Dissertation

Functional Heteroleptic Coordination Cages Based on a Modular Approach

submitted by

André Platzek

Prepared at the

Department of Chemistry and Chemical Biology

TU Dortmund University

Dortmund 2024

The experimental work has been prepared from December 2018 to December 2022 at the Department of Chemistry and Chemical Biology at TU Dortmund University under supervision of Prof. Dr. Guido H. Clever.

Examiner: **Prof. Dr. Guido H. Clever**

Department of Chemistry and Chemical Biology,
TU Dortmund University,
Otto-Hahn-Straße 6, 44227 Dortmund

Coexaminer: **Prof. Dr. Wolf-G. Hiller**

Department of Chemistry and Chemical Biology,
TU Dortmund University,
Otto-Hahn-Straße 6, 44227 Dortmund

Submission Date: 26.02.2024

Grau is im Leben alle Theorie − aber entscheidend is auf'm Platz.

Adi Preißler

Für meine lieben Mensafreunde

Jonathan, Lars, Marvin & Stefan

Eidesstattliche Versicherung (Affidavit)

Name, Vorname
(Surname, first name)

Matrikel-Nr.
(Enrolment number)

Belehrung:

Wer vorsätzlich gegen eine die Täuschung über Prüfungsleistungen betreffende Regelung einer Hochschulprüfungsordnung verstößt, handelt ordnungswidrig. Die Ordnungswidrigkeit kann mit einer Geldbuße von bis zu 50.000,00 € geahndet werden. Zuständige Verwaltungsbehörde für die Verfolgung und Ahndung von Ordnungswidrigkeiten ist der Kanzler/die Kanzlerin der Technischen Universität Dortmund. Im Falle eines mehrfachen oder sonstigen schwerwiegenden Täuschungsversuches kann der Prüfling zudem exmatrikuliert werden, § 63 Abs. 5 Hochschulgesetz NRW.

Die Abgabe einer falschen Versicherung an Eides statt ist strafbar.

Wer vorsätzlich eine falsche Versicherung an Eides statt abgibt, kann mit einer Freiheitsstrafe bis zu drei Jahren oder mit Geldstrafe bestraft werden, § 156 StGB. Die fahrlässige Abgabe einer falschen Versicherung an Eides statt kann mit einer Freiheitsstrafe bis zu einem Jahr oder Geldstrafe bestraft werden, § 161 StGB.

Die oben stehende Belehrung habe ich zur Kenntnis genommen:

Official notification:

Any person who intentionally breaches any regulation of university examination regulations relating to deception in examination performance is acting improperly. This offence can be punished with a fine of up to EUR 50,000.00. The competent administrative authority for the pursuit and prosecution of offences of this type is the chancellor of the TU Dortmund University. In the case of multiple or other serious attempts at deception, the candidate can also be unenrolled, Section 63, paragraph 5 of the Universities Act of North Rhine-Westphalia.

The submission of a false affidavit is punishable.

Any person who intentionally submits a false affidavit can be punished with a prison sentence of up to three years or a fine, Section 156 of the Criminal Code. The negligent submission of a false affidavit can be punished with a prison sentence of up to one year or a fine, Section 161 of the Criminal Code.

I have taken note of the above official notification.

Ort, Datum
(Place, date)

Unterschrift
(Signature)

Titel der Dissertation:
(Title of the thesis):

Ich versichere hiermit an Eides statt, dass ich die vorliegende Dissertation mit dem Titel selbstständig und ohne unzulässige fremde Hilfe angefertigt habe. Ich habe keine anderen als die angegebenen Quellen und Hilfs- mittel benutzt sowie wörtliche und sinngemäße Zitate kenntlich gemacht.
Die Arbeit hat in gegenwärtiger oder in einer anderen Fassung weder der TU Dortmund noch einer anderen Hochschule im Zusammenhang mit einer staatlichen oder akademischen Prüfung vorgelegen.

I hereby swear that I have completed the present dissertation independently and without inadmissible external support. I have not used any sources or tools other than those indicated and have identified literal and analogous quotations.

The thesis in its current version or another version has not been presented to the TU Dortmund University or another university in connection with a state or academic examination.*

*Please be aware that solely the German version of the affidavit ("Eidesstattliche Versicherung") for the PhD thesis is the official and legally binding version.

Ort, Datum
(Place, date)

Unterschrift
(Signature)

Abstract

This work describes the rational design of a family of endohedrally functionalized heteroleptic coordination cages of the type $Pd_2\mathbf{A}_2\mathbf{B}_2$. These were assembled out of a modular toolbox of banana shaped ligands **A** based on carbazole and shape complementary ligands **B** with different aromatic backbones and lengths. The obtained structures were characterized by NMR spectroscopy and ESI mass spectrometry as well as for some examples with X-ray diffraction in the solid state. With installing different functional groups to the free secondary amine at the carbazole moiety, namely amides and methyl substituents a variety of coordination cages with unique properties inside the cavities were formed. The coordination cages were investigated in their ability to bind hydrogen bond acceptors. For this, alkyl- and aryl phosphate ester salts were used as guest molecules. Binding constants were obtained via ^{1}H NMR titration experiments and it was shown that the binding event was mainly driven by the formation of hydrogen bonds. Here, the modular system was used to group the heteroleptic coordination cages and the different phosphate guests in regard of their binding strengths. By blocking the hydrogen bond donor site, the binding constants dropped significantly, however binding was still observed, due to ionic interactions as well as π–π stacking with the aromatic backbones of ligands **B** with the aromatic phosphate ester salts. This was also supported by MD simulations as well as ion-mobility mass spectrometry. Using the latter, inside-binding of the guest was proven since the obtained molecular structures of a few host-guest complexes showed that the guest was located outside the cavity in the solid state.

Another goal of this work was the NMR spectroscopic investigation of coordination assemblies. With the help of tailor-made NMR experiments new cage compounds were characterized. The main focus was laid on DOSY NMR experiments. With this technique, the size of interpenetrated cage dimers was determined, and it was proposed to calculate unique shape factors for the normally non-spherical cage compounds. Furthermore, the effect of different exohedral side chains attached to the ligand backbones on the spatial extend of the so-called double cages was investigated. It was shown that these alkyl substituents fold back to the ligand backbones and, most likely, exhibit non-polar interactions in solution. Additionally, the DOSY experiment itself was illuminated in a

more detailed way, since the effect of convection inside an NMR tube has a huge effect on the diffusion measurement and could lead to wrong radii of the analytes.

Zusammenfassung

Diese Arbeit beschreibt den rationalen Entwurf einer Familie von endohedral funktionalisierten heteroleptischen Koordinationskäfigen des Typs $Pd_2\mathbf{A}_2\mathbf{B}_2$. Diese wurden aus einer modularen Bibliothek von bananenförmigen Liganden **A**, basierend auf Carbazol und dazu formkomplementären Liganden **B** mit verschiedenen aromatischen Rückgraten und Längen zusammengesetzt. Die erhaltenen Strukturen wurden mittels NMR-Spektroskopie und ESI-Massenspektrometrie charakterisiert sowie für einige Beispiele mittels Einkristallröntgenstrukturanalyse im Festkörper. Indem verschiedene funktionelle Gruppen wie Amide oder Methylsubstituenten am freien sekundären Amin der Carbazoleinheit installiert wurden, entstanden eine Vielfalt von Koordinationskäfigen mit einzigartigen Eigenschaften innerhalb deren Kavitäten. Die Koordinationskäfige wurden in ihrer Fähigkeit hin untersucht, Wasserstoffbrückenakzeptoren zu binden. Dazu wurden Alkyl- und Arylphosphatestersalze als Gastmoleküle genutzt. Mittels ^{1}H-NMR-Titrationsexperimenten wurden Bindungskonstanten bestimmt und es wurde gezeigt, dass die Bildung von Wasserstoffbrückenbindungen hauptsächlich zu den Bindungsereignissen geführt hat. Die Modularität des Systems wurde dazu genutzt, die heteroleptischen Koordinationskäfige entsprechend ihrer Fähigkeit die verschiedenen Phosphatester zu binden in Gruppen einzuteilen. Durch die Blockierung der Wasserstoffbrückendonorstelle sank die Bindungskonstante signifikant ab, jedoch fand trotzdem eine Bindung statt, was an ionischen Interaktionen sowie der Bildung von π–π Wechselwirkungen zwischen den aromatischen Phosphatestern mit den Rückgraten der Liganden **B** lag. Diese Beobachtungen wurden sowohl durch MD-Simulationen als auch durch Ionenmobilitätsmassenspektrometrie bestätigt. Mit letztgenannter Methode wurde auch die Bindung des Gastes innerhalb der Kavität bewiesen, nachdem bei Einkristallröntgenstrukturanalysen von einigen Wirt-Gast-Komplexen sich der Gast im Festkörper außerhalb der Kavität befand.

Ein weiteres Ziel dieser Arbeit war die NMR-spektroskopische Untersuchung von Koordinationsverbindungen. Mit Hilfe maßgeschneiderter NMR-Experimente wurden

neuartige Käfigverbindungen charakterisiert. Der Schwerpunkt lag hierbei auf DOSY NMR-Experimenten. Mit dieser Methode wurden die Größen von interpenetrierten Käfigdimeren bestimmt und es wurde geplant einzigartige Formfaktoren für die, im Normalfall nicht kugelförmigen Käfigverbindungen zu berechnen. Darüber hinaus wurde der Effekt von verschiedenen exohedralen Seitenketten, die an das Ligandenrückgrat angebracht wurden, in Hinblick auf die räumliche Ausdehnung der sog. Doppelkäfige untersucht. Hierbei wurde gezeigt, dass die Alkylsubstituenten zum Ligandenrückgrat falten und dort, höchstwahrscheinlich, nicht-polare Wechselwirkungen mit diesen in Lösung eingehen. Zusätzlich wurde das DOSY-Experiment selbst detailliert beleuchtet, da der Effekt der Konvektion in einem NMR-Röhrchen die Diffusionsmessung massiv beeinflussen und zu falsch berechneten Radien der Analyten führen kann.

Content

1 Introduction

1.1 Supramolecular Coordination Cages

Supramolecular chemistry is widely regarded as a subfield in chemistry, that deals with non-covalent interactions like hydrogen bonds, VAN DER WAALS or electrostatic interactions as well as coordination bonding. While the initial concept is commonly found in nature, for example in the formation of the three-dimensional structures of proteins and DNA, chemists have been using this concept in the last decades to mimic these structures and make use of the given functionalities to access complex synthetic supramolecules.[1] Pioneering work on synthetic host molecules has been done by LEHN (cryptands), PEDERSEN (crown ethers) and CRAM (spherands) who described cation receptors selectively binding Na^+ and K^+.[2–8] While these studies where based on single molecule hosts with a certain repetitive unit, the use of coordination bonding came into focus in the last decades highlighted by e.g. FUJITA.[9–17] The host molecule is no longer one fully covalent structure, but a self-assembled architecture consisting of different smaller subunits. This strategy saves time and resources by using very simple, yet diverse building blocks. By choosing the correct ligand and suitable metal ions numerous different structures such as links, knots, spheres, grids, helicates, boxes, rings, polyhedrons and cages has evolved in a very controlled way.[16,18–36] Both, ligand geometry and metal coordination environment contribute to the structure of the final assembly. Metal coordination chemistry ranges from linear coordinated metal ions like Ag(I) or Au(I), octahedral coordinated Fe(II) or Ni(II), tetrahedral coordination as found in Zn(II) complexes to square planar coordination in Pd(II) and Pt(II) assemblies.[18,37–40]

From the vast variety of metallo-supramolecular structures utilizing the diverse array of coordination geometries, self-assembled coordination cages with a defined cavity were studied extensively in the last decades.[41–43] In our group we are using naked, square-planar Pd(II) cations and concave or so-called banana-shaped ligands to build up very predictable homoleptic lantern-shaped coordination cages of the type $Pd_2\mathbf{L}_4$ that are able to bind small guest molecules (Figure 1.1).[44]

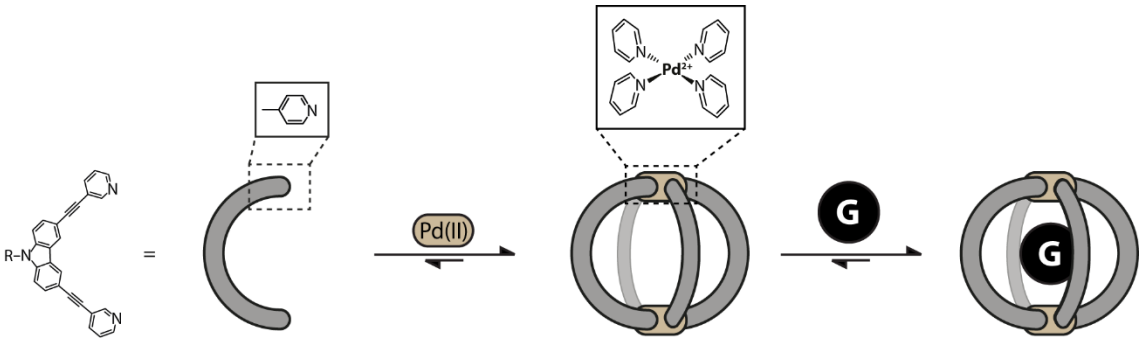

Figure 1.1: Example of a metal-mediated, self-assembled coordination cage with a concave carbazole-based ligand **L** and square planar palladium(II) cations and guest uptake inside the cavity.

These structures feature a confined cavity that is accessible for guest molecules like small anions (e.g. BF_4^- or Cl^-), or, with the right ligand design, even larger guests like fullerenes.[45–49] Figure 1.1 shows a concave ligand with a carbazole backbone, alkinyl linkers and pyridyl donor groups serving as the organic part and naked Pd(II) cations as the inorganic component. The self-assembly is carried out in organic solvents such as DMSO or acetonitrile and is nearly quantitative. The cavities of coordination cages are of special interest in regard to the investigation of guest encapsulation, recognition and sensing applications.[50]

While chemists are spoilt for choice regarding the ligands backbone which yielded a diverse array of different cages there are two ways to further increase complexity in Pd(II) coordination compounds. The first one is using ligands with reduced symmetry as shown by LEWIS and CROWLEY.[51,52] The second option to access more complex structures is using multiple types of ligands in one cage to form a heteroleptic coordination cage as it is shown in Figure 1.2.

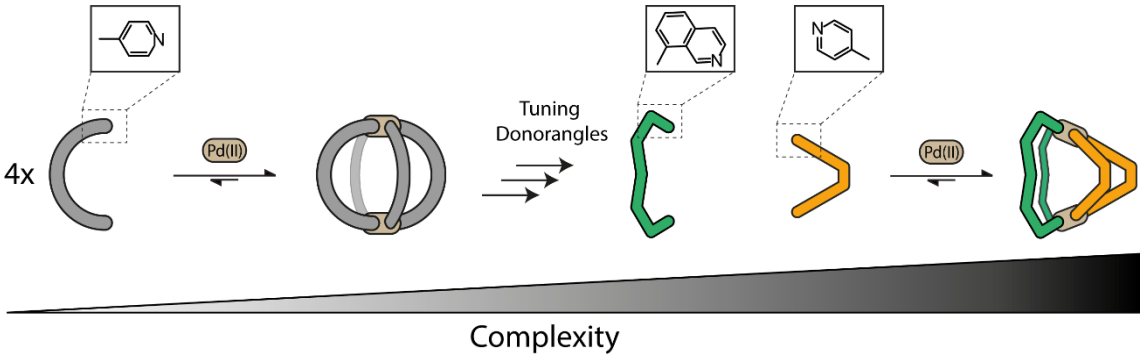

Figure 1.2: Increasing the complexity: From homoleptic $Pd_2\mathbf{L}_4$ coordination cages to heteroleptic structures.

1.1.1 Heteroleptic $Pd_2A_2B_2$ Coordination Cages

To access architectures that are structurally more diverse than highly symmetric lantern shaped $Pd_2\mathbf{L}_4$ cages, two different types of ligands could be used for the self-assembly. However, if we were to use two different colored LEGO™ bricks there are three different outcomes if we combine them in a 1:1 manner and stack them in pairs of four (Figure 1.3).

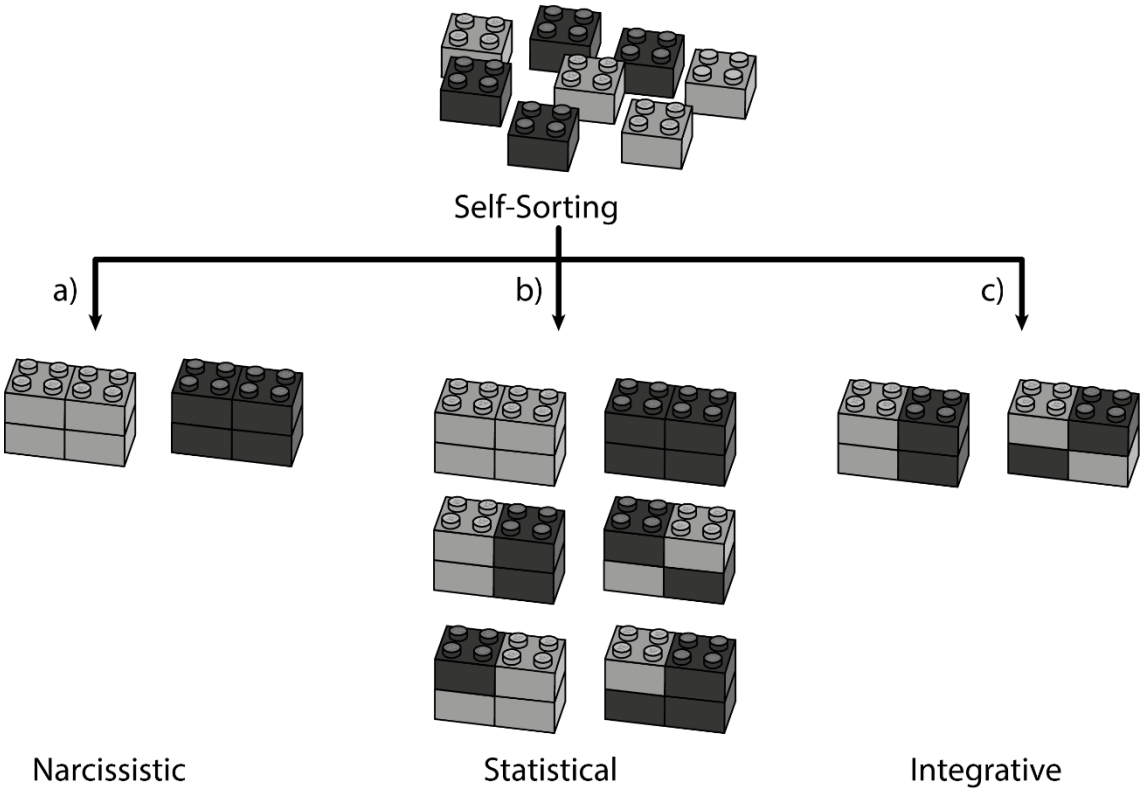

Figure 1.3: Illustration of the three different types of self-sorting when mixing two types of ligands (depicted as bricks): a) narcissistic, b) statistical and c) integrative behavior.

The same goes for ligands in the aforementioned ratio if they were combined with Pd(II) cations. First, the corresponding homoleptic species form exclusively, this is called narcissistic self-sorting (Figure 1.3a). A second, non-desired outcome is shown in Figure 1.3b) and is called statistical self-sorting. Here, a mixture of all possible species forms in a completely statistical fashion. By rational design of the ligands the third outcome, integrative self-sorting (Figure 1.3c), occurs and the desired heteroleptic structures with 1:1 ligand ratio form exclusively. It is noted however, that a $Pd_2\mathbf{A}_2\mathbf{B}_2$ system can yield either *cis* or *trans* isomer depending on the used ligands.

To still get a controlled, non-statistical heteroleptic cage formation, multiple strategies were shown in the past.[53,54] These however require a more sophisticated ligand design.

Continuing the LEGO™ analogy, we have to move on from using simple 2x2-bricks to more complex brick structures as depicted in Figure 1.4.

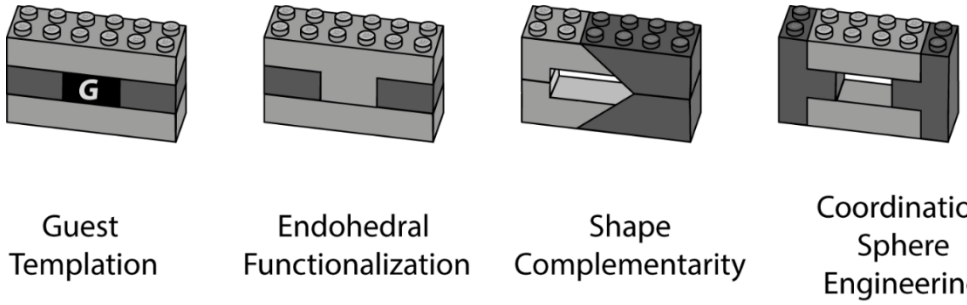

Figure 1.4: Illustration of different strategies to form heteroleptic coordination cages.

With guest templation a central brick is needed to form the final structure, occupying the central space. The same happens with endohedral functionalization, which uses a special space demanding brick, whose special form enables the formation of a heteroleptic structure but blocks the central space while doing so. Another strategy would be coordination sphere engineering (CSE) using bricks that connect in defined way, with steric bulk around the connection area preventing the formation of homoleptic assemblies. The last strategy is shape complementarity which uses bricks with a certain shape that fit exactly to their counterpart. Switching from LEGO™ to chemistry now, Figure 1.5 shows examples for the aforementioned strategies.

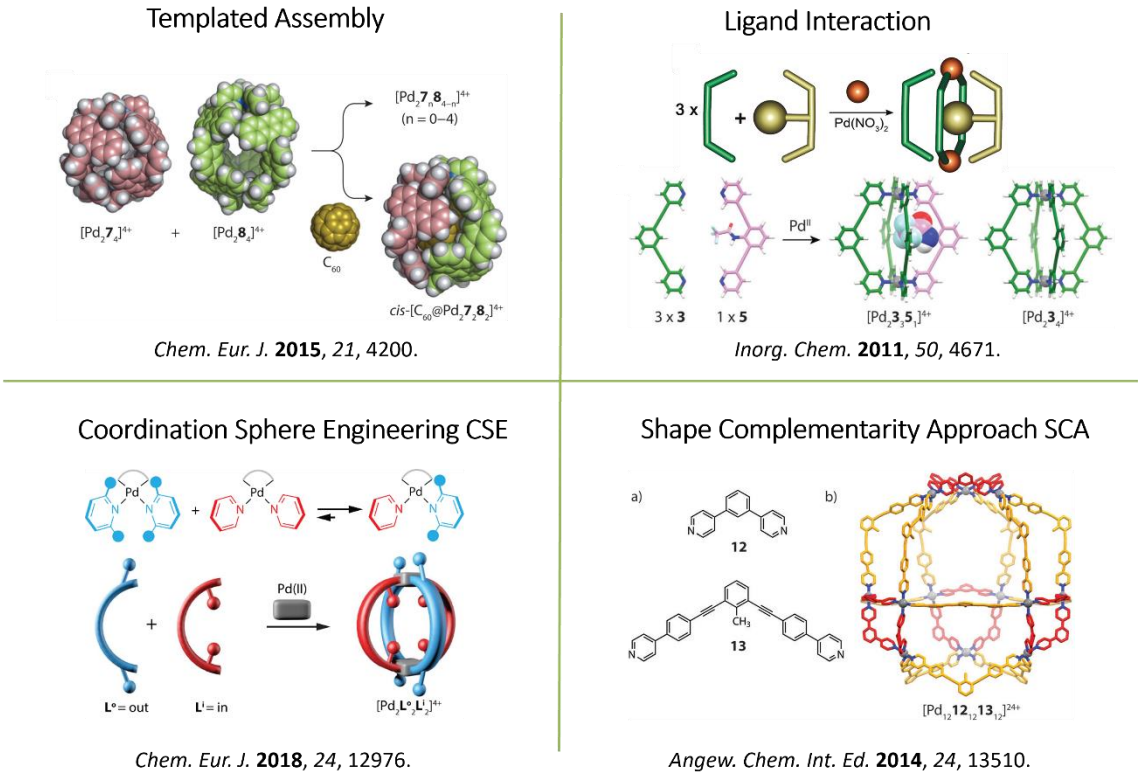

Figure 1.5: Strategies to form heteroleptic coordination cages. Figures used with permission from[10,55–57].

In the early 2000s FUJITA showed that the formation of homo- and heteroleptic cages based on *cis*-protected palladium and tritopic ligands is depending on the templating guest molecule added to the self-assembly process.[58] Moreover, the group of YOSHIZAWA used a fullerene C_{60} molecule to template the formation of a heteroleptic $Pd_2\mathbf{A}_2\mathbf{B}_2$ coordination cage out of a mixture of the two corresponding previously formed homoleptic structures.[55] However, in the case of guest templation the cavity of the coordination cage is no longer accessible for other guests, since the cage often breaks apart and the ligands would reassemble to the homoleptic coordination cages if the template is removed. Another strategy to form heteroleptic coordination cages was shown by the group of HOOLEY.[56] They used different endohedral functionalized ligands to use their steric effects in the controlled formation of $Pd_2\mathbf{AB}_3$ assemblies. However, the cavity is already occupied by the steric bulk and therefore only accessible for very much smaller guest molecules.

Strategies that will not directly involve the cavities of the heteroleptic cage structures are the CSE (Coordination Sphere Engineering) and the SCA (Shape-Complementary Assembly) approach that have been studied by our group, among others, extensively in the last years.[54] Installing steric bulk around the coordination environment of the ligands leads to strain in the homoleptic assemblies or them not forming at all anymore, thus self-assembly to the corresponding heteroleptic coordination cages is favored. Our group demonstrated this approach with a series of heteroleptic $Pd_2\mathbf{A}_2\mathbf{B}_2$ coordination cages based on concave picolyl ligands as well as bowl-type $Pd_2\mathbf{A}_3$ with one vacant coordination site occupied by a solvent molecule at the Pd-center and ring-type $Pd_2\mathbf{A}_2$ structures, based on ligands with naphthyridine or acridine donor sites.[47,57] In 2016 the group of CROWLEY showed the clean formation of heteroleptic *cis*-$Pd_2\mathbf{A}_2\mathbf{B}_2$ coordination cages by installing NH_2 groups next to the coordination sphere to interact via hydrogen bonds with the counter ligand.[59]

The SCA approach uses ligands that are geometrically matching to each other in respect to their binding vectors to form a distinct species and avoiding statistical mixtures. Often homoleptic assemblies of these ligands are disfavored due to a certain strain. In 2014 the group of FUJITA reported a large heteroleptic $Pd_{12}\mathbf{A}_{12}\mathbf{B}_{12}$ coordination polyhedron based on banana-shaped ligands of different sizes.[10] In 2021 the group of SEVERIN reported the formation of heteroleptic $Pd_6\mathbf{A}_6\mathbf{B}_6$ barrel-shaped cages based on either simple bis-pyridyl ligands but also with bulky, iron-containing clathrochelate ligands.[60] The first example

of heteroleptic coordination cages by using the SCA in our group was published by BLOCH in 2016. Here, a set of three banana-shaped ligands based on phenanthrene, acridone and carbazole that are geometrically matching to each other were used to form either *cis*- or *trans*-$Pd_2\mathbf{A}_2\mathbf{B}_2$ assemblies. All of these coordination cages were also formed when the corresponding homoleptic assemblies were mixed in a 1:1 manner.[36,53,61] Extending this system with a larger array of banana-shaped ligands, EBBERT could show the formation of a mixture of ten different heteroleptic coordination cages of the type $Pd_2\mathbf{A}_2\mathbf{B}_2$ but also $Pd_2\mathbf{A}_2\mathbf{BC}$ and even $Pd_2\mathbf{ABCD}$, with two sets of ligands of which two each were shape complementary, limiting the number of possible outcomes to ten, including one *cis*/*trans* isomer. Interestingly, all of these structures could be identified by using ion-mobility mass spectrometry.[62] Besides using the beforehand mentioned strategies, TESSAROLO reported a series of tetrahedral and octahedral coordination cages that were able to form heteroleptic structures using the effect of steric hindrance at the ligand backbones.[30]

1.1.2 Functional Coordination Cages

In the past the focus moved from accessing fancy new structures to obtain functional coordination cages. Our group reported a series of different functions in assemblies like light-switchable cages that alter their cavity size upon irradiation,[63,64] interpenetrated double cages that were able to bind neutral guests after a chemical trigger and generating singlet oxygen for a cycloaddition reaction of cyclopentadiene,[65–68] chromophore-based cages that interact with chiral molecules,[69] donor-acceptor systems for light-powered charge separation[70] as well as heteroleptic coordination cages that bind guest molecules selectively based on their shape[36] and exohedral functionalized ones that act as amphiphiles that were able to form vesicles enabling the use of coordination cages in material science.[71]

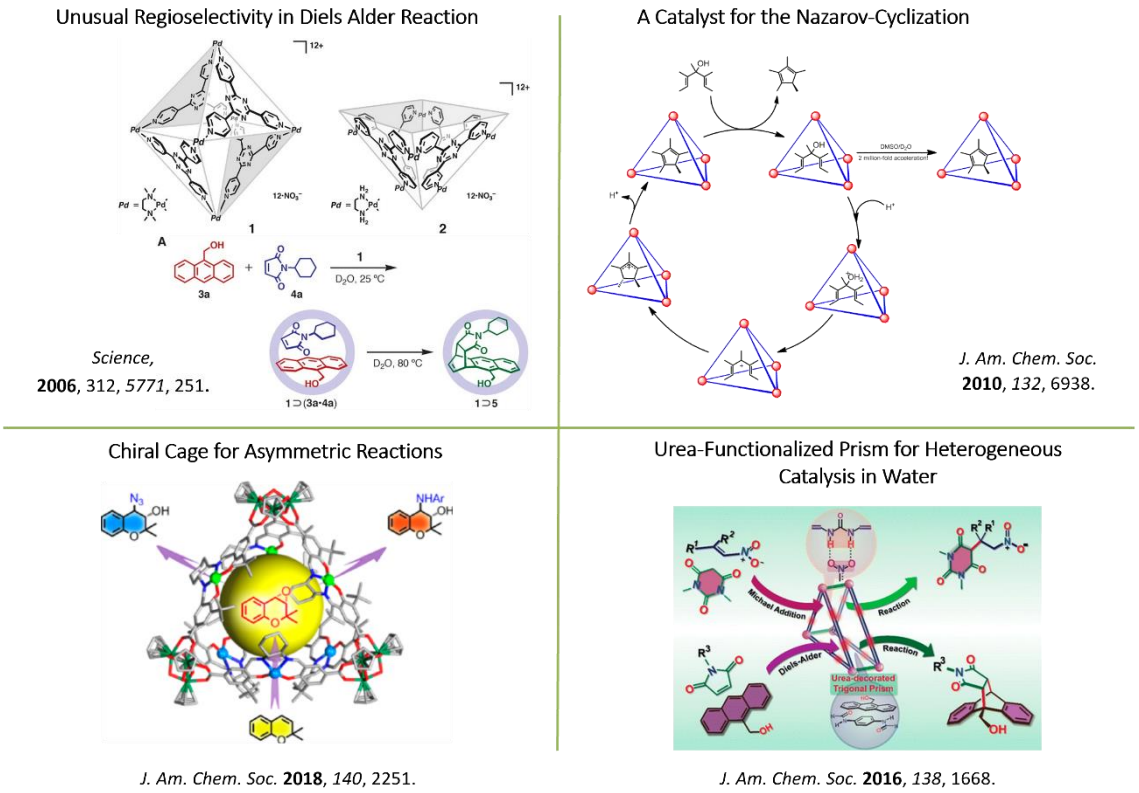

Figure 1.6: Overview on functional coordination cages. Figures used with permission from[72,74–76].

Especially the potential to perform chemical reactions inside coordination cages, thus using them as nano-reaction chambers, have been in the interest of plenty of groups. In 2006 the group of FUJITA presented an octahedral $Pd_6\mathbf{L}_4$ cage that promotes the DIELS-ALDER reaction of anthracene derivatives with *N*-cyclohexyl phthalimide at the normally unfavored 1,4-position. Without the coordination cage the reaction took place at the central ring of the anthracene system.[72] RAYMOND and BERGMAN reported a series of tetrahedral Ga(III) based coordination cages that were used for the binding of neutral guests.[73] One of these anionic $Ga_4\mathbf{L}_6$ cage acts as catalyst for the NAZAROV cyclization of pentadienoles.[74] In 2018 CUI and co-workers reported chiral coordination cages based on M(salen) complexes (M = Cr, Mn, Fe) that act as catalysts for asymmetric epoxidation/ring-opening tandem reactions where *ee*-values up to 93% were obtained.[75] The use of hydrogen bonds to bind guests and substrates in coordination assemblies has been reported in recent years.[77,78] The group of MUKHERJEE used a molecular prism equipped with urea-based hydrogen bond donors to preorganize substrates that then could perform MICHAEL additions and DIELS-ALDER reactions in water effectively enabling catalysis inside a coordination cage.[76]

1.2 Nuclear Magnetic Resonance Spectroscopy

Spectroscopy is, most generally speaking, the detection of the interaction between any matter with electromagnetic radiation. To analyze supramolecular coordination cages numerous of spectroscopic and spectrometric methods have been established.[79] As outstanding methods especially mass spectrometry, X-ray structure analysis and nuclear magnetic resonance (NMR) spectroscopy have been and are used in this field of chemistry. Since the first two methods indeed have their benefits, the latter is the most powerful one as it analyzes the molecules of interest in solution state and is not an invasive method. However, NMR spectroscopy is a comparable slow analytical method.

NMR spectroscopy[80,81] is based on the interactions of nuclei with radio wave frequencies in a strong magnetic field. Only nuclei that have a spin $I > 0$ (e.g. ^{1}H, ^{2}H, ^{6}Li, ^{11}B, ^{13}C, ^{15}N, ^{19}F, ^{29}Si, ^{31}P, ^{119}Sn, ^{195}Pt) can be detected with radio waves because they have a magnetic moment μ and an angular momentum P in the direction of the spin axis.

$$P = \sqrt{I(I+1)}\hbar \tag{1.1}$$

with reduced PLANCK constant $\hbar$. P and μ are related through the gyromagnetic ratio γ that is characteristic for each nucleus:

$$\mu = \gamma \cdot P \tag{1.2}$$

$$\Rightarrow \mu = \gamma\sqrt{I(I+1)}\hbar \tag{1.3}$$

Nuclei having a large γ are more sensitive and nuclei with a small γ are less sensitive to an NMR experiment.

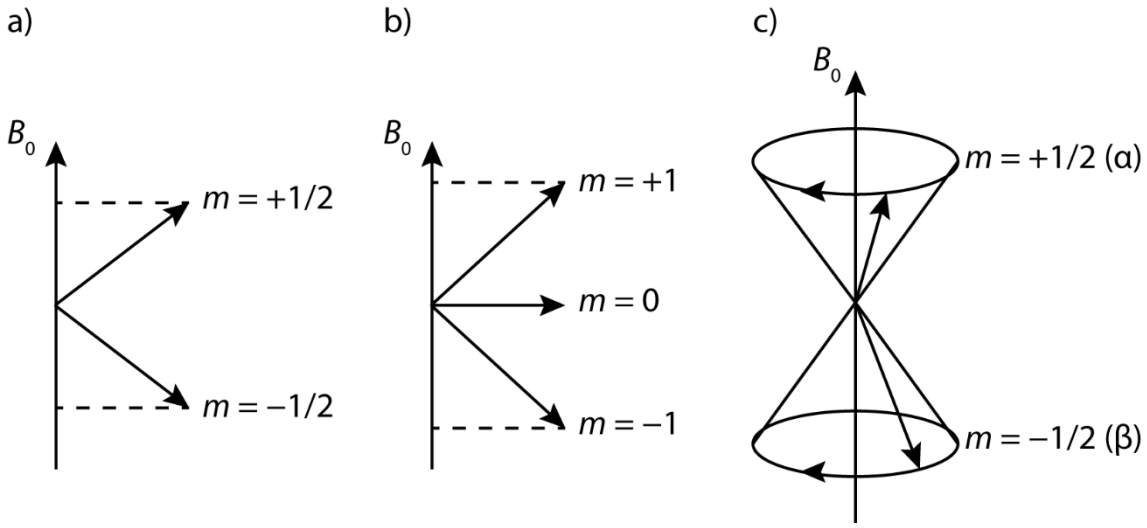

Figure 1.7: Quantization of direction of *P* in a magnetic field B_0 for a) a nucleus with $I = ½$ and b) a nucleus with $I = 1$ and c) double precession cone for a nucleus with $I = ½$.

Figure 1.7a describes the orientation of *P* in a magnetic field B_0 for a nucleus that has a spin of $I = ½$ (e.g. ^{1}H) that can have two magnetic quantum states $m = +½$ or $m = -½$. If a nucleus has a spin of $I = 1$, *m* can attain three values (+1, 0, −1, Figure 1.7b). These spins precess around the direction of the magnetic field (z-axis in a cartesian coordinate system) with a particular frequency that is unique for every nucleus and proportional to B_0, the so-called LARMOR frequency ν_L (Figure 1.7c). This is described by the resonance condition:

$$\nu_L = \left|\frac{\gamma}{2\pi}\right| B_0 \tag{1.4}$$

Without an external magnetic field, the quantum states *m* are degenerated but applying a magnetic field leads to energy differences what is called ZEEMAN effect and shown in Figure 1.8. Furthermore, the energy differences are proportional to B_0.

$$E = -m \cdot \gamma \cdot \hbar \cdot B_0 \tag{1.5}$$

$$\Rightarrow \Delta E = \gamma \cdot \hbar \cdot B_0 \tag{1.6}$$

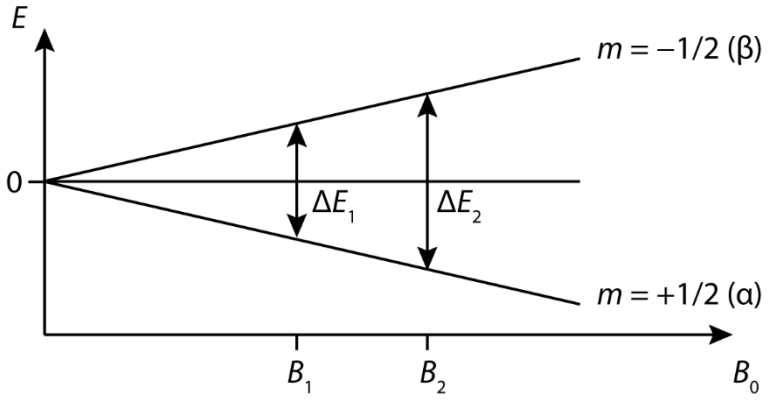

Figure 1.8: Energy differences of two states α and β depending on the magnetic field.

The problem here is that these differences are really small, normally around thousandth of per mil, due to BOLTZMANN statistic:

$$\frac{N_\beta}{N_\alpha} = \exp\left(\frac{-\Delta E}{k_B \cdot T}\right) \approx 1 - \frac{\gamma \cdot \hbar \cdot B_0}{k_B \cdot T} \tag{1.7}$$

with N_α the number of nuclei in the energetically lower state, N_β the number of nucleus in the energetically higher state, temperature T and BOLTZMANN constant k_B. That implies that the intensity of an NMR signal gets higher with a stronger magnetic field:

$$\frac{S}{N} \propto B_0^{3/2} \tag{1.8}$$

with the signal to noise ratio S/N. To obtain a spectrum, one can vary the magnetic field B_0 and keep the frequency ν_1 constant or the other way around. This is called continuous wave (CW) method and was used until the early 70s and was replaced by the pulse fourier transform (PFT) method that is until now the state of the art in NMR spectroscopy. All spins of the nucleus of interest are irradiated at the same time with the PFT method. By using the correct pulse length, the magnetization of the excited spins will be brought perpendicular to the B_0 field followed by an oscillation back to the transversal plane. This is displayed by a free induction decay (FID) and can be transformed to a usual NMR spectrum by applying the FOURIER transform.

The described relaxation process after the irradiation of a spin system after an applied pulse is called longitudinal or spin-lattice relaxation time T_1. It is absolutely important to know the relaxation time T_1 of the investigated spin system, since this defines the delay between two pulses. The obtained signal intensity would decrease if not all spins are relaxed back to their initial state and a pulse is already applied. This delay should not be

shorter than $5 \cdot T_1$. A second relaxation process that can be observed is the transversal or spin-spin relaxation time T_2 that is normally shorter than T_1. T_2 defines the spectral resolution in an NMR experiment since this is proportional to T_2^{-1}. It also means that the line broadening gets larger if T_2 is short. As it was mentioned before, the PFT method is repeated after the delay defined by T_1 to accumulate the FID. That is because the signal intensity gets larger with a higher number of scans (NS):

$$\frac{S}{N} \propto \sqrt{\mathrm{NS}} \tag{1.9}$$

The obtained resonances of the spins in a molecule are dependent by each other. This effect is called shielding and can be described by equation 1.10:

$$B_{\mathrm{eff}} = (1 - \sigma) B_0 \tag{1.10}$$

with the effective magnetic field B_{eff} and the shielding constant σ. σ is only dependent by the electronic and magnetic environment of a spin in a molecule but not by B_0. Combining equation 1.10 with the resonance condition leads to:

$$\upsilon_1 = \left|\frac{\gamma}{2\pi}\right| (1 - \sigma) B_0 \tag{1.11}$$

with the resonance frequency υ_1. From this it follows that nuclei that are chemically inequivalent will resonate at different frequencies because of their unique shielding. To make spectra that were recorded at different magnetic fields comparable the nondimensional chemical shift δ (given in parts per million, ppm) to a standard (tetramethylsilane, TMS with δ = 0 ppm) was introduced:

$$\delta = \frac{\upsilon_1 - \upsilon_{\mathrm{ref}}}{\upsilon_{\mathrm{ref}}} \tag{1.12}$$

with the measured frequency υ_1 and the reference frequency υ_{ref}.

However, not every spin resonates as a singlet. Normally, a fine splitting structure is observed. This is due to the interactions of neighbouring magnetic dipoles that lead to an indirect coupling to other spins in the investigated system. Depending on the quantity and the spin of the so-called *J*-coupling nuclei the signal splits with the following multiplicity:

$$M = 2 \cdot N \cdot I + 1 \tag{1.13}$$

with multiplicity *M*, number of coupling nuclei *N* and spin *I*.

Beside the observed splitting, *J*-coupling can also be visualized by two-dimensional NMR experiments, e.g. by correlation spectroscopy (COSY). Here, two frequency axes of the same nucleus are measured and crosspeaks appears for coupling signals. However, coupling over bonds is not the only observable with 2D NMR experiments. For example, contacts through space can be measured by nuclear overhauser enhancement spectroscopy (NOESY). To measure the NOE, the nuclear spin polarization will be transferred from one nucleus to another. This will be visualized by the change of the intensity of one signal that happens if another one gets saturated by the irradiation with a frequency pulse. In particular for large, three-dimensional chemical structures (e.g. coordination cages) the NOESY experiment is indispensable for the structural assignment. With equation 1.14 the distance between two spins can be calculated if a NOE contact can be measured:

$$I_{\mathrm{NOE}} \propto \frac{1}{r^6} \tag{1.14}$$

With the intensity of the NOE crosspeak I_{NOE} and the distance between the dipolar-coupled nuclei *r*.

1.2.1 DOSY and Diffusion

Another powerful NMR experiment to characterize in particular supramolecular structures is diffusion ordered spectroscopy (DOSY) NMR.[82] This is because one could obtain information about the size, the shape or the aggregation state of compounds with this method (e.g. two-dimensional ring vs. three-dimensional cage or monomeric vs. dimeric species) as well as providing reliable information about association constants (e.g. inside or outside binding of a guest, slow or fast exchange). The first example where DOSY NMR was used in supramolecular chemistry was shown by COHEN and MAYZEL who determined association constants ammonium salts in crown ethers.[83] In this pseudo-2D NMR experiment the frequency will be measured against the diffusion coefficient of the substance.[81] This technique is mainly used for the analysis of mixtures, since every NMR resonance could be assigned to a diffusion coefficient und if this is the same, the signals belong to the same substance. By using the STOKES-EINSTEIN-equation 1.15 the hydrodynamic radius of a substance can be calculated:[84]

$$r_{\mathrm{H}} = \frac{k_{\mathrm{B}} \cdot T}{6 \cdot \pi \cdot \eta \cdot D} \tag{1.15}$$

with the hydrodynamic radius r_{H}, BOLTZMANN constant k_{B}, temperature T, viscosity of the analyte η[85] and diffusion coefficient D. In diluted systems the viscosity of the analyte is assumed to be the same as the solvent. However, equation 1.15 is only valid for spherical molecules. To also calculate the radius of molecules with different shapes, a shape factor f has to be introduced to the equation:

$$r_{\mathrm{H}} = \frac{k_{\mathrm{B}} \cdot T \cdot f}{6 \cdot \pi \cdot \eta \cdot D} \tag{1.16}$$

For the most common shapes like stick, prolate or plate values for f can be found in the literature.[86–89] Often supramolecular structures could not be described by these common shapes in an adequate way. This problem will be described in a more detailed way in chapter 3.5.2.

(Self-)Diffusion is a natural physical process which describes the movement of particles (e.g. atoms or molecules) in a medium or solvent without external actions. This leads to a consistent distribution of the particles and an enhancement of the entropy of the system.[90] Besides other physical methods, diffusion can be detected by NMR by using pulsed-field-gradients (PFG).[91] The first approach to measure DOSY NMR was done by a HAHN-Spin-Echo experiment.[92] In the last decades numerous pulse sequences for diffusion measurements were published.[93–96] PFGs create an inhomogeneous magnetic field for a short time (~ms) and are normally applied in the direction of the B_0 field. By applying the gradient, the position of a nuclear spin can be followed in the sample tube during the diffusion time. This is illustrated in Figure 1.9.

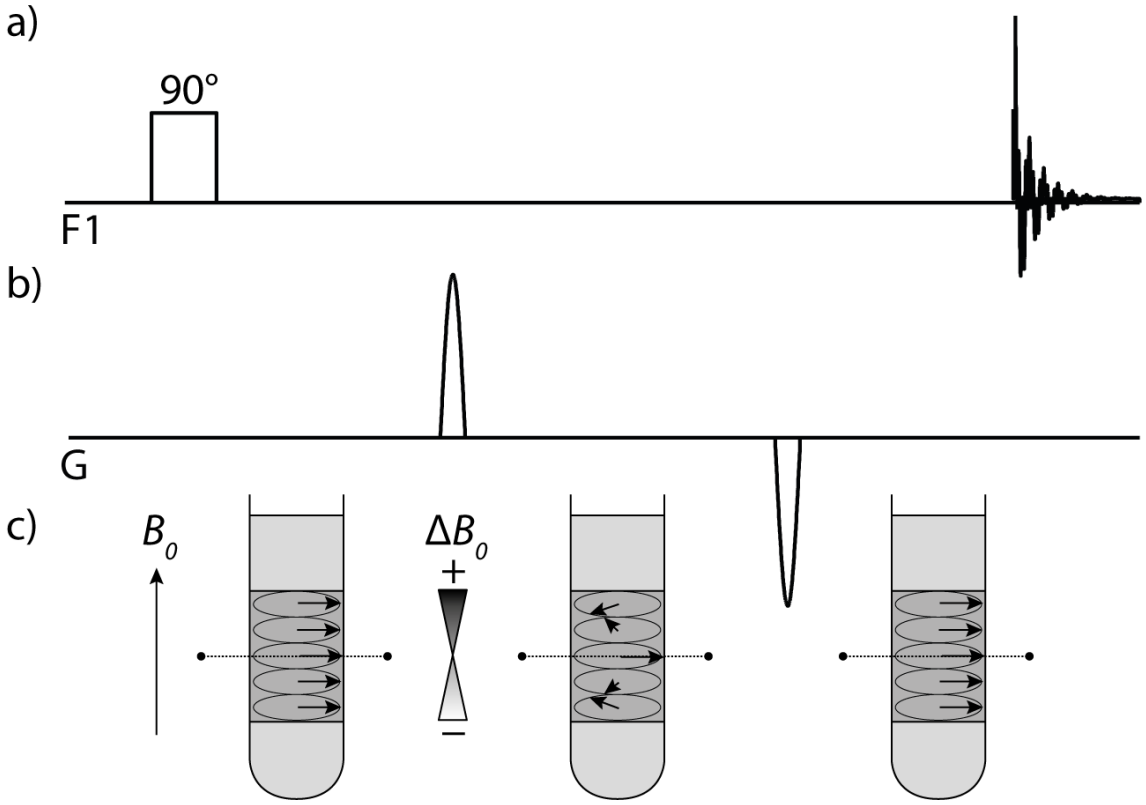

Figure 1.9: a) Frequency channel F1 with 90° pulse and FID, b) gradient channel G with encoding and decoding gradients and c) illustration of an ensemble of spins in an NMR tube with the volume that is irradiated in dark grey and their behavior after the applied 90° pulse (left), the encoding gradient (middle) and the decoding gradient (right). Figure reproduced from[81].

The change on the signal intensity depending on the gradient parameters (length and power) is described by the STEJSKAL-TANNER-equation:

$$I = I_0 \cdot \exp\left(-\gamma^2 \cdot g^2 \cdot \delta^2 \cdot D\left(\Delta - \frac{\delta}{3}\right)\right) \tag{1.17}$$

with the observed signal intensity I, the reference signal intensity I_0, the gyromagnetic ratio γ, the gradient power g, the gradient length δ, diffusion coefficient D and the diffusion time Δ. From this equation it follows that nuclei with a larger gyromagnetic ratio are more sensitive for the measurement of diffusion than nuclei with a small γ. The maximum gradient power g is given by the spectrometer hardware. The parameters δ and Δ have to be tuned for every measurement since their values are depending on the sample (solvent and size of the molecule). To avoid homonuclear J-coupling during the diffusion time, δ should be short, preferably. Typical values are Δ = 0.08 s for the diffusion time and δ = 1500 µs for the gradient length in the case of the supramolecular structures investigated in this work. In an ideal case, less than 5% observed signal intensity is left when the gradient is at the highest power (e.g. 98%) compared to the reference signal

intensity where only 3-5% of the gradient power is applied. The decrease of the signal intensity should be sigmoidal if plotted against the gradient power.

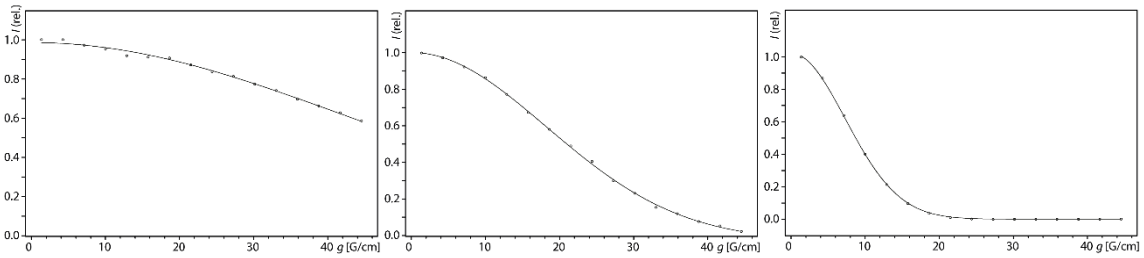

Figure 1.10: Plot of gradient strengths *g* against the relative signal intensity *I* with a to low value of δ (left), an ideal value of δ (middle) and a to high value of δ (right).

One of the most common ways to measure DOSY NMR is using a led-based pulse sequence (ledbpgp2s, Figure 1.11a).[97] However, this is not covering one of the major problems during diffusion measurement, the compensation of convection. Convection is a thermal induced movement of particles in solution.[90] If this effect is not compensated, wrong diffusion data could be obtained. Movement due to convection can be especially observed in low viscous solvents (e.g. chloroform) and in tubes with a larger diameter. To compensate convection by a technical way, JERSCHOW and MÜLLER published pulse sequences that contains additional gradients for convection compensation (Figure 1.11b).[98,99]

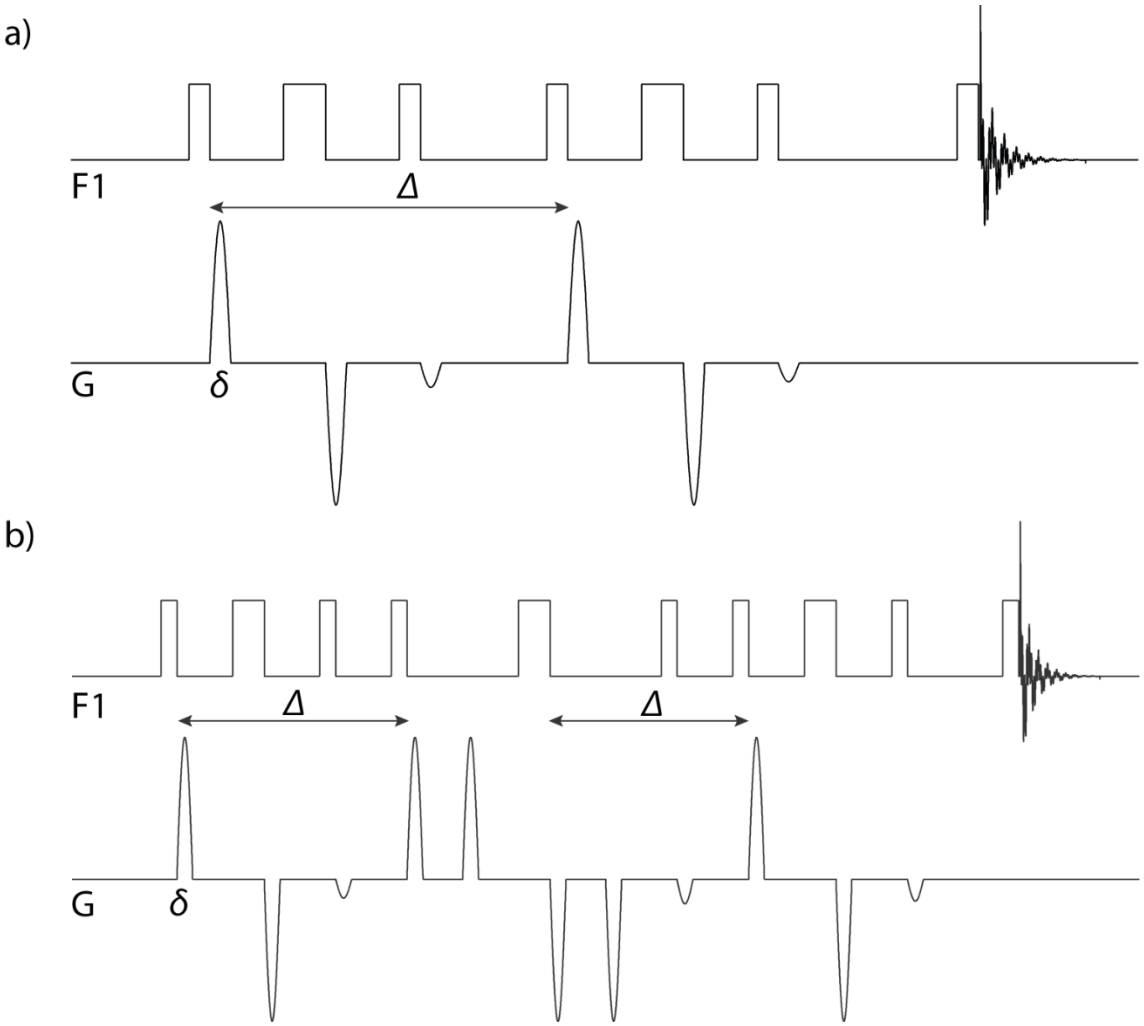

Figure 1.11: ^{1}H DOSY NMR pulse sequences: a) ledbpgp2s and b) dstebpgp3s with diffusion times Δ and gradient lengths δ.

Beside the compensation of convection via gradient pulses, it is also possible to use NMR tube with a smaller diameter or solvents with a higher viscosity. In this thesis, the effect of convection was investigated for several NMR spectrometer with different probes as well as for many commonly used deuterated solvents.

2 Scope of the Thesis

Rational design of novel coordination cage structures is one of the major goals in the Clever-Lab. In the past, numerous heteroleptic coordination assemblies have been described. To utilize the unique properties of these structures the focus shifted from purely structural analysis to the implementation of functionalities into the cage systems. The scope of this thesis is the proposal of a modular heteroleptic coordination cage system by using endohedral functionalized ligands with hydrogen bond donor sites pointing into the formed cavities to investigate hydrogen-bond driven guest binding.

The characterization of the structures and the investigation of e.g. guest binding or guest exchange is mainly carried out by one- and two-dimensional NMR spectroscopy. One outstanding method hereby is the DOSY NMR experiment. In this thesis, the technique was illuminated in close detail with special regard to the optimization of the measurement for our cage systems.

In particular, the following points were investigated during the doctoral research:

- Design and synthesis of endohedral functionalized ligands with hydrogen bond donor sites
- Self-assembly and characterization of novel heteroleptic coordination cages using the SCA
- Guest binding studies of organophosphates inside the coordination cages via NMR, ESI-MS and X-ray diffraction as well as MD-simulations
- Development and optimization of tailor-made NMR experiments for coordination cages
- Determination of hydrodynamic radii for non-spherical molecules
- Investigation and compensation of convection effects during the DOSY measurement

3 Results and Discussion

Contents of this chapter were published in: *Endohedrally Functionalized Heteroleptic Coordination Cages for Phosphate Ester Binding* (**A. Platzek**, S. Juber, C. Yurtseven, S. Hasegawa, L. Schneider, C. Drechsler, K. E. Ebbert, R. Rudolf, Q.-Q. Yan, J. J. Holstein, L. V. Schäfer, G. H. Clever, *Angew. Chem. Int. Ed.*, **2022**, *61*, e202209305.) (Hot Paper)[100]

3.1 Design of Ligands for a Modular Host System

9*H*-Carbazole is a heterocyclic aromatic molecule that is naturally available in fossil oil as well as in coal tar, from which it was firstly isolated and characterized by GRAEBE and GLASER in the end of the 19th century.[101] The molecule contains a secondary amine that can be easily functionalized with aliphatic and aromatic compounds.[102–111] It is quite reactive at the 3,6-position due to the +M effect of the nitrogen atom, so it is possible to introduce bromine or iodine atoms to obtain precursors for bis-monodentate ligands that were already used in the group of CLEVER for coordination cages.[61,62,112] The disadvantage is that the amine is pointing out of the cavity of these cage structures. To obtain ligands that are based on carbazole but having the secondary amine pointing into the cavity, the donor sites have to be attached to the 2,7-positions. To obtain better fitting donor angles, isoquinoline donor groups were attached instead of the classically used pyridine moieties.

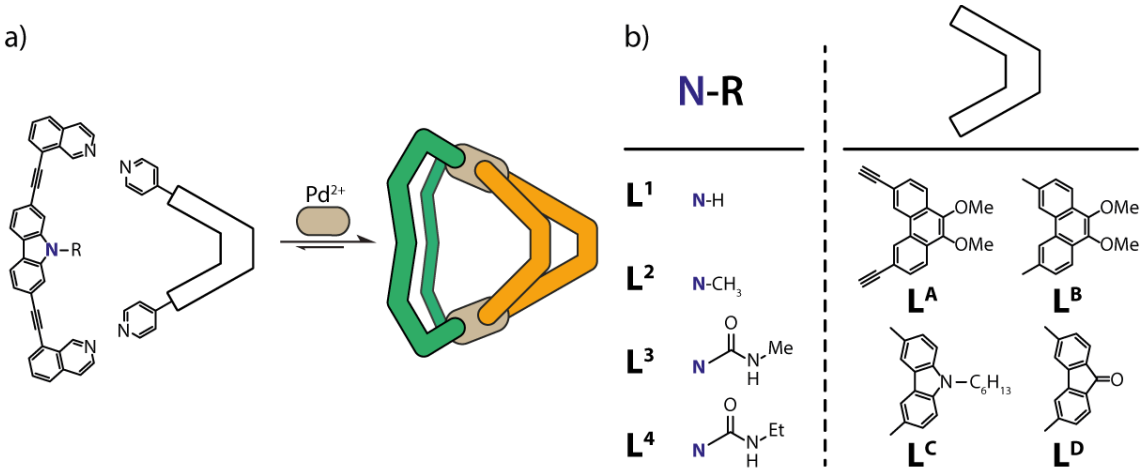

Figure 3.1: Design of a modular system of a) heteroleptic coordination cages based on shape complementary ligands b).

Ligand **L**^{1} was synthesized via SONOGASHIRA cross coupling reaction of commercially available 2,7-dibromo-9*H*-carbazole (2,7-DBC) with 8-ethinylisoquinoline **1** in a 1:1 mixture of DMF and DIPEA at 115 °C for 48 h. However, the yield was quite poor since it was not possible to purify the crude product via column chromatography due to the very low solubility of **L**^{1} in common organic solvents. It was figured out, that **L**^{1} is only decent enough soluble in either DMSO or DMF, so the purification was done via gel permeation chromatography (GPC) of the crude reaction mixture in DMF with a lot of cycles to obtain the pure ligand in yields up to 24%. Compared to classic column chromatography, the separation of compounds via GPC is done by the size of the molecules, smaller ones interact with the column material and therefore eluate slower than larger ones. To get a proper separation, the analytes are passing the column multiple times through a loop. To optimize the overall yield, a *tert*-butyloxycarbonyl (Boc) protection group was introduced to the secondary amine to increase the solubility (chapter 4.2.15). The following cross coupling reaction lead to the formation of Boc-**L**^{1} which could not be isolated as a single compound, since the protection group dissociated during the workup procedure via column chromatography with chloroform/MeOH (9:1) as the eluent. After the following GPC cycles with DMF as the eluent **L**^{1} could be obtained in slightly better yields up to 35%.

L^{1} was characterized by NMR spectroscopy as well as ESI mass spectrometry. A ^{1}H NMR spectrum of **L**^{1} in DMSO-d_6 shows nine signals in the aromatic region which could be unambiguously assigned to the structure with the help of homo- and hetero-correlation

NMR experiments as well as one prominent singlet at 11.7 ppm which could be assigned to the resonance of the secondary amine proton.

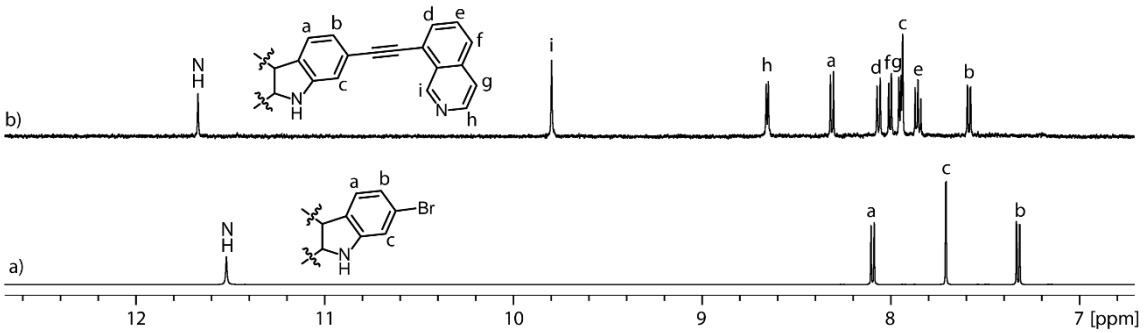

Figure 3.2: Partial ^{1}H NMR (500 MHz, DMSO-d_6) spectra of a) 2,7-DBC and b) $\mathbf{L^1}$.

As it was mentioned in chapter 2, one reason 2,7-carbazole was chosen as a ligand backbone is that it is modifiable at the secondary amine with ease. The following Scheme 3.1 shows the different approaches of modification, namely methylation, implementing amide functionalities and amination of $\mathbf{L^1}$.

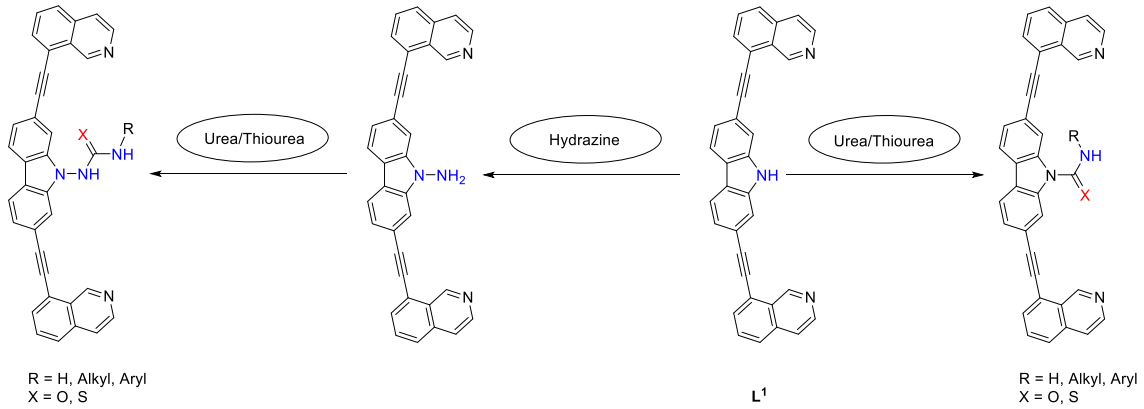

Scheme 3.1: Possible functionalization routes of $\mathbf{L^1}$.

These approaches lead to a series of proposed ligands with different functionalities for unique guest binding properties and catalysis applications. The ligands were synthesized via cross coupling reactions of the substituted 2,7-DBC backbone with isoquinoline donor groups. The methylated backbone **2** was obtained by the reaction of the unmodified backbone with iodomethane. The followed cross coupling reaction lead to ligand $\mathbf{L^2}$ in slightly better yields compared to $\mathbf{L^1}$, due to better solubility and therefor easier workup and purification steps. A ^{1}H NMR spectrum of $\mathbf{L^2}$ in DMSO-d_6 shows nine signals in the aromatic regions and a singlet resonance at around 4.0 ppm which could be assigned to the introduced methyl-group that is shifted downfield compared to the precursor molecule.

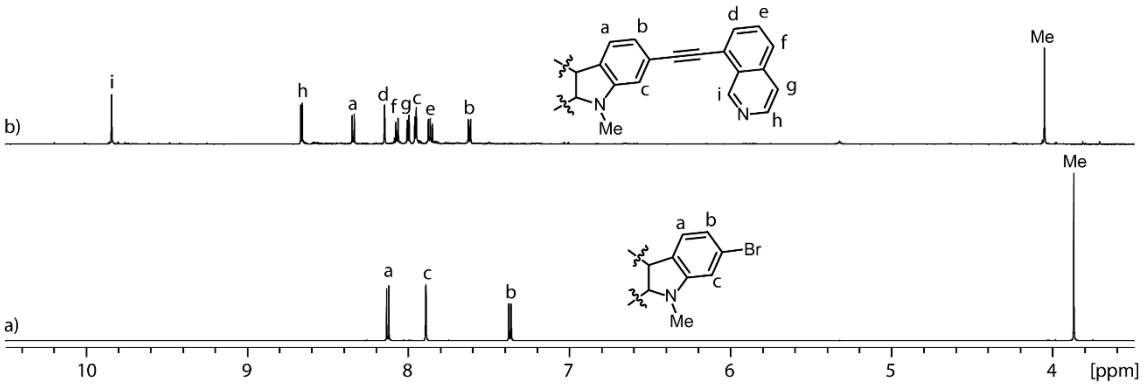

Figure 3.3: Partial ^{1}H NMR (600 MHz, DMSO-d_6) spectra of a) N-methyl substituted 2,7-DBC and b) $\mathbf{L^2}$.

For forming the amide bond in ligands $\mathbf{L^3}$ and $\mathbf{L^4}$ two different pathways where used: Backbone **3** was synthesized by a nucleophilic substitution reaction of 2,7-DBC with ethyl-*N*-methyl carbamate and backbone **4** via a nucleophilic substitution reaction of 2,7-DBC with ethyl isocyanate, respectively. Both ligands were obtained by following cross coupling reaction of the respective backbones with isoquinoline donor groups in poor yields of 6 to 12%. Further optimization of the reactions was not realized. ^{1}H NMR spectra of ligands $\mathbf{L^3}$ and $\mathbf{L^4}$ showing both nine signals in the aromatic regions as well as a quartet resonance at 8.5 ppm ($\mathbf{L^3}$) and a triplet resonance at 8.6 ppm ($\mathbf{L^4}$) which could be assigned to the amide proton in both cases. Compared to **3** and **4**, respectively, the signals of the NH protons are slightly downfield shifted.

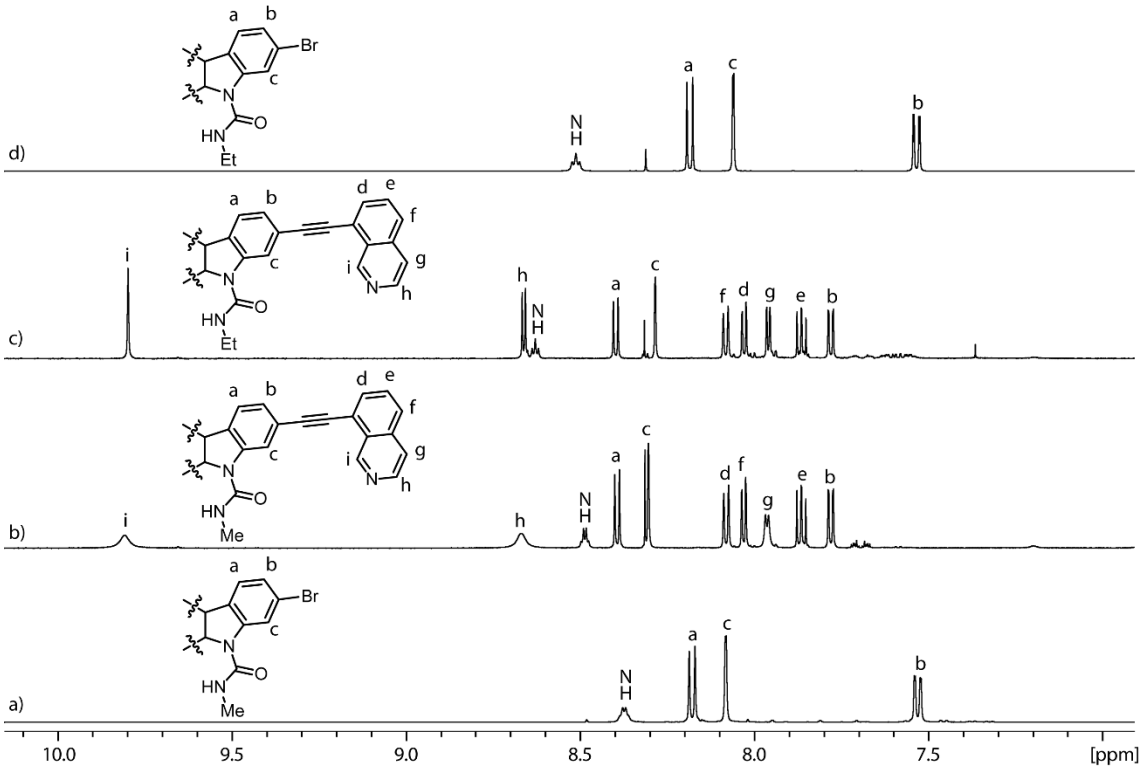

Figure 3.4: Partial ^{1}H NMR (DMSO-d_6) spectra of a) precursor **3**, b) $\mathbf{L^3}$, c) $\mathbf{L^4}$ and d) precursor **4**.

The proposed ligand containing a hydrazine functionality could not be realized. The corresponding backbone was synthesized (chapter 4.2.13 and 4.2.14), however, the hydrazine functional group was not stable under the cross coupling reaction condition and therefore only ligand $\mathbf{L^1}$ was isolated.

Based on the studies of shape-complementary ligands by BLOCH and EBBERT, ligands $\mathbf{L^{A\text{-}D}}$ where used for cage formation studies (Figure 3.1b).[61,62] Both could show that a ligand with carbazole backbone that was substituted with alkinyl-para-pyridine linkers in 3,6-position is able to form exclusively heteroleptic coordination cages with the phenanthrene based ligands $\mathbf{L^A}$ and $\mathbf{L^B}$. The illustration in Figure 3.5 shows that if the carbazole backbone is mirrored and will be substituted with donor sites in the 2,7-position it will have similar donor angles and therefore, most likely, will form heteroleptic coordination cages with $\mathbf{L^A}$ and $\mathbf{L^B}$ as well.

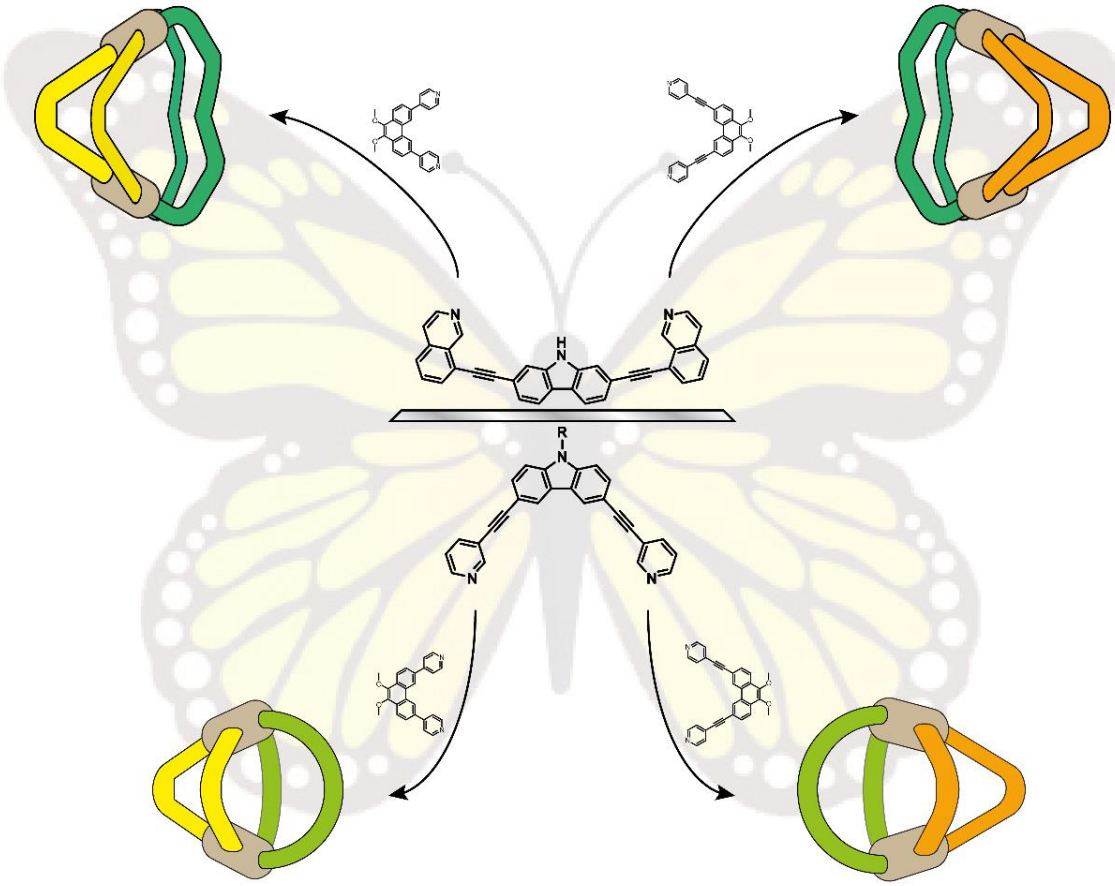

Figure 3.5: Comparison of ligand $\mathbf{L^1}$ (top) with 3,6-substituted carbazole-based ligand (bottom) and both phenanthrene-based ligands $\mathbf{L^A}$ (right) and $\mathbf{L^B}$ (left) as well as proposed (top) and reported (bottom) heteroleptic coordination cages.

3.2 Synthesis of Coordination Cages

Adding 0.55 eq of a $[Pd^{II}(CH_3CN)_4](BF_4)_2$ solution in the respective solvent (just named "Pd(II) cations") to a solution of $\mathbf{L^1}$ in DMSO-d_6 or DMF-d_7 at room temperature or heating to 70 °C did not lead to a clear formation of a homoleptic $Pd_2\mathbf{L^1}_4$ cage structure (Figure 3.6) but to a not further analyzed mixture of different species.

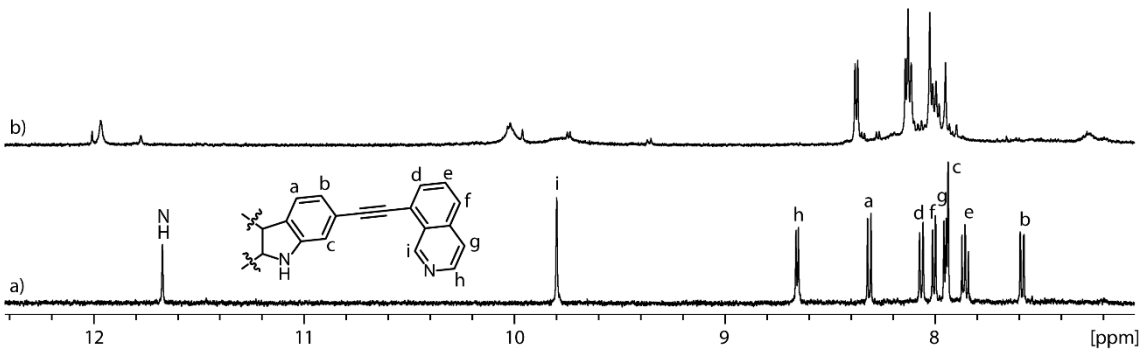

Figure 3.6: Partial ^{1}H NMR (500 MHz, DMSO-d_6) spectra of a) ligand $\mathbf{L^1}$ and b) adding 0.55 eq Pd(II) to $\mathbf{L^1}$, 24 h at rt.

Figure 3.6b showing new signals in the aromatic region of the ^{1}H NMR spectrum as well as new signals at about 12 ppm which likely correspond to the resonance of the NH proton of the newly formed species. However, no signals of the free ligand were observed. Heating the sample to 70 °C over time also did not lead to a single species formation (chapter 4.3).

In the ESI-MS spectrum (Figure 3.7) peaks at *m/z* = 522.5886 for $[Pd_2\mathbf{L^1}_4]^{4+}$, 725.7852 for $[Pd_2\mathbf{L^1}_4 + BF_4]^{3+}$ and 1132.1787 for $[Pd_2\mathbf{L^1}_4 + 2\ BF_4]^{2+}$ were observed as well as a peak at *m/z* = 845.5755 which could be assigned to the bowl-type structure $[Pd_2\mathbf{L^1}_3Cl_2]^{2+}$.

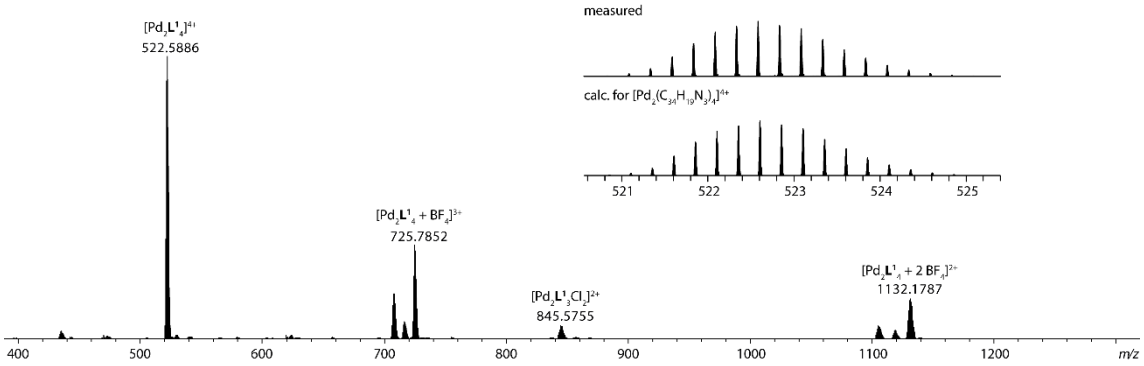

Figure 3.7: ESI-MS spectrum of $Pd_2\mathbf{L^1}_4$.

However, mixing $\mathbf{L^1}$ in a 1:1 fashion with one of the ligands $\mathbf{L^{A-D}}$ in DMSO-d_6 or DMF-d_7 followed by the addition of 0.55 eq Pd(II) cations lead to a quantitative formation of heteroleptic coordination cages of the type $Pd_2\mathbf{L^1}_2\mathbf{L^{A-D}}_2$ after a few minutes at room temperature. Additionally, mixing ligands $\mathbf{L^{2-4}}$ with $\mathbf{L^{A-D}}$ under the same conditions stated above lead to in total 16 novel heteroleptic cage structures as well. All of these architectures were characterized by NMR spectroscopy in solution state and ESI-MS in gas phase.

3.2.1 Heteroleptic Coordination Cages with $\mathbf{L^1}$

In a ^{1}H NMR spectrum (Figure 3.8c) of the heteroleptic cage $Pd_2\mathbf{L^1}_2\mathbf{L^A}_2$ a singlet at 11.8 ppm is observed which could be assigned to the NH proton, so the signal was shifted downfield compared to the free ligand. Also, the signals of the protons around the coordination sphere (h, i, e') undergo a downfield shift, indicating the formation of a coordinative bond between the nitrogen and the palladium atom. Overall, the observed signals in the aromatic regions are shifted compared to the ones of the free ligands. Signals

of the protons pointing inside the cavity are shifted downfield, the signals of proton b and b' are shifted upfield.

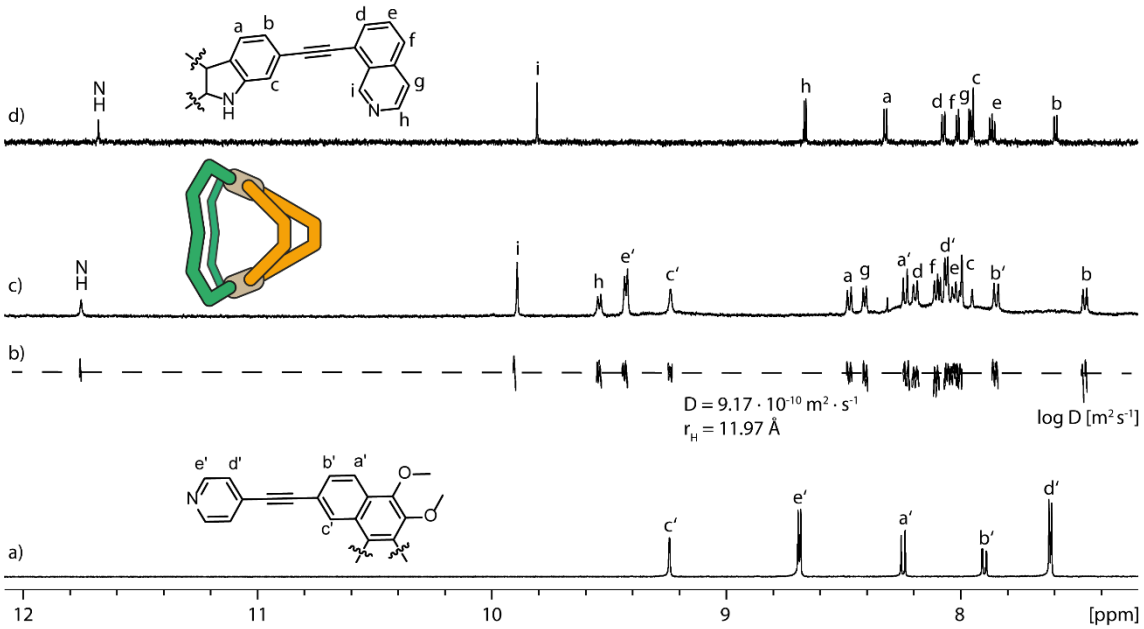

Figure 3.8: Partial ^{1}H NMR (DMSO-d_6) spectra of a) ligand $\mathbf{L^A}$, b) ^{1}H DOSY trace of $Pd_2\mathbf{L^1}_2\mathbf{L^A}_2$ with diffusion coefficient *D* and hydrodynamic radius r_H, c) heteroleptic coordination cage $Pd_2\mathbf{L^1}_2\mathbf{L^A}_2$ and d) ligand $\mathbf{L^1}$.

From a ^{1}H DOSY NMR spectrum (Figure 3.8b) of $Pd_2\mathbf{L^1}_2\mathbf{L^A}_2$ it is clear, that only one single species is present in solution state, with a hydrodynamic radius of r_H = 11.97 Å. This is in good accordance to the radii of previously reported heteroleptic coordination cages.[47,61] Furthermore, the heteroleptic cage formation was observed in the gas-phase by ESI mass spectrometry (Figure 4.54). Peaks for different charged species of the title compound, namely the most prominent ones for $[Pd_2\mathbf{L^1}_2\mathbf{L^A}_2]^{4+}$, $[Pd_2\mathbf{L^1}_2\mathbf{L^A}_2 + BF_4]^{3+}$, $[Pd_2\mathbf{L^1}_2\mathbf{L^A}_2 + 2\ BF_4]^{2+}$ were observed.

Fortunately, single crystals of $Pd_2\mathbf{L^1}_2\mathbf{L^A}_2$ that were suitable for X-ray diffraction were obtained from slow vapor diffusion of toluene into a solution of the cage in DMF-d_7. In the crystal structure (Figure 3.9) the arrangement of the two different ligands $\mathbf{L^1}$ and $\mathbf{L^A}$ in *cis*-configuration to each other is confirmed. The two palladium centres have a distance of 14.403(5) Å to each other and the N−N distance of the, almost parallel to each other, carbazole backbone moieties of ligand $\mathbf{L^1}$ amounts to 6.727(7) Å. Since the ligands $\mathbf{L^1}$ are such close to each other, the cavity is wide open from the other side where ligands $\mathbf{L^A}$ are placed and this makes it easily accessible for potential guests from this direction. The coordination cage contains two distinct BF_4^- anions inside the cavity, both in a very close proximity to the NH functions of ligand $\mathbf{L^1}$. The closest H−F distance (2.109 Å) found is

inside the range of hydrogen bonds.[113] Moreover, two DMF solvent molecules that are encapsulated as well could be found in the molecular structure, each of them pointing towards the Pd centre with their oxygen atoms and in between the narrow channel that is formed by the two ligands $\mathbf{L^1}$.

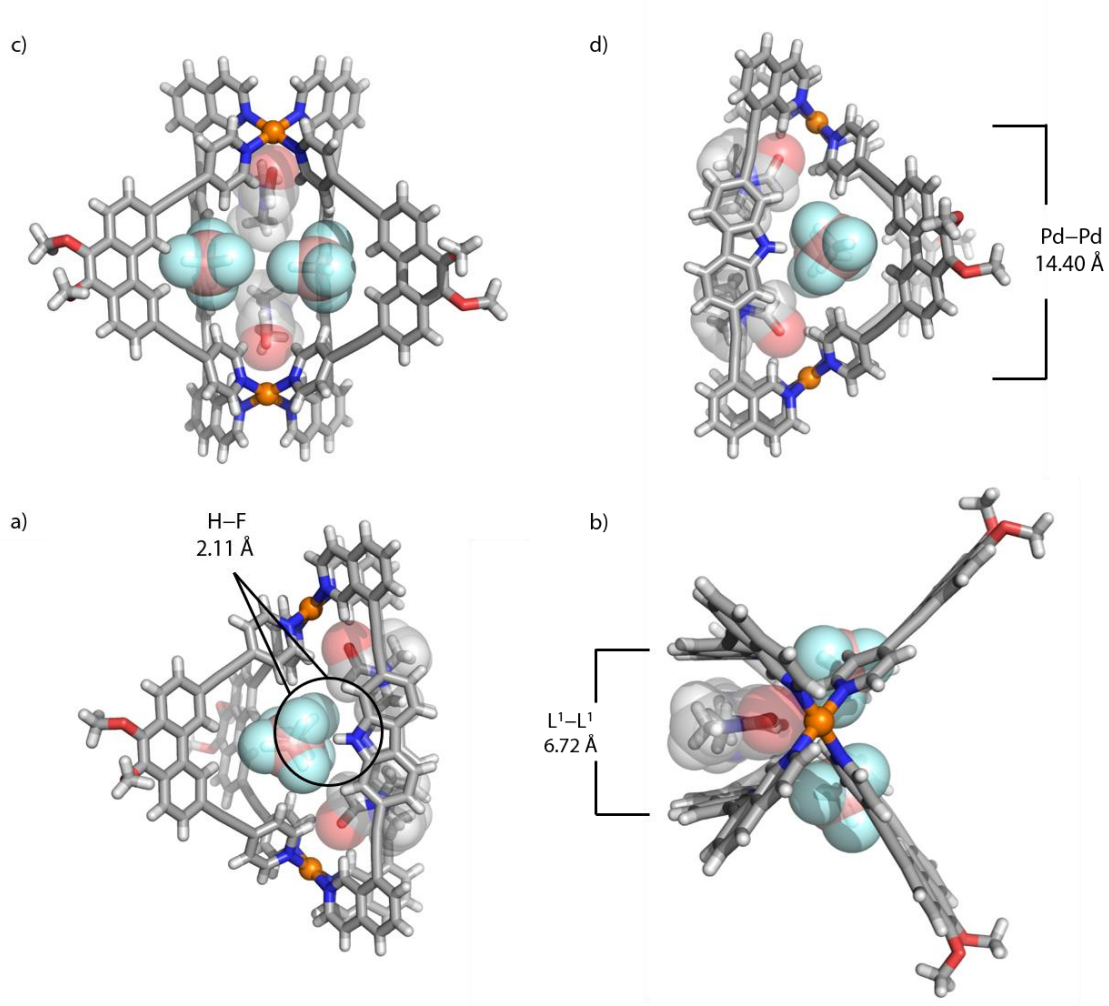

Figure 3.9: Molecular structure of $Pd_2\mathbf{L^1}_2\mathbf{L^A}_2$ in the solid state, determined by X-ray diffraction, a) side, b) top, c) front and d) side view and selected distances in Å.

Mixing ligands $\mathbf{L^1}$ and $\mathbf{L^B}$ with Pd under the conditions described above lead to the formation of heteroleptic cage $Pd_2\mathbf{L^1}_2\mathbf{L^B}_2$. In a ^{1}H NMR spectrum (Figure 3.10b) of this species comparable shifts of the signals are observed. Most prominent are again the downfield shift of the signal of the secondary amine proton as well as the downfield shifts of the signals of the inner protons i and e'. In contrast to cage $Pd_2\mathbf{L^1}_2\mathbf{L^A}_2$, the signal of proton c' is shifted upfield, indicating a larger shielding effect and therefore a smaller cavity size.

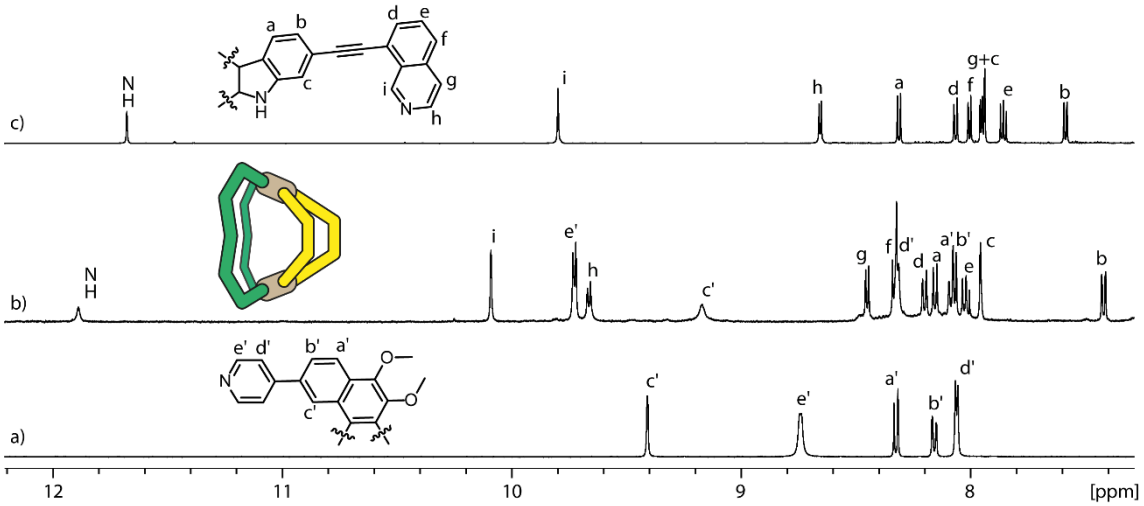

Figure 3.10: Partial ^{1}H NMR (DMSO-d_6) spectra of a) ligand $\mathbf{L^B}$, b) heteroleptic coordination cage $Pd_2\mathbf{L^1}_2\mathbf{L^B}_2$ and c) ligand $\mathbf{L^1}$.

Additionally, the self-assembly was confirmed by ES-MS (Figure 4.60), peaks for different charged species, namely $[Pd_2\mathbf{L^1}_2\mathbf{L^B}_2]^{4+}$, $[Pd_2\mathbf{L^1}_2\mathbf{L^B}_2 + BF_4]^{3+}$, $[Pd_2\mathbf{L^1}_2\mathbf{L^B}_2 + 2\ BF_4]^{2+}$ were observed.

Very recently, single crystals of $Pd_2\mathbf{L^1}_2\mathbf{L^B}_2$ were obtained via slow vapor diffusion of toluene into the cage solution in DMF. Preliminary analysis of X-ray diffraction data revealed, that the cage structure looks pretty much like the one obtained with the combination of $\mathbf{L^1}$ and $\mathbf{L^A}$.

Figure 3.11b shows a ^{1}H NMR spectrum of the heteroleptic coordination cage $Pd_2\mathbf{L^1}_2\mathbf{L^C}_2$ in which again a strong downfield shift of the signal of the secondary amine proton of ligand $\mathbf{L^1}$ could be observed. Downfield shifts of the signals of the protons in proximity to the coordination sphere confirming the formation of a dative nitrogen palladium bond. Similar to cage $Pd_2\mathbf{L^1}_2\mathbf{L^B}_2$, a upfield shift and therefor a larger shielding effect of the signal of proton c' is observed, indicating the smaller cavity compared to coordination cage $Pd_2\mathbf{L^1}_2\mathbf{L^A}_2$.

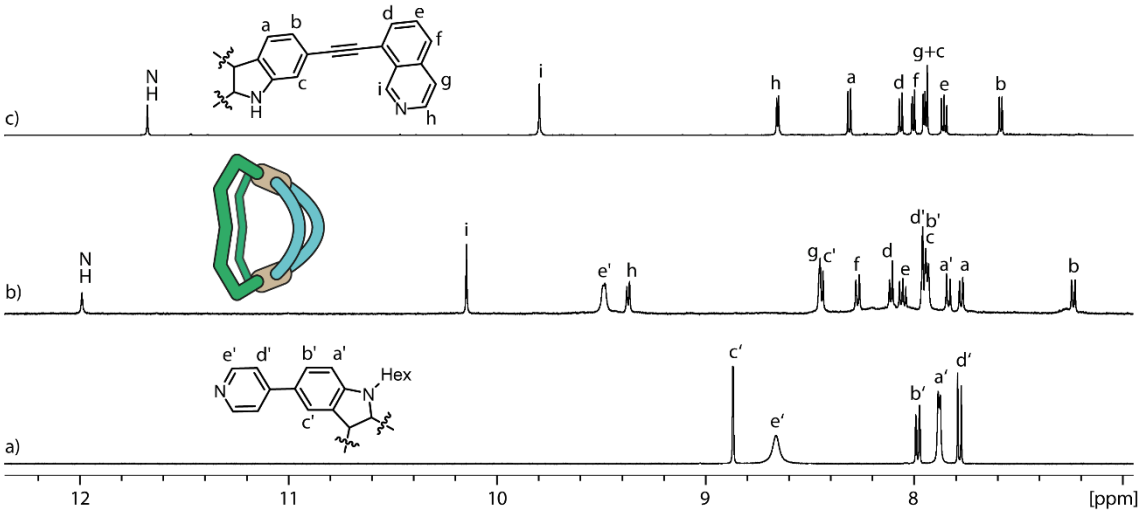

Figure 3.11: Partial ^{1}H NMR (DMSO-d_6) spectra of a) ligand $\mathbf{L^C}$, b) heteroleptic coordination cage $Pd_2\mathbf{L^1}_2\mathbf{L^C}_2$ and c) ligand $\mathbf{L^1}$.

Furthermore, the cage formation was confirmed by ESI-MS (Figure 4.66), peaks of different charged species, namely $[Pd_2\mathbf{L^1}_2\mathbf{L^C}_2]^{4+}$, $[Pd_2\mathbf{L^1}_2\mathbf{L^C}_2 + BF_4]^{3+}$, $[Pd_2\mathbf{L^1}_2\mathbf{L^C}_2 + 2\ BF_4]^{2+}$ were observed.

Also in this case, single crystals of $Pd_2\mathbf{L^1}_2\mathbf{L^C}_2$ were obtained via slow vapor diffusion of toluene into the cage solution in DMF. The preliminary analysis of the X-ray diffraction data revealed, that the structure of the assembly looks similar to the one obtained with the combination of $\mathbf{L^1}$ and $\mathbf{L^A}$.

Addition of Pd(II) cations to a 1:1 mixture of $\mathbf{L^1}$ and $\mathbf{L^D}$ also lead to formation of a heteroleptic coordination cage, a ^{1}H NMR spectrum is shown in Figure 3.12. The observed shifts of the signals are again comparable to the previous examples.

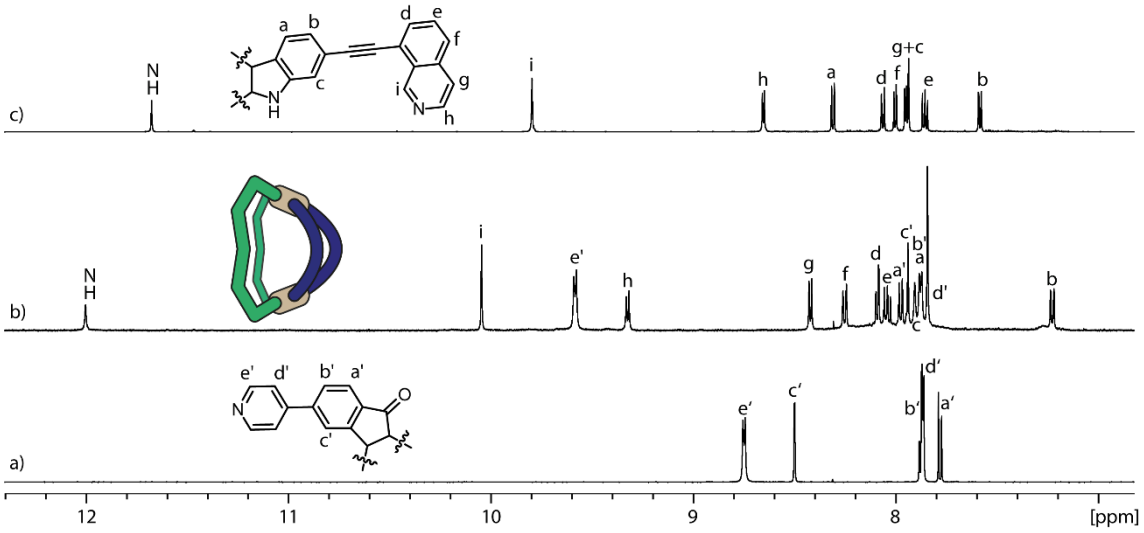

Figure 3.12: Partial ^{1}H NMR (DMSO-d_6) spectra of a) ligand $\mathbf{L^D}$, b) heteroleptic coordination cage $Pd_2\mathbf{L^1}_2\mathbf{L^D}_2$ and c) ligand $\mathbf{L^1}$.

In an ESI-MS spectrum peaks for species $[Pd_2\mathbf{L^1}_2\mathbf{L^D}_2 + BF_4]^{3+}$ and $[Pd_2\mathbf{L^1}_2\mathbf{L^D}_2 + 2\ BF_4]^{2+}$ were found (Figure 4.72).

The described decrease of the cavity size going from $Pd_2\mathbf{L^1}_2\mathbf{L^A}_2$ over $Pd_2\mathbf{L^1}_2\mathbf{L^B}_2$ to $Pd_2\mathbf{L^1}_2\mathbf{L^D}_2$ is shown by the overlay of the geometry optimized cage structures in the following figure.

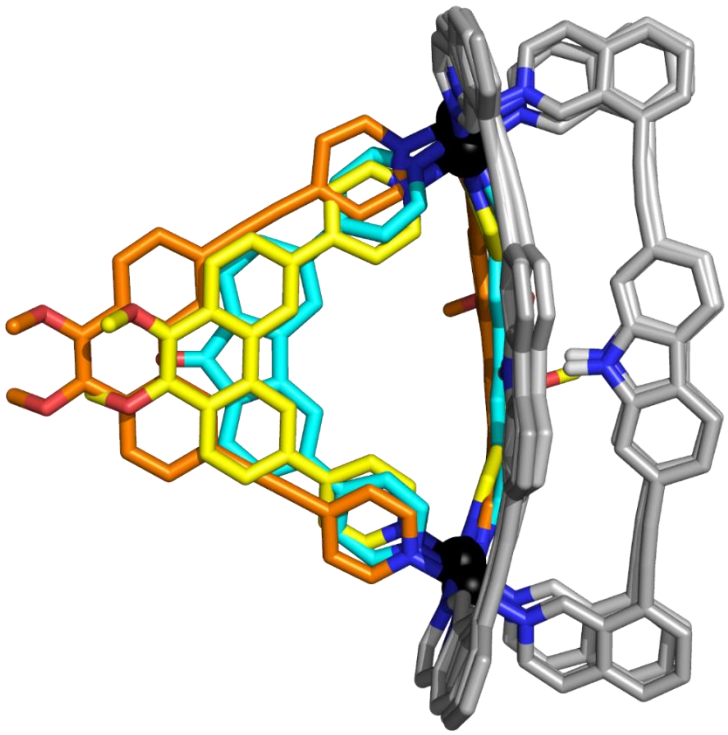

Figure 3.13: Overlay of PM6 optimized structures of $Pd_2\mathbf{L^1}_2\mathbf{L^A}_2$ (orange), $Pd_2\mathbf{L^1}_2\mathbf{L^B}_2$ (yellow) and $Pd_2\mathbf{L^1}_2\mathbf{L^D}_2$ (turquoise).

The average distances between the two different ligands through the cavity decreases from 8.4 Å (measured from the NH atom of $\mathbf{L^1}$ to hydrogen atom c' of $\mathbf{L^A}$) to 6.2 Å (measured from the NH atom of $\mathbf{L^1}$ to hydrogen atom c' of $\mathbf{L^B}$) and 5.5 Å (measured from the NH atom of $\mathbf{L^1}$ to hydrogen atom c' of $\mathbf{L^D}$). This already allows the presumption that larger guest molecules most likely bind to $Pd_2\mathbf{L^1}_2\mathbf{L^A}_2$ rather than to the smaller cage derivatives.

3.2.2 Heteroleptic Coordination Cages with $\mathbf{L^2}$

Next, the capability of heteroleptic cage formation of the methylated ligand $\mathbf{L^2}$ with $\mathbf{L^{A-D}}$ was tested. The ligands were as well mixed in a 1:1 fashion and 0.55 eq Pd(II) cations in DMSO-d_6 to obtain the corresponding self-assembled cages at room temperature within minutes. For example, a ^{1}H NMR spectrum (Figure 3.14b) of $Pd_2\mathbf{L^2}_2\mathbf{L^A}_2$ showing a downfield shift of the signals in close proximity to the coordination sphere and the inner protons, respectively. However, the shift for the signal of proton c' is not at as strong as it was observed for $Pd_2\mathbf{L^1}_2\mathbf{L^A}_2$, because of the sterically more demanding methyl-groups inside the cavity.

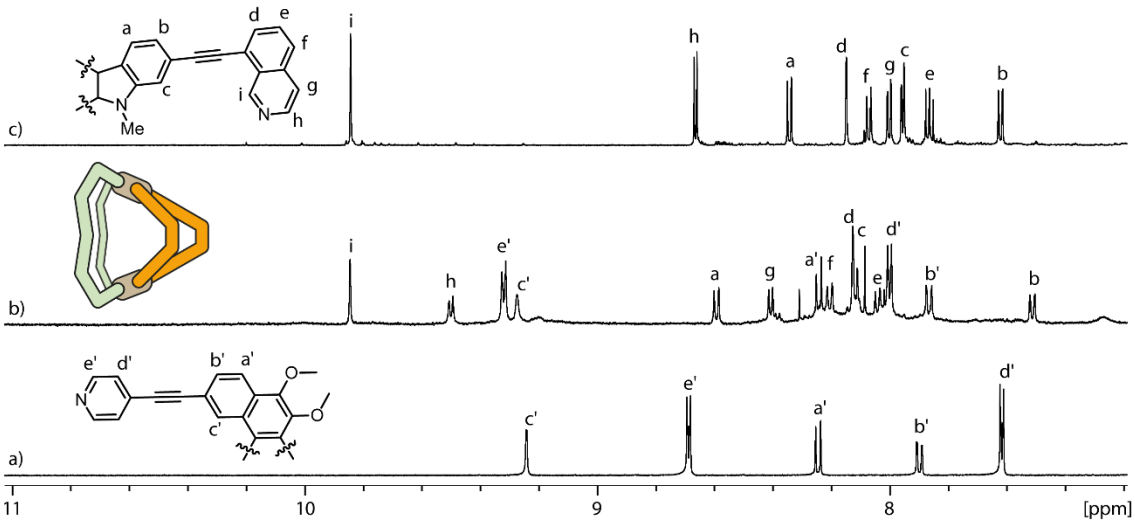

Figure 3.14: Partial ^{1}H NMR (DMSO-d_6) spectra of a) ligand $\mathbf{L^A}$, b) heteroleptic coordination cage $Pd_2\mathbf{L^2}_2\mathbf{L^A}_2$ and c) ligand $\mathbf{L^2}$.

The coordination cage formation was also shown by ESI-MS, most prominent peaks were found for $[Pd_2\mathbf{L^2}_2\mathbf{L^A}_2]^{4+}$, $[Pd_2\mathbf{L^2}_2\mathbf{L^A}_2 + BF_4]^{3+}$, $[Pd_2\mathbf{L^2}_2\mathbf{L^A}_2 + 2\ BF_4]^{2+}$ (Figure 4.78).

The ^{1}H NMR spectra (Figure 3.15, Figure 3.16 and Figure 3.17) of the assemblies of $\mathbf{L^2}$ with the shorter ligands $\mathbf{L^{B-D}}$ are comparable with the ones from $Pd_2\mathbf{L^1}_2\mathbf{L^{B-D}}_2$. The signals of the protons in proximity to the coordination spheres are shifted downfield compared to

the free ligands and the signals of the inward pointing protons, especially proton c', are shifted upfield as they are more shielded due to the smaller cavity.

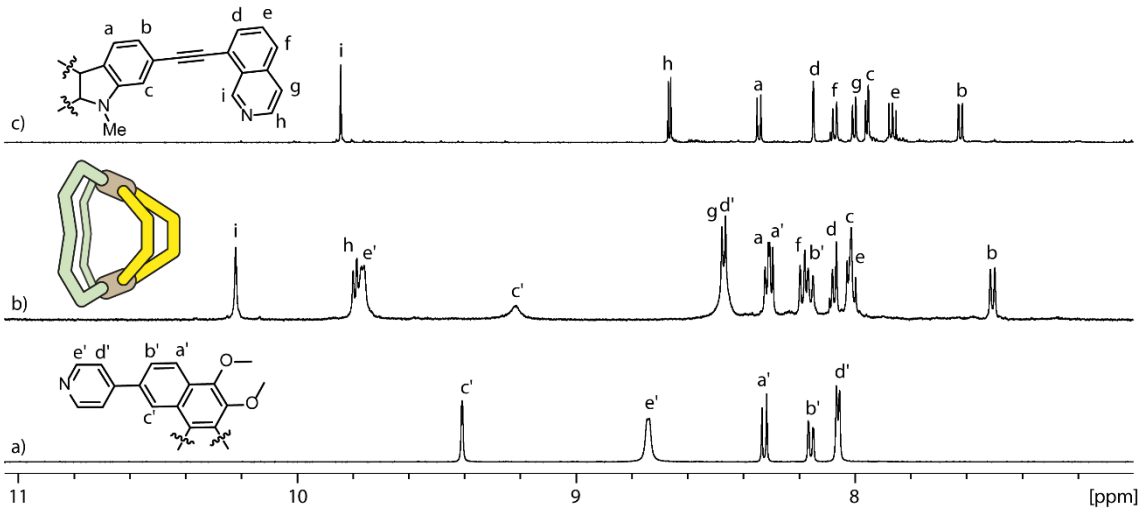

Figure 3.15: Partial ^{1}H NMR (DMSO-d_6) spectra of a) ligand $\mathbf{L^B}$, b) heteroleptic coordination cage $Pd_2\mathbf{L^2}_2\mathbf{L^B}_2$ and c) ligand $\mathbf{L^2}$.

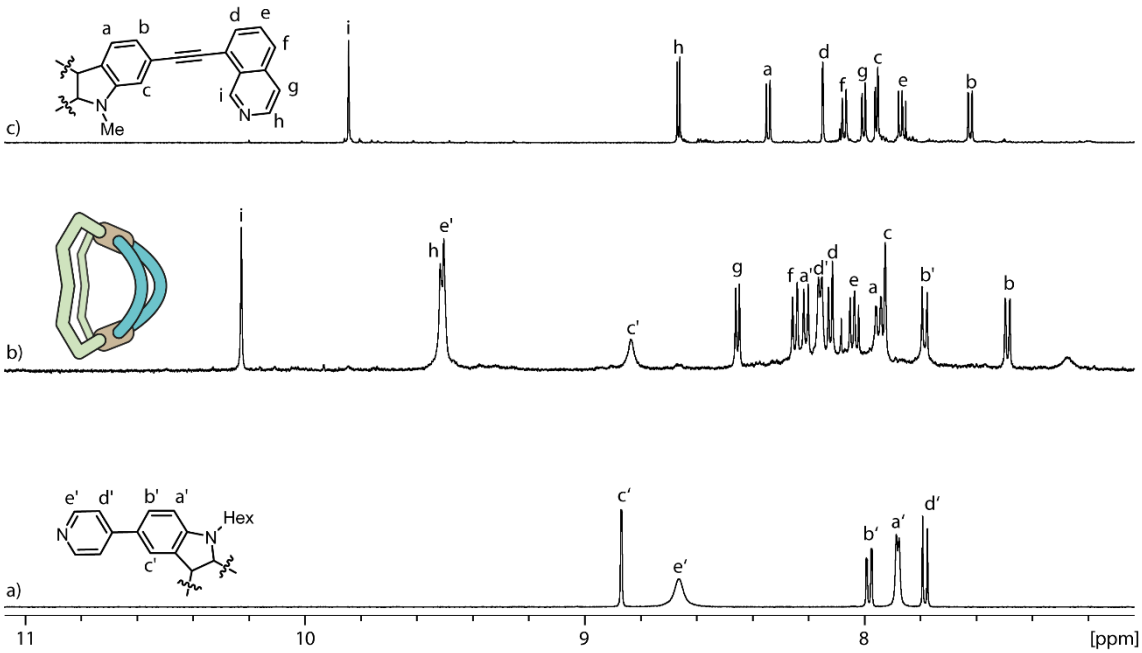

Figure 3.16: Partial ^{1}H NMR (DMSO-d_6) spectra of a) ligand $\mathbf{L^C}$, b) heteroleptic coordination cage $Pd_2\mathbf{L^2}_2\mathbf{L^C}_2$ and c) ligand $\mathbf{L^2}$.

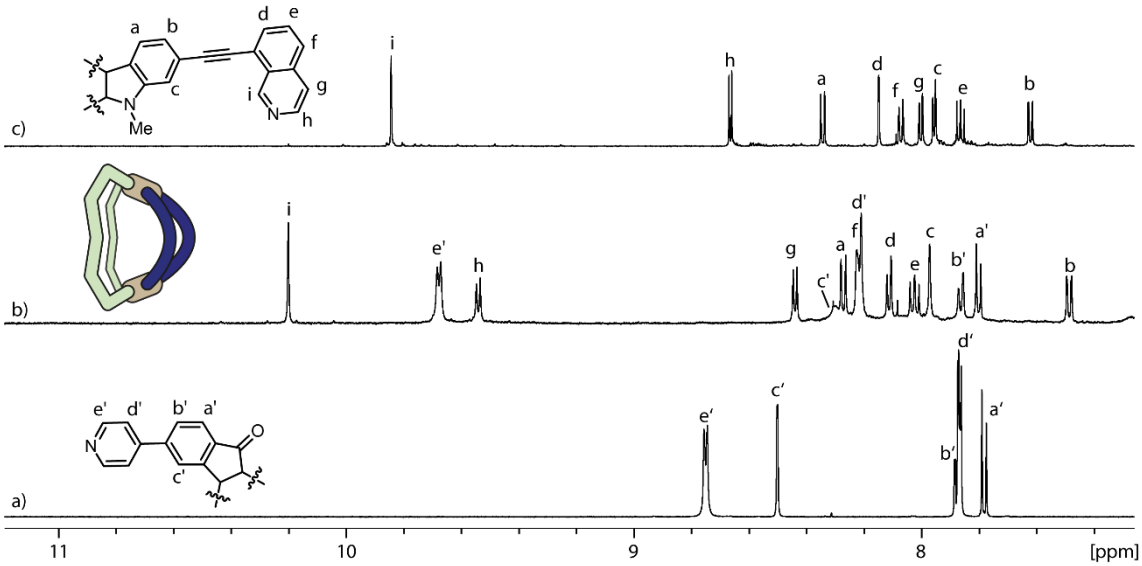

Figure 3.17: Partial ^{1}H NMR (DMSO-d_6) spectra of a) ligand $\mathbf{L^D}$, b) heteroleptic coordination cage $Pd_2\mathbf{L^2}_2\mathbf{L^D}_2$ and c) ligand $\mathbf{L^2}$.

All of these assemblies were analyzed by ESI-MS as well (Figure 4.84, Figure 4.90 and Figure 4.96). Peaks of different charged species of the cage structure were observed, namely the 4^+ species without BF_4^- anions as well as the 3^+ and 2^+ species with one and two BF_4^- anions, respectively.

3.2.3 Heteroleptic Coordination Cages with L^3

Formation of the heteroleptic coordination cage $Pd_2\mathbf{L^3}_2\mathbf{L^A}_2$ was also observed via ^{1}H NMR spectroscopy. The signals of the protons around the coordination sphere (h, i, e') are shifted downfield compared to the free ligands due to the formation of the dative N−Pd bond. However, the signal of the inward pointing proton c' is shifted upfield strongly, indicating a stronger shielding. This can be explained by the sterically more demanding endohedral substituents. Therefore, the signal of the NH proton as well as the signal of the methyl group are also shifted upfield compared to the free ligand.

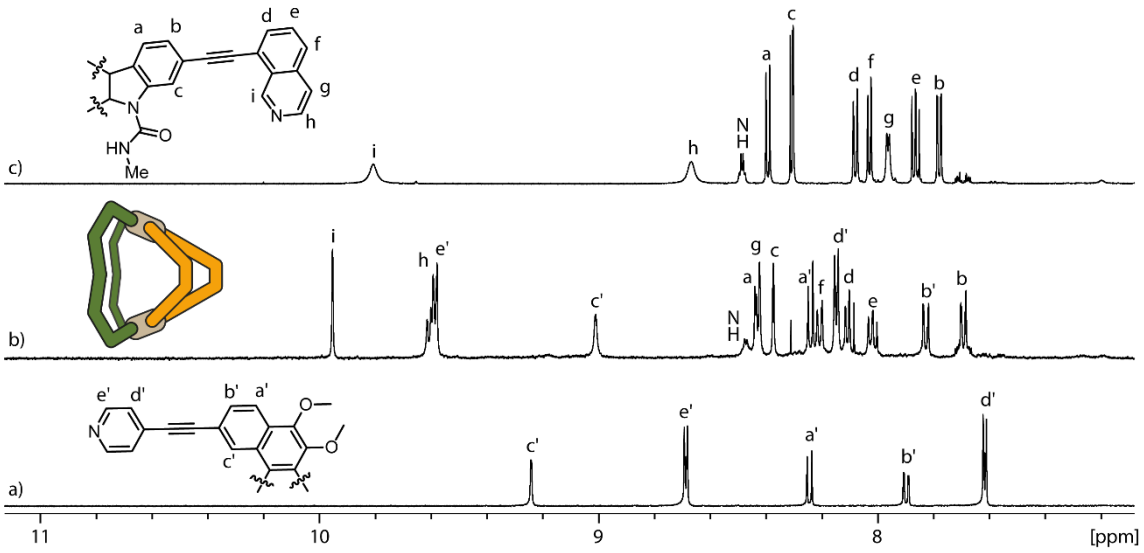

Figure 3.18: Partial ^{1}H NMR (DMSO-d_6) spectra of a) ligand $\mathbf{L^A}$, b) heteroleptic coordination cage $Pd_2\mathbf{L^3}_2\mathbf{L^A}_2$ and c) ligand $\mathbf{L^3}$.

The coordination cage formation was also shown by ESI-MS, most prominent peaks were found for $[Pd_2\mathbf{L^3}_2\mathbf{L^A}_2]^{4+}$, $[Pd_2\mathbf{L^3}_2\mathbf{L^A}_2 + BF_4]^{3+}$, $[Pd_2\mathbf{L^3}_2\mathbf{L^A}_2 + 2\ BF_4]^{2+}$ (Figure 4.102).

Next, the cage formation of ligand $\mathbf{L^3}$ with the other shape complementary ligands $\mathbf{L^{B\text{-}D}}$ was tested. However, in all three cases a mixture of species was observed in the corresponding ^{1}H NMR spectra. Some prominent signals could be assigned to the protons around the coordination sphere as well as to the amide proton. A possible reason why $\mathbf{L^3}$ is not forming distinct heteroleptic species with those ligands cannot be given at this point since these results are still under investigation. Steric hindrance of the bulky endohedral moiety can be disregarded because clean cage formation with the even bulkier ligand $\mathbf{L^4}$ was observed with all of the ligands $\mathbf{L^{A\text{-}D}}$ (see chapter 3.2.4). Nevertheless, a peak of species $[Pd_2\mathbf{L^3}_2\mathbf{L^C}_2]^{4+}$ could be observed in the ESI-MS spectrum (Figure 4.107).

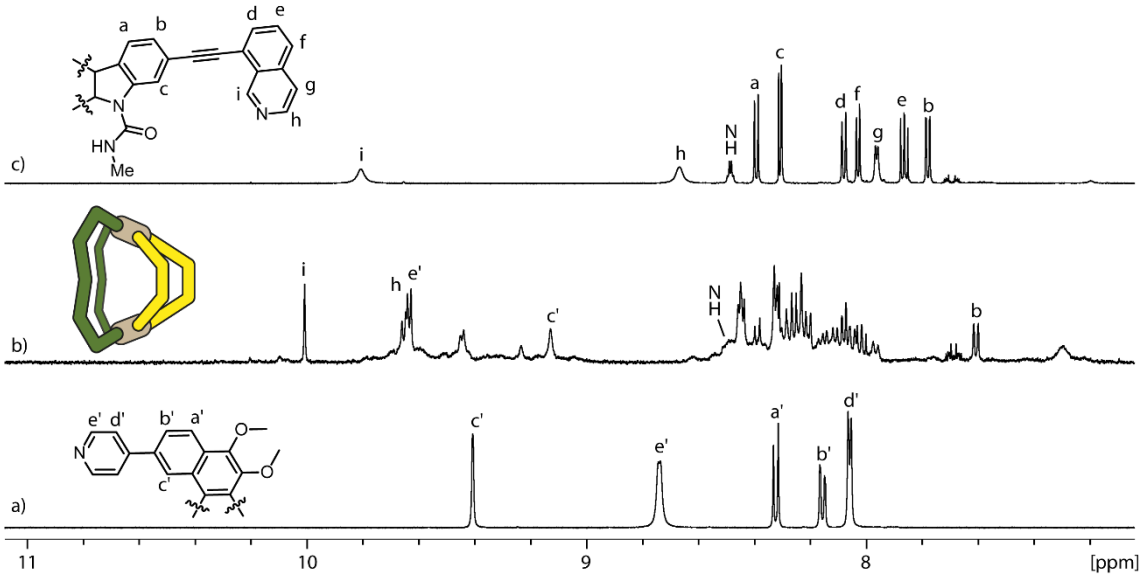

Figure 3.19: Partial ^{1}H NMR (DMSO-d_6) spectra of a) ligand $\mathbf{L^B}$, b) heteroleptic coordination cage $Pd_2\mathbf{L^3}_2\mathbf{L^B}_2$ and c) ligand $\mathbf{L^3}$.

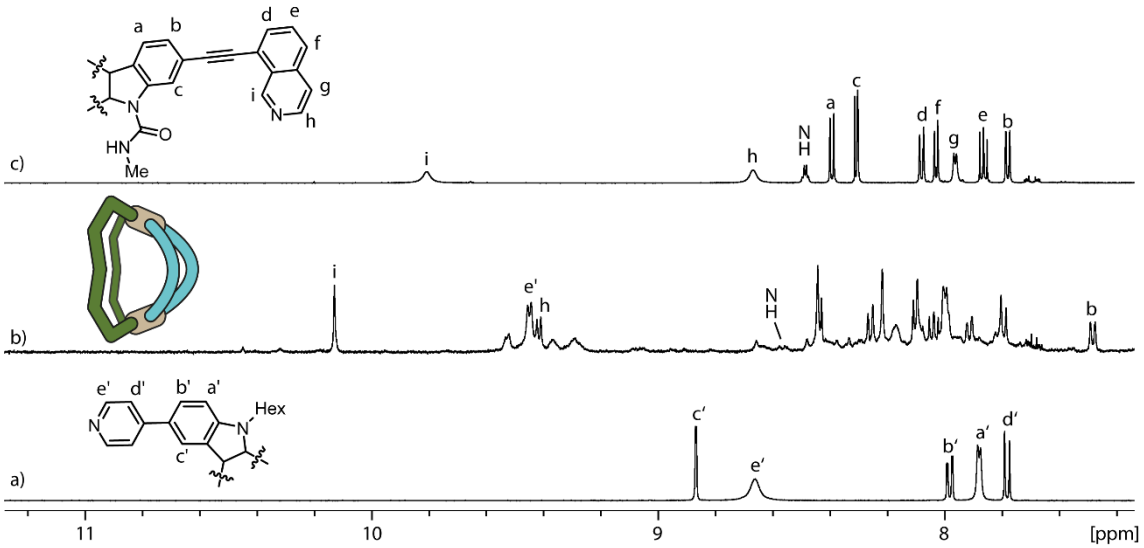

Figure 3.20: Partial ^{1}H NMR (DMSO-d_6) spectra of a) ligand $\mathbf{L^C}$, b) heteroleptic coordination cage $Pd_2\mathbf{L^3}_2\mathbf{L^C}_2$ and c) ligand $\mathbf{L^3}$.

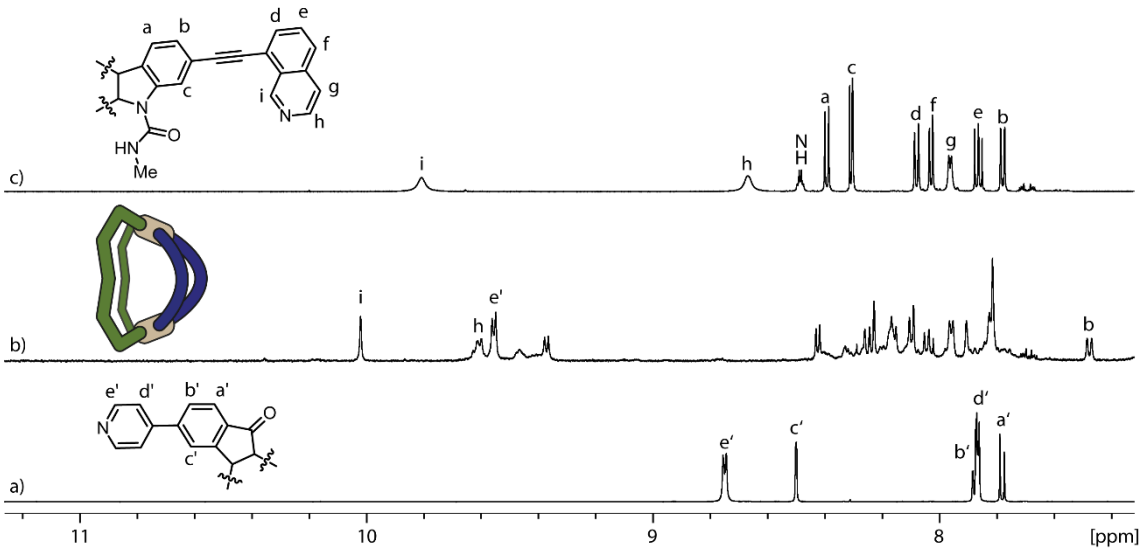

Figure 3.21: Partial ^{1}H NMR (DMSO-d_6) spectra of a) ligand $\mathbf{L^D}$, b) heteroleptic coordination cage $Pd_2\mathbf{L^3}_2\mathbf{L^D}_2$ and c) ligand $\mathbf{L^3}$.

3.2.4 Heteroleptic Coordination Cages with L^4

While combining ligand $\mathbf{L^4}$ with large ligand $\mathbf{L^A}$ a heteroleptic coordination cage was obtained and characterized by ^{1}H NMR spectroscopy (Figure 3.22). The spectrum is again comparable to the systems above, downfield shifts of the signals of the protons around the coordination sphere (h, i, e') are observed. The signal of the amide proton is also slightly shifted downfield and the signal of inward pointing proton c' shifts upfield.

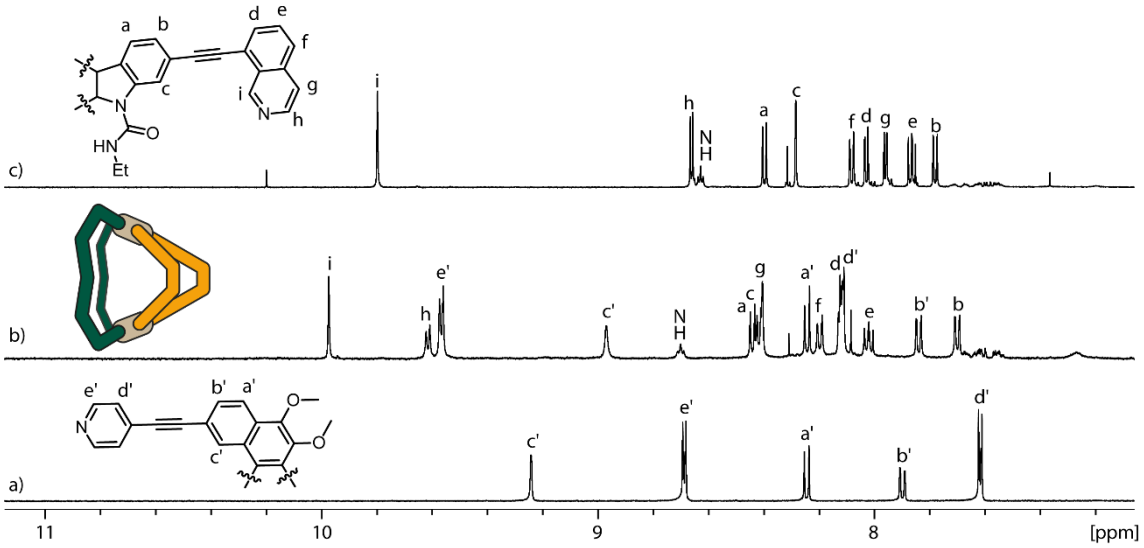

Figure 3.22: Partial ^{1}H NMR (DMSO-d_6) spectra of a) ligand $\mathbf{L^A}$, b) heteroleptic coordination cage $Pd_2\mathbf{L^4}_2\mathbf{L^A}_2$ and c) ligand $\mathbf{L^4}$.

The formation of the coordination cage was also confirmed by ESI mass spectrometry, namely the different charged species $[Pd_2\mathbf{L^4}_2\mathbf{L^A}_2]^{4+}$, $[Pd_2\mathbf{L^4}_2\mathbf{L^A}_2 + BF_4]^{3+}$, $[Pd_2\mathbf{L^4}_2\mathbf{L^A}_2 + 2\ BF_4]^{2+}$ were found (Figure 4.115).

Surprisingly, clean NMR spectra (Figure 3.23, Figure 3.24 and Figure 3.25) were obtained while mixing $\mathbf{L^4}$ with $\mathbf{L^{B\text{-}D}}$, considering the even more sterically demanding endohedral substituent at $\mathbf{L^4}$ compared to the results with $\mathbf{L^3}$ in the chapter above. In all three cases, downfield shifts of the signals of the protons around the coordination spheres (h, i, e') are observed as well as the upfield shift of the signal of the amide proton due to the already discussed shielding effect of the smaller cavity. The same effect is also shown by the upfield shifts of the signal of proton c' that points into the corresponding cavity.

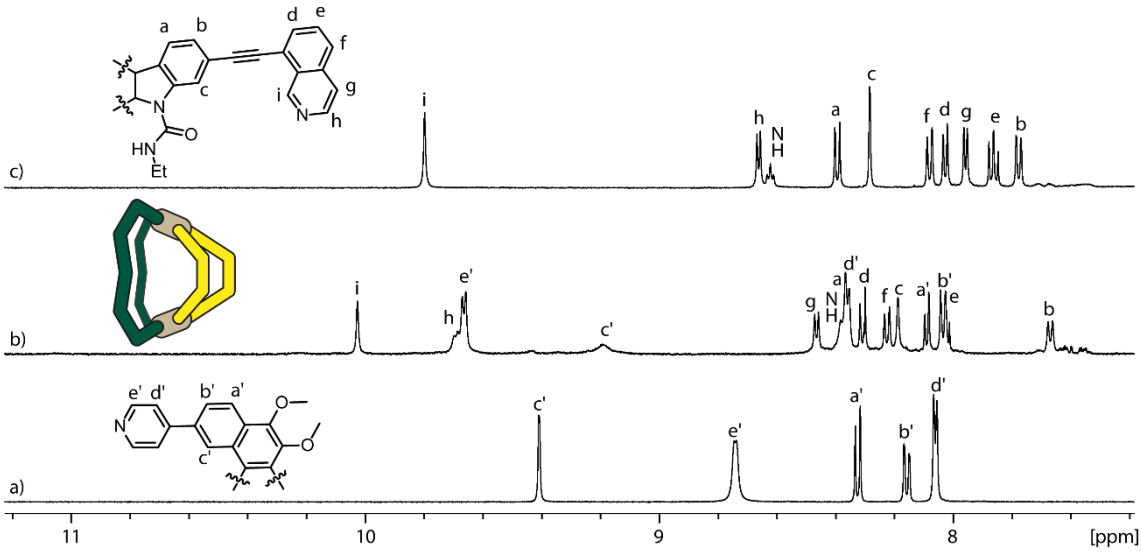

Figure 3.23: Partial ^{1}H NMR (DMSO-d_6) spectra of a) ligand $\mathbf{L^B}$, b) heteroleptic coordination cage $Pd_2\mathbf{L^4}_2\mathbf{L^B}_2$ and c) ligand $\mathbf{L^4}$.

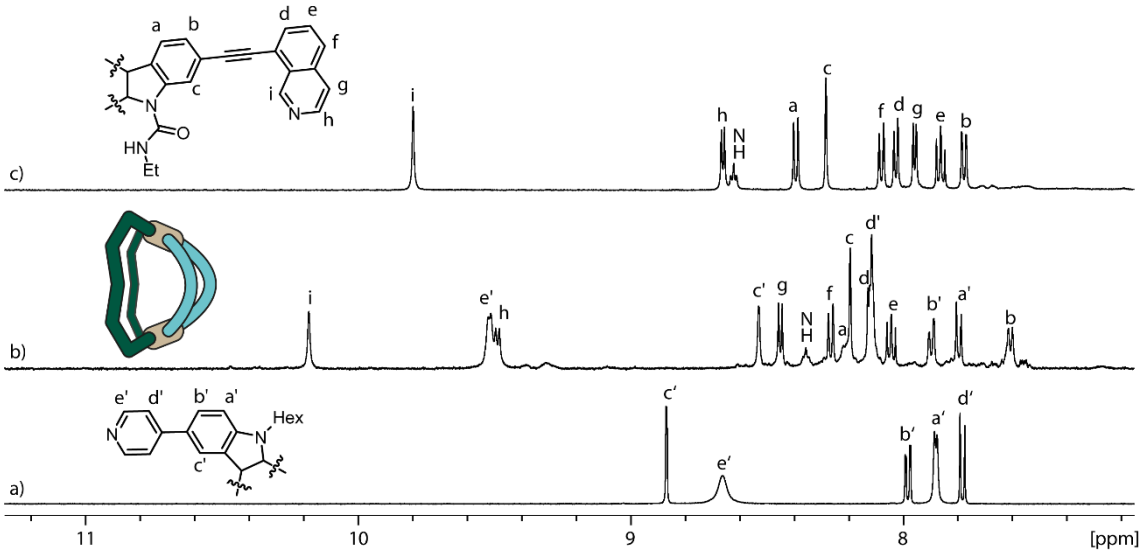

Figure 3.24: Partial ^{1}H NMR (DMSO-d_6) spectra of a) ligand $\mathbf{L^C}$, b) heteroleptic coordination cage $Pd_2\mathbf{L^4}_2\mathbf{L^C}_2$ and c) ligand $\mathbf{L^4}$.

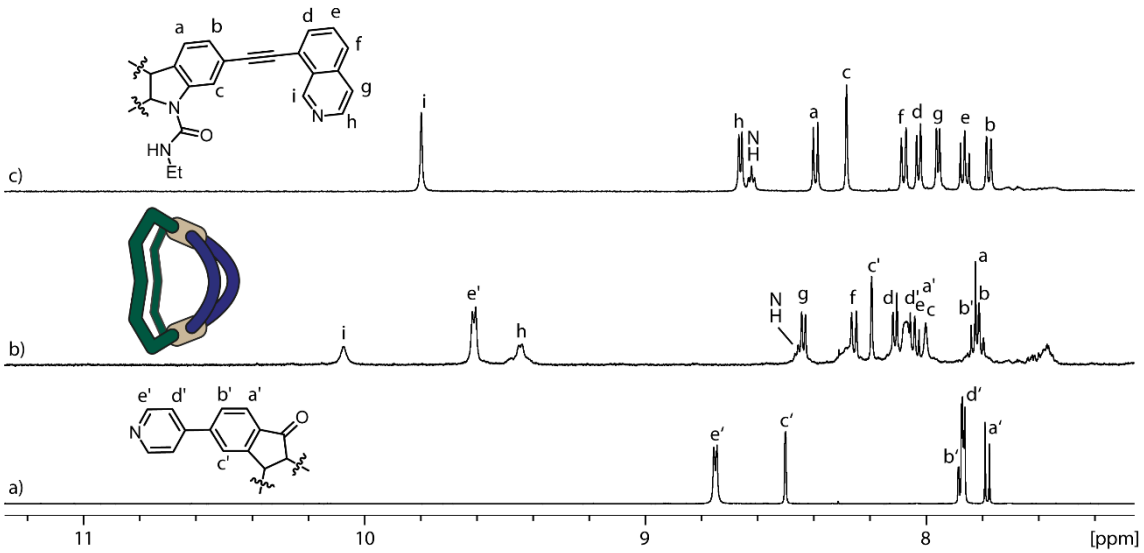

Figure 3.25: Partial ^{1}H NMR (DMSO-d_6) spectra of a) ligand $\mathbf{L^D}$, b) heteroleptic coordination cage $Pd_2\mathbf{L^4}_2\mathbf{L^D}_2$ and c) ligand $\mathbf{L^4}$.

All of these three heteroleptic cages were also observed in their ESI mass spectra (Figure 4.121, Figure 4.127 and Figure 4.133). Peaks of the species $[Pd_2\mathbf{L^4}_2\mathbf{L^{B\text{-}D}}_2]^{4+}$ and $[Pd_2\mathbf{L^4}_2\mathbf{L^C}_2 + BF_4]^{3+}$ could be found.

In summary, 16 novel heteroleptic coordination cages of the type $Pd_2\mathbf{L^{1\text{-}4}}_2\mathbf{L^{A\text{-}D}}_2$ were synthesized out of a modular toolbox of shape complementary ligands with on the one hand different endohedral functionalities ($\mathbf{L^{1\text{-}4}}$) and on the other hand different sizes and backbones ($\mathbf{L^{A\text{-}D}}$) to obtain cages with unique environments inside their cavities. All of these assemblies were characterized by NMR spectroscopy and ESI mass spectrometry as well as X-ray crystallography in the case of $Pd_2\mathbf{L^1}_2\mathbf{L^A}_2$, respectively.

3.3 Phosphate Binding

3.3.1 Principles of Host-Guest Chemistry

Guest interactions in supramolecular coordination cages have been studied extensively in the last decades.[1,18,77,114–117] In our group we mainly focus on the binding of anions inside our cationic cages.[36,65,69,112,118–120] In particular, strong binding of aromatic and aliphatic bis-sulfonates could be shown. For example, BLOCH could show in his work on heteroleptic $Pd_2\mathbf{A}_2\mathbf{B}_2$ coordination cages, that bent bis-sulfonate guest molecules have a higher binding affinity to the asymmetric hosts than linear ones.[36]

One powerful technique to characterize host-guest interactions in solution is NMR spectroscopy.[82,96,121,122] In principle, two different outcomes could be observed: slow (ms to s) and fast (ns to µs) guest exchange compared to the NMR timescale.[79,123] While in the fashion of slow guest exchange, two sets of signals, one for the free host **H** and one for the host-guest-complex **HG**, could be observed, only one averaged signal for the complex is visible in a fast exchange process. This signal is gradually shifted compared to the free host if more guest **G** is added to the solution.

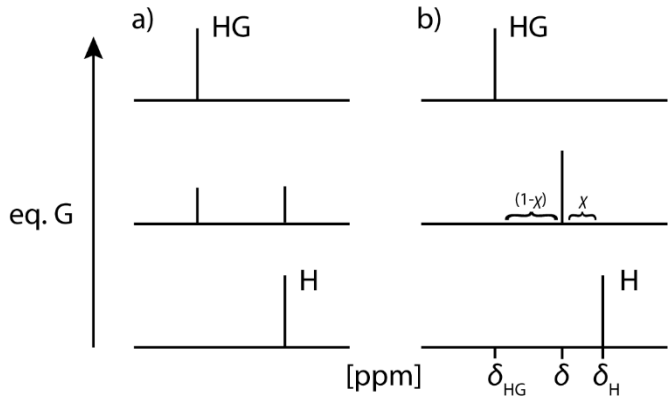

Figure 3.26: Comparison of NMR spectra of a supramolecular host-guest system in a) slow and b) fast exchange compared to the NMR timescale. With host **H**, guest **G**, host-guest complex **HG**, observed chemical shift δ, initial chemical shift of the host $\delta_{\mathbf{H}}$, chemical shift of the host-guest complex $\delta_{\mathbf{HG}}$ and the ratio of the complexed host at the equilibrium over the total host χ.

To characterize the binding affinity in a simple 1:1 system, the so-called binding or association constant K of the equilibrium equation can be determined:

$$\mathbf{H} + \mathbf{G} \overset{K}{\rightleftharpoons} \mathbf{HG}$$

Scheme 3.2: Equilibrium reaction of host **H** with guest **G** to host-guest complex **HG** with binding constant K.

Herein, *K* can be calculated by the equations (3.1-3.4)

$$K = \frac{[\mathbf{HG}]}{[\mathbf{H}][\mathbf{G}]} \tag{3.1}$$

$$[\mathbf{H}]_0 = [\mathbf{H}] + [\mathbf{HG}] \tag{3.2}$$

$$[\mathbf{G}]_0 = [\mathbf{G}] + [\mathbf{HG}] \tag{3.3}$$

$$\Rightarrow K = \frac{[\mathbf{HG}]}{([\mathbf{H}]_0 - [\mathbf{HG}]) \cdot ([\mathbf{G}]_0 - [\mathbf{HG}])} \tag{3.4}$$

with concentration of the free host [**H**], concentration of the free guest [**G**], concentration of the host-guest complex [**HG**], initial host concentration $[\mathbf{H}]_0$ and initial guest concentration $[\mathbf{G}]_0$.

In a fast exchange system, that is illustrated in Figure 3.26b, the chemical shift δ of **HG** appears at the weighted average of the chemical shift of the free host and the host-guest complex. To calculate [**HG**] equations (3.5) to (3.7) are used

$$\delta = \delta_{\mathbf{H}}(1 - \chi) + \delta_{\mathbf{HG}} \cdot \chi \tag{3.5}$$

$$\Rightarrow [\mathbf{H}]_0 \cdot (\delta - \delta_{\mathbf{H}}) = [\mathbf{HG}] \cdot (\delta_{\mathbf{HG}} - \delta_{\mathbf{H}}) \tag{3.6}$$

$$\Leftrightarrow [\mathbf{HG}] = \frac{[\mathbf{H}]_0(\delta - \delta_{\mathbf{H}})}{\delta_{\mathbf{HG}} - \delta_{\mathbf{H}}} \tag{3.7}$$

with observed chemical shift δ, initial chemical shift of the host $\delta_{\mathbf{H}}$, chemical shift of the host-guest complex $\delta_{\mathbf{HG}}$ and the ratio of the complexed host at the equilibrium over the total host χ. The herein investigated host-guest systems are all in a fast exchange compared to the ^{1}H NMR timescale. *K* was obtained by plotting the Δ of the chemical shifts of the cage signals against the guest concentration and the data was fitted by using the software Bindfit.[122,124,125]

Besides calculating the binding constant to describe guest affinity and selectivity to a supramolecule, obtaining the thermodynamic parameters (free GIBBS energy ΔG, enthalpy ΔH and entropy ΔS) is another criterium to investigate host-guest complexes. *K* is related to ΔG trough the temperature *T*:

$$\Delta G = -RT \ln K \tag{3.8}$$

with molar gas constant *R*. Using the GIBBS-HELMHOLTZ equation (3.9) and the VAN'T HOFF equation (3.10) the enthalpy and entropy of the binding process can be calculated:

$$\Delta G = \Delta H - T\Delta S \tag{3.9}$$

$$\ln K = -\frac{\Delta H}{RT} + \frac{\Delta S}{R} \tag{3.10}$$

Here, equation 3.10 is of the type y = mx+b so it describes a straight line if ln K is plotted against T^{-1} where the offset is determined by the entropic term and the slope by the enthalpic one. With this technique one could easily get access to these parameters only by measuring the association constant at variable temperature.

3.3.2 Phosphate Esters and Phosphate Recognition

Phosphates are salts or esters of phosphoric acid and consisting of four oxygen atoms and a phosphorus atom in the oxidation state +V. Phosphate ester molecules can be produced by the reaction of the acid with alcohols and depending on the stoichiometry mono-, di- and triesters could be obtained. Organophosphates can be found in a numerous amount in nature, for example in biomolecules like nucleic acids, lipids, proteins and sugars as well as in form of hydroxyapatite in biominerals.[126,127]

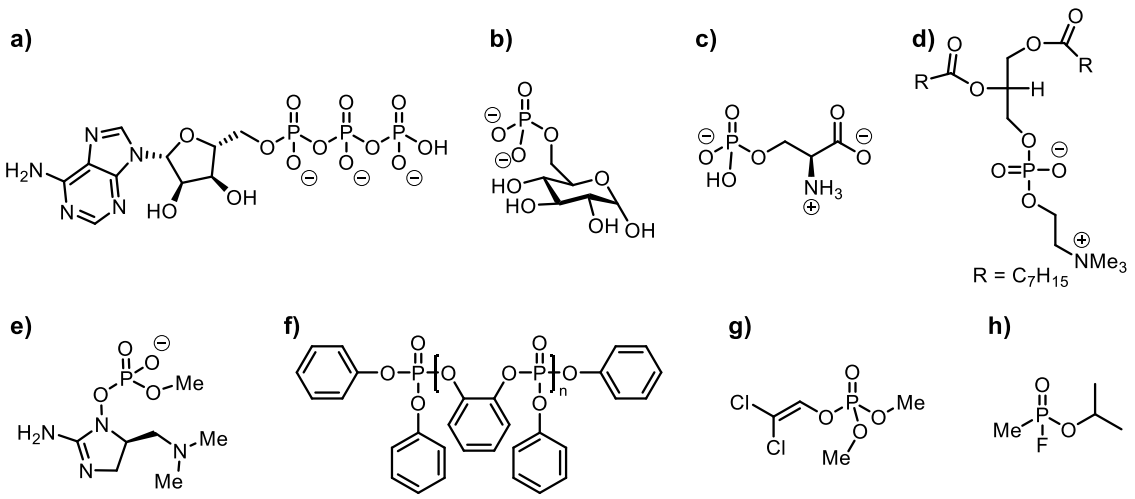

Scheme 3.3: Chemical structures of naturally available and synthetic organophosphates.

ATP (adenosine triphosphate, **a**) is a nucleotide that is responsible for energy transfer and regulation in cells. Phosphorylated sugars like D-Glucose-6-phosphate **b**) are common

metabolites in cellular processes like the glycolysis of glucose. Phosphoserine **c**) is an example of a phosphorylated amino acid that is found in several proteins. DOPC **d**) is a representative of phospholipids that are forming cell membranes and lipid bilayers due to its amphiphilic character. As a last example for naturally available phosphates guanitoxin **e**) is shown, that is produced by cyanobacteria.[128] Besides the natural occurrence, phosphate esters are broadly common in synthetic and industrial products like pesticides, fertilizers, flame retardants and nerve agents.[129–134] Polyphosphate **f**) is broadly used as a flame retardant due to its high melting point, dichlorvos **g**) is a widely used and highly potent insecticide and organophosphonate sarin **h**) is a nerve agent that was used as a chemical weapon in World War II and acts as an acetylcholinesterase inhibitor.

In the last decades, scores of synthetic receptors for the recognition of phosphate esters have been described.[135–141] Environmental pollution, e.g. water contamination by fertilizers and therefore an increase of algae growth caused by phosphates zoomed up a lot in the past decades, phosphate receptors are already broadly used by industry.[142] The receptor molecules can be distinguished by their recognition mode of the phosphates, for example charge-charge interactions, hydrogen-bonding, macrocyclic interactions or the coordination by several metals are described in the literature. Besides these synthetic receptors, phosphates can also be recognized by specific proteins in nature.[143–145]

The first described organic receptors for phosphates were polyammonium cations. These molecules were especially used to bind nucleotides AMP, ADP and ATP in aqueous solutions.[146–149]

Another extensively studied compound class of phosphate receptors are amide- and urea-based systems that are able to form hydrogen bonds to the anion.[142]

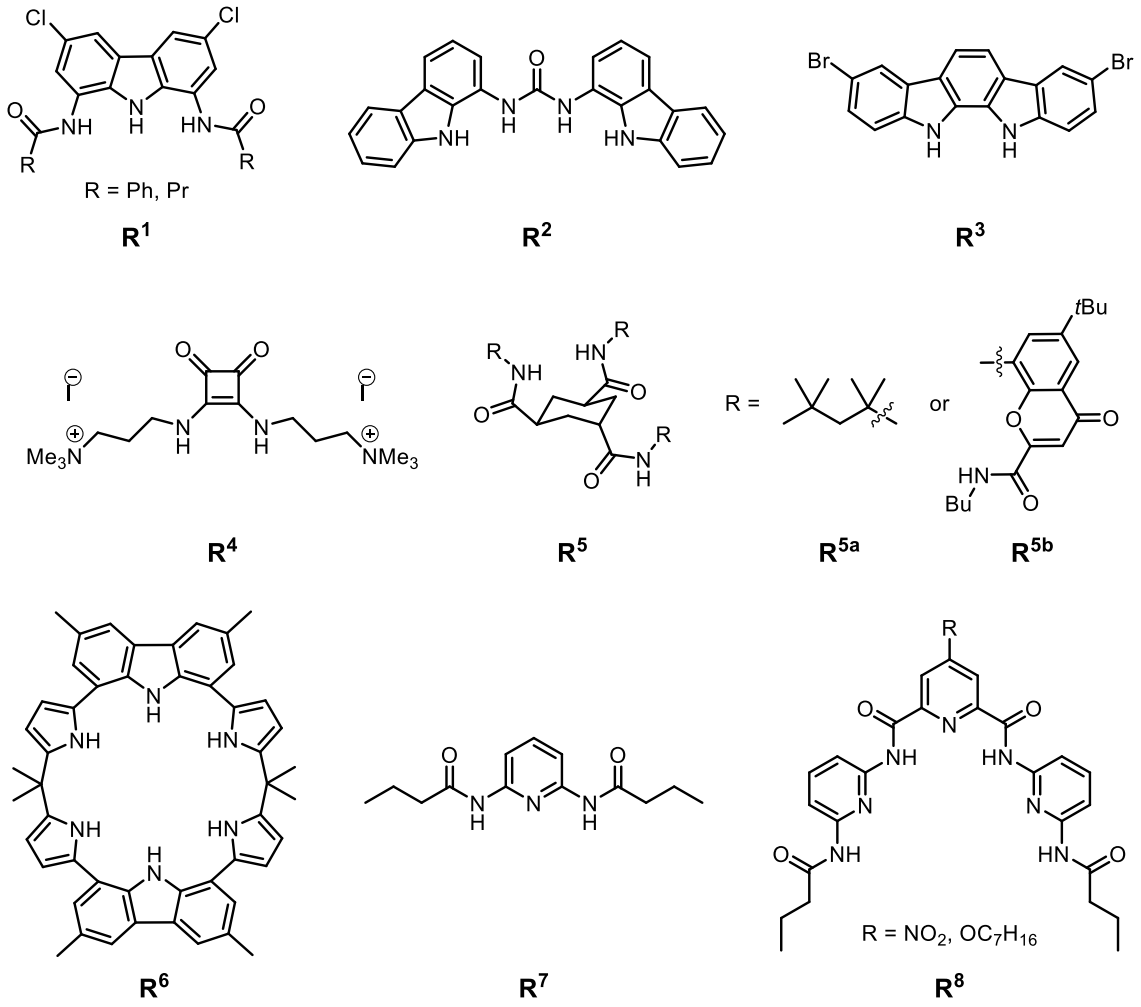

Scheme 3.4: Chemical structures of receptor molecules **R**[1]-**R**[8].

Receptor **R**[1] was reported by the group of JURCZAK in 2004 and featuring beside the amide functionalities a carbazole moiety to act as hydrogen bond donors.[150] It was shown that this molecule was able to bind $H_2PO_4^-$ selectively with a 5000-fold higher binding constant over chloride in a DMSO/H_2O mixture. This was reasoned by the size of the groove of the receptor that is too wide for the chloride anion.

In 2009 the group of GALE reported a series of receptor molecules based on a urea moiety.[151] **R**[2] is additionally equipped with two carbazole moieties attached to the urea backbone and acts as a sensor for different anions, including dihydrogen phosphate. It was shown that the fluorescence of **R**[2] decreased upon addition of $H_2PO_4^-$.

Receptor **R**[3] also consisting of a carbazole moiety was published by the group of BEER in 2004 as part of a series of indolocarbazole sensors.[152] With NMR titration experiments in acetone it was shown that $H_2PO_4^-$ was recognized with an association constant of log K = 5.3 M^{-1} stronger than fluoride, chloride or hydrogen sulfate. A derivative of **R**[3]

(methyl groups instead of the bromine atoms) also acts as a fluorescent sensor with $H_2PO_4^-$ enhancing the emission.

Another interesting class of receptors are composed of square amide motifs and were reported by the group of COSTA in 2004.[153] In a 9:1 mixture of ethanol and water an association constant of $K = 2.2 \cdot 10^4\ M^{-1}$ for HPO_4^{2-}@**R**^{4} was determined, however the receptor was found to be more selective for sulfate anions.

One of the first amide-based receptors for phosphates are the triangular molecules **R**^{5a} and **R**^{5b} reported by the group of RAPOSO in 1995.[154] They could show that the association of propylphosphonate to **R**^{5a} is quite weak in $CDCl_3$. However, using **R**^{5b} that has additional hydrogen bond donor site lead to an increase of the association constants for propyl- and phenylphosphonate. Changing the solvent to more polar DMSO or methanol yields again in an increase of K. Additionally, the recognition of PO_4^{3-} by **R**^{5b} was followed by NMR titration in DMSO and gave the in this work highest reported association constant of $K > 10^5\ M^{-1}$. This was explained by the high charge and the additional hydrogen bond acceptor sites.

SESSLER et al. reported a series of macrocyclic anion receptors in the last years with **R**^{6} as an example that comprises of carbazole and pyrrole units.[155] It was shown that this receptor was able to form emissive 1:1 complexes with a numerous amount of anions, including dihydrogen phosphate and hydrogen pyrophosphate, respectively. Binding constants in the range of $K = 7 \cdot 10^4\ M^{-1}$ were reported for the phosphates, however the receptor showed the highest affinity for carboxylates.

The amidopyridyl receptors **R**^{7} and **R**^{8} were reported by the group of HAMILTON in 1992.[156] They investigated the binding of different mono- and diphosphate esters to the receptor molecules with NMR and UV/Vis titration experiments. It was shown, that bis-(4-nitrophenyl)-phosphate was forming a 1:1 complex with **R**^{7} and a 2:1 with **R**^{8}. Titration of the monoester dodecylphosphate to **R**^{7} led to a binding constant of $K = 2.8 \cdot 10^4\ M^{-1}$ in chloroform.

Beside these examples of fully organic and quite flexible phosphate receptors, a large number of metal-containing receptor molecules were reported, a selection is shown in Scheme 3.5.

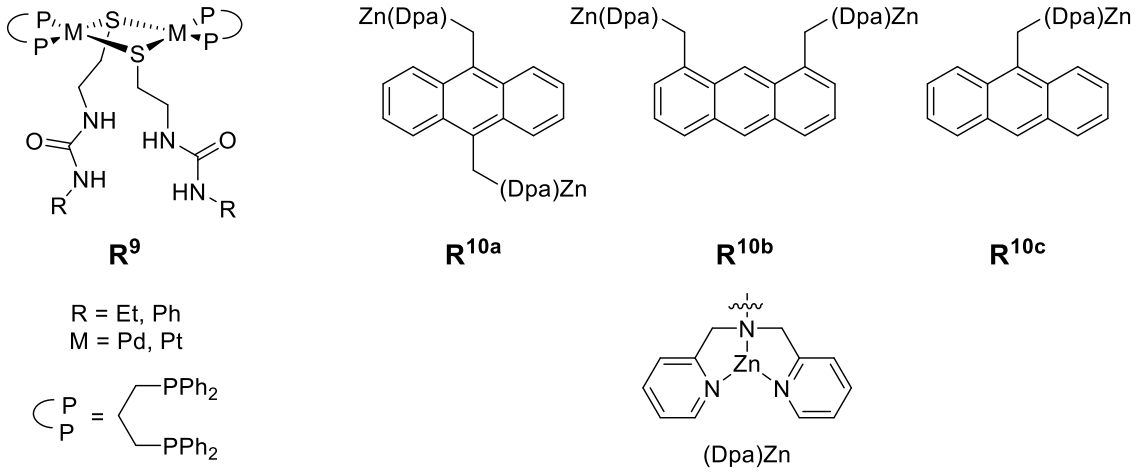

R^{9} **R**^{10a} **R**^{10b} **R**^{10c}

Scheme 3.5: Chemical structures of receptor molecules **R**^{9} and **R**$^{10a-c}$.

In the 2000s the group of VILAR reported dinuclear palladium and platinum compounds bridged by sulfides yielding receptor molecules **R**^{9} with urea motifs as hydrogen bond donor sites.[157–159] With NMR titration experiments in DMSO-d_6 it was shown that **R**^{9} with M = Pd shows a selectivity for the recognition of dihydrogen phosphate and phenylphosphate over anions like bromide or hydrogen sulfate with a binding constant of log K = 3.4 M^{-1} for the organophosphate. Since it was observed that the palladium complexes were not stable for long, the more stable platinum containing receptors were synthesized. The binding affinity for the investigated phosphates did not change significantly.

The group of HAMACHI showed that zinc(II) dipicolylamine (Zn(Dpa), **R**$^{10a-c}$) could be used as a phosphate receptor, in particular for oligopeptides containing phosphorylated amino acids.[160–167] On the other hand, also the selective recognition of inorganic phosphate and methylphosphate in water over anions like carbonate and acetate was shown for receptor **R**^{10a}. Furthermore, an association constant of $K = 2.2 \cdot 10^6$ M^{-1} was obtained via ^{31}P NMR titration experiments for ATP@**R**^{10a}, which binds stronger than ADP or AMP due to its higher charge. Similar results and association constants were observed for receptor **R**^{10b}. However, with receptor **R**^{10c} lower association constants (1-2 magnitudes) were obtained since this molecule features only one Zn(Dpa) binding motif. Additionally, HAMACHI et al. could show that **R**^{10a} and **R**^{10b} were able to recognize peptide sequences that consists out of 8-9 amino acids with one of these was phosphorylated. No association was found for non-phosphorylated peptides.

While organic receptor molecules for organophosphates are extensively studied, only a few examples for coordination cages that incorporate phosphates as guest molecules were shown in the past. For example, WARD et al. reported a highly charged cubic $[Co_8L_{12}]^{16+}$ coordination cage that acts as a host for several alkylphosphonates as simulants for nerve agents like sarin.[168] However, the reported binding constants in acetonitrile or water obtained by NMR and luminescence titrations were quite low in the range of $K \approx 10$ to 400 M^{-1}. The group also reported binding studies of organophosphates that are used as insecticides in their cubic coordination cage.[169] They further investigated the hydrolysis of dichlorvos that is one order of magnitude higher if the guest is bound to the coordination cage.

Additionally, in 2013 the group of NITSCHKE presented a water-soluble Fe_4L_6 tetrahedral coordination cage that was able to bind neutral guest molecules, including dichlorvos.[170] Further, the hydrolysis of this guest was demonstrated to be more effective if the host was present.

In 2020 LUSBY et al. reported a Pd_2L_4 coordination cage that was able to incorporate benzoquinone as a guest in the cages' cavity.[171] However, they could show that the association of $Ph_3P(O)$ at the metal centres outside the coordination cage modulates the binding affinity of the guest molecule as well as the catalytic properties of the host-guest-system.

One advantage to use coordination cages for anion recognition and binding instead of (fully) organic receptors is the rigidity of the system. The size and shape of the binding site is more predictable inside a cage structure and therefor the selectivity for a particularly shaped anion is much higher. Another benefit for using coordination cages is that the synthetic effort is mostly lower and ligands can be easily functionalized and replaced according to the necessities. Therefore, the modular system of heteroleptic coordination cages presented and described in the previous chapters was proposed to act as a suitable host of organophosphate esters.

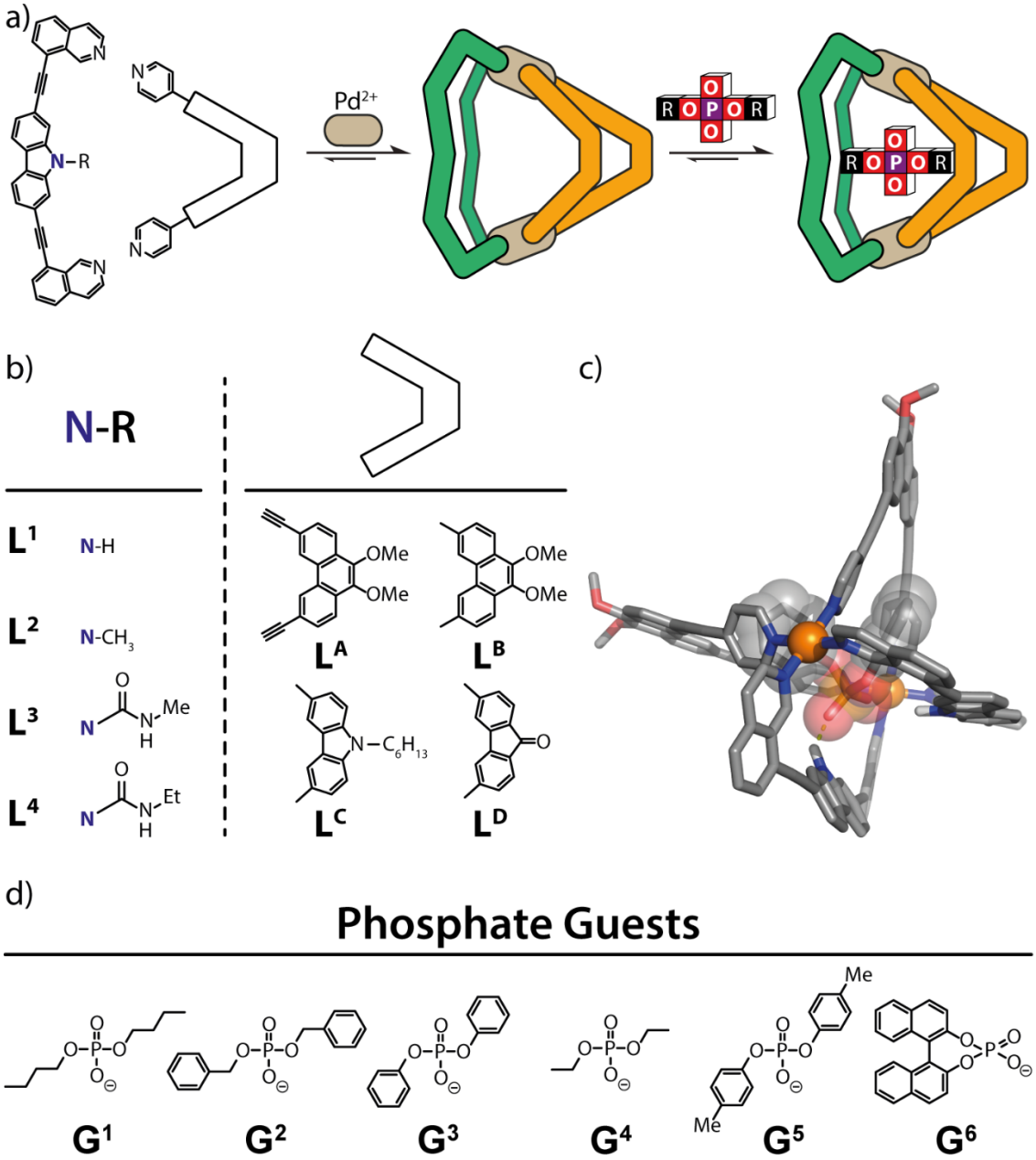

Figure 3.27: a) Formation of heteroleptic coordination cages and uptake of phosphate esters, b) modular ligand toolbox, c) MD-simulated structure of $\mathbf{G^3}@Pd_2\mathbf{L^1}_2\mathbf{L^A}_2$ and d) investigated phosphate guests $\mathbf{G^{1\text{-}6}}$.

In the following chapters the modularity of the system will be used to investigate the effects of H-bond donors and cavity size to the binding affinity of phosphate ester $\mathbf{G^3}$ (Figure 3.27). Furthermore, the effect of different residue moieties attached to the phosphate (aliphatic and aromatic groups) on the binding strength was evaluated.

3.3.3 Cavity Size Variation

While titrating $\mathbf{G^3}$ into a solution of $Pd_2\mathbf{L^1}_2\mathbf{L^A}_2$ in DMSO-d_6 continuous shifts of the signals in the ^{1}H NMR spectrum were observed (Figure 3.28). Most prominent downfield

shift was observed for the signal of the NH proton as well as a broadening, indicating the formation of a hydrogen bond to the guest molecule, most likely to one of the phosphate oxygen atoms. Another strong evidence for inside guest binding is given by the shifts of the signals of inward pointing protons by guest addition, e.g. protons c, i, c' and e'. Furthermore, crosspeaks between the phenyl proton signals of $\mathbf{G^3}$ and the signals of proton c' and d' could be found in a ^{1}H–^{1}H-NOESY NMR spectrum (Figure 4.160). This also shows that the phosphate is most likely orientated with its phenyl backbones to the phenanthrene ligand $\mathbf{L^A}$. forming π-π-interactions. As it was mentioned above, the guest binds in a fast exchange fashion to the host compared to the NMR timescale. From the analysis of $\Delta\delta$ against the guest concentration with the software Bindfit a binding constant of K = 2062 ± 31 M^{-1} was obtained. Since DMSO-d$_6$ is known to be a strong competitor in regards of hydrogen bonding the titration was also performed in DMF-d$_7$ which led to a similar binding constant of K = 1734 ± 97 M^{-1} (Figure 4.185).

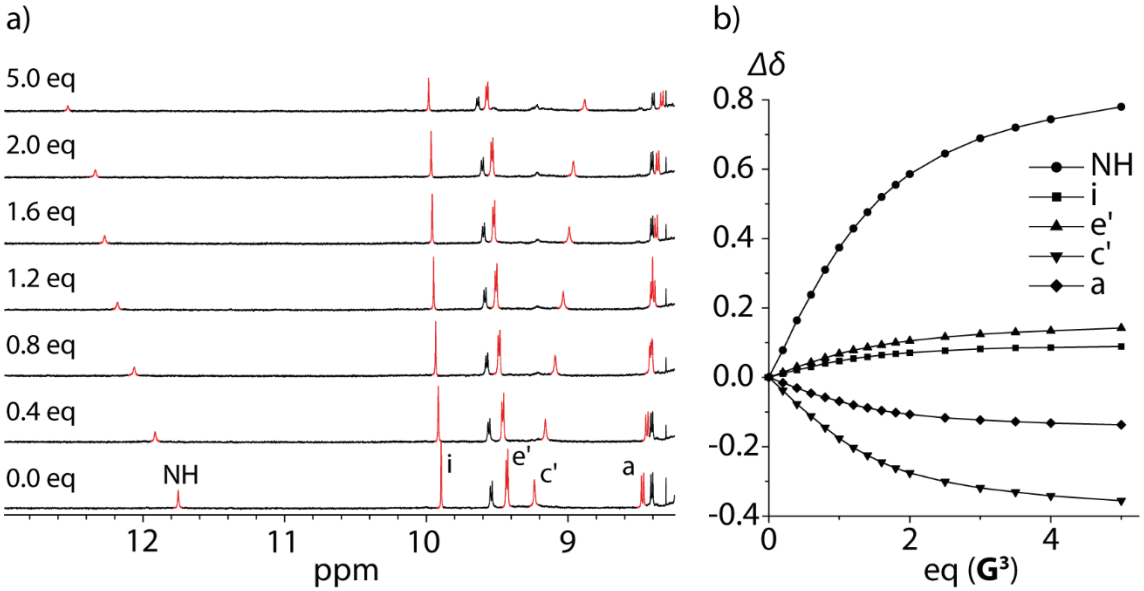

Figure 3.28: a) Stacked partial ^{1}H NMR spectra (500 MHz, DMSO-d$_6$) of the titration of $\mathbf{G^3}$ to $Pd_2\mathbf{L^1}_2\mathbf{L^A}_2$ and b) plot of $\Delta\delta$ of selected proton signals against guest concentration.

In addition, single crystals suitable for X-ray diffraction of $\mathbf{G^3}$@$Pd_2\mathbf{L^1}_2\mathbf{L^A}_2$ were obtained from slow vapor diffusion of Et_2O into the solution of the host-guest complex in DMF. Surprisingly, the phosphate ester guest molecule was not found inside the cavity, but two guest molecules are closely stacked each on top of the Pd−Pd axis of the cage interacting with the Pd atoms from the outside. Inside the cavity, two BF_4^- anions are located, exactly at the same position as for the structure of $Pd_2\mathbf{L^1}_2\mathbf{L^A}_2$ forming hydrogen bonds with the NH protons. In addition, two DMF molecules could be found again in the same position

like for the empty cage structure, pointing to the palladium atoms with their oxygen atoms.

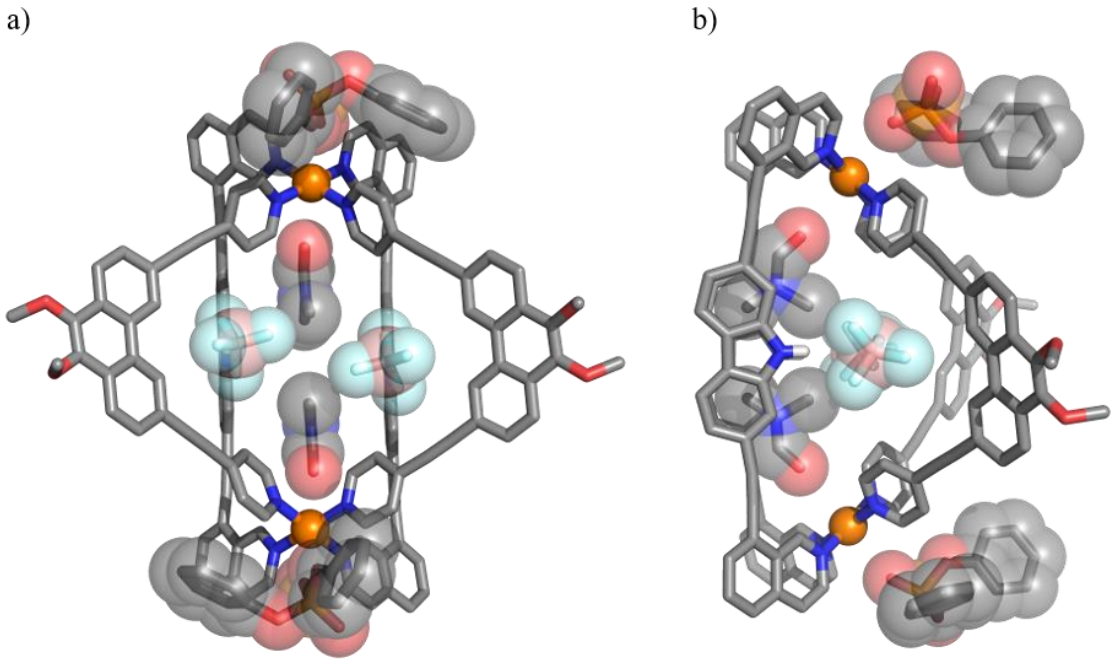

Figure 3.29: Molecular structure of $\mathbf{G^3}@Pd_2\mathbf{L^1}_2\mathbf{L^A}_2$ in the solid state, determined by X-ray diffraction, a) front and b) side view.

The guest uptake was also confirmed by ESI mass spectrometry (Figure 3.30a). Peaks for the host-guest complex, namely $[Pd_2\mathbf{L^1}_2\mathbf{L^A}_2 + \mathbf{G^3}]^{3+}$, $[Pd_2\mathbf{L^1}_2\mathbf{L^A}_2 + BF_4 + \mathbf{G^3}]^{2+}$ and $[Pd_2\mathbf{L^1}_2\mathbf{L^A}_2 + 2\ \mathbf{G^3}]^{2+}$ could be assigned. To confirm that the guest is located inside the cages´ cavity, ion mobility spectra of the empty host and the host-guest complex were recorded (in collaboration with L. SCHNEIDER and C. DRECHSLER) (Figure 3.30b). For the empty cage an experimental collisional cross section (eCCS) of 595.1 $Å^2$ was obtained whereas the eCCS value for the host-guest complex slightly increased to 603.7 $Å^2$. A comparison with the theoretically obtained collisional cross sections (tCCS) revealed the same trend (Table 4.3). Furthermore, the simulation of the complex where the phosphate guest was placed outside the cavity gave a tCCS of 688.8 $Å^2$ to show that the guest binding is most likely inside the cavity.

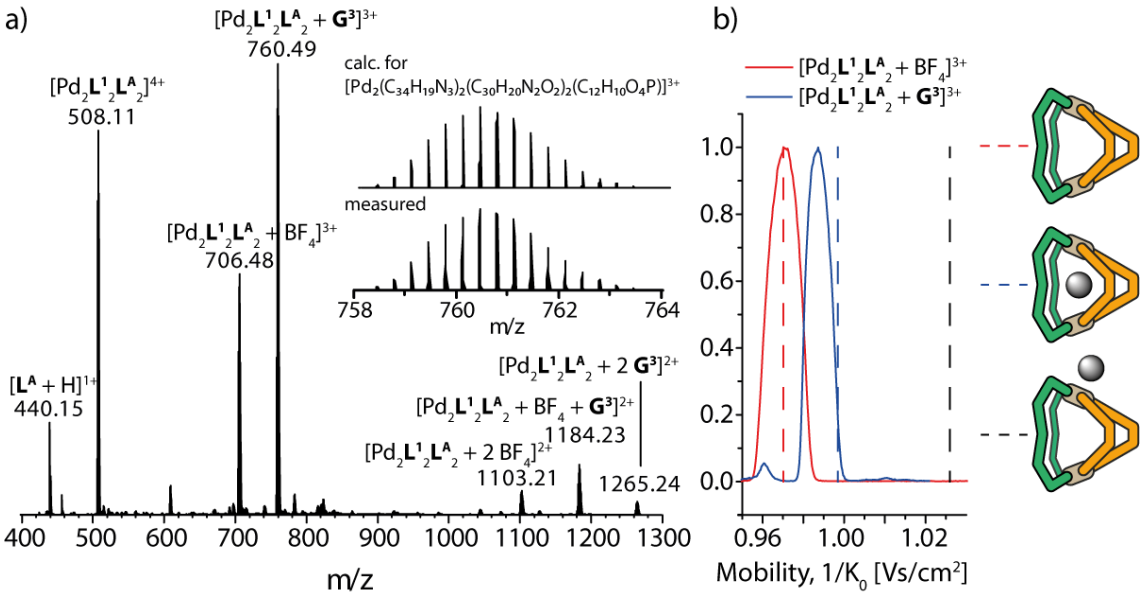

Figure 3.30: a) ESI-MS spectrum of [$\mathbf{G^3}$@$Pd_2\mathbf{L^1}_2\mathbf{L^A}_2$], b) experimental ion mobilities of [BF_4@$Pd_2\mathbf{L^1}_2\mathbf{L^A}_2$]$^{3+}$ (solid red line) and [$\mathbf{G^3}$@$Pd_2\mathbf{L^1}_2\mathbf{L^A}_2$]$^{3+}$ (solid blue line) and theoretically determined mobilities of [BF_4@$Pd_2\mathbf{L^1}_2\mathbf{L^A}_2$]$^{3+}$ (dashed red line) and [$\mathbf{G^3}$@$Pd_2\mathbf{L^1}_2\mathbf{L^A}_2$]$^{3+}$ (dashed blue line) compared to the mobility of complex where $\mathbf{G^3}$ is placed outside of [$Pd_2\mathbf{L^1}_2\mathbf{L^A}_2$]$^{4+}$ (dashed black line). The theoretical values were scaled by a factor of 0.934.

To study the effect of the cavity size on the guest binding, the ^{1}H NMR titration experiment of $\mathbf{G^3}$ to $Pd_2\mathbf{L^1}_2\mathbf{L^B}_2$ was performed. Like for the first titration experiment, shifts of the signals of the inward pointing cage protons could be observed. For example, the signal of the NH proton shifts downfield gradually upon guest addition, but the $\Delta\delta$ of about 0.2 ppm is much lower compared to $\mathbf{G^3}$@$Pd_2\mathbf{L^1}_2\mathbf{L^A}_2$. This could be already an indication for a lower binding affinity. Also, the observed shifts of the other signals of interest are way lower. Here, the signal of proton c' is shifting downfield. A possible reason could be the more shielding effect due to the smaller cavity. From the fit of the binding isotherms with Bindfit a binding constant of $K = 98 \pm 1$ M^{-1} was obtained.

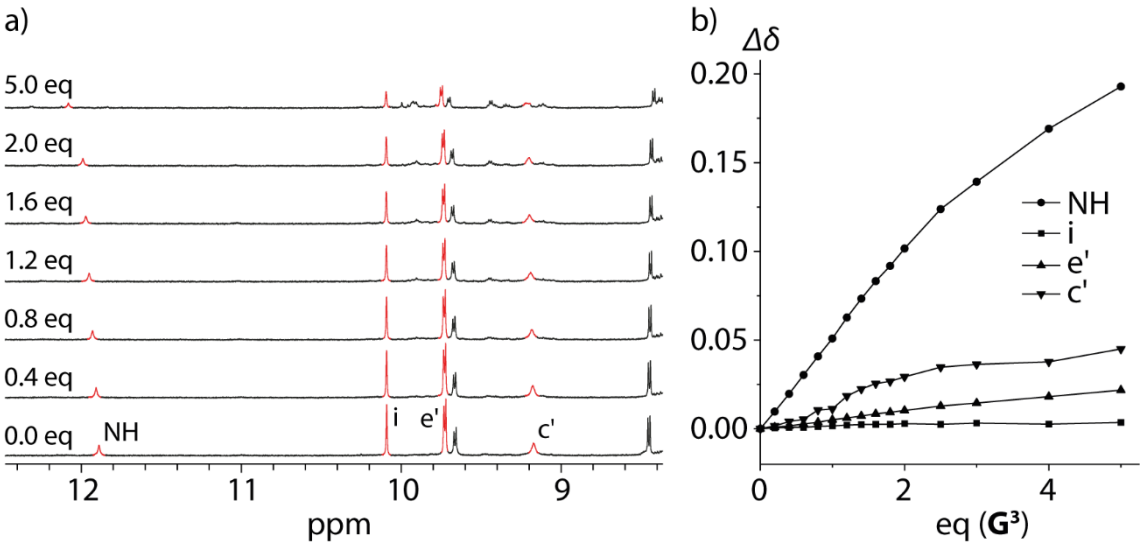

Figure 3.31: a) Stacked partial ^{1}H NMR spectra (500 MHz, DMSO-d_6) of the titration of $\mathbf{G^3}$ to $Pd_2\mathbf{L^1}_2\mathbf{L^B}_2$ and b) plot of $\Delta\delta$ of selected proton signals against guest concentration.

The formation of the host-guest complex was also confirmed by ESI mass spectrometry (Figure 4.173). Most prominent peaks were obtained for following charged species of the host-guest complex: $[Pd_2\mathbf{L^1}_2\mathbf{L^B}_2 + \mathbf{G^3}]^{3+}$, $[Pd_2\mathbf{L^1}_2\mathbf{L^B}_2 + BF_4 + \mathbf{G^3}]^{2+}$ and $[Pd_2\mathbf{L^1}_2\mathbf{L^B}_2 + 2\ \mathbf{G^3}]^{2+}$. Ion mobility studies showed an eCCS of 545.6 Å^2 for the empty host and an eCCS of 549.2 Å^2 for the host-guest complex, showing the comparable slight increase of the ion size and therefor showing the inside binding of $\mathbf{G^3}$ (Figure 4.189).

Next, the ^{1}H NMR titration experiment of $\mathbf{G^3}$ to $Pd_2\mathbf{L^1}_2\mathbf{L^C}_2$ was performed. Slight shifting of the signals of the inward pointing protons was observed, as well as a slight downfield shift of the signal of the NH proton of $\Delta\delta \approx 0.1$ ppm upon 5 eq addition of $\mathbf{G^3}$. This indicates an even lower binding affinity of $\mathbf{G^3}$@$Pd_2\mathbf{L^1}_2\mathbf{L^C}_2$ compared to $\mathbf{G^3}$@$Pd_2\mathbf{L^1}_2\mathbf{L^B}_2$. Fitting of the binding isotherms lead to a binding constant of $K = 33 \pm 1\ M^{-1}$. The addition of 5 eq guest lead also to a partial disassembly of the coordination cage.

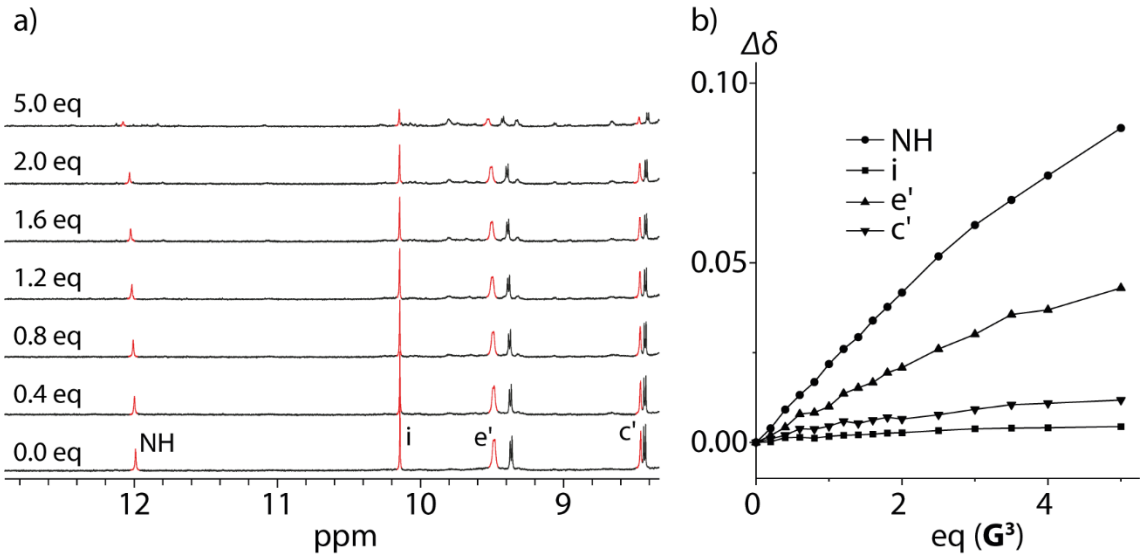

Figure 3.32: a) Stacked partial ^{1}H NMR spectra (500 MHz, DMSO-d_6) of the titration of $\mathbf{G^3}$ to $Pd_2\mathbf{L^1}_2\mathbf{L^C}_2$ and b) plot of $\Delta\delta$ of selected proton signals against guest concentration.

The formation of the host-guest complex was also confirmed by ESI mass spectrometry (Figure 4.175). Most prominent peaks were obtained for following charged species of the host-guest complex: $[Pd_2\mathbf{L^1}_2\mathbf{L^C}_2 + \mathbf{G^3}]^{3+}$, $[Pd_2\mathbf{L^1}_2\mathbf{C}_2 + BF_4 + \mathbf{G^3}]^{2+}$ and $[Pd_2\mathbf{L^1}_2\mathbf{L^C}_2 + 2\ \mathbf{G^3}]^{2+}$. Ion mobility studies showed an eCCS of 555.1 Å^2 for the empty host and an eCCS of 562.7 Å^2 for the host-guest complex, showing the comparable slight increase of the ion size and therefor showing the inside binding of $\mathbf{G^3}$ (Figure 4.190).

In a last experiment of this series, $\mathbf{G^3}$ was titrated to $Pd_2\mathbf{L^1}_2\mathbf{L^D}_2$ followed by ^{1}H NMR spectroscopy. The observed slight shift of the signal of the NH proton ($\Delta\delta \approx 0.2$ ppm) indicates again a lower binding constant compared to $\mathbf{G^3}$@$Pd_2\mathbf{L^1}_2\mathbf{L^A}_2$. Slight downfield shifting of the signals of the inward pointing protons and the protons around the coordination sphere, respectively, was also observed. Interestingly, the signal of proton i does not shift at all as it was observed for the other host-guest titration experiments.

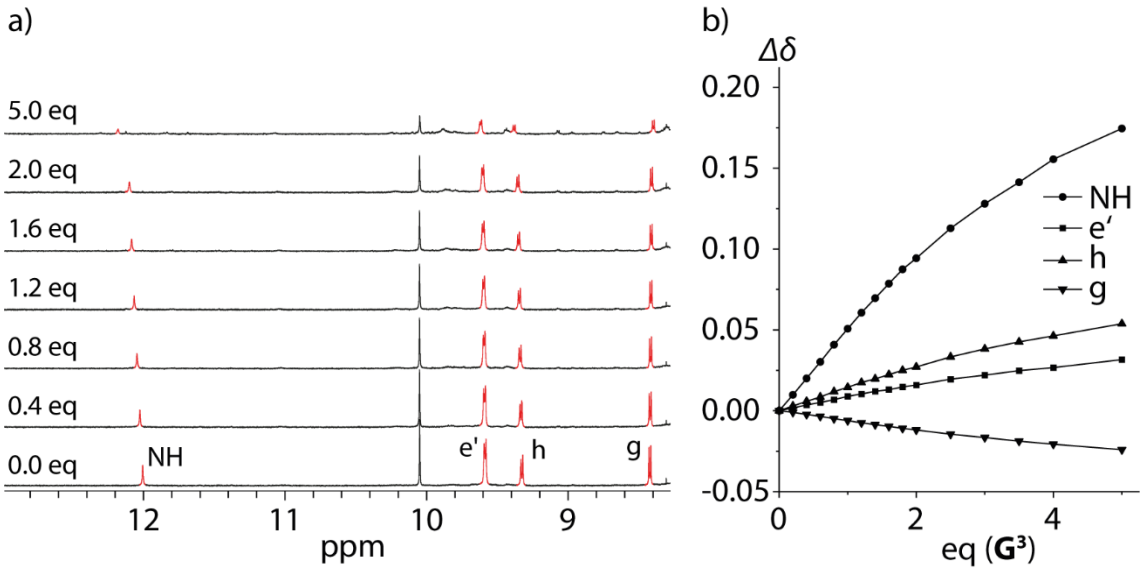

Figure 3.33: a) Stacked partial ^{1}H NMR spectra (500 MHz, DMSO-d_6) of the titration of $\mathbf{G^3}$ to $Pd_2\mathbf{L^1}_2\mathbf{L^D}_2$ and b) plot of $\Delta\delta$ of selected proton signals against guest concentration.

The formation of the host-guest complex was also confirmed by ESI mass spectrometry (Figure 4.177). Most prominent peaks were obtained for following charged species of the host-guest complex: $[Pd_2\mathbf{L^1}_2\mathbf{L^D}_2 + \mathbf{G^3}]^{3+}$, $[Pd_2\mathbf{L^1}_2\mathbf{L^D}_2 + BF_4 + \mathbf{G^3}]^{2+}$ and $[Pd_2\mathbf{L^1}_2\mathbf{L^D}_2 + 2\ \mathbf{G^3}]^{2+}$. Ion mobility studies showed an eCCS of 555.1 Å^2 for the empty host and an eCCS of 562.7 Å^2 for the host-guest complex, showing the comparable slight increase of the ion size and therefor showing the inside binding of $\mathbf{G^3}$ (Figure 4.191).

Table 3.1: Overview of binding constants K for encapsulation of $\mathbf{G^3}$.

$\mathbf{G^3}$@	$Pd_2\mathbf{L^1}_2\mathbf{L^A}_2$	$Pd_2\mathbf{L^1}_2\mathbf{L^B}_2$	$Pd_2\mathbf{L^1}_2\mathbf{L^C}_2$	$Pd_2\mathbf{L^1}_2\mathbf{L^D}_2$
K [M^{-1}]	2062 ± 31	98 ± 1	33 ± 1	149 ± 1

In summary, it can be stated that the decrease of the cavity size has a substantial impact on the binding affinity of the phosphate guest $\mathbf{G^3}$ to the hosts. The binding constants decrease by a factor of about 20 when $\mathbf{L^A}$ is substituted by $\mathbf{L^B}$ and even by a factor of about 60 when $\mathbf{L^A}$ is substituted by $\mathbf{L^C}$. In all four cases the downfield shift and the broadening of the NH signal observed in the ^{1}H NMR titration experiments revealed that the binding of $\mathbf{G^3}$ is mainly driven by the formation of hydrogen bonds. Ion mobility studies could show that the guest is most likely located inside the cavities of the hosts.

3.3.4 Donor Site Variation

In a next series of experiments, the influence of the NH donor site on the binding strength of $\mathbf{G^3}$ was investigated. Initially, the ^{1}H NMR titration of $\mathbf{G^3}$ to the methylated

coordination cage $Pd_2\mathbf{L^2}_2\mathbf{L^A}_2$ was performed. Most prominent downfield shift of the signals of the inward pointing protons i and h was observed as well as an upfield shift of the signal of proton c'. Additionally, the signal of the methyl group undergoes a upfield shift as well compared to the empty host. Upon addition of 5 eq $\mathbf{G^3}$, the coordination cage starts to partially disassemble. From the signal shifts inside binding of the phosphate guest is assumed. A binding constant of $K = 77 \pm 3\ M^{-1}$ was obtained, so the binding affinity is about 25 times lower than for $\mathbf{G^3}$ inside the coordination cage $Pd_2\mathbf{L^1}_2\mathbf{L^A}_2$ that has the hydrogen bond donor functionalities installed. However, binding of $\mathbf{G^3}$ was still expected since the coordination cage is a positively charged species.

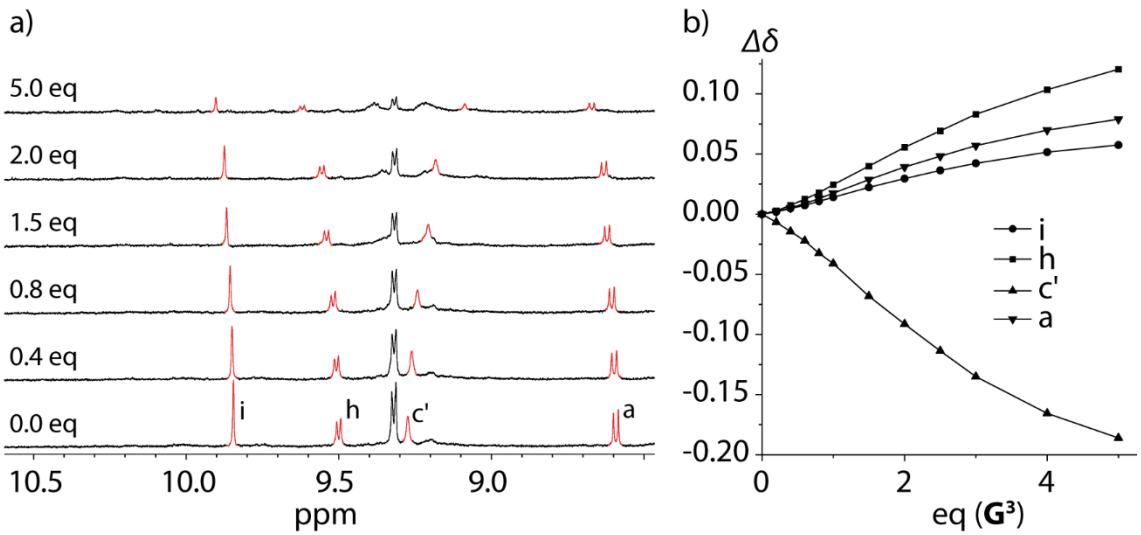

Figure 3.34: a) Stacked partial ^{1}H NMR spectra (500 MHz, DMSO-d_6) of the titration of $\mathbf{G^3}$ to $Pd_2\mathbf{L^2}_2\mathbf{L^A}_2$ and b) plot of $\Delta\delta$ of selected proton signals against guest concentration.

The same trend of decreasing the binding affinity compared to the coordination cage $Pd_2\mathbf{L^1}_2\mathbf{L^A}_2$ with the free amine functionality installed was observed when changing the solvent to DMF-d_7 (Figure 4.186). Here, a binding constant of $K = 199 \pm 6\ M^{-1}$ was obtained.

The formation of the host-guest complex was also observed via ESI mass spectrometry (Figure 4.179). Most prominent peaks were obtained for following charged species of the host-guest complex: $[Pd_2\mathbf{L^2}_2\mathbf{L^A}_2 + \mathbf{G^3}]^{3+}$, $[Pd_2\mathbf{L^2}_2\mathbf{A}_2 + BF_4 + \mathbf{G^3}]^{2+}$ and $[Pd_2\mathbf{L^2}_2\mathbf{L^A}_2 + 2\ \mathbf{G^3}]^{2+}$. To proof inside binding, ion mobility studies showed an eCCS of 597.0 Å^2 for the empty host and a slightly increased eCCS of 600.3 Å^2 for the host-guest complex (Figure 4.192).

Next, the binding of $\mathbf{G^3}$ inside the urea-type cage $Pd_2\mathbf{L^3}_2\mathbf{L^A}_2$ was investigated. However, this coordination cage contains sterically more demanding endohedral moieties but

compared to the methylated derivative a hydrogen bond donor is again present in this case. In the ^{1}H NMR titration experiment slight downfield shifts of the signals of the inward pointing protons was observed, as well as a downfield shift and broadening of the signal of the NH proton. Fitting of the binding isotherm led to a low binding constant of $K = 46 \pm 2\ M^{-1}$. There are two possible explanations for this low binding affinity, one is the sterically overcrowded host that prevents the guest molecule to stay inside the host in an energetically favorable manner. On the other hand, the hydrogen bond donor functions ate not pointing directly to the center of the cavity like in the unmodified coordination cage $Pd_2\mathbf{L^1}_2\mathbf{L^A}_2$.

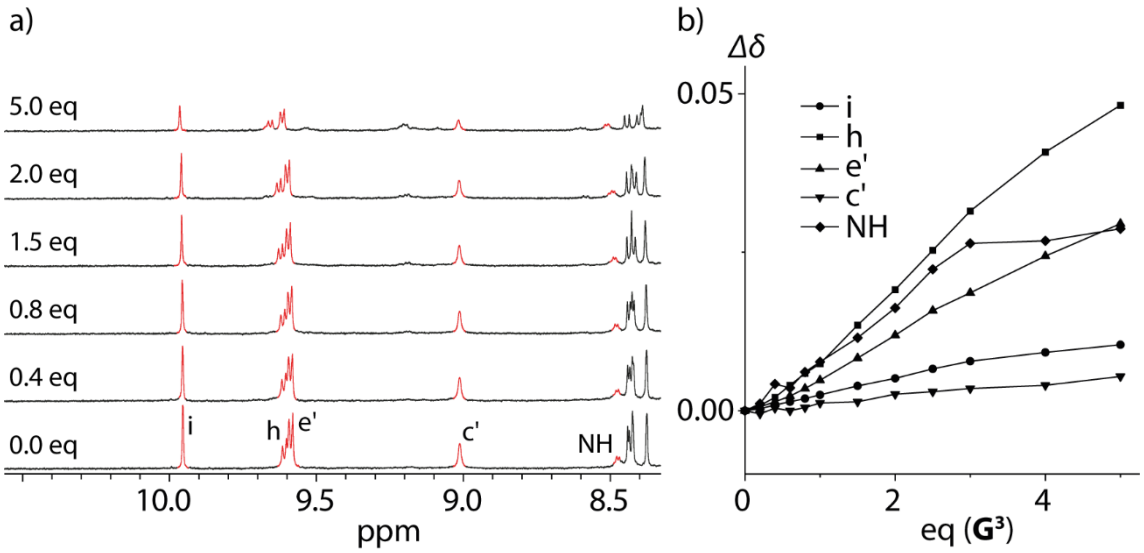

Figure 3.35: a) Stacked partial ^{1}H NMR spectra (500 MHz, DMSO-d_6) of the titration of $\mathbf{G^3}$ to $Pd_2\mathbf{L^3}_2\mathbf{L^A}_2$ and b) plot of $\Delta\delta$ of selected proton signals against guest concentration.

The guest uptake was also confirmed by ESI mass spectrometry (Figure 4.182). Most prominent peaks were obtained for following charged species of the host-guest complex: $[Pd_2\mathbf{L^3}_2\mathbf{L^A}_2 + \mathbf{G^3}]^{3+}$, $[Pd_2\mathbf{L^3}_2\mathbf{A}_2 + BF_4 + \mathbf{G^3}]^{2+}$ and $[Pd_2\mathbf{L^3}_2\mathbf{L^A}_2 + 2\ \mathbf{G^3}]^{2+}$. To proof inside binding, ion mobility studies showed an eCCS of 590.5 Å^2 for the empty host and a slightly increased eCCS of 592.7 Å^2 for the host-guest complex (Figure 4.193).

In a last experiment, the binding of G3 to the coordination cage $Pd_2\mathbf{L^4}_2\mathbf{L^A}_2$ was investigated. In the ^{1}H NMR titration experiment downfield shifts of the signals of the inward pointing proton was observed, comparable to the previous host-guest system. Furthermore, a downfield shift and broadening of the signal of the NH proton was observed, indicating the formation of hydrogen bonds. The obtained binding constant $K = 128 \pm 3\ M^{-1}$ is in the same low range as for the previous described examples. The

hydrogen bonding here is again not strong enough to compensate the less space due to the endohedral overcrowding functionalities inside the host.

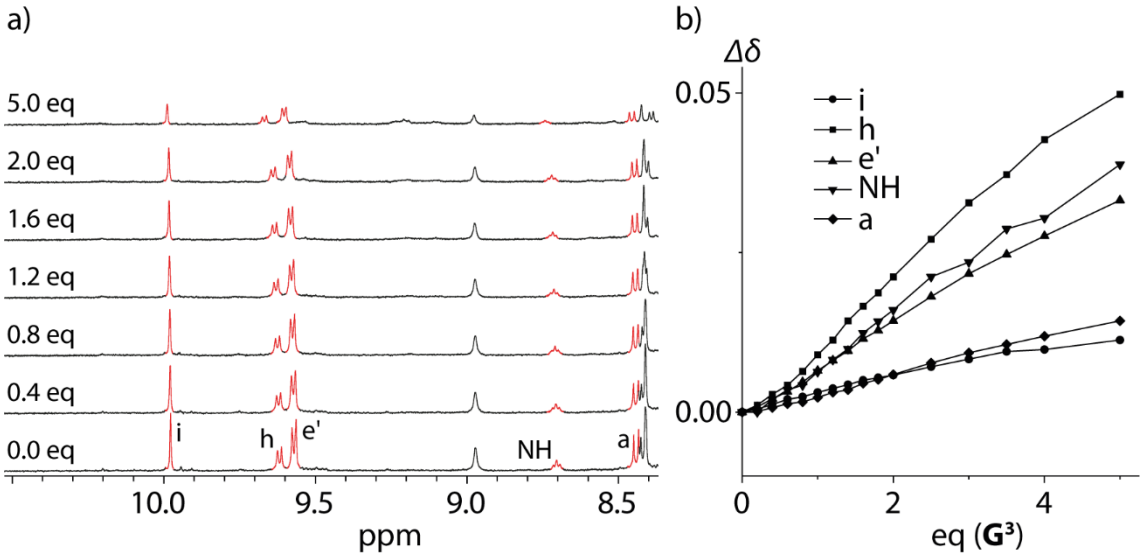

Figure 3.36: a) Stacked partial ^{1}H NMR spectra (500 MHz, DMSO-d_6) of the titration of $\mathbf{G^3}$ to $Pd_2\mathbf{L^4}_2\mathbf{L^A}_2$ and b) plot of $\Delta\delta$ of selected proton signals against guest concentration.

Again, guest uptake was confirmed by ESI mass spectrometry (Figure 4.184). Most prominent peaks were obtained for following charged species of the host-guest complex: $[Pd_2\mathbf{L^4}_2\mathbf{L^A}_2 + \mathbf{G^3}]^{3+}$, $[Pd_2\mathbf{L^4}_2\mathbf{A}_2 + BF_4 + \mathbf{G^3}]^{2+}$ and $[Pd_2\mathbf{L^4}_2\mathbf{L^A}_2 + 2\ \mathbf{G^3}]^{2+}$. To proof inside binding, ion mobility studies showed an eCCS of 592.3 Å^2 for the empty host and a slightly increased eCCS of 597.0 Å^2 for the host-guest complex (Figure 4.194).

Table 3.2: Overview of binding constants K for encapsulation of $\mathbf{G^3}$.

$\mathbf{G^3}$@	$Pd_2\mathbf{L^1}_2\mathbf{L^A}_2$	$Pd_2\mathbf{L^2}_2\mathbf{L^A}_2$	$Pd_2\mathbf{L^3}_2\mathbf{L^A}_2$	$Pd_2\mathbf{L^4}_2\mathbf{L^A}_2$
K [M^{-1}]	2062 ± 31	77 ± 3	46 ± 2	128 ± 3

In conclusion, it was shown that the main driving force for binding the organophosphate $\mathbf{G^3}$ is the formation of hydrogen bonds, since the binding constant drops significantly when the NH donor of ligand $\mathbf{L^1}$ is blocked by the methyl group in the case of $\mathbf{L^2}$. A weak binding process is still happening since the coordination cage is a cationic species. The binding of $\mathbf{G^3}$ is still much weaker compared to cage $Pd_2\mathbf{L^1}_2\mathbf{L^A}_2$ when exchanging ligand $\mathbf{L^1}$ with $\mathbf{L^3}$ or $\mathbf{L^4}$, respectively. Admittedly, both containing hydrogen bond donor functions, but these are not pointing inside the center of the cavity. Furthermore, the cavity space is much more limited with these more sterically demanding moieties.

3.3.5 Guest Variation

In the previous chapters it was described that the binding event of the phosphate ester **G^{3}** is the best if the hydrogen bond donor functionality is given by **L^{1}** and the cavity is large like it is the case for the long phenanthrene based ligand **L^{A}**. This coordination cage $Pd_2\mathbf{L^1}_2\mathbf{L^A}_2$ was then used for the binding studies of the other phosphate ester guests **G^{1}**-**G^{6}** (see Figure 3.27d).

The titration with the aliphatic guest molecules containing ethyl (**G^{4}**) and butyl (**G^{1}**) sidechains, respectively, did not lead to a clear formation of a host-guest complex (Figure 4.154 and Figure 4.162). However, shifts of the signals in the ^{1}H NMR titration experiments were observed for e.g. the NH proton and the inward pointing protons as well. After the addition of more than two equivalents of the guests, the signals broadened a lot and new, not further analyzed, species appeared. Due to the signal broadening, it was not possible to determine the chemical shifts and therefore no binding constants for the titration of **G^{1}** and **G^{4}** to $Pd_2\mathbf{L^1}_2\mathbf{L^A}_2$ were obtained. But from the shift and the comparison with the other obtained titration data it could be assumed that the aliphatic ester **G^{1}** and **G^{4}** also weakly bind to the host most likely.

However, ESI-MS analysis of the two experiments showed formation of the respective host-guest complexes in the gas phase (Figure 4.156 and Figure 4.164). Namely, peaks were obtained for following charged species of the host-guest complexes: $[Pd_2\mathbf{L^1}_2\mathbf{L^A}_2 + \mathbf{G^1}]^{3+}$, $[Pd_2\mathbf{L^1}_2\mathbf{A}_2 + BF_4 + \mathbf{G^1}]^{2+}$, $[Pd_2\mathbf{L^1}_2\mathbf{L^A}_2 + \mathbf{G^4}]^{3+}$ and $[Pd_2\mathbf{L^1}_2\mathbf{A}_2 + BF_4 + \mathbf{G^4}]^{2+}$. Ion mobility measurements revealed that in both cases the guest is likely bound inside the cavity, since eCCS values of 604.2 Å^2 (**G^{1}**) and 601.1 Å^2 (**G^{4}**) were obtained (in comparison empty cage had an eCCS of 595.1 Å^2) (Figure 3.42).

The ^{1}H NMR titration of $Pd_2\mathbf{L^1}_2\mathbf{L^A}_2$ with the benzyl substituted phosphate **G^{2}** gave similar results to the titration with the aliphatic guests (Figure 4.157). Shifting of the signals of the NH proton as well as the inward pointing protons were observed, and the signals starts to broaden a lot after the addition of more than two equivalents of guest. Like described above, a new, not further analyzed species appeared after two equivalents of **G^{2}**. Due to the signal broadening, it was not possible to determine a binding constant for the titration, however, binding of **G^{2}** can be assumed as well. In the ESI-MS spectrum the host-guest complex, namely the charged species $[Pd_2\mathbf{L^1}_2\mathbf{L^A}_2 + \mathbf{G^2}]^{3+}$, $[Pd_2\mathbf{L^1}_2\mathbf{A}_2 + BF_4 + \mathbf{G^2}]^{2+}$ and

$[Pd_2\mathbf{L^1}_2\mathbf{L^A}_2 + 2\ \mathbf{G^2}]^{2+}$ were observed (Figure 4.158). To proof inside binding, the ion mobility of the complex was measured to obtain an eCCS of 605.4 Å^2 (Figure 3.42).

A possible explanation why the binding event of the aliphatic guests $\mathbf{G^1}$ and $\mathbf{G^4}$ is not so clear from the obtained NMR data could be the missing π–π-interactions with ligand $\mathbf{L^A}$ like it was observed for $\mathbf{G^3}$@$Pd_2\mathbf{L^1}_2\mathbf{L^A}_2$. This could increase the movement of the guest inside the cavity and lead to the observed signal broadening. Furthermore, the flexibility of the benzyl group also leads to an increased movement of $\mathbf{G^2}$ inside the cavity and therefore to the observed signal broadening. In the case of the aliphatic guests, it could also be possible, that two guests are bound by the host and would therefore lead to a signal broadening and new signals arising in the NMR spectra. However, a 2:1 complex was not observed in the ESI mass spectra. To proof, that the binding of the diethyl ester is less strong than the binding of the diphenyl ester in the host $Pd_2\mathbf{L^1}_2\mathbf{L^A}_2$, a competition experiment was performed (see chapter 3.3.6).

In the ^{1}H NMR titration experiment of toluyl ester $\mathbf{G^5}$ to $Pd_2\mathbf{L^1}_2\mathbf{L^A}_2$, a strong downfield shift and signal broadening of the NH proton was again observed after guest addition (Figure 3.37). Furthermore, the signals of the inward pointing protons (i, e', c') are shifted, comparable to the observed shifts of the complex $\mathbf{G^3}$@$Pd_2\mathbf{L^1}_2\mathbf{L^A}_2$. From the binding isotherm a binding constant of K = 1432 ± 117 M^{-1} was obtained. Compared to $\mathbf{G^3}$@$Pd_2\mathbf{L^1}_2\mathbf{L^A}_2$ the binding affinity decreases and could be explained by the larger size of the guest molecule.

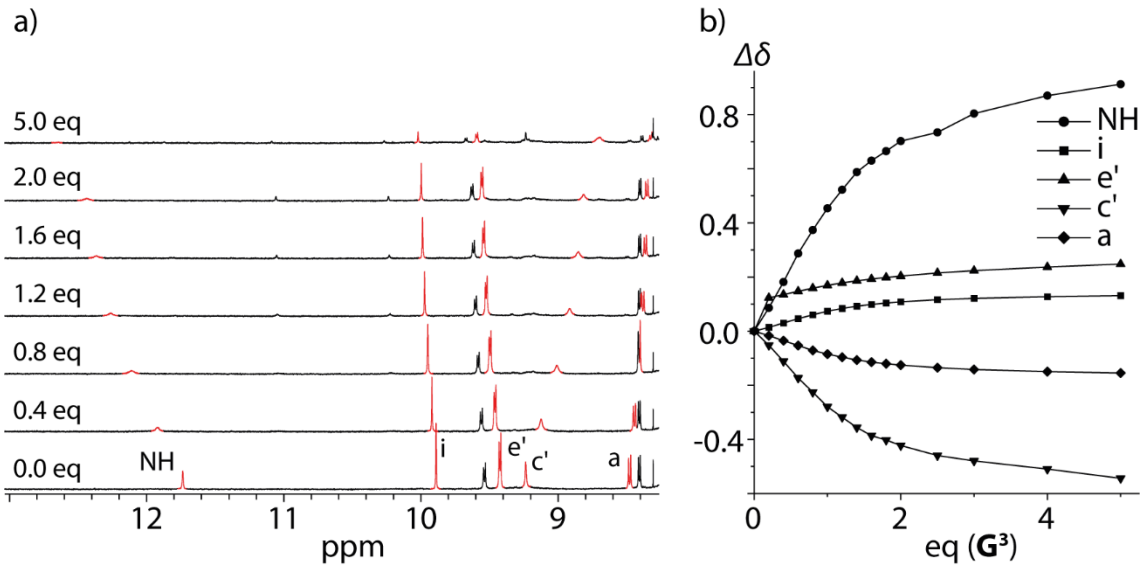

Figure 3.37: a) Stacked partial ^{1}H NMR spectra (500 MHz, DMSO-d_6) of the titration of $\mathbf{G^5}$ to $Pd_2\mathbf{L^1}_2\mathbf{L^A}_2$ and b) plot of $\Delta\delta$ of selected proton signals against guest concentration.

The guest uptake was also confirmed by ESI mass spectrometry (Figure 4.166). Most prominent peaks were obtained for following charged species of the host-guest complex: $[Pd_2\mathbf{L^1}_2\mathbf{L^A}_2 + \mathbf{G^5}]^{3+}$, $[Pd_2\mathbf{L^1}_2\mathbf{A}_2 + BF_4 + \mathbf{G^5}]^{2+}$ and $[Pd_2\mathbf{L^1}_2\mathbf{L^A}_2 + 2\ \mathbf{G^5}]^{2+}$. To proof inside binding, ion mobility studies showed an eCCS of 595.1 Å^2 for the empty host and a slightly increased eCCS of 601.7 Å^2 for the host-guest complex (Figure 3.42).

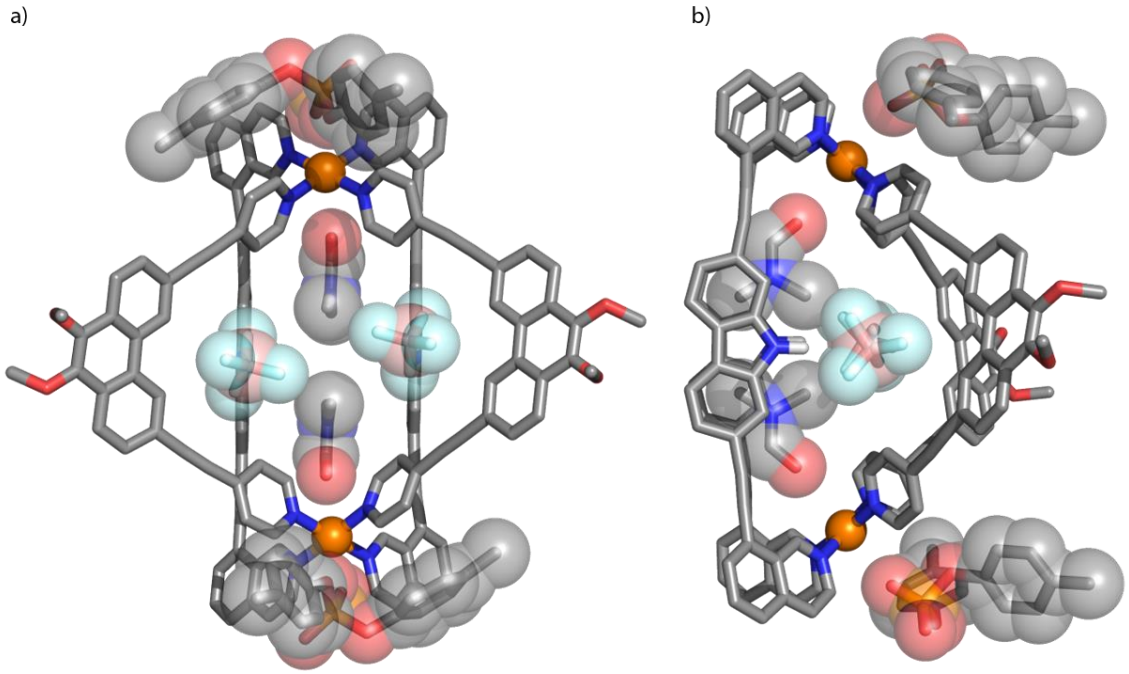

Figure 3.38: Molecular structure of $\mathbf{G^5}@Pd_2\mathbf{L^1}_2\mathbf{L^A}_2$ in the solid state, determined by X-ray diffraction, a) front and b) side view.

In addition, single crystals suitable for X-ray diffraction of $\mathbf{G^5}@Pd_2\mathbf{L^1}_2\mathbf{L^A}_2$ were obtained from slow vapor diffusion of Et_2O into the solution of the host-guest complex in DMF. The obtained molecular structure is, beside of the toluyl groups attached to the phosphate backbone, the same as in the case for $\mathbf{G^3}@Pd_2\mathbf{L^1}_2\mathbf{L^A}_2$. The guest molecules are again placed outside the cavity and interacting with the palladium atoms of the coordination cage. Inside the cavity, two BF_4^- anions are found as well as the two templating DMF molecules that were described for the previous structures.

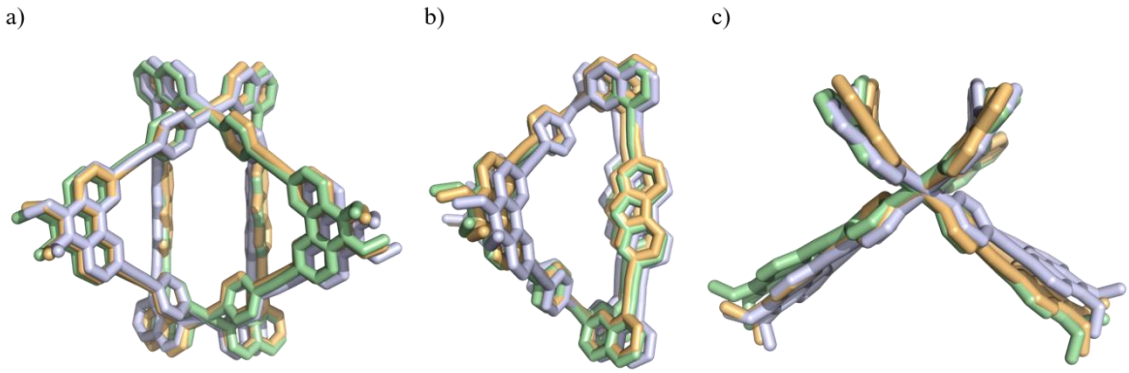

Figure 3.39: Superimpositions of the molecular structures in the solid state of $Pd_2\mathbf{L^1}_2\mathbf{L^A}_2$ (orange), $\mathbf{G^3}$@$Pd_2\mathbf{L^1}_2\mathbf{L^A}_2$ (green) and $\mathbf{G^5}$@$Pd_2\mathbf{L^1}_2\mathbf{L^A}_2$ (purple) from a) the front, b) side and c) top.

In Figure 3.39 the three obtained molecular structures were superimposed to illustrate the described similarity of these.

The last investigated guest molecule was the chiral BINOL derivative $\mathbf{G^6}$. Interestingly, also this comparable large guest binds to the coordination cage $Pd_2\mathbf{L^1}_2\mathbf{L^A}_2$. In the ^{1}H NMR titration experiment a downfield shift and broadening of the signal of the NH proton was observed (Figure 3.40). The signals of the inward pointing protons (i, c', e') are also shifted upon guest addition, however the shift is not as large as it was observed for $\mathbf{G^3}$@$Pd_2\mathbf{L^1}_2\mathbf{L^A}_2$. A binding constant of $K = 513 \pm 17$ M^{-1} was obtained, so about one quarter less strong then the binding of $\mathbf{G^3}$.

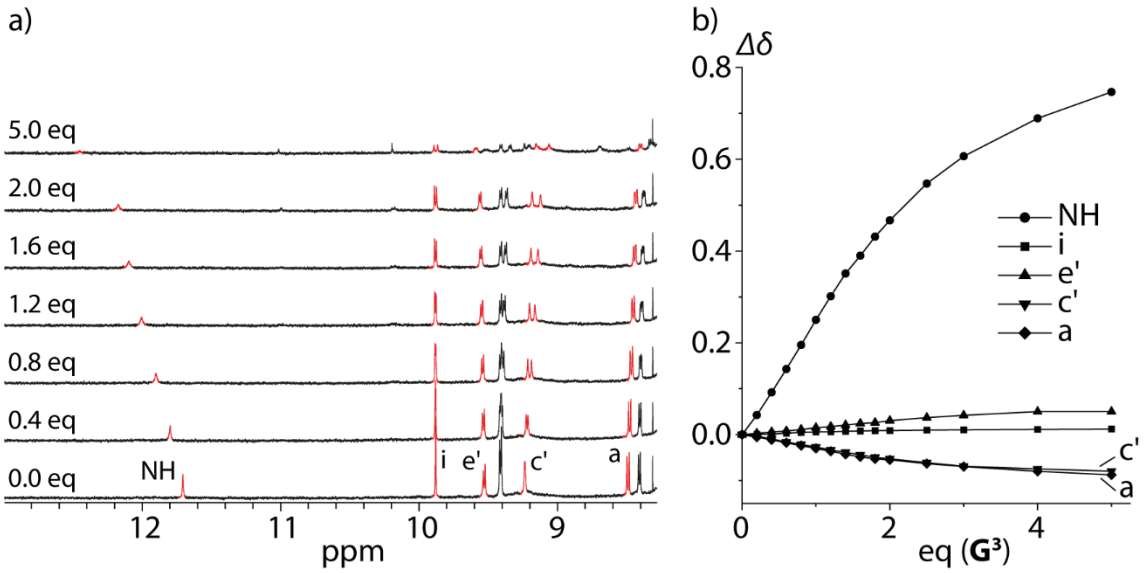

Figure 3.40: a) Stacked partial ^{1}H NMR spectra (500 MHz, DMSO-d_6) of the titration of $\mathbf{G^6}$ to $Pd_2\mathbf{L^1}_2\mathbf{L^A}_2$ and b) plot of $\Delta\delta$ of selected proton signals against guest concentration.

Furthermore, all signals split into a set of two during the addition of $\mathbf{G^6}$, except the signal of the NH proton. This could be explained by the chirality of the guest molecule. The upper and the lower part of the coordination cage (plain through the coordination cage from the NH groups to the central phenyl rings of $\mathbf{L^A}$) are not chemically equivalent anymore, since one of the naphthyl moieties is pointing up whereas the other naphthyl moiety is pointing down (see PM6 optimized structure in Figure 3.41). NOE data of the host-guest complex could not provide information of the orientation of the guest.

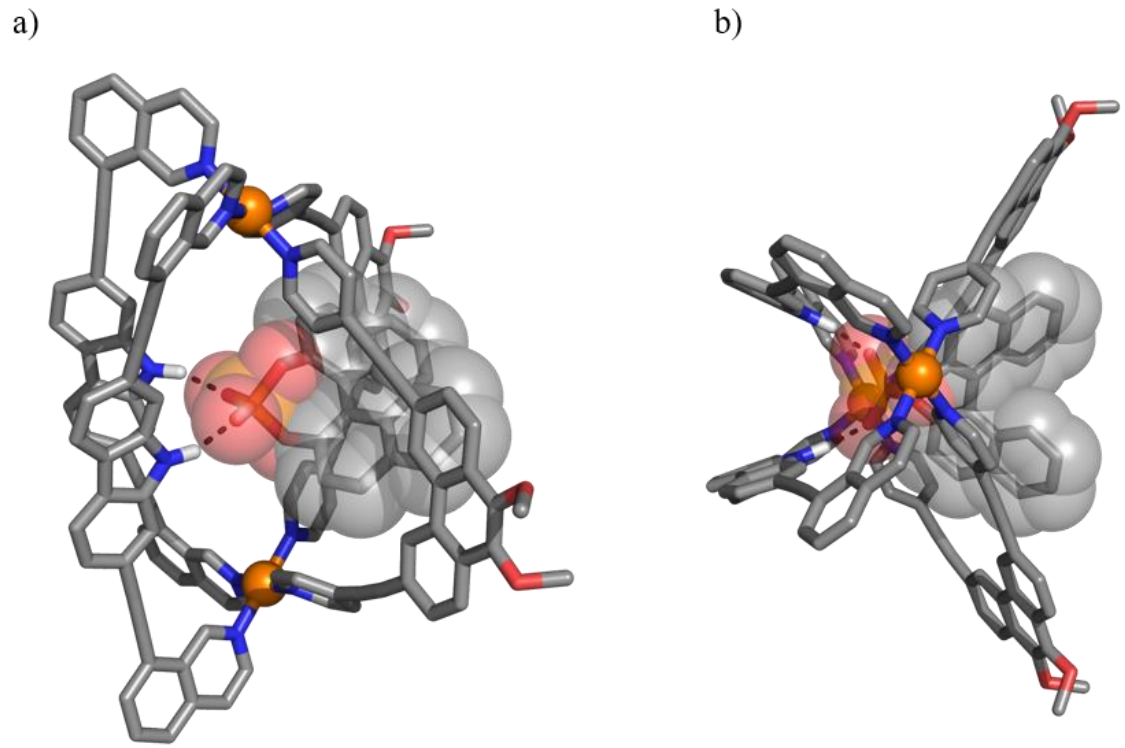

Figure 3.41: PM6 optimized structure of $\mathbf{G^6}$@$Pd_2\mathbf{L^1}_2\mathbf{L^A}_2$ from a) side and b) top to illustrate the hydrogen bond formation (dashed lines) and the orientation of the naphthyl moieties.

Very recently, single crystals of $\mathbf{G^6}$@$Pd_2\mathbf{L^1}_2\mathbf{L^A}_2$ were obtained by slow vapor diffusion of toluene into the cage solution in DMF. Preliminary analysis of the X-ray diffraction data showed the similarity of the host-guest complex with the other obtained structures, with the guest molecules outside the cavity.

The guest uptake was also confirmed by ESI mass spectrometry (Figure 4.168). Most prominent peaks were obtained for following charged species of the host-guest complex: $[Pd_2\mathbf{L^1}_2\mathbf{L^A}_2 + \mathbf{G^6}]^{3+}$, $[Pd_2\mathbf{L^1}_2\mathbf{A}_2 + BF_4 + \mathbf{G^6}]^{2+}$ and $[Pd_2\mathbf{L^1}_2\mathbf{L^A}_2 + 2\ \mathbf{G^6}]^{2+}$. To proof inside binding, ion mobility studies showed an eCCS of 595.1 $Å^2$ for the empty host and a slightly increased eCCS of 599.0 $Å^2$ for the host-guest complex (Figure 3.42).

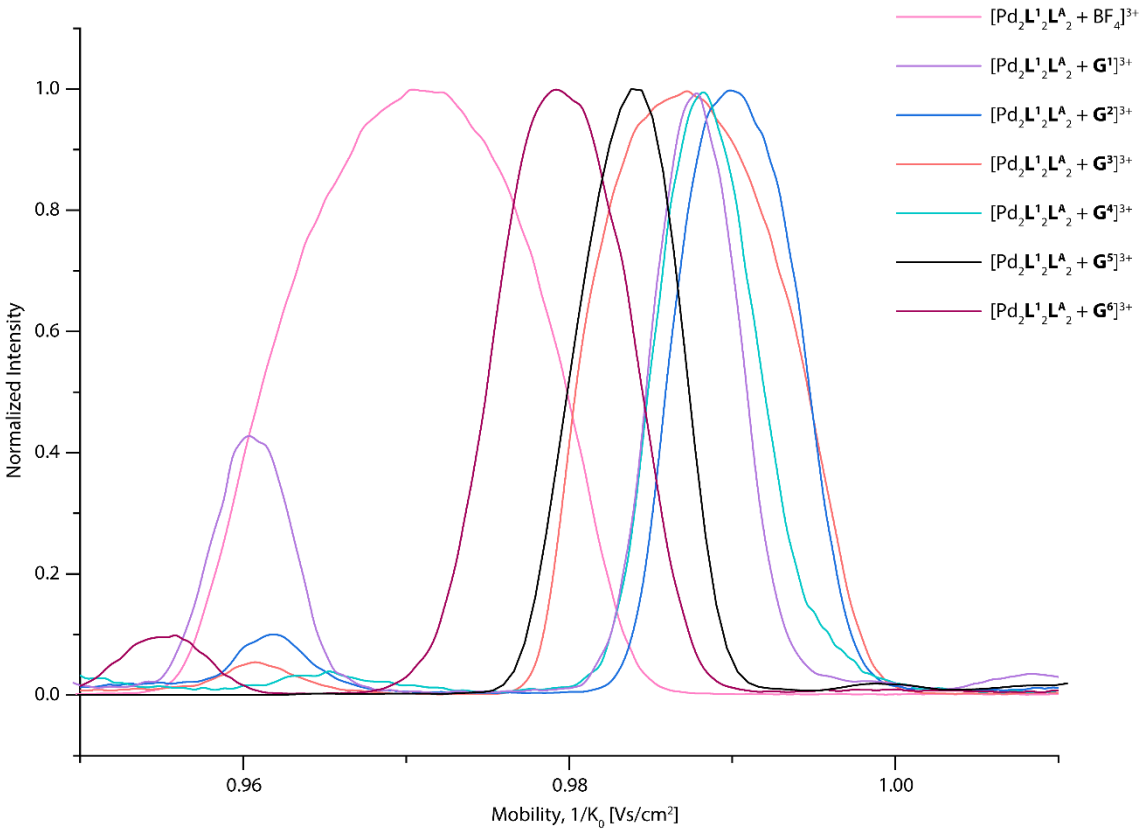

Figure 3.42: Overlay of the normalized ion-mobility spectra of $[Pd_2\mathbf{L}^{\mathbf{1}}{}_2\mathbf{L}^{\mathbf{A}}{}_2 + BF_4]^{3+}$ and $[Pd_2\mathbf{L}^{\mathbf{1}}{}_2\mathbf{L}^{\mathbf{A}}{}_2 + \mathbf{G}^{\mathbf{1-6}}]^{3+}$.

Additionally, the photophysical properties of the host-guest complex $\mathbf{G}^{\mathbf{6}}@Pd_2\mathbf{L}^{\mathbf{1}}{}_2\mathbf{L}^{\mathbf{A}}{}_2$ were investigated (Figure 3.43). In the UV/Vis spectrum a broad local absorption maximum at around 400 nm of the coordination cage and the host-guest complex is found. Local absorption maxima at around 300 nm of the cage and the host-guest complex are overlaid by the absorption of the free guest $\mathbf{G}^{\mathbf{6}}$. In the CD spectrum a small signal in the absorption range of the host-guest complex at around 420 nm was observed, indicating a weak chirality transfer from the guest to the achiral host.

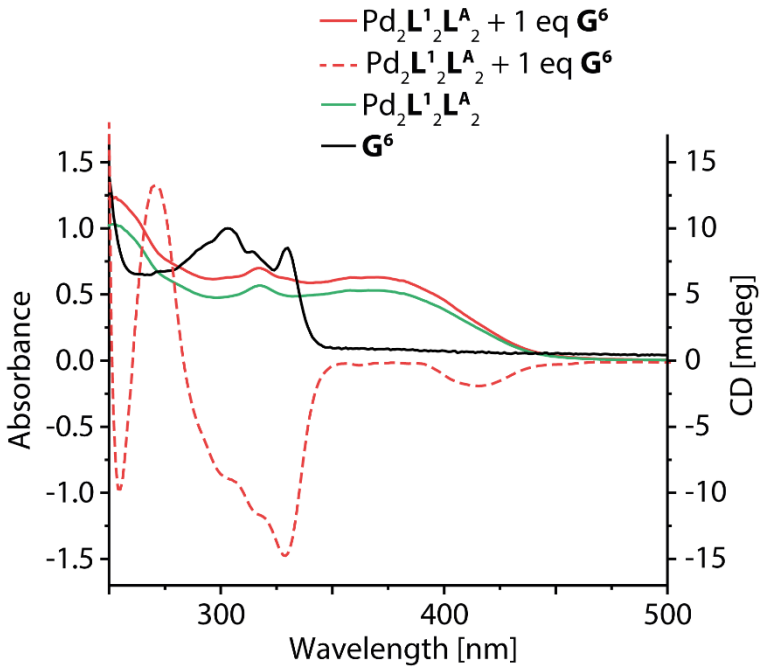

Figure 3.43: Overlay of UV/Vis (solid lines) and CD (dashed line) spectra of $Pd_2\mathbf{L^1}_2\mathbf{L^A}_2$ (green, c = 0.07 mM), $\mathbf{G^6}$@$Pd_2\mathbf{L^1}_2\mathbf{L^A}_2$ (1 eq red, c = 0.07 mM) and $\mathbf{G^6}$ (black, c = 0.7 mM).

In conclusion, it was shown that beside the investigated binding of $\mathbf{G^3}$ inside the coordination cage $Pd_2\mathbf{L^1}_2\mathbf{L^A}_2$ this supramolecule can also acts as a host for a variety of organophosphate ester. Aliphatic and therefore more flexible guests ($\mathbf{G^1}$ and $\mathbf{G^4}$) show weaker binding than to $\mathbf{G^3}$, however, binding constants could not be obtained due to intense signal broadening. Same was observed for the benzyl ester $\mathbf{G^2}$. The larger toluyl ester $\mathbf{G^5}$ shows binding to the host but with a lower binding constant than $\mathbf{G^3}$@ $Pd_2\mathbf{L^1}_2\mathbf{L^A}_2$. Interestingly, the largest evaluated guest $\mathbf{G^6}$ binds to the cage as well and moreover transferring its chiral information to the host.

Table 3.3: Overview of binding constants K for guest encapsulation.

	$\mathbf{G^3}$@$Pd_2\mathbf{L^1}_2\mathbf{L^A}_2$	$\mathbf{G^5}$@$Pd_2\mathbf{L^1}_2\mathbf{L^A}_2$	$\mathbf{G^6}$@$Pd_2\mathbf{L^1}_2\mathbf{L^A}_2$
K [M^{-1}]	2062 ± 31	1432 ± 117	513 ± 17

3.3.6 Guest Competition Experiments

As it was discussed in the previous chapter, binding constants for the aliphatic phosphate ester molecules could not be obtained. However, from the NMR titration data it was assumed that the binding affinity should be much lower compared to $\mathbf{G^3}$. To proof this assumption, guest competition experiments were performed in which $\mathbf{G^3}$ was added to a

solution of $\mathbf{G^4}$@ $Pd_2\mathbf{L^1}_2\mathbf{L^A}_2$ and $\mathbf{G^4}$ to a solution of $\mathbf{G^3}$@ $Pd_2\mathbf{L^1}_2\mathbf{L^A}_2$, respectively, to compare the relative binding affinities of the guest molecules.

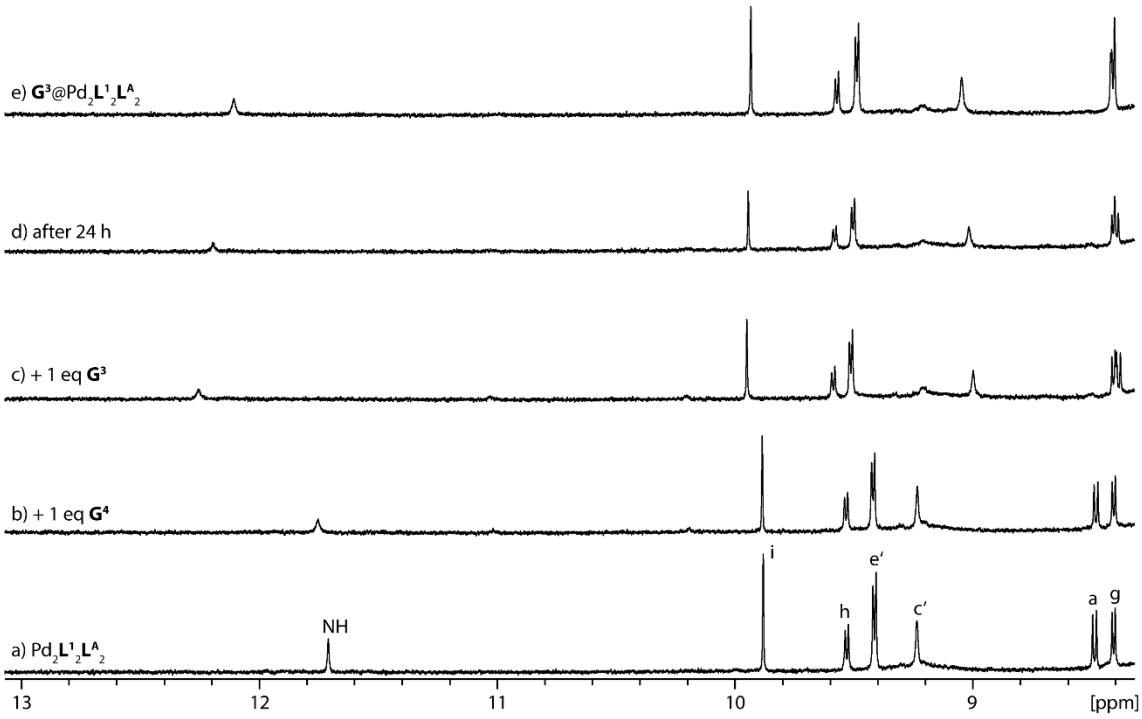

Figure 3.44: Stacked partial ^{1}H NMR spectra (500 MHz, 298 K, DMSO-d_6) of guest competition titration experiments.

While adding one equivalent of the aliphatic guest $\mathbf{G^4}$ to the coordination cage solution the signal of the NH proton is shifted slightly downfield in the ^{1}H NMR spectrum, like it was described in the previous chapter (Figure 3.44). After measuring, aromatic phosphate $\mathbf{G^3}$ was added to the solution of $\mathbf{G^4}$@$Pd_2\mathbf{L^1}_2\mathbf{L^A}_2$. In the ^{1}H NMR spectrum measured immediately and after 24 h shifting of the signals was observed, especially a large downfield shift for the NH proton signal. The signals of the inward pointing protons (i, c', e') shifting downfield as well. All in all, the observed shifts are comparable to the ^{1}H NMR spectrum of $\mathbf{G^3}$@$Pd_2\mathbf{L^1}_2\mathbf{L^A}_2$ (Figure 3.44e), leading to the assumption that $\mathbf{G^4}$ is replaced by $\mathbf{G^3}$ inside the host. The additional downfield shift of the NH proton signal could be explained by the overall larger concentration of phosphates in the solution. In a control experiment where $\mathbf{G^4}$ was added to $\mathbf{G^3}$@$Pd_2\mathbf{L^1}_2\mathbf{L^A}_2$ the same result was shown, the ^{1}H NMR spectrum is not changing after addition of the aliphatic guest (Figure 4.188). This indicates that the binding affinity of the diethyl phosphate ester is way less pronounced than binding of $\mathbf{G^3}$. This can be explained by the lack of π–π-interactions of the guest with $\mathbf{L^A}$.

3.3.7 Molecular Dynamics Simulations

To get a more detailed look into the binding process also from a theoretical point of view, all-atom molecular dynamics (MD) simulations in an explicit solvent (DMSO) were performed in collaboration with the group of SCHÄFER at the Ruhr-University Bochum. In the simulations the contribution of the different cages' parts to the binding of $\mathbf{G^3}$ was evaluated in the case of $Pd_2\mathbf{L^1}_2\mathbf{L^A}_2$ (Figure 3.45b) containing the hydrogen bond donor function and its methylated version $Pd_2\mathbf{L^2}_2\mathbf{L^A}_2$ (Figure 3.45a).

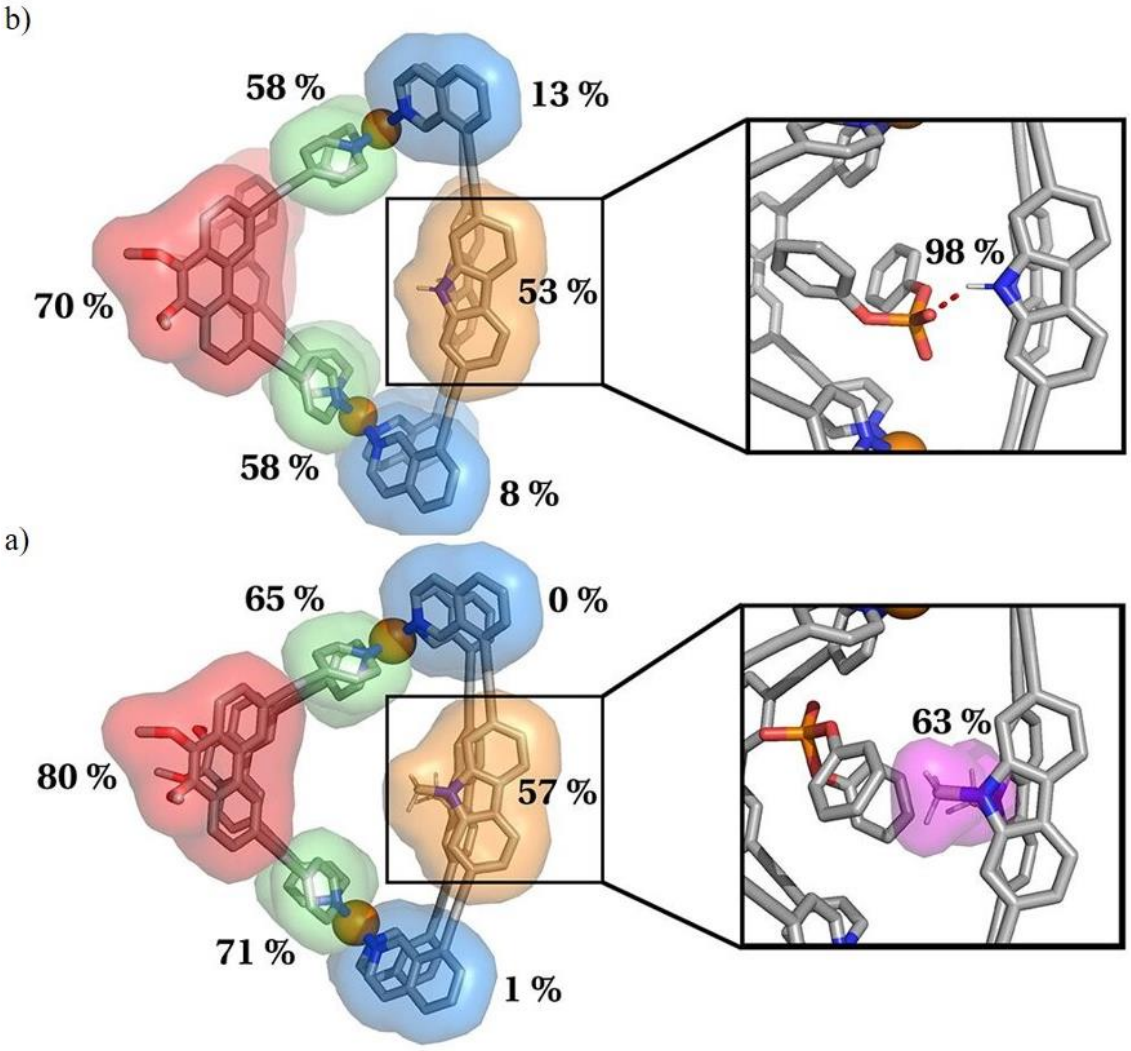

Figure 3.45: Illustration of the host-guest contacts during the MD simulation of a) $\mathbf{G^3}$@$\mathbf{Pd_2L^2_2L^A_2}$ and b) $\mathbf{G^3}$@$\mathbf{Pd_2L^1_2L^A_2}$ with the possibility of the different cage compounds contributing to the formation of bonds to the guest given in percentage.

The analysis showed that the free binding energy decreases from -6.6 ± 0.2 kJ · mol^{-1} for $Pd_2\mathbf{L^2}_2\mathbf{L^A}_2$ to -13.3 ± 1.4 kJ · mol^{-1} for $Pd_2\mathbf{L^1}_2\mathbf{L^A}_2$ making it more favourable for $\mathbf{G^3}$ to bind inside the coordination cage with the hydrogen bond donor function installed. This is in good accordance with the experimentally obtained values for *K* described before.

Since the difference in the obtained energies is quite low, a contact analysis was performed describing the possibilities of molecular interactions between the guest, in particular the phosphate group and the phenyl moieties and the different parts of the host molecule highlighted in Figure 3.45. In the case of $Pd_2\mathbf{L^1}_2\mathbf{L^A}_2$ it was shown that the binding of $\mathbf{G^3}$ is driven by the H-bond formation as well as non-polar contacts between the guest's phenyl moieties and the backbone of $\mathbf{L^A}$. The lack of the H-bond donor in the methylated cage led to an increase of the non-polar contacts, in particular with $\mathbf{L^A}$, during the binding events.

Furthermore, MD simulations of the binding of the aliphatic guest $\mathbf{G^4}$ inside $Pd_2\mathbf{L^2}_2\mathbf{L^A}_2$ were performed to confirm the binding selectivity of the cage that was shown in the guest competition experiments (chapter 3.3.6). MD simulations of the binding of $\mathbf{G^4}$ to $Pd_2\mathbf{L^1}_2\mathbf{L^A}_2$ were not possible to perform, since there was a large kinetic barrier for the guest release and therefore no statistically reliable data was obtained. However, the binding affinity for $\mathbf{G^4}$@$Pd_2\mathbf{L^2}_2\mathbf{L^A}_2$ was much lower with a value for the binding energy of $\Delta G = -1 \pm 1$ kJ · mol^{-1}. This increase of ΔG is most likely due to the lack of π-surfaces of the guest that could interact with ligand $\mathbf{L^A}$.

In summary it was shown that the binding of $\mathbf{G^3}$ is more favourable if hydrogen bonds are formed. However, it is also quite important for the guest to form π-π-interactions with ligand $\mathbf{L^A}$ for a higher binding affinity. All these theoretical results support the experimentally obtained ones in a decent manner.

3.3.8 Additional Guest Titration Experiments

In addition to the guests $\mathbf{G^1}$-$\mathbf{G^6}$ that showed binding to $Pd_2\mathbf{L^1}_2\mathbf{L^A}_2$ the molecule $\mathbf{G^7}$ and the biologically relevant phosphates $\mathbf{G^8}$ and $\mathbf{G^9}$ were also tested in regard of their binding affinities to the heteroleptic coordination cage (Figure 3.46a and b). These differ from the former guests in their overall charge, since $\mathbf{G^7}$ and $\mathbf{G^8}$ are dianions and $\mathbf{G^9}$ even equipped with three negative charges.

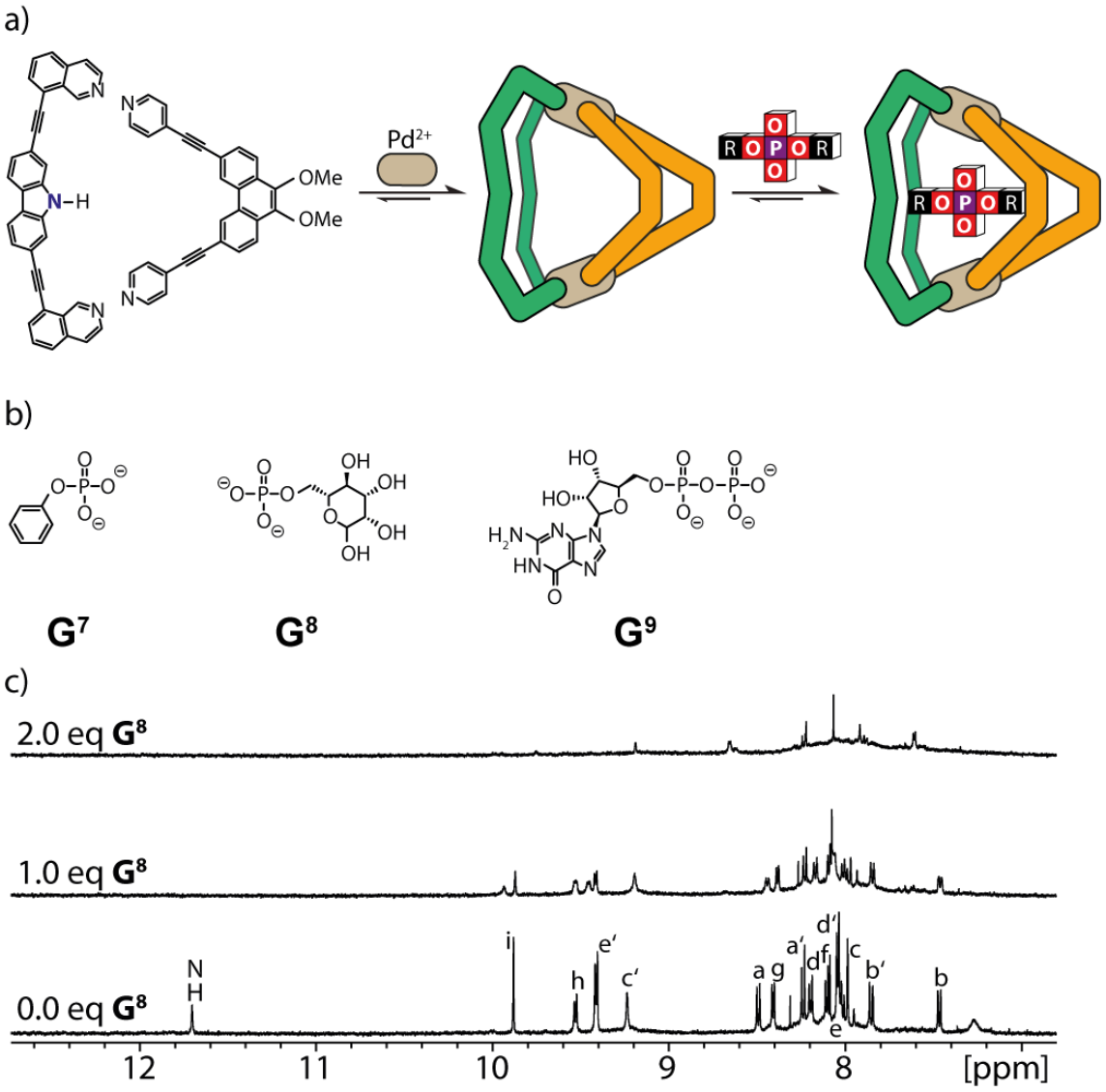

Figure 3.46: a) Formation of coordination cage $Pd_2\mathbf{L^1}_2\mathbf{L^A}_2$, illustration of guest uptake, b) investigated guest molecules $\mathbf{G^{7\text{-}9}}$ and c) stacked partial ^{1}H NMR spectra (500 MHz, 298 K, DMSO-d_6) of the titration of $\mathbf{G^8}$ to $Pd_2\mathbf{L^1}_2\mathbf{L^A}_2$.

However, the titration of theses guest to the latter cage did not show binding. In the corresponding ^{1}H NMR spectra (Figure 4.169 - Figure 4.171) the signals of the amine proton were found to be broadened intensively in all three cases upon addition of 1 eq of the guest molecules. After the addition of more guest solution the host starts to disassemble and after 2 eq of guest only unidentifiable signals were observed in the ^{1}H NMR spectra. As an example, the titration of mannose phosphate ($\mathbf{G^8}$) is shown in Figure 3.46c. While the signal of the NH proton is strongly broadened the signals of the inward pointing protons are only weakly shifted compared to the previous titrations. Furthermore, new signals arise after addition of one equivalent guest. After two equivalents of guest, the titration was aborted since no host signals were identified anymore as well as the

signals for free ligand appeared. These results could be explained by the increased basicity of the divalent phosphates that could interact with the Pd(II) cations. Furthermore, the guest molecules carrying a lot of functional groups that are known to interact with Pd(II) cations in a preferred manner, like the hydroxy and amine functionalities.

3.4 Conclusion and Outlook

In summary, 16 novel heteroleptic coordination cages of the type $Pd_2\mathbf{L}^{\mathbf{1\text{-}4}}{}_2\mathbf{L}^{\mathbf{A\text{-}D}}{}_2$ were synthesized out of a modular toolbox of endohedral functionalized ligands $\mathbf{L}^{\mathbf{1\text{-}4}}$ and shape-complementary ligands $\mathbf{L}^{\mathbf{A\text{-}D}}$. All assemblies were characterized by NMR spectroscopy as well as ESI mass spectrometry as well as X-ray diffraction for distinct cages and host-guest complexes, respectively. To get use of the endohedral hydrogen bond donor sites in the cavities, organophosphate ester molecules carrying aromatic and aliphatic residues were evaluated in regard of their binding affinities to the coordination cages via NMR titration experiments and ion-mobility mass spectrometry. It was shown that the formation of hydrogen bonds plays a major role for the binding event. If the free amine donor site was blocked by a methyl group or substituted by amides where the hydrogen bond donor site is not pointing to the centre of the cavity anymore, the binding constants decreases significantly. The binding still took place because of a) the electrostatic interactions between the cationic host and the anionic guest and b) because of π-π interactions between the aromatic organophosphates and the backbones of ligands $\mathbf{L}^{\mathbf{A\text{-}D}}$. In the case of aliphatic guest molecules, a clear formation of host-guest complexes could not be observed by NMR spectroscopy, however guest competition experiments were performed to estimate the binding affinity qualitively compared to $\mathbf{G}^{\mathbf{3}}$.

Based on these systematic studies, a next possible step could be the investigation of transesterification reactions inside the cavity.

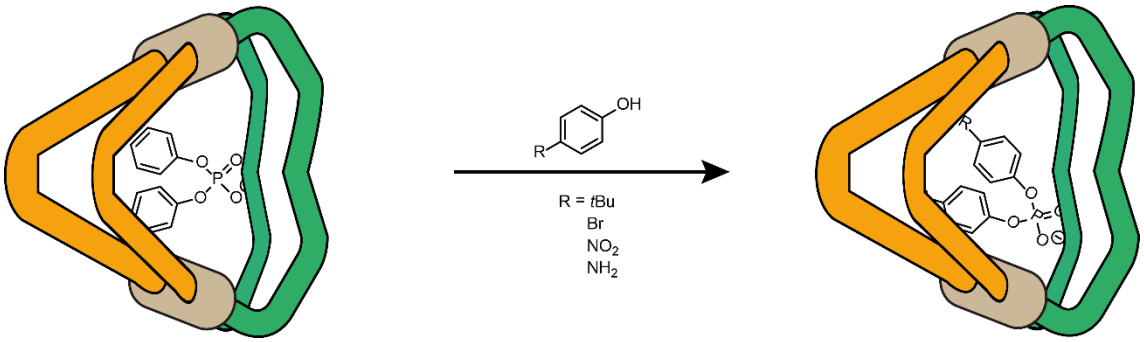

Figure 3.47: Proposed transesterification reactions of bound $\mathbf{G^3}$ inside $Pd_2\mathbf{L^1}_2\mathbf{L^A}_2$ with different phenols.

First results could show the formation of new, yet not identified species via time-dependent ^{1}H NMR experiments.

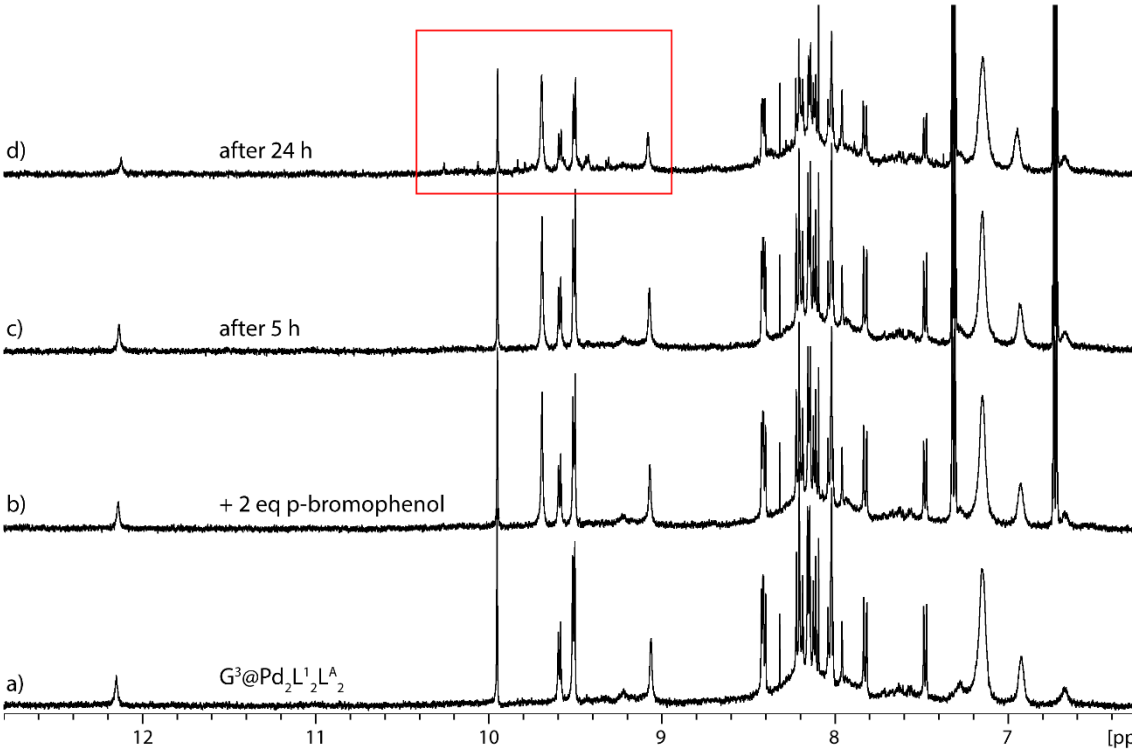

Figure 3.48: Stacked partial ^{1}H NMR spectra (500 MHz, 298 K, DMSO-d_6) of a) $\mathbf{G^3}$@$Pd_2\mathbf{L^1}_2\mathbf{L^A}_2$ and b) the addition of 2 eq *p*-bromophenol to $\mathbf{G^3}$@$Pd_2\mathbf{L^1}_2\mathbf{L^A}_2$ after c) 5 h and d) 24 h. New signals are visible in the red marked area.

Another way to explore the usage of hydrogen bonding in catalysis is the proposed coordination cage shown in figure that was done in collaboration with K. EBBERT. Here, $\mathbf{L^1}$ was combined with a fluorenone-based ligand $\mathbf{L^{FAm}}$ that contains two secondary amine groups in proximity to the coordination sphere. This highly functionalized coordination cage contains six hydrogen bond donor sites and would be a perfect candidate for MICHAEL addition reactions inside the cavity.[172]

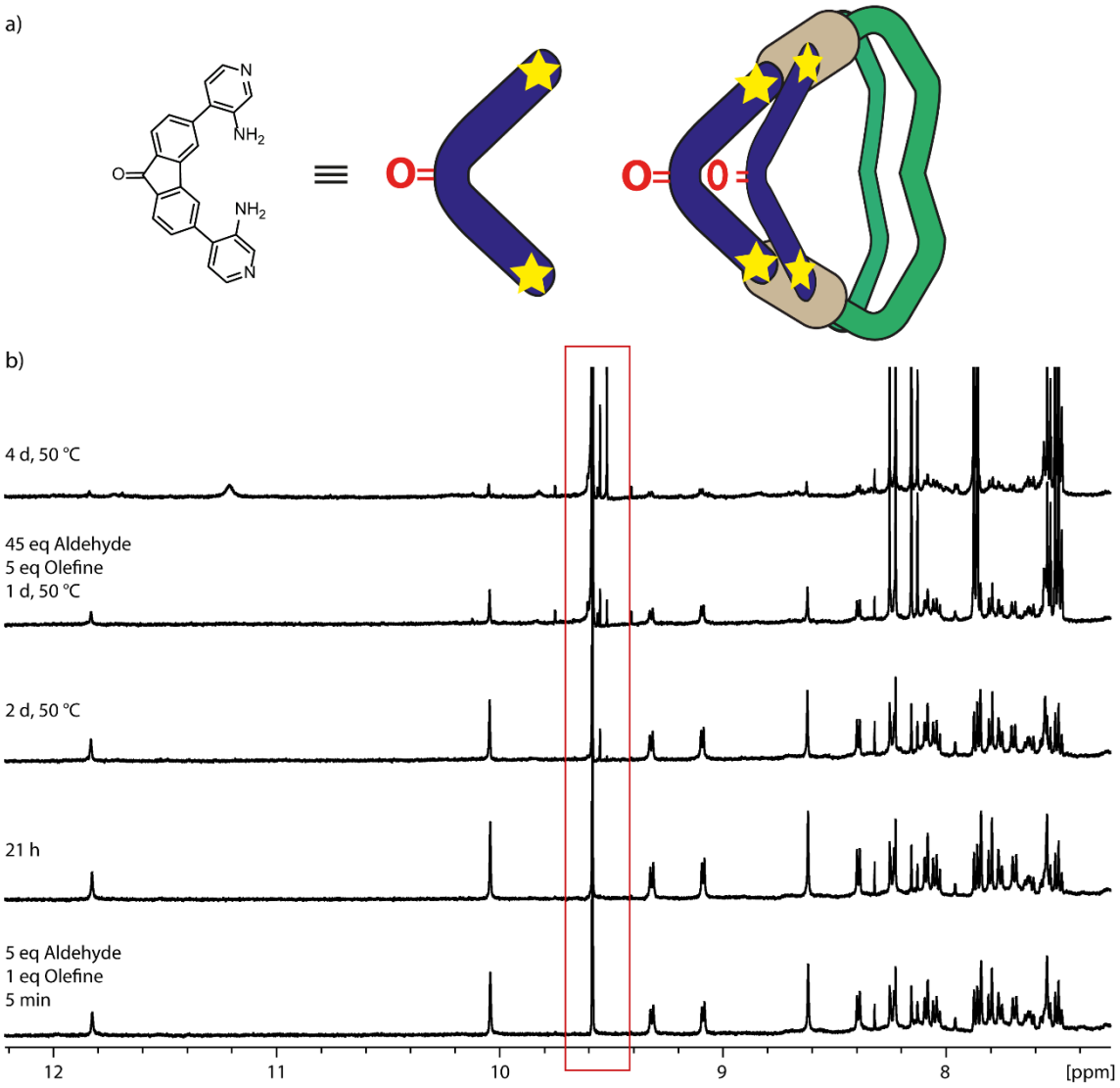

Figure 3.49: a) Formation of $Pd_2\mathbf{L}^1{}_2\mathbf{L}^{\mathbf{FAm}}{}_2$ and b) stacked partial ^{1}H NMR spectra (500 MHz, 298 K, DMSO-d_6) of $Pd_2\mathbf{L}^1{}_2\mathbf{L}^{\mathbf{FAm}}{}_2$ with addition of 5 eq isopropyl aldehyde and 1 eq β-nitrostyrene, after 21 h, 2 d at 50 °C, addition of 45 eq isopropyl aldehyde and 5 eq β-nitrostyrene and heating at 50 °C for one day and after heating at 50 °C for additional 4 days.

It was shown that the cage stayed intact after the addition of 5 eq isopropyl aldehyde and 1 eq *trans*-β-nitrostyrene. After heating the sample at 50 °C for two days new signals appeared, indicating that a new species was formed. These signals enlarged after the addition of more reactants to the cage solution. However, the process is still under investigation.

3.5 Interpenetrated Coordination Cages

Another class of coordination cages, that have been studied in our group are interpenetrated coordination cages.[173] Here, two monomeric Pd_2L_4 coordination cages dimerize into a single Pd_4L_8 species in which the two monomers are catenated or mechanically interlocked to each other. The cavities of these molecules were investigated extensively by our group, as for example, halide binding and exchange was observed.[65] In acridone-based interpenetrated coordination cages the binding of neutral guest molecules was shown after the central cavity was activated by the addition of chloride into the outer pockets.[66,67] That lead to an overall shrinking of the system on the Pd-Pd axis and therefore an enlargement of the central cavity that was then available for small neutral guests like benzene, cyclohexane or heterocycles.

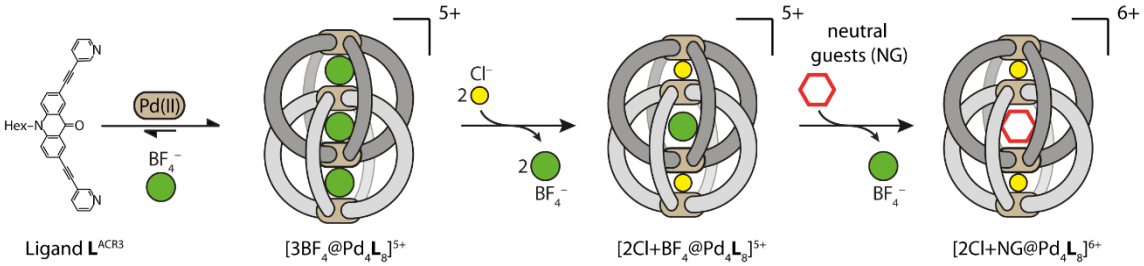

Figure 3.50: Formation of an interpenetrated coordination cage $3BF_4@Pd_4\mathbf{L}^{\mathbf{ACR3}}{}_8$, the uptake of chloride ions in the outer pocket and the exchange of BF_4^- by a neutral guest molecule NG.

Most of the interpenetrated structures described by our group contain alkyl chains attached to the ligand backbones to increase solubility, however it is not well understood how these behave in solution. In this work, the behaviour of these sidechains attached to an acridone backbone was investigated by DOSY NMR spectroscopy. This project is a continuation and extension of previous work from my master thesis.[174] The results will be recapped shortly for better understanding.

The ligands $\mathbf{L}^{\mathbf{ACR1,3,4,6}}$ were synthesized and the interpenetrated coordination cages were formed in acetonitrile. From the obtained diffusion coefficients of the ^{1}H DOSY experiments the hydrodynamic radii were calculated, using in the one hand the unmodified Stokes-Einstein equation (1.15) and on the other hand using equation (3.12) with a shape factor for a prolate particle. Here it was shown that the values for r_H calculate with the mentioned shape factor suits the dimensions of the coordination cage obtained by X-ray analysis.

Especially for $\mathbf{L}^{\mathbf{ACR1,3,4}}$ the differences in the obtained radii were extremely small. This indicates that the side chains will not contribute to the spatial extent of the coordination cages. The obtained radius for $\mathbf{L}^{\mathbf{ACR6}}$ was about 1 Å larger than the beforehand mentioned, most likely due to an interaction of the long carbon chain with itself. Distance analyses of the geometry optimized structures (PM6-level) confirmed the experimentally obtained trend. Most likely, the sidechains fold back to the coordination cage and forming dispersive interactions with the acridone backbone. In the case of the C_{12} chain additional backfolding to the chain itself promotes a larger radius.

In the case for $Pd_4\mathbf{L}^{\mathbf{ACR3}}{}_8$ the two, in chapter 1.2.1 mentioned pulse sequences were used for the ^{1}H DOSY measurement on the AV NEO 500 equipped with BBFOsmart probe. Furthermore, the measurements were performed at a temperature ramp from −80 to 70 °C. Especially at high and low temperatures a huge deviation in the obtained diffusion coefficients was found due to convection. Surprisingly, also at room temperature a significant difference in the values for *D* was measured.

3.5.1 Side Chain Interactions

In this work, firstly, alkyl sidechains of different lengths were attached to the ligand (C_{2n} with n = 1 - 6) backbone and the interpenetrated coordination cages of the type $Pd_4\mathbf{L}^{\mathbf{ACR1\text{-}6}}{}_8$ were formed in acetone-d_6 and acetonitrile-d_3 according the reported self-assembly.[66] It is noted that the ligand $\mathbf{L}^{\mathbf{ACR5}}$ containing a decyl side chain has not been synthesized by the end of this doctoral research.

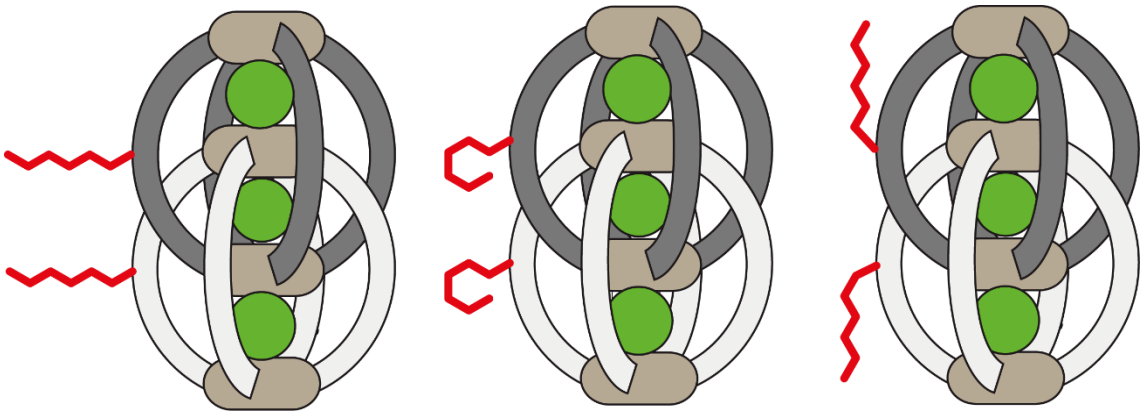

Figure 3.51: Illustration of possible folded and unfolded positions of the sidechains attached to the interpenetrated coordination cage.

^{1}H DOSY NMR spectra were measured, and the hydrodynamic radii of the structures were calculated using the obtained diffusion coefficients. It was shown that the diffusion

coefficients and therefore the hydrodynamic radii were in a similar range independent from the different chain length (Figure 3.52). This is most likely based to a backfolding of the sidechains to the ligand backbone forming dispersive interactions with each other, therefore no significant increase of the spatial extent could be observed.

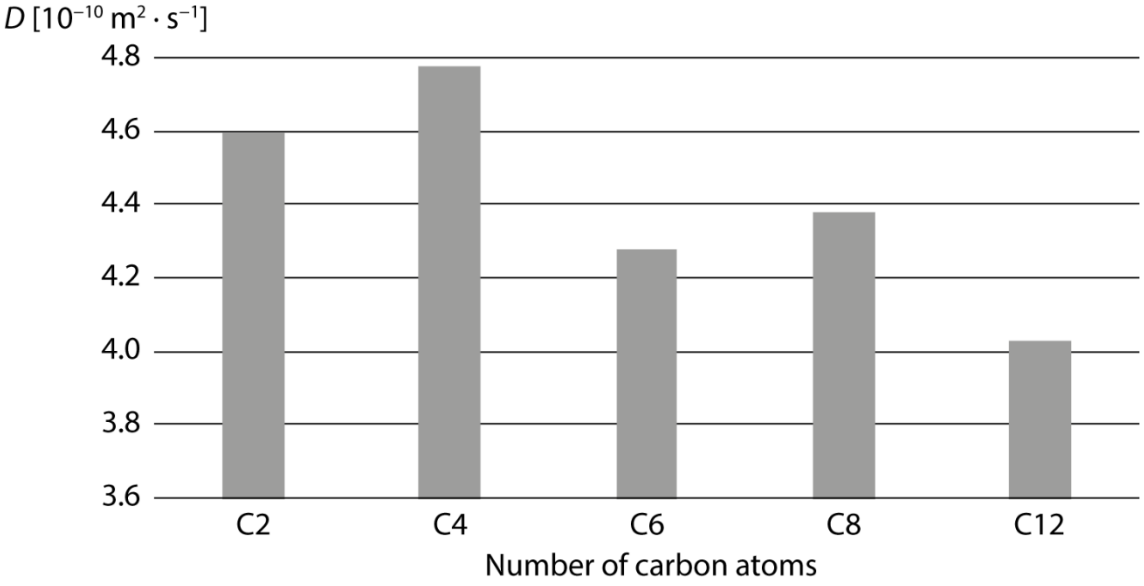

Figure 3.52: Number of carbon atoms in the side chains against the obtained diffusion coefficients *D* in 10^{-10} m^2 · s^{-1} of the corresponding coordination cages $Pd_4\mathbf{L}^{\mathbf{ACR1\text{-}6}}{}_8$.

For $Pd_4\mathbf{L}^{\mathbf{ACR1}}{}_8$ and $Pd_4\mathbf{L}^{\mathbf{ACR2}}{}_8$ the largest diffusion coefficients of $D = 4.593 \pm 0.008 \cdot 10^{-10}$ m^2 · s^{-1} and $D = 4.779 \pm 0.011 \cdot 10^{-10}$ m^2 · s^{-1}, respectively, were obtained. Since the value for the coordination cage with the C_4 chain is larger than for the shorter C_2 chain indicates that the dispersive interaction between carbon chain and ligand backbone is stronger and therefore the spatial extent of the molecule is smaller. The differences between a hexyl-substituted coordination cage and an octyl-substituted one is close to zero, indicating the same interaction strength between the side chain and the ligand backbone. Still these obtained values are with $D = 4.278 \pm 0.007 \cdot 10^{-10}$ m^2 · s^{-1} and $D = 4.382 \pm 0.006 \cdot 10^{-10}$ m^2 · s^{-1} smaller, and therefore the spatial extent larger than the beforehand mentioned. For $Pd_4\mathbf{L}^{\mathbf{ACR6}}{}_8$ a diffusion coefficient of $D = 4.031 \pm 0.003 \cdot 10^{-10}$ m^2 · s^{-1} was obtained, which results in a hydrodynamic radius about 1 Å larger than the other assemblies. These data are in good accordance to the already obtained values during my master thesis.

Similar behaviour was observed in studies by DRECHSLER who used DOSY NMR and ion-mobility mass spectrometry, respectively, to investigate the effect of sidechains attached to coordination cages.[175] In this work, lantern-shaped, carbazole-based $Pd_2\mathbf{L}_4$

and 3Br@$Pd_4\mathbf{L}_8$ coordination cages with different side chains were evaluated. Guest addition to the monomeric cage triggered the dimerization.

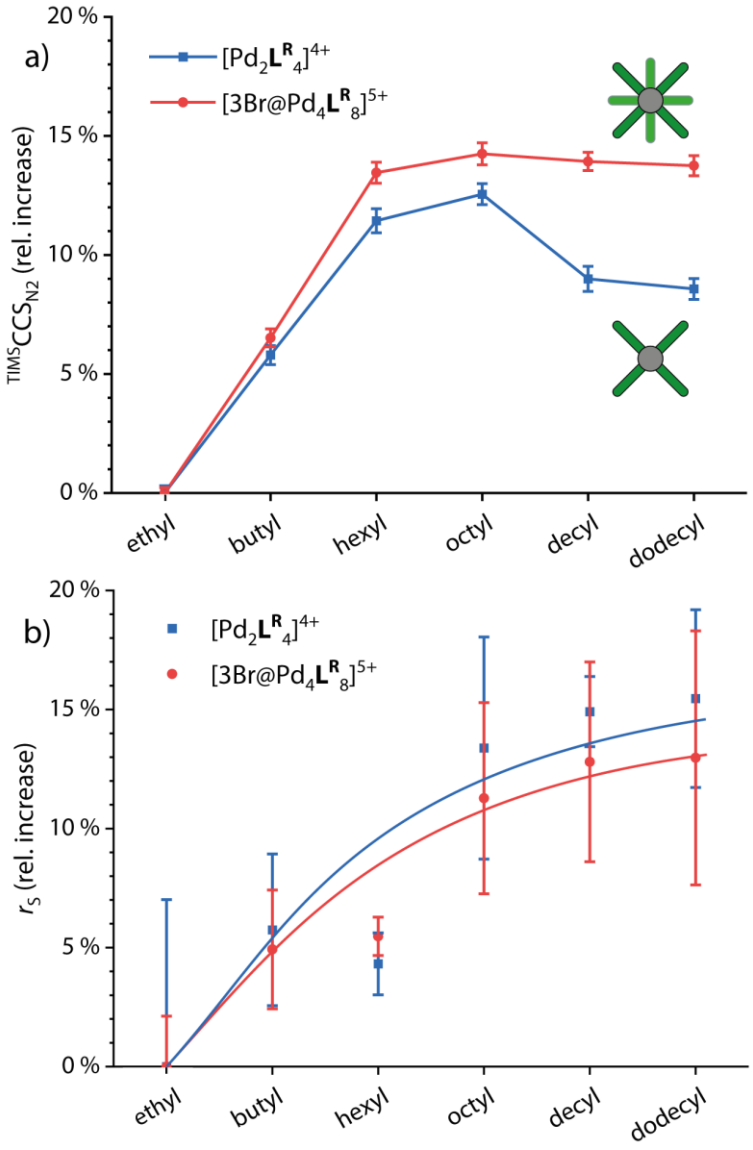

Figure 3.53: Increase of b) the hydrodynamic radii compared to the ethyl functionalized coordination cage and a) the increase of the collisional cross section compared to the ethyl functionalized coordination cage, in both cases with (red) and without (blue) guest molecule.

In this work it was shown that the hydrodynamic radius increased if longer side chains are installed. However, like the results obtained for the acridone based interpenetrated cages, the value dropped for the cage with hexyl sidechain. If the side chain length increases from octyl to dodecyl the hydrodynamic radius still increases but only by a few percentages compared to the ethyl functionalized cage. For the $Pd_2\mathbf{L}_4$ cages, the CCS values also increased with longer chain length from ethyl to octyl but decreases for decyl and dodecyl. However, in the case of the interpenetrated $Pd_4\mathbf{L}_8$ cage the CCS value increases from ethyl to hexyl and stays nearly constant with longer chain length. This

could be explained by dispersion interactions between the chains and the ligand backbones.

3.5.2 Hydrodynamic Radius and Shape

As described in chapter 1.2.1 it is common to calculate a hydrodynamic radius r_H from the obtained diffusion coefficient via STOKES-EINSTEIN equation. Aforementioned, this equation applies only to spherical molecules and is therefore not useful for a quantitative comparison of sizes of coordination cages, especially interpenetrated dimers or heteroleptic coordination cages whose form resembles an elongated ellipsoid more. However, most sizes of supramolecular structures reported in the literature were calculated by using the unmodified Stokes-Einstein equation and therefore prone to a certain error.[176]

A good way to describe the shape of a $Pd_2\mathbf{L}_4$ cage is to assume the particle to be a prolate ellipsoid, albeit drawbacks will appear. Most of the time, the surfaces of the cages are not "flat" as they are carrying functional groups or aliphatic sidechains to increase the solubility. To calculate the hydrodynamic radius of a prolate ellipsoid a modified STOKES-EINSTEIN equation 3.11 is proposed as follows:

$$r_H = \frac{k_B \cdot T \cdot f}{6 \cdot \pi \cdot \eta \cdot D} \tag{3.11}$$

with a shape factor *f*:

$$f = \frac{\ln\left(\frac{a}{b} + \sqrt{\left(\frac{a}{b}\right)^2 - 1}\right)}{\sqrt{\left(\frac{a}{b}\right)^2 - 1}} \tag{3.12}$$

with the major semi axis *a* und the minor semi axis *b* of the ellipsoid.

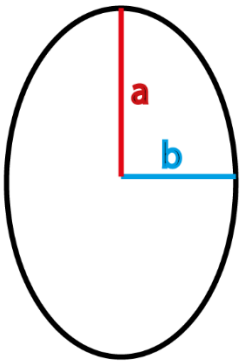

Figure 3.54: Illustration of the semi-axes *a* and *b* of an ellipsoid.

In case of the interpenetrated acridone-based coordination cage the values for r_H were calculated using the unmodified STOKES-EINSTEIN equation as well as equation 3.11 to compare the obtained results. The shape factor $f = 0.837$ was determined from distance measurement inside the molecular structure obtained by X-ray diffraction of $Pd_4\mathbf{L}^{\mathbf{ACR3}}{}_8$.[174] However, this method did first not take the side chains into consideration and second the structure in the solid state is more static compared to the liquid state.

Table 3.4: Diffusion coefficients D in 10^{-10} m^2 · s^{-1} in and calculated hydrodynamic radii r_H in Å for both spherical (Eq. 1.15) and prolate (Eq. 3.11) shape and difference between the two radii for the coordination cages.

	D [10^{-10} m^2 · s^{-1}]	r_H (Eq. 1.15) [Å]	r_H (Eq. 3.11) [Å]	Δ r_H [Å]
$Pd_4\mathbf{L}^{\mathbf{ACR1}}{}_8$	4.593 ± 0.008	15.39 ± 0.02	12.88 ±0.02	2.51
$Pd_4\mathbf{L}^{\mathbf{ACR2}}{}_8$	4.779 ± 0.011	14.79 ± 0.03	12.38 ±0.03	2.41
$Pd_4\mathbf{L}^{\mathbf{ACR3}}{}_8$	4.278 ± 0.007	16.52 ± 0.03	13.83 ± 0.03	2.69
$Pd_4\mathbf{L}^{\mathbf{ACR4}}{}_8$	4.382 ± 0.006	16.13 ± 0.02	13.50 ± 0.02	2.63
$Pd_4\mathbf{L}^{\mathbf{ACR6}}{}_8$	4.031 ± 0.003	17.54 ± 0.01	14.68 ± 0.01	2.86

The obtained differences for the hydrodynamic radii calculated with the two equations are with 2.4 to 2.9 Å in a similar range to the one obtained in the studies before.[174] Here, the values for the size of the coordination cages are more precise respectively more similar to the dimension of the molecular structure in the solid state when using the modified Stokes-Einstein equation for an ellipsoid.

One disadvantage of using the proposed shape factor is that the side chains will not be taken into consideration when calculating the hydrodynamic radius. Another drawback is that the values of the semi axes of the ellipsoid have to be either taken from a molecular structure in the solid state or from geometry optimized, calculated structures. Due to this,

it was contrived to develop a tailor-made shape factor for the calculation of the hydrodynamic radius of these interpenetrated coordination cage in collaboration with the NMR department at TU Dortmund University, Prof. W. HILLER. It was planned to fit the obtained diffusion coefficient from a temperature-dependent ^{1}H DOSY measurement.

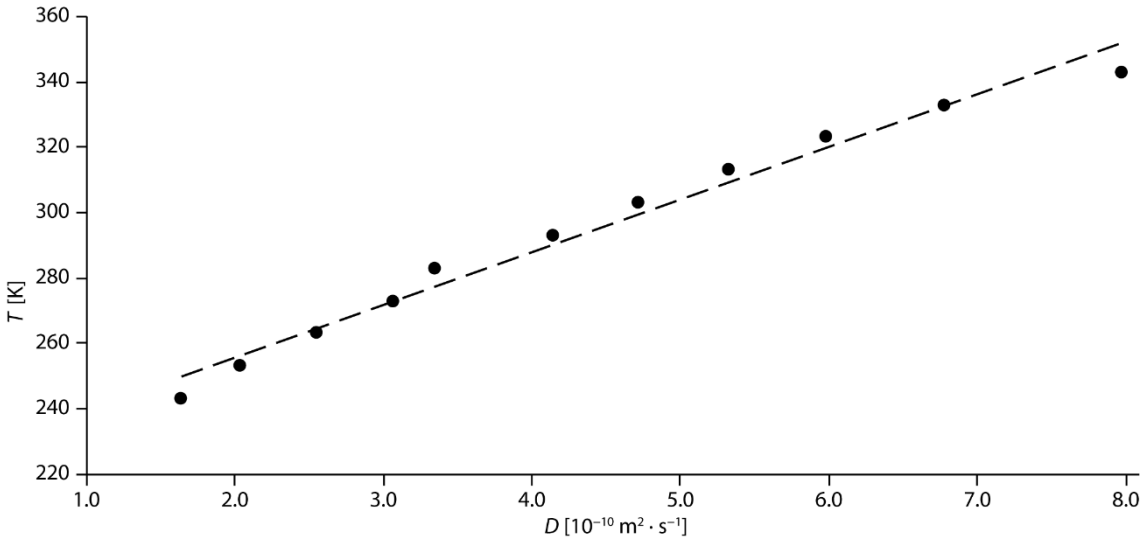

Figure 3.55: Obtained diffusion coefficients D in $10^{-10} \cdot m^2 \cdot s^{-1}$ of $Pd_4\mathbf{L}^{\mathbf{ACR3}}{}_8$ in acetone-d_6 against the temperature T in K.

As an example, the values for D at different temperatures are shown in Figure 3.55 for $Pd_4\mathbf{L}^{\mathbf{ACR3}}{}_8$. However, this work has not yet finished until the end of this doctoral thesis and is still under investigation. First results showed that the cage seems to shrink along the Pd-Pd axis and lead to a sphere-shape, which would give a shape factor of one.

3.5.3 Convection Compensation

As previously mentioned in the introduction one major problem while measuring diffusion by NMR spectroscopy is convection inside the analyte. To evaluate how the obtained diffusion coefficients of small molecules in various common solvents differ we evaluate a) two different pulse sequences for the ^{1}H DOSY experiments and b) used different NMR spectrometers that vary in magnetic field strength as well as being equipped with different probes. Especially NMR spectrometers that are equipped with nitrogen (N_2) or helium (He) chilled cryo-probes are prone to convection due to the huge temperature gradient between the coils and the sample. The molecules that were analyzed are *p*-toluene sulfonic acid (dissolved in D_2O, CD_3CN, acetone-d_6, DMF-d_7, DMSO-d_6, CD_3OD, $c = 1\ mg \cdot mL^{-1}$) and 2-phenoxyethanol (dissolved in CD_2Cl_2, $CDCl_3$, $c = 1\ mg \cdot mL^{-1}$). These molecules were chosen because of their broad solubility in polar

and non-polar solvents with diverse viscosities and because they show ^{1}H NMR signals in both the aromatic and aliphatic region. The investigated spectrometers and probes are the following: Bruker AVANCE III HD 400 MHz equipped with BBFO probe (**A**), AVANCE NEO 500 MHz equipped with BBFO*smart* probe (**B**), AVANCE III HD 500 MHz equipped with prodigy cryo-probe (N_2 chilled) (**C**), AVANCE III HD 600 MHz equipped with BBFO cryo-probe (He chilled) (**D**), AVANCE III HD 700 MHz equipped with QCI cryo-probe (He chilled) (**E**) and Agilent DD2 500 MHz equipped with H(F,X) triple resonance probe (**F**). All samples were measured with (*D*cc) and without (*D*) convection compensation with the pulse sequences mentioned above.

Table 3.5: Obtained diffusion coefficients $\boldsymbol{D_{cc}}$ and $\boldsymbol{D}$ in $10^{-10} \cdot m^2 \cdot s^{-1}$ for the ^{1}H DOSY NMR measurements of the samples in D_2O and CD_2Cl_2 measured on spectrometers **A**-**F**.

D_2O	**A**	**B**	**C**	**D**	**E**	**F**
$\boldsymbol{D_{cc}}$	6.688 ± 0.005	6.738 ± 0.004	6.857 ± 0.003	6.486 ± 0.004	6.646 ± 0.007	7.490 ± 0.002
$\boldsymbol{D}$	6.693 ± 0.005	6.799 ± 0.001	6.778 ± 0.002	6.303 ± 0.003	6.792 ± 0.001	7.370 ± 0.001
CD_2Cl_2	**A**	**B**	**C**	**D**	**E**	**F**
$\boldsymbol{D_{cc}}$	21.19 ± 0.04	21.07 ± 0.09	22.73 ± 0.11	21.46 ± 0.07	20.75 ± 0.10	22.10 ± 0.10
$\boldsymbol{D}$	25.87 ± 0.04	24.42 ± 0.01	61.47 ± 0.05	56.81 ± 0.06	73.75 ± 0.07	22.50 ± 0.02

If comparing the obtained diffusion coefficients for the measurements in the quite viscous solvent D_2O (Figure 3.56a) that the deviation if changing the spectrometer is low. This applies for both the measurement with and without the convection compensating gradients. However, changing the solvent to a less viscous one like CD_2Cl_2 the deviation for *D* especially measured without convection compensation between the spectrometers is quite high (Figure 3.56b). The largest effect can be seen for the cryo-probes (**C**, **D** and **E**), what could be explained by the huge temperature gradient between the sample and the coils.

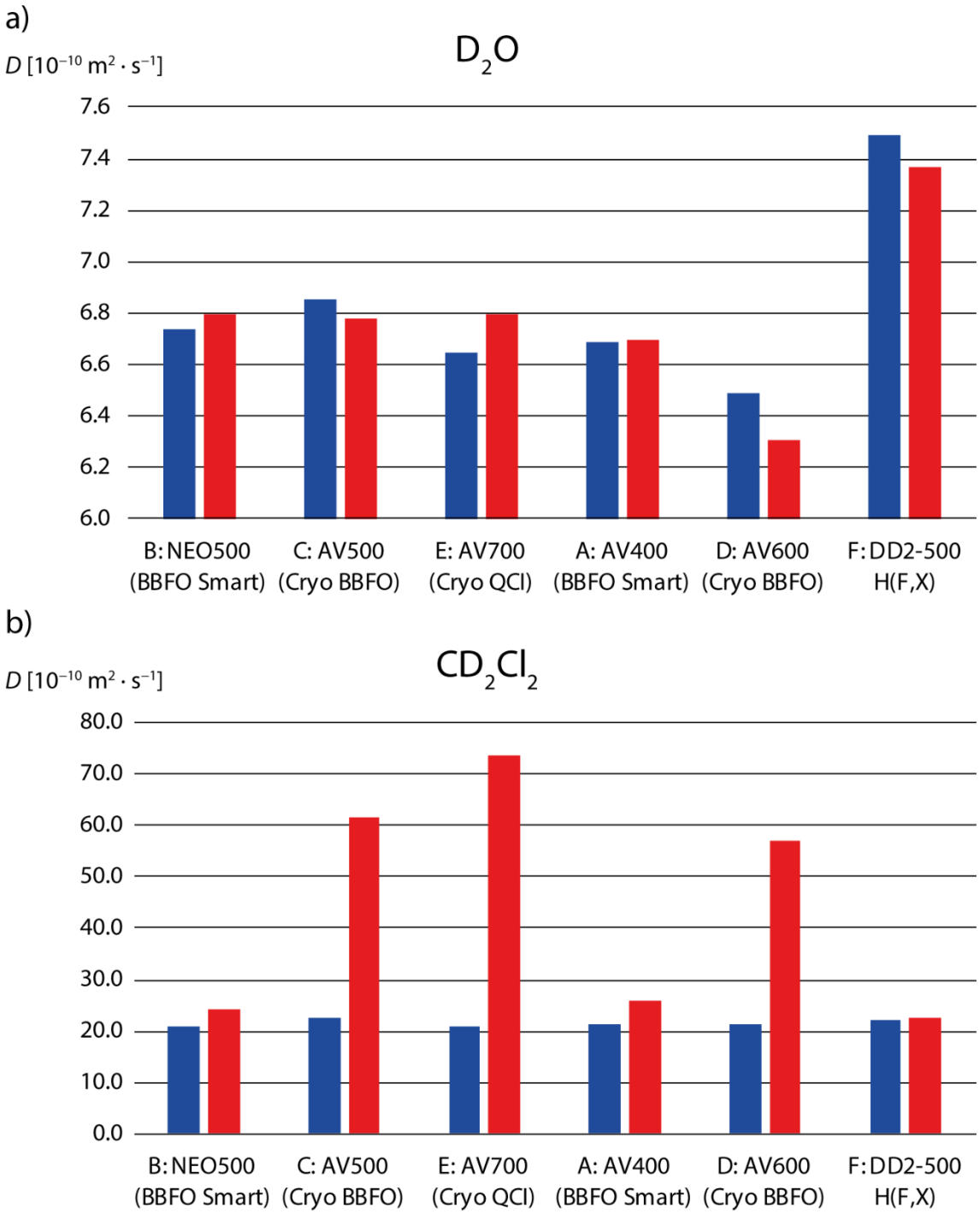

Figure 3.56: Obtained diffusion coefficients D_{cc} (blue) in $10^{-10} \cdot m^2 \cdot s^{-1}$ and D (red) in $10^{-10} \cdot m^2 \cdot s^{-1}$ for the samples in D_2O and CD_2Cl_2 measured on spectrometers **A-F**.

The same trends could be observed if the solvents were grouped according to their viscosity: high viscous one like DMSO-d_6, DMF-d_7 and CD_3OD showed similar behavior like D_2O. The deviation between the obtained diffusion coefficients of the samples in CD_3CN and acetone-d_6 using the different pulse sequences is low when spectrometers with room temperature probes are used but high for the ones equipped with cryo probes.

Comparatively high deviations were obtained for the measurements in less viscous $CDCl_3$, both for the spectrometers equipped with room temperature and cryo probes.

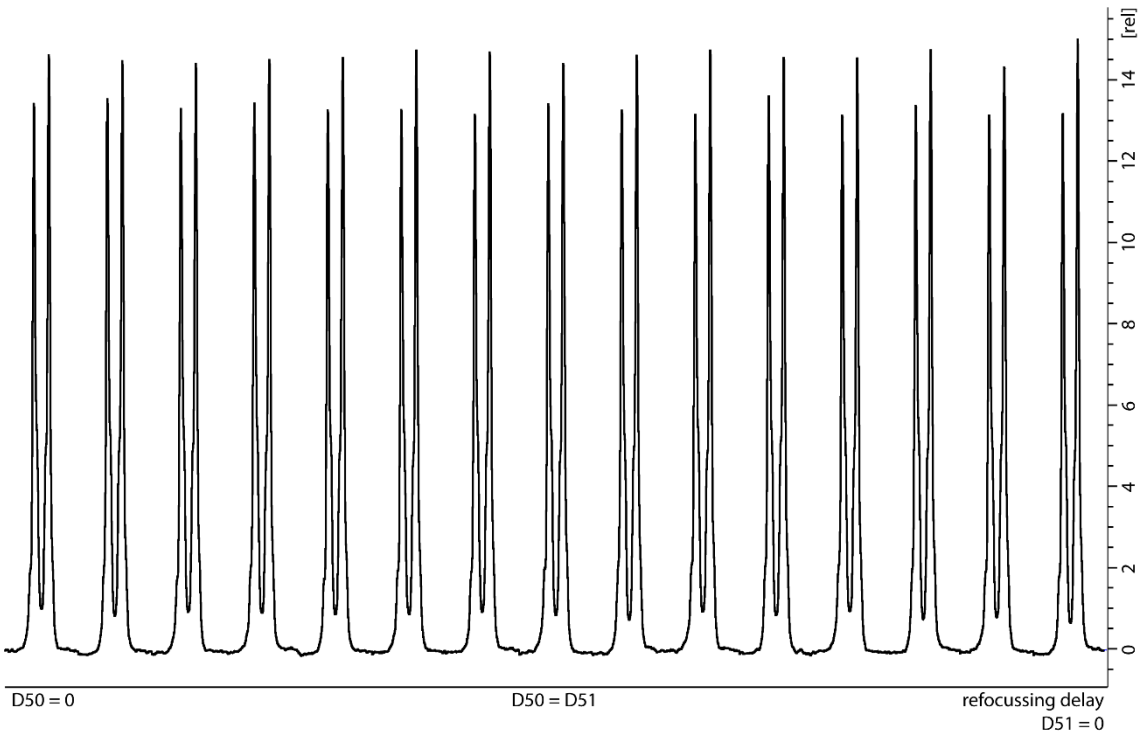

Figure 3.57: Plot of the signal intensity (700 MHz, T = 298 K, D_2O) of proton blah against the refocusing delays D50 and D51.

To proof if the signal intensity decrease is due to convection during the ^1H DOSY measurement, the refocusing delays were varied and the signal was plotted. If there are no significantly differences in the signal intensities visible, no convection would take place. This is the case for the measurement in D_2O, shown in Figure 3.57. In the case of convection, the highest signal intensity would be observed when the two delay times are the same, if one of the delays is shortened until 0 ms, the signal would have the lowest intensity. This is the case for the measurement in a less viscous solvent, for example CD_2Cl_2. This situation is shown in Figure 3.58.

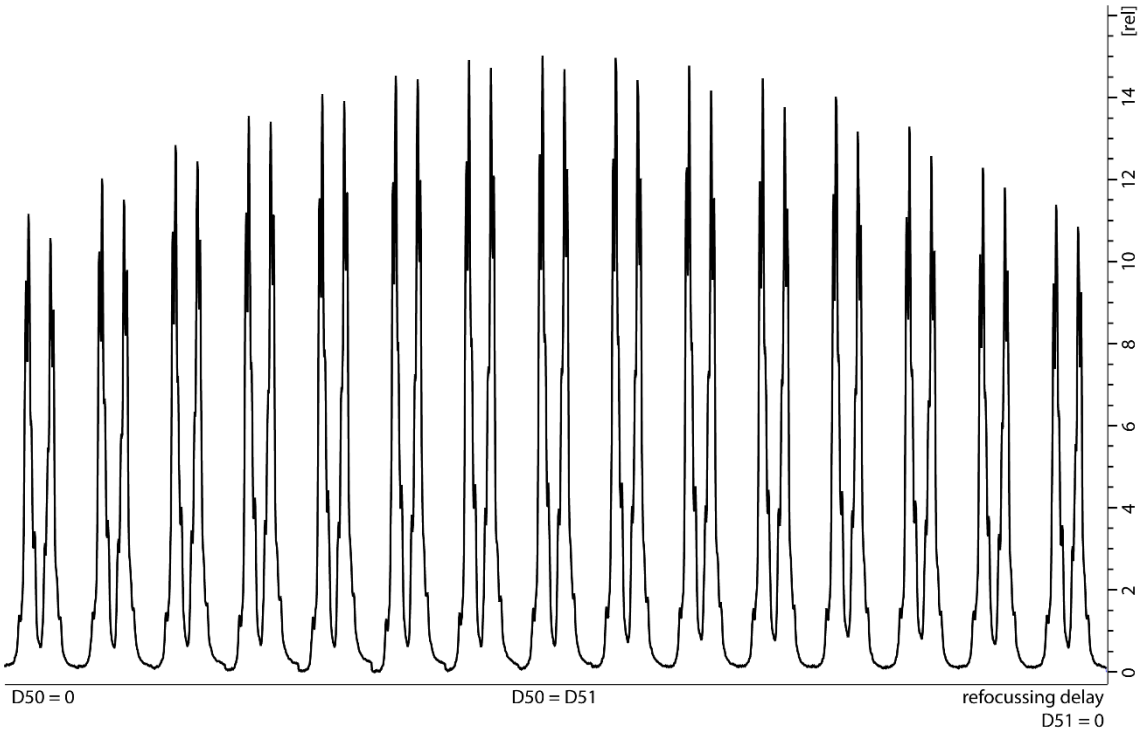

Figure 3.58: Plot of the signal intensity (700 MHz, T = 298 K, CD_2Cl_2) of proton blah against the refocusing delays D50 and D51.

As a conclusion, it is really important to understand the difference between diffusion and convection. It is absolutely necessary to use the correct pulse sequences for the measurements of DOSY NMR spectra. The obtained deviation in the diffusion coefficients is enormous if the contribution of convection is not compensated.

3.6 Conclusion and Outlook

Since the cavity of acridone-based interpenetrated coordination cages has been investigated extensively in former work of the group it was time to scrutinize the outer part of the cages: what is the behavior of the side chains attached to the ligand backbone? It was shown with ^{1}H DOSY NMR analysis, that the side chains most likely fold back in solution and forming dispersive interactions to the ligand backbone. If the chain length increases, the hydrodynamic radius of the system decreases as an indication of stronger interactions. The longest attached C_{12} chain also showed an interaction with itself as the increase of r_H of about 1 Å compared to the other ones depicts. Here, comparisons with ion-mobility mass spectrometry measurements could be helpful.

One disadvantage of using DOSY NMR for size calculation of coordination cages are the assumption of the shape that has to be made. The Stokes-Einstein equation is only valid

for spherical molecules. For shapes like ellipsoids, sticks or plates modified equations could be found in the literature. In this work and in continuing studies a tailor-made shape factor for coordination cages was proposed based on VT DOSY NMR experiments.

The last part of this chapter dealt with the influence of convection during DOSY measurements and showed ways to compensate it via PFG methods. The highest deviation in the diffusion coefficients between the investigated pulse sequences were obtained with less viscous solvents and spectrometers that were equipped with nitrogen or helium chilled probes.

3.7 Further NMR Experiments

Apart from the own research described in the previous chapters, I was involved in miscellaneous projects of the group with advanced NMR spectroscopic methods. Literally hundreds of DOSY NMR spectra were recorded and processed. Among others, VT NMR experiments, variable pressure experiments, solvent suppression (presat, excitation sculpting), selective 1D NOESY, EXSY, X-nuclei (1D, 2D, DOSY), T1 relaxation measurements and kinetics were performed to support the research in the group. Furthermore, NMR measurements for external collaborations were performed.[177,178] Outstanding examples, were advanced NMR spectroscopy helped to reveal structural information are the following.

3.7.1 $^{1}H\{^{1}H\}$ Homodecoupling

In the work of TESSAROLO it was unclear from ^{1}H NMR data as well from the 2D analysis if a coordination assembly consists of an interlocked octahedron or if a triple catenated species is present in solution.[179] By using PSYCHE NMR,[180–182] the overlapping signals could be distinguished because of the loss of multiplicity and therefore it was shown, that the interlocked species with a split into five signals with a ratio of 1:1:2:1:1 exists in solution (Figure 3.59).

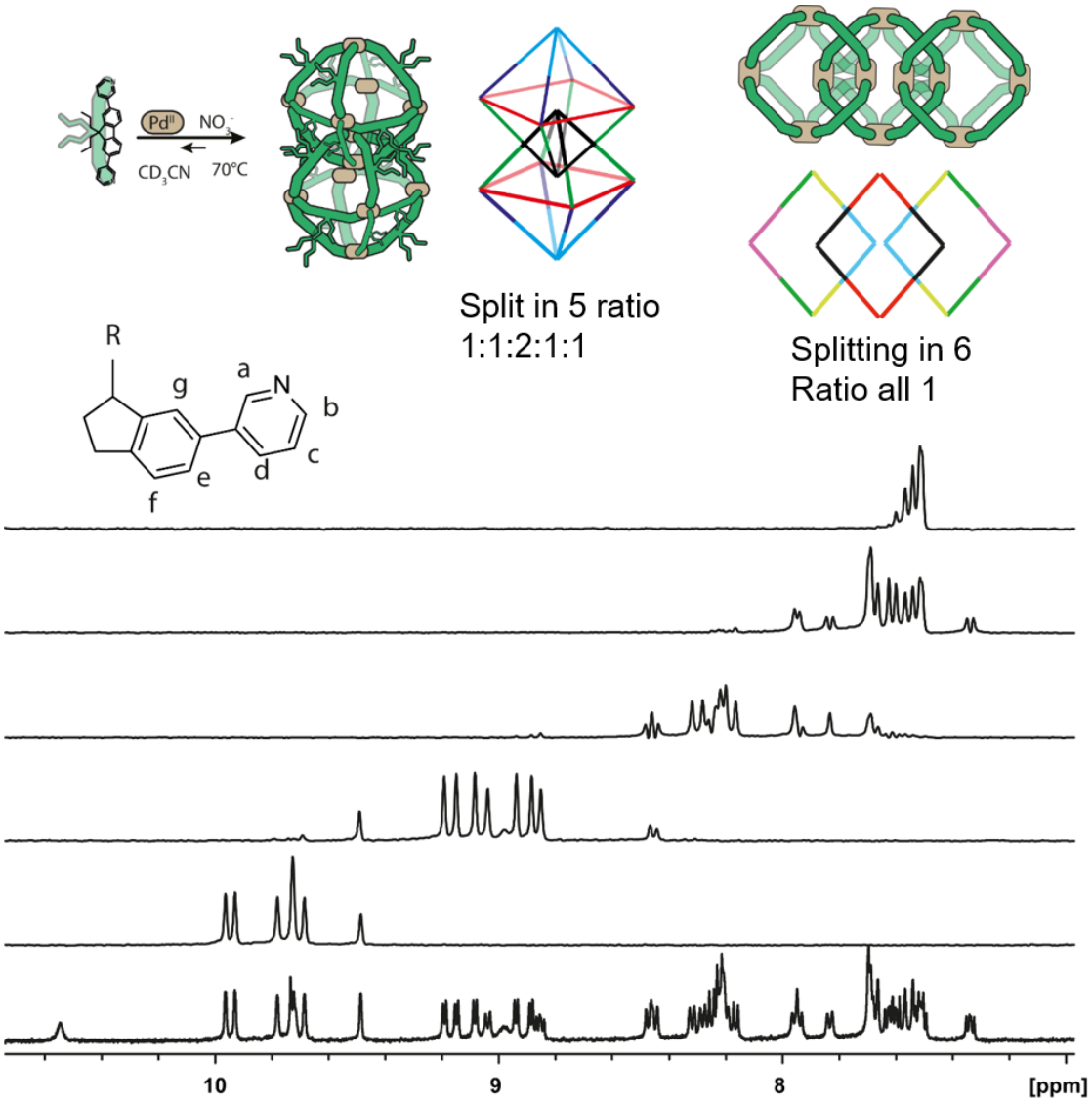

Figure 3.59: Partially stacked ^{1}H NMR spectra (500 MHz, CD_3CN, 298 K) with coupled ^{1}H NMR (bottom) and ^{1}H{^{1}H} PSYCHE spectra of the octahedral assemblies (top).

3.7.2 Conformational Analysis by NOESY NMR

In the work of EBBERT it was unclear how the ligands are oriented to one another in different heteroleptic $Pd_4A_4B_4$ assemblies.[183] With the help of ^{1}H–^{1}H NOESY NMR spectroscopy it was shown that in one example all of ligands A are pointing up making the so-called UFO-type structure (Figure 3.60 left). In this case, the intensity of the NOE crosspeak between the signal of proton **1** and **a** dominates the spectrum, however nearly no crosspeak between the signal of proton **1** and **2** could be identified. For the so-called saddle-type structure (Figure 3.60 right), the intensity of the NOE contact between the signals of protons **1** and **2** increases significantly.

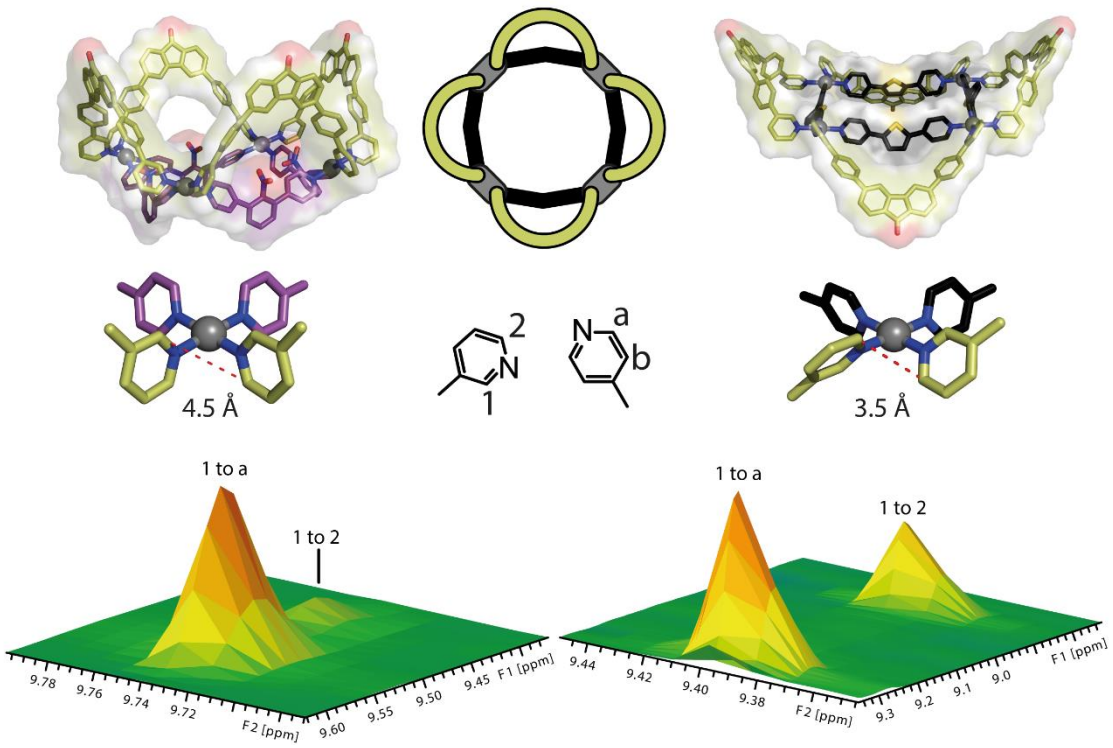

Figure 3.60: Conformational analysis of an UFO-type $Pd_4A_4B_4$ structure (left) and a saddle type $Pd_4A_4B_4$ structure (right) by the corresponding 1H−1H NOESY NMR spectra (500 MHz, DMSO-d_6, 298 K). The intensities of the NOE crosspeaks of the signals **1** to **a** and **1** to **2**, respectively, are shown within a 3D plot.

4 Experimental Section I

4.1 General Information

4.1.1 Nuclear Magnetic Resonance Spectroscopy (NMR)

NMR spectroscopic data was measured on the spectrometers Bruker AV 500 Avance NEO, Bruker AV 400 Avance III HD NanoBay, AV 500 Avance III HD, AV 600 Avance III HD, AV 700 Avance III HD and Agilent Technologies DD2 500 MHz. For ^{1}H and ^{13}C NMR spectra, chemical shifts were calibrated to the solvent lock signal.[184] For ^{31}P NMR spectra, 85% H_3PO_4 in H_2O (^{31}P, 0 ppm) was used as external standard. Chemical shifts δ are given in ppm, coupling constants J in Hz. All spectra were recorded in standard 5 mm NMR tubes at 25 °C, if not mentioned otherwise. ^{13}C{^{1}H} NMR spectra were processed using automatic BLP (backwards linear prediction, "cryoproc1d") to optimize the baseline. Due to overlapping signals and low signal-to-noise ratio in the aromatic regions not every ^{13}C signal of the carbon atoms of the coordination cages could be observed. ^{1}H–^{1}H NOESY NMR spectra were recorded with a mixing time D8 of 0.5 s. ^{1}H DOSY NMR spectra were recorded with a *dstebpgp3s* pulse sequence with diffusion delays D20 of 0.08 s and gradient durations P30 of 2500 to 3000 µs.[98,99] T1 analyses of the corresponding signals in the 1D spectra were performed to obtain the diffusion coefficients D using the STEJSKAL-TANNER-Equation.[185,186] Hydrodynamic radii r_H were calculated using the STOKES-EINSTEIN-Equation.[84]

4.1.2 Electrospray Ionisation Mass Spectrometry (ESI-MS)

Mass spectrometry and trapped ion mobility data were measured on Bruker ESI-timsTOF (electrospray ionization-trapped ion mobility-time of flight) and Bruker compact high-resolution LC mass spectrometers (positive/negative mode). For calibration of the TIMS and TOF devices, Agilent ESI-Low Concentration Tuning Mix was used. All measured and calculated values are given in *m/z*.

4.1.3 Gaschromatography Electron Ionization Mass Spectrometry (GC/EIMS)

GC/EI-MS analysis was obtained using an Agilent 7890B GC system (column: Agilent HP-5MS, 30 m, 0.25 mm, 0.25 μm) with an Agilent 5977A Mass Selective Detector.

4.1.4 X-Ray Single Crystal Structure Determination

Synchrotron beamline P11@DESY: Single crystal X-ray diffraction data was collected at macromolecular beamline P11, Petra III, DESY (a member of the Helmholtz Association, HGF), Hamburg, Germany. Samples were mounted using the Stäubli TX60L robotic arm. A wavelength of l = 0.6889 Å was chosen using a liquid N_2 cooled double crystal monochromator. Single crystal X-ray diffraction data was collected at 100(2) K on a single axis goniometer, equipped with an Oxford Cryostream 800 device and an Eiger 2 12M detector.

4.1.5 GPC

Recycling gel permeation chromatography was performed on Japan Analytical Industry NEXT and LaboACE instruments using JAIGEL 1-HH and 2-HH columns, 20 mm x 600 mm, flowrate 7 mL/min.

4.1.6 UV/Vis Spectroscopy

UV vis spectra were recorded on a DAD HP-8453 UV-Vis spectrometer.

4.1.7 CD Spectroscopy

Circular dichroism spectra were recorded on an Applied Photophysis qCD Chirascan CD spectrometer with a temperature-controlled cuvette holder.

4.2 Experimental Procedures

Where necessary, experiments were performed under argon atmosphere using standard Schlenk techniques. Chemicals and standard solvents were purchased from Sigma Aldrich, Acros Organics, Carl Roth, TCI Europe, VWR, ABCR or other suppliers and used as received, if not mentioned differently. Dry solvents were purchased or purified and dried over absorbent-filled columns on a GS-Systems solvent purification system

(SPS). Reactions were monitored with thin layer chromatography (TLC) using silica coated aluminum plates (Merck, silica 60, fluorescence indicator F254, thickness 0.25 mm). For column chromatography, silica (Merck, silica 60, 0.02–0.063 mesh ASTM) was used as the stationary phase, if not mentioned otherwise. The syntheses of the compounds $\mathbf{L^A}$ and $\mathbf{L^B}$ were reported in previous studies.[36,62]

4.2.1 Synthesis of 8-ethinylisoquinoline 1

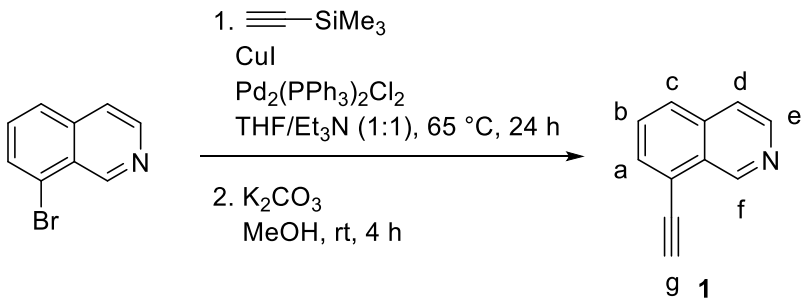

Scheme 4.1: Synthesis of 8-ethinylisoquinoline **1**.

To a degassed mixture of THF and Et_3N (1:1, 40 mL) 8-bromoisoquinoline (2.00 g, 9.61 mmol, 1 eq), ethinyltrimethylsilane (1.23 g, 12.50 mmol, 1.3 eq), copper(I)-iodide (0.37 g, 1.92 mmol, 0.2 eq) and dichloridobis(triphenylphosphine) palladium(II) (0.67 g, 0.96 mmol, 0.1 eq) were added under argon and heated to 65 °C for 24 h. The reaction mixture was cooled to rt and the solvent was removed. The crude product was purified via column chromatography (pentane/diethyl ether 1:1) to obtain 8-((trimethylsilyl)ethinyl)isoquinoline **1** as an orange oil. The obtained oil was dissolved in MeOH (100 mL) and K_2CO_3 as an excess was added. The reaction mixture was stirred at rt for 4 h. The reaction mixture was dissolved in $CHCl_3$ and carefully washed with water and brine and dried over $MgSO_4$. The solvent was removed in vacuo to obtain 8-ethinylisoquinoline **1** as a dark brown solid (1.39 g, 9.05 mmol, 95%).

^{1}H NMR (700 MHz, 298 K, $CDCl_3$): δ = 9.73 (s, 1H, f), 8.60 (d, ^3J = 5.7, 1H, e), 7.82 (m, 2H, a, c), 7.64 (m, 2H, b, d), 3.55 (s, 1H, g).

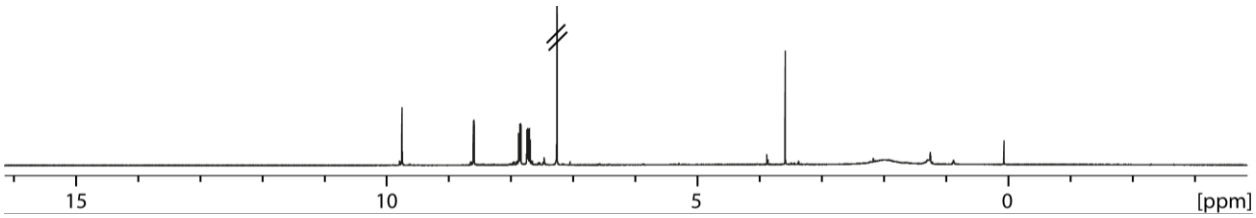

Figure 4.1: ^{1}H NMR (700 MHz, 298 K, $CDCl_3$) of **1**.

4.2.2 Synthesis of 2,7-bis(isoquinolin-8-ylethinyl)-9H-carbazole L^1

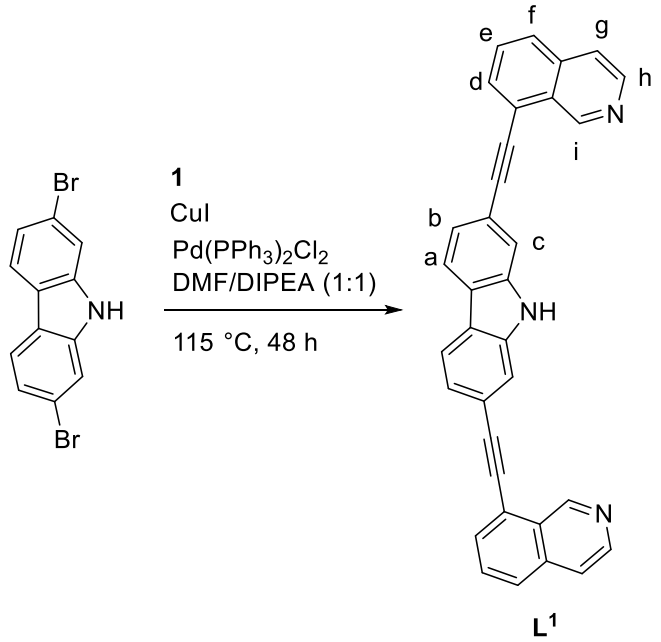

Scheme 4.2: Synthesis of $\mathbf{L^1}$.

To a degassed mixture of DMF and DIPEA (1:1, 15 mL) 2,7-dibromo-9*H*-carbazole (100.00 mg, 0.31 mmol, 1.0 eq), 8-ethinylisoquinoline **1** (141.40 mg, 0.93 mmol, 3.0 eq), copper(I)-iodide (11.27 mg, 0.06 mmol, 0.2 eq) and dichloridobis(triphenylphosphine)palladium(II) (21.60 mg, 0.03 mmol, 0.1 eq) were added under argon in a pressure flask and heated to 115 °C for 48 h. The reaction mixture was allowed to cool down to rt, dissolved in ethyl acetate and was washed with water and brine and dried over $MgSO_4$. The solvent was removed *in vacuo*. The crude product was dissolved in DMF and purified via GPC to obtain $\mathbf{L^1}$ as a yellowish-brown solid (35.00 mg, 0.07 mmol, 24%).

^{1}H NMR (500 MHz, 298 K, DMSO-d_6): δ = 11.67 (s, 1H, N*H*), 9.80 (s, 2H, i), 8.65 (d, ^3J = 5.5, 2H, h), 8.31 (d, ^3J = 8.0, 2H, a), 8.06 (d, ^3J = 8.2, 2H, d), 8.01 (d, ^3J = 6.5, 2H, f), 7.95 (d, ^3J = 5.4, 2H, g), 7.94 (s, 2H, c), 7.86 (t, ^3J = 7.4, 2H, e), 7.58 (dd, ^3J = 8.1, ^4J = 1.2, 2H, b).

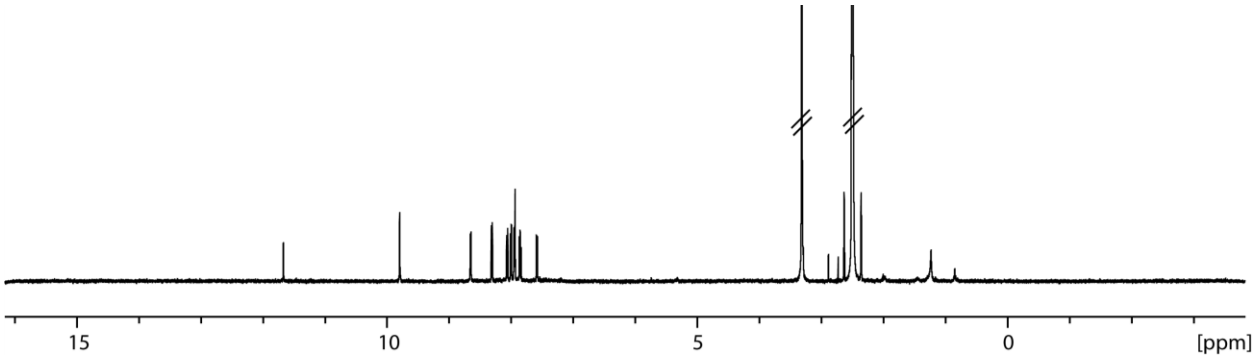

Figure 4.2: ^{1}H NMR (500 MHz, 298 K, DMSO-d_6) of $\mathbf{L^1}$.

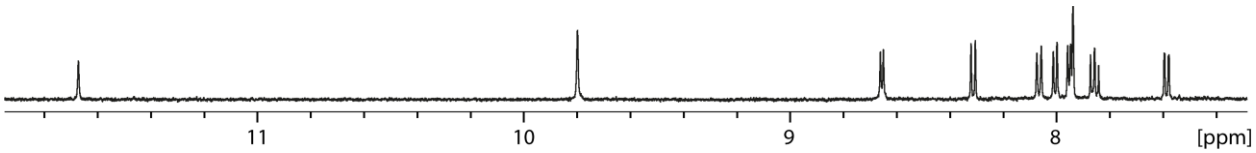

Figure 4.3: Partial ^{1}H NMR (500 MHz, 298 K, DMSO-d_6) of $\mathbf{L^1}$.

^{13}C{^{1}H} NMR (151 MHz, 298 K, DMSO-d_6): δ = 162.32, 150.14, 143.86, 140.22, 135.45, 131.75, 130.39, 127.48, 127.13, 122.76, 121.21, 120.81, 120.43, 119.10, 114.56, 97.05, 85.36.

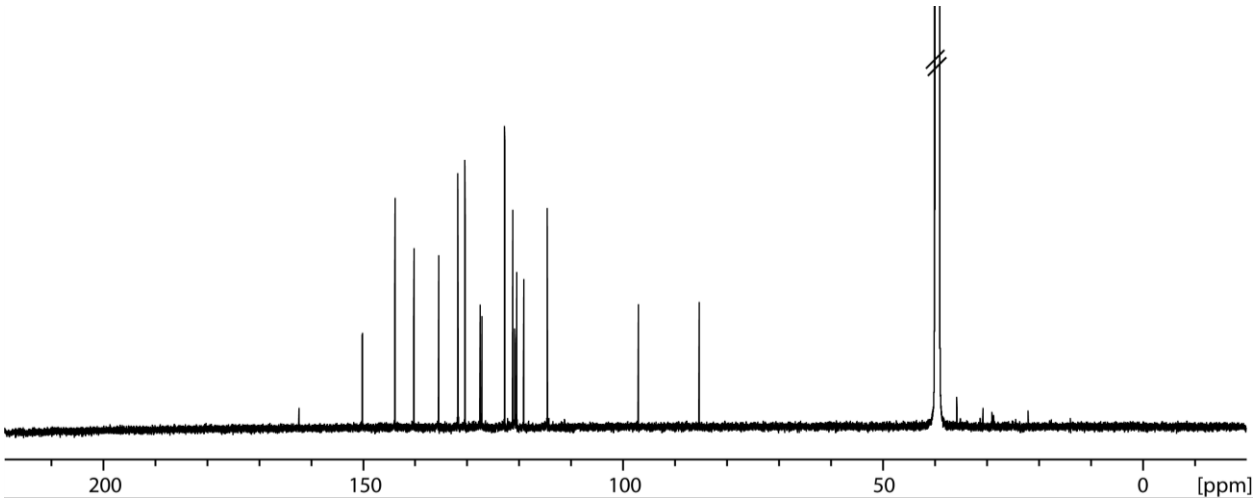

Figure 4.4: ^{13}C{^{1}H} NMR (151 MHz, 298 K, DMSO-d_6) of $\mathbf{L^1}$.

HR-ESI-MS (positive mode): measured for: $[C_{34}H_{19}N_3+H]^+$: 411.1623

calculated: 411.1598

4.2.3 Synthesis of 2,7-dibromo-9-methyl-9*H*-carbazole 2

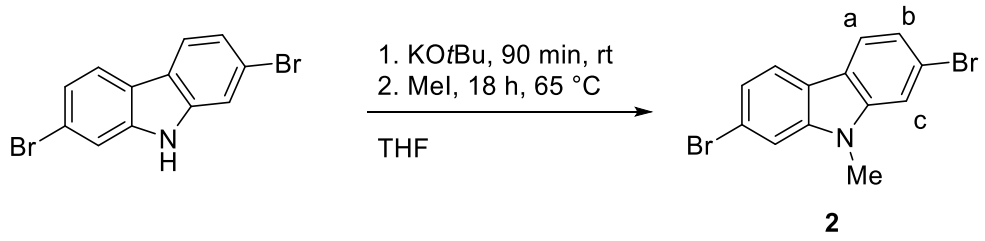

2

Scheme 4.3: Synthesis of 2,7-dibromo-9-methyl-9*H*-carbazole.

To a suspension of 2,7-dibromo-9*H*-carbazole (500.00 mg, 1.54 mmol, 1.0 eq)) in dry THF (10 mL) KO*t*Bu (345.27 mg, 3.08 mmol, 2.0 eq) was slowly added and the reaction mixture was stirred at rt for 90 min. Then a solution of MeI (240.20 mg, 1.69 mmol, 1.1 eq) in dry THF (3 mL) was added and the reaction mixture was stirred at 65 °C for 18 h. After cooling to rt, the reaction mixture was dissolved in DCM and washed with water and brine and dried over $MgSO_4$. The solvent was removed *in vacuo*. The crude product was purified via column chromatography (pentane/ethyl acetate 9:1) to obtain the desired product as a white solid (140 mg, 0.4 mmol, 27%).

^{1}H NMR (700 MHz, 298 K, $CDCl_3$): δ = 7.89 (d, ^3J = 8.2, 2H, a), 7.55 (d, ^4J = 1.6, 2H, c), 7.35 (dd, ^3J = 8.2, ^4J = 1.6, 2H, b), 3.80 (s, 3H, NCH_3).

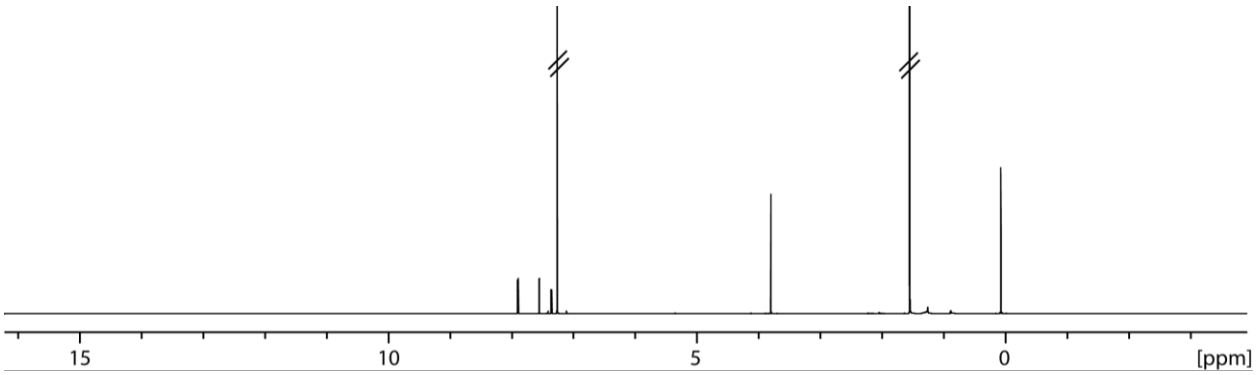

Figure 4.5: ^{1}H NMR (700 MHz, 298 K, $CDCl_3$) of **2**.

^{13}C NMR (176 MHz, 298 K, $CDCl_3$): δ = 140.92, 121.63, 120.42, 120.23, 118.75, 110.89, 28.30.

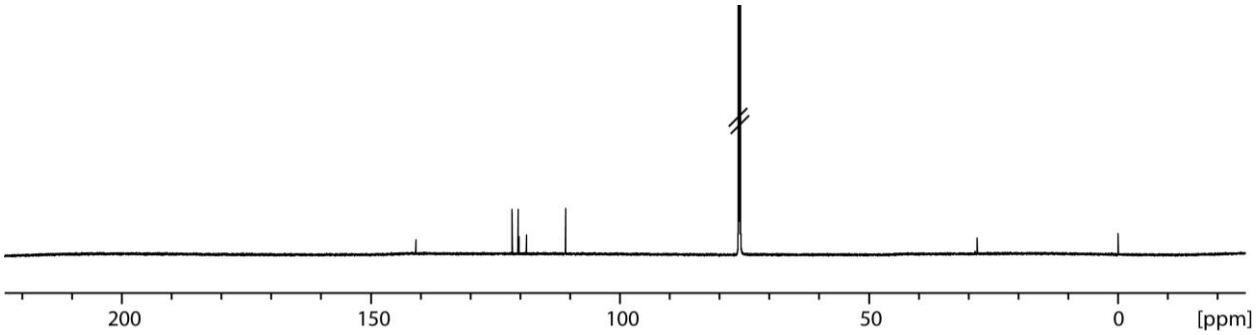

Figure 4.6: $^{13}C\{^{1}H\}$ NMR (176 MHz, 298 K, $CDCl_3$) of **2**.

GC-EI-MS: [80 °C (1 min) – 270 °C (5.5 min), heat rate 40 °C min^{-1}] (70 eV, retention time: 7.58 min): *m*/*z* (%) = 339 (100) $[M]^{+\cdot}$, 324 (3) $[M - Me]^+$, 258 (13) $[M - Br]^+$, 179 (44) $[M - 2\ Br]^+$, 164 (47) $[M - Me - 2\ Br]^+$.

4.2.4 Synthesis of 2,7-bis(isoquinolin-8-ylethinyl)-9-methyl-9*H*-carbazole L^2

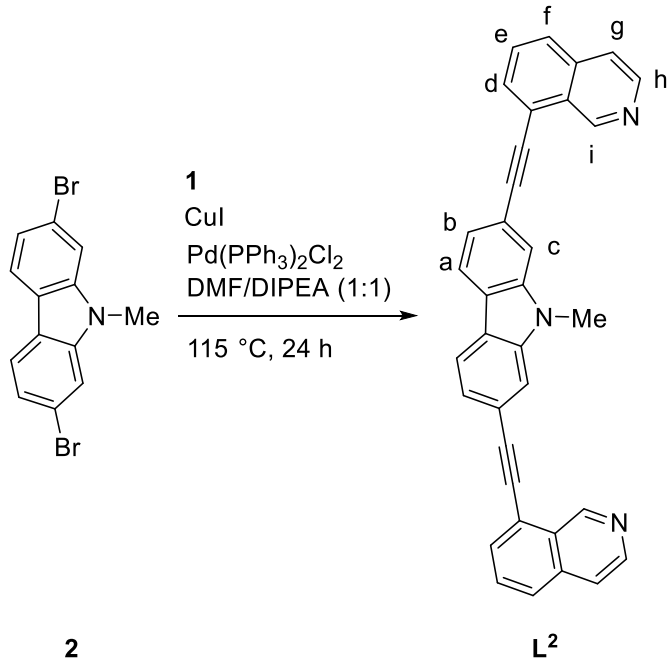

Scheme 4.4: Synthesis of L^2.

To a degassed mixture of DMF and DIPEA (1:1, 15 mL) 2,7-dibromo-9-methyl-9*H*-carbazole **2** (100.00 mg, 0.29 mmol, 1.0 eq), 8-ethinylisoquinoline **1** (135.55 mg, 0.87 mmol, 3.0 eq), copper(I)-iodide (11.24 mg, 0.06 mmol, 0.2 eq) and dichloridobis(triphenylphosphine)palladium(II) (20.70 mg, 0.03 mmol, 0.1 eq) were added under argon in a pressure flask and the reaction was heated to 115 °C for 24 h. The reaction mixture was allowed to cool down to rt, dissolved in $CHCl_3$ and was washed

with water and brine and dried over $MgSO_4$. The solvent was removed *in vacuo*. The crude product was dissolved in DMF and purified via GPC to obtain **L²** as a yellowish solid (55.00 mg, 0.11 mmol, 39%).

^{1}H NMR (600 MHz, 298 K, DMSO-d_6): δ = 9.48 (s, 2H, i), 8.66 (d, ^3J = 5.6, 2H, h), 8.34 (d, ^3J = 8.0, 2H, a), 8.15 (s (br), 2H, d), 8.07 (d, ^3J = 8.3, 2H, f), 8.00 (dd, ^3J = 7.1, ^5J = 0.9, 2H, g), 7.96 (d, ^3J = 5.6, 2H, c), 7.86 (dt, ^3J = 7.2, 2H, e), 7.62 (dd, ^3J = 8.0, ^4J = 1.3, 2H, b), 4.05 (s, 3H, NCH_3).

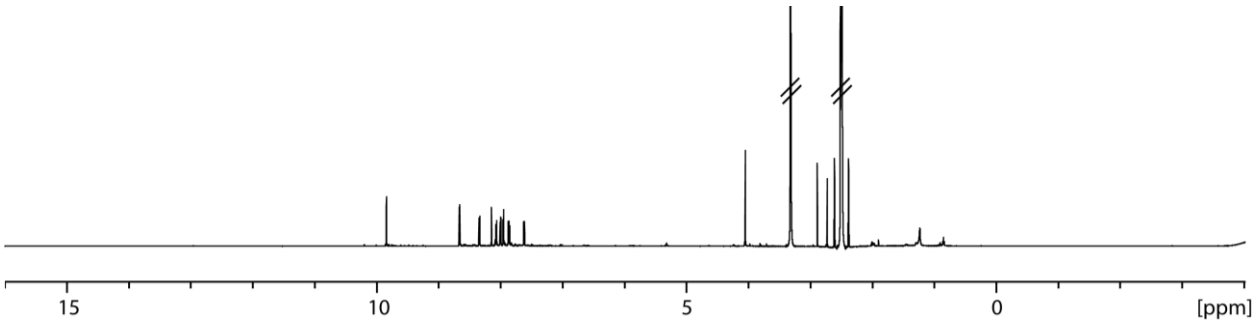

Figure 4.7: ^{1}H NMR (600 MHz, 298 K, DMSO-d_6) of **L²**.

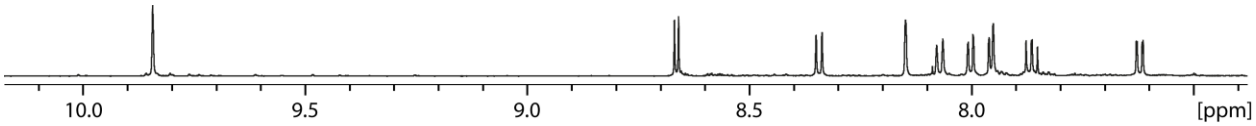

Figure 4.8: Partial ^{1}H NMR (600 MHz, 298 K, DMSO-d_6) of **L²**.

^{13}C{^{1}H} NMR (151 MHz, 298 K, DMSO-d_6): δ = 150.22, 143.90, 141.20, 135.46, 131.73, 130.39, 127.52, 127.12, 122.85, 122.29, 121.18, 120.79, 120.41, 119.30, 113.08, 97.07, 85.51, 29.38.

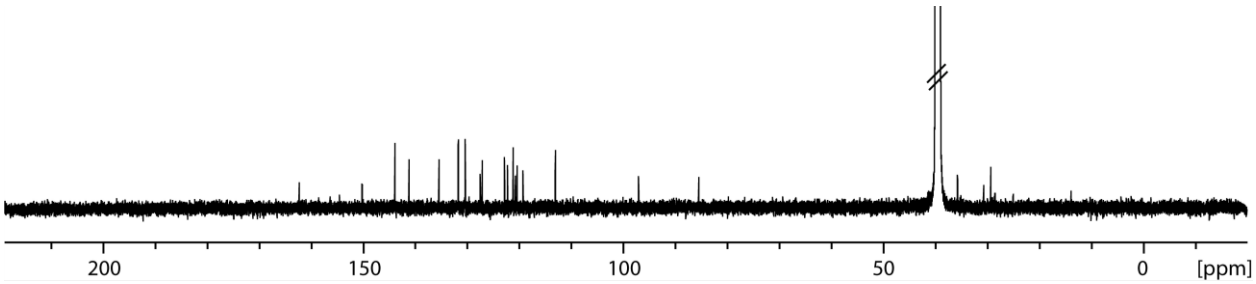

Figure 4.9: ^{13}C{^{1}H} NMR (151 MHz, 298 K, DMSO-d_6) of **L²**.

HR-ESI-MS (positive mode): measured for: $[C_{35}H_{21}N_3+H]^+$: 484.1763

calculated: 484.1808

4.2.5 Synthesis of 2,7-dibromo-*N*-methyl-9*H*-carbazole-9-carboxamide 3

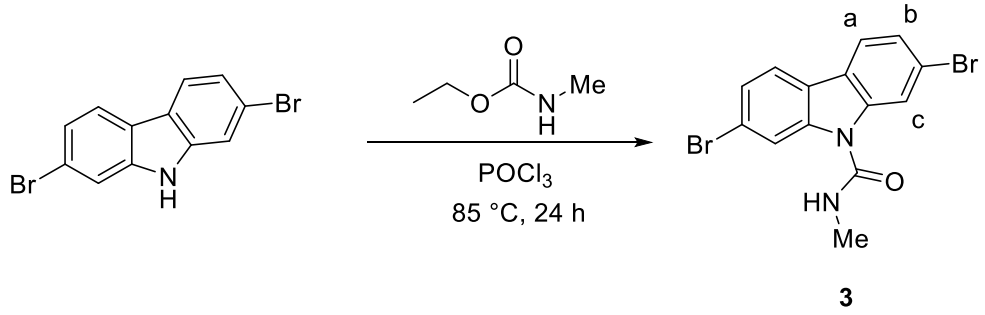

3

Scheme 4.5: Synthesis of 2,7-dibromo-*N*-methyl-9*H*-carbazole-9-carboxamide **3**.

2,7-dibromo-9*H*-carbazole (1.00 g, 3.08 mmol, 1.0 eq) and ethyl-*N*-methylcarbamate (1.27 g, 12.31 mmol, 4.0 eq) were dissolved in freshly distilled phosphoryl trichloride (20 mL) and heated to 85 °C for 24 h. The reaction mixture was cooled to rt and diluted with ice-cold water. Saturated $NaHCO_3$ solution was added until the mixture was pH-neutral. The reaction mixture was extracted with DCM and the combined organic layers were washed with water and brine and dried over $MgSO_4$. The solvent was removed *in vacuo* and the crude product was purified via column chromatography (pentane/ethyl acetate 9:1) to obtain **3** as a white solid (0.29 g, 0.75 mmol, 24%).

^{1}H NMR (600 MHz, 298 K, DMSO-d_6): δ = 8.38 (q, ^3J = 4.2, 1H, N*H*), 8.18 (d, ^3J = 8.3, 2H, a), 8.08 (d, ^4J = 1.6, 2H, c), 7.53 (dd, ^3J = 8.3, ^4J = 1.7, 2H, b), 2.94 (d, ^3J = 4.2, 3H, C*H*$_3$).

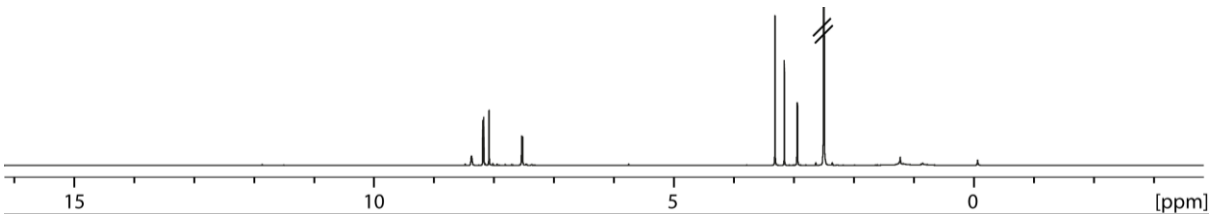

Figure 4.10: ^{1}H NMR (500 MHz, 298 K, DMSO-d_6) of **3**.

^{13}C{^{1}H} NMR (126 MHz, 298 K, DMSO-d_6): δ = 151.9, 138.7, 124.9, 122.3, 122.2, 119.7, 116.4, 28.9.

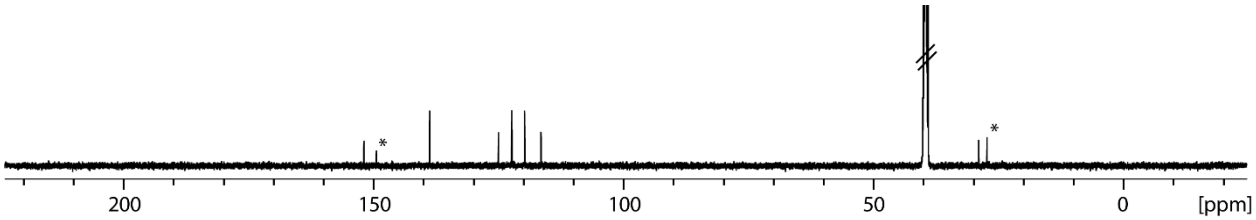

Figure 4.11: $^{13}C\{^{1}H\}$ NMR (126 MHz, 298 K, DMSO-d_6) of **3**. Reagent residues are marked with a star *.

HR-ESI-MS (positive mode): measured for: $[C_{14}H_{10}Br_2N_2O+Na]^+$: 404.9023

calculated: 404.9032

4.2.6 Synthesis of 2,7-bis(isoquinolin-8-ylethinyl)-*N*-methyl-9*H*-carbazole-9-carboxamide L^3

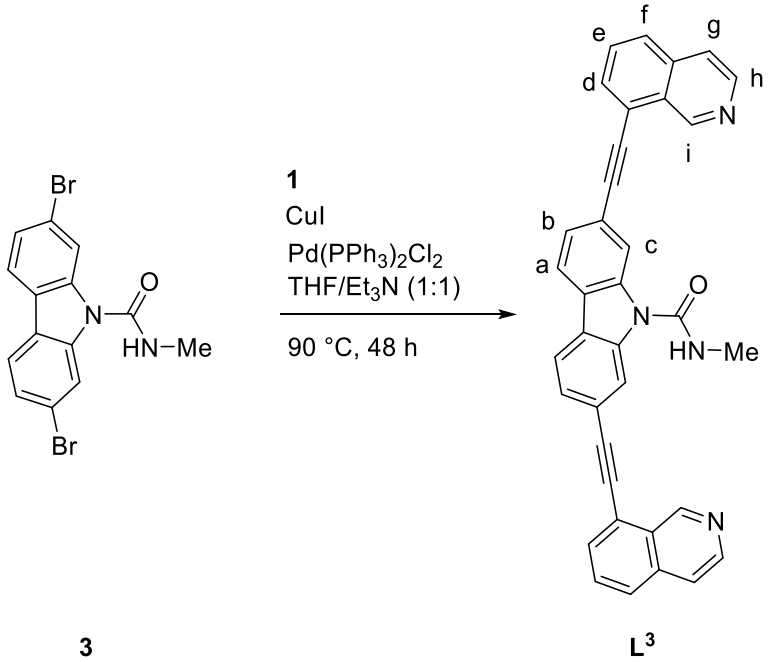

Scheme 4.6: Synthesis of 2,7-bis(isoquinolin-8-ylethinyl)-*N*-methyl-9*H*-carbazole-9-carboxamide $\mathbf{L^3}$.

To a degassed mixture of dry THF and Et_3N (1:1, 20 mL) **3** (250.00 mg, 0.65 mmol, 1.0 eq), **1** (250.59 mg, 1.64 mmol, 2.5 eq), copper(I)-iodide (24.92 mg, 0.13 mmol, 0.2 eq) and dichloridobis(triphenylphosphine)palladium(II) (45.93 mg, 0.07 mmol, 0.1 eq) were added under argon in a pressure flask and heated to 90 °C for 48 h. The reaction mixture was allowed to cool down to rt, dissolved in EtOAc and washed with water and brine and dried over $MgSO_4$. The solvent was removed *in vacuo*. The crude product was purified via column chromatography (EtOAc 100%) and GPC ($CHCl_3$) to obtain $\mathbf{L^3}$ as an orange solid (20 mg, 0.04 mmol, 6%).

^{1}H NMR (600 MHz, 298 K, DMSO-d_6): δ = 9.81 (s (br), 2H, i), 8.67 (s (br), 2H, h), 8.49 (q, ^{3}J = 4.4, 1H, N*H*), 8.39 (d, ^{3}J = 8.0, 2H, a), 8.30 (d, ^{4}J = 0.5, 2H, c), 8.08 (d, ^{3}J = 8.3, 2H, d), 8.03 (dd, ^{3}J = 7.1, ^{4}J = 0.9 Hz, 2H, f), 7.96 (d, ^{3}J = 5.3 Hz, 2H, g), 7.86 (m, 2H, e), 7.78 (dd, ^{3}J = 8.0 Hz, ^{4}J = 1.3 Hz, 2H, b), 3.04 (d, ^{3}J = 4.4 Hz, 3H, C*H*$_3$).

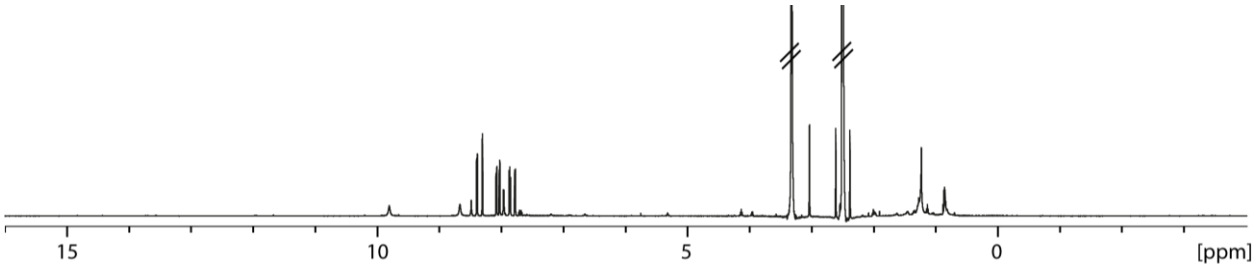

Figure 4.12: ^{1}H NMR (600 MHz, 298 K, DMSO-d_6) of **L^{3}**.

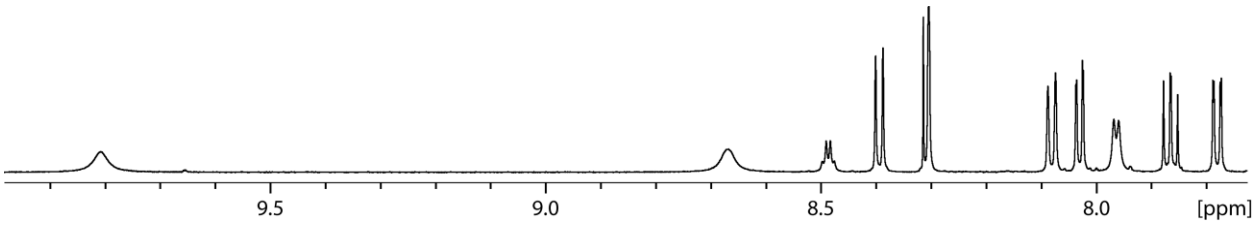

Figure 4.13: Partial ^{1}H NMR (600 MHz, 298 K, DMSO-d_6) of **L^{3}**.

^{13}C{^{1}H} NMR (151 MHz, 298 K, DMSO-d_6): δ = 152.62, 150.58, 144.38, 138.80, 135.90, 132.43, 130.85, 129.14, 128.19, 126.11, 124.49, 121.78, 120.71, 120.62, 117.37, 96.92, 86.48, 79.65, 27.90.

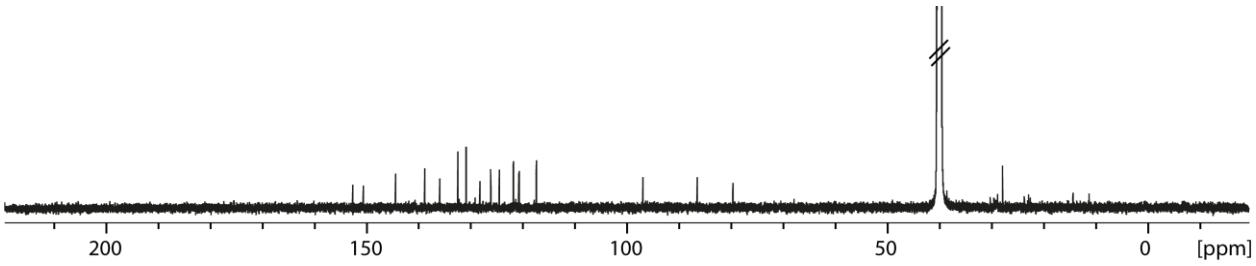

Figure 4.14: ^{13}C{^{1}H} NMR (151 MHz, 298 K, DMSO-d_6) of **L^{3}**.

HR-ESI-MS (positive mode): measured for: $[C_{36}H_{22}N_4O+H]^+$: 527.1859

calculated: 527.1866

4.2.7 Synthesis of 2,7-dibromo-*N*-ethyl-9*H*-carbazole-9-carboxamide 4

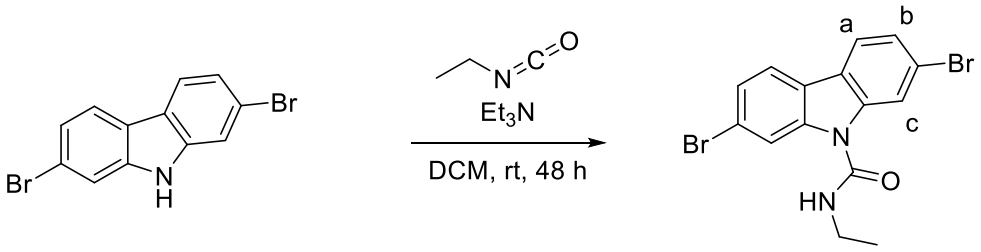

4

Scheme 4.7: Synthesis of 2,7-dibromo-*N*-ethyl-9*H*-carbazole-9-carboxamide **4**.

2,7-dibromo-9*H*-carbazole (250.00 mg, 0.77 mmol, 1.0 eq) was dissolved in dry DCM (20 mL). Ethyl isocyanate (82.01 mg, 1.15 mmol, 1.5 eq) and Et_3N (116.76 mg, 1.15 mmol, 1.5 eq) were added and the reaction mixture was stirred at rt for 48 h. The reaction mixture was diluted with water (30 mL) and extracted with DCM. The combined organic phases were washed with water and brine and dried over $MgSO_4$. The solvent was removed *in vacuo*. The crude product was purified via column chromatography (pentane/EtOAc, 9:1) and GPC ($CHCl_3$) to obtain **4** as a white solid (94.00 mg, 0.24 mmol, 31%).

^{1}H NMR (500 MHz, 298 K, DMSO-d_6): δ = 8.51 (t, ^3J = 5.3, 1H, N*H*), 8.18 (d, ^3J = 8.3, 2H, a), 8.06 (d, ^4J = 1.6, 2H, c), 7.53 (dd, ^3J = 8.3, ^4J = 1.6, 2H, b), 3.41 (m, 2H, CH_2), 1.25 (t, ^3J = 7.2, 3H, CH_3).

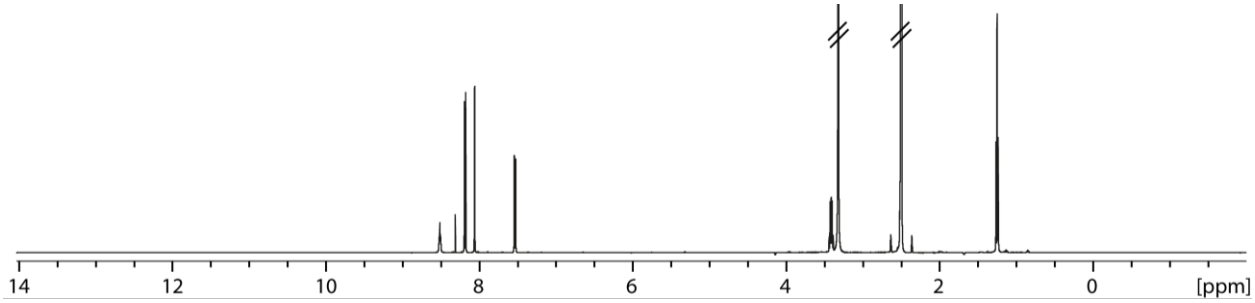

Figure 4.15: ^{1}H NMR (500 MHz, 298 K, DMSO-d_6) of **4**.

^{13}C{^{1}H} NMR (126 MHz, 298 K, DMSO-d_6): δ = 151.1, 138.8, 124.9, 122.3, 122.2, 119.7, 116.4, 35.4, 14.6.

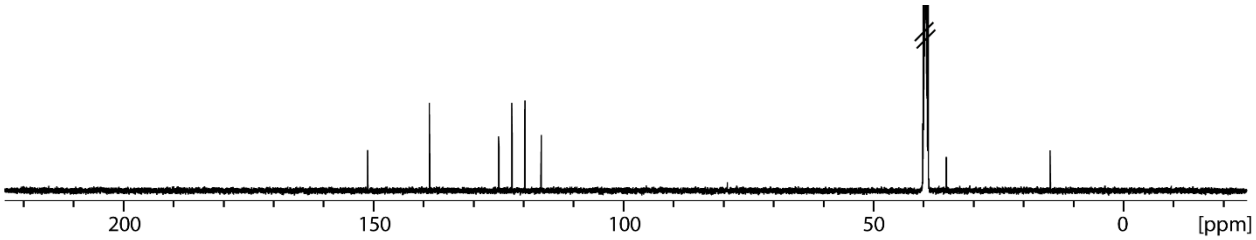

Figure 4.16: $^{13}C\{^{1}H\}$ NMR (126 MHz, 298 K, DMSO-d_6) of **4**.

HR-ESI-MS (positive mode): measured for: $[C_{15}H_{12}Br_2N_2O+Na]^+$: 418.9186

calculated: 418.9189

4.2.8 Synthesis of 2,7-bis(isoquinolin-8-ylethinyl)-*N*-ethyl-9*H*-carbazole-9-carboxamide L[4]

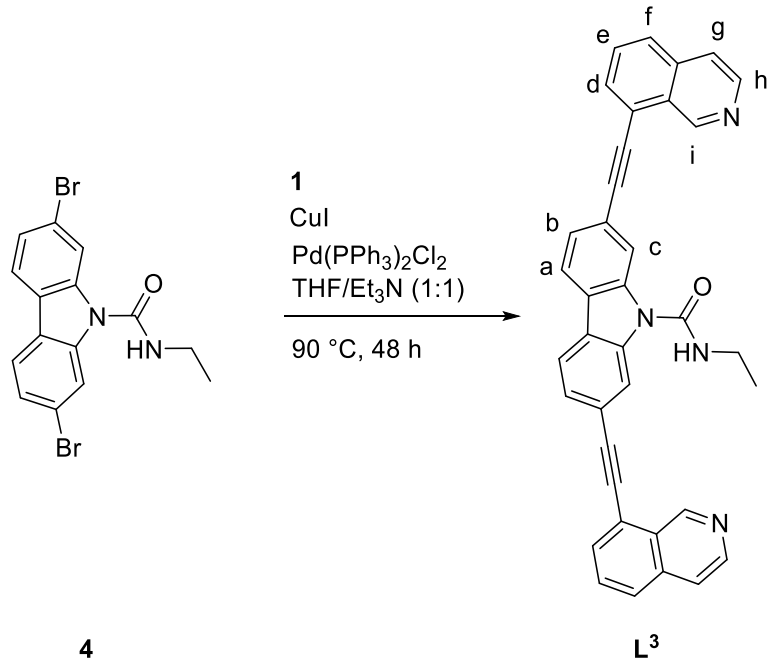

4 **L[3]**

Scheme 4.8: Synthesis of 2,7-bis(isoquinolin-8-ylethinyl)-*N*-ethyl-9*H*-carbazole-9-carboxamide **L[4]**.

To a degassed mixture of THF and Et_3N (1:1, 10 mL) **4** (94.00 mg, 0.24 mmol, 1.0 eq), **1** (90.89 mg, 0.59 mmol, 2.5 eq), copper(I)-iodide (13.6 mg, 0.07 mmol, 0.3 eq) and dichloridobis(triphenylphosphine)palladium(II) (25.03 mg, 0.04 mmol, 0.15 eq) were added under argon in a pressure flask and heated to 90 °C for 48 h. The reaction mixture was allowed to cool down to rt, dissolved in $CHCl_3$ and washed with water and brine and dried over $MgSO_4$. The solvent was removed *in vacuo*. The crude product was purified via column chromatography ($CHCl_3$/MeOH, 10:1) and GPC ($CHCl_3$) to obtain **L[3]** as an orange solid (15.00 mg, 0.03 mmol, 12%).

^{1}H NMR (600 MHz, 298 K, DMSO-d_6): δ = 9.80 (s, 2H, i), 8.66 (d, ^{3}J = 5.6, 2H, h), 8.63 (t, ^{3}J = 5.4, 1H, N*H*), 8.40 (d, ^{3}J = 8.0, 2H, a), 8.28 (d, ^{4}J = 0.5, 2H, c), 8.08 (d, ^{3}J = 8.3, 2H, f), 8.03 (dd, ^{3}J = 7.1, ^{4}J = 0.9, 2H, d), 7.96 (dd, ^{3}J = 5.6, ^{4}J = 0.5, 2H, g), 7.86 (m, 2H, e), 7.78 (dd, ^{3}J = 8.1, ^{4}J = 1.7, 2H, b), 3.51 (m, 2H, CH_2), 1.34 (t, ^{3}J = 7.2, 3H, CH_3).

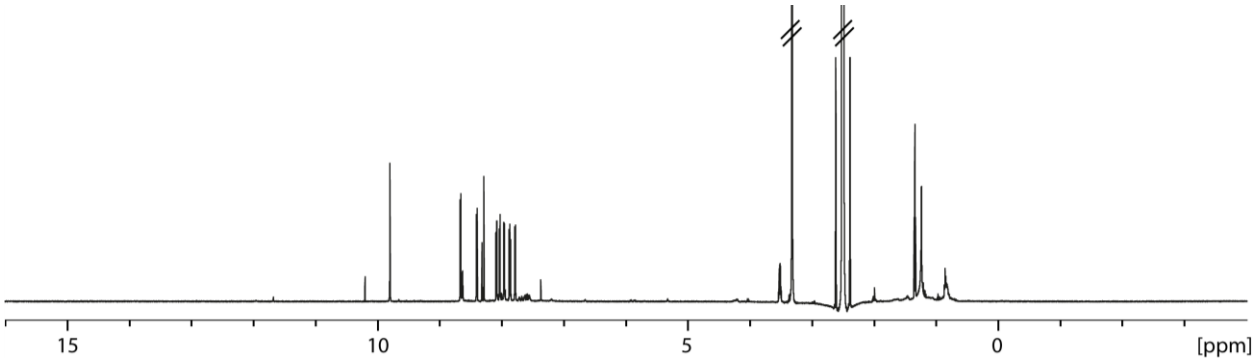

Figure 4.17: ^{1}H NMR (600 MHz, 298 K, DMSO-d_6) of **L^{4}**.

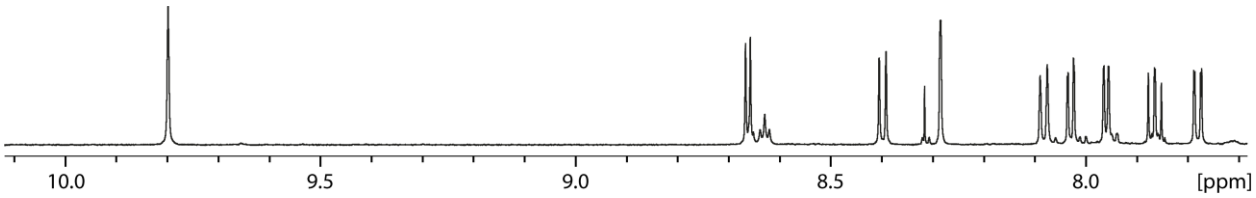

Figure 4.18: Partial ^{1}H NMR (600 MHz, 298 K, DMSO-d_6) of **L^{4}**.

^{13}C{^{1}H} NMR (151 MHz, 298 K, DMSO-d_6, lb = 2 Hz): δ = 151.4, 150.1, 143.9, 138.4, 135.4, 131.9, 130.4, 127.7, 127.1, 125.6, 124.0, 121.3, 120.8, 120.2, 120.1, 116.9, 96.5, 86.0, 35.5, 14.8.

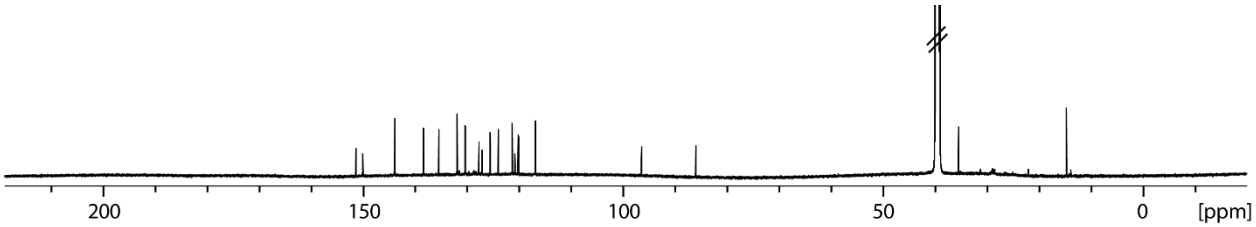

Figure 4.19: ^{13}C{^{1}H} NMR (151 MHz, 298 K, DMSO-d_6, lb = 2 Hz) of **L^{4}**.

HR-ESI-MS (positive mode): measured for: $[C_{37}H_{24}N_4O+H]^+$: 541.2018

calculated: 541.2023

4.2.9 Synthesis of 2,7-bis(pyridine-3-yl)- 9*H*-carbazole L^5

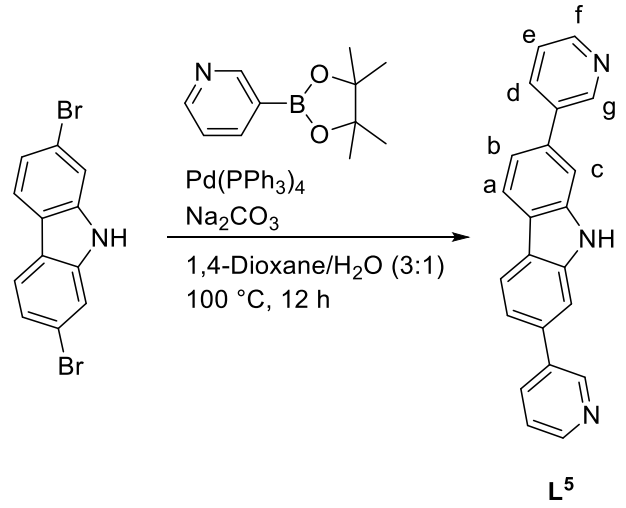

Scheme 4.9: Synthesis of $\mathbf{L^5}$.

To a degassed mixture of 1,4-dioxane and water (20 mL, 3:1) 2,7-dibromo-9*H*-carbazole (500.00 mg, 1.54 mmol, 1.0 eq), 3-(4,4,5,5-tetramethyl-1,3,2-dioxaborolan-2-yl)pyridine (946.44 mg, 4.62 mmol, 3.0 eq), tetrakis(triphenylphosphine)palladium(0) (53.33 mg, 0.05 mmol, 0.03 eq) and sodium carbonate (489.17 mg, 4.62 mmol, 3.0 eq) were added under argon and heated to 100 °C for 12 h. After the reaction mixture was cooled to rt DCM was added and washed with water and brine and dried over $MgSO_4$. The solvent was removed *in vacuo* and the crude product was purified via column chromatography ($CHCl_3$/MeOH, 9:1) and GPC ($CHCl_3$) to obtain $\mathbf{L^5}$ as a slightly yellow solid (454.88 mg, 1.42 mmol, 92%).

^{1}H NMR (500 MHz, 298 K, DMSO-d_6): δ = 11.54 (s, 1H, N*H*), 9.00 (d, ^5J = 2.2, 2H, g), 8.59 (dd, ^3J = 4.7, ^4J = 1.4, 2H, f), 8.28 (d, ^3J = 8.1, 2H, a), 8.17 (dt, ^3J = 7.9, ^4J = 1.8, 2H, e), 7.82 (d, ^4J = 1.2, 2H, c), 7.53 (m, 4H, b, d).

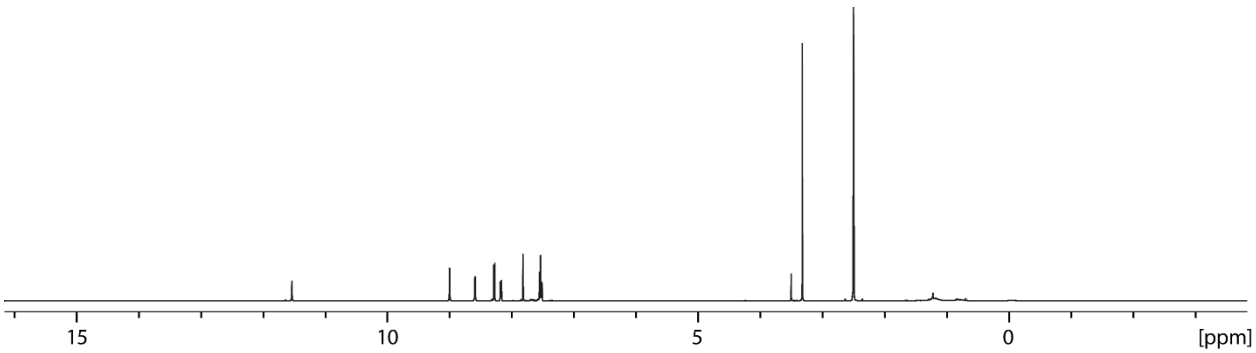

Figure 4.20: ^{1}H NMR (500 MHz, 298 K, DMSO-d_6) of $\mathbf{L^5}$.

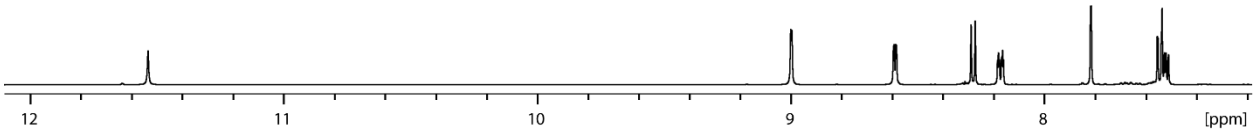

Figure 4.21: Partial ^{1}H NMR (500 MHz, 298 K, DMSO-d_6) of **L^5**.

^{13}C{^{1}H} NMR (126 MHz, 298 K, DMSO-d_6): δ = 148.2, 147.9, 140.9, 136.5, 134.9, 134.4, 123.9, 122.0, 121.1, 118.1, 109.3.

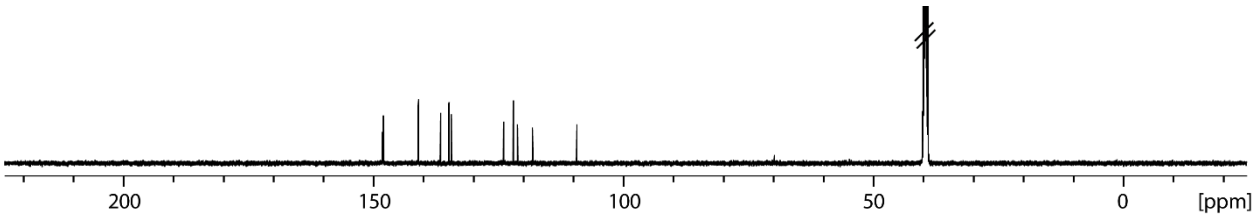

Figure 4.22: ^{13}C{^{1}H} NMR (126 MHz, 298 K, DMSO-d_6) of **L^5**.

HR-ESI-MS (positive mode): measured for: $[C_{22}H_{15}N_3+H]^+$: 321.1261

calculated: 321.1266

4.2.10 Synthesis of 9-methyl-2,7-bis(pyridine-3-yl)- 9*H*-carbazole L^6

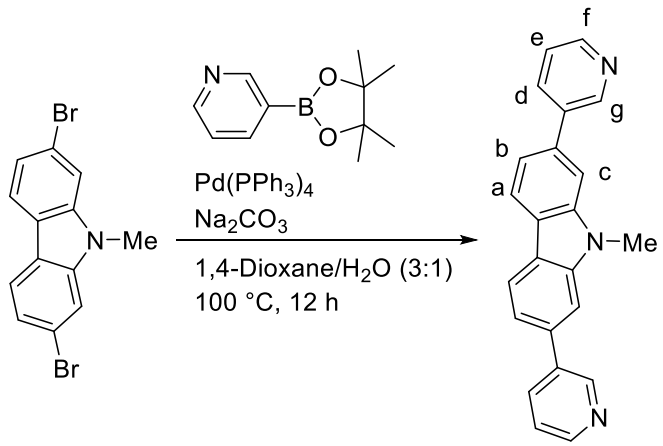

2 **L^6**

Scheme 4.10: Synthesis of **L^6**.

To a degassed mixture of 1,4-dioxane and water (12 mL, 3:1) **2** (120.00 mg, 0.35 mmol, 1.0 eq), 3-(4,4,5,5-tetramethyl-1,3,2-dioxaborolan-2-yl)pyridine (217.75 mg, 1.06 mmol, 3.0 eq), tetrakis(triphenylphosphine)palladium(0) (16.36 mg, 0.01 mmol, 0.04 eq) and sodium carbonate (112.54 mg, 1.06 mmol, 3.0 eq) were added under argon in a pressure flask and heated to 105 °C for 24 h. After the reaction mixture was cooled to rt DCM was added and washed with water and brine and dried over $MgSO_4$. The solvent was removed

in vacuo and the crude product was purified via GPC ($CHCl_3$) to obtain **L^6** as a yellow solid (117.53 mg, 0.35 mmol, 99%).

^{1}H NMR (600 MHz, 298 K, DMSO-d_6): δ = 9.09 (s, 2H, g), 8.60 (d, ^3J = 4.2, 2H, f), 8.31 (d, ^3J = 8.1, 2H, a), 8.25 (dt, ^3J = 8.5, ^5J = 1.9, 2H, e), 8.01 (d, ^4J = 1.1, 2H, c), 7.60 (dd, ^3J = 8.1, ^4J = 1.1, 2H, b), 7.54 (dd, ^3J = 7.9, ^4J = 4.7, 2H, d), 4.04 (s, 3H, NCH_3).

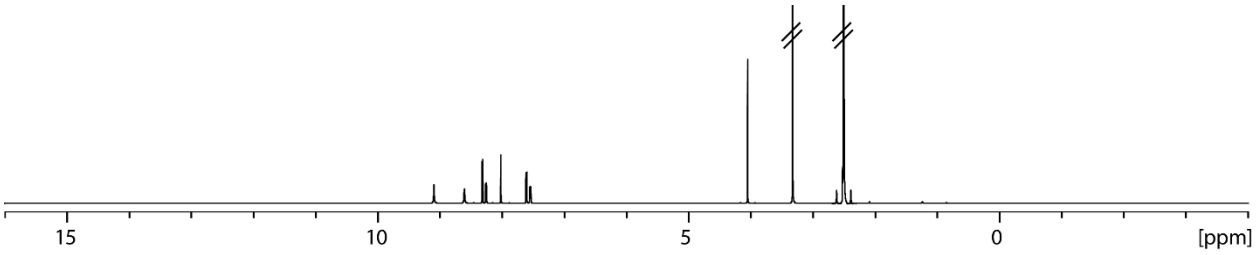

Figure 4.23: ^{1}H NMR (600 MHz, 298 K, DMSO-d_6) of **L^6**.

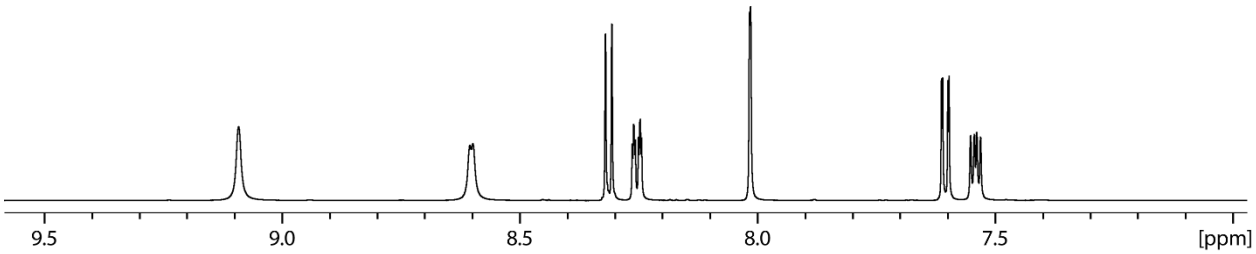

Figure 4.24: Partial ^{1}H NMR (600 MHz, 298 K, DMSO-d_6) of **L^6**.

^{13}C{^{1}H} NMR (151 MHz, 298 K, DMSO-d_6): δ = 148.2, 148.1, 141.9, 136.4, 135.0, 134.4, 123.9, 121.5, 121.2, 118.1, 107.7, 29.2.

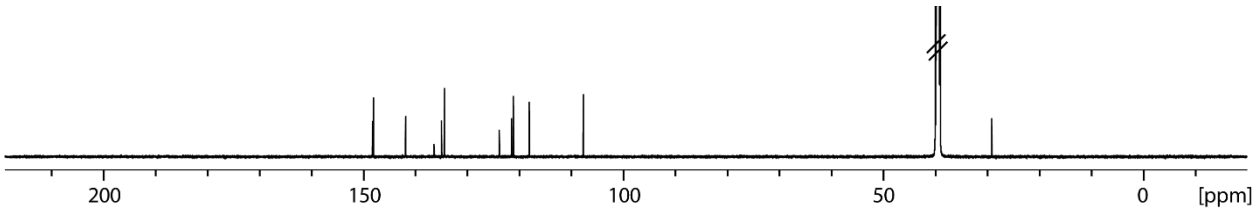

Figure 4.25: ^{13}C{^{1}H} NMR (151 MHz, 298 K, DMSO-d_6) of **L^6**.

HR-ESI-MS (positive mode): measured for: $[C_{23}H_{17}N_3+H]^+$: 336.1509

calculated: 336.1501

4.2.11 Synthesis of 9-phenyl-2,7-dibromo-9*H*-carbazole 5

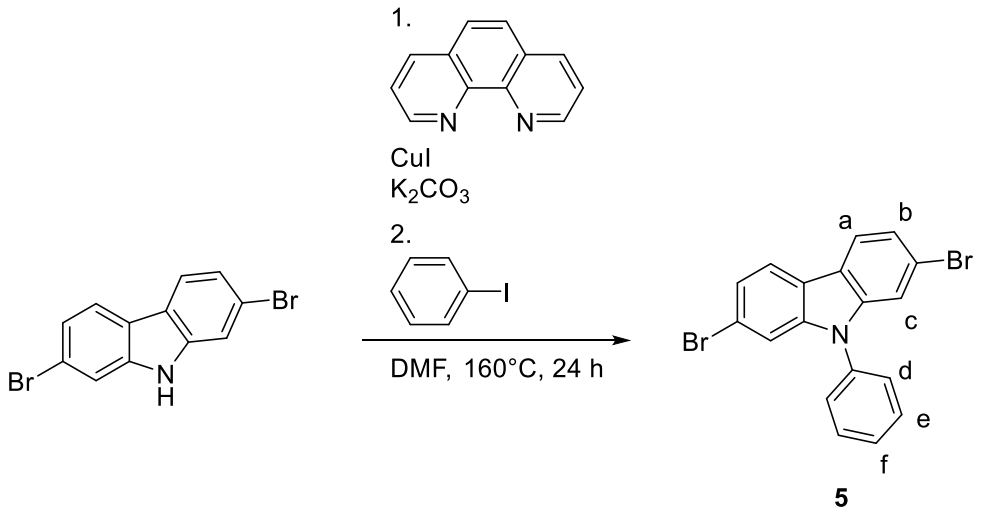

Scheme 4.11: Synthesis of 9-phenyl-2,7-dibromo-9*H*-carbazole **5**.

To a suspension of 2,7-dibromo-9*H*-carbazole (250.00 mg, 0.77 mmol, 1.0 eq), 1,10-phenanthroline (27.72 mg, 0.15 mmol, 0.2 eq), copper(I) iodide (29.30 mg, 0.15 mmol, 0.2 eq) and potassium carbonate (318.93 mg, 2.31 mmol, 3.0 eq) in 20 mL DMF iodobenzene (103.13 µL, 0.92 mmol, 1.2 eq) was added dropwise under argon and heated to 160 °C for 24 h. After the reaction mixture was cooled to rt DCM was added and washed with water and brine. The solvent was removed *in vacuo*. The crude product was purified via column chromatography (pentane/DCM, 1:1) to obtain **5** as a yellowish solid (61.50 mg, 0.15 mmol, 20%).

^{1}H NMR (500 MHz, 298 K, DMSO-d_6): δ = 8.25 (d, ^3J = 8.3, 2H, a), 7.71 (m, 2H, d), 7.64 (m, 2H, e), 7.60 (m, 1H, f), 7.47 (dd, ^3J = 8.4, ^4J = 1.6, 2H, b), 7.42 (d, ^4J = 1.6, 2H, c).

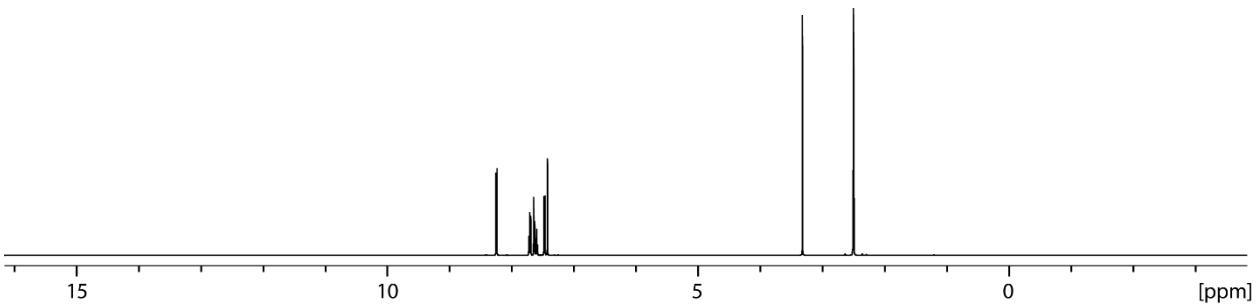

Figure 4.26: ^{1}H NMR (500 MHz, 298 K, DMSO-d_6) of **5**.

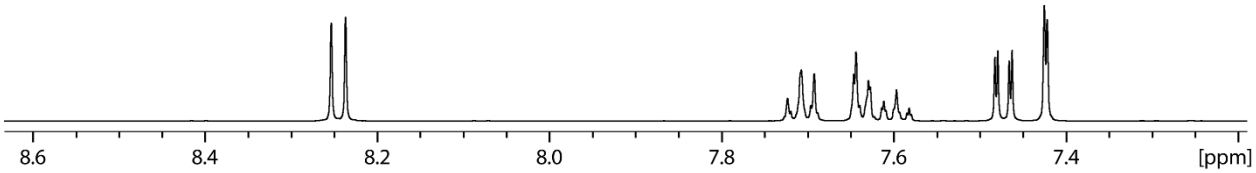

Figure 4.27: Partial ^{1}H NMR (500 MHz, 298 K, DMSO-d_6) of **5**.

^{13}C{^{1}H} NMR (126 MHz, 298 K, DMSO-d_6): δ = 141.3, 135.6, 130.5, 128.6, 126.9, 123.4, 122.6, 121.3, 119.5, 112.4.

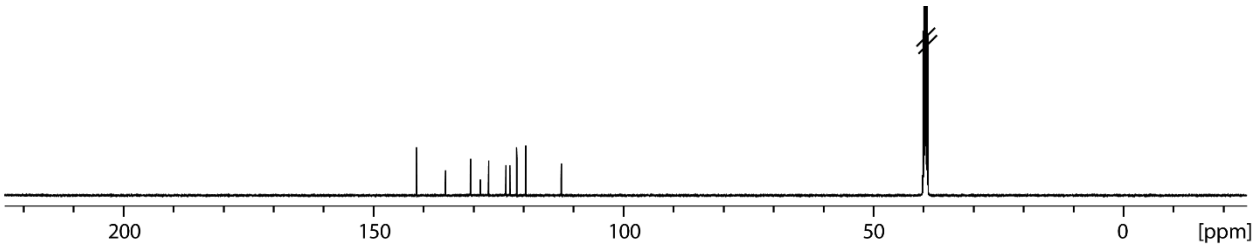

Figure 4.28: ^{13}C{^{1}H} NMR (126 MHz, 298 K, DMSO-d_6) of **5**.

HR-ESI-MS (positive mode): measured for: $[C_{18}H_{11}Br_2N+H]^+$: 402.1098

calculated: 402.1090

4.2.12 Synthesis of 9-phenyl-2,7-bis(pyridine-3-yl)- 9*H*-carbazole L^7

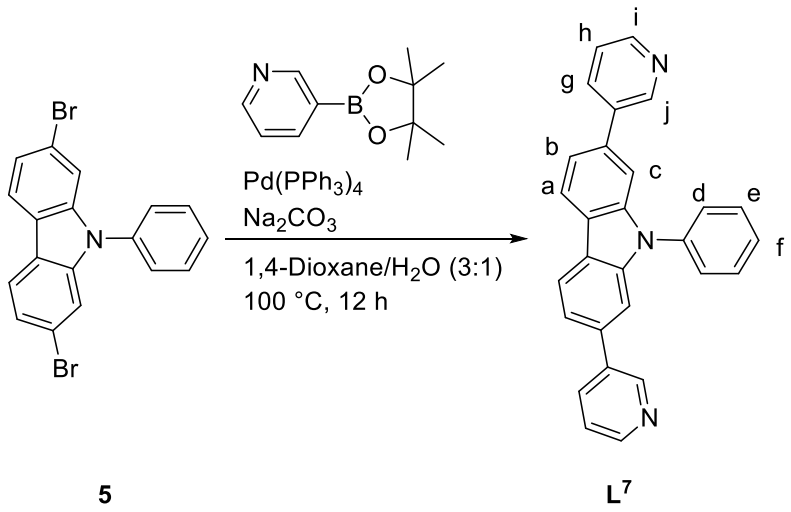

5 **L^7**

Scheme 4.12: Synthesis of **L^7**.

To a degassed mixture of 1,4-dioxane and water (20 mL, 3:1) **5** (250.00 mg, 0.62 mmol, 1.0 eq), 3-(4,4,5,5-tetramethyl-1,3,2-dioxaborolan-2-yl)pyridine (383.43 mg, 1.86 mmol, 3.0 eq), tetrakis(triphenylphosphine)palladium(0) (21.61 mg, 0.02 mmol, 0.03eq) and sodium carbonate (914.68 mg, 1.86 mmol, 3.0 eq) were added under argon in a pressure

flask and heated to 100 °C for 24 h. After the reaction mixture was cooled to rt DCM was added and washed with water and brine and dried over $MgSO_4$. The solvent was removed *in vacuo* and the crude product was purified via GPC ($CHCl_3$) to obtain **L**^{7} as a yellow solid (241.51 mg, 0.61 mmol, 98%).

^{1}H NMR (600 MHz, 298 K, DMSO-d_6): δ = 8.94 (s (br), 2H, j), 8.58 (d, ^{3}J = 3.3, 2H, i), 8.44 (d, ^{3}J = 8.0, 2H, a), 8.12 (dt, ^{3}J = 7.9, ^{4}J = 1.8, 2H, h), 7.80 (dd, ^{3}J = 8.5, ^{4}J = 1.2, 2H, d), 7.72 (dt, ^{3}J = 7.6, ^{3}J = 2.1, 2H, e), 7.68 (dd, ^{3}J = 8.1, ^{4}J = 1.5, 2H, b), 7.63 (d, ^{4}J = 1.5, 2H, c), 7.58 (dt, ^{3}J = 7.5, ^{4}J = 1.2, 1H, f), 7.49 (dd, ^{3}J = 7.8, ^{4}J = 4.7, 2H, g).

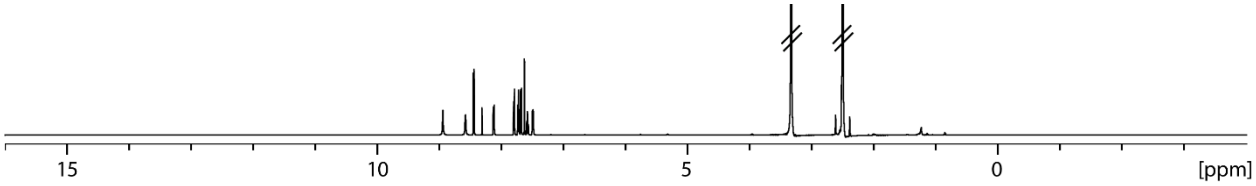

Figure 4.29: ^{1}H NMR (600 MHz, 298 K, DMSO-d_6) of **L**^{7}.

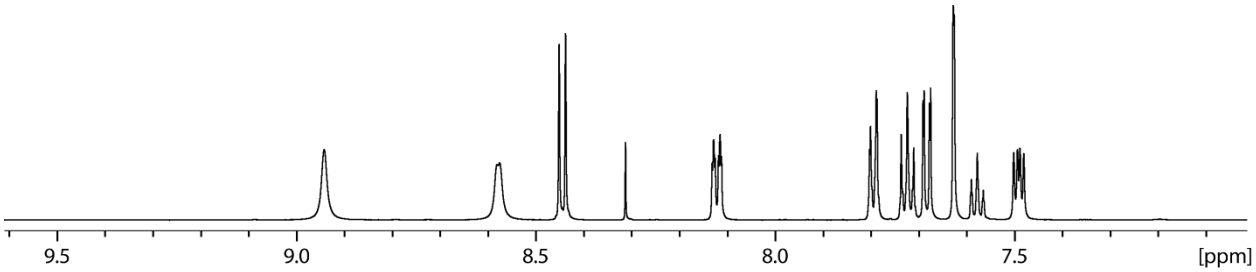

Figure 4.30: Partial ^{1}H NMR (600 MHz, 298 K, DMSO-d_6) of **L**^{7}.

^{13}C{^{1}H} NMR (151 MHz, 298 K, DMSO-d_6): δ = 148.4, 148.0, 141.3, 136.4, 136.3, 135.7, 134.6, 130.4, 127.9, 126.9, 123.9, 122.3, 121.6, 119.7, 108.1.

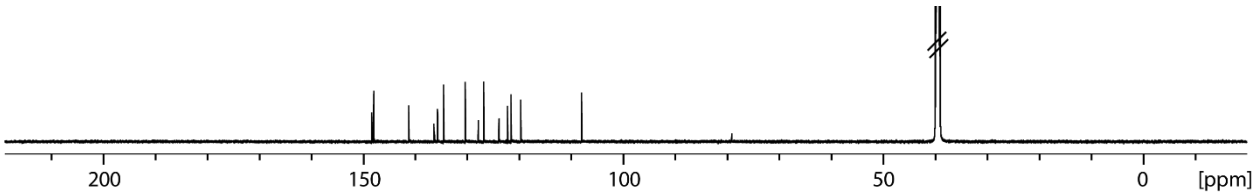

Figure 4.31: ^{13}C{^{1}H} NMR (151 MHz, 298 K, DMSO-d_6) of **L**^{7}.

HR-ESI-MS (positive mode): measured for: $[C_{28}H_{19}N_3+H]^+$: 397.1588

calculated: 397.1579

4.2.13 Synthesis of 2,7-dibromo-9-nitroso-9*H*-carbazole 6

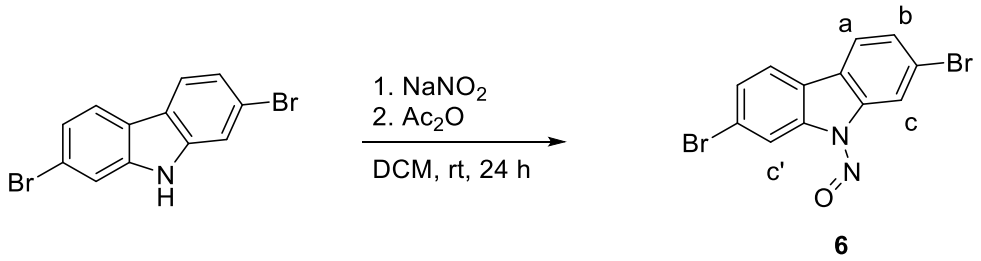

Scheme 4.13: Synthesis of 2,7-dibromo-9-nitroso-9*H*-carbazole **6**.

To a solution of 2,7-dibromo-9*H*-carbazole (1.00 g, 3.08 mmol, 1.0 eq) in DCM (50 mL) sodium nitrite (636.87 mg, 9.23 mmol, 3.0 eq) was added at rt under extreme stirring. After a few minutes, acetic anhydride (0.87 mL, 9.23 mmol, 3.0 eq) was added dropwise and mixture was allowed to stir at rt for 24 h. The reaction mixture was filtrated, washed with DCM and the solvent was removed *in vacuo*. The crude product was purified via column chromatography (pentane/EtOAc, 9:1) to obtain **6** as a bright yellow solid (1.06 g, 2.99 mmol, 97%).

^{1}H NMR (500 MHz, 298 K, DMSO-d_6): δ = 8.57 (s, 1H, c/c'), 8.44 (s, 1H, c/c'), 8.21 (d, ^3J = 8.3, 2H, a), 7.80 (s (br), 2H, b).

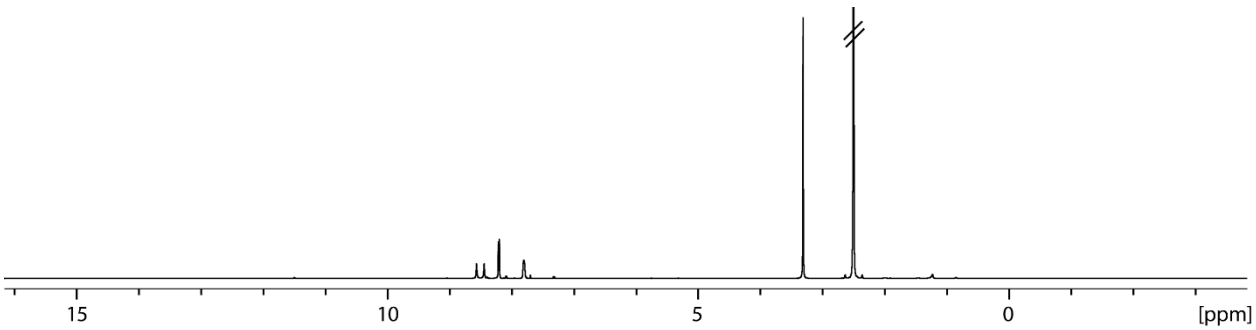

Figure 4.32: ^{1}H NMR (500 MHz, 298 K, DMSO-d_6) of **6**.

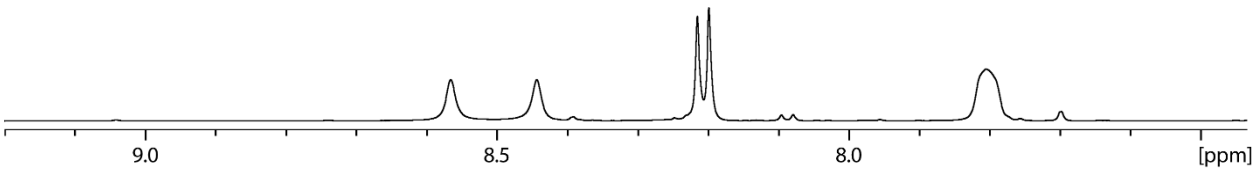

Figure 4.33: Partial ^{1}H NMR (500 MHz, 298 K, DMSO-d_6) of **6**.

HR-ESI-MS (positive mode): measured for: $[C_{12}H_6Br_2N_2O+H]^+$: 355.0102

calculated: 355.0090

4.2.14 Synthesis of 2,7-dibromo-9*H*-carbazole-9-amine 7

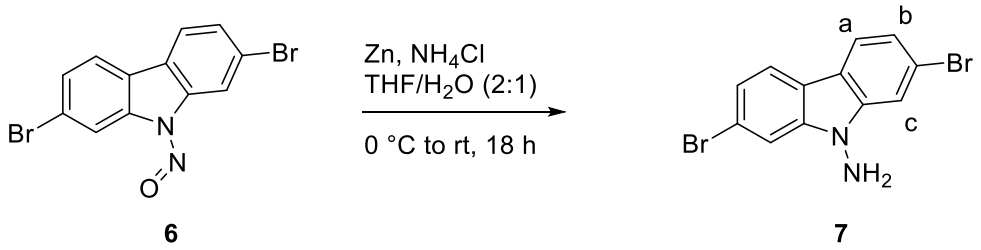

6 **7**

Scheme 4.14: Synthesis of 2,7-dibromo-9*H*-carbazole-9-amine **7**.

A suspension of zinc powder (1.85 g, 28.25 mmol, 20 eq) and NH_4Cl (1.51 g, 28.25 mmol, 20 eq) in a 2:1 mixture of THF and water (20 mL) was cooled to 0 °C under argon. A solution of **6** (0.50 g, 1.41 mmol, 1 eq) in 20 mL THF was added dropwise and the mixture was stirred vigorously for 18 h. The mixture was diluted with EtOAc and filtered over celite and the solvent was removed *in vacuo*. The crude product was purified via GPC to yield **7** as a white solid (86.45 mg, 0.25 mmol, 18%).

^{1}H NMR (600 MHz, 298 K, DMSO-d_6): δ = 8.10 (d, ^3J = 8.3, 2H a), 7.76 (d, ^4J = 1.6, 2H, c), 7.35 (dd, ^3J = 8.3, ^4J = 1.7, 2H, b), 5.95 (s, 2H, NH_2).

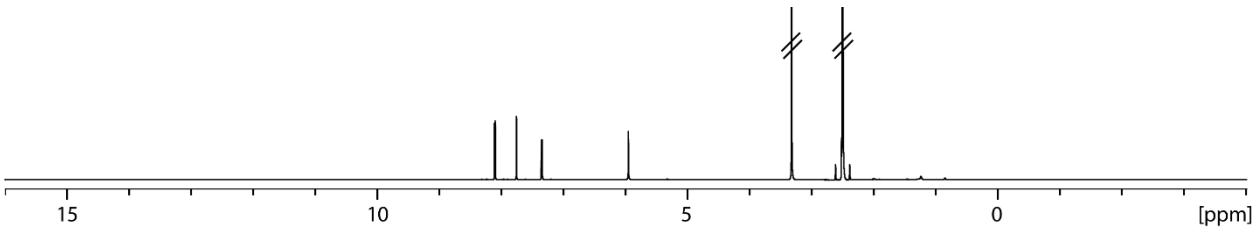

Figure 4.34: ^{1}H NMR (600 MHz, 298 K, DMSO-d_6) of **7**.

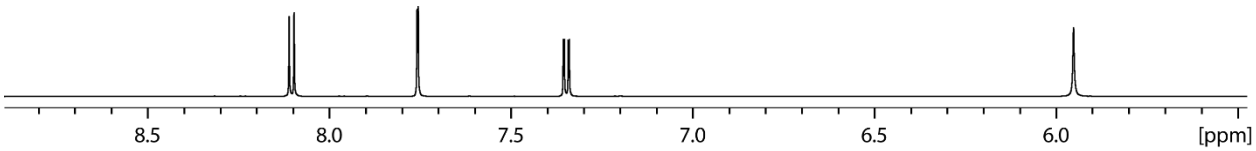

Figure 4.35: Partial ^{1}H NMR (600 MHz, 298 K, DMSO-d_6) of **7**.

HR-ESI-MS (positive mode): measured for: $[C_{12}H_8Br_2N_2+H]^+$: 338.9141

calculated: 338.9132

4.2.15 Synthesis of *t*-butyl 2,7-dibromo-9*H*-carbazole-9-carboxylate 8

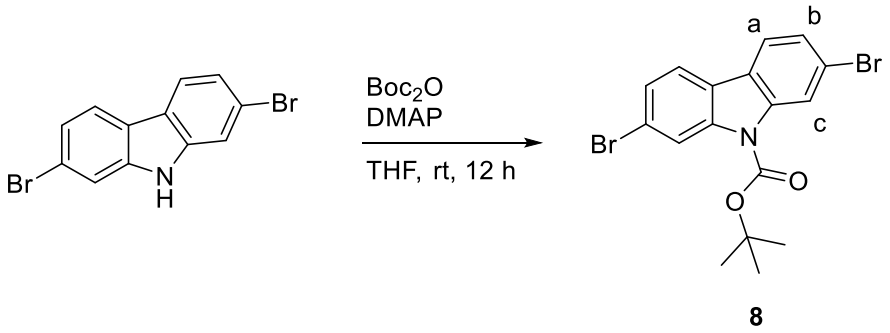

8

Scheme 4.15: Synthesis of *t*-butyl 2,7-dibromo-9*H*-carbazole-9-carboxylate **8**.

A suspension of 2,7-dibromo-9H-carbazole (1.00 g, 3.08 mmol, 1.0 eq), di-*tert*-butyl dicarbonate (Boc_2O) (1.34 g, 6.15 mmol, 2.0 eq) and 4-dimethylaminopyridine (DMAP) (0.38 g, 3.08 mmol, 1.0 eq) in 50 mL THF was stirred at rt for 12 h. The solvent was removed and the crude mixture was dissolved in 300 mL water and extracted with EtOAc (3x 250 mL). The combined organic layers were washed with 200 mL HCl (1 M in H_2O) and brine (300 mL) and dried with $MgSO_4$. The solvent was removed *in vacuo* to yield 8 as a white solid (1.28 g, 3.00 mmol, 98%).

^{1}H NMR (500 MHz, 298 K, DMSO-d_6): δ = 8.37 (s, 2H, c), 8.16 (d, ^3J = 8.2, 2H, a), 7.60 (d, ^3J = 7.94, 2H, b), 1.72 (s (br), 9H, C(CH_3)$_3$).

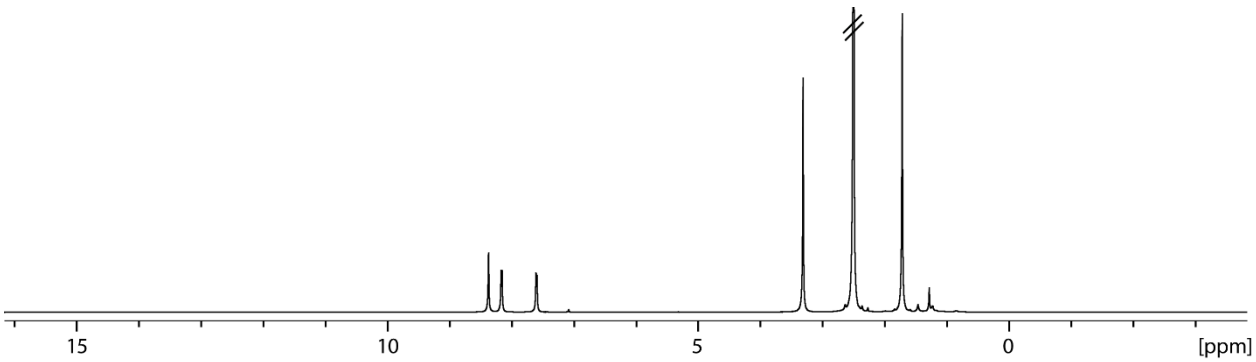

Figure 4.36: ^{1}H NMR (500 MHz, 298 K, DMSO-d_6) of **8**.

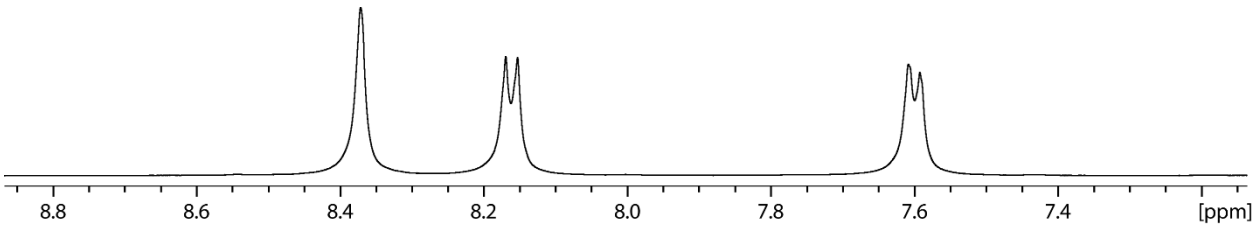

Figure 4.37: Partial ^{1}H NMR (500 MHz, 298 K, DMSO-d_6) of **8**.

$^{13}C\{^{1}H\}$ NMR (126 MHz, 298 K, DMSO-d_6): δ = 149.6, 138.5, 126.4, 123.5, 122.1, 120.3, 118.6, 85.4, 27.6.

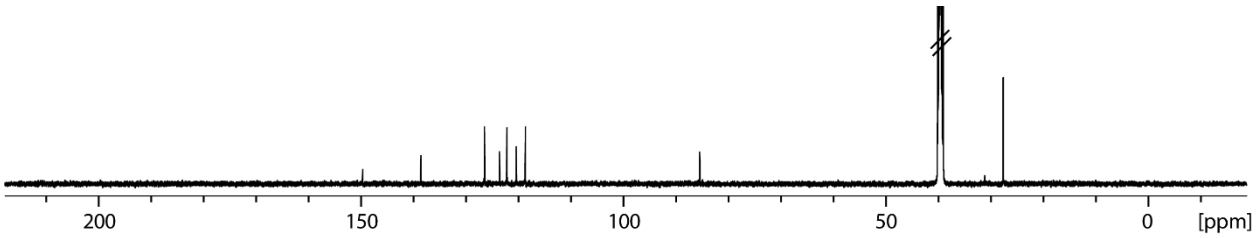

Figure 4.38: $^{13}C\{^{1}H\}$ NMR (126 MHz, 298 K, DMSO-d_6) of **8**.

HR-ESI-MS (positive mode): measured for: $[C_{17}H_{15}Br_2NO_2+H]^+$: 426.1295

calculated: 426.1280

4.2.16 Synthesis of 3,6-dibromo-9-hexyl-9*H*-carbazole 9

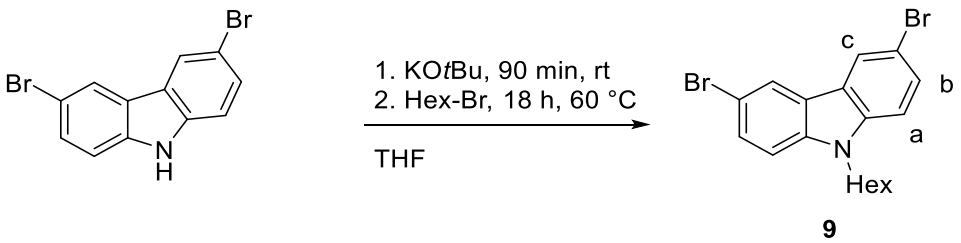

9

Scheme 4.16: Synthesis of 3,6-dibromo-hexyl-9*H*-carbazole **9**.

3,6-dibromo-9*H*-carbazole (1.00 g, 3.08 mmol, 1.0 eq) and KO*t*Bu (0.38 g, 3.38 mmol, 1.1 eq) were suspended in dry THF (50 mL) and stirred at rt for 90 min. After adding 1-bromo hexane (1.02 g, 6.15 mmol, 2.0 eq) dropwise to the reaction mixture, it was heated to 60 °C for 18 h. The reaction mixture was cooled to rt, filtered over celite and washed with EtOAc. The solvent was removed *in vacuo*. The crude product was purified via column chromatography (pentane/EtOAc, 20:1) to obtain **9** as a yellow solid (1.04 g, 2.53 mmol, 82%).

^{1}H NMR (500 MHz, 298 K, $CDCl_3$): δ = 8.13 (s, 2H, c), 7.54 (dd, ^{3}J = 8.8, ^{4}J = 1.7, 2H, b), 7.26 (d, ^{3}J = 8.8, 2H, a), 4.23 (t, ^{3}J = 7.2, 2H, NCH_2), 1.81 (quint, ^{3}J = 7.2, 2H, NCH$_2$CH_2), 1.30 (m, 6H), 0.85 (t, ^{3}J = 6.9, 3H, CH_3).

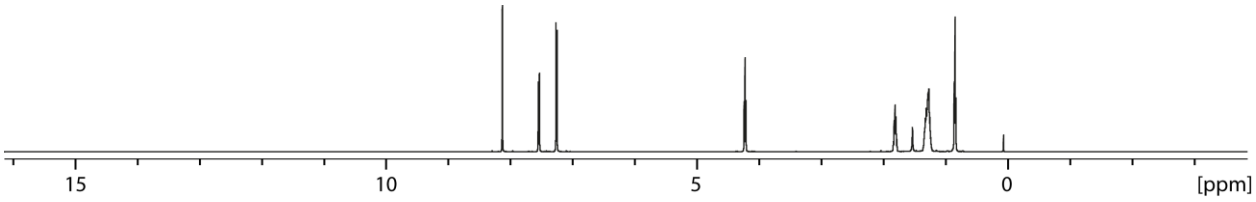

Figure 4.39: ^{1}H NMR (500 MHz, 298 K, $CDCl_3$) of **9**.

^{13}C{^{1}H} NMR (126 MHz, 298 K, $CDCl_3$): δ = 139.5, 129.1, 123.6, 123.4, 112.1, 110.5, 43.5, 31.6, 29.0, 27.0, 22.6, 14.1.

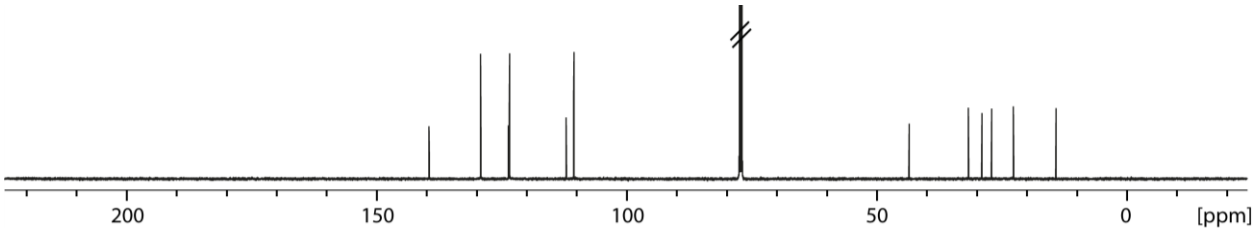

Figure 4.40: ^{13}C{^{1}H} NMR (126 MHz, 298 K, $CDCl_3$) of **9**.

HR-ESI-MS (positive mode): measured for: $[C_{18}H_{19}Br_2N_2+K]^+$: 447.9480

calculated: 447.9496

4.2.17 Synthesis of 9-hexyl-3,6-di(pyridine-4-yl)-9H-carbazole L^{C}

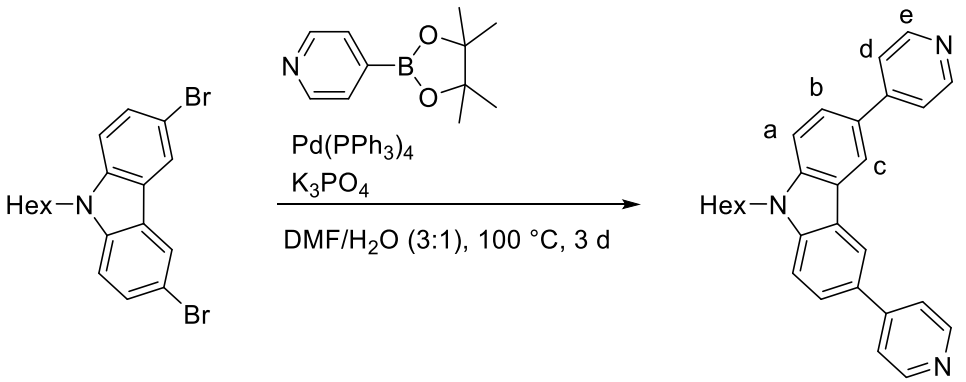

9 **L^{C}**

Scheme 4.17: Synthesis of **L^{C}**.

To a degassed mixture of DMF and water (3:1, 30 mL) **9** (100.00 mg, 0.24 mmol, 1.0 eq), 4-(4,4,5,5-tetramethyl-1,3,2-dioxaborolan-2-yl)pyridine (300.71 mg, 1.47 mmol, 6.0 eq), tetrakis(triphenylphosphine)palladium(0) (28.24 mg, 0.02 mmol, 0.1 eq) and potassium phosphate (155.63 mg, 0.73 mmol, 3.0 eq) were added under argon in a pressure flask and heated to 100 °C for 3 d. After the reaction mixture was cooled down to rt, $CHCl_3$

(90 mL) was added. The mixture was consecutively washed with water, brine and saturated ammonium chloride solution and dried over $MgSO_4$. The solvent was removed *in vacuo*. The crude product was purified via column chromatography (pentane/acetone, 1:1) and GPC ($CHCl_3$) to yield $\mathbf{L^C}$ as a yellow solid (60.00 mg, 0.15 mmol, 61%).

^{1}H NMR (500 MHz, 298 K, $CDCl_3$): δ = 8.75 (s (br), 4H, e), 8.46 (d, ^4J = 1.3, 2H, c), 7.81 (dd, ^3J = 8.5, ^4J = 1.6, 2H, b), 7.70 (s (br), 4H, d), 7.54 (d, ^3J = 8.5, 2H, a), 4.37 (t, ^3J = 7.2, 2H, NCH_2), 1.93 (quint., ^3J = 7.2, 2H, NCH$_2$CH_2), 1.41 (m, 2H, NCH$_2$CH$_2$CH_2), 1.32 (m, 4H), 0.88 (t, ^3J = 7.1, 3H, CH_3).

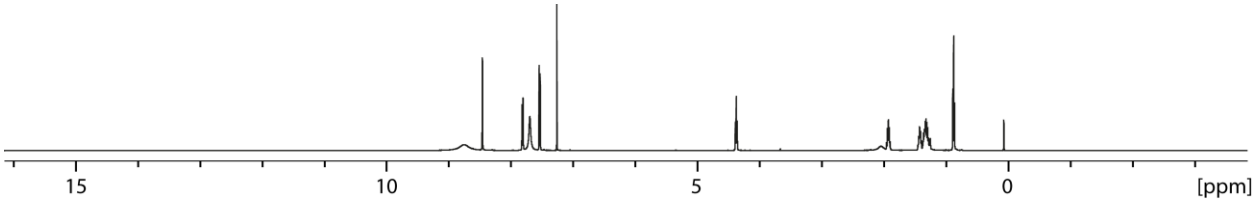

Figure 4.41: ^{1}H NMR (500 MHz, 298 K, $CDCl_3$) of $\mathbf{L^C}$.

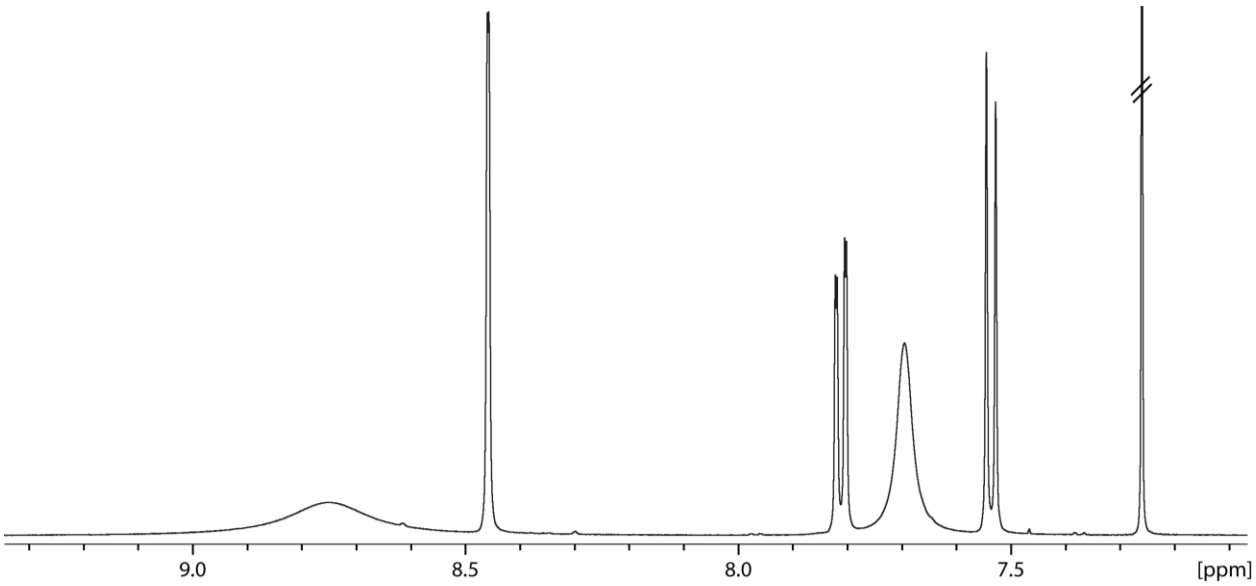

Figure 4.42: Partial ^{1}H NMR (500 MHz, 298 K, $CDCl_3$) of $\mathbf{L^C}$.

^{13}C NMR (126 MHz, 298 K, $CDCl_3$): δ = 150.1, 149.2, 141.6, 129.5, 125.4, 123.7, 122.1, 119.3, 109.8, 43.7, 31.7, 29.1, 27.1, 22.7, 14.1.

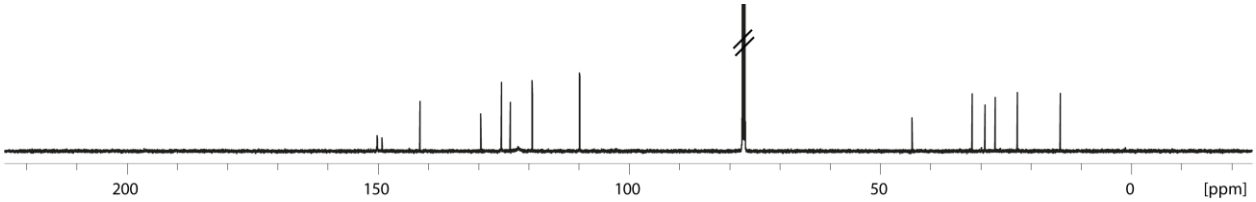

Figure 4.43: ^{13}C{^{1}H} NMR (126 MHz, 298 K, $CDCl_3$) of $\mathbf{L^C}$.

HR-ESI-MS (positive mode): measured for: $[C_{28}H_{27}N_3+H]^+$: 406.2293

calculated: 406.2278

4.2.18 Synthesis of 3,6-di(pyridine-4-yl)-9*H*-fluoren-9-one L^D

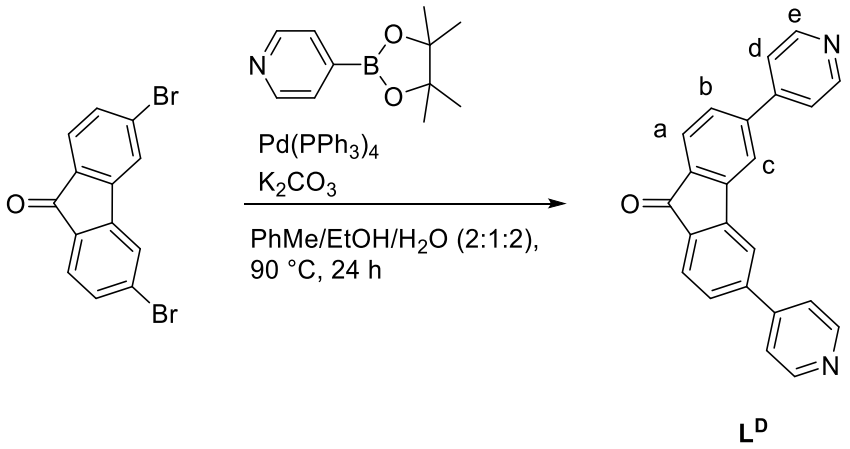

L^D

Scheme 4.18: Synthesis of $\mathbf{L^D}$.

To a degassed mixture of toluene, ethanol and water (2:1:2, 25 mL), 2,6-dibromo-9*H*-fluoren-9-one (200.00 mg, 0.59 mmol, 1.0 eq), 4-(4,4,5,5-tetramethyl-1,3,2-dioxaborolan-2-yl)pyridine (485.36 mg, 2.37 mmol, 4.0 eq), tetrakis(triphenylphosphine)palladium(0) (68.38 mg, 0.06 mmol, 0.1 eq) and potassium carbonate (245.34 mg, 1.78 mmol, 3.0 eq) were added under argon in a pressure flask and heated to 90 °C for 24 h. The reaction mixture was allowed to cool down to rt and extracted with DCM. The combined organic layers were washed with water and brine and dried over $MgSO_4$. The solvent was removed *in vacuo*. The crude product was purified via column chromatography (DCM/MeOH, 10:1) to obtain $\mathbf{L^D}$ as a yellow solid (401.00 mg, 1.20 mmol, 81%).

^{1}H NMR (700 MHz, 298 K, DMSO-d_6): δ = 8.75 (d, ^3J = 4.54, 4H, e), 8.50 (s, 2H, c), 7.87 (m, 6H, b, d), 7.78 (d, ^3J = 7.60, 2H, a).

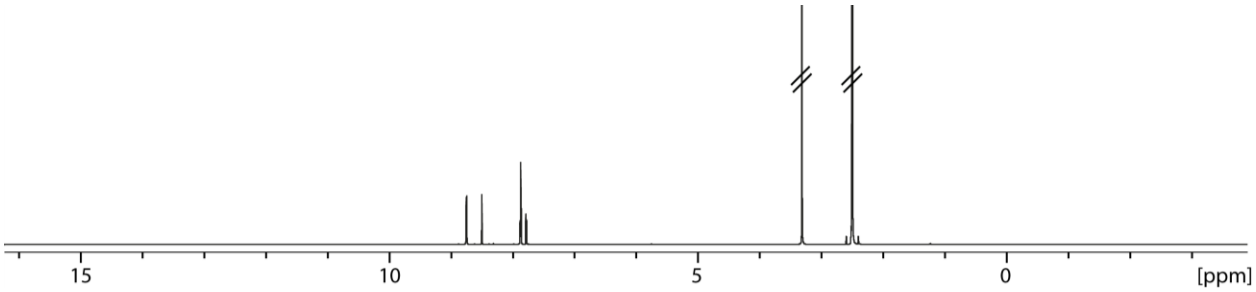

Figure 4.44: ^{1}H NMR (700 MHz, 298 K, DMSO-d_6) of $\mathbf{L^D}$.

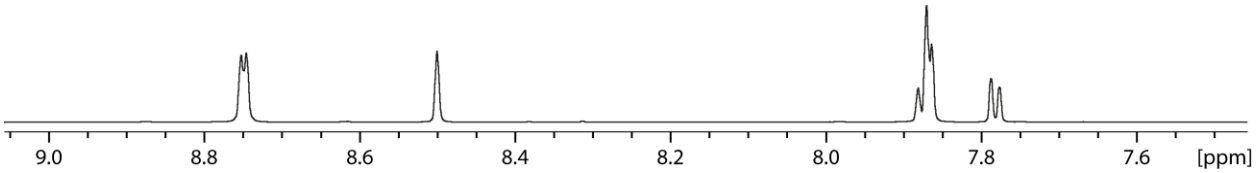

Figure 4.45: Partial ^{1}H NMR (700 MHz, 298 K, DMSO-d_6) of $\mathbf{L^D}$.

^{13}C{^{1}H} NMR (176 MHz, 298 K, DMSO-d_6): δ = 192.0, 150.4, 145.8, 144.5, 143.9, 133.9, 128.3, 124.6, 121.4, 120.3.

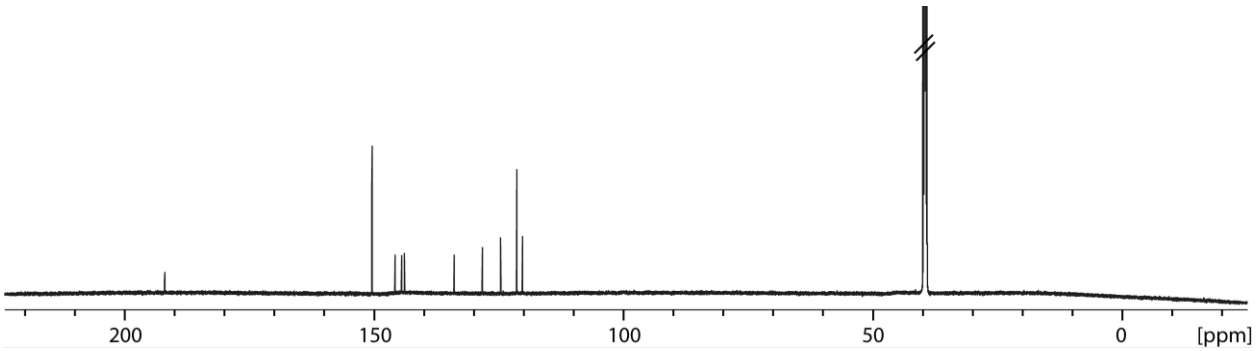

Figure 4.46: ^{13}C{^{1}H} NMR (176 MHz, 298 K, DMSO-d_6) of $\mathbf{L^D}$.

HR-ESI-MS (positive mode): measured for: $[C_{23}H_{14}N_2O+H]^+$: 335.1199

calculated: 335.1184

4.3 Attempts of Homoleptic Cage Formation $Pd_2L^1_4$

To a solution of L1 (540 µL, 2.8 mM, DMSO-d_6) a solution of $[Pd(MeCN)_4](BF_4)_2$ (60 µL, 15.0 mM, 0.55 eq, DMSO-d_6) was added in a NMR tube and shaken for 5 min at rt. 1H NMR was measured after 2 h at rt, 4 h at rt and heating for 5 min at 70 °C, 48 h at

rt and 18 h at 70 °C, respectively.

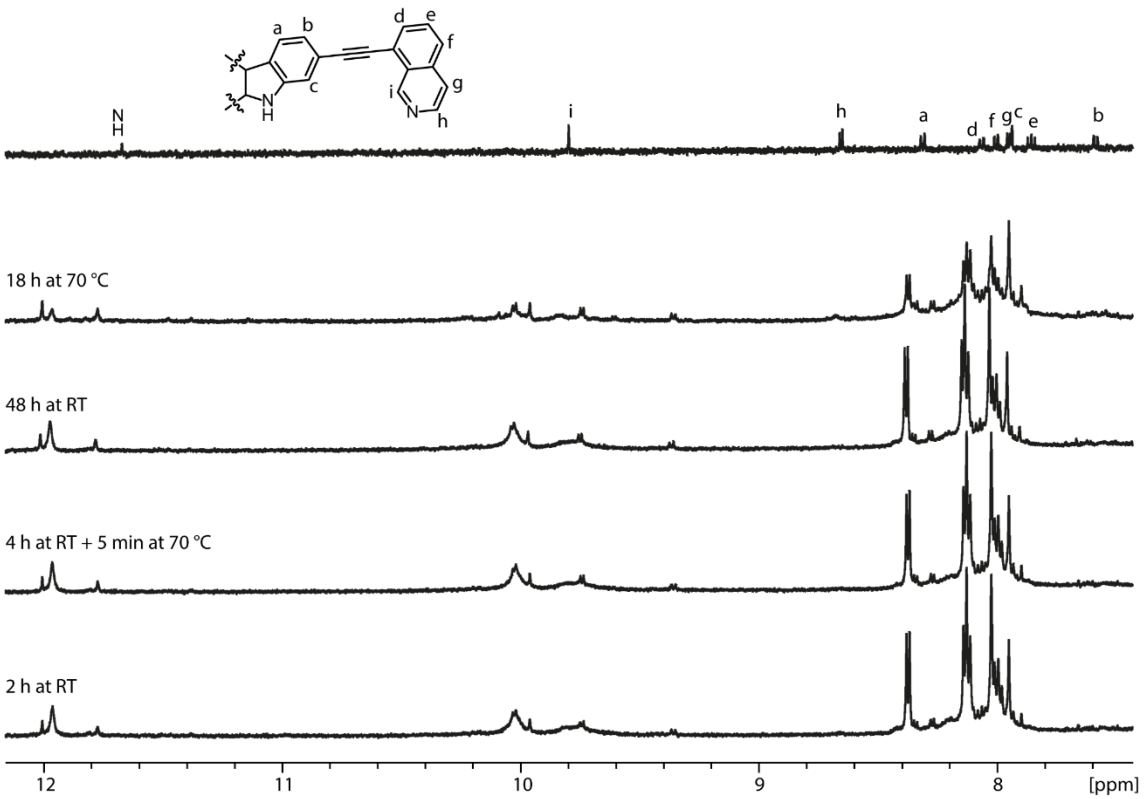

Figure 4.47: Stacked partial ^{1}H NMR spectra (500 MHz, 298 K, DMSO-d_6) of $\mathbf{L^1}$ (top) and different conditions after adding Pd(II) to assemble $Pd_2\mathbf{L^1}_4$.

4.4 General Synthesis of Heteroleptic Coordination Cages

To a 1:1 mixture of the corresponding ligands (270 µL each, 2.8 mM, DMSO-d_6) a solution of $[Pd(MeCN)_4](BF_4)_2$ (60 µL, 15.0 mM, 0.55 eq, DMSO-d_6) was added in a NMR tube and shaken for 5 min at rt. The coordination cages were formed in a quantitative yield within minutes. Cage formation was also observed when using ligands and Pd-salt solution in DMF-d_7 under the same conditions.

4.4.1 $Pd_2\mathbf{L^1}_2\mathbf{L^A}_2$

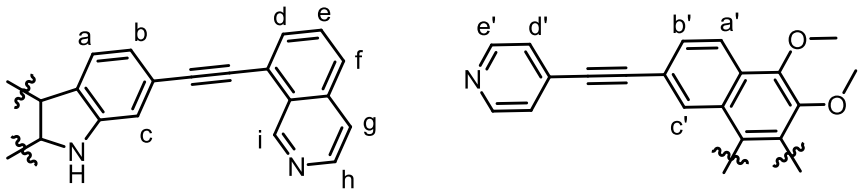

Scheme 4.19: Ligand Assignment for $Pd_2\mathbf{L^1}_2\mathbf{L^A}_2$.

^{1}H NMR (500 MHz, 298 K, DMSO-d_6): δ = 11.76 (s, 2H, N*H*), 9.90 (s, 4H, i), 9.54 (d, ^3J = 6.5, 4H, h), 9.43 (d, ^3J = 6.7, 8H, e'), 9.24 (s, 4H, c'), 8.47 (d, ^3J = 8.0, 4H, a), 8.41 (d, ^3J = 6.5, 4H, g), 8.23 (d, ^3J = 8.6, 4H, a'), 8.19 (d, ^3J = 8.3, 4H, d), 8.10 (m, 4H, f), 8.06 (m, 8H, d'), 8.02 (m, 4H, e), 7.99 (s, 4H, c), 7.85 (dd, ^3J = 8.5, ^5J = 1.0, 4H, b'), 7.47 (dd, ^3J = 7.9, ^4J = 1.2, 4H, b), 4.01 (s, 12H, OCH_3).

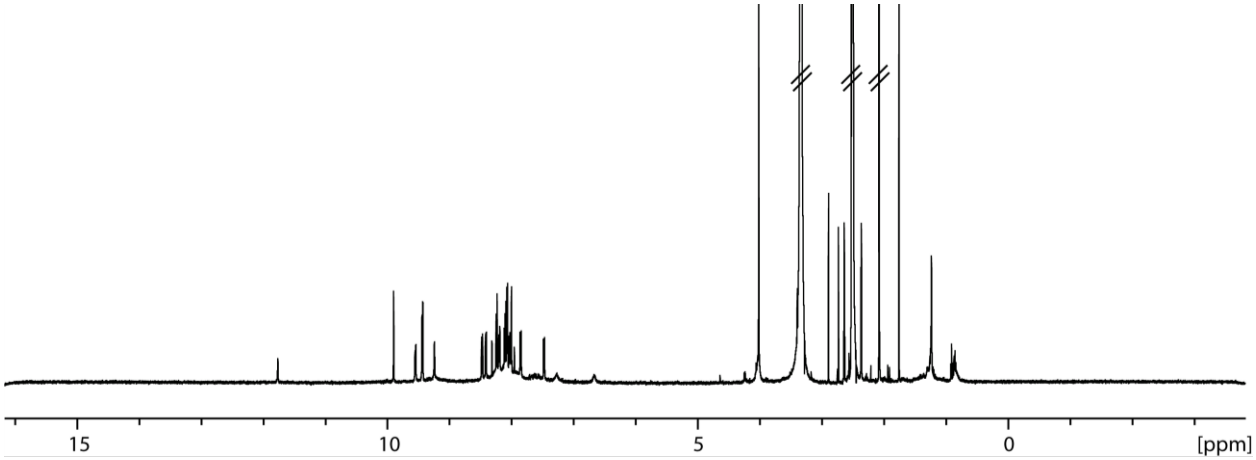

Figure 4.48: ^{1}H NMR (500 MHz, 298 K, DMSO-d_6) of $Pd_2\mathbf{L^1}_2\mathbf{L^A}_2$.

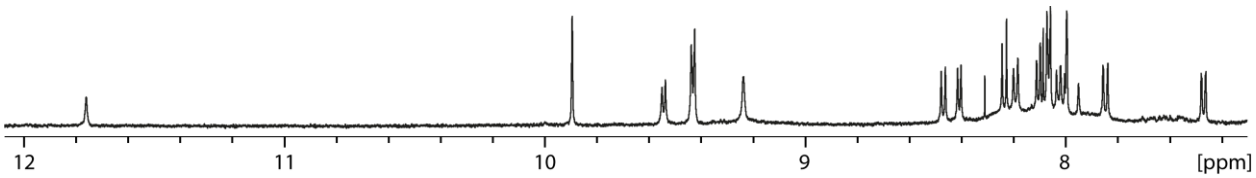

Figure 4.49: Partial ^{1}H NMR (500 MHz, 298 K, DMSO-d_6) of $Pd_2\mathbf{L^1}_2\mathbf{L^A}_2$.

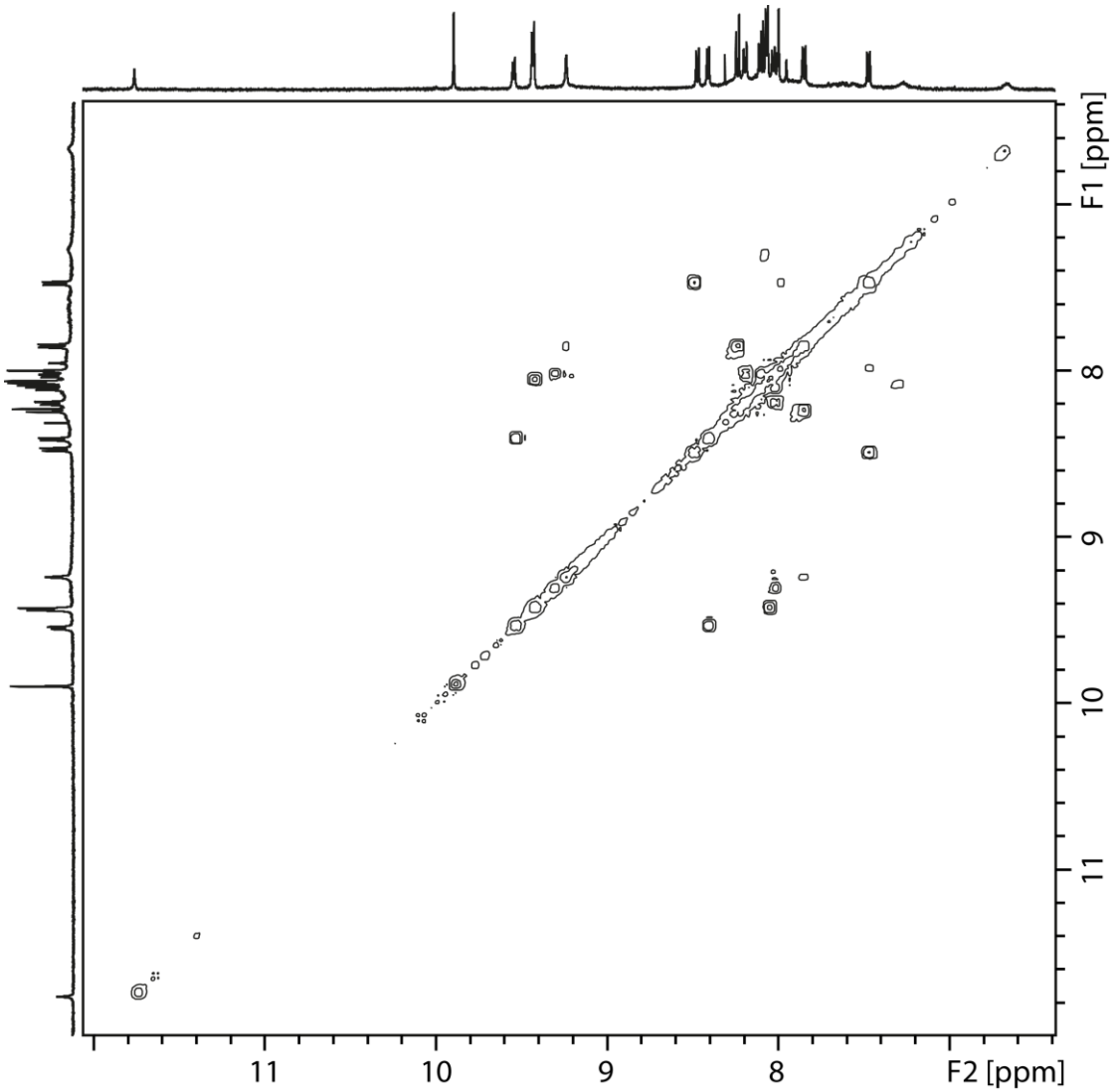

Figure 4.50: Partial $^{1}H-^{1}H$ COSY NMR (500 MHz, 298 K, DMSO-d_6) of $Pd_2\mathbf{L^1}_2\mathbf{L^A}_2$.

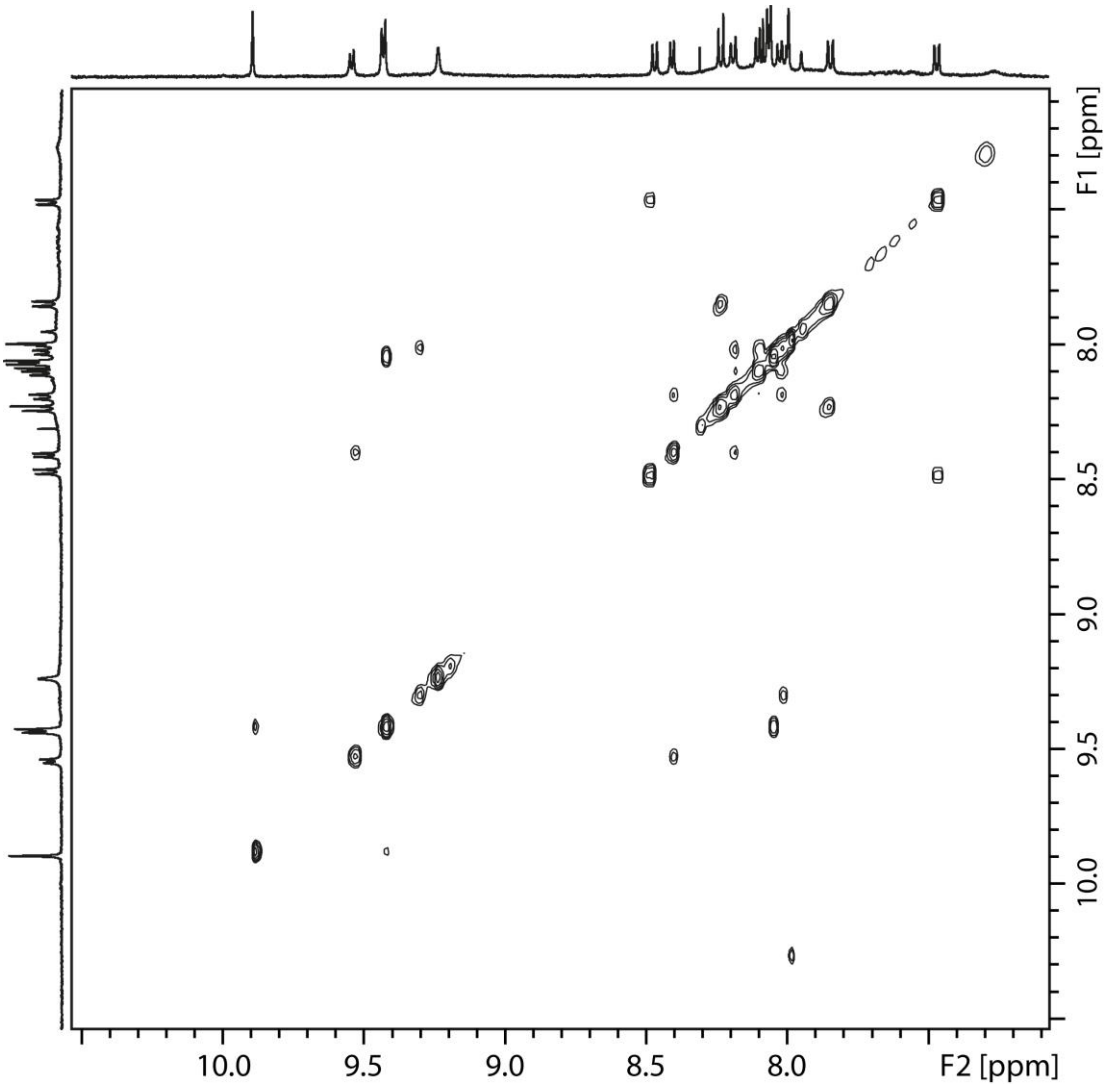

Figure 4.51: Partial $^{1}H-^{1}H$ NOESY NMR (500 MHz, 298 K, DMSO-d_6) of $Pd_2\mathbf{L^1}_2\mathbf{L^A}_2$.

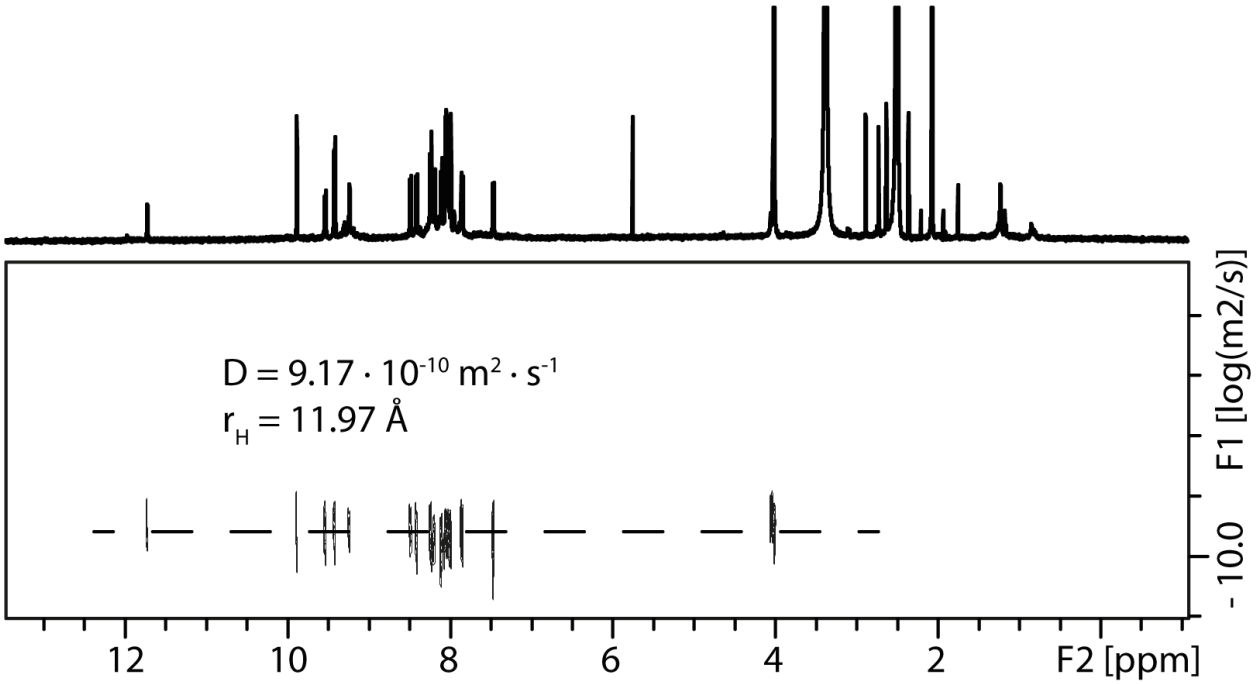

Figure 4.52: ^{1}H DOSY NMR (500 MHz, 298 K, DMSO-d_6) of $Pd_2\mathbf{L^1}_2\mathbf{L^A}_2$.

^{13}C{^{1}H} NMR (151 MHz, 298 K, DMSO-d_6): δ = 171.6, 162.4, 153.8, 151.0, 144.8, 142.4, 140.2, 136.2, 134.9, 133.9, 130.0, 129.0, 128.0, 127.2, 123.4, 123.0, 121.6, 121.1, 119.0, 118.1, 114.7, 99.4, 98.5, 86.3, 84.7, 79.2, 61.2.

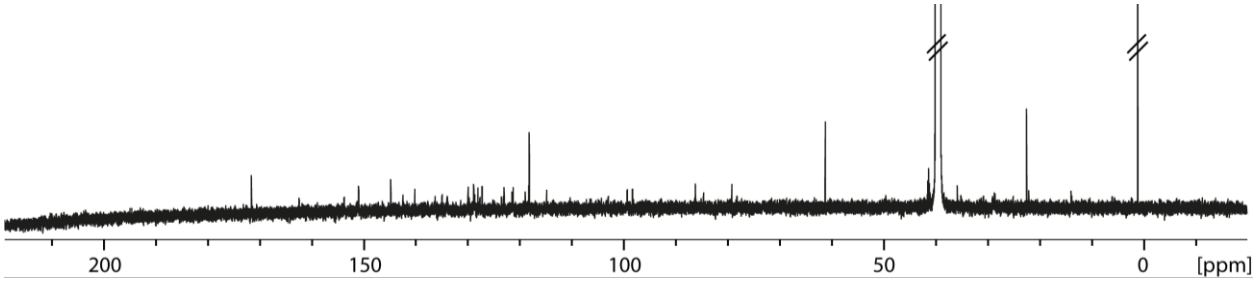

Figure 4.53: ^{13}C{^{1}H} NMR (151 MHz, 298 K, DMSO-d_6) of $Pd_2\mathbf{L^1}_2\mathbf{L^A}_2$.

HR-ESI-MS (positive mode):

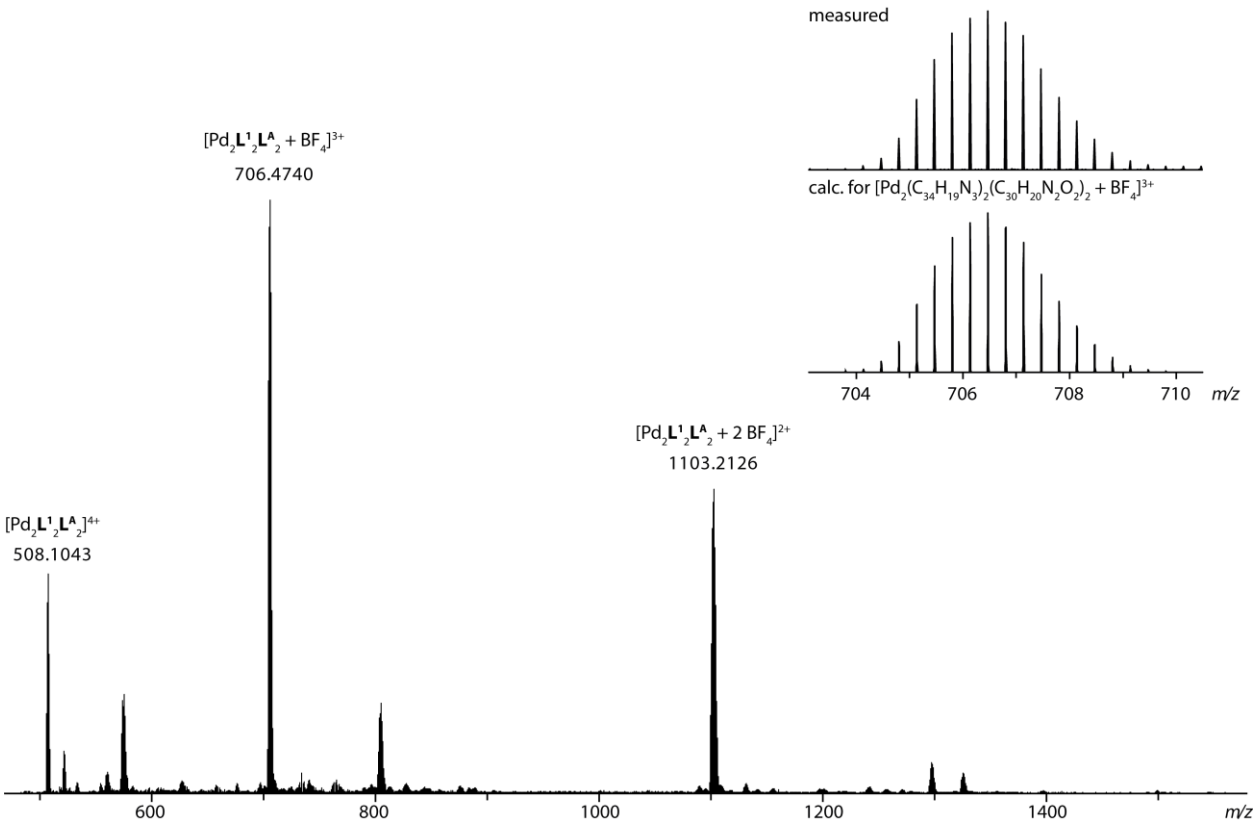

Figure 4.54: ESI-MS spectrum of $[Pd_2\mathbf{L^1}_2\mathbf{L^A}_2 + n\ BF_4]^{(4-n)+}$ and inset of comparison of measured and calculated mass.

4.4.2 $Pd_2\mathbf{L^1}_2\mathbf{L^B}_2$

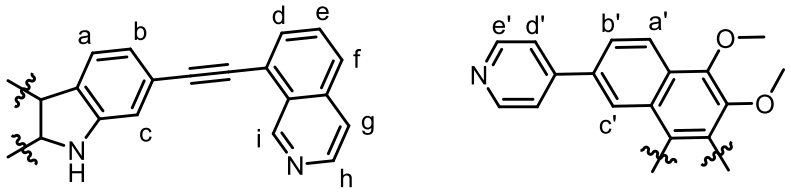

Scheme 4.20: Ligand Assignment for $Pd_2\mathbf{L^1}_2\mathbf{L^B}_2$.

^{1}H NMR (500 MHz, 298 K, DMSO-d_6): δ = 11.89 (s, 2H, N*H*), 10.09 (s, 4H, i), 9.73 (d, ^3J = 6.4, 8H, e'), 9.66 (d, ^3J = 6.6, 4H, h), 9.17 (s (br), 4H, c'), 8.45 (d, ^3J = 6.5, 4H, g), 8.32 (m, 12H, d',f), 8.20 (d, ^3J = 8.3, 4H, d), 8.15 (d, ^3J = 8.1, 4H, a), 8.08 (m, 8H, a', b'), 8.01 (m, 4H, e), 7.96 (s, 4H, c), 7.42 (dd, ^3J = 7.9, ^4J = 1.2 , 4H, b)

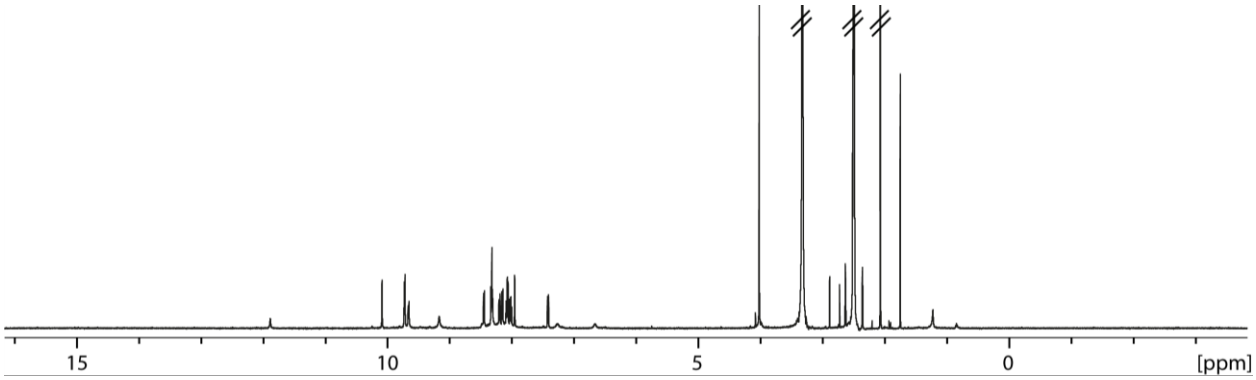

Figure 4.55: ^{1}H NMR (500 MHz, 298 K, DMSO-d_6) of $Pd_2\mathbf{L^1}_2\mathbf{L^B}_2$.

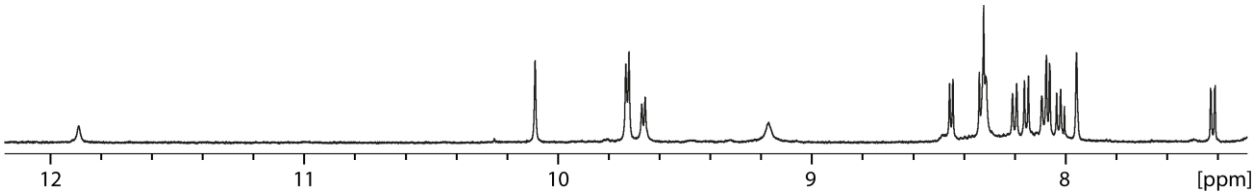

Figure 4.56: Partial ^{1}H NMR (500 MHz, 298 K, DMSO-d_6) of $Pd_2\mathbf{L^1}_2\mathbf{L^B}_2$.

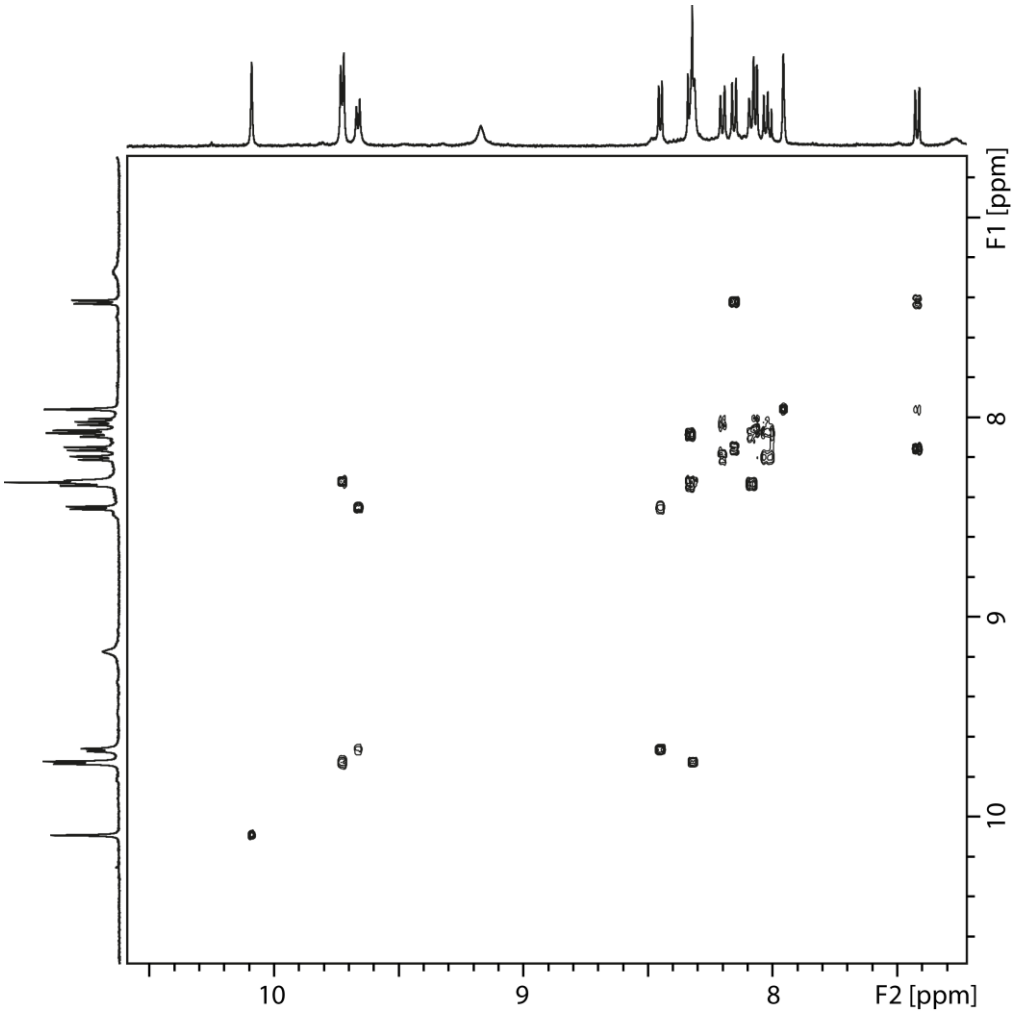

Figure 4.57: Partial ^{1}H–^{1}H COSY NMR (500 MHz, 298 K, DMSO-d_6) of $Pd_2\mathbf{L^1}_2\mathbf{L^B}_2$.

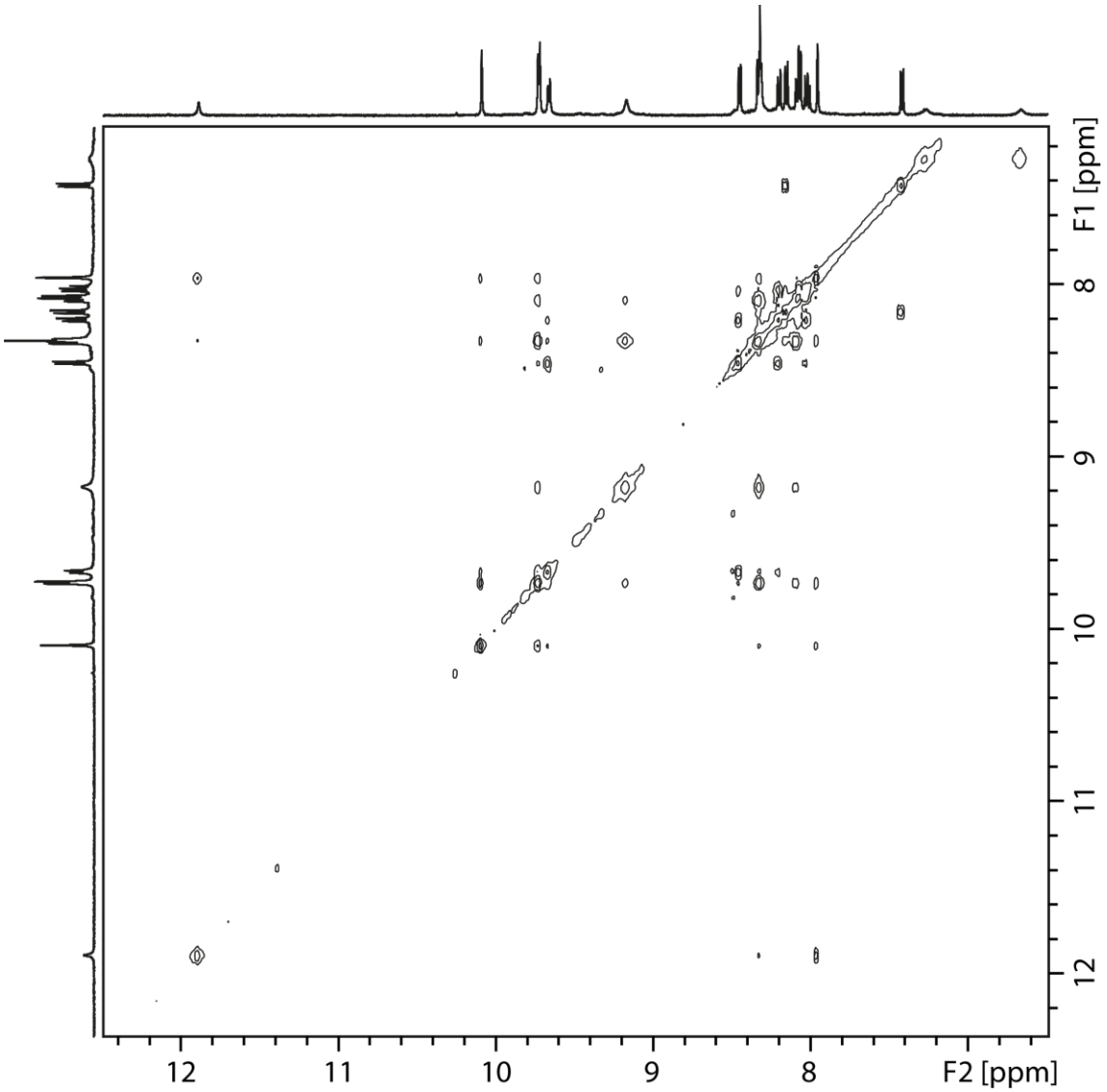

Figure 4.58: Partial $^{1}H-^{1}H$ NOESY NMR (500 MHz, 298 K, DMSO-d_6) of $Pd_2\mathbf{L^1}_2\mathbf{L^B}_2$.

$^{13}C\{^{1}H\}$ NMR (151 MHz, 298 K, DMSO-d_6): δ = 171.5, 162.3, 151.5, 151.1, 144.2, 142.4, 140.0, 136.2, 133.0, 130.2, 128.2, 125.4, 123.1, 121.5, 121.2, 119.0, 118.1, 115.3, 98.5, 84.5, 61.2.

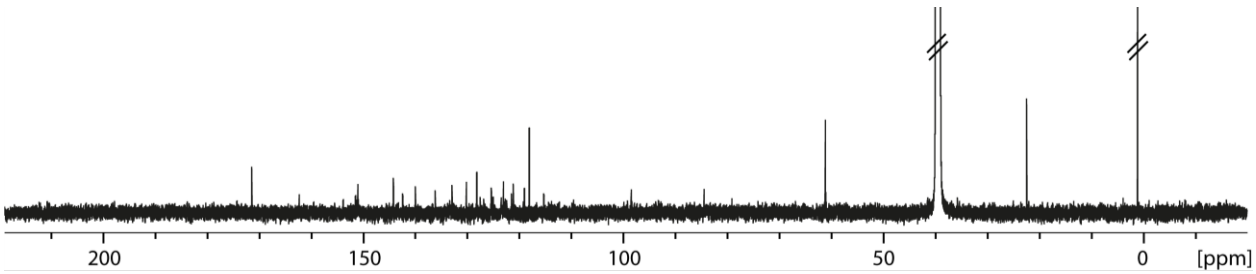

Figure 4.59: $^{13}C\{^{1}H\}$ NMR (151 MHz, 298 K, DMSO-d_6) of $Pd_2\mathbf{L^1}_2\mathbf{L^B}_2$.

HR-ESI-MS (positive mode):

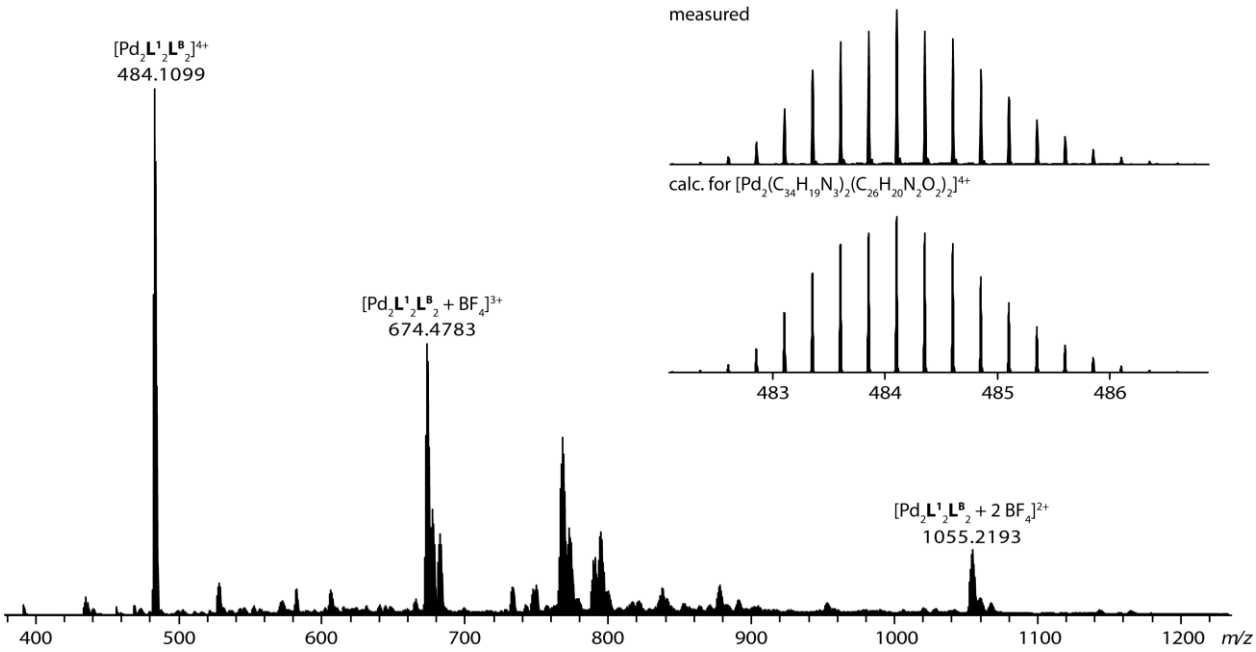

Figure 4.60: ESI-MS spectrum of $[Pd_2\mathbf{L^1}_2\mathbf{L^B}_2 + n\ BF_4]^{(4-n)+}$ and inset of comparison of measured and calculated mass.

4.4.3 $Pd_2\mathbf{L^1}_2\mathbf{L^C}_2$

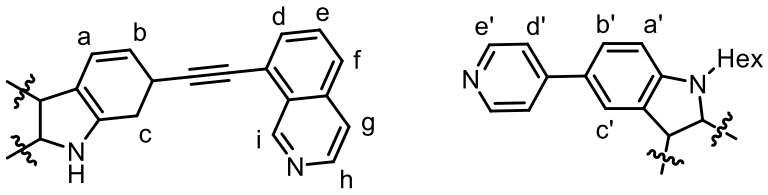

Scheme 4.21: Ligand Assignment for $Pd_2\mathbf{L^1}_2\mathbf{L^C}_2$.

^{1}H NMR (500 MHz, 298 K, DMSO-d_6): δ = 11.98 (s, 2H, N*H*), 10.14 (s, 4H, i), 9.45 (s (br), 8H, e'), 9.36 (d, ^3J = 6.6, 4H, h), 8.44 (m, 8H, g, c'), 8.26 (d, ^3J = 8.4, 4H, f), 8.10 (m, 4H, d), 8.05 (t, ^3J = 8.0, 4H, e), 7.93 (m, 16H, c, b', d'), 7.83 (d, ^3J = 8.7, 4H, a'), 7.77 (d, ^3J = 7.9, 4H, a), 7.23 (dd, ^3J = 7.9, ^4J = 1.0, 4H, b), 4.47 (s (br), 4H, NCH_2), 1.24−1.04 (m, 16H, CH_2), 0.65 (t, ^3J = 7.3, 6H, CH_3).

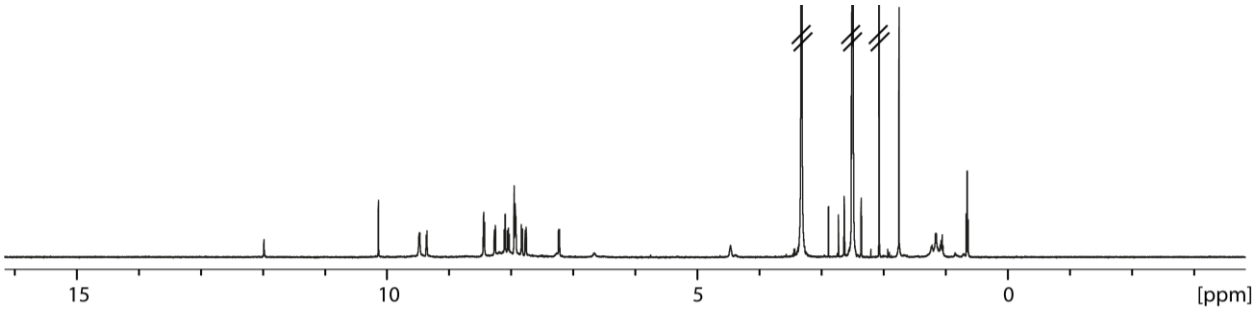

Figure 4.61: ^{1}H NMR (500 MHz, 298 K, DMSO-d_6) of $Pd_2\mathbf{L^1}_2\mathbf{L^C}_2$.

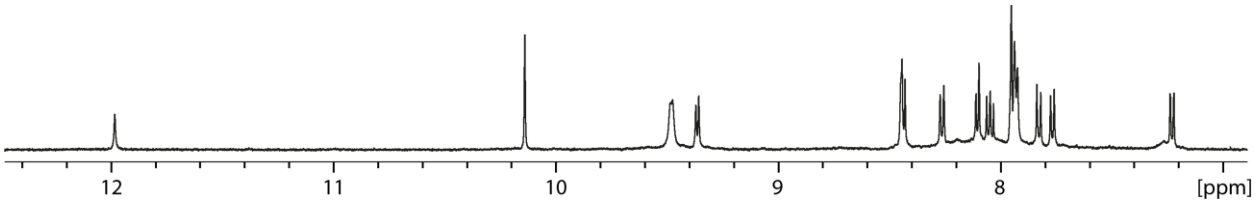

Figure 4.62: Partial ^{1}H NMR (500 MHz, 298 K, DMSO-d_6) of $Pd_2\mathbf{L^1}_2\mathbf{L^C}_2$.

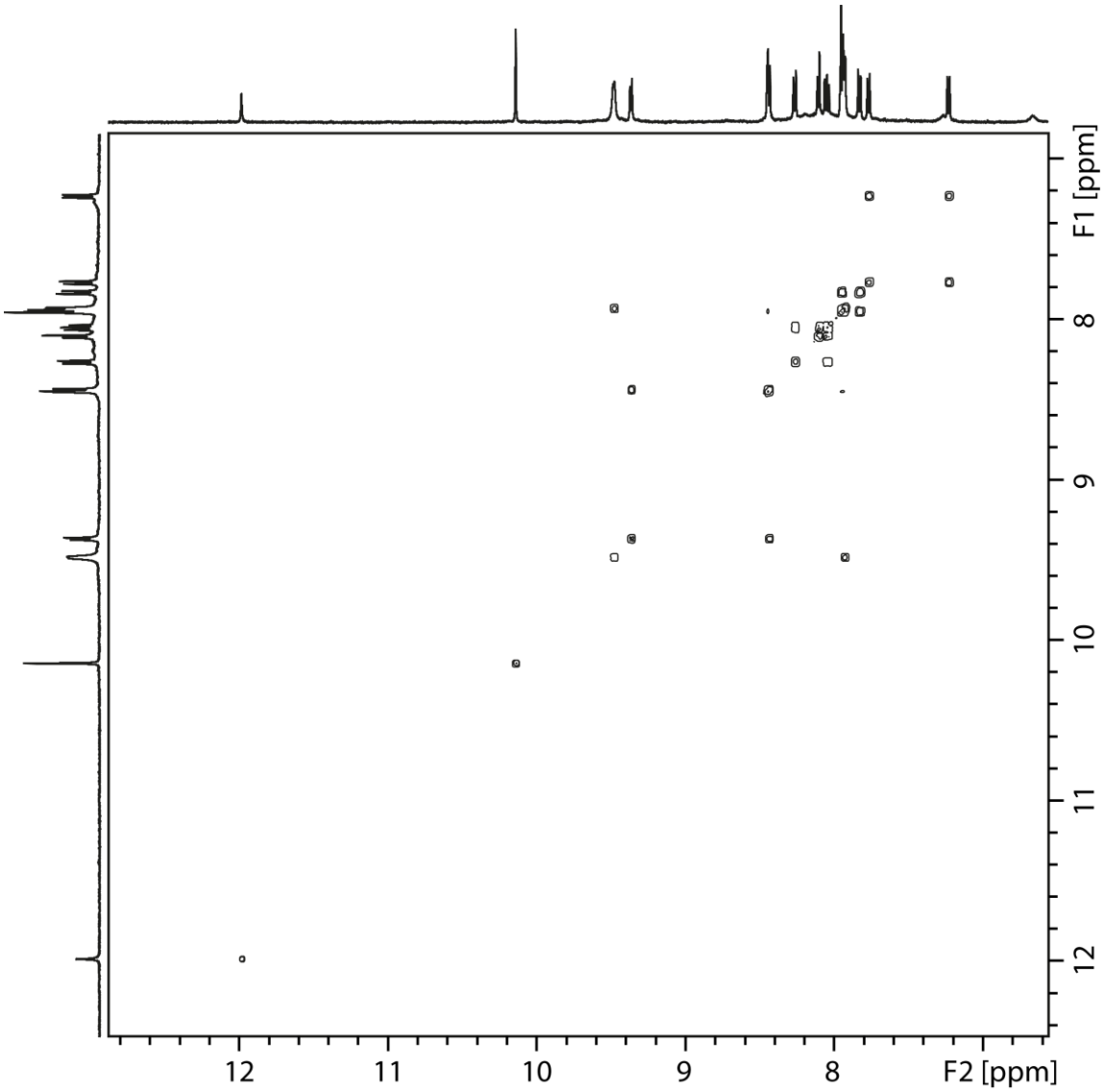

Figure 4.63: Partial $^{1}H-^{1}H$ COSY NMR (600 MHz, 298 K, DMSO-d_6) of $Pd_2\mathbf{L}^{\mathbf{1}}{}_2\mathbf{L}^{\mathbf{C}}{}_2$.

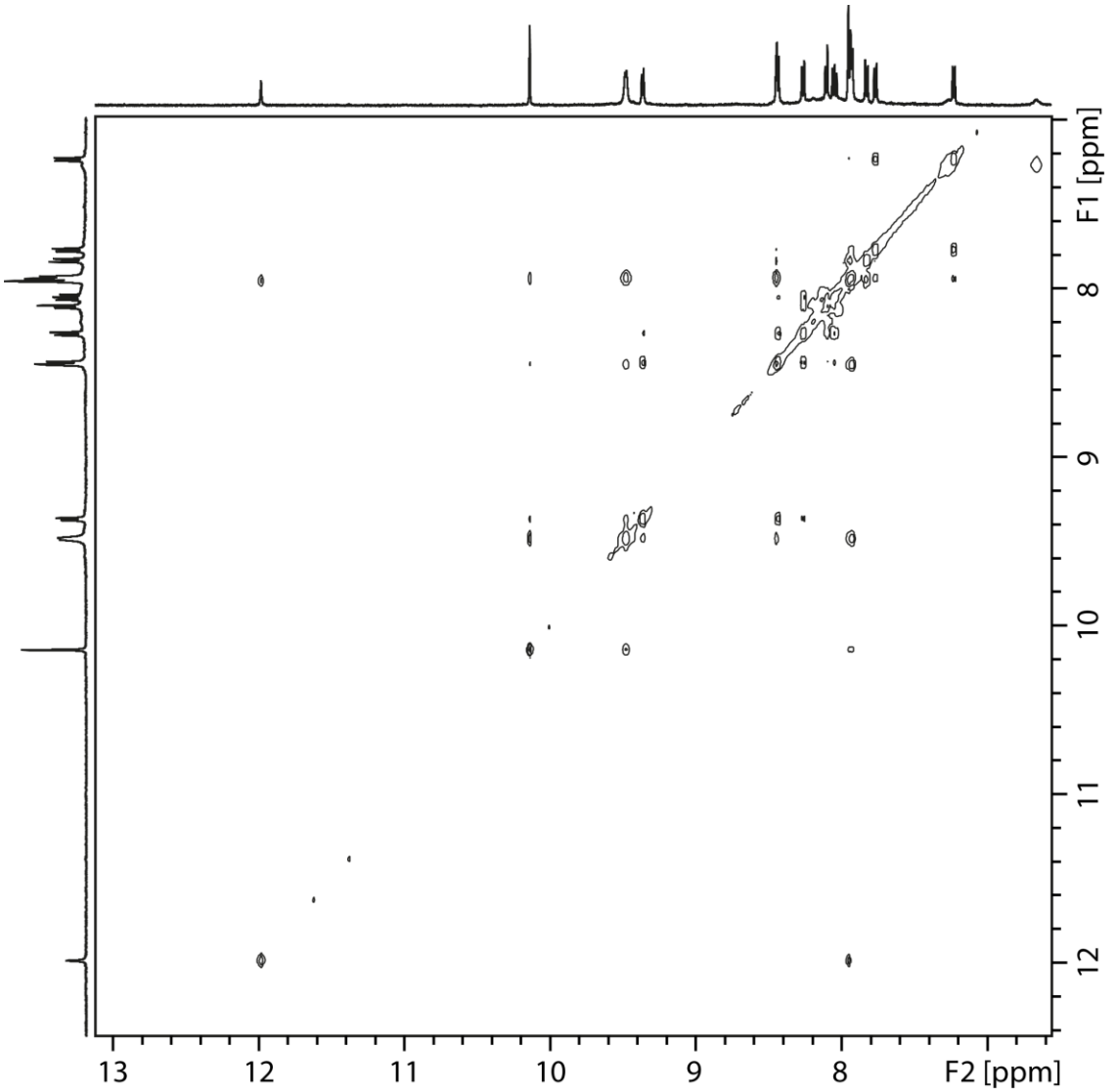

Figure 4.64: Partial ^{1}H–^{1}H NOESY NMR (600 MHz, 298 K, DMSO-d$_6$) of $Pd_2\mathbf{L^1}_2\mathbf{L^C}_2$.

^{13}C{^{1}H} NMR (151 MHz, 298 K, DMSO-d$_6$): δ = 171.4, 162.3, 153.4, 151.9, 150.4, 142.7, 142.1, 140.3, 136.3, 133.9, 127.7, 125.8, 125.0, 124.2, 123.3, 123.1, 122.8, 121.5, 121.1, 119.1, 118.1, 114.0, 111.2, 98.2, 84.1, 30.7, 28.5, 25.8, 22.5, 21.9, 13.6.

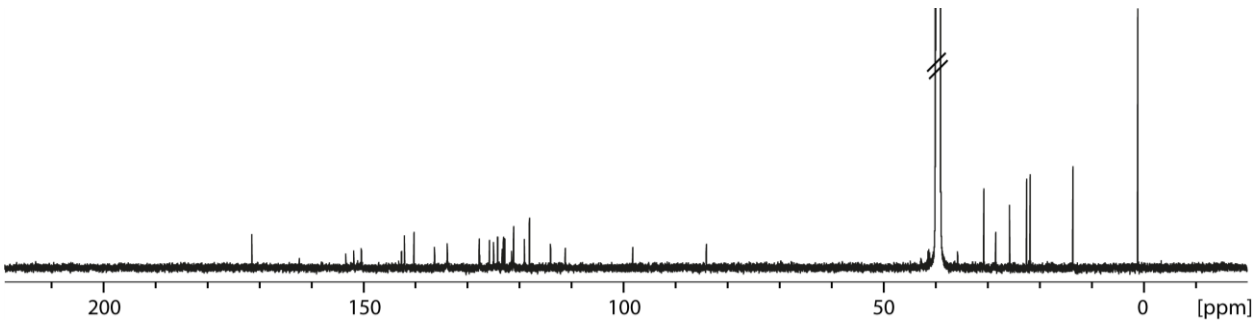

Figure 4.65: ^{13}C{^{1}H} NMR (151 MHz, 298 K, DMSO-d$_6$) of $Pd_2\mathbf{L^1}_2\mathbf{L^C}_2$.

HR-ESI-MS (positive mode):

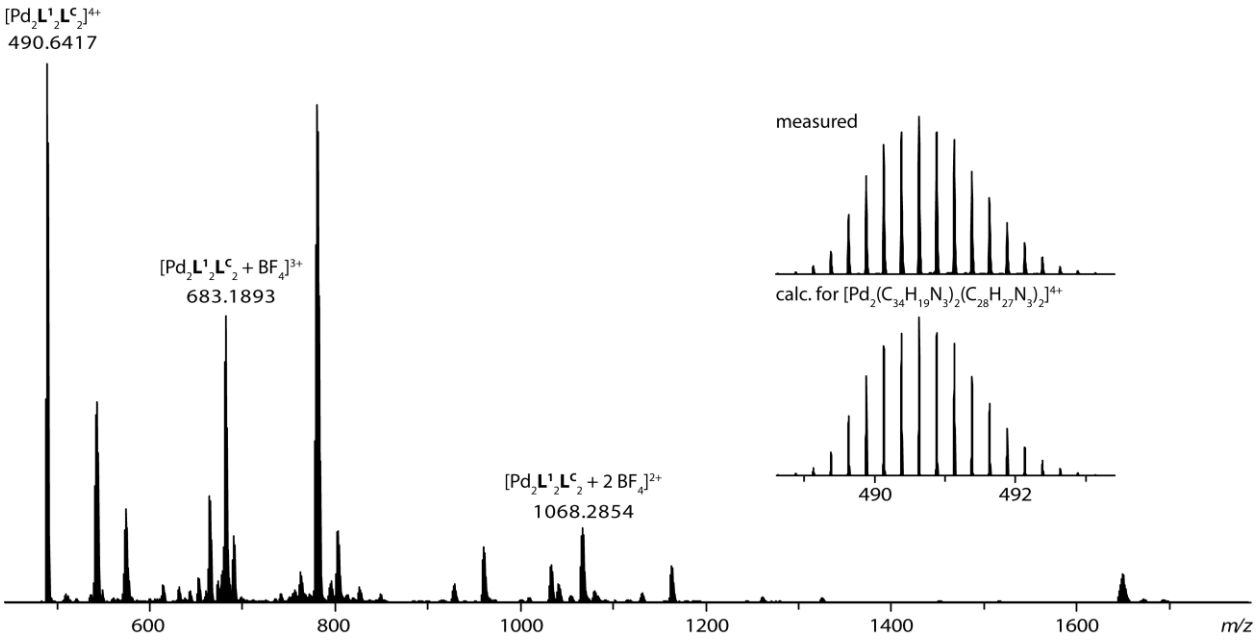

Figure 4.66: ESI-MS spectrum of $[Pd_2\mathbf{L^1}_2\mathbf{L^C}_2 + n\ BF_4]^{(4-n)+}$ and inset of comparison of measured and calculated mass.

4.4.4 $Pd_2\mathbf{L^1}_2\mathbf{L^D}_2$

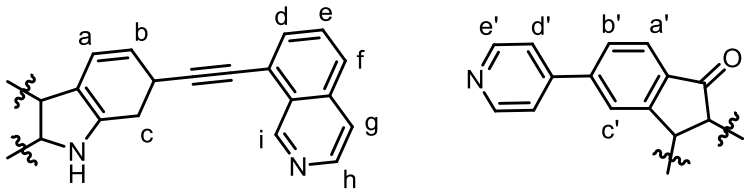

Scheme 4.22: Ligand Assignment for $Pd_2\mathbf{L^1}_2\mathbf{L^D}_2$.

^{1}H NMR (500 MHz, 298 K, DMSO-d_6): δ = 12.00 (s, 2H, N*H*), 10.04 (s, 4H, i), 9.58 (d, ^3J = 6.3, 8H, e'), 9.33 (d, ^3J = 6.5, 4H, h), 8.42 (d, ^3J = 6.4, 4H, g), 8.25 (d, ^3J = 8.3, 4H, f), 8.09 (dd, ^3J = 7.1, ^4J = 1.1, 4H, d), 8.05 (m, 4H, e), 7.98 (d, ^3J = 8.1, 4H, a'), 7.94 (s, 4H, c'), 7.91 (s, 4H, c), 7.88 (d, ^3J = 6.2, 8H, a, b'), 7.84 (s, 8H, d'), 7.23 (dd, ^3J = 7.9, ^4J = 1.1, 4H, b).

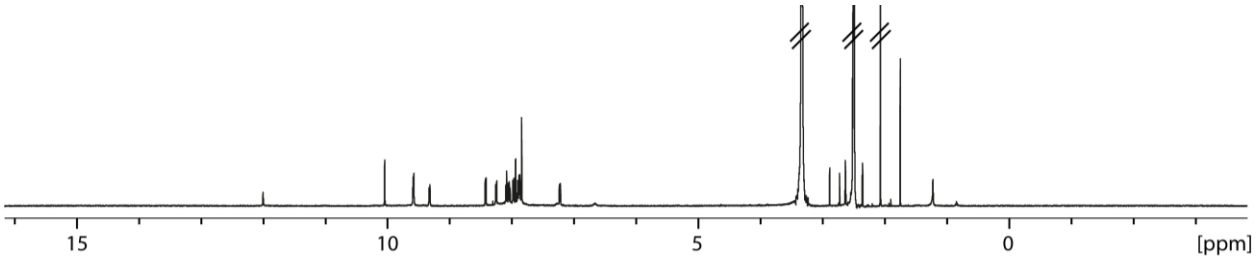

Figure 4.67: ^{1}H NMR (500 MHz, 298 K, DMSO-d_6) of $Pd_2\mathbf{L^1}_2\mathbf{L^D}_2$.

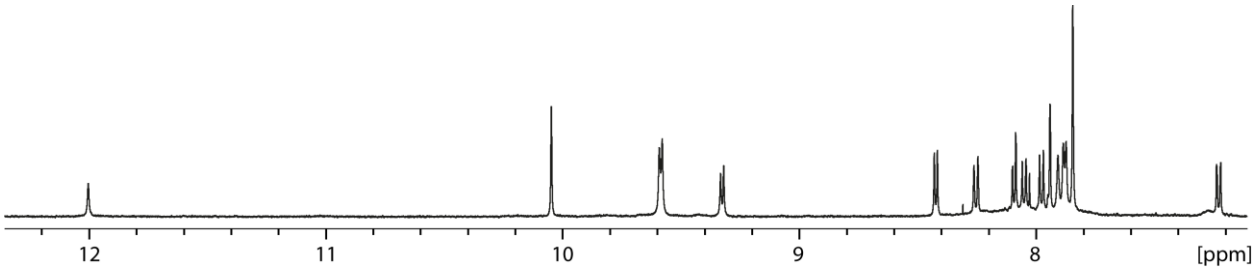

Figure 4.68: Partial ^{1}H NMR (500 MHz, 298 K, DMSO-d_6) of $Pd_2\mathbf{L^1}_2\mathbf{L^D}_2$.

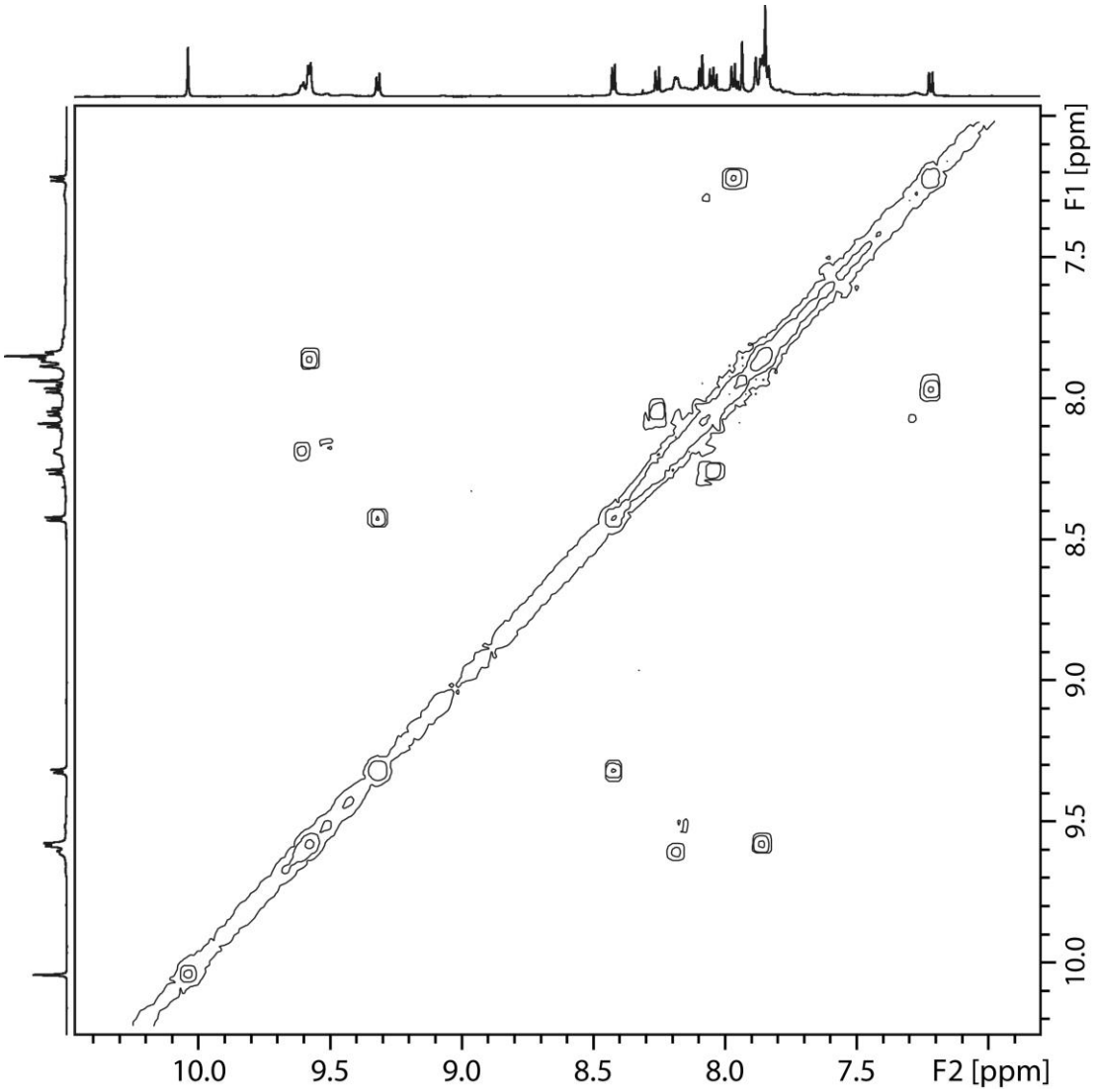

Figure 4.69: Partial $^{1}H-^{1}H$ COSY NMR (600 MHz, 298 K, DMSO-d_6) of $Pd_2\mathbf{L^1}_2\mathbf{L^D}_2$.

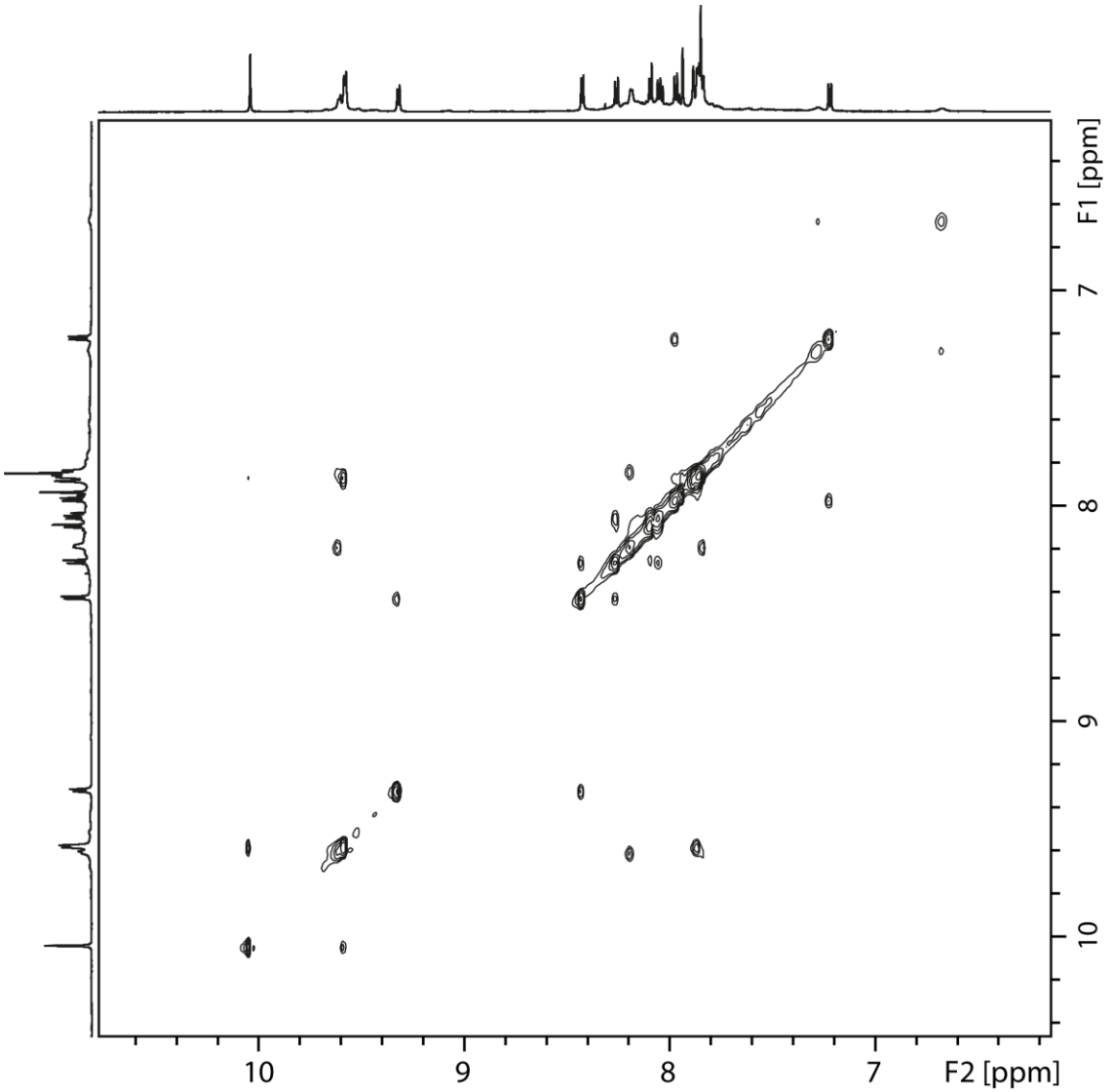

Figure 4.70: Partial $^{1}H-^{1}H$ NOESY NMR (600 MHz, 298 K, DMSO-d_6) of $Pd_2\mathbf{L^1}_2\mathbf{L^D}_2$.

$^{13}C\{^{1}H\}$ NMR (151 MHz, 298 K, DMSO-d_6): δ = 191.6, 171.4, 162.3, 153.4, 150.9, 150.1, 143.8, 142.6, 141.1, 140.3, 136.3, 134.8, 134.0, 133.7, 128.8, 127.8, 127.7, 125.2, 123.2, 123.0, 121.4, 121.1, 119.0, 118.1, 114.1, 98.2, 83.8.

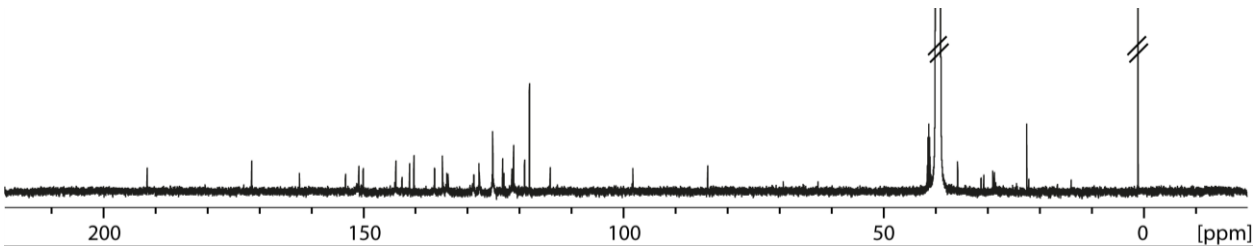

Figure 4.71: $^{13}C\{^{1}H\}$ NMR (151 MHz, 298 K, DMSO-d_6) of $Pd_2\mathbf{L^1}_2\mathbf{L^D}_2$.

HR-ESI-MS (positive mode):

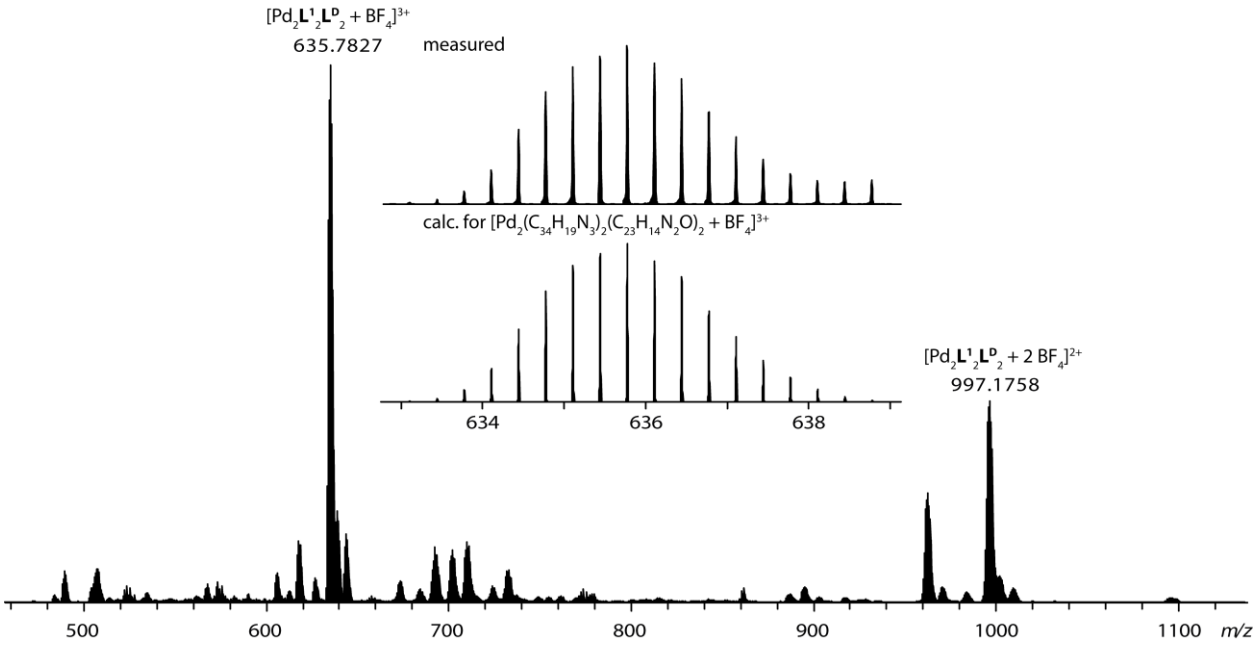

Figure 4.72: ESI-MS spectrum of $[Pd_2\mathbf{L}^{\mathbf{1}}{}_2\mathbf{L}^{\mathbf{D}}{}_2 + n\ BF_4]^{(4-n)+}$ and inset of comparison of measured and calculated mass.

4.4.5 $Pd_2L^2{}_2L^A{}_2$

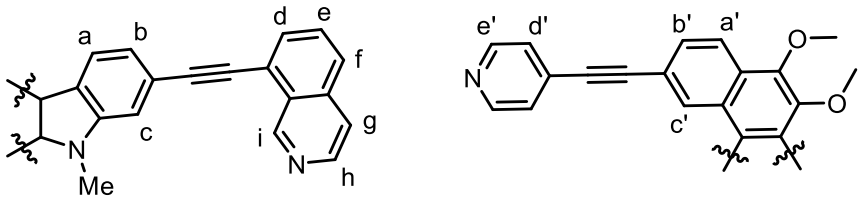

Scheme 4.23: Ligand Assignment for $Pd_2\mathbf{L}^{\mathbf{2}}{}_2\mathbf{L}^{\mathbf{A}}{}_2$.

^{1}H NMR (500 MHz, 298 K, DMSO-d_6): δ = 9.84 (s, 4H, i), 9.50 (d, ^3J = 6.7, 4H, h), 9.32 (d, ^3J = 6.8, 8H, e'), 9.27 (s, 4H, c'), 8.59 (d, ^3J = 8.0, 4H, a), 8.41 (d, ^3J = 6.7, 4H, g), 8.24 (d, ^3J = 8.6, 4H, a'), 8. 21 (d, ^3J = 8.4, 4H, f), 8.12 (m, 8H, c, d), 8.03 (m, 4H, e), 8.00 (d, ^3J = 6.8, 8H, d'), 7.87 (d, ^3J = 8.5, 4H, b'), 7.51 (dd, ^3J = 7.6, ^4J = 1.1, 4H, b), 4.05 (s, 6H, NCH_3), 4.01 (s, 12H, OCH_3).

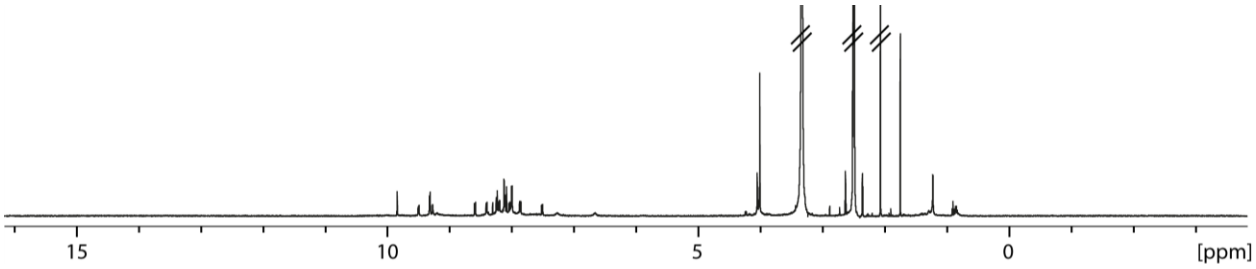

Figure 4.73: ^{1}H NMR (500 MHz, 298 K, DMSO-d_6) of $Pd_2\mathbf{L}^{\mathbf{2}}{}_2\mathbf{L}^{\mathbf{A}}{}_2$.

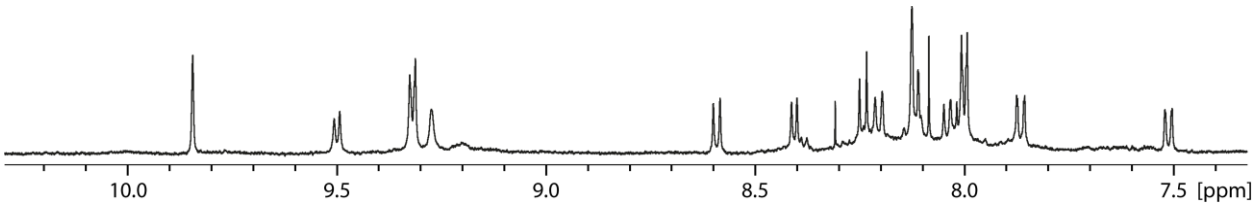

Figure 4.74: Partial ^{1}H NMR (500 MHz, 298 K, DMSO-d_6) of $Pd_2\mathbf{L}^{\mathbf{2}}{}_2\mathbf{L}^{\mathbf{A}}{}_2$.

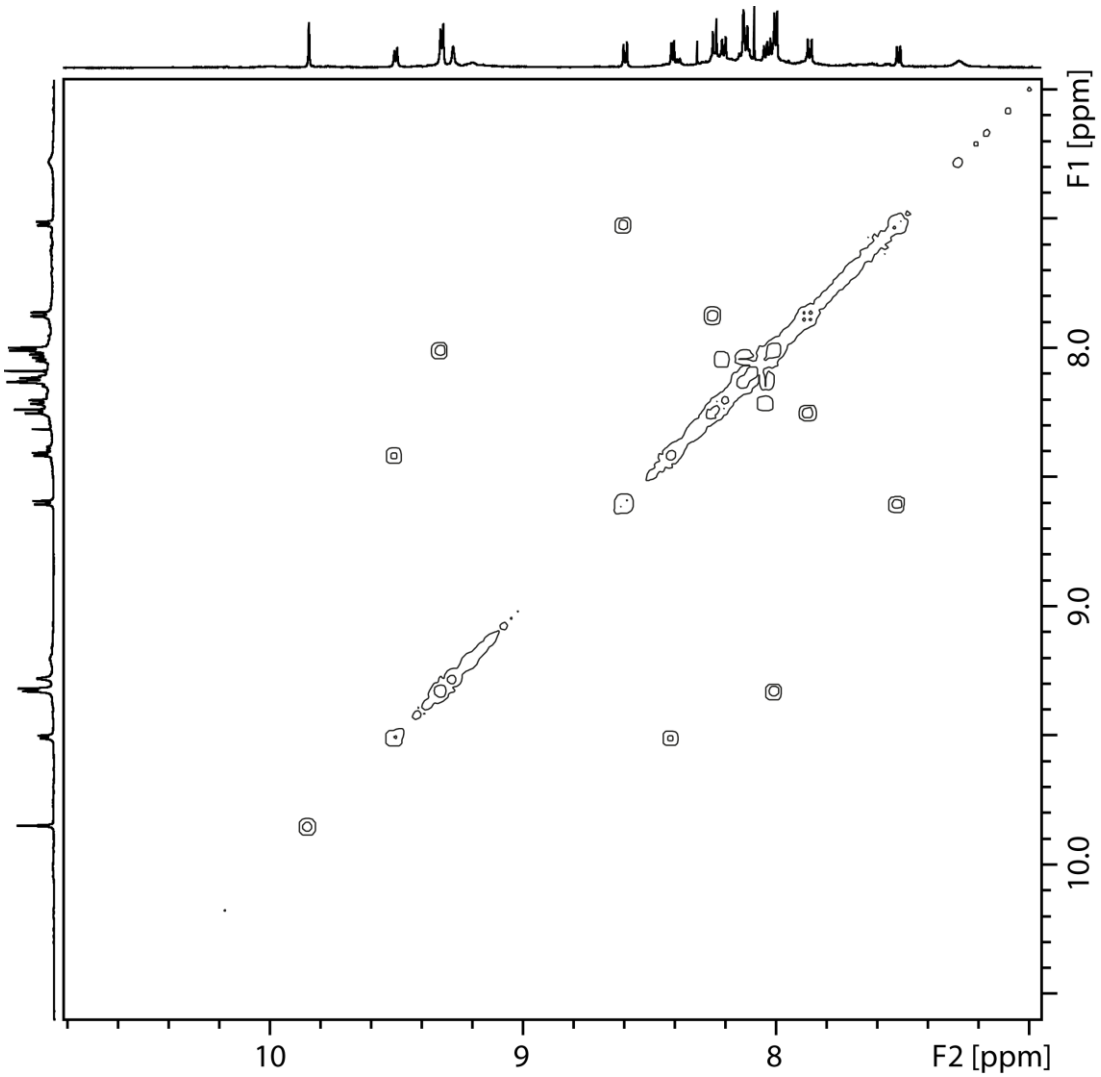

Figure 4.75: Partial ^{1}H–^{1}H COSY NMR (600 MHz, 298 K, DMSO-d_6) of $Pd_2\mathbf{L}^{\mathbf{2}}{}_2\mathbf{L}^{\mathbf{A}}{}_2$.

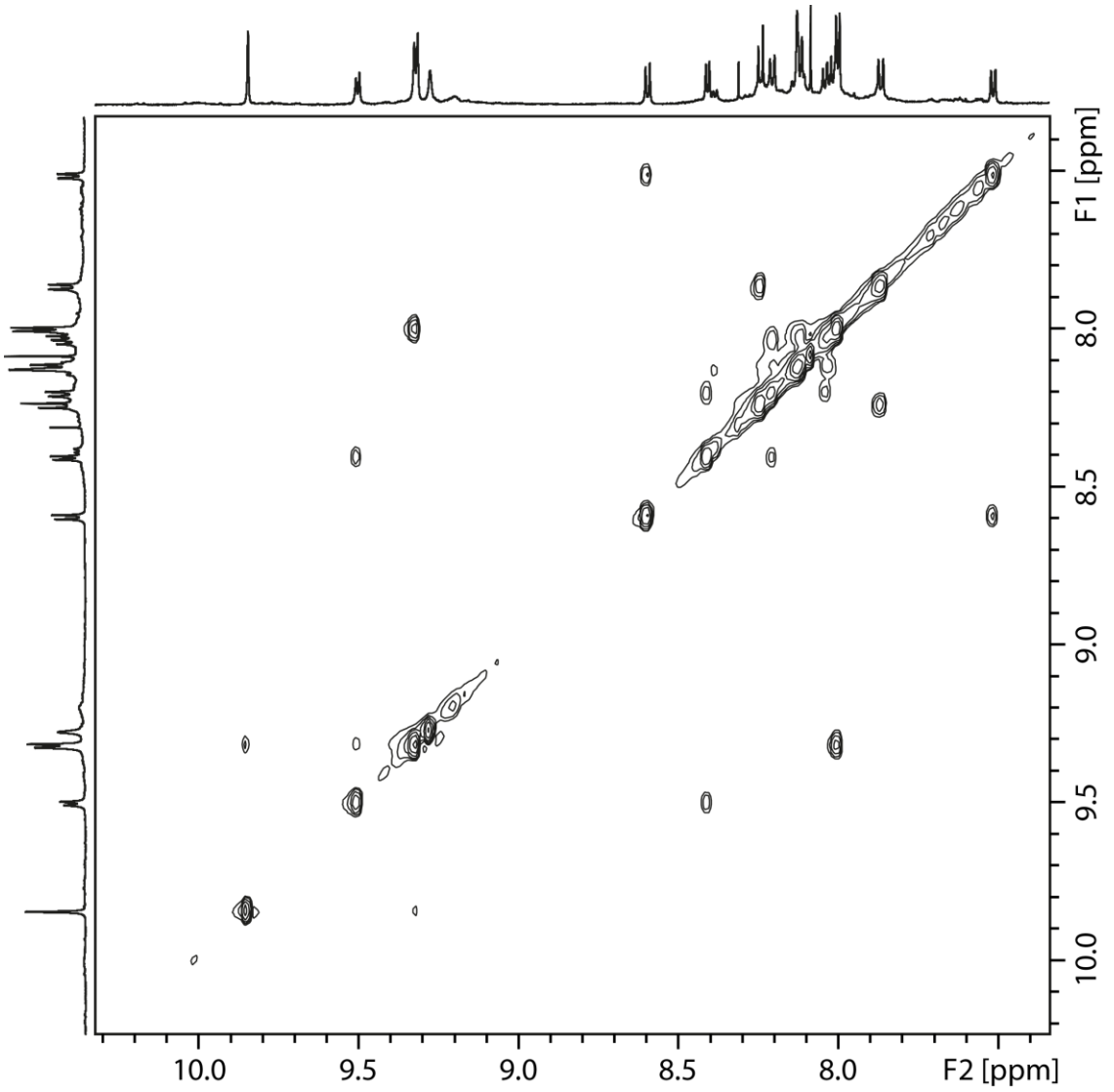

Figure 4.76: Partial ^{1}H–^{1}H NOESY NMR (600 MHz, 298 K, DMSO-d$_6$) of $Pd_2\mathbf{L}^{\mathbf{2}}{}_2\mathbf{L}^{\mathbf{A}}{}_2$.

^{13}C{^{1}H} NMR (151 MHz, 298 K, DMSO-d$_6$): δ = 171.5, 151.1, 144.7, 141.1, 136.2, 134.8, 133.8, 129.9, 129.5, 128.8, 128.6, 128.1, 127.8, 127.2, 123.0, 122.5, 121.5, 121.1, 119.0, 118.2, 118.1, 113.4, 99.4, 98.1, 86.2, 84.6, 61.2, 22.5.

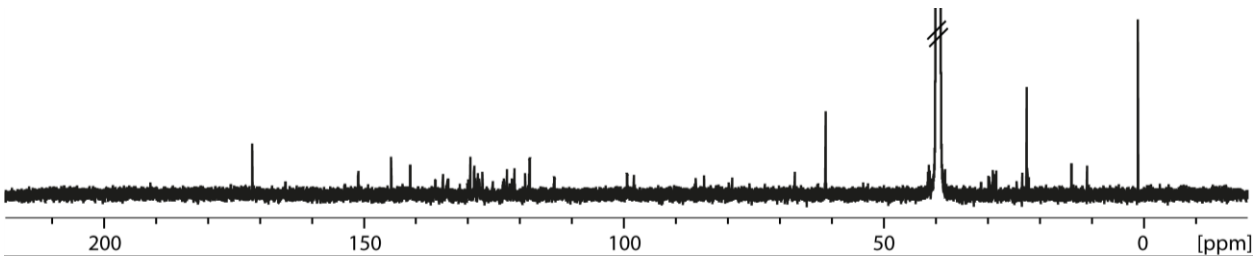

Figure 4.77: ^{13}C{^{1}H} NMR (151 MHz, 298 K, DMSO-d$_6$) of $Pd_2\mathbf{L}^{\mathbf{2}}{}_2\mathbf{L}^{\mathbf{A}}{}_2$.

HR-ESI-MS (positive mode):

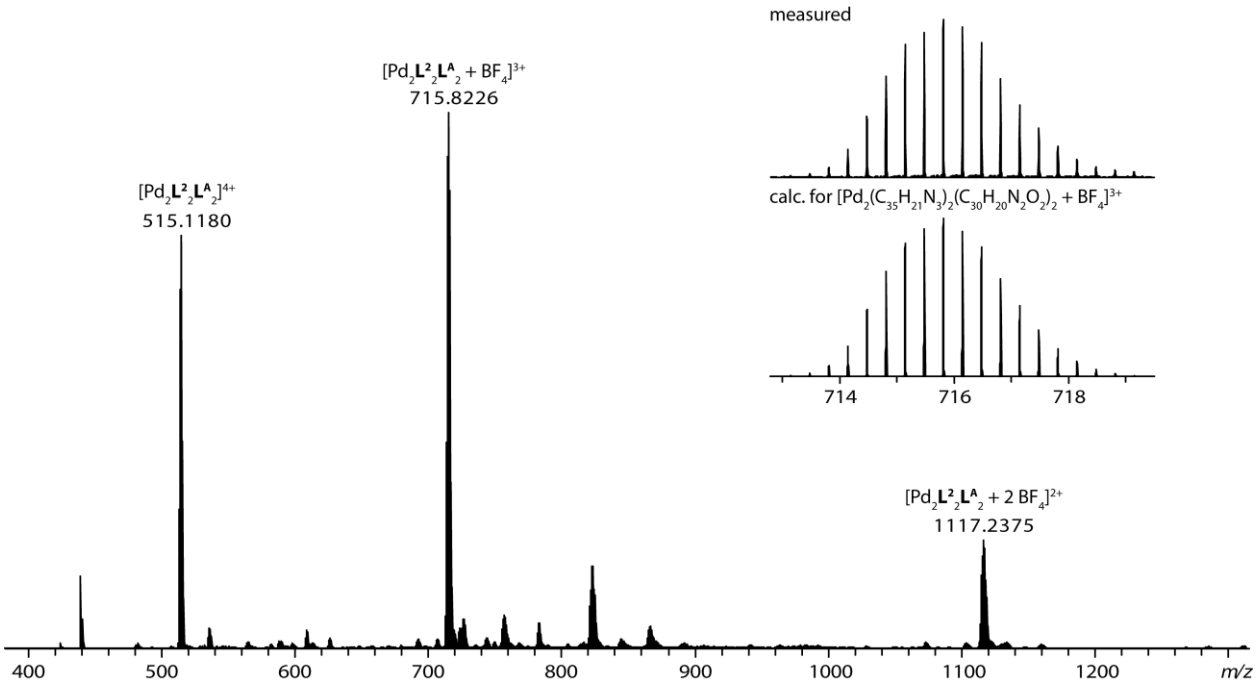

Figure 4.78: ESI-MS spectrum of $[Pd_2\mathbf{L}^{2}{}_2\mathbf{L}^{\mathbf{A}}{}_2 + n\ BF_4]^{(4-n)+}$ and inset of comparison of measured and calculated mass.

4.4.6 $Pd_2\mathbf{L}^{2}{}_2\mathbf{L}^{\mathbf{B}}{}_2$

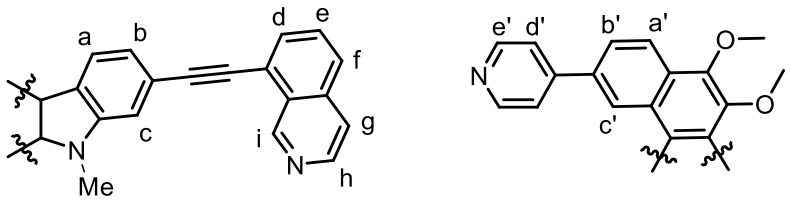

Scheme 4.24: Ligand Assignment for $Pd_2\mathbf{L}^{2}{}_2\mathbf{L}^{\mathbf{B}}{}_2$.

^{1}H NMR (500 MHz, 298 K, DMSO-d_6): δ = 10.21 (s, 4H, i), 9.79 (d, ^3J = 6.5, 4H, h), 9.75 (d, ^3J = 6.2, 8H, e'), 9.20 (s (br), 4H, c'), 8.46 (d, ^3J = 6.2, 12H, g, d'), 8.30 (m, 8H, a, a'), 8.17 (m, 8H, f, b'), 8.07 (d, ^3J = 6.5, 4H, d), 8.01 (m, 8H, c, e), 7.50 (d, ^3J = 8.7, 4H, b), 4.37 (s, 6H, NCH_3), 4.00 (s, 12H, OCH_3).

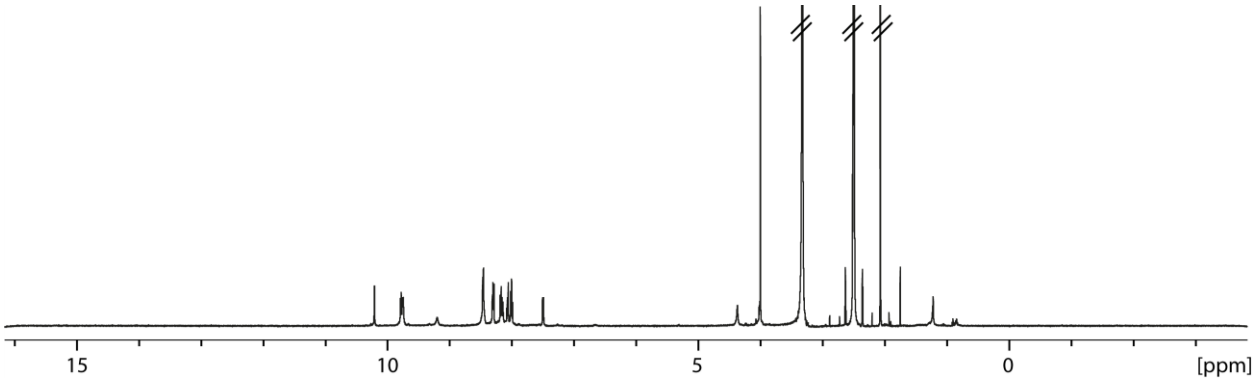

Figure 4.79: ^{1}H NMR (500 MHz, 298 K, DMSO-d_6) of $Pd_2\mathbf{L}^{\mathbf{2}}{}_2\mathbf{L}^{\mathbf{B}}{}_2$.

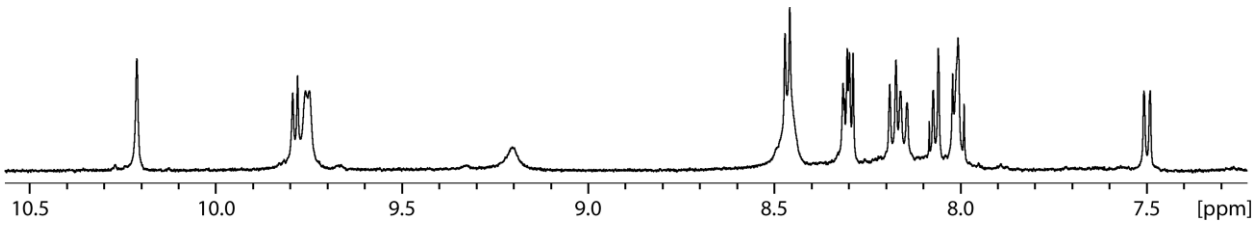

Figure 4.80: Partial ^{1}H NMR (500 MHz, 298 K, DMSO-d_6) of $Pd_2\mathbf{L}^{\mathbf{2}}{}_2\mathbf{L}^{\mathbf{B}}{}_2$.

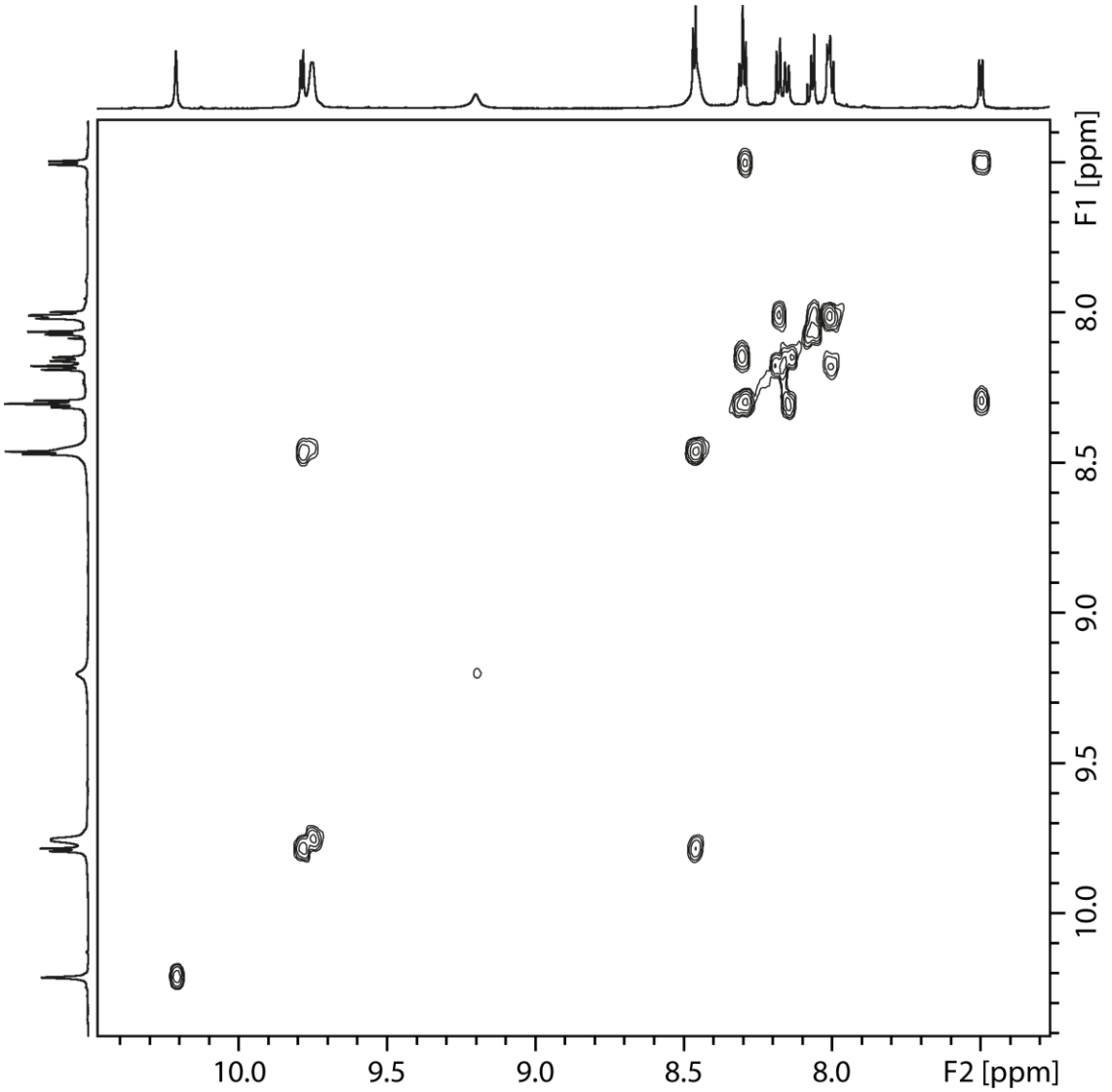

Figure 4.81: Partial $^{1}H-^{1}H$ COSY NMR (700 MHz, 298 K, DMSO-d_6) of $Pd_2\mathbf{L}^{\mathbf{2}}{}_2\mathbf{L}^{\mathbf{B}}{}_2$.

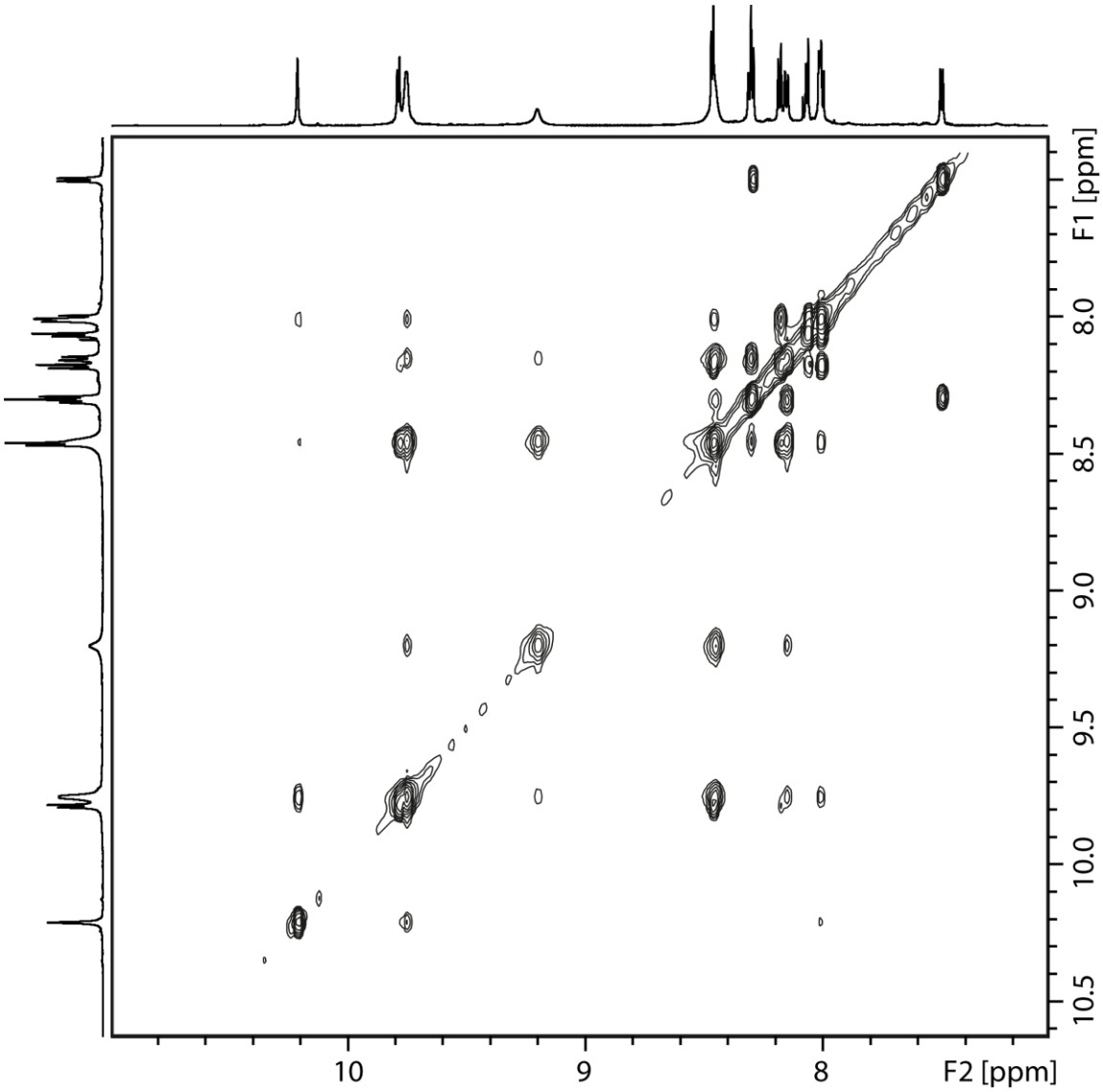

Figure 4.82: Partial $^{1}H-^{1}H$ NOESY NMR (700 MHz, 298 K, DMSO-d_6) of $Pd_2\mathbf{L}^{\mathbf{2}}{}_2\mathbf{L}^{\mathbf{B}}{}_2$.

$^{13}C\{^{1}H\}$ NMR (176 MHz, 298 K, DMSO-d_6): δ = 154.4, 151.4, 150.3, 144.3, 142.3, 140.9, 136.1, 133.7, 133.4, 132.6, 130.3, 128.1, 127.5, 125.0, 124.6, 122.4, 121.5, 121.3, 118.9, 118.1, 114.2, 98.4, 84.8, 61.1, 22.5.

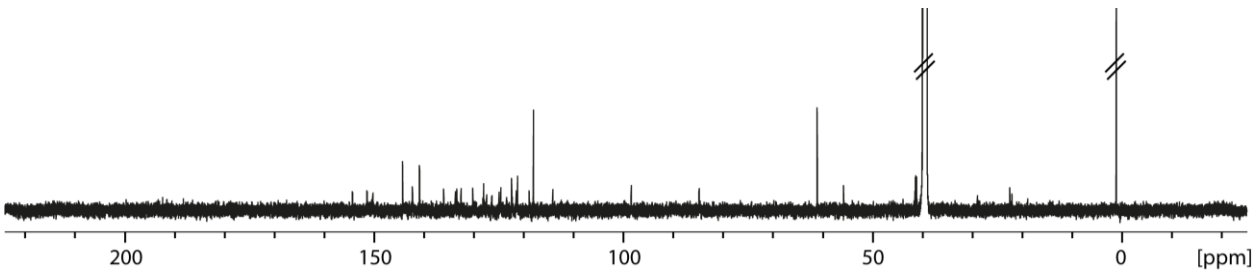

Figure 4.83: $^{13}C\{^{1}H\}$ NMR (176 MHz, 298 K, DMSO-d_6) of $Pd_2\mathbf{L}^{\mathbf{2}}{}_2\mathbf{L}^{\mathbf{B}}{}_2$.

HR-ESI-MS (positive mode):

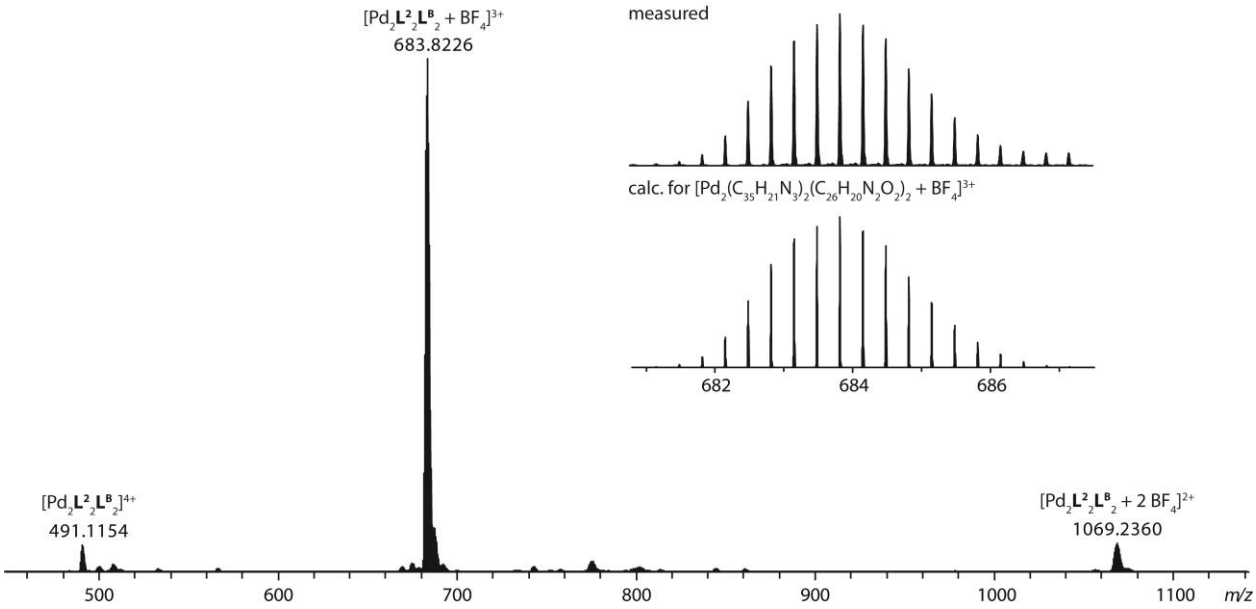

Figure 4.84: ESI-MS spectrum of $[Pd_2\mathbf{L}^{2}_{2}\mathbf{L}^{\mathbf{B}}_{2}$ + n $BF_4]^{(4-n)+}$ and inset of comparison of measured and calculated mass.

4.4.7 $Pd_2\mathbf{L}^{2}_{2}\mathbf{L}^{\mathbf{C}}_{2}$

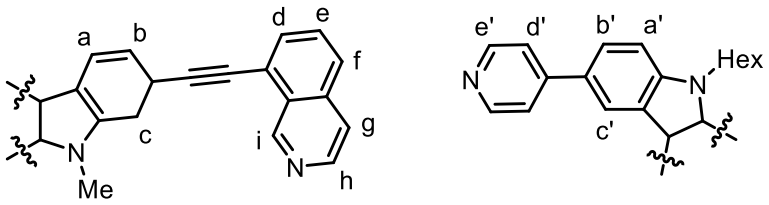

Scheme 4.25: Ligand Assignment for $Pd_2\mathbf{L}^{2}_{2}\mathbf{L}^{\mathbf{C}}_{2}$.

^{1}H NMR (500 MHz, 298 K, DMSO-d_6): δ = 10.23 (s, 4H, i), 9.51 (m, 12H, h, e'), 8.83 (s (br), 4H, c'), 8.45 (d, ^3J = 6.5, 4H, g), 8.25 (d, ^3J = 8.4, 4H, f), 8.21 (d, ^3J = 8.0, 4H, a), 8.16 (d, ^3J = 6.2, 8H, d'), 8.12 (d, ^3J = 6.9, 4H, d), 8.03 (t, ^3J = 8.1, 4H, e), 7.94 (m, 8H, c, a'), 7.78 (d, ^3J = 8.7, 4H, b'), 7.49 (dd, ^3J =8.0, ^4J = 1.1, 4H, b), 4.42 (t (br), 4H, NCH_2), 4.22 (s, 6H, NCH_3), 1.73 (m, 4H, NCH_2CH_2), 1.22−1.08 (m, 12H, CH_2), 0.68 (t, ^3J = 7.1, 6H, CH_3).

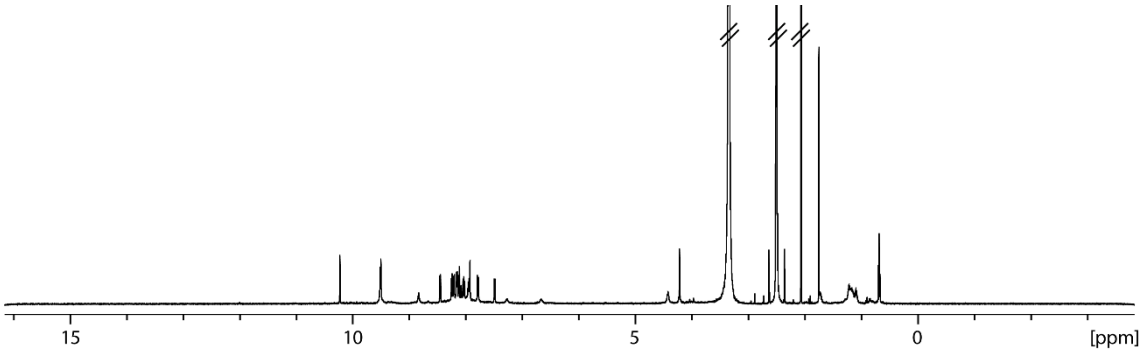

Figure 4.85: ^{1}H NMR (500 MHz, 298 K, DMSO-d_6) of $Pd_2\mathbf{L}^{\mathbf{2}}{}_2\mathbf{L}^{\mathbf{C}}{}_2$.

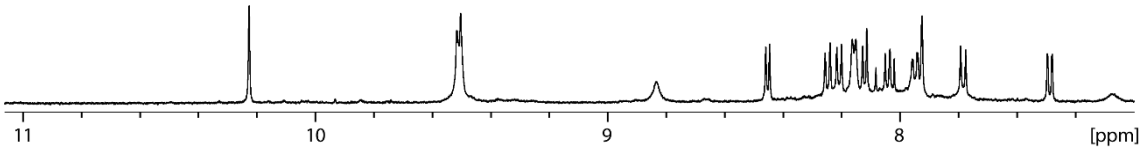

Figure 4.86: Partial ^{1}H NMR (500 MHz, 298 K, DMSO-d_6) of $Pd_2\mathbf{L}^{\mathbf{2}}{}_2\mathbf{L}^{\mathbf{C}}{}_2$.

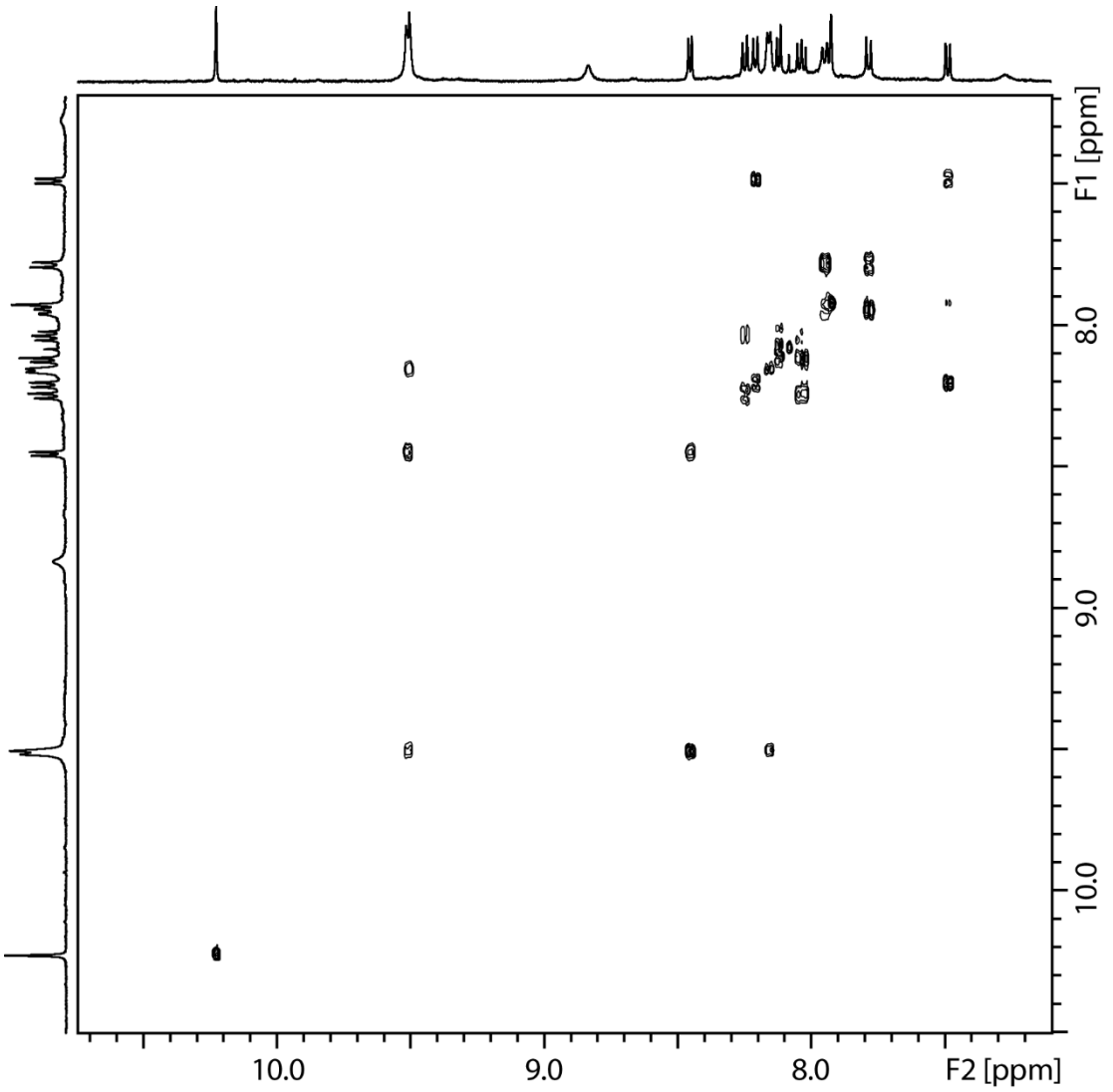

Figure 4.87: Partial ^{1}H–^{1}H COSY NMR (500 MHz, 298 K, DMSO-d_6) of $Pd_2\mathbf{L}^{\mathbf{2}}{}_2\mathbf{L}^{\mathbf{C}}{}_2$.

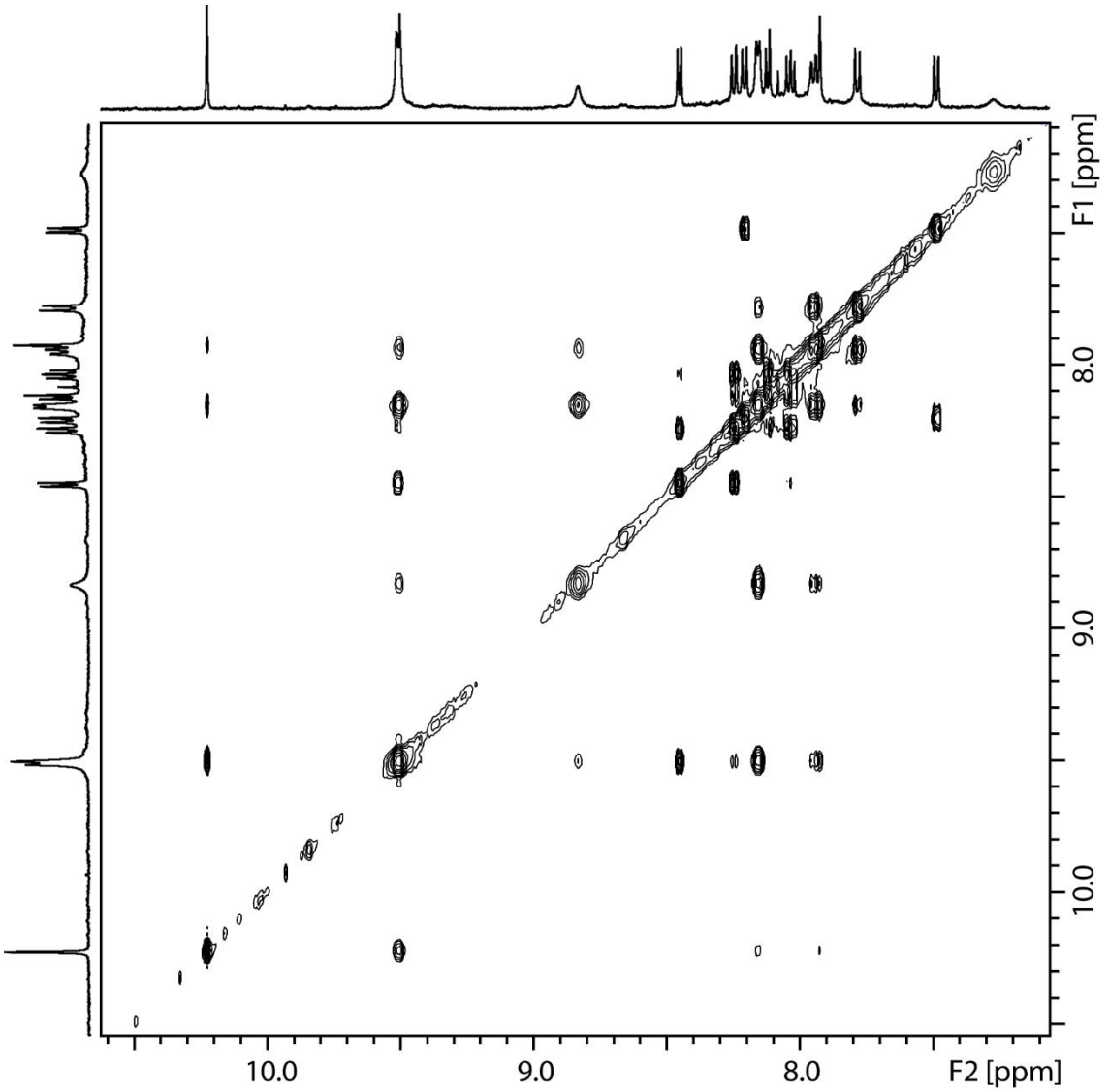

Figure 4.88: Partial ^{1}H–^{1}H NOESY NMR (500 MHz, 298 K, DMSO-d_6) of $Pd_2\mathbf{L^2}_2\mathbf{L^C}_2$.

^{13}C{^{1}H} NMR (151 MHz, 298 K, DMSO-d_6): δ = 171.5, 153.4, 151.5, 150.5, 142.7, 142.1, 136.3, 134.2, 133.9, 129.5, 127.7, 125.9, 125.0, 124.9, 124.1, 123.5, 123.1, 122.5, 121.4, 121.1, 120.9, 119.2, 118.1, 112.5, 111.0, 98.2, 84.4, 30.8, 29.2, 28.6, 25.9, 22.5, 21.9, 13.7.

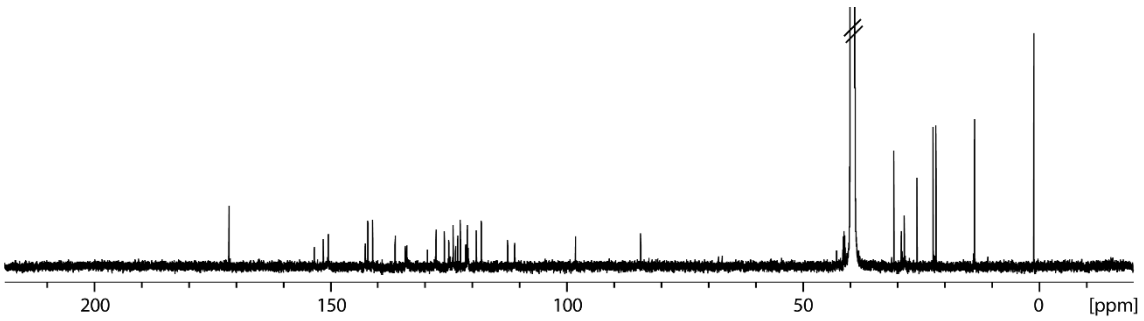

Figure 4.89: ^{13}C{^{1}H} NMR (151 MHz, 298 K, DMSO-d_6) of $Pd_2\mathbf{L^2}_2\mathbf{L^C}_2$.

HR-ESI-MS (positive mode):

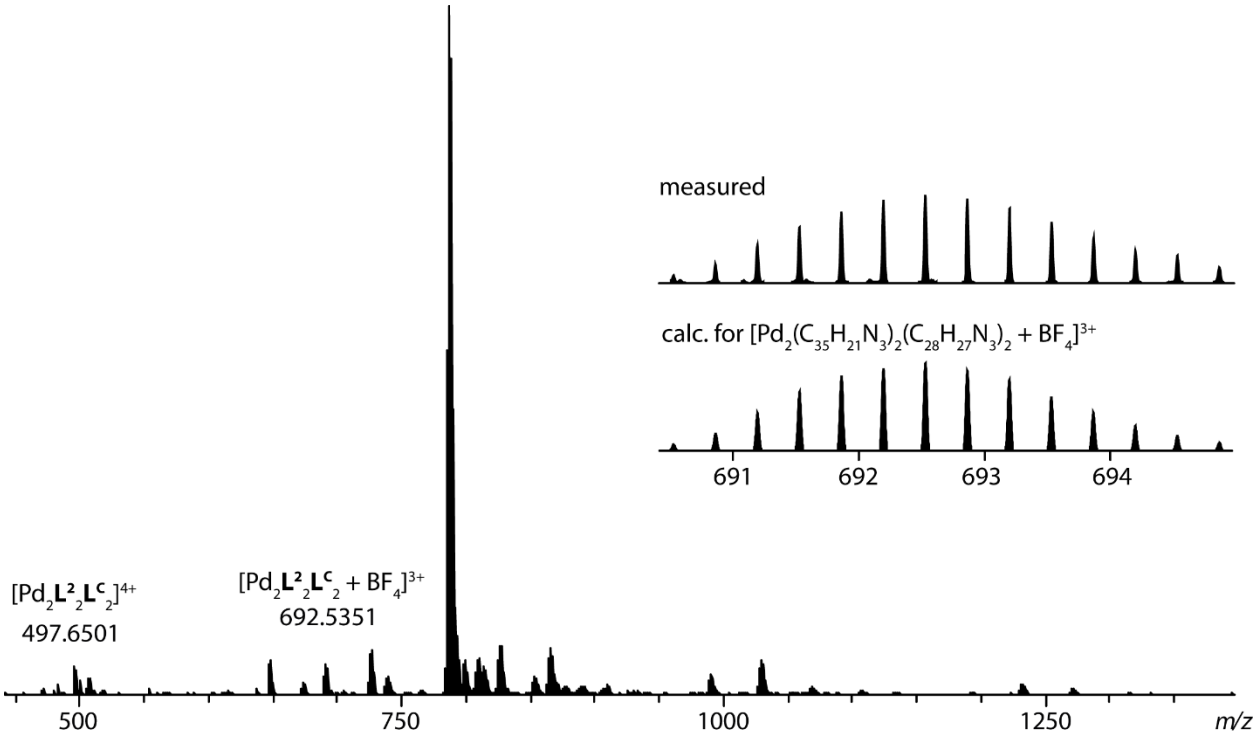

Figure 4.90: ESI-MS spectrum of $[Pd_2\mathbf{L}^{\mathbf{2}}{}_2\mathbf{L}^{\mathbf{C}}{}_2 + n\ BF_4]^{(4-n)+}$ and inset of comparison of measured and calculated mass.

4.4.8 $Pd_2\mathbf{L}^{\mathbf{2}}{}_2\mathbf{L}^{\mathbf{D}}{}_2$

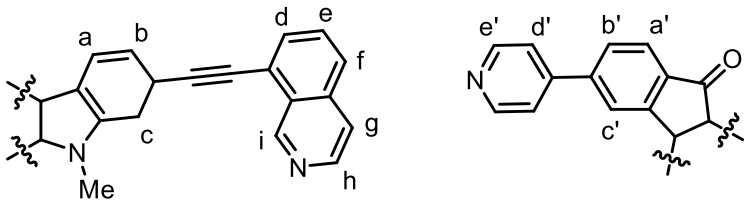

Scheme 4.26: Ligand Assignment for $Pd_2\mathbf{L}^{\mathbf{2}}{}_2\mathbf{L}^{\mathbf{D}}{}_2$.

^{1}H NMR (500 MHz, 298 K, DMSO-d_6): δ = 10.20 (s, 4H, i), 9.68 (d, ^3J = 6.1, 8H, e'), 9.54 (d, ^3J = 6.5, 4H, h), 8.44 (d, ^3J = 6.5, 4H, g), 8.30 (s (br), 4H, c'), 8.27 (d, ^3J = 8.0, 4H, a), 8.22 (m, 12H, f, d'), 8.11 (d, ^3J = 7.3, 4H, d), 8.02 (t, ^3J = 7.6, 4H, e), 7.97 (s, 4H, c), 7.86 (dd, ^3J = 7.7, ^4J = 1.1, 4H, b'), 7.80 (d, ^3J = 7.7, 4H, a'), 7.49 (dd, ^3J = 8.0, ^4J = 1.1, 4H, b), 4.28 (s, 6H, NCH_3).

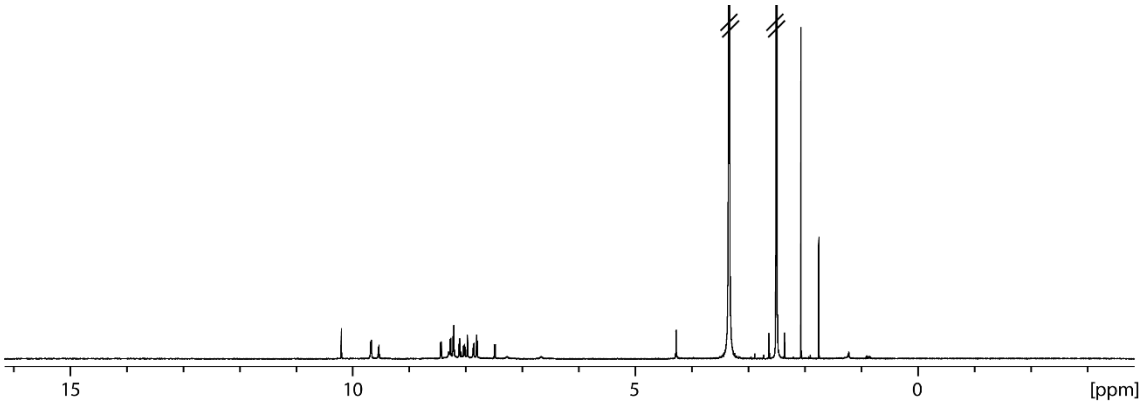

Figure 4.91: ^{1}H NMR (500 MHz, 298 K, DMSO-d_6) of $Pd_2\mathbf{L^2}_2\mathbf{L^D}_2$.

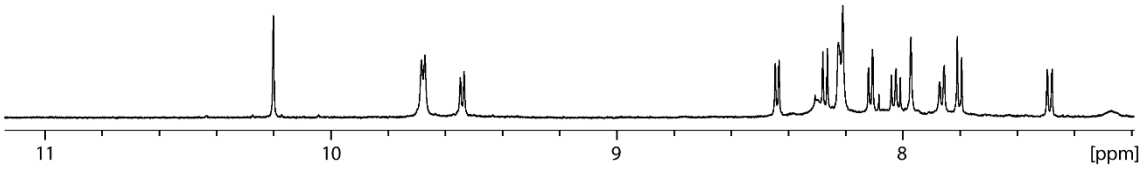

Figure 4.92: Partial ^{1}H NMR (500 MHz, 298 K, DMSO-d_6) of $Pd_2\mathbf{L^2}_2\mathbf{L^D}_2$.

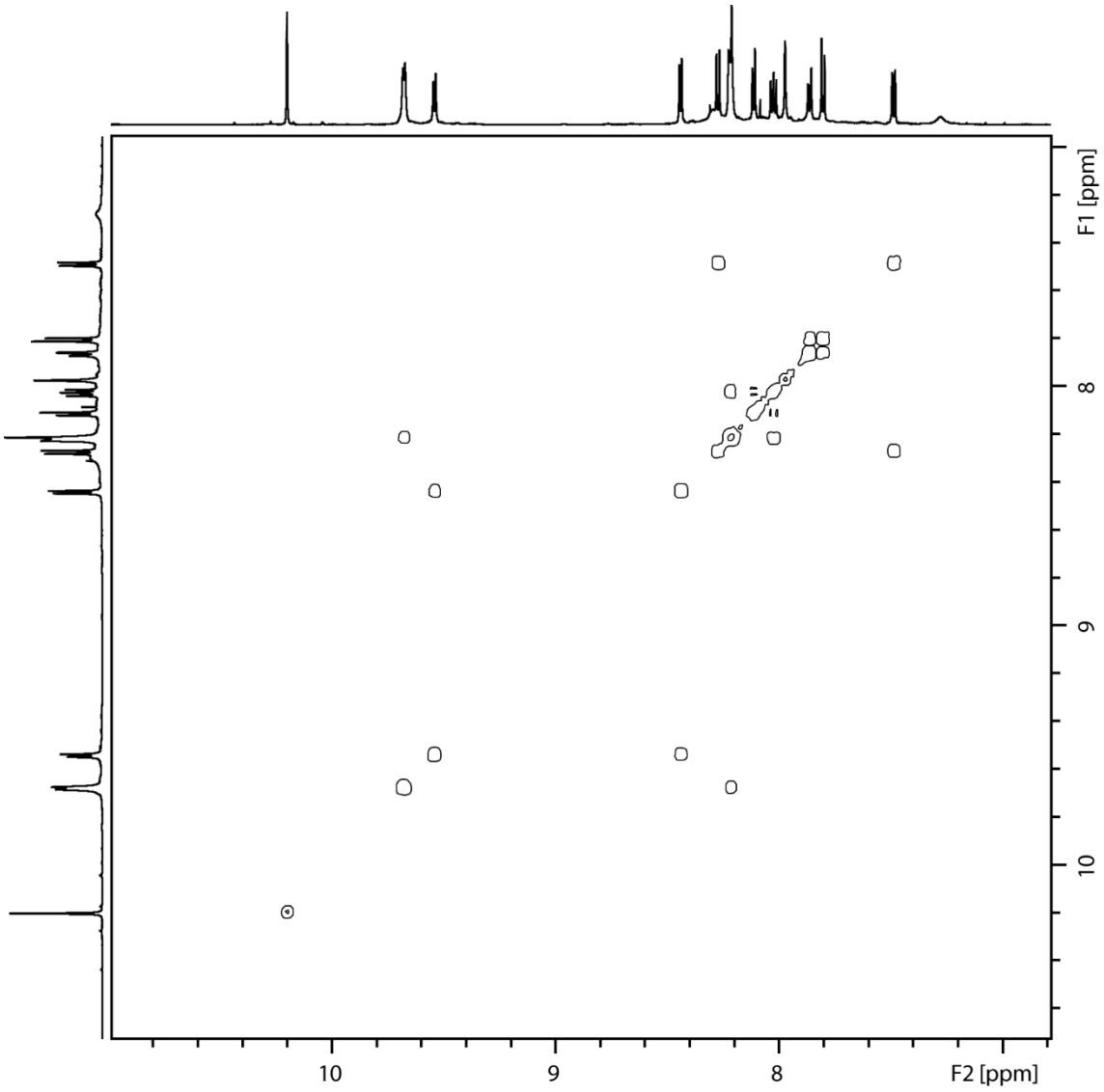

Figure 4.93: Partial $^{1}H-^{1}H$ COSY NMR (600 MHz, 298 K, DMSO-d_6) of $Pd_2\mathbf{L^2}_2\mathbf{L^D}_2$.

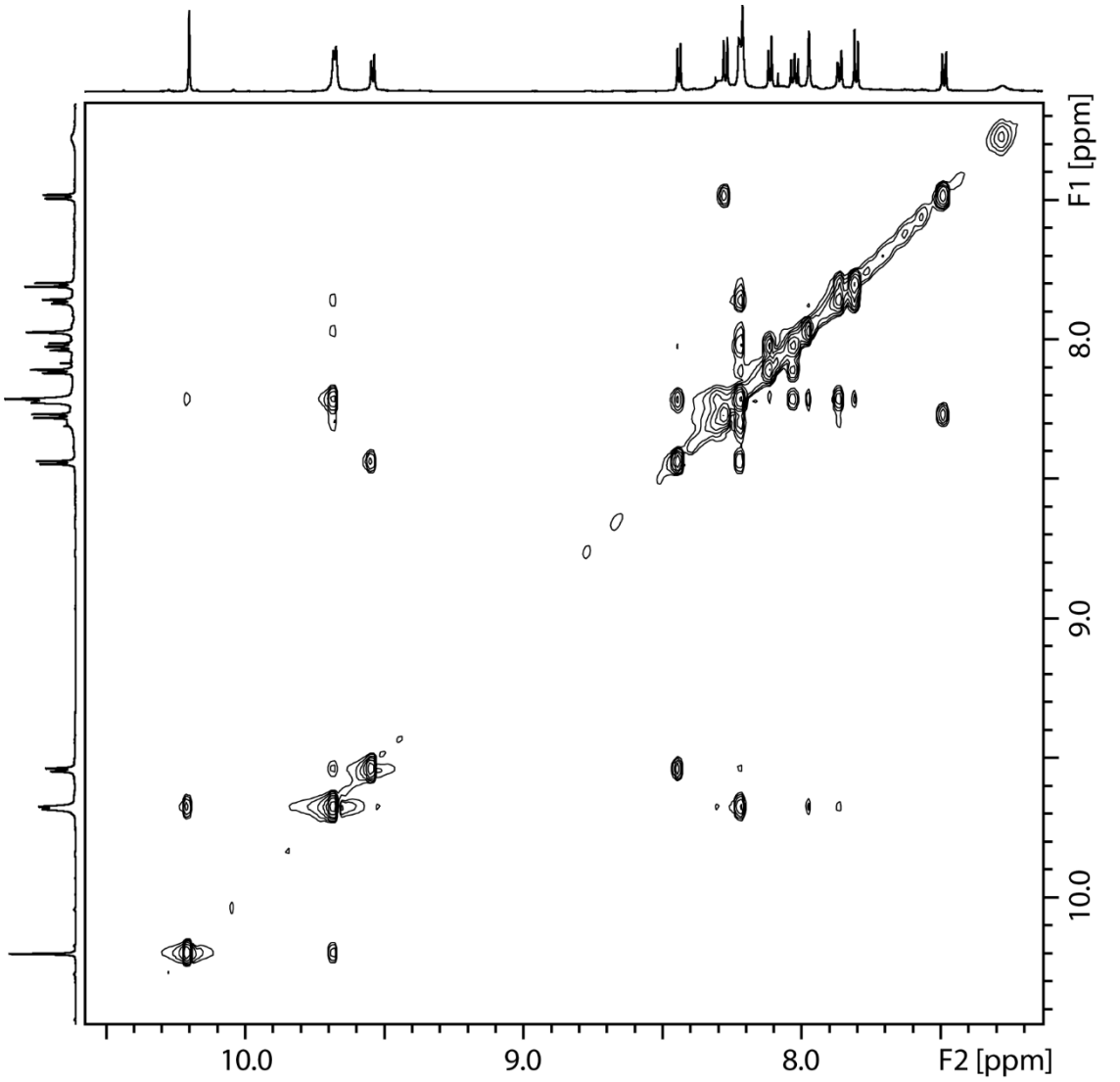

Figure 4.94: Partial $^{1}H-^{1}H$ NOESY NMR (600 MHz, 298 K, DMSO-d_6) of $Pd_2\mathbf{L}^{\mathbf{2}}{}_2\mathbf{L}^{\mathbf{D}}{}_2$.

$^{13}C\{^{1}H\}$ NMR (151 MHz, 298 K, DMSO-d_6): δ = 191.5, 171.5, 153.6, 151.1, 149.5, 144.0, 142.5, 141.4, 141.0, 136.3, 134.7, 134.1, 133.9, 129.5, 128.6, 127.8, 127.6, 125.1, 125.0, 123.2, 122.5, 121.5, 121.2, 120.2, 119.2, 118.1, 113.1, 98.3, 84.5, 22.5.

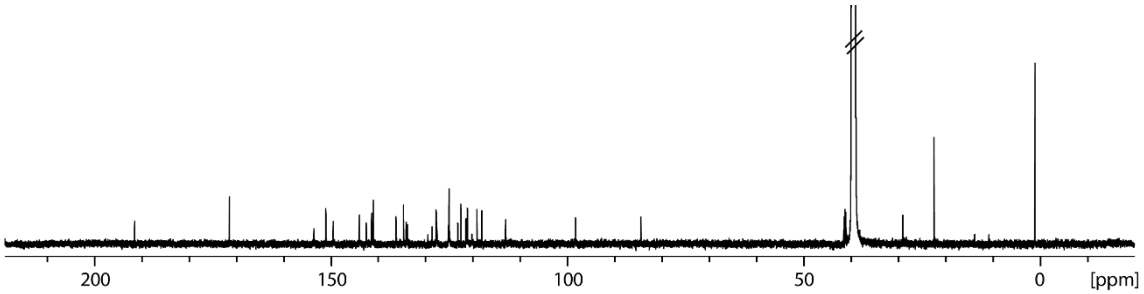

Figure 4.95: $^{13}C\{^{1}H\}$ NMR (151 MHz, 298 K, DMSO-d_6) of $Pd_2\mathbf{L}^{\mathbf{2}}{}_2\mathbf{L}^{\mathbf{D}}{}_2$.

HR-ESI-MS:

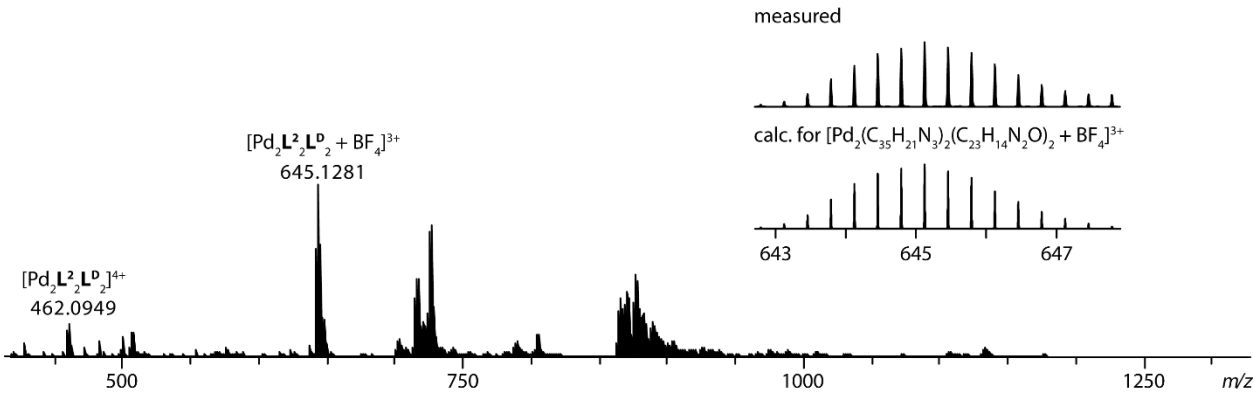

Figure 4.96: ESI-MS spectrum of $[Pd_2\mathbf{L}^{2}{}_2\mathbf{L}^{\mathbf{D}}{}_2$ + n $BF_4]^{(4-n)+}$ and inset of comparison of measured and calculated mass.

4.4.9 $Pd_2\mathbf{L}^{3}{}_2\mathbf{L}^{\mathbf{A}}{}_2$

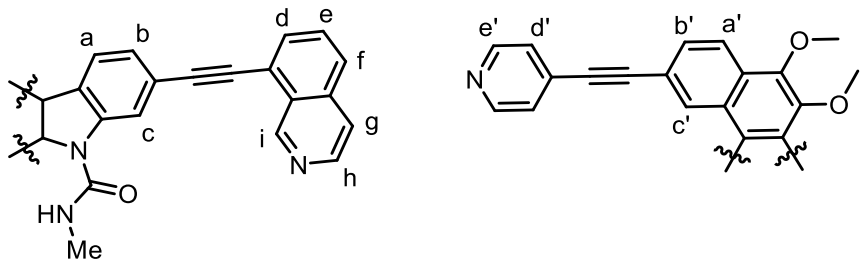

Scheme 4.27: Ligand Assignment for $Pd_2\mathbf{L}^{3}{}_2\mathbf{L}^{\mathbf{A}}{}_2$.

^{1}H NMR (500 MHz, 298 K, DMSO-d_6): δ = 9.95 (s, 4H, i), 9.60 (m, 12H, h, e'), 9.01 (s, 4H, c'), 8.47 (m, 2H, N*H*), 8.43 (m, 8H, a, g), 8.37 (s, 4H, c), 8.24 (d, ^3J = 8.6, 4H, a') 8.21 (d, ^3J = 8.3, 4H, f), 8.15 (d, ^3J = 6.7, 8H, d'), 8.11 (d, ^3J = 6.4, 4H, d), 8.02 (t, ^3J = 8.0, 4H, e), 7.83 (d, ^3J = 9.7, 4H, b'), 7.69 (dd, ^3J = 7.8, ^4J = 1.0, 4H, b), 4.02 (s, 12H, OCH_3), 3.48 (d, ^3J = 4.4, 6H, CH_3).

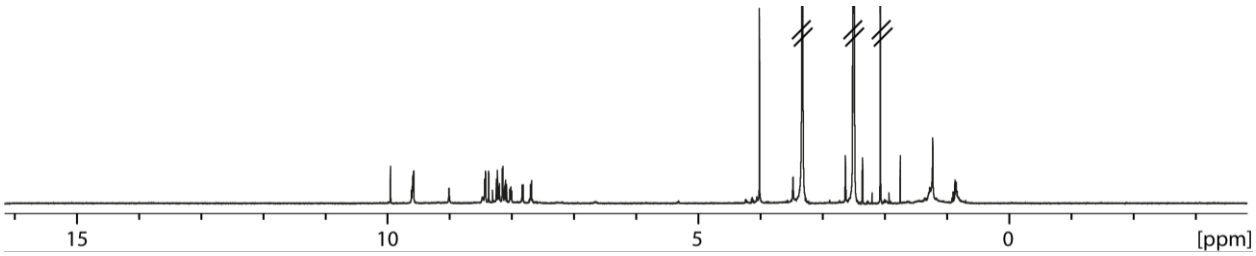

Figure 4.97: ^{1}H NMR (500 MHz, 298 K, DMSO-d_6) of $Pd_2\mathbf{L}^{3}{}_2\mathbf{L}^{\mathbf{A}}{}_2$.

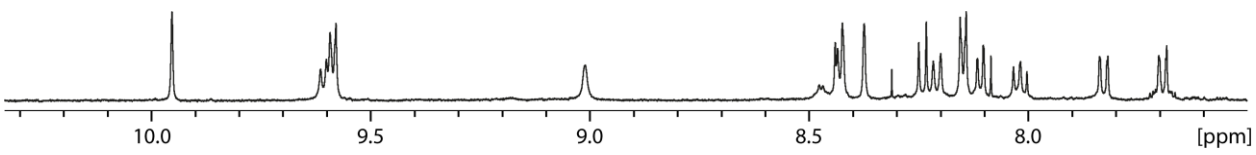

Figure 4.98: Partial ^{1}H NMR (500 MHz, 298 K, DMSO-d_6) of $Pd_2\mathbf{L}^{3}{}_2\mathbf{L}^{\mathbf{A}}{}_2$.

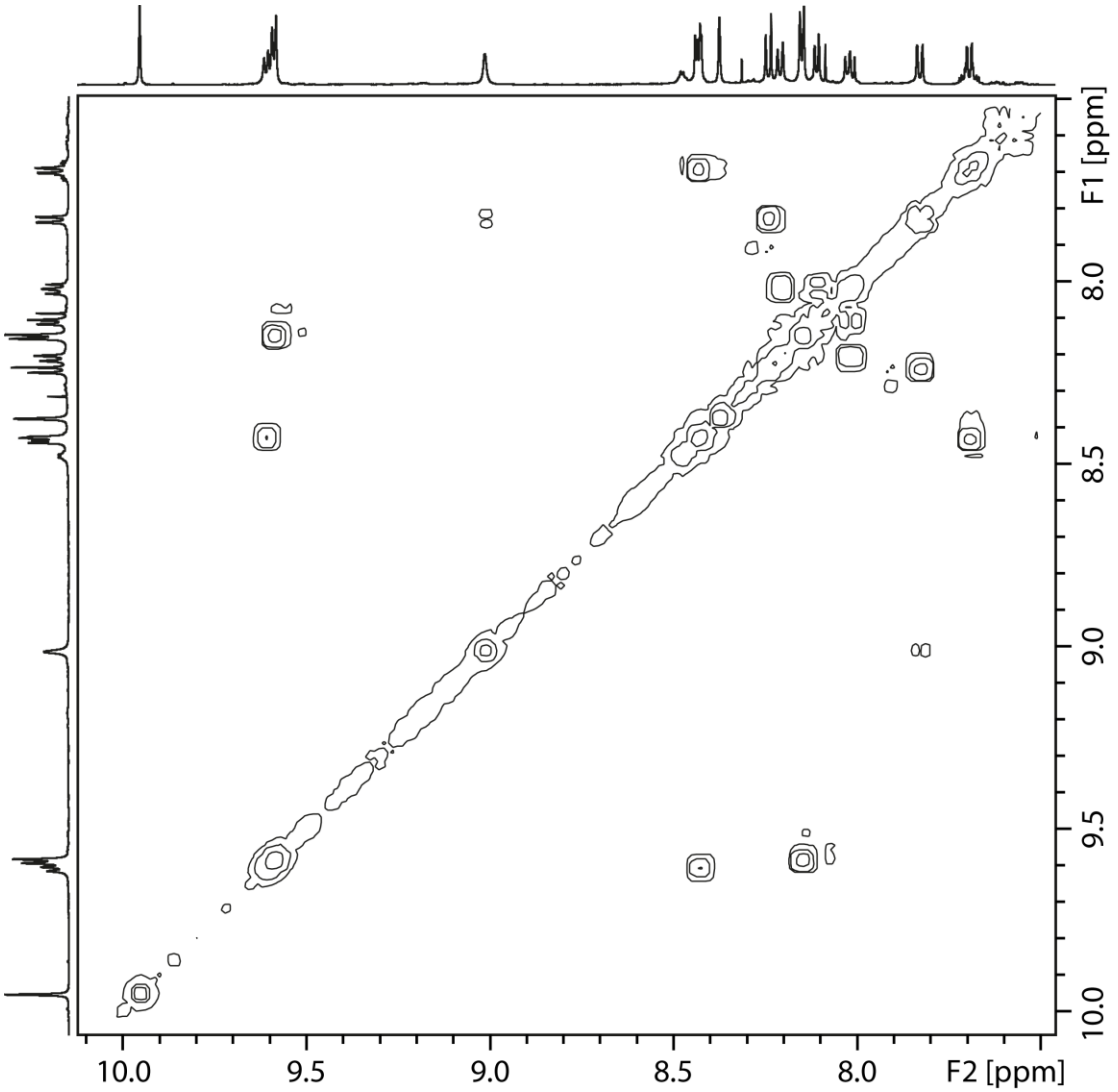

Figure 4.99: Partial $^{1}H-^{1}H$ COSY NMR (600 MHz, 298 K, DMSO-d_6) of $Pd_2\mathbf{L^3}_2\mathbf{L^A}_2$.

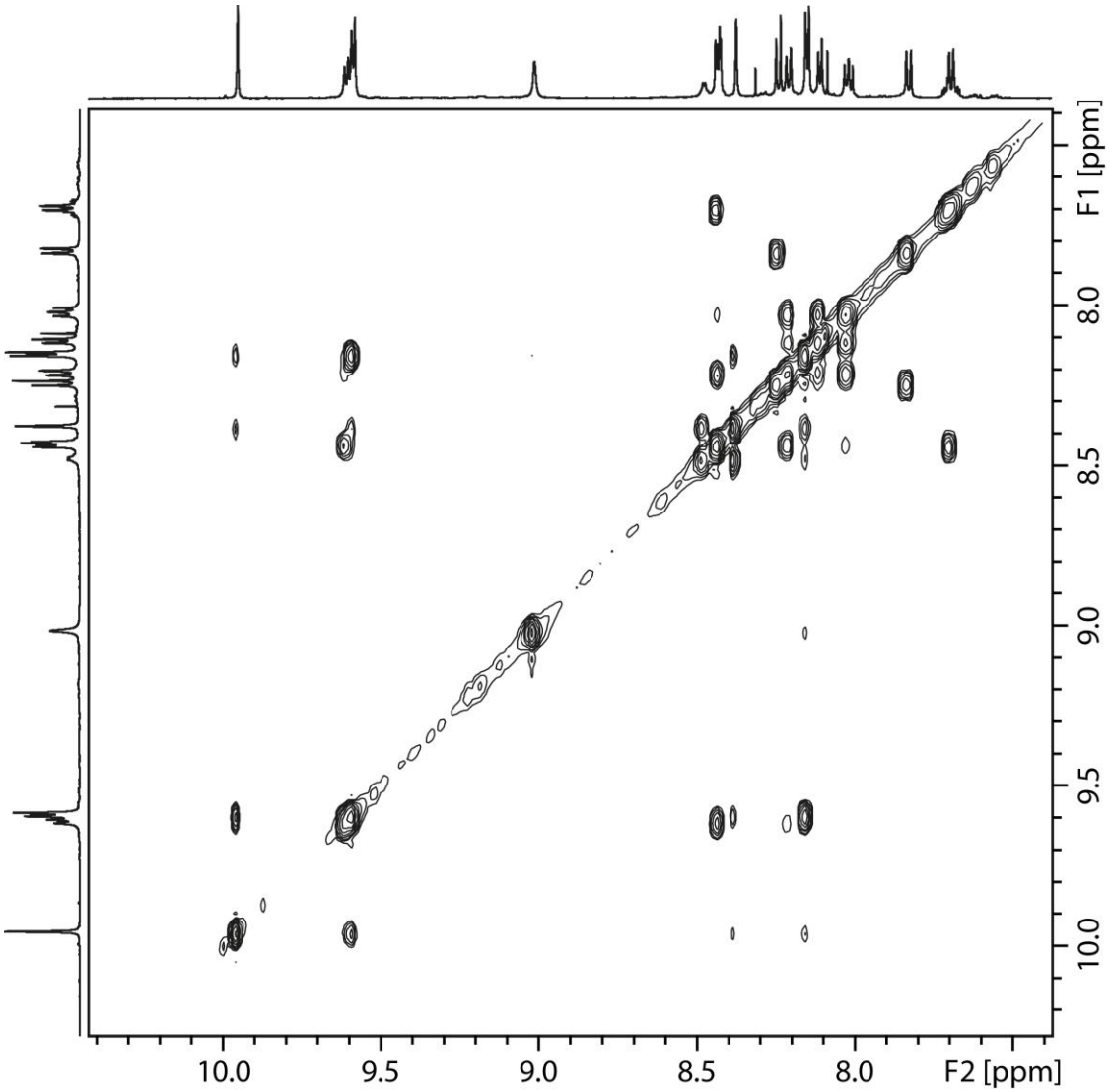

Figure 4.100: Partial ^{1}H–^{1}H NOESY NMR (600 MHz, 298 K, DMSO-d_6) of $Pd_2\mathbf{L}^{3}{}_2\mathbf{L}^{A}{}_2$.

^{13}C{^{1}H} NMR (151 MHz, 298 K, DMSO-d_6): δ = 152.8, 151.0, 144.8, 142.3, 138.1, 136.1, 134.7, 134.2, 133.8, 131.7, 131.6, 129.8, 129.6, 129.5, 128.9, 128.7, 128.3, 127.7, 126.8, 126.2, 125.1, 124.3, 123.2, 121.6, 120.9, 120.1, 118.1, 117.4, 98.9, 97.6, 86.3, 85.1, 61.2, 13.9.

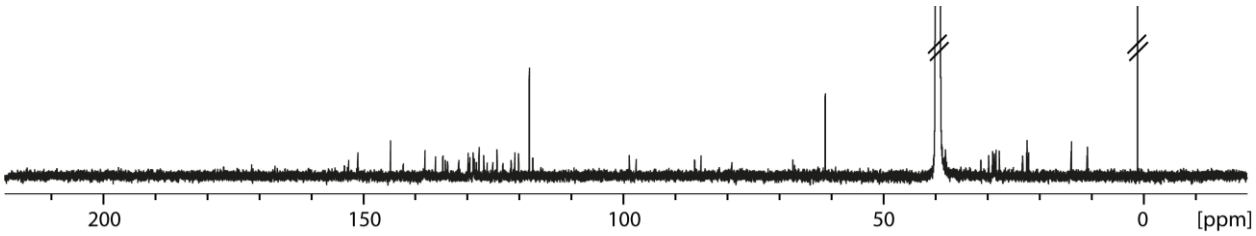

Figure 4.101: ^{13}C{^{1}H} NMR (151 MHz, 298 K, DMSO-d_6) of $Pd_2\mathbf{L}^{3}{}_2\mathbf{L}^{A}{}_2$.

HR-ESI-MS (positive mode):

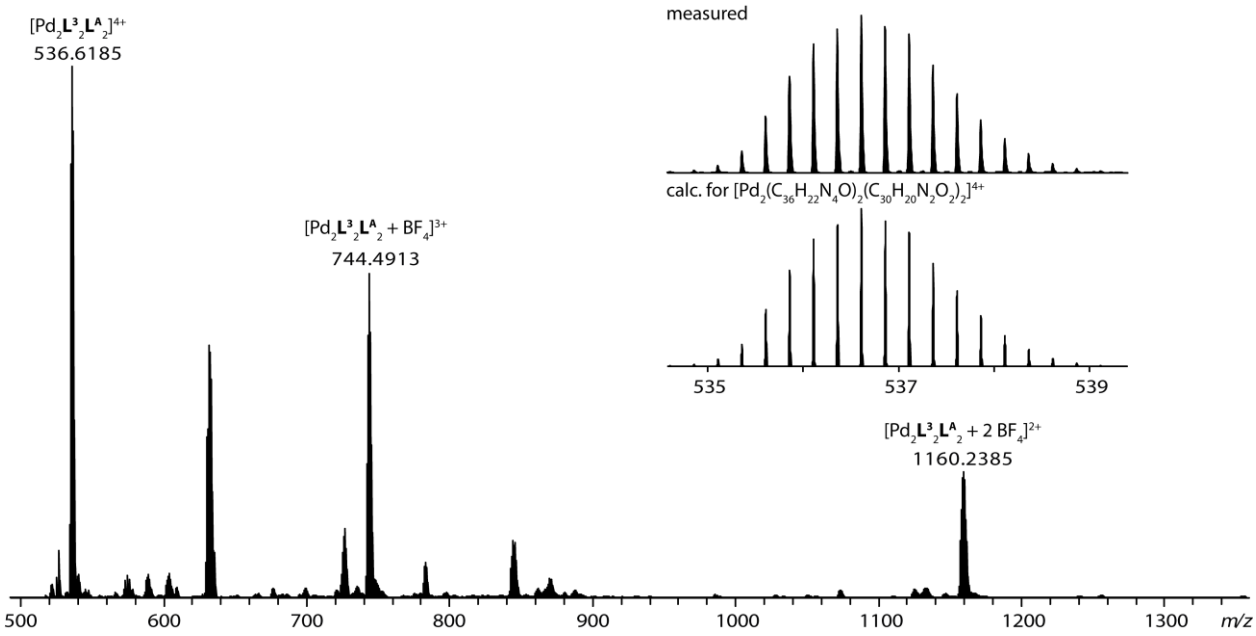

Figure 4.102: ESI-MS spectrum of $[Pd_2\mathbf{L^3}_2\mathbf{L^A}_2 + n\ BF_4]^{(4-n)+}$ and inset of comparison of measured and calculated mass.

4.4.10 $Pd_2L^3{}_2L^B{}_2$

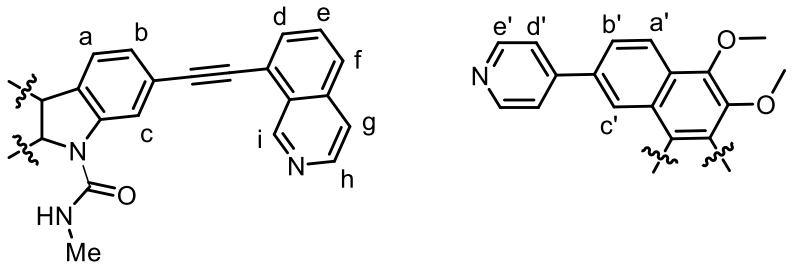

Scheme 4.28: Ligand Assignment for $Pd_2\mathbf{L^3}_2\mathbf{L^B}_2$.

Due to overlapping signals of different species (see discussion in chapter 3.2.3), the assignment of the signals was only performed for a number of distinct signals. The assignment is based on the comparison to the other heteroleptic cages as well as the signals of the free ligands. ESI-MS data could not be obtained of this compound.

^{1}H NMR (500 MHz, 298 K, DMSO-d_6): δ = 10.01 (s, 4H, i), 9.65 (m, 12H, h, e'), 9.13 (s, 4H, c'), 8.49 (m, 2H, N*H*), 7.61 (d, ^3J = 7.8, 4H, b).

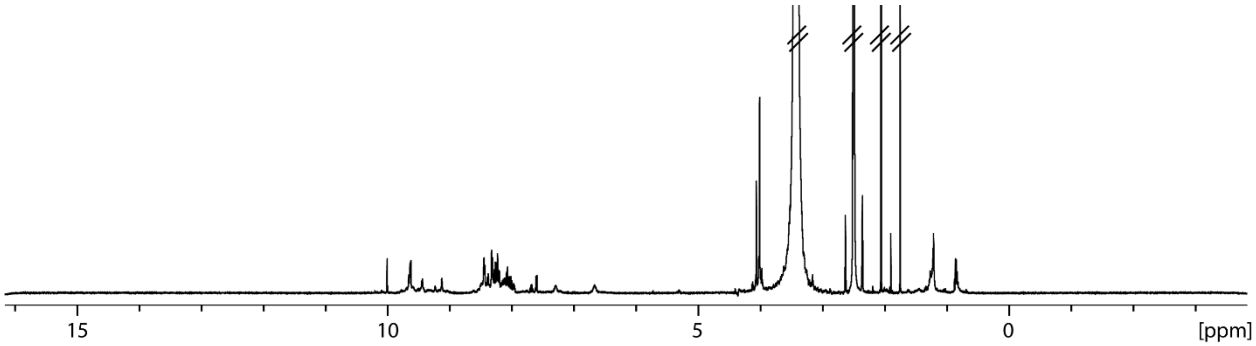

Figure 4.103: ^{1}H NMR (500 MHz, 298 K, DMSO-d$_6$) of $Pd_2\mathbf{L}^{\mathbf{3}}{}_2\mathbf{L}^{\mathbf{B}}{}_2$.

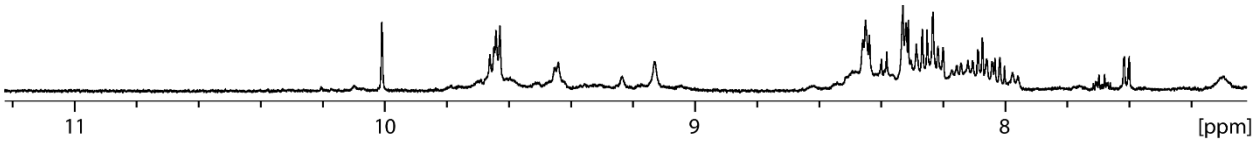

Figure 4.104: Partial ^{1}H NMR (500 MHz, 298 K, DMSO-d$_6$) of $Pd_2\mathbf{L}^{\mathbf{3}}{}_2\mathbf{L}^{\mathbf{B}}{}_2$.

4.4.11 $Pd_2\mathbf{L}^{\mathbf{3}}{}_2\mathbf{L}^{\mathbf{C}}{}_2$

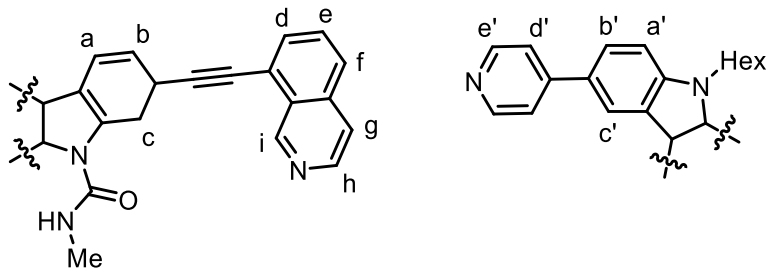

Scheme 4.29: Ligand Assignment for $Pd_2\mathbf{L}^{\mathbf{3}}{}_2\mathbf{L}^{\mathbf{C}}{}_2$.

Due to overlapping signals of different species (see discussion in chapter 3.2.3), the assignment of the signals was only performed for a number of distinct signals. The assignment is based on the comparison to the other heteroleptic cages as well as the signals of the free ligands.

^{1}H NMR (500 MHz, 298 K, DMSO-d$_6$): δ = 10.13 (s, 4H, i), 9.45 (d, ^{3}J = 6.1, 8H, e'), 9.42 (d, ^{3}J = 6.7, 4H, h), 8.57 (m, 2H, N*H*), 7.48 (d, ^{3}J = 8.2, 4H, b).

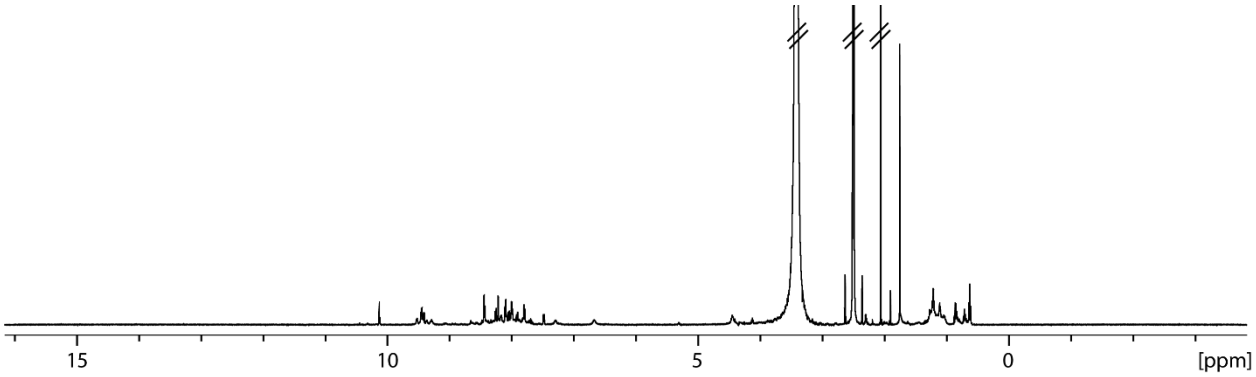

Figure 4.105: ^{1}H NMR (500 MHz, 298 K, DMSO-d_6) of $Pd_2\mathbf{L}^{\mathbf{3}}{}_2\mathbf{L}^{\mathbf{C}}{}_2$.

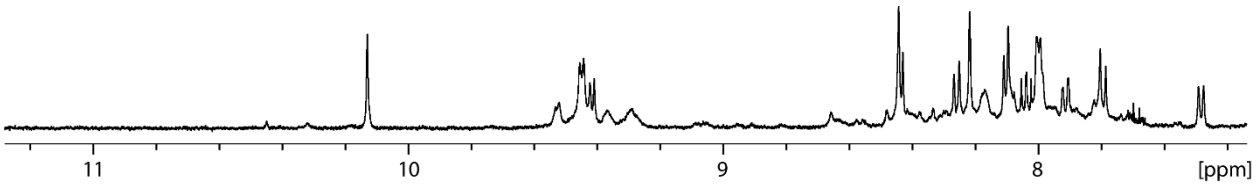

Figure 4.106: Partial ^{1}H NMR (500 MHz, 298 K, DMSO-d_6) of $Pd_2\mathbf{L}^{\mathbf{3}}{}_2\mathbf{L}^{\mathbf{C}}{}_2$.

HR-ESI-MS: Only very weak intense mass peak of the species $[Pd_2\mathbf{L}^{\mathbf{3}}{}_2\mathbf{L}^{\mathbf{C}}{}_2]^{4+}$ could be observed. However, the measured peak matches perfectly with the calculation.

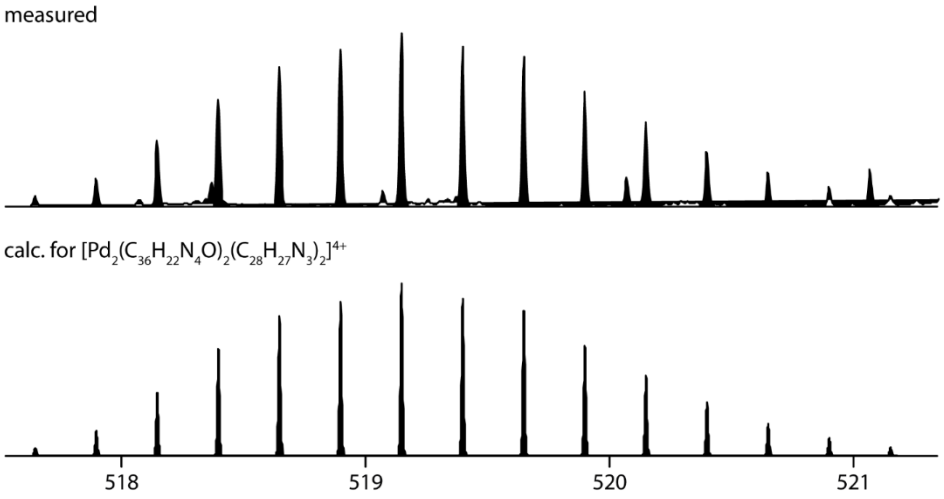

Figure 4.107: Partial ESI-MS spectrum of $[Pd_2\mathbf{L}^{\mathbf{3}}{}_2\mathbf{L}^{\mathbf{C}}{}_2]^{4+}$ and comparison with calculated mass.

4.4.12 $Pd_2L^3{}_2L^D{}_2$

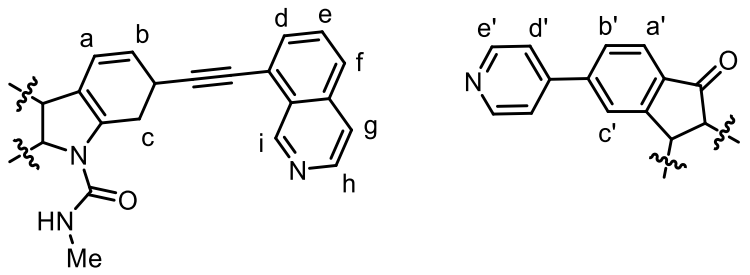

Scheme 4.30: Ligand Assignment for $Pd_2\mathbf{L}^3{}_2\mathbf{L}^D{}_2$.

Due to overlapping signals of different species (see discussion in chapter 3.2.3), the assignment of the signals was only performed for a number of distinct signals. The assignment is based on the comparison to the other heteroleptic cages as well as the signals of the free ligands. ESI-MS data could not be obtained of this compound.

^{1}H NMR (500 MHz, 298 K, DMSO-d_6): δ = 10.02 (s, 4H, i), 9.61 (m, 4H, h), 9.56 (d, ^3J = 6.3, 8H, e'), 7.48 (d, ^3J = 8.1, 4H, b).

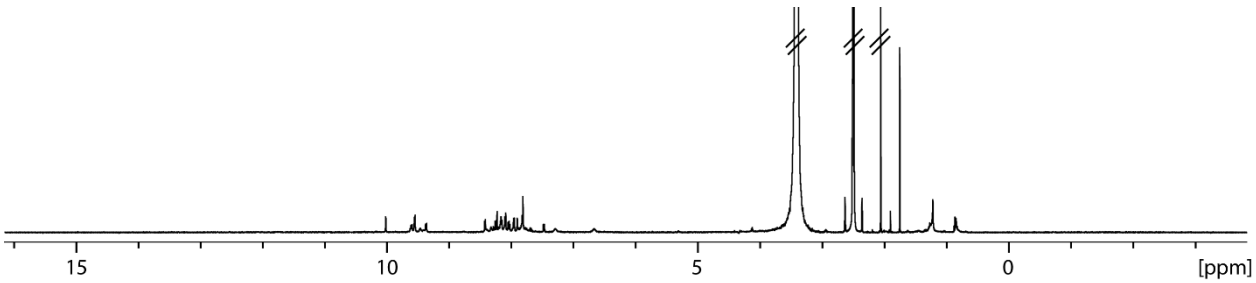

Figure 4.108: ^{1}H NMR (500 MHz, 298 K, DMSO-d_6) of $Pd_2\mathbf{L}^3{}_2\mathbf{L}^D{}_2$.

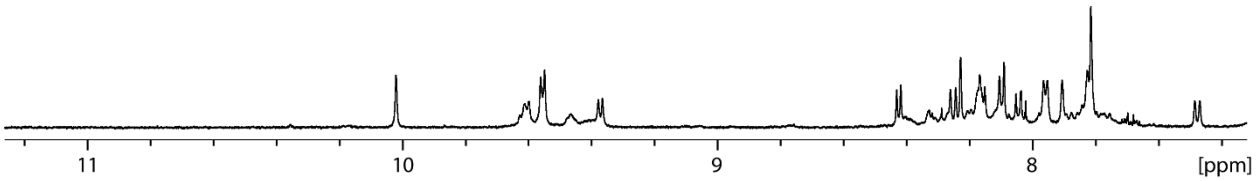

Figure 4.109: Partial ^{1}H NMR (500 MHz, 298 K, DMSO-d_6) of $Pd_2\mathbf{L}^3{}_2\mathbf{L}^D{}_2$.

4.4.13 $Pd_2L^4{}_2L^A{}_2$

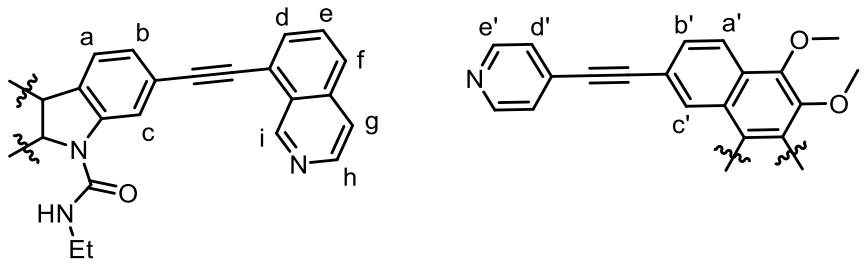

Scheme 4.31: Ligand Assignment for $Pd_2\mathbf{L}^4{}_2\mathbf{L}^A{}_2$.

^{1}H NMR (500 MHz, 298 K, DMSO-d_6): δ = 9.97 (s, 4H, i), 9.62 (d, ^3J = 6.5, 4H, h), 9.57 (d, ^3J = 6.6, 8H, e'), 8.97 (s, 4H, c'), 8.70 (t, ^3J = 5.1, 2H, N*H*), 8.42 (m, 12H, a, c, g), 8.24 (d, ^3J = 8.6, 4H, a'), 8.20 (d, ^3J = 8.4, 4H, f), 8.12 (m, 12H, d, d'), 8.02 (t, ^3J = 8.0, 4H, e), 7.84 (d, ^3J = 8.5, 4H, b'), 7.70 (dd, ^3J = 7.9, ^4J = 1.2, 4H, b), 4.02 (s, 12H, OCH_3), 3.83 (m, 4H, NCH_2), 1.49 (t, ^3J = 7.1, 6H, NCH_2CH_3).

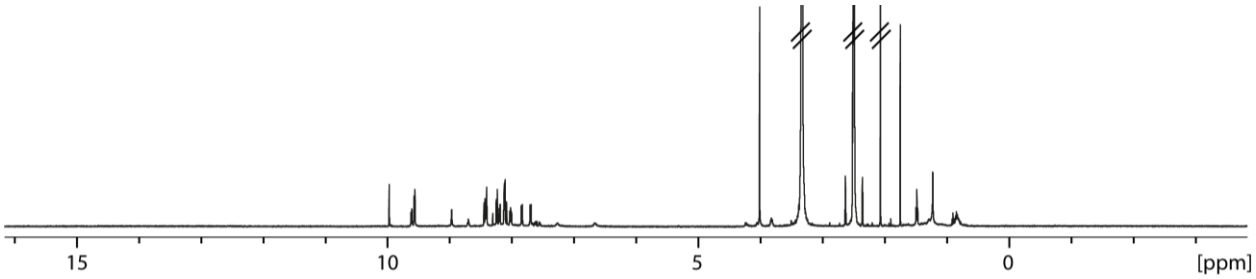

Figure 4.110: ^{1}H NMR (500 MHz, 298 K, DMSO-d_6) of $Pd_2\mathbf{L}^4{}_2\mathbf{L}^A{}_2$.

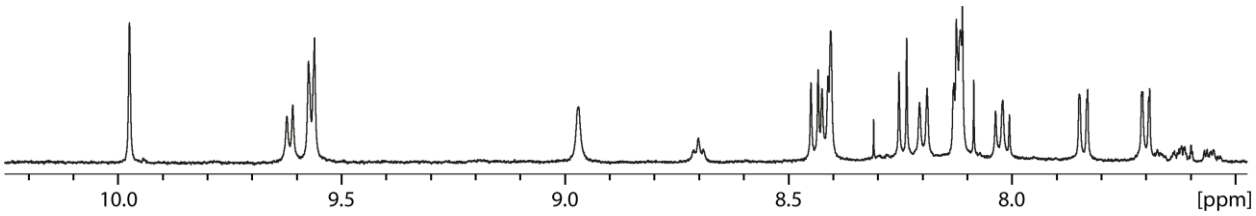

Figure 4.111: Partial ^{1}H NMR (500 MHz, 298 K, DMSO-d_6) of $Pd_2\mathbf{L}^4{}_2\mathbf{L}^A{}_2$.

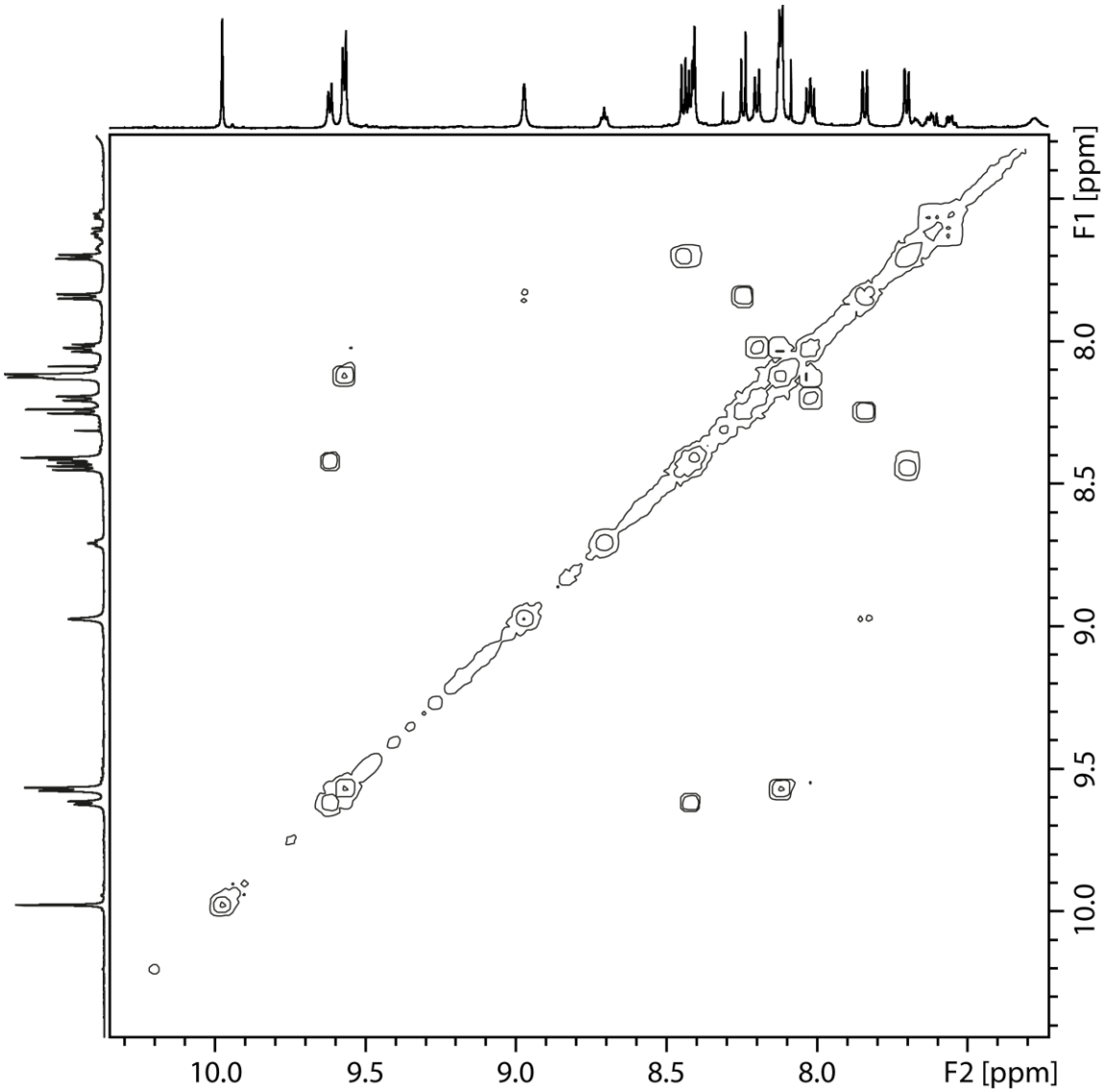

Figure 4.112: Partial $^{1}H-^{1}H$ COSY NMR (600 MHz, 298 K, DMSO-d_6) of $Pd_2\mathbf{L^4}_2\mathbf{L^A}_2$.

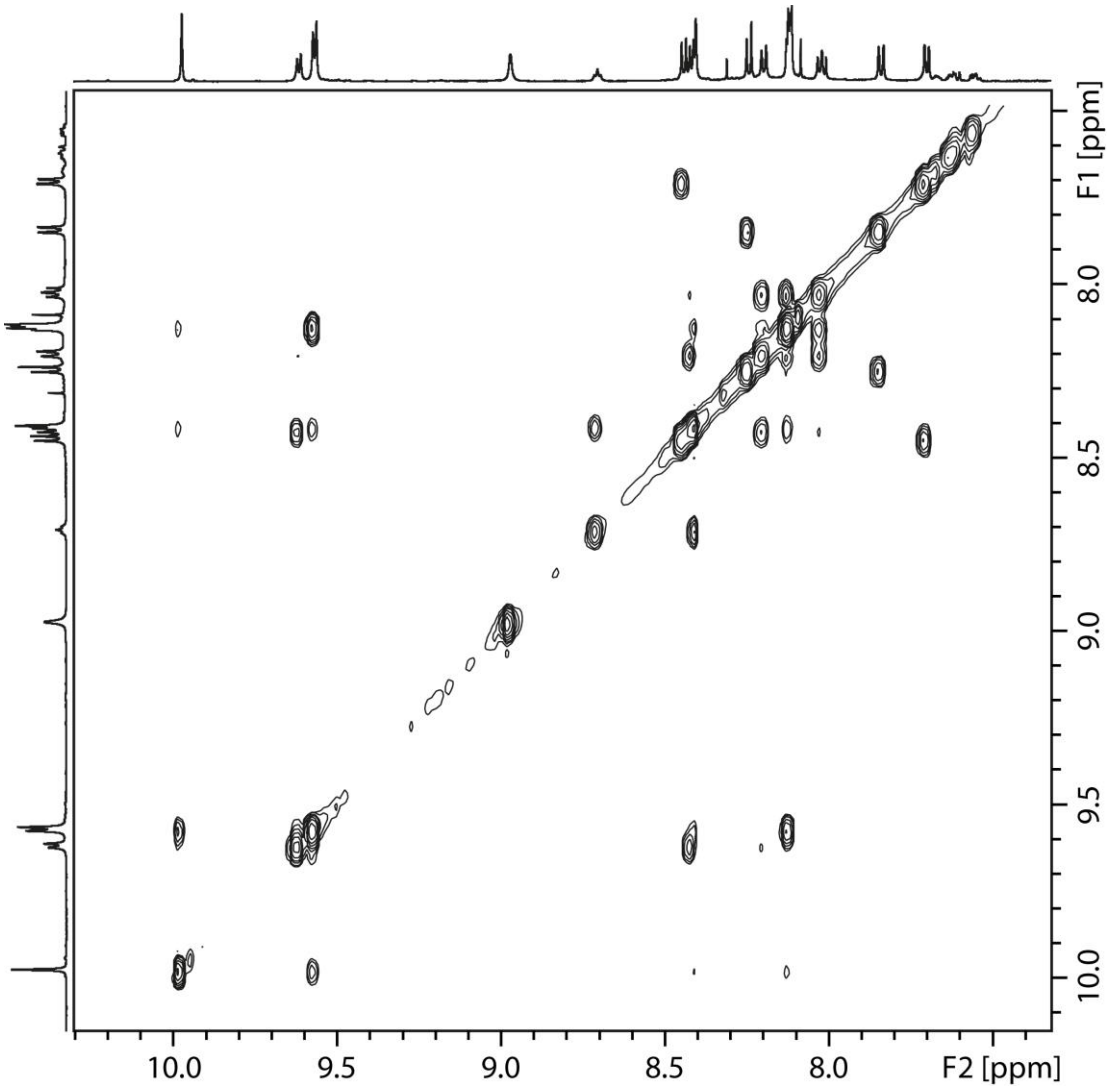

Figure 4.113: Partial ^{1}H–^{1}H NOESY NMR (600 MHz, 298 K, DMSO-d_6) of $Pd_2\mathbf{L^4}_2\mathbf{L^A}_2$.

^{13}C{^{1}H} NMR (151 MHz, 298 K, DMSO-d_6): δ = 171.5, 153.7, 152.0, 151.0, 144.7, 142.4, 138.2, 136.1, 134.7, 134.4, 133.8, 132.1, 131.5, 131.4, 129.9, 129.7, 129.5, 128.9, 128.8, 128.7, 128.0, 127.7, 126.8, 126.2, 125.1, 124.3, 123.2, 121.7, 121.0, 120.1, 118.1, 117.5, 98.8, 97.6, 86.2, 85.3, 61.2, 22.5, 15.2.

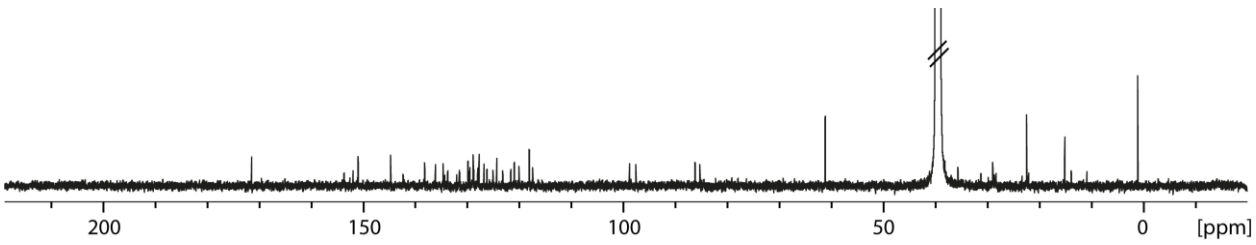

Figure 4.114: ^{13}C{^{1}H} NMR (151 MHz, 298 K, DMSO-d_6) of $Pd_2\mathbf{L^4}_2\mathbf{L^A}_2$.

HR-ESI-MS (positive mode):

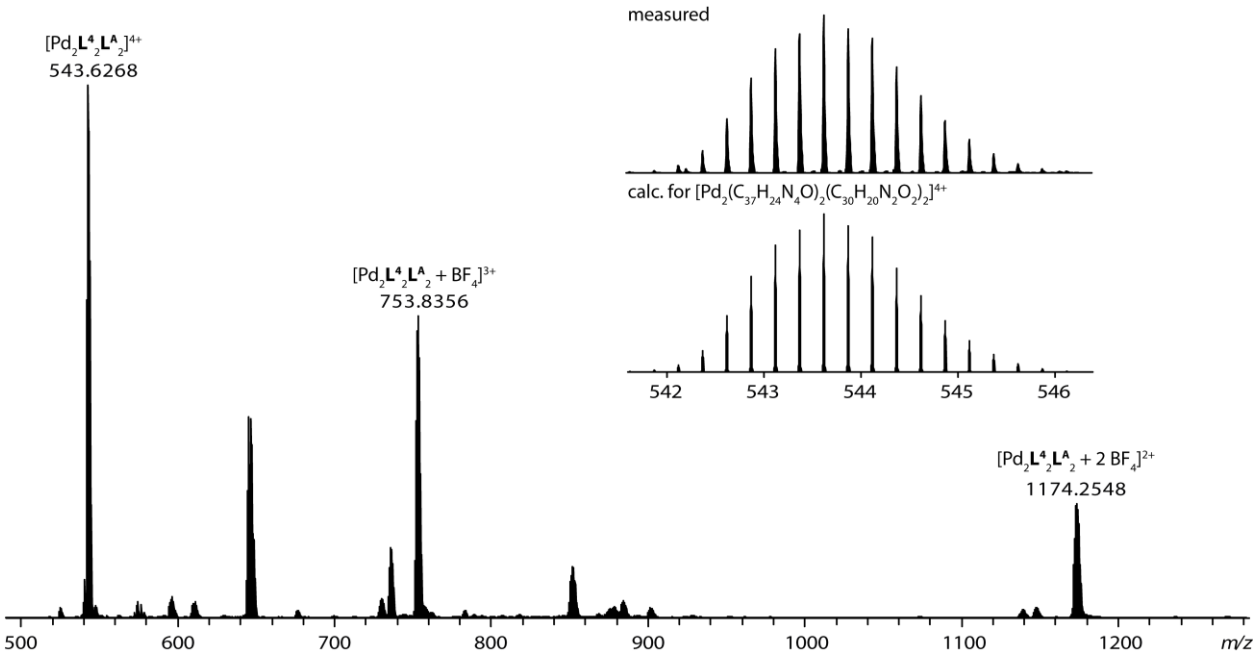

Figure 4.115: ESI-MS spectrum of $[Pd_2\mathbf{L^4}_2\mathbf{L^A}_2 + n\ BF_4]^{(4-n)+}$ and inset of comparison of measured and calculated mass.

4.4.14 $Pd_2L^4{}_2L^B{}_2$

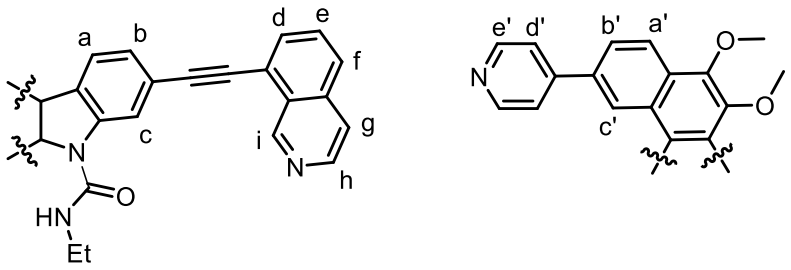

Scheme 4.32: Ligand Assignment for $Pd_2\mathbf{L^4}_2\mathbf{L^B}_2$.

^{1}H NMR (500 MHz, 298 K, DMSO-d_6): δ = 10.03 (s, 4H, i), 9.67 (m, 12H, h, e'), 9.19 (s (br), 4H, c'), 8.46 (d, ^3J = 6.8, 4H, g), 8.37 (m, 14H, N*H*, a, d'), 8.31 (d, 4H, ^3J = 8.7, 4H, d), 8.23 (d, ^3J = 8.3, 4H, f), 8.19 (s, 4H, c), 8.09 (d, ^3J = 6.6, 4H, a'), 8.03 (m, 8H, e, b'), 7.67 (d, ^3J = 7.7, 4H, b), 4.00 (s, 12H, OC*H*$_3$), 1.22 (s (br), 6H, NCH$_2$C*H*$_3$).

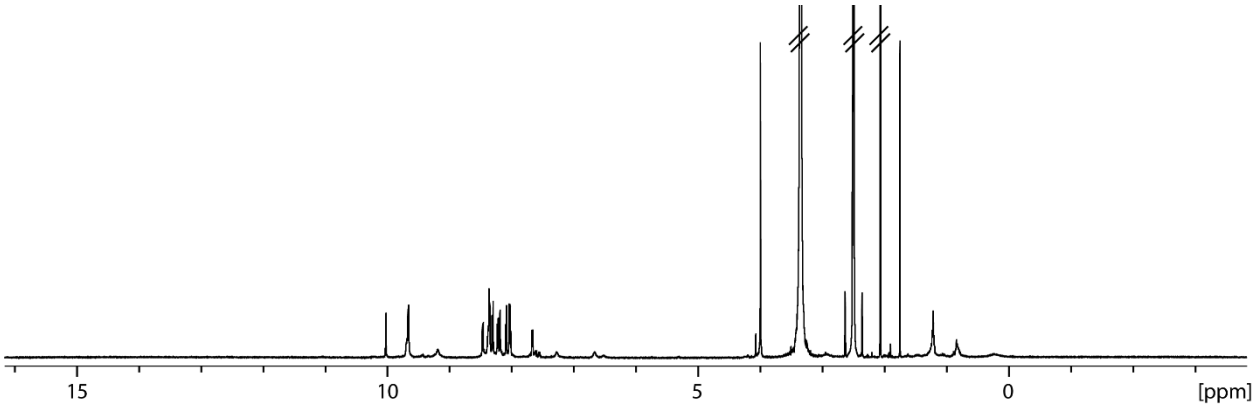

Figure 4.116: ^{1}H NMR (500 MHz, 298 K, DMSO-d_6) of $Pd_2\mathbf{L}^{\mathbf{4}}{}_2\mathbf{L}^{\mathbf{B}}{}_2$.

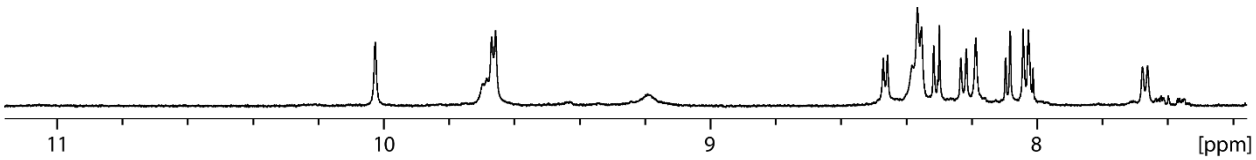

Figure 4.117: Partial ^{1}H NMR (500 MHz, 298 K, DMSO-d_6) of $Pd_2\mathbf{L}^{\mathbf{4}}{}_2\mathbf{L}^{\mathbf{B}}{}_2$.

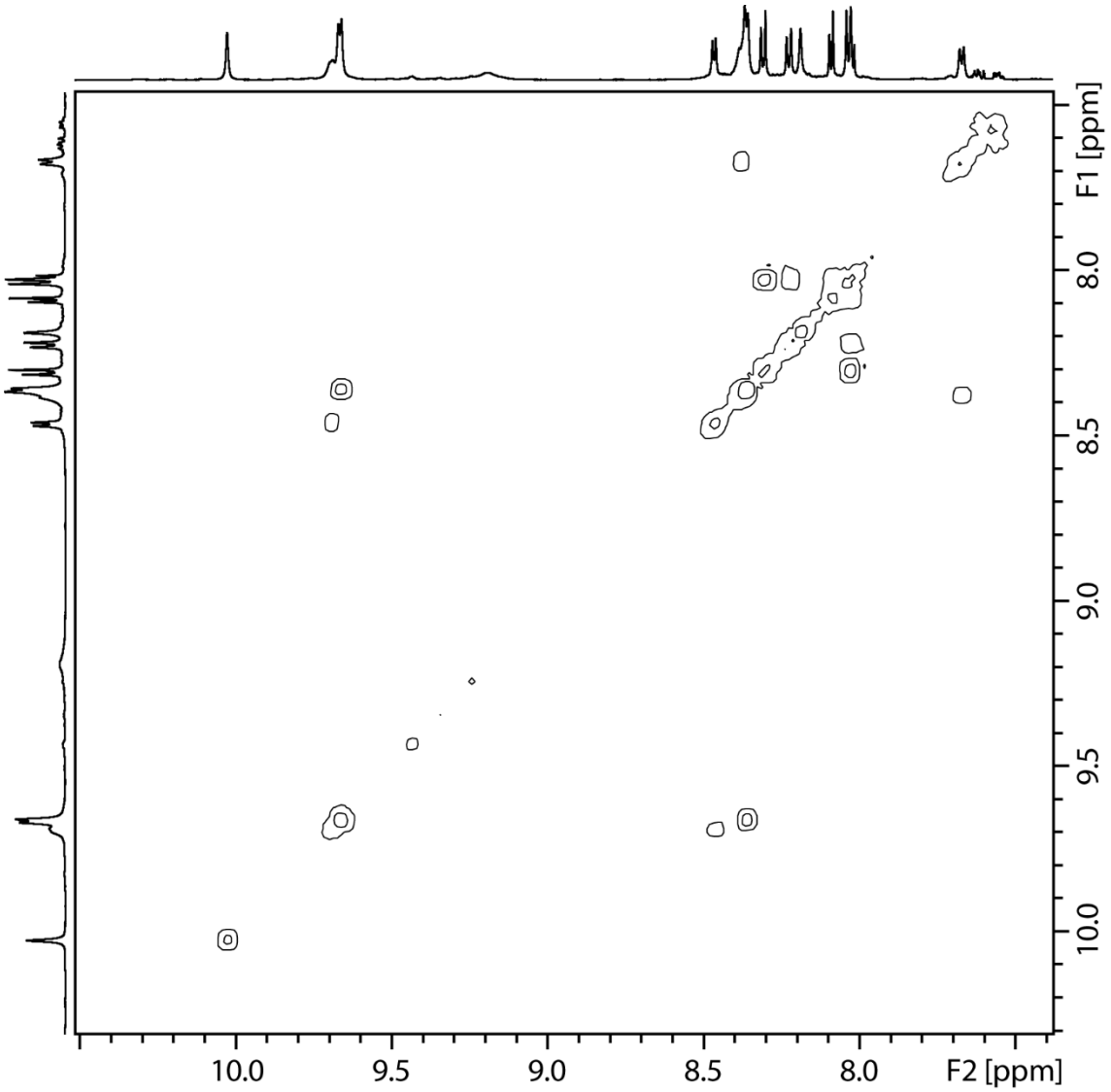

Figure 4.118: Partial $^{1}H-^{1}H$ COSY NMR (600 MHz, 298 K, DMSO-d_6) of $Pd_2\mathbf{L}^{\mathbf{4}}{}_2\mathbf{L}^{\mathbf{B}}{}_2$.

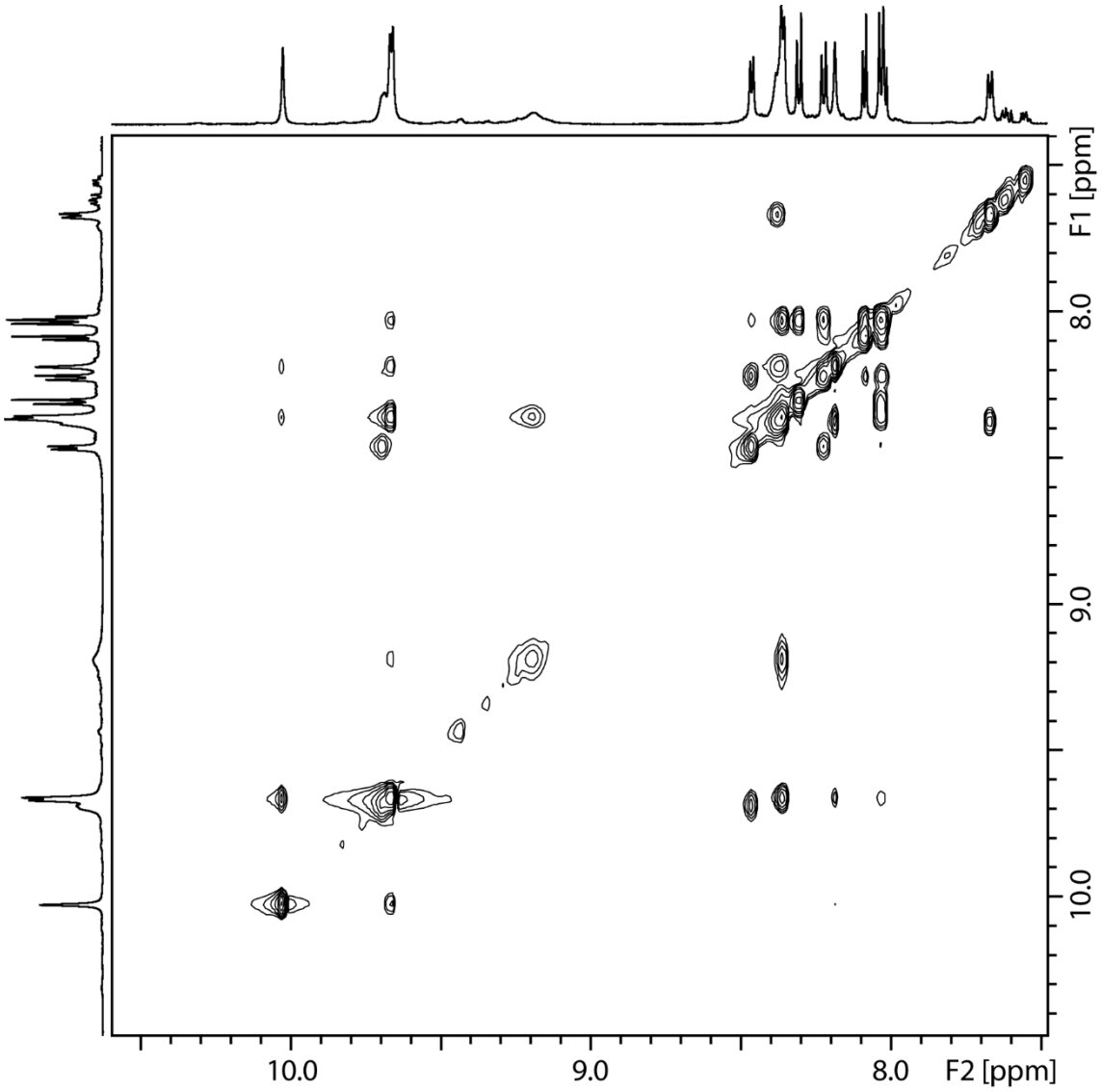

Figure 4.119: Partial ^{1}H–^{1}H NOESY NMR (600 MHz, 298 K, DMSO-d_6) of $Pd_2\mathbf{L}^{\mathbf{4}}{}_2\mathbf{L}^{\mathbf{B}}{}_2$.

^{13}C{^{1}H} NMR (151 MHz, 298 K, DMSO-d_6): δ = 171.5, 153.6, 151.5, 150.9, 144.2, 142.5, 138.4, 136.3, 133.8, 133.1, 131.6, 131.5, 130.2, 128.8, 128.7, 128.1, 128.0, 127.9, 127.0, 125.6, 125.1, 123.9, 123.5, 122.4, 121.8, 120.8, 120.1, 118.1, 116.8, 97.7, 85.1, 61.2, 22.5.

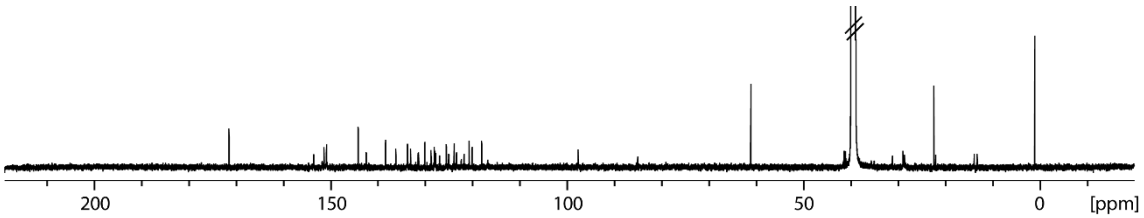

Figure 4.120: ^{13}C{^{1}H} NMR (151 MHz, 298 K, DMSO-d_6) of $Pd_2\mathbf{L}^{\mathbf{4}}{}_2\mathbf{L}^{\mathbf{B}}{}_2$.

HR-ESI-MS: Only very weak intense mass peak of the species $[Pd_2\mathbf{L}^{\mathbf{4}}{}_2\mathbf{L}^{\mathbf{B}}{}_2]^{4+}$ could be observed. However, the measured peak matches perfectly with the calculation.

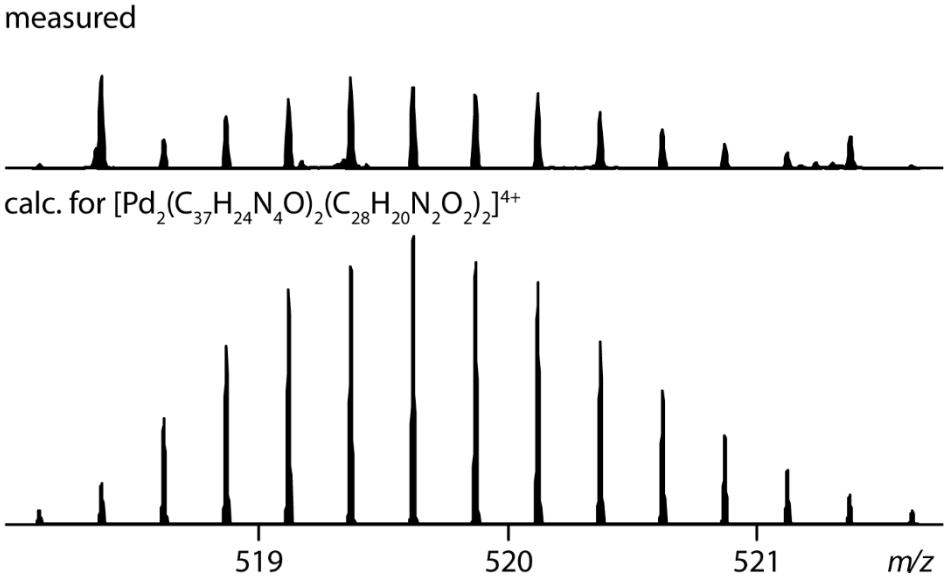

Figure 4.121: Partial ESI-MS spectrum of $[Pd_2\mathbf{L}^{\mathbf{4}}{}_2\mathbf{L}^{\mathbf{B}}{}_2]^{4+}$ and comparison with calculated mass.

4.4.15 $Pd_2\mathbf{L}^{\mathbf{4}}{}_2\mathbf{L}^{\mathbf{C}}{}_2$

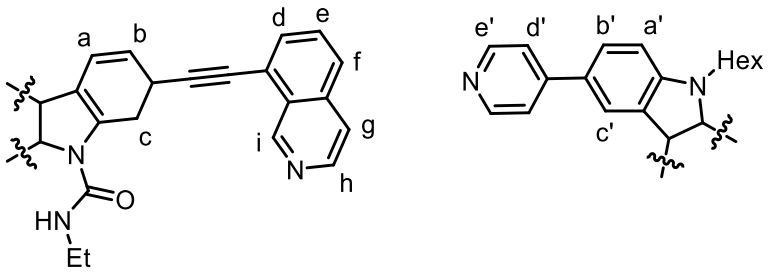

Scheme 4.33: Ligand Assignment for $Pd_2\mathbf{L}^{\mathbf{4}}{}_2\mathbf{L}^{\mathbf{C}}{}_2$.

^{1}H NMR (500 MHz, 298 K, DMSO-d_6): δ = 10.18 (s, 4H, i), 9.50 (m, 12H, h, e'), 8.53 (s, 4H, c'), 8.45 (d, ^3J = 6.6, 4H, g), 8.36 (t, ^3J = 5.3, 2H, N*H*), 8.27 (d, ^3J = 8.4, 4H, f), 8.20 (m, 8H, a, c), 8.12 (m, 12H, d, d'), 8.04 (t, ^3J = 8.0, 4H, e), 7.90 (dd, ^3J = 8.7, ^4J = 1.2, 4H, b'), 7.80 (d, ^3J = 8.7, 4H, a'), 7.61 (d, ^3J = 7.5, 4H, b), 4.45 (t (br), 4H, NCH_2), 2.88 (s (br), 4H, C(O)NCH_2), 1.73 (m, 4H, NCH$_2$CH_2), 1.22 – 1.03 (m, 12H, CH_2), 0.65 (t, ^3J = 7.3, 6H, CH_3), 0.33 (s (br), 6H, C(O)NCH$_2$CH_3).

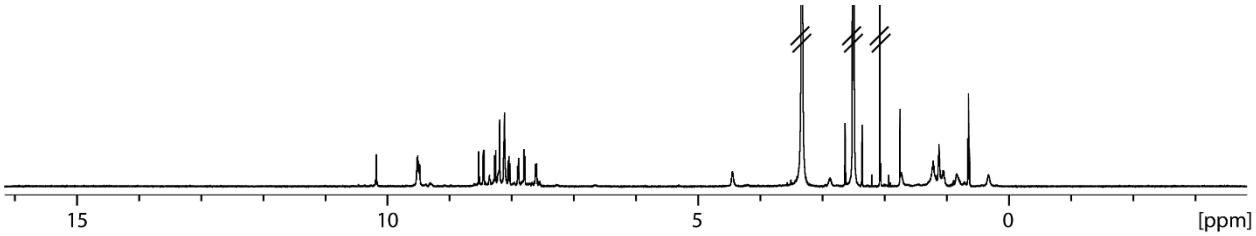

Figure 4.122: ^{1}H NMR (500 MHz, 298 K, DMSO-d_6) of $Pd_2\mathbf{L}^{\mathbf{4}}{}_2\mathbf{L}^{\mathbf{C}}{}_2$.

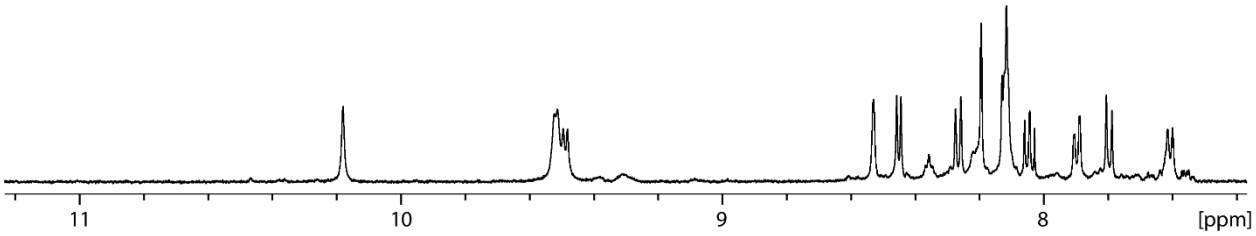

Figure 4.123: Partial ^{1}H NMR (500 MHz, 298 K, DMSO-d_6) of $Pd_2\mathbf{L}^{\mathbf{4}}{}_2\mathbf{L}^{\mathbf{C}}{}_2$.

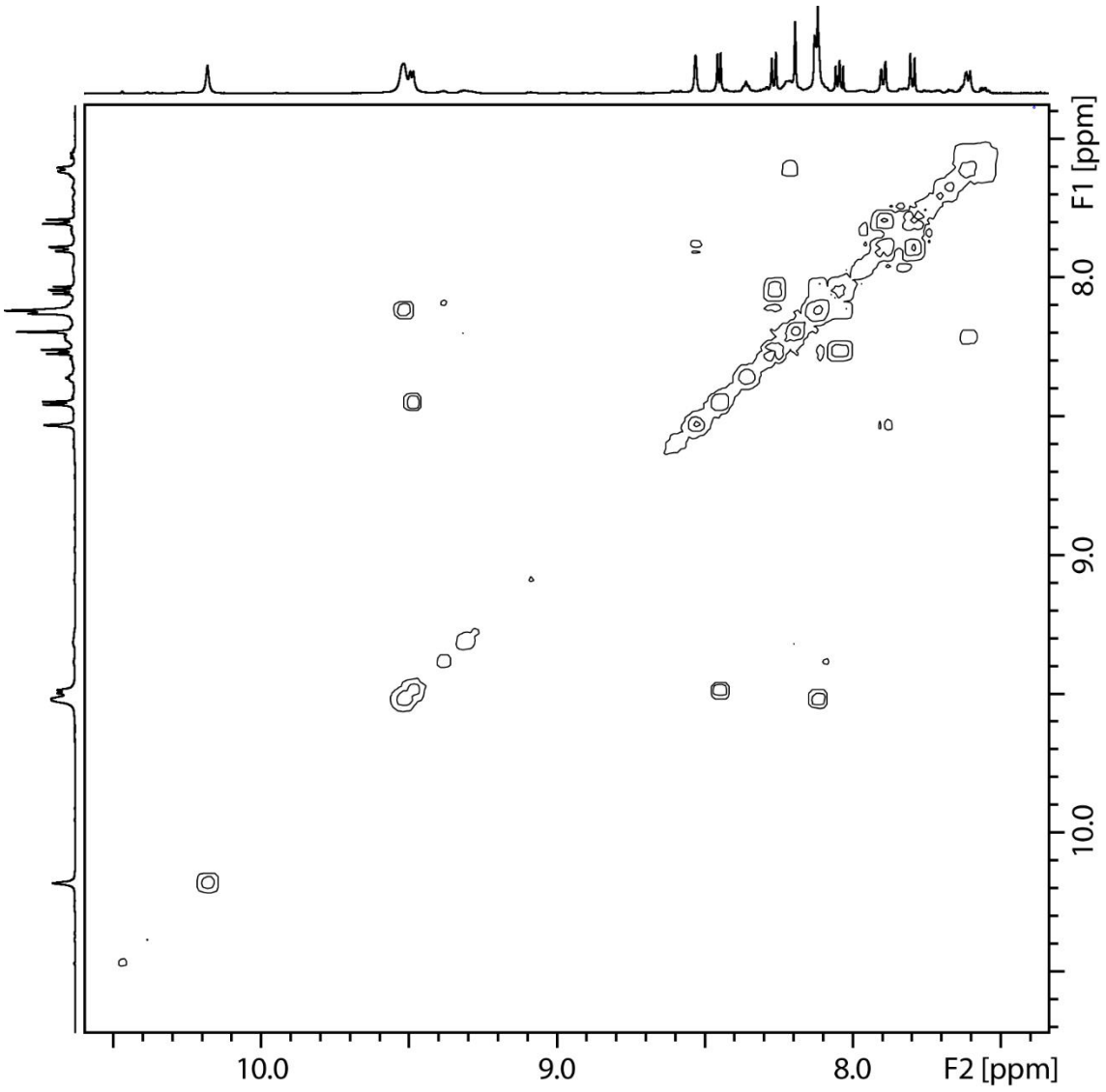

Figure 4.124: Partial ^{1}H–^{1}H COSY NMR (600 MHz, 298 K, DMSO-d_6) of $Pd_2\mathbf{L}^{\mathbf{4}}{}_2\mathbf{L}^{\mathbf{C}}{}_2$.

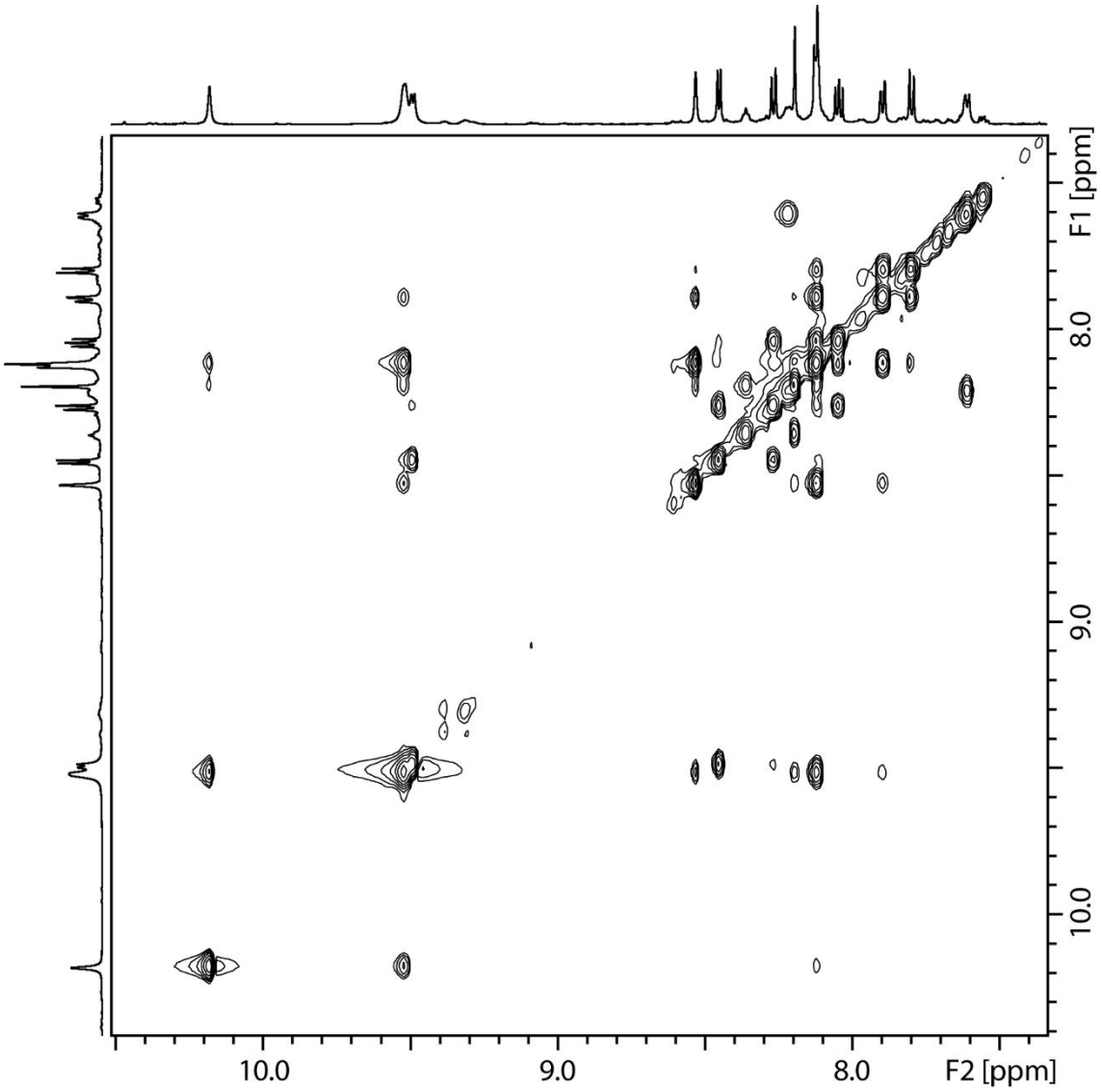

Figure 4.125: Partial ^{1}H–^{1}H NOESY NMR (600 MHz, 298 K, DMSO-d$_6$) of $Pd_2\mathbf{L}^{\mathbf{4}}{}_2\mathbf{L}^{\mathbf{C}}{}_2$.

^{13}C{^{1}H} NMR (151 MHz, 298 K, DMSO-d$_6$): δ = 171.4, 153.3, 152.1, 150.5, 142.7, 142.0, 138.5, 136.3, 134.3, 133.8, 132.0, 131.5, 131.4, 128.8, 128.7, 127.9, 127.7, 125.9, 125.8, 124.9, 124.2, 124.0, 122.7, 121.6, 120.8, 120.2, 118.1, 116.2, 111.1, 97.4, 84.8, 35.3, 30.8, 28.5, 25.8, 22.5, 21.9, 13.6, 13.4.

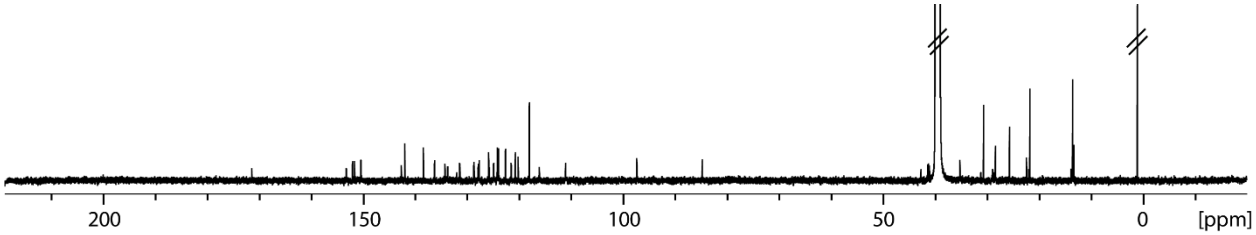

Figure 4.126: ^{13}C{^{1}H} NMR (151 MHz, 298 K, DMSO-d$_6$) of $Pd_2\mathbf{L}^{\mathbf{4}}{}_2\mathbf{L}^{\mathbf{C}}{}_2$.

HR-ESI-MS:

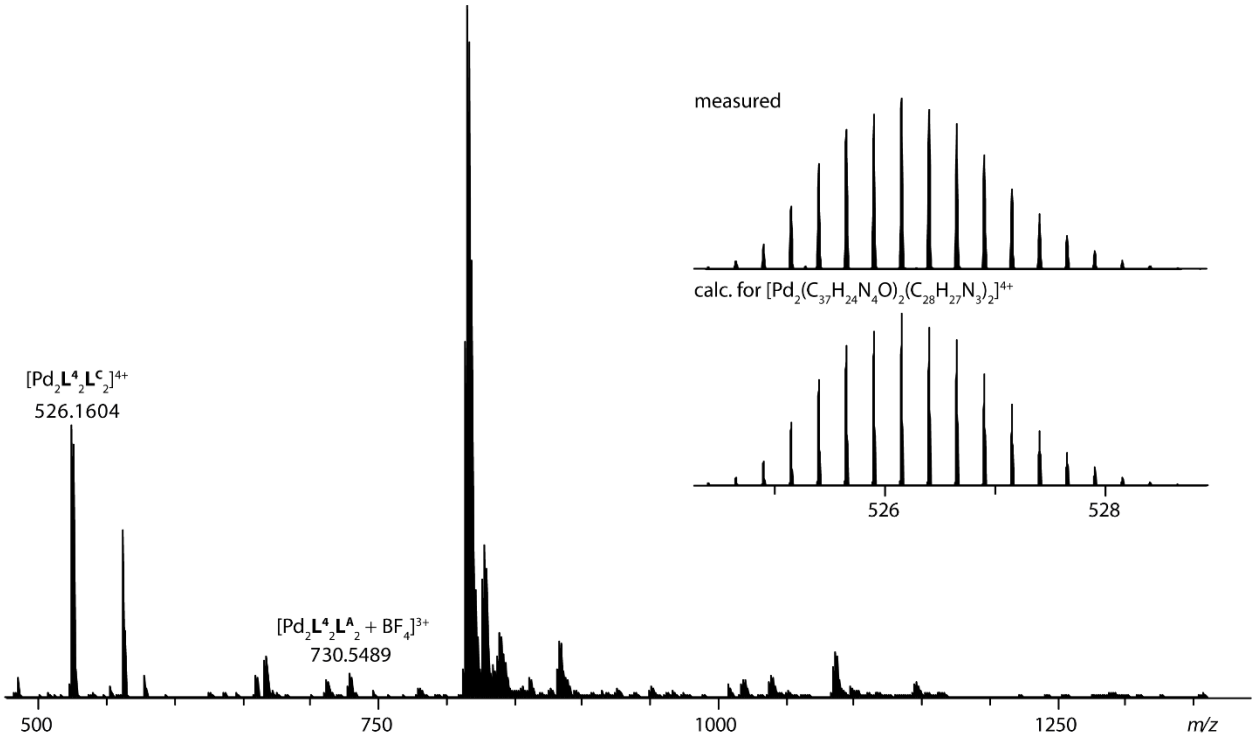

Figure 4.127: ESI-MS spectrum of $[Pd_2\mathbf{L}^4{}_2\mathbf{L}^C{}_2 + n\ BF_4]^{(4-n)+}$ and inset of comparison of measured and calculated mass.

4.4.16 $Pd_2L^4{}_2L^D{}_2$

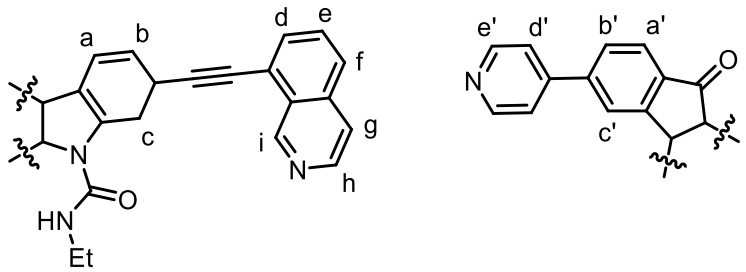

Scheme 4.34: Ligand Assignment for $Pd_2\mathbf{L}^4{}_2\mathbf{L}^D{}_2$.

^{1}H NMR (500 MHz, 298 K, DMSO-d_6): δ = 10.07 (s (br), 4H, i), 9.61 (d, ^3J = 6.1, 8H, e'), 9.44 (d (br), ^3J = 5.2, 4H, h), 8.45 (m, 6H, g, N*H*), 8.26 (d, ^3J = 8.4, 4H, f), 8.19 (s, 4H, c'), 8.11 – 8.02 (m, 20H, d, e, a', d'), 8.00 (s (br), 4H, c), 7.82 (m, 12H, a, b, b'), 3.03 (s (br), 4H, C(O)NHCH_2), 0.57 (s (br), 6H, C(O)NHCH$_2$CH_3).

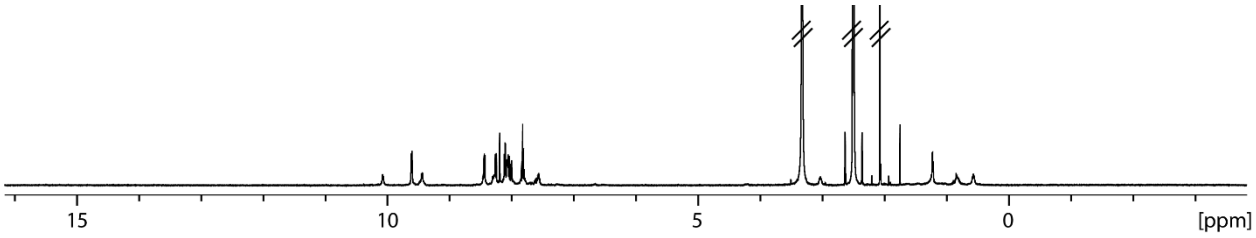

Figure 4.128: ^{1}H NMR (500 MHz, 298 K, DMSO-d_6) of $Pd_2\mathbf{L^4}_2\mathbf{L^D}_2$.

Figure 4.129: Partial ^{1}H NMR (500 MHz, 298 K, DMSO-d_6) of $Pd_2\mathbf{L^4}_2\mathbf{L^D}_2$.

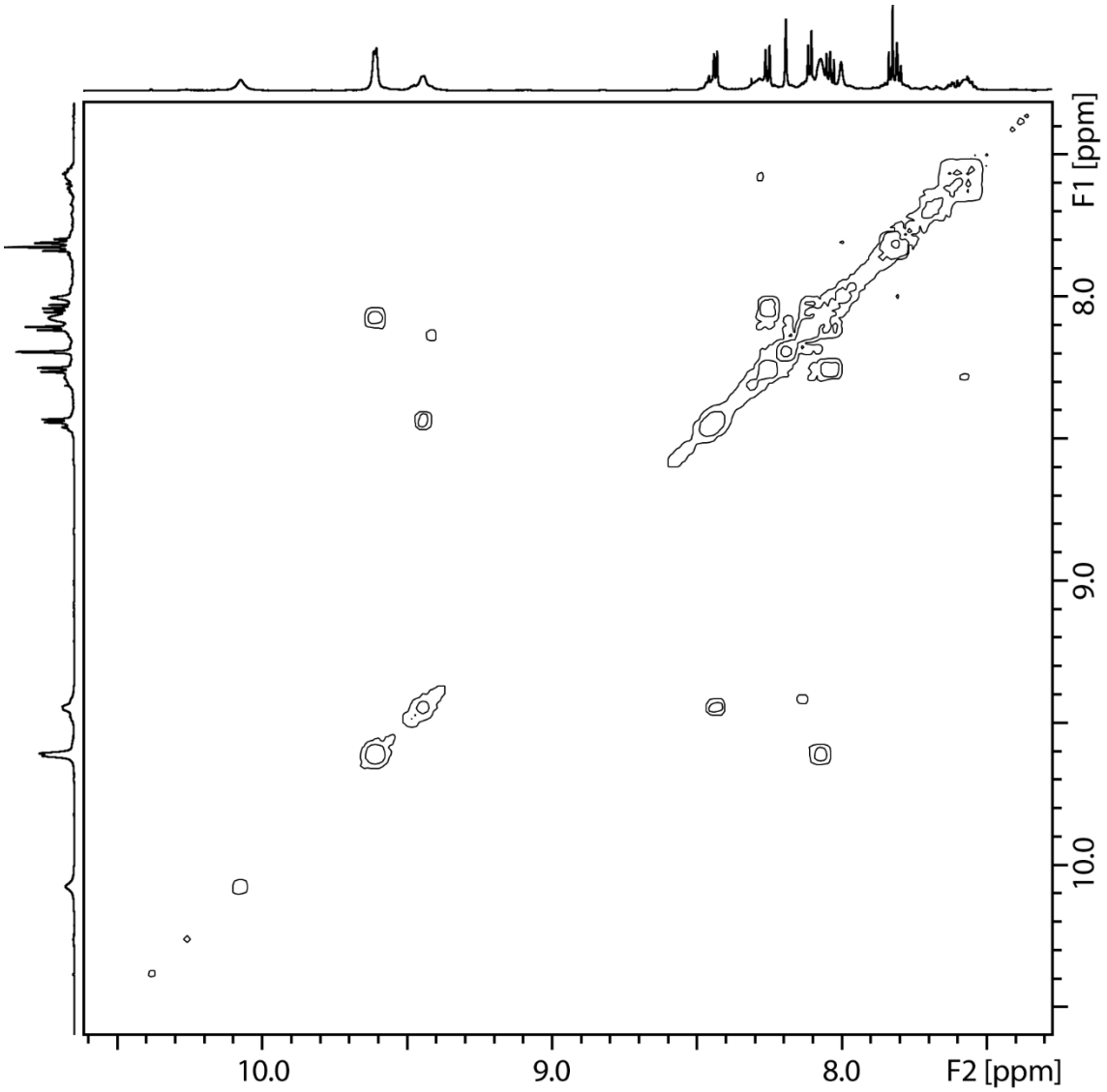

Figure 4.130: Partial ^{1}H–^{1}H COSY NMR (600 MHz, 298 K, DMSO-d_6) of $Pd_2\mathbf{L^4}_2\mathbf{L^D}_2$.

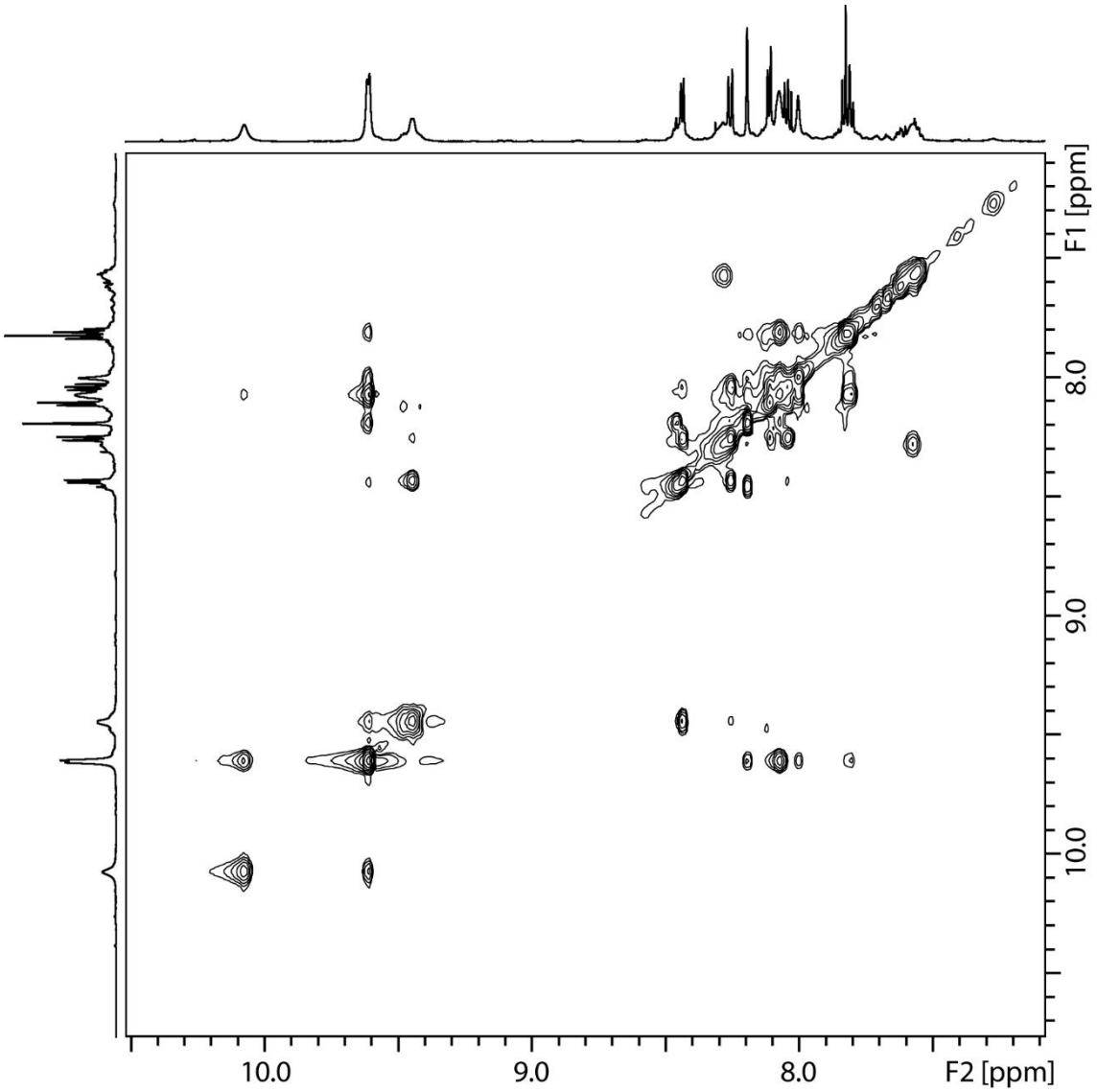

Figure 4.131: Partial ^{1}H–^{1}H NOESY NMR (600 MHz, 298 K, DMSO-d_6) of $Pd_2\mathbf{L}^{\mathbf{4}}{}_2\mathbf{L}^{\mathbf{D}}{}_2$.

^{13}C{^{1}H} NMR (151 MHz, 298 K, DMSO-d_6): δ = 191.4, 171.4, 153.4, 151.8, 151.0, 150.2, 143.6, 142.6, 141.3, 138.4, 136.3, 134.7, 134.1, 133.8, 131.5, 131.4, 128.8, 128.7, 127.9, 127.8, 125.6, 125.2, 124.0, 121.7, 121.2, 120.8, 120.2, 116.3, 97.4, 84.7, 22.5, 13.8.

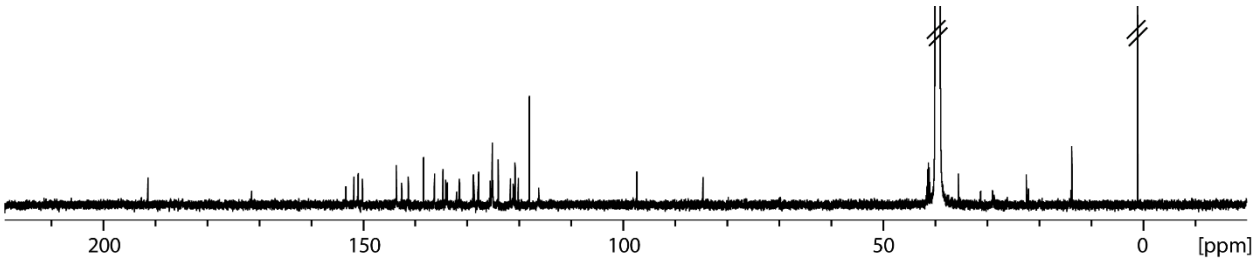

Figure 4.132: ^{13}C{^{1}H} NMR (151 MHz, 298 K, DMSO-d_6) of $Pd_2\mathbf{L}^{\mathbf{4}}{}_2\mathbf{L}^{\mathbf{D}}{}_2$.

HR-ESI-MS: Only very weak intense mass peak of the species $[Pd_2\mathbf{L}^{\mathbf{4}}{}_2\mathbf{L}^{\mathbf{D}}{}_2]^{4+}$ could be observed. However, the measured peak matches perfectly with the calculation.

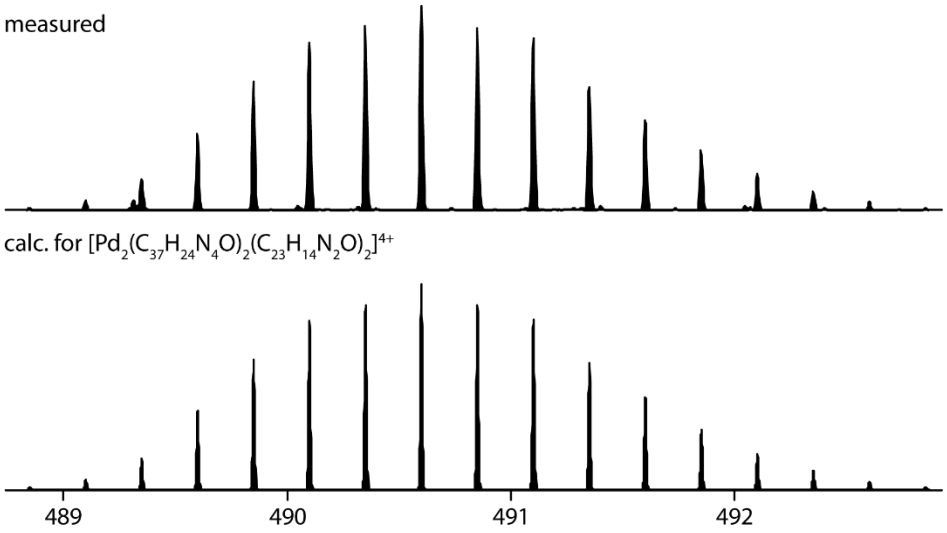

Figure 4.133: Partial ESI-MS spectrum of $[Pd_2\mathbf{L}^{\mathbf{4}}{}_2\mathbf{L}^{\mathbf{D}}{}_2]^{4+}$ and comparison with calculated mass.

4.5 General synthesis of phosphate ester salts $\mathbf{G^1}$-$\mathbf{G^6}$

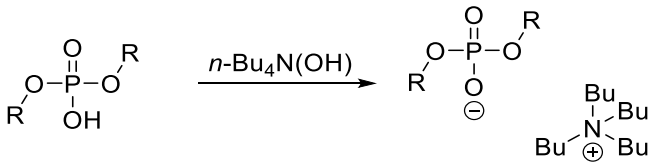

Scheme 4.35: General synthesis of phosphate ester salts.

100 mg of the commercially available organic phosphoric acids of the type $P(O)(OR)_2OH$ (R = Ph, Bn, Tol, Et, Bu, (*S*)-Binaphtyl) were dissolved in 50 mL HPLC-grade MeOH. A solution of tetra-*n*-butyl ammonium hydroxide (10% *ww* in HPLC-grade MeOH) was added dropwise until a neutral pH was reached. The solvent was removed *in vacuo* and the salts were dried at high vacuum for 24 h. The correct ratio of phosphate to TBA was checked via ^{1}H NMR spectroscopy. For titration experiments, stock solutions in DMSO-d_6 (c = 15 mM) were used. (*D*)-Mannose-6-phosphate sodium salt ($\mathbf{G^8}$) and guanosine diphosphate sodium salt ($\mathbf{G^9}$) were commercially available and used as received. Due to solubility stock solutions in D_2O (c = 15 mM) were used.

4.5.1 Dibutylphosphate G[1]

^{1}H NMR (700 MHz, 298 K, DMSO-d_6): δ = 3.56 (q, ^{3}J = 7.42, 2H, d), 3.16 (m, 2H, NCH_2), 1.57 (m, 2H, NCH$_2$CH_2), 1.43 (m, 2H, c), 1.30 (m, 4H, b, NCH$_2$CH$_2$CH_2), 0.93 (t, ^{3}J = 7.31, 3H, CH_3), 0.87 (t, ^{3}J = 7.42, 3H, a).

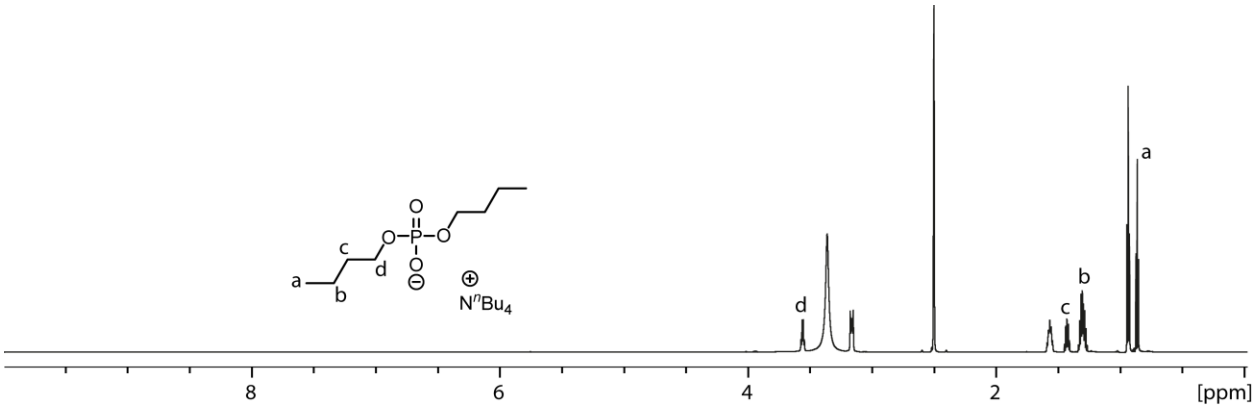

Figure 4.134: ^{1}H NMR spectrum (700 MHz, 298 K, DMSO-d_6) and structure assignment of **G[1]**.

^{13}C{^{1}H} NMR (176 MHz, 298 K, DMSO-d_6): δ = 63.3, 57.5, 32.7, 23.1, 19.2, 18.7, 13.7, 13.5.

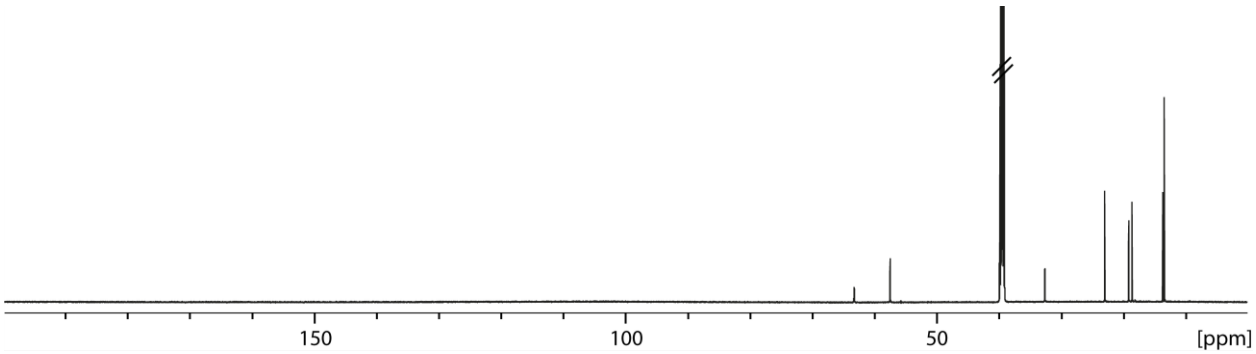

Figure 4.135: ^{13}C{^{1}H} NMR spectrum (176 MHz, 298 K, DMSO-d_6) of **G[1]**.

^{31}P{^{1}H} NMR (283 MHz, 298 K, DMSO-d_6, lb = 5 Hz): δ = −1.0.

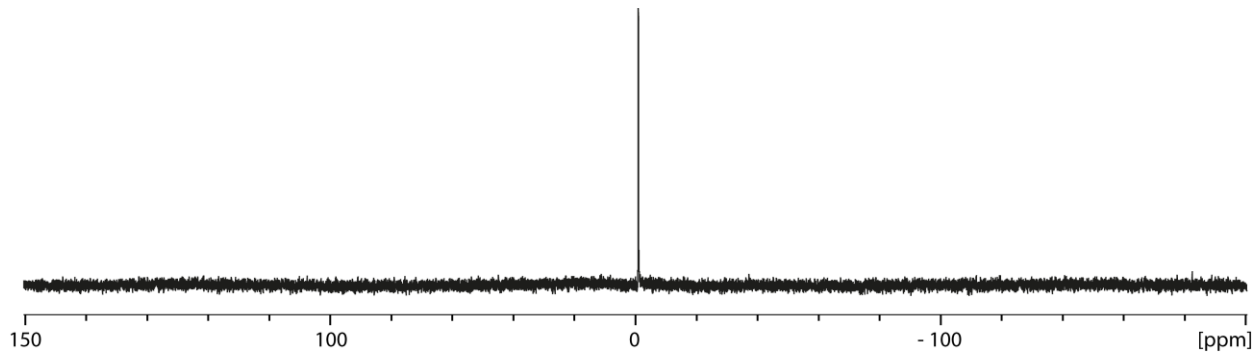

Figure 4.136: ^{31}P{^{1}H} NMR spectrum (283 MHz, 298 K, DMSO-d_6, lb = 5 Hz) of **G[1]**.

4.5.2 Dibenzylphosphate G²

¹H NMR (700 MHz, 298 K, DMSO-d₆): δ = 7.30 (m, 4H, b, c), 7.22 (m, 1H, a), 4.7 (d, 2H, ^{2}J = 6.46, d), 3.16 (m, 2H, NC*H*₂), 1.56 (m, 2H, NCH₂C*H*₂), 1.30 (m, 2H, NCH₂CH₂C*H*₂), 0.93 (t, ^{3}J = 7.30, 3H, C*H*₃).

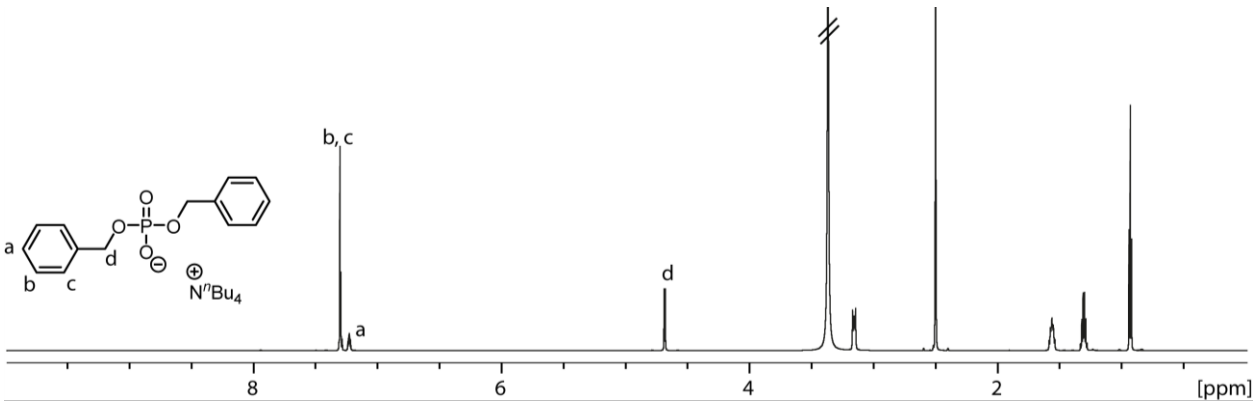

Figure 4.137: ¹H NMR spectrum (700 MHz, 298 K, DMSO-d₆) and structure assignment of **G²**.

¹³C{¹H} NMR (176 MHz, 298 K, DMSO-d₆): δ = 139.9, 128.0, 127.0, 126.8, 65.7, 57.5, 23.0, 19.2, 13.5.

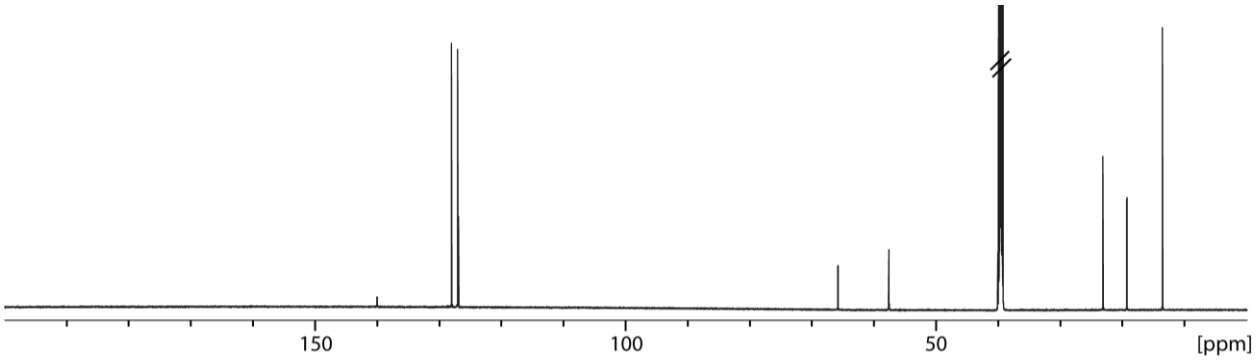

Figure 4.138: ¹³C{¹H} NMR spectrum (176 MHz, 298 K, DMSO-d₆) of **G²**.

³¹P{¹H} NMR (283 MHz, 298 K, DMSO-d₆, lb = 5 Hz): δ = −0.8.

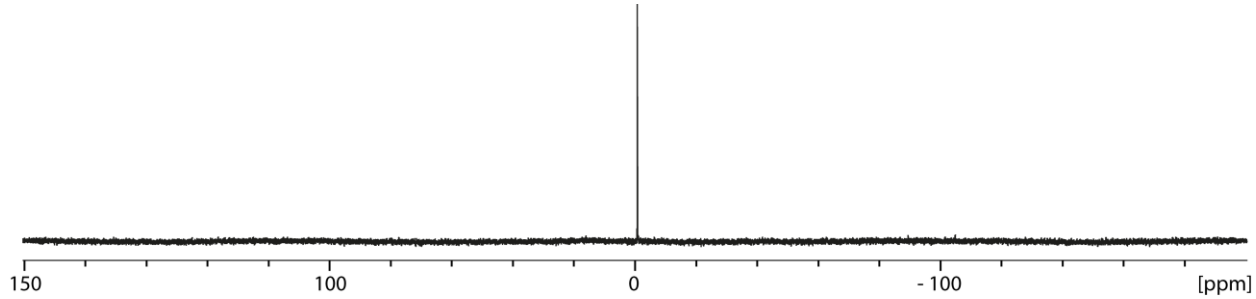

Figure 4.139: ³¹P{¹H} NMR spectrum (283 MHz, 298 K, DMSO-d₆, lb = 5 Hz) of **G²**.

4.5.3 Diphenylphosphate G^3

^{1}H NMR (700 MHz, 298 K, DMSO-d$_6$): δ = 7.20 (m, 2H, b), 7.11 (m, 2H, c), 6.93 (t, ^3J = 7.30, 1H, a), 3.16 (m, 2H, NC*H*$_2$), 1.56 (m, 2H, NCH$_2$C*H*$_2$), 1.31 (tq, ^3J = 7.31, 2H, NCH$_2$CH$_2$C*H*$_2$), 0.93 (t, ^3J = 7.31, 3H, C*H*$_3$).

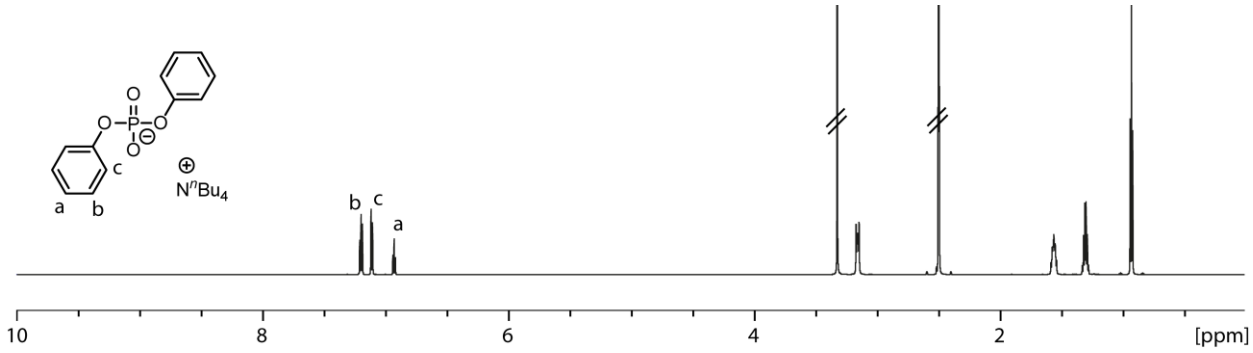

Figure 4.140: ^{1}H NMR spectrum (700 MHz, 298 K, DMSO-d$_6$) and structure assignment of **G^3**.

^{13}C{^{1}H} NMR (176 MHz, 298 K, DMSO-d$_6$): δ = 154.1, 128.7, 121.6, 119.8, 57.5, 23.0, 19.2, 13.5.

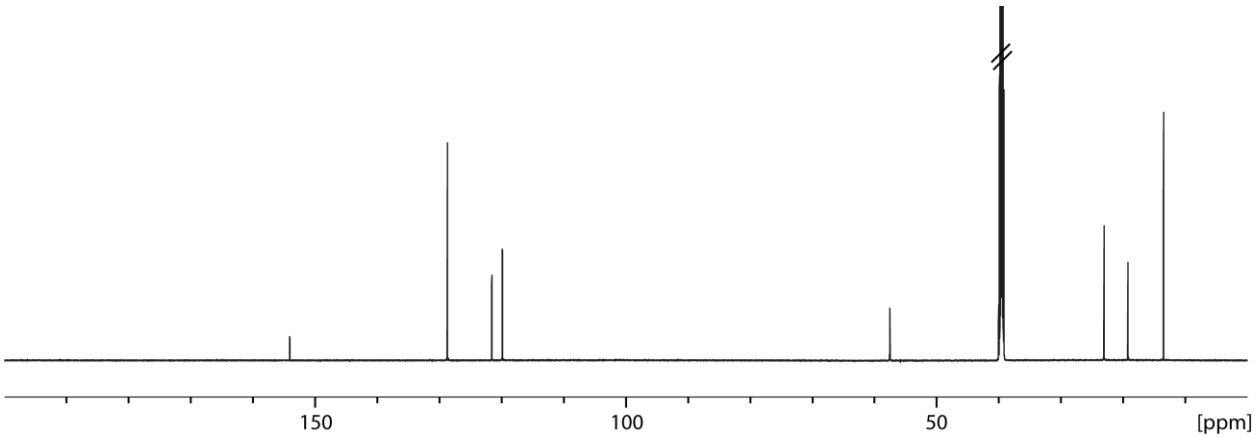

Figure 4.141: ^{13}C{^{1}H} NMR spectrum (176 MHz, 298 K, DMSO-d$_6$) of **G^3**.

^{31}P{^{1}H} NMR (283 MHz, 298 K, DMSO-d$_6$, lb = 5 Hz): δ = −11.3.

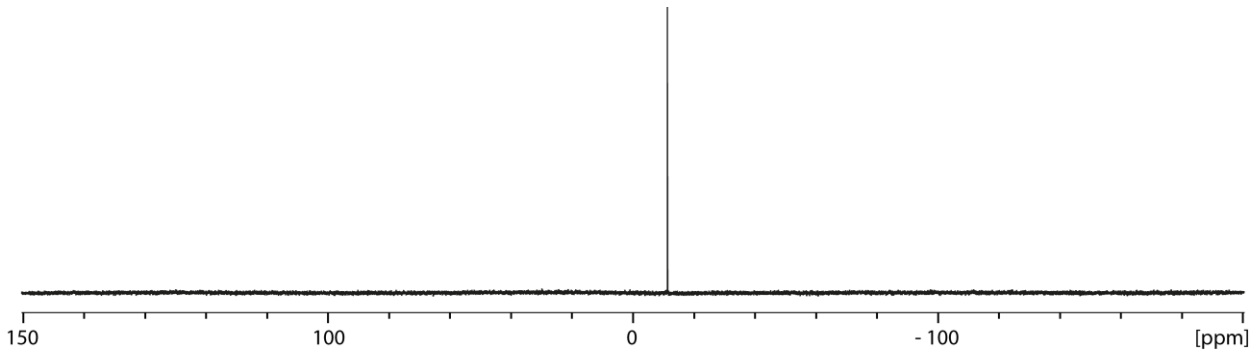

Figure 4.142: ^{31}P{^{1}H} NMR spectrum (283 MHz, 298 K, DMSO-d$_6$, lb = 5 Hz) of **G^3**.

4.5.4 Diethylphosphate G[4]

[1]H NMR (700 MHz, 298 K, DMSO-d$_6$): δ = 3.60 (m, 2H, b), 3.16 (m, 2H, NC*H*$_2$), 1.57 (m, 2H, NCH$_2$C*H*$_2$), 1.31 (m, 2H, NCH$_2$CH$_2$C*H*$_2$), 1.06 (t, ^3J = 7.05, 3H, a), 0.93 (t, ^3J = 7.31, 3H, C*H*$_3$).

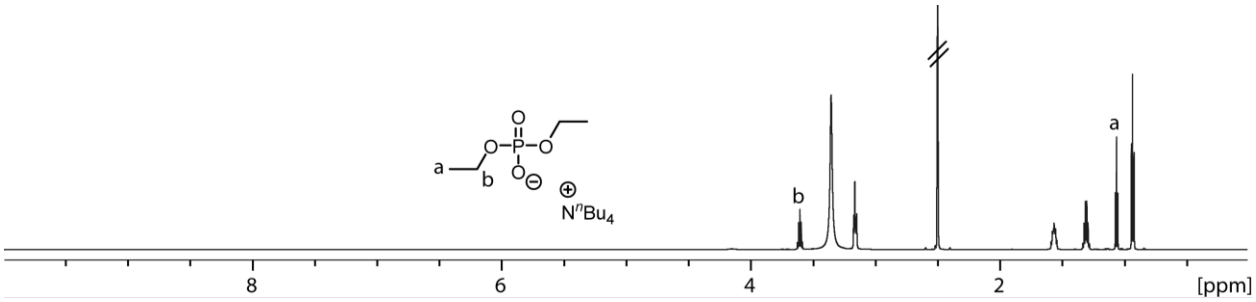

Figure 4.143: ^{1}H NMR spectrum (700 MHz, 298 K, DMSO-d$_6$) and structure assignment of **G[4]**.

[13]C{[1]H} NMR (176 MHz, 298 K, DMSO-d$_6$): δ = 59.0, 57.5, 23.1, 19.2, 16.7, 13.5.

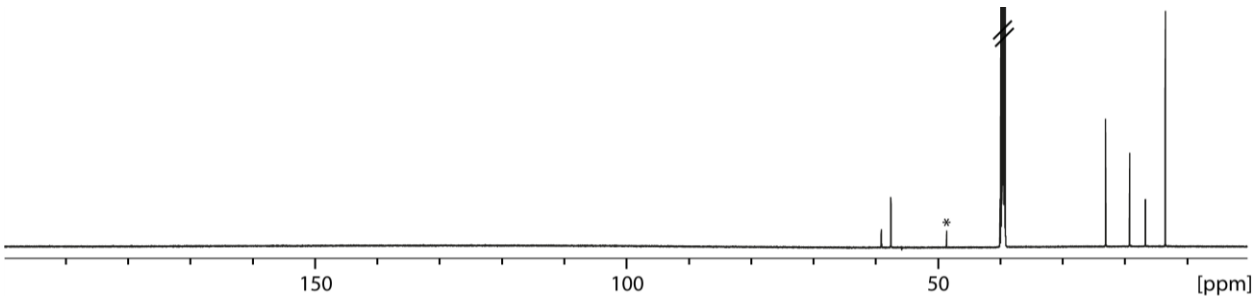

Figure 4.144: ^{13}C{^{1}H} NMR spectrum (176 MHz, 298 K, DMSO-d$_6$) of **G[4]**, solvent residue signal (MeOH) marked with a star *.

[31]P{[1]H} NMR (283 MHz, 298 K, DMSO-d$_6$, lb = 5 Hz): δ = −1.0.

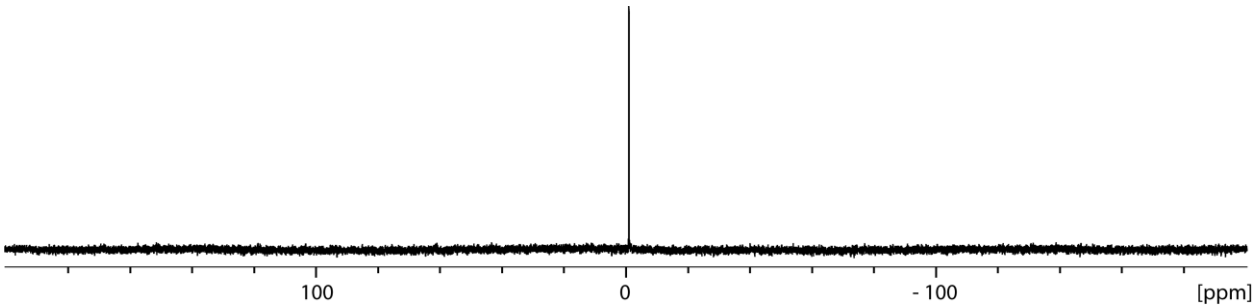

Figure 4.145: ^{31}P{^{1}H} NMR spectrum (283 MHz, 298 K, DMSO-d$_6$, lb = 5 Hz) of **G[4]**.

4.5.5 Di-*p*-toluylphosphate G[5]

^{1}H NMR (700 MHz, 298 K, DMSO-d$_6$): δ = 6.98 (s, 4H, b, c), 3.16 (m, 2H, NC*H*$_2$), 2.20 (s, 3H, a), 1.56 (m, 2H, NCH$_2$C*H*$_2$), 1.31 (m, 2H, NCH$_2$CH$_2$C*H*$_2$), 0.93 (t, ^{3}J = 7.31, 3H, C*H*$_3$).

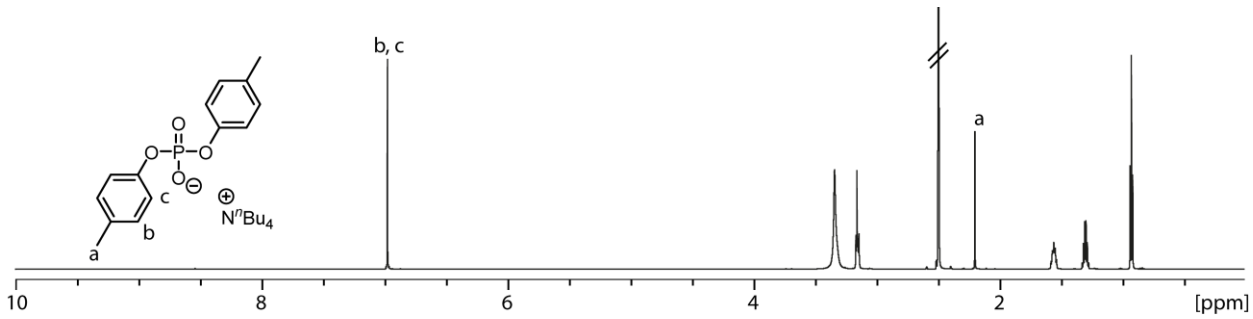

Figure 4.146: ^{1}H NMR spectrum (700 MHz, 298 K, DMSO-d$_6$) and structure assignment of **G[5]**.

^{13}C{^{1}H} NMR (176 MHz, 298 K, DMSO-d$_6$): δ = 151.9, 130.1, 129.0, 119.8, 57.5, 23.1, 20.2, 19.2, 13.5.

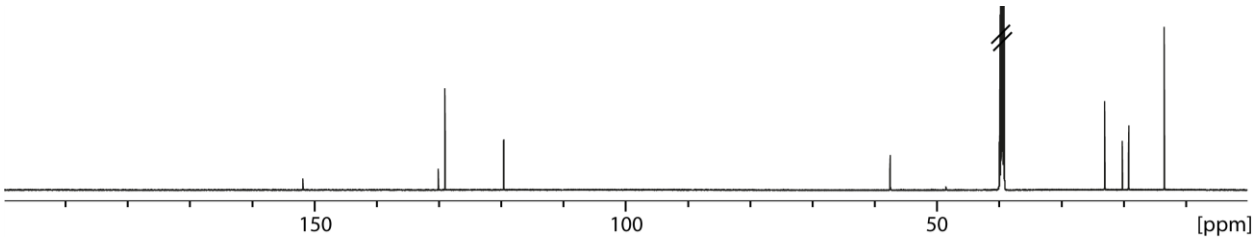

Figure 4.147: ^{13}C{^{1}H} NMR spectrum (176 MHz, 298 K, DMSO-d$_6$) of **G[5]**.

^{31}P{^{1}H} NMR (283 MHz, 298 K, DMSO-d$_6$, lb = 5 Hz): δ = −11.1.

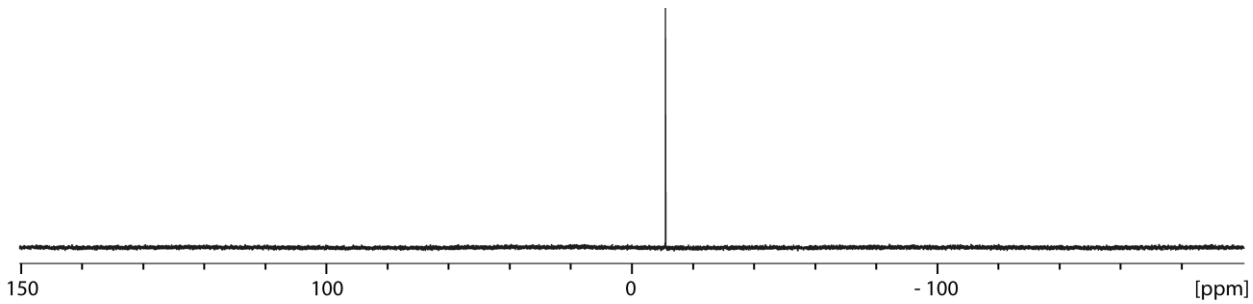

Figure 4.148: ^{31}P{^{1}H} NMR spectrum (283 MHz, 298 K, DMSO-d$_6$, lb = 5 Hz) of **G[5]**.

4.5.6 (*S*)-Binaphtylphosphate G[6]

^{1}H NMR (700 MHz, 298 K, DMSO-d$_6$): δ = 8.01 (m, 4H, b, c), 7.42 (m, 2H, e), 7.38 (d, ^{3}J = 8.69, 2H, a), 7.28 (m, 2H, d), 7.20 (d, ^{3}J = 8.50, 2H, f), 3.16 (m, 2H, NC*H*$_2$), 1.56 (m, 2H, NCH$_2$C*H*$_2$), 1.31 (m, 2H, NCH$_2$CH$_2$C*H*$_2$), 0.93 (t, ^{3}J = 7.31, 3H, C*H*$_3$).

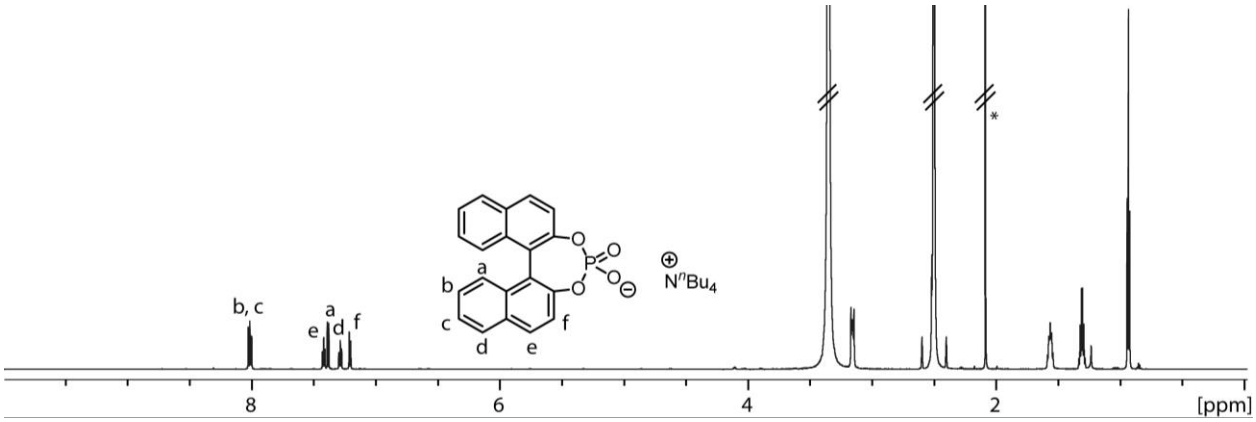

Figure 4.149: ^{1}H NMR spectrum (700 MHz, 298 K, DMSO-d_6) and structure assignment of **G^6**, solvent residue signal (acetone) marked with a star *.

^{13}C{^{1}H} NMR (176 MHz, 298 K, DMSO-d_6): δ = 150.3, 132.0, 130.2, 129.6, 128.4, 126.0, 125.9, 124.3, 122.8, 121.8, 57.5, 20.2, 19.2, 13.5.

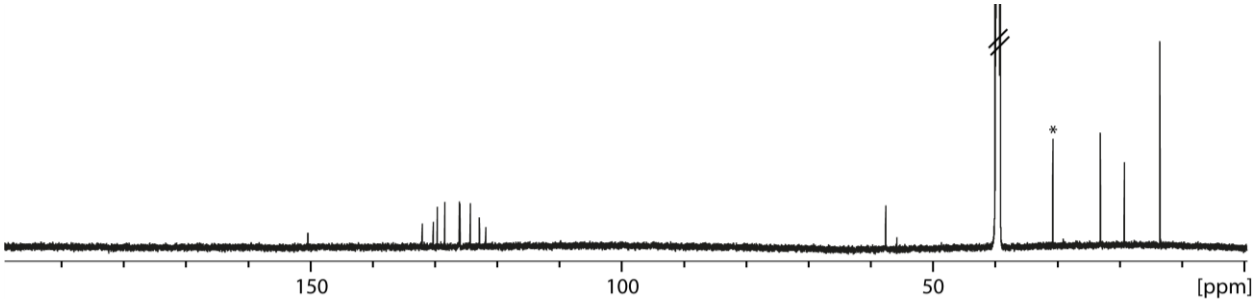

Figure 4.150: ^{13}C{^{1}H} NMR spectrum (176 MHz, 298 K, DMSO-d_6) of **G^6**, solvent residue signal (acetone) marked with a star *.

^{31}P{^{1}H} NMR (283 MHz, 298 K, DMSO-d_6, lb = 5 Hz): δ = 5.2.

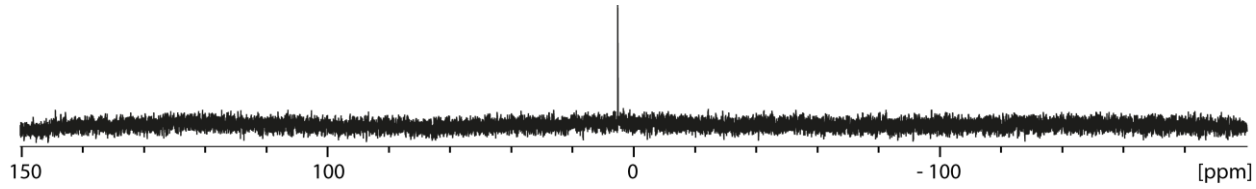

Figure 4.151: ^{31}P{^{1}H} NMR spectrum (283 MHz, 298 K, DMSO-d_6, lb = 5 Hz) of **G^6**.

4.5.7 Monophenylphosphate G^7

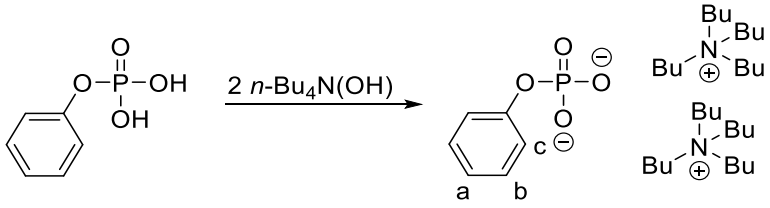

Scheme 4.36: Synthesis of **G^7**.

^{1}H NMR (500 MHz, 298 K, DMSO-d_6): δ = 7.11 (m, 2H, b), 7.07 (m, 2H, c), 6.71 (t, ^{3}J = 6.9, 1H, a), 3.17 (m, 4H, NCH_2), 1.56 (m, 4H, NCH$_2$CH_2), 1.31 (m, 4H, NCH$_2$CH$_2$CH_2), 0.93 (t, ^{3}J = 7.3, 6H, CH_3).

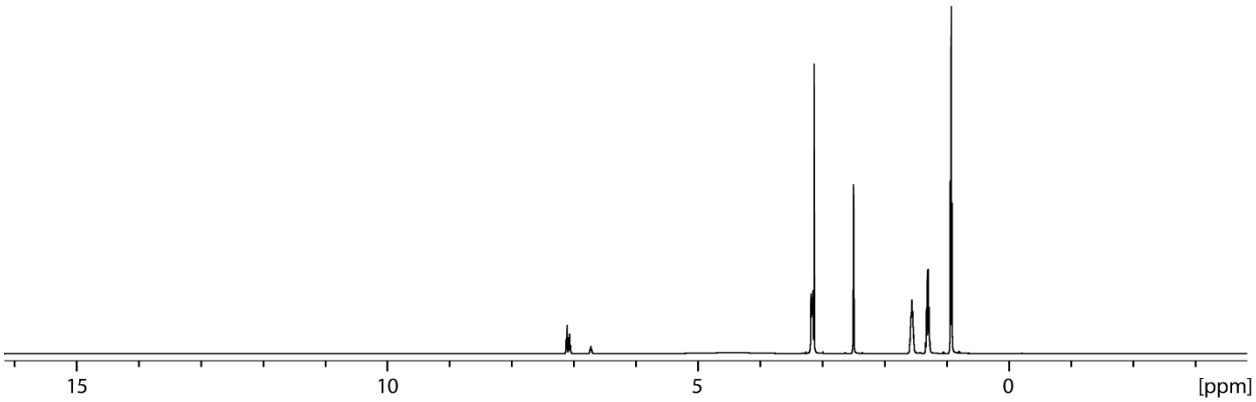

Figure 4.152: ^{1}H NMR spectrum (500 MHz, 298 K, DMSO-d_6) of **G^{7}**.

^{31}P{^{1}H} NMR (202 MHz, 298 K, DMSO-d_6, lb = 5 Hz): δ = −1.9.

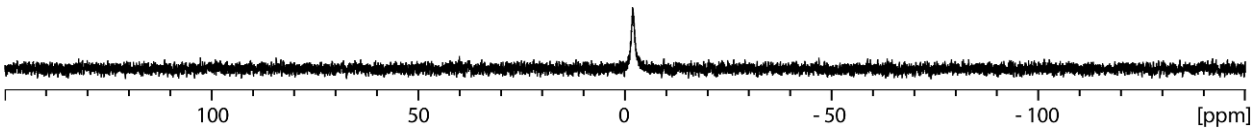

Figure 4.153: ^{31}P{^{1}H} NMR spectrum (202 MHz, 298 K, DMSO-d_6, lb = 5 Hz) of **G^{7}**.

4.6 Guest Titration Experiments

^{1}H NMR Titration experiments were carried out in the following way: The guest solution (15 mM in DMSO-d_6) was added to the host solution (0.7 mM in DMSO-d_6) in steps of 0.2 eq (until reaching 2 eq in total, then 2.5, 3.0, 3.5, 4.0 and 5.0 eq, if not mentioned otherwise). After adding, the sample was shaken briefly and measured directly. Owing to clarity, only every second recorded spectrum is shown in the following figures. ESI MS measurements were carried out after 1 eq guest was added to the host solution.

4.6.1 Titration of G^1 to $Pd_2L^1{}_2L^A{}_2$

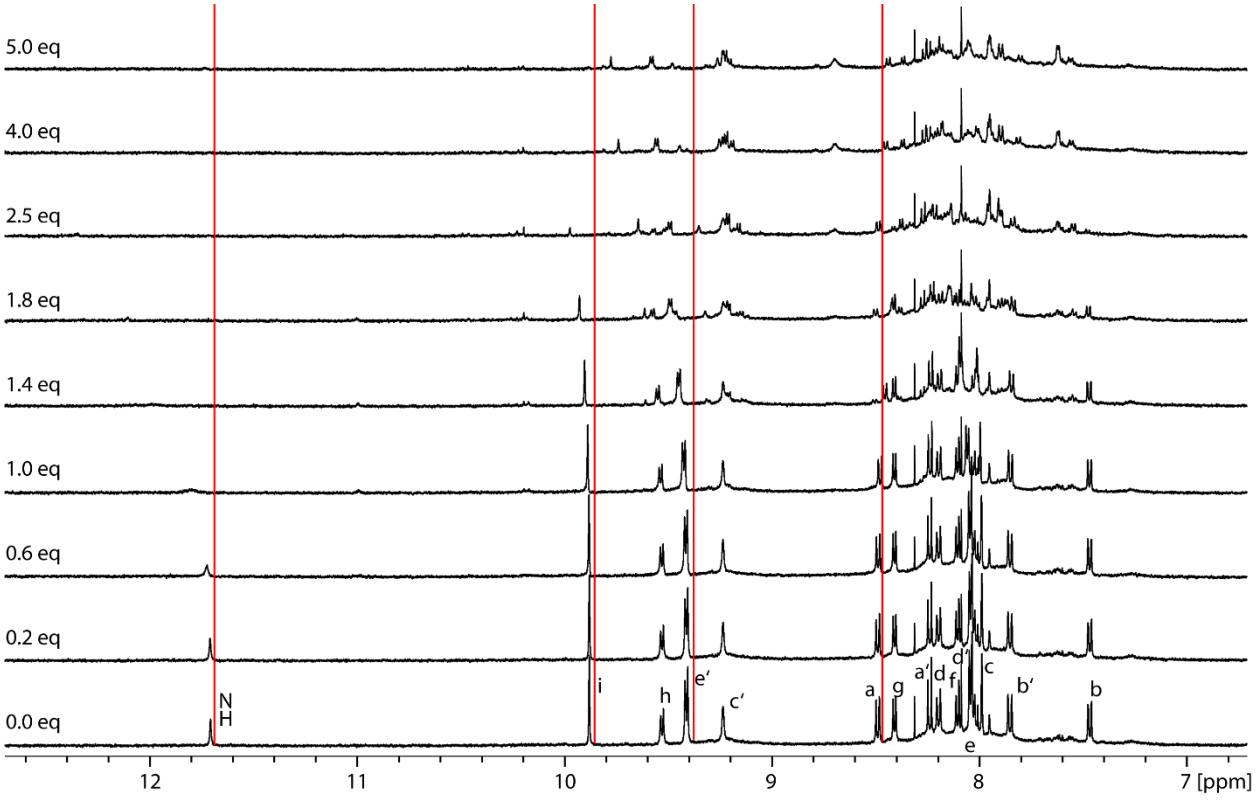

Figure 4.154: Stacked partial ^{1}H NMR spectra (500 MHz, 298 K, DMSO-d_6) of $\mathbf{G^1}$@$Pd_2\mathbf{L^1}_2\mathbf{L^A}_2$.

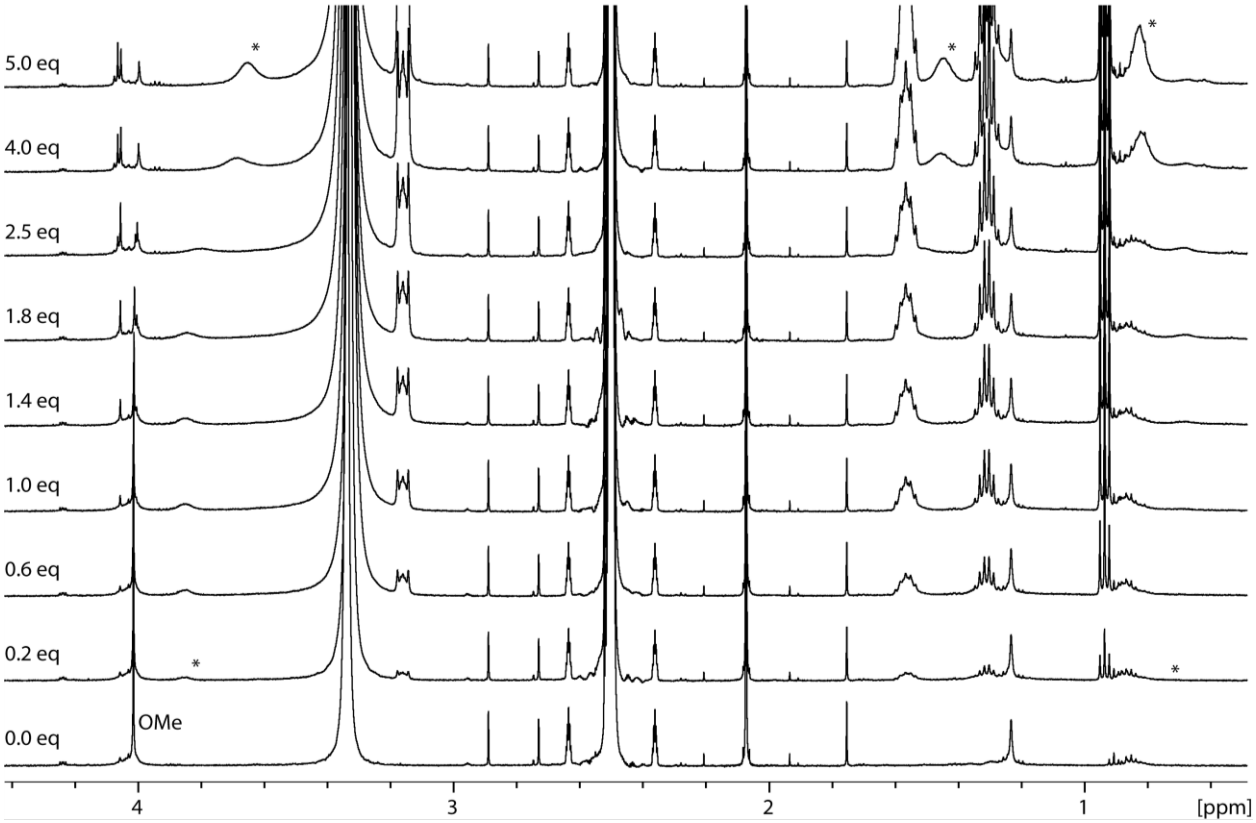

Figure 4.155: Stacked partial ^{1}H NMR spectra (500 MHz, 298 K, DMSO-d_6) of $\mathbf{G^1}$@$Pd_2\mathbf{L^1}_2\mathbf{L^A}_2$. Guest signals are indicated with a star *.

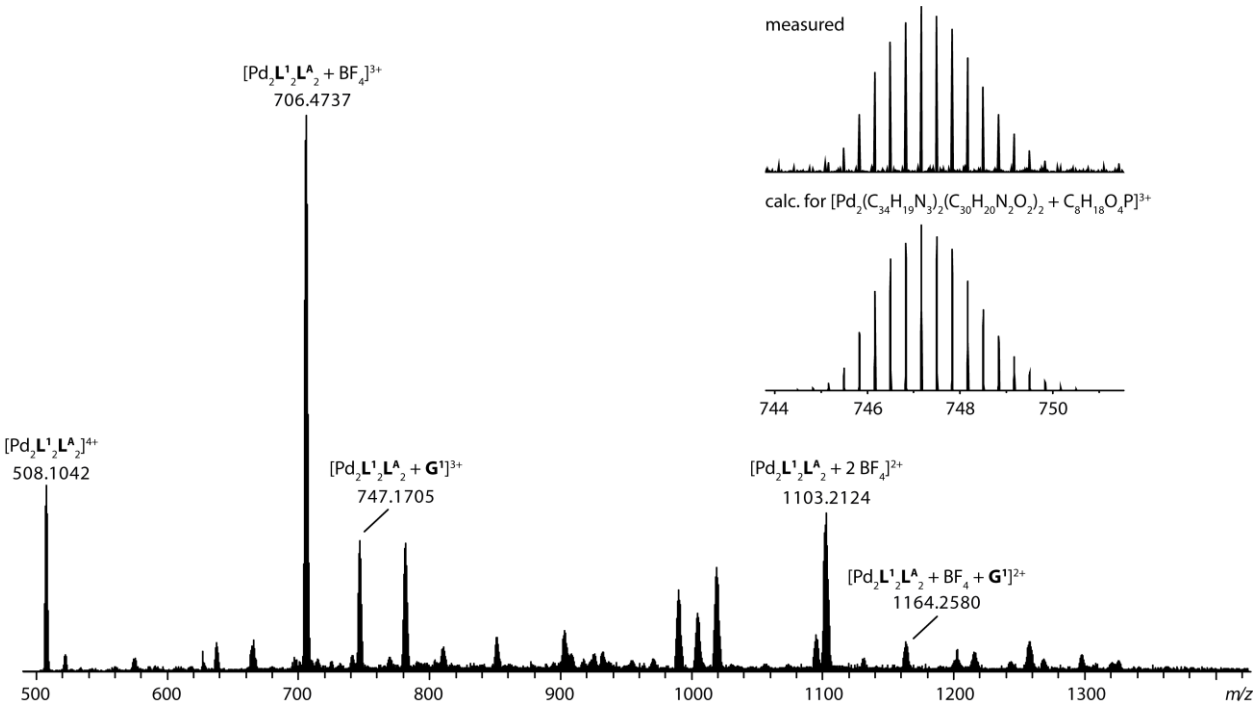

Figure 4.156: ESI-MS spectrum of $[Pd_2\mathbf{L^1}_2\mathbf{L^A}_2$ + m $\mathbf{G^1}$ + n $BF_4]^{(4-[m+n])+}$ and inset of comparison of measured and calculated mass.

4.6.2 Titration of G^2 to $Pd_2L^1{}_2L^A{}_2$

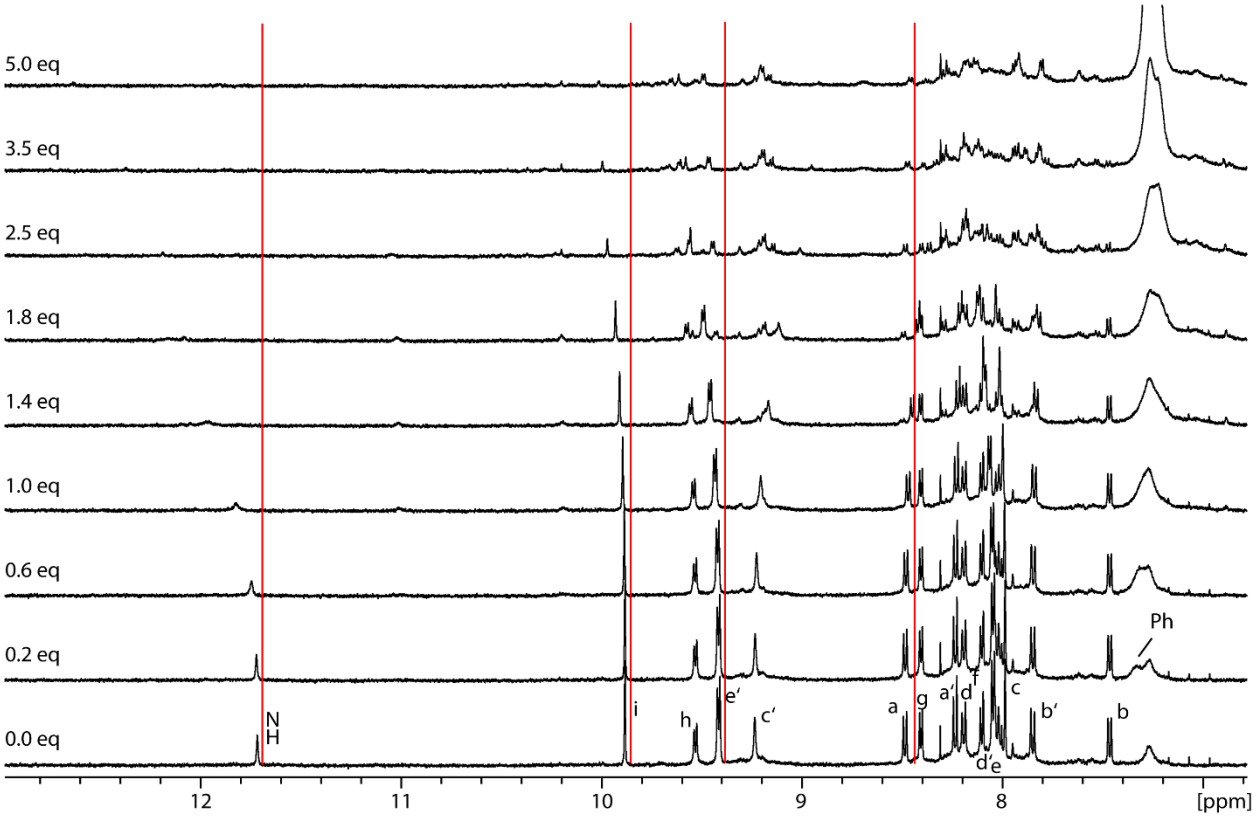

Figure 4.157: Stacked partial ^{1}H NMR spectra (500 MHz, 298 K, DMSO-d_6) of $\mathbf{G^2}$@$Pd_2\mathbf{L^1}_2\mathbf{L^A}_2$.

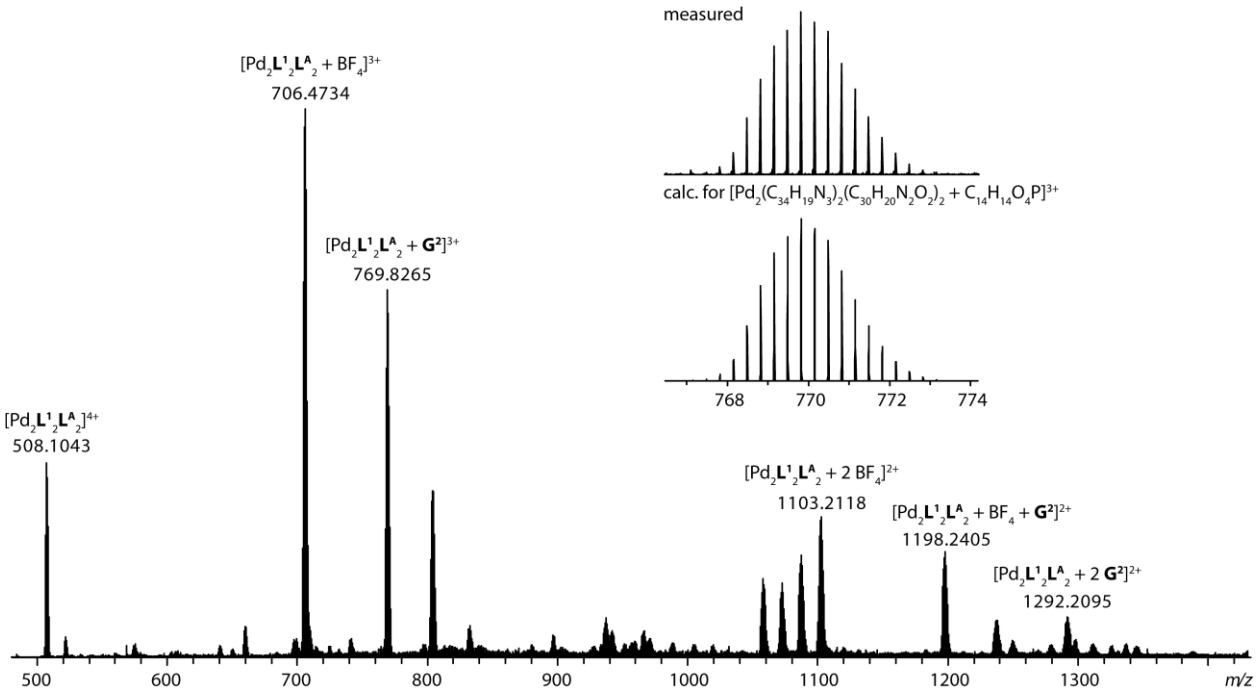

Figure 4.158: ESI-MS spectrum of $[Pd_2\mathbf{L^1}_2\mathbf{L^A}_2$ + m $\mathbf{G^2}$ + n $BF_4]^{(4-[m+n])+}$ and inset of comparison of measured and calculated mass.

4.6.3 Titration of G^3 to $Pd_2L^1{}_2L^A{}_2$

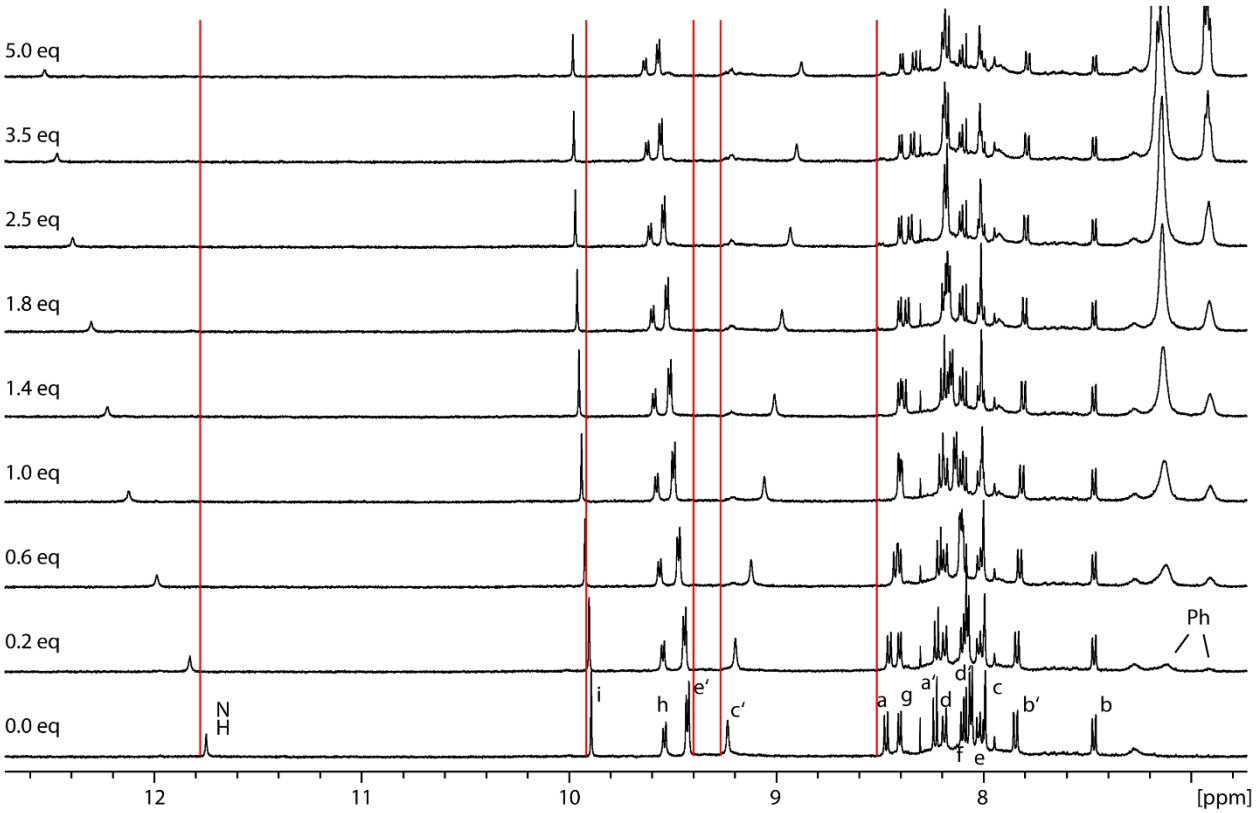

Figure 4.159: Stacked partial ^{1}H NMR spectra (500 MHz, 298 K, DMSO-d_6) of $\mathbf{G^3}$@$Pd_2\mathbf{L^1}_2\mathbf{L^A}_2$.

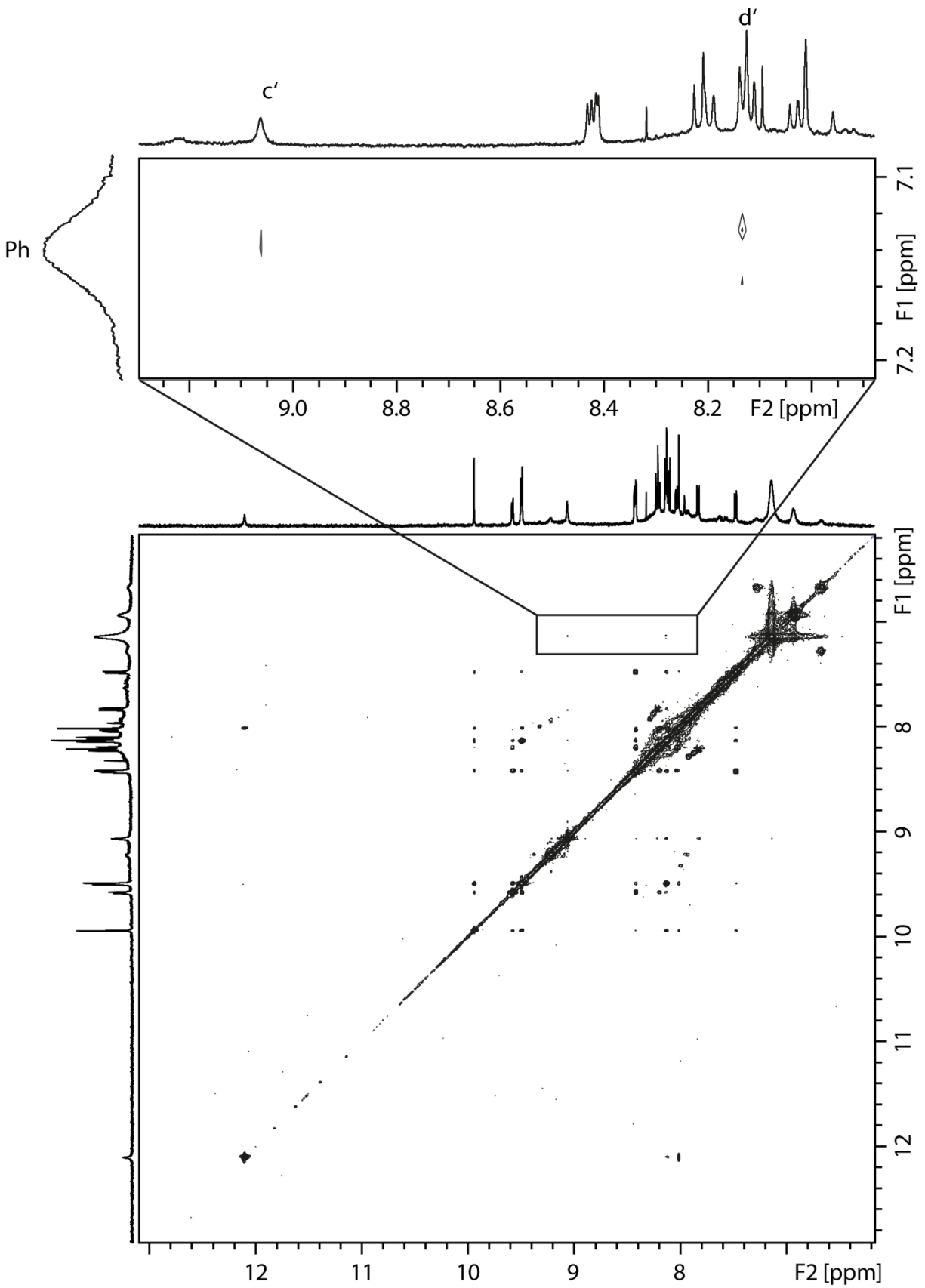

Figure 4.160: Partial ^{1}H–^{1}H NOESY NMR (600 MHz, 298 K, DMSO-d_6) of 1 eq $\mathbf{G^3}$@$Pd_2\mathbf{L^1}_2\mathbf{L^A}_2$ with cutout region to visualize NOE crosspeaks between phenyl proton signals of $\mathbf{G^3}$ and proton signals c' and d'.

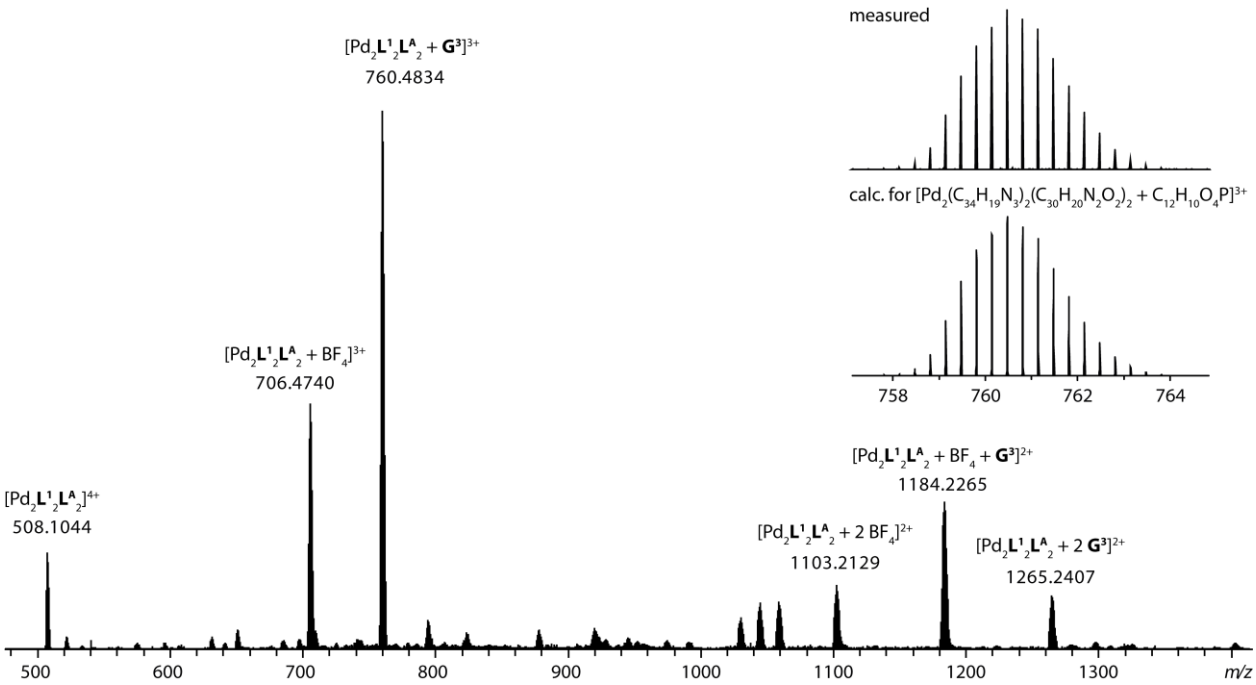

Figure 4.161: ESI-MS spectrum of $[Pd_2\mathbf{L^1}_2\mathbf{L^A}_2$ + m $\mathbf{G^3}$ + n $BF_4]^{(4-[m+n])+}$ and inset of comparison of measured and calculated mass.

4.6.4 Titration of G^4 to $Pd_2L^1{}_2L^A{}_2$

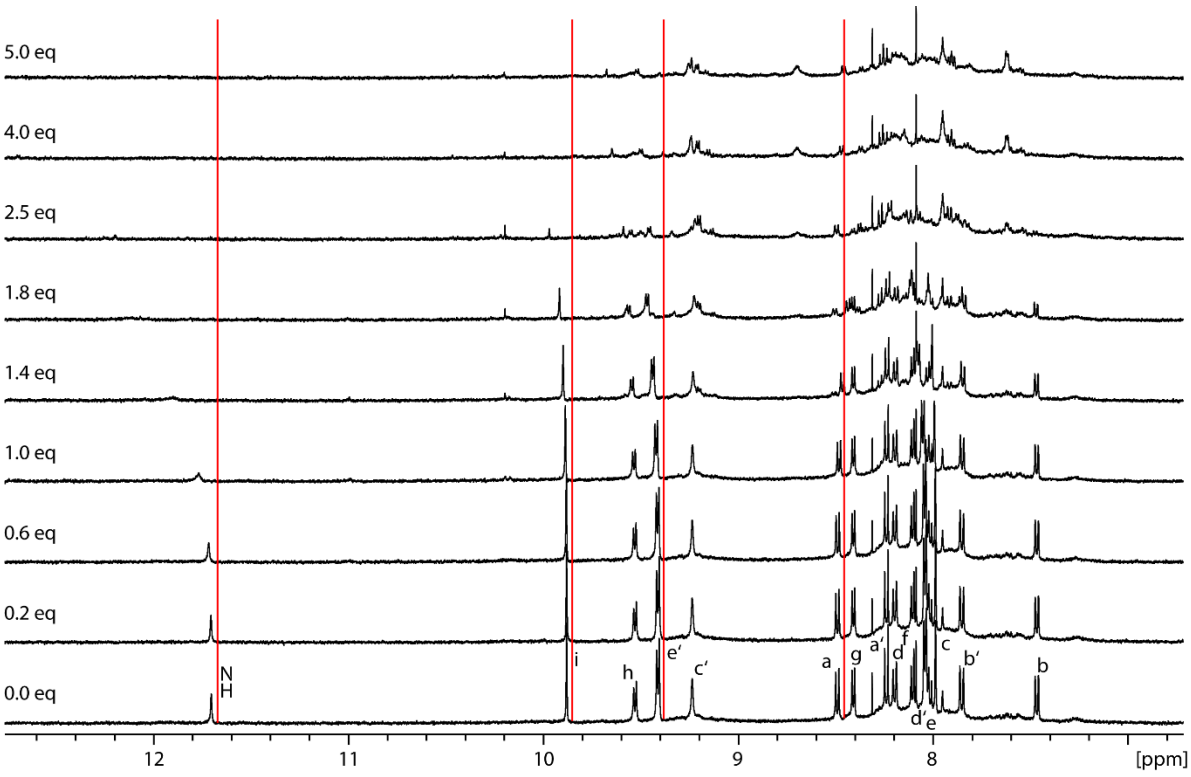

Figure 4.162: Stacked partial ^{1}H NMR spectra (500 MHz, 298 K, DMSO-d_6) of $\mathbf{G^4}$@$Pd_2\mathbf{L^1}_2\mathbf{L^A}_2$.

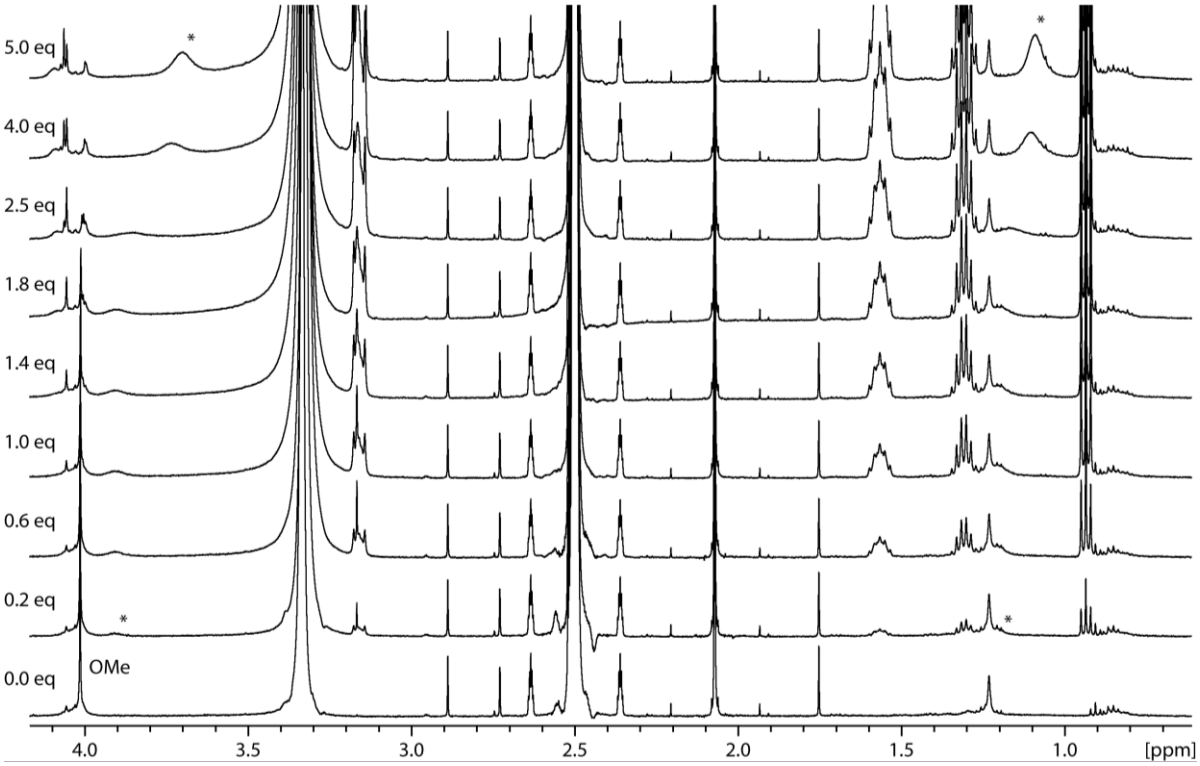

Figure 4.163: Stacked partial ^{1}H NMR spectra (500 MHz, 298 K, DMSO-d_6) of $\mathbf{G^4}$@$Pd_2\mathbf{L^1}_2\mathbf{L^A}_2$. Guest signals are indicated with a star *.

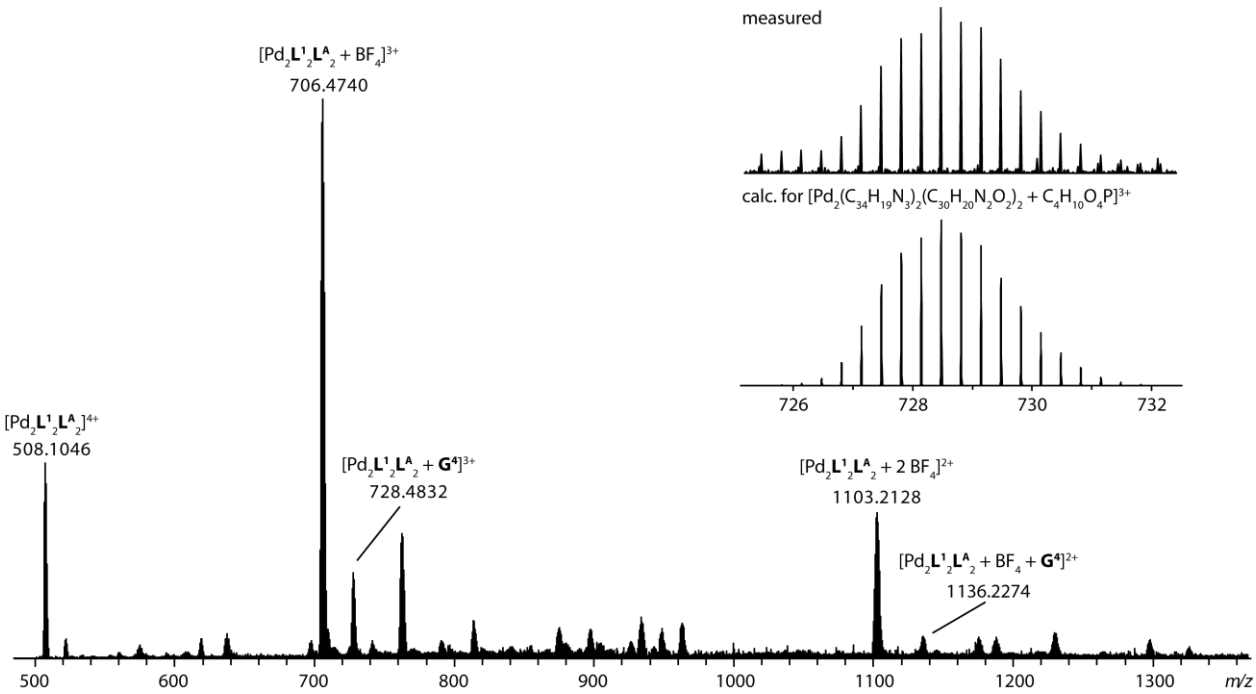

Figure 4.164: ESI-MS spectrum of $[Pd_2\mathbf{L^1}_2\mathbf{L^A}_2$ + m $\mathbf{G^4}$ + n $BF_4]^{(4-[m+n])+}$ and inset of comparison of measured and calculated mass.

4.6.5 Titration of G^5 to $Pd_2L^1{}_2L^A{}_2$

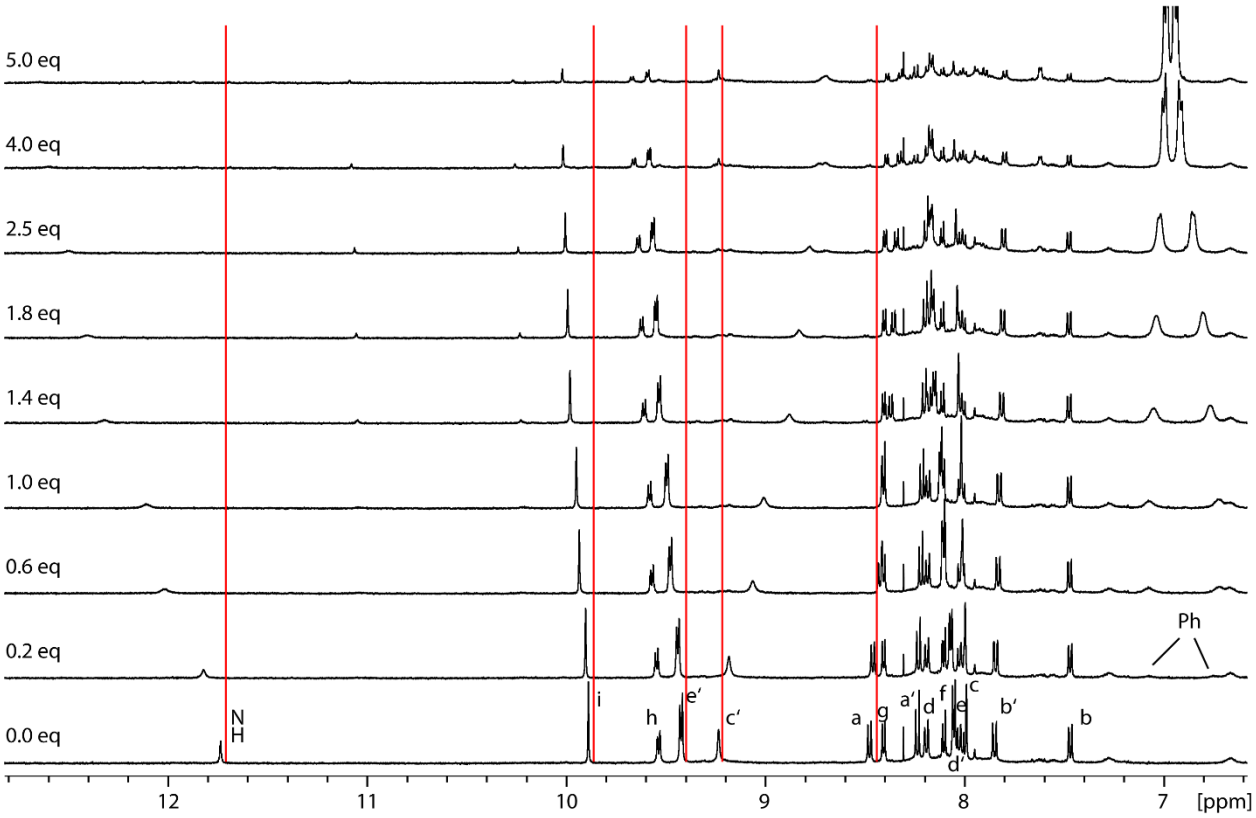

Figure 4.165: Stacked partial ^{1}H NMR spectra (500 MHz, 298 K, DMSO-d_6) of $\mathbf{G^5}$@$Pd_2\mathbf{L^1}{}_2\mathbf{L^A}{}_2$.

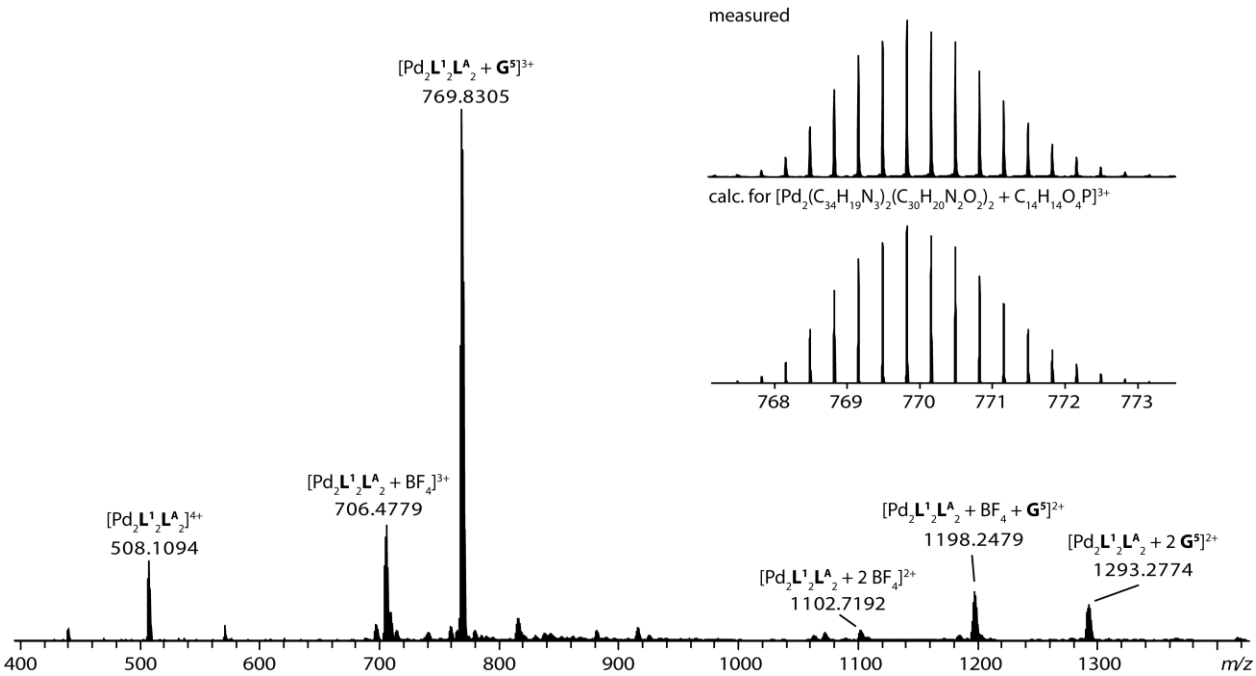

Figure 4.166: ESI-MS spectrum of $[Pd_2\mathbf{L^1}{}_2\mathbf{L^A}{}_2$ + m $\mathbf{G^5}$ + n $BF_4]^{(4-[m+n])+}$ and inset of comparison of measured and calculated mass.

4.6.6 Titration of G^6 to $Pd_2L^1{}_2L^A{}_2$

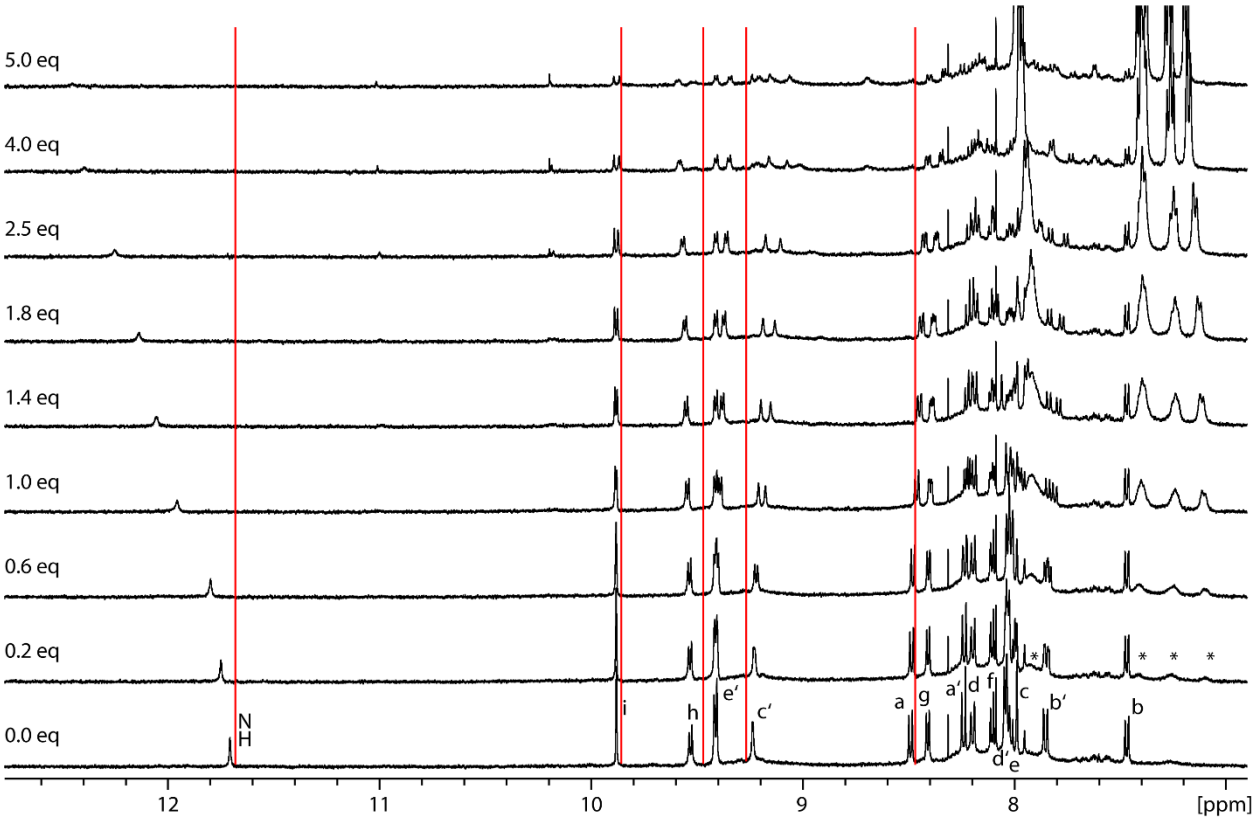

Figure 4.167: Stacked partial ^{1}H NMR spectra (500 MHz, 298 K, DMSO-d_6) of $\mathbf{G^6}$@$Pd_2\mathbf{L^1}_2\mathbf{L^A}_2$. Guest signals are marked with a star *.

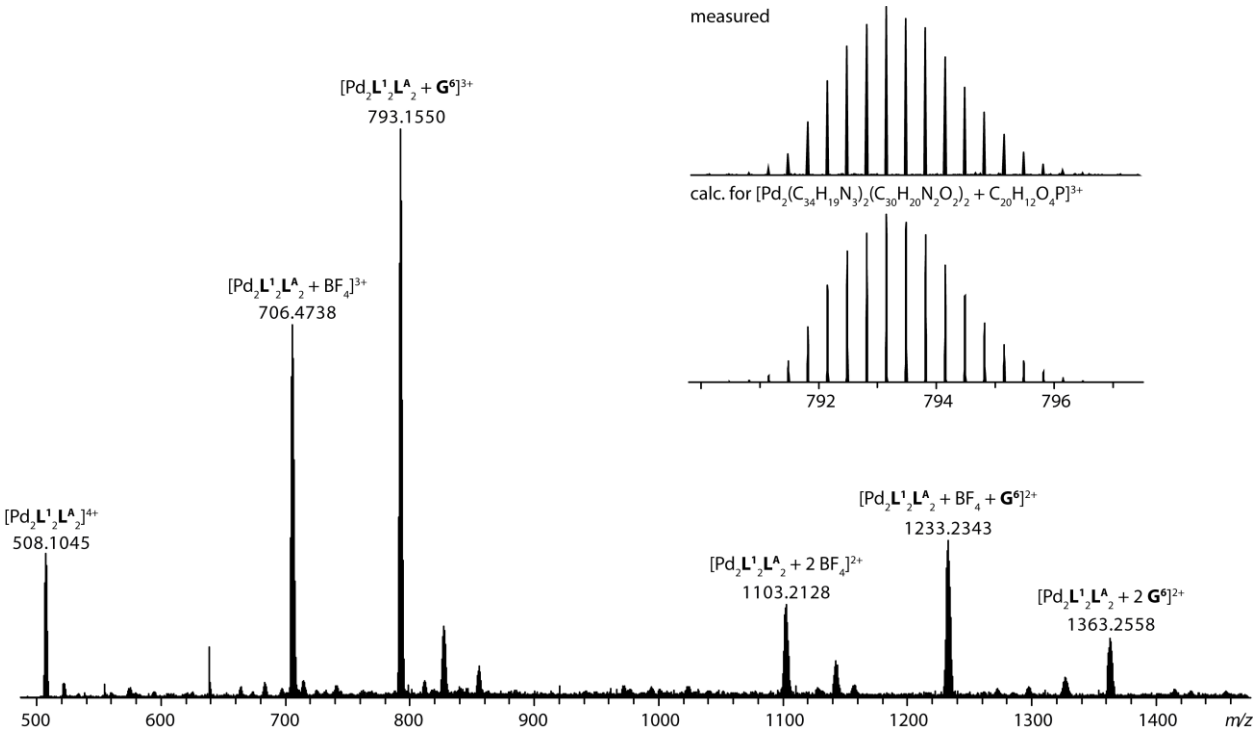

Figure 4.168: ESI-MS spectrum of $[Pd_2\mathbf{L^1}_2\mathbf{L^A}_2$ + m $\mathbf{G^6}$ + n $BF_4]^{(4-[m+n])+}$ and inset of comparison of measured and calculated mass.

4.6.7 Titration of G^7 to $Pd_2L^1{}_2L^A{}_2$

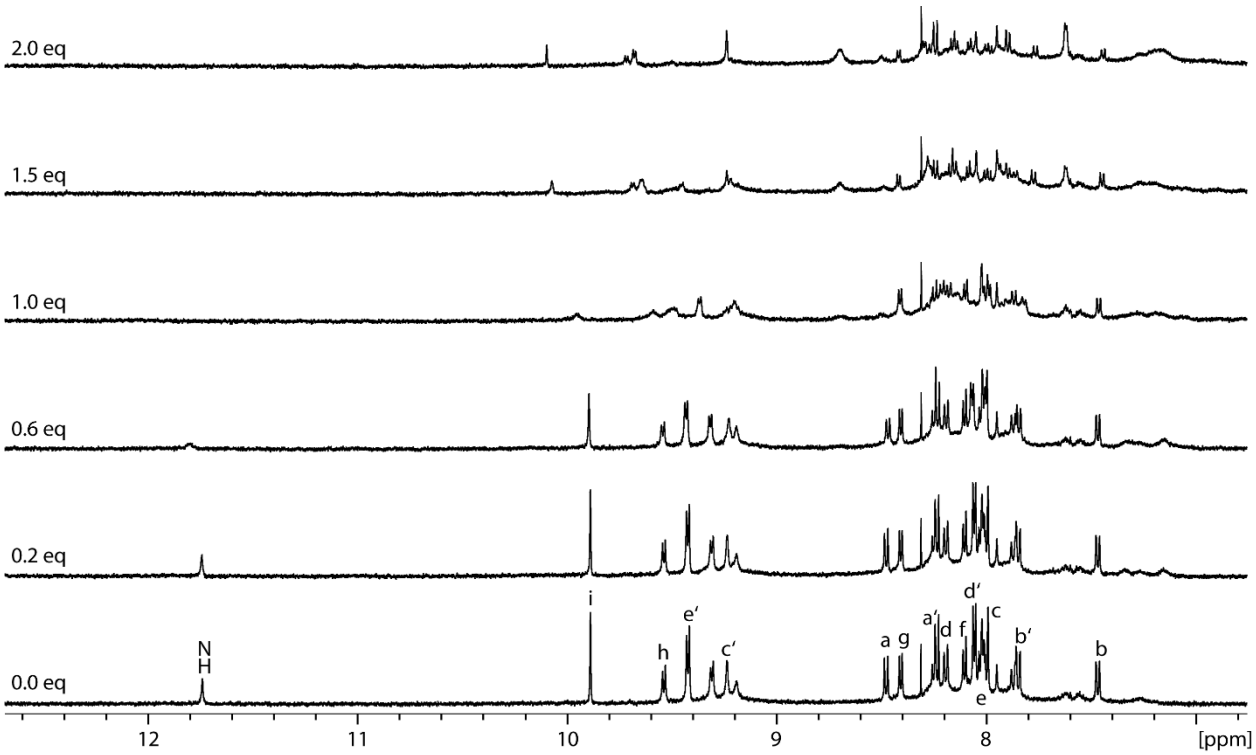

Figure 4.169: Stacked partial ^{1}H NMR spectra (500 MHz, 298 K, DMSO-d_6) of $\mathbf{G^7}$@$Pd_2\mathbf{L^1}_2\mathbf{L^A}_2$.

4.6.8 Titration of G^8 to $Pd_2L^1{}_2L^A{}_2$

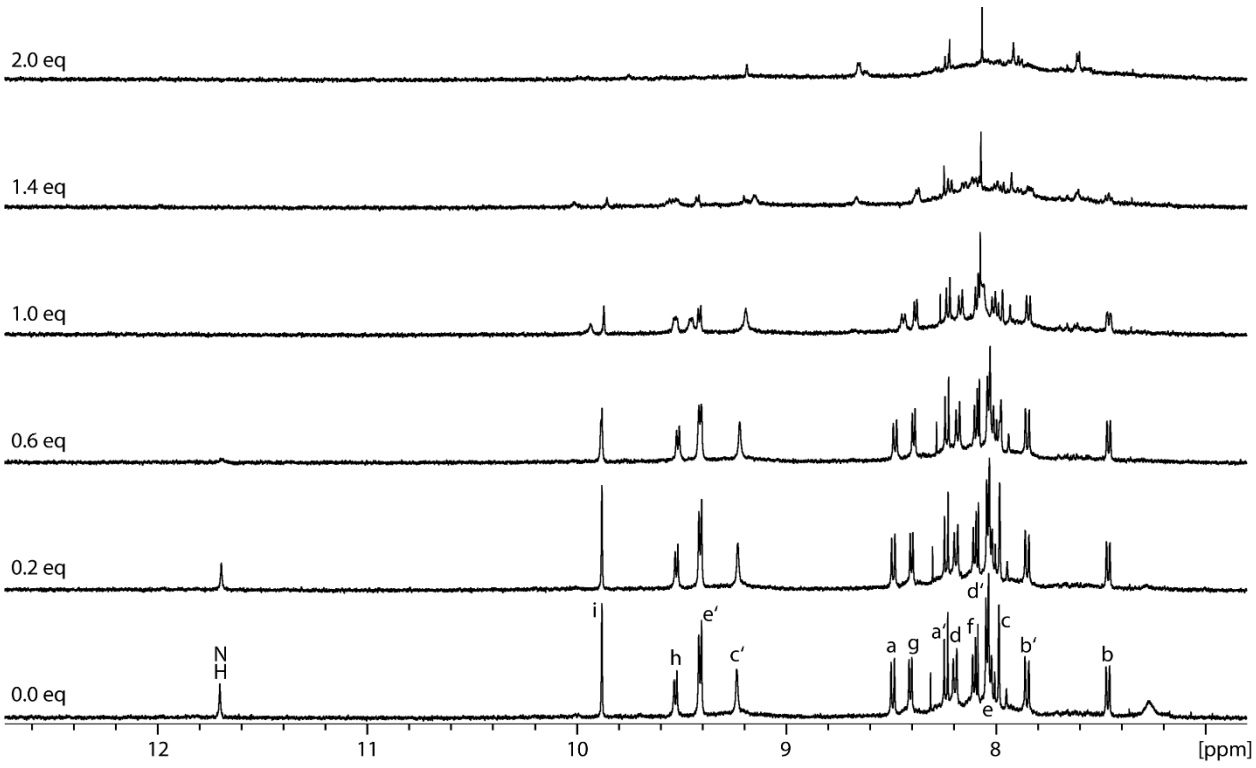

Figure 4.170: Stacked partial ^{1}H NMR spectra (500 MHz, 298 K, DMSO-d_6) of $\mathbf{G^8}$@$Pd_2\mathbf{L^1}_2\mathbf{L^A}_2$.

4.6.9 Titration of G^9 to $Pd_2L^1{}_2L^A{}_2$

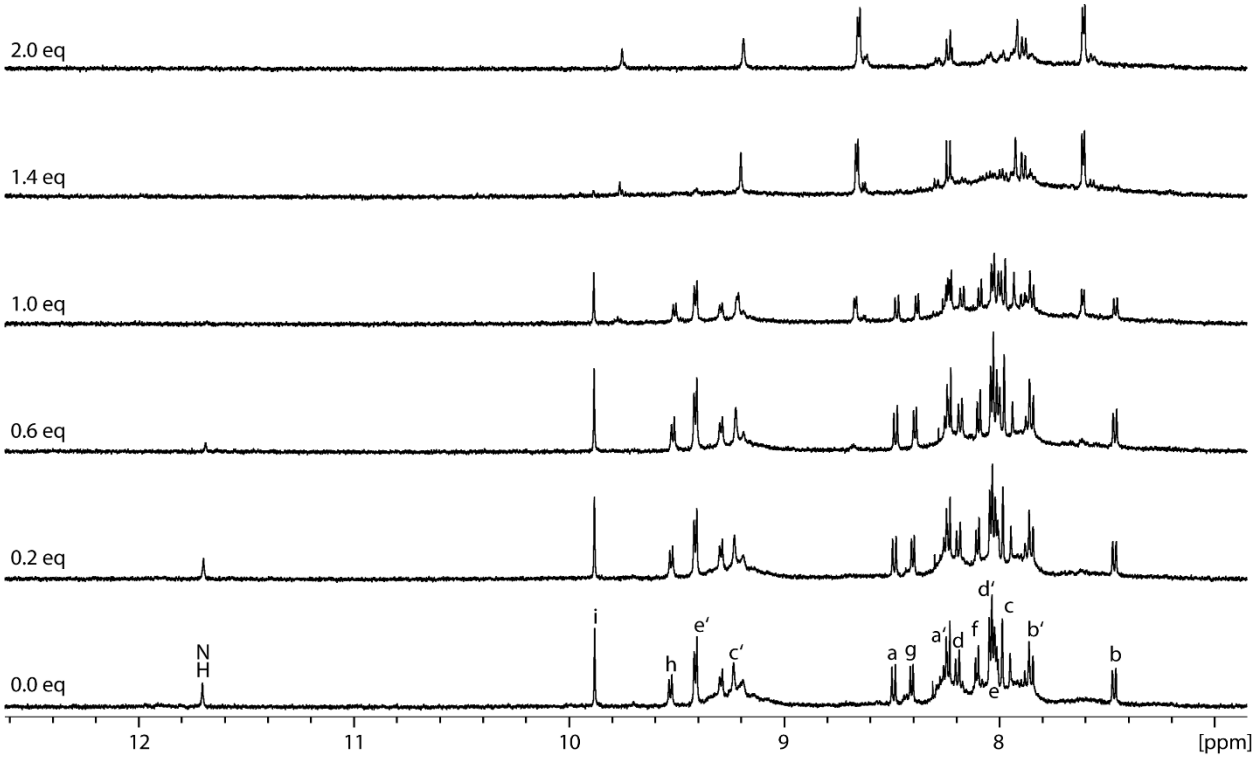

Figure 4.171: Stacked partial ^{1}H NMR spectra (500 MHz, 298 K, DMSO-d_6) of $\mathbf{G^9}$@$Pd_2\mathbf{L^1}_2\mathbf{L^A}_2$.

4.6.10 Titration of G^3 to $Pd_2L^1{}_2L^B{}_2$

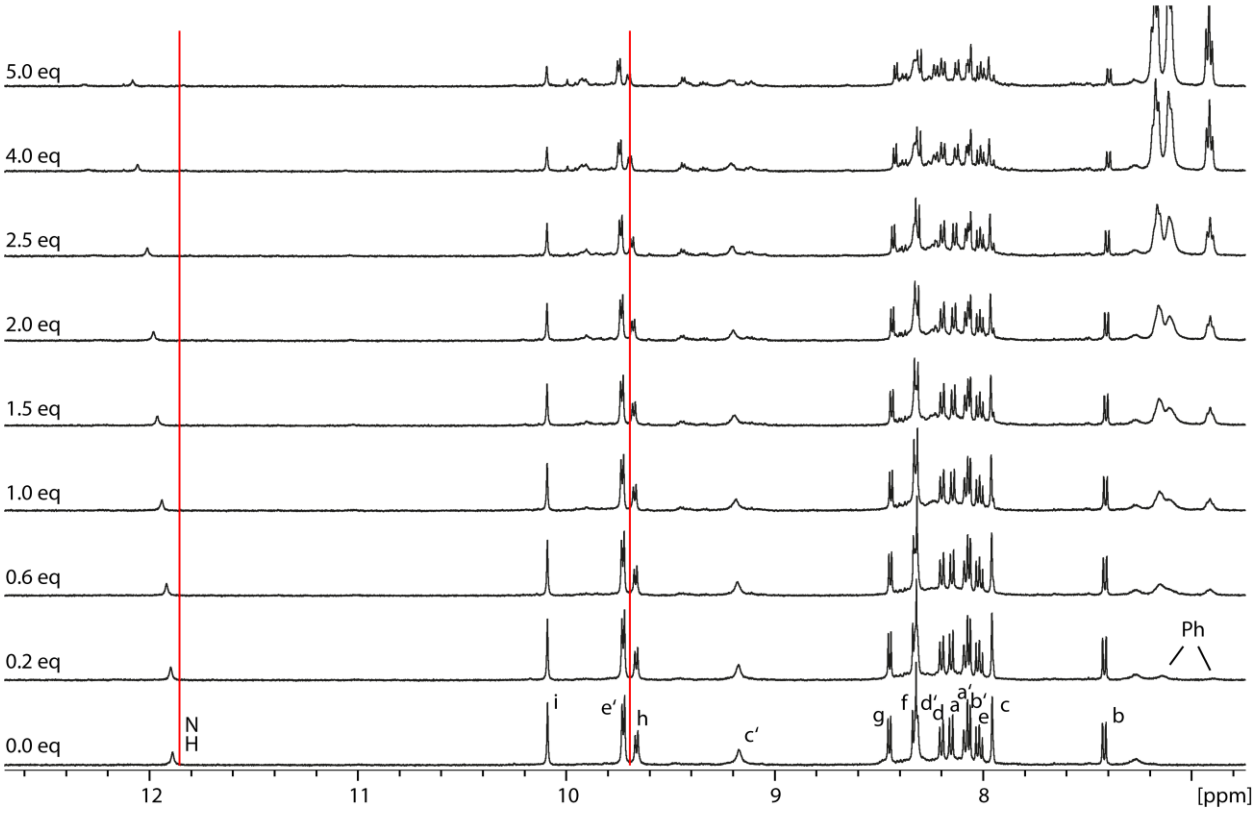

Figure 4.172: Stacked partial ^{1}H NMR spectra (500 MHz, 298 K, DMSO-d_6) of $\mathbf{G^3}$@$Pd_2\mathbf{L^1}_2\mathbf{L^B}_2$.

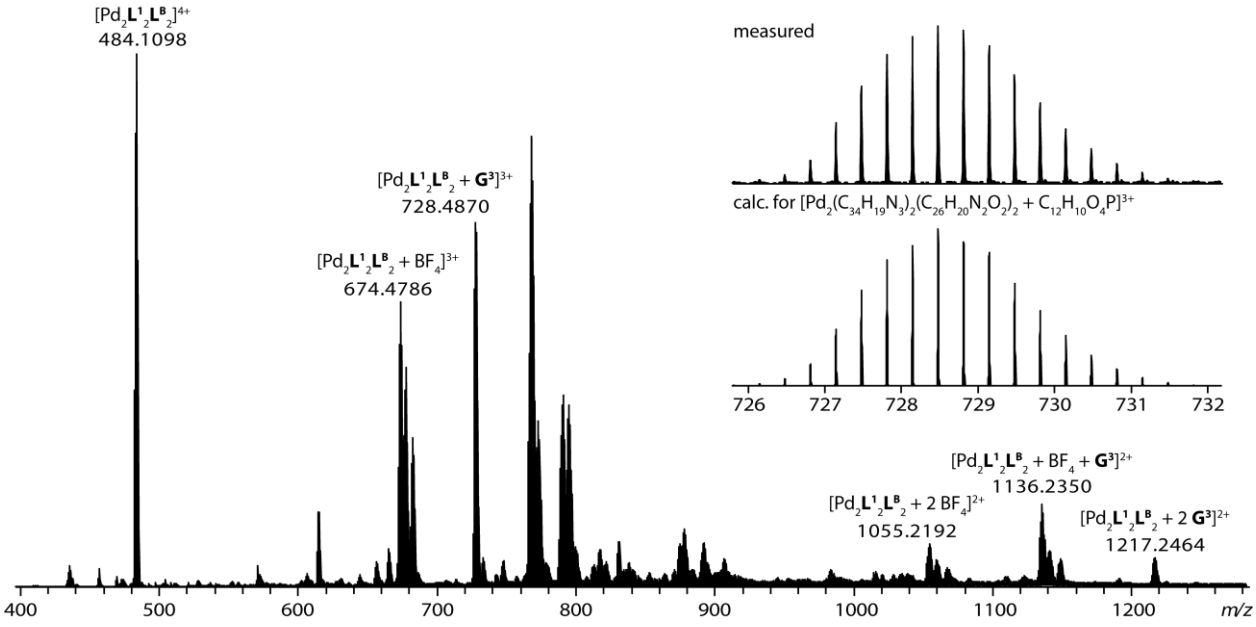

Figure 4.173: ESI-MS spectrum of $[Pd_2\mathbf{L^1}_2\mathbf{L^B}_2$ + m $\mathbf{G^3}$ + n $BF_4]^{(4-[m+n])+}$ and inset of comparison of measured and calculated mass.

4.6.11 Titration of G^3 to $Pd_2L^1{}_2L^C{}_2$

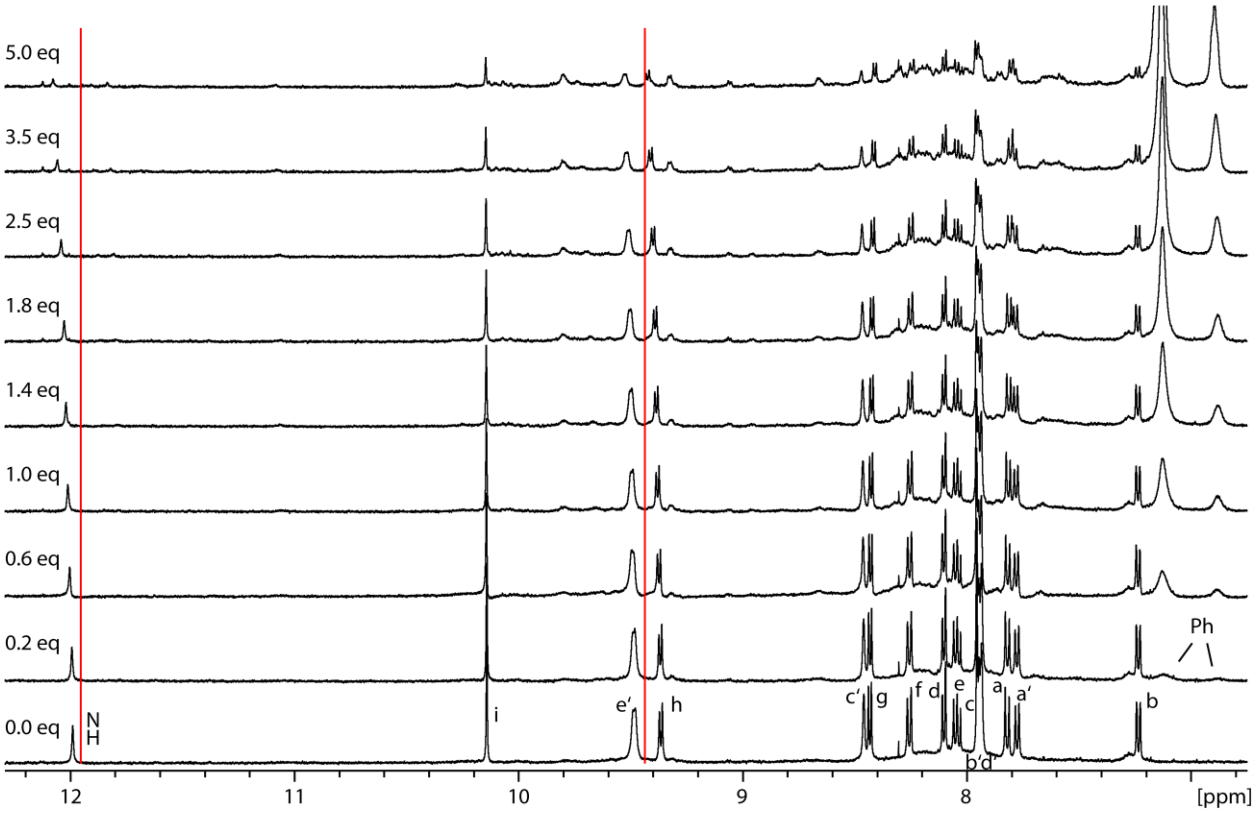

Figure 4.174: Stacked partial ^{1}H NMR spectra (500 MHz, 298 K, DMSO-d$_6$) of $\mathbf{G^3}$@$Pd_2\mathbf{L^1}_2\mathbf{L^C}_2$.

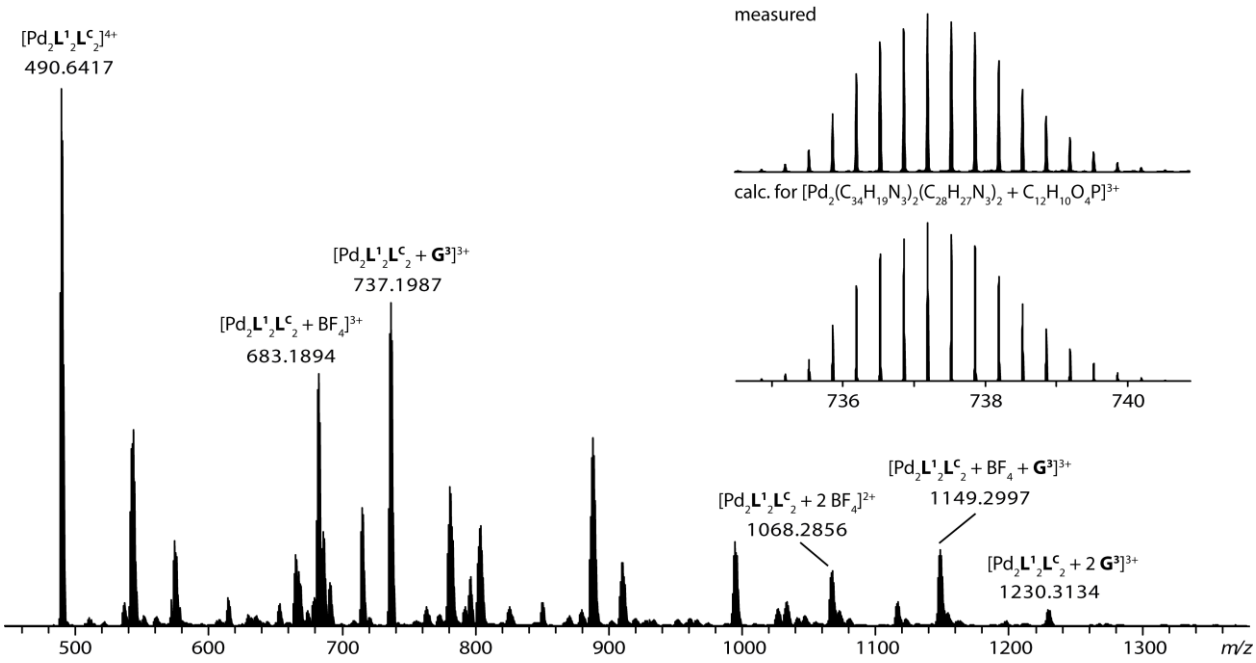

Figure 4.175: ESI-MS spectrum of $[Pd_2\mathbf{L^1}_2\mathbf{L^C}_2$ + m $\mathbf{G^3}$ + n $BF_4]^{(4-[m+n])+}$ and inset of comparison of measured and calculated mass.

4.6.12 Titration of G^3 to $Pd_2L^1{}_2L^D{}_2$

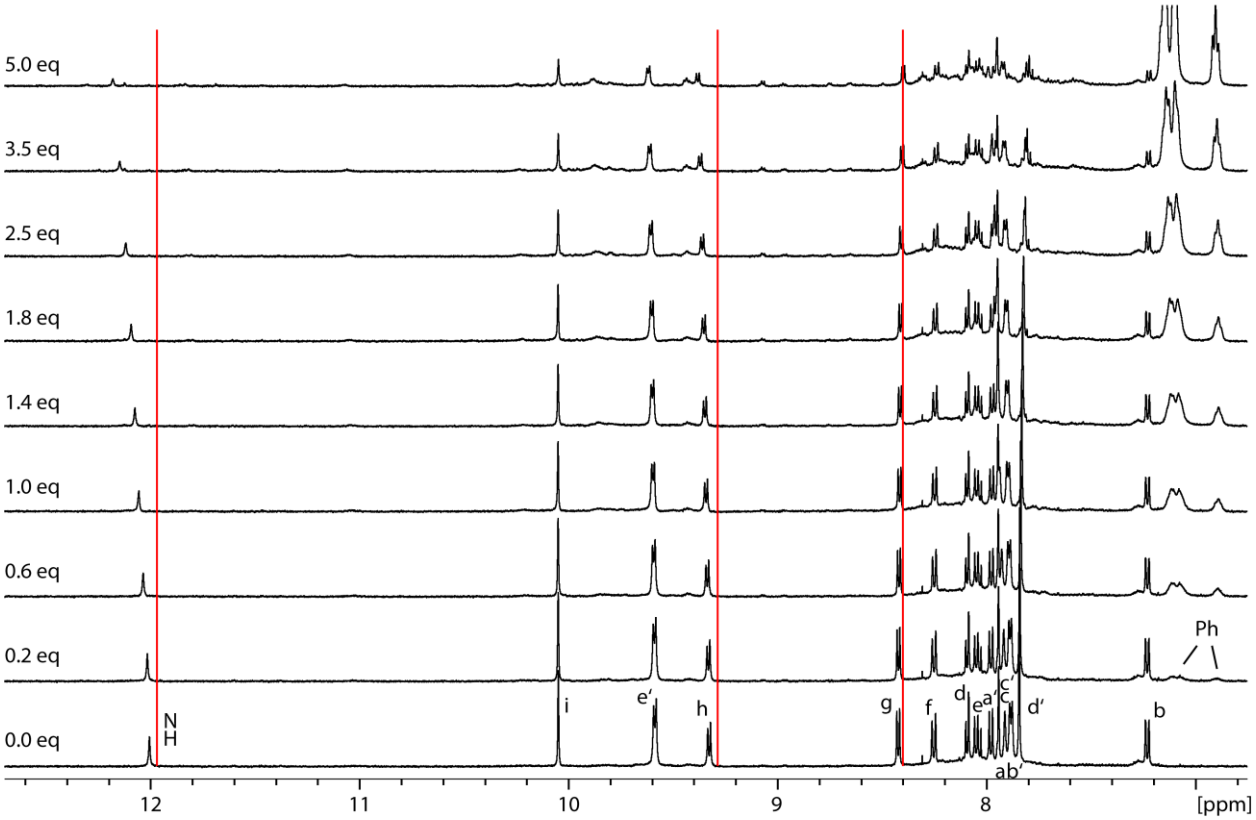

Figure 4.176: Stacked partial ^{1}H NMR spectra (500 MHz, 298 K, DMSO-d_6) of $\mathbf{G^3}$@$Pd_2\mathbf{L^1}_2\mathbf{L^D}_2$.

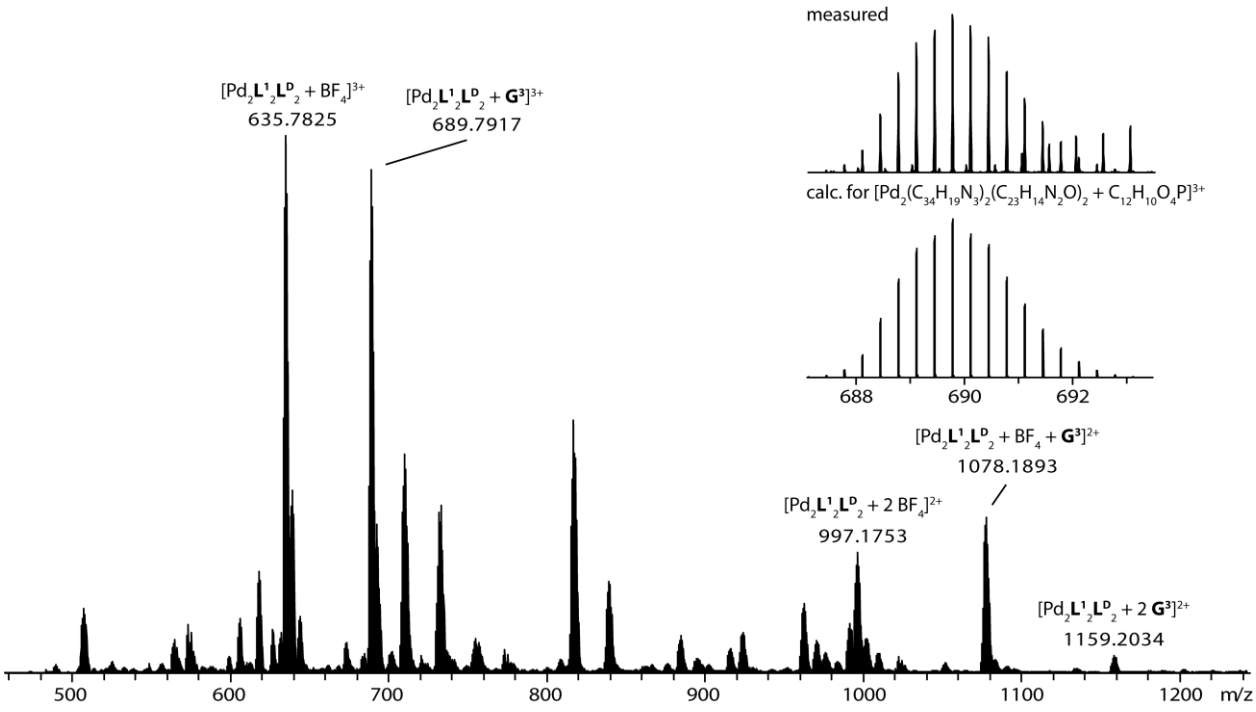

Figure 4.177: ESI-MS spectrum of $[Pd_2\mathbf{L^1}_2\mathbf{L^D}_2$ + m $\mathbf{G^3}$ + n $BF_4]^{(4-[m+n])+}$ and inset of comparison of measured and calculated mass.

4.6.13 Titration of G^3 to $Pd_2L^2{}_2L^A{}_2$

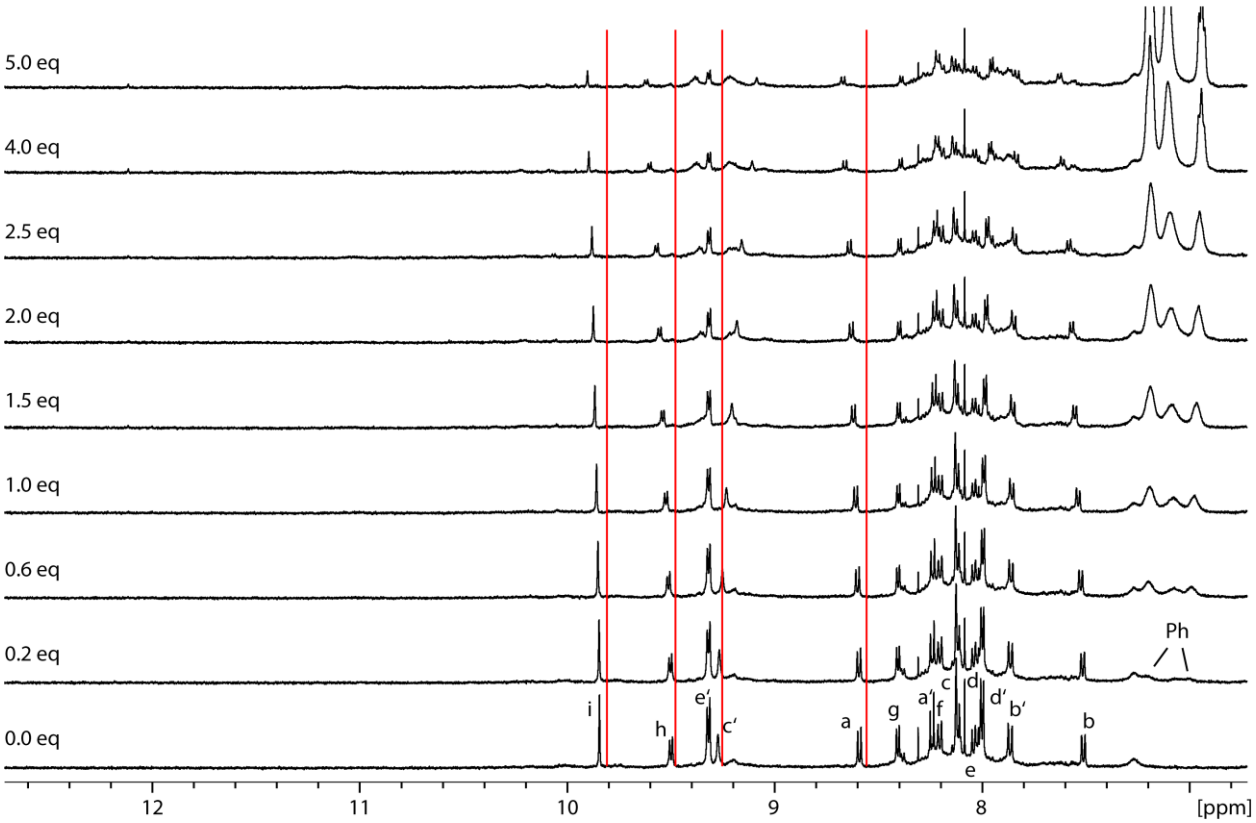

Figure 4.178: Stacked partial ^{1}H NMR spectra (500 MHz, 298 K, DMSO-d_6) of $\mathbf{G^3}$@$Pd_2\mathbf{L^2}_2\mathbf{L^A}_2$.

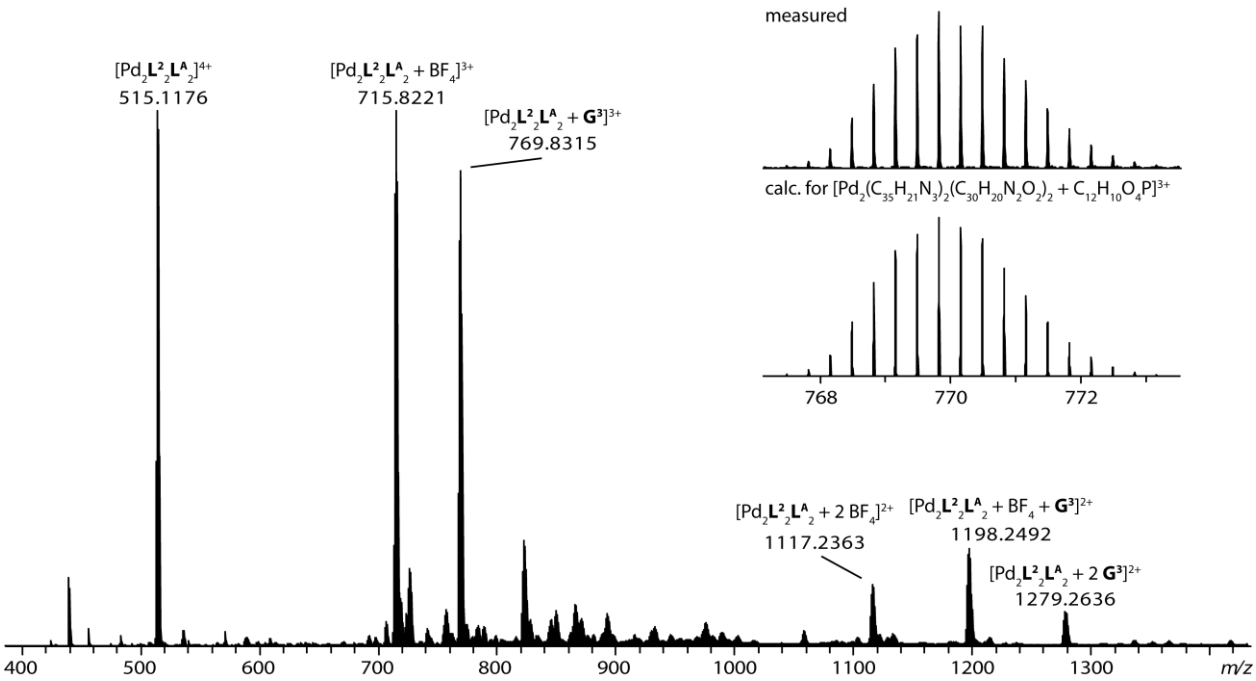

Figure 4.179: ESI-MS spectrum of $[Pd_2\mathbf{L^2}_2\mathbf{L^A}_2 + m\ \mathbf{G^3} + n\ BF_4]^{(4-[m+n])+}$ and inset of comparison of measured and calculated mass.

4.6.14 Titration of G^3 to $Pd_2L^2{}_2L^B{}_2$

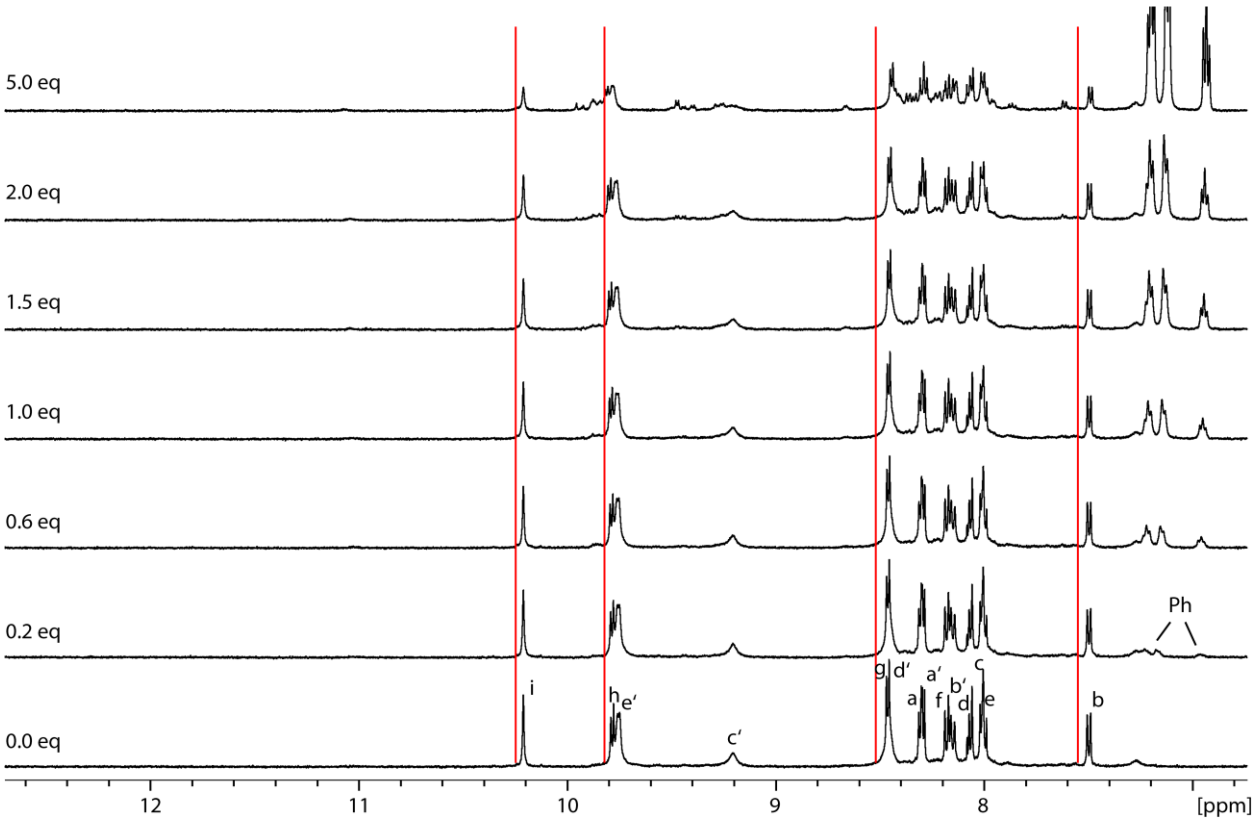

Figure 4.180: Stacked partial ^{1}H NMR spectra (500 MHz, 298 K, DMSO-d_6) of $\mathbf{G^3}$@$Pd_2\mathbf{L^2}_2\mathbf{L^B}_2$.

4.6.15 Titration of G^3 to $Pd_2L^3{}_2L^A{}_2$

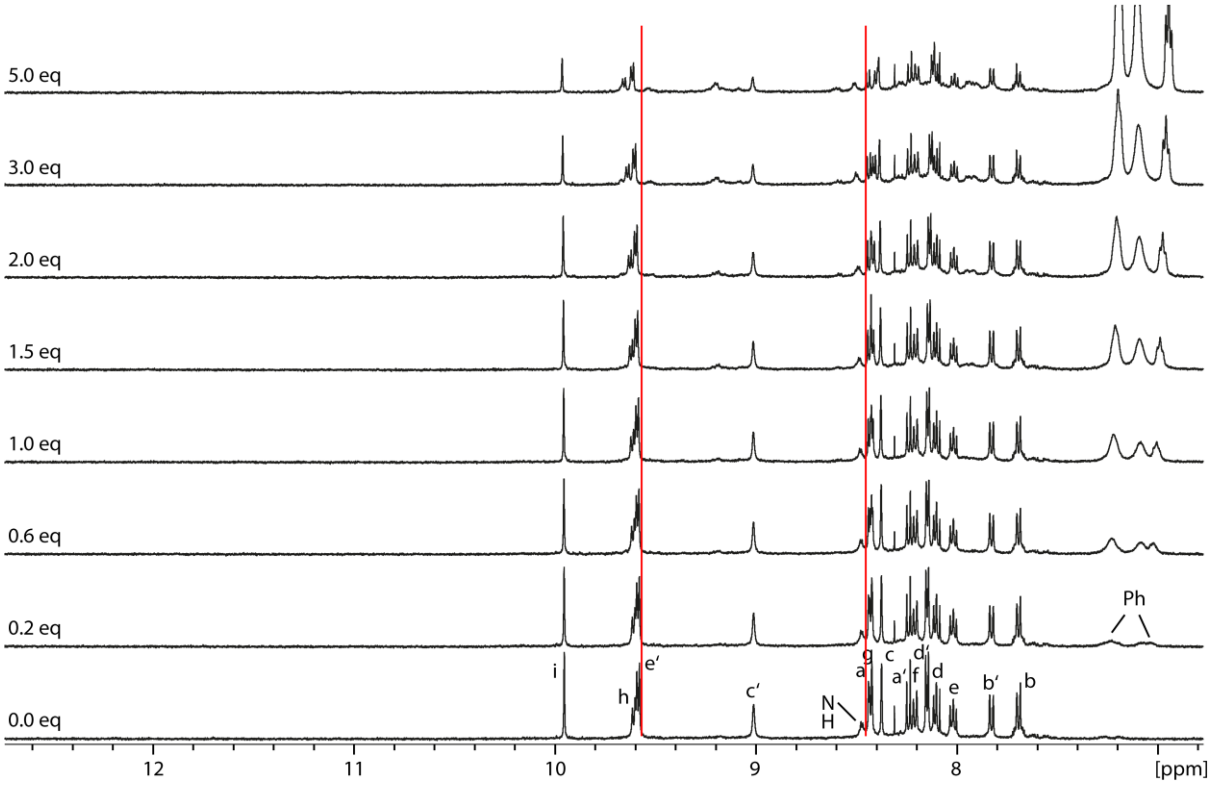

Figure 4.181: Stacked partial ^{1}H NMR spectra (500 MHz, 298 K, DMSO-d_6) of $\mathbf{G^3}$@$Pd_2\mathbf{L^3}{}_2\mathbf{L^A}{}_2$.

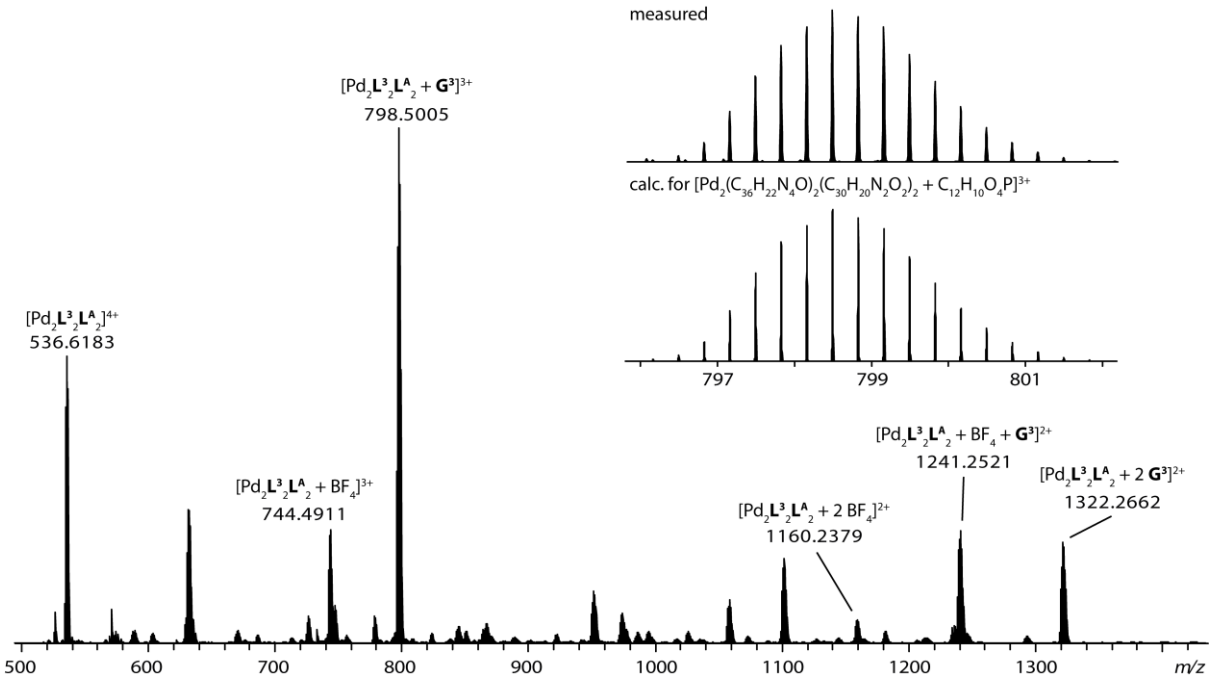

Figure 4.182: ESI-MS spectrum of $[Pd_2\mathbf{L^3}{}_2\mathbf{L^A}{}_2$ + m $\mathbf{G^3}$ + n $BF_4]^{(4-[m+n])+}$ and inset of comparison of measured and calculated mass.

4.6.16 Titration of G^3 to $Pd_2L^4{}_2L^A{}_2$

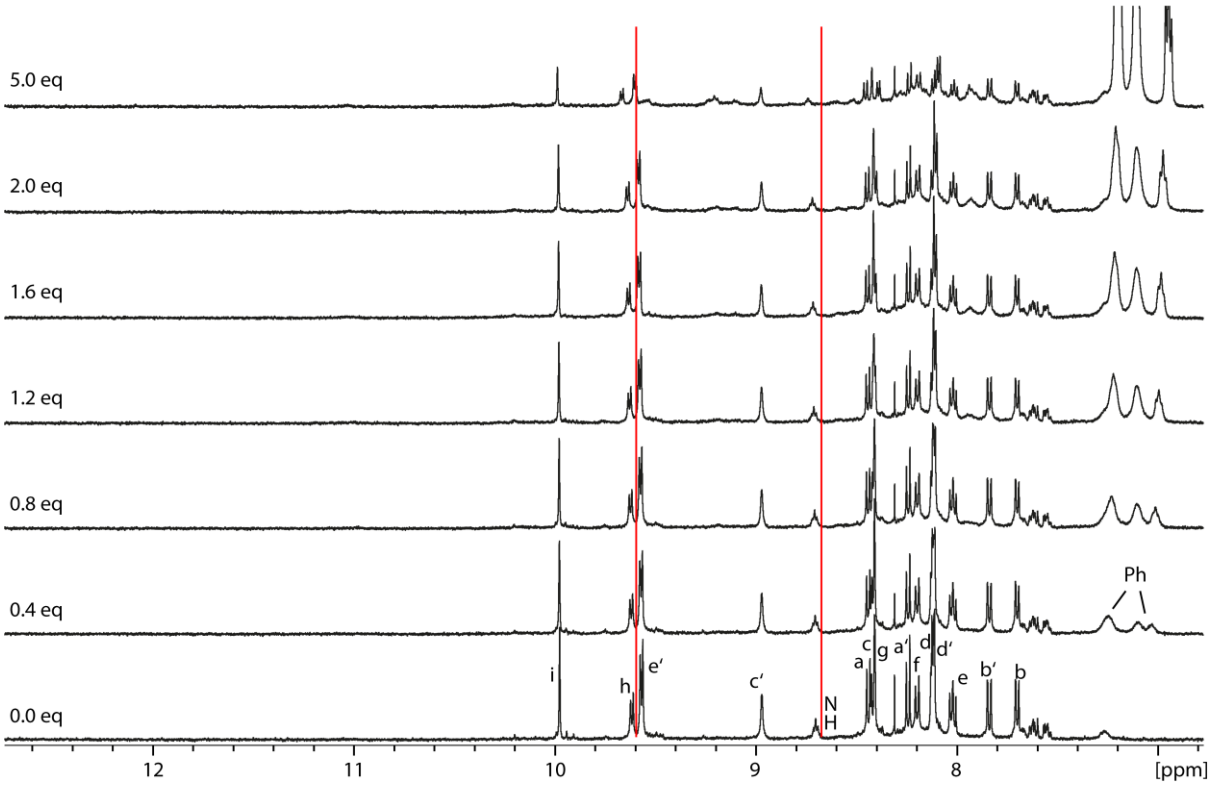

Figure 4.183: Stacked partial ^{1}H NMR spectra (500 MHz, 298 K, DMSO-d_6) of $\mathbf{G^3}$@$Pd_2\mathbf{L^4}{}_2\mathbf{L^A}{}_2$.

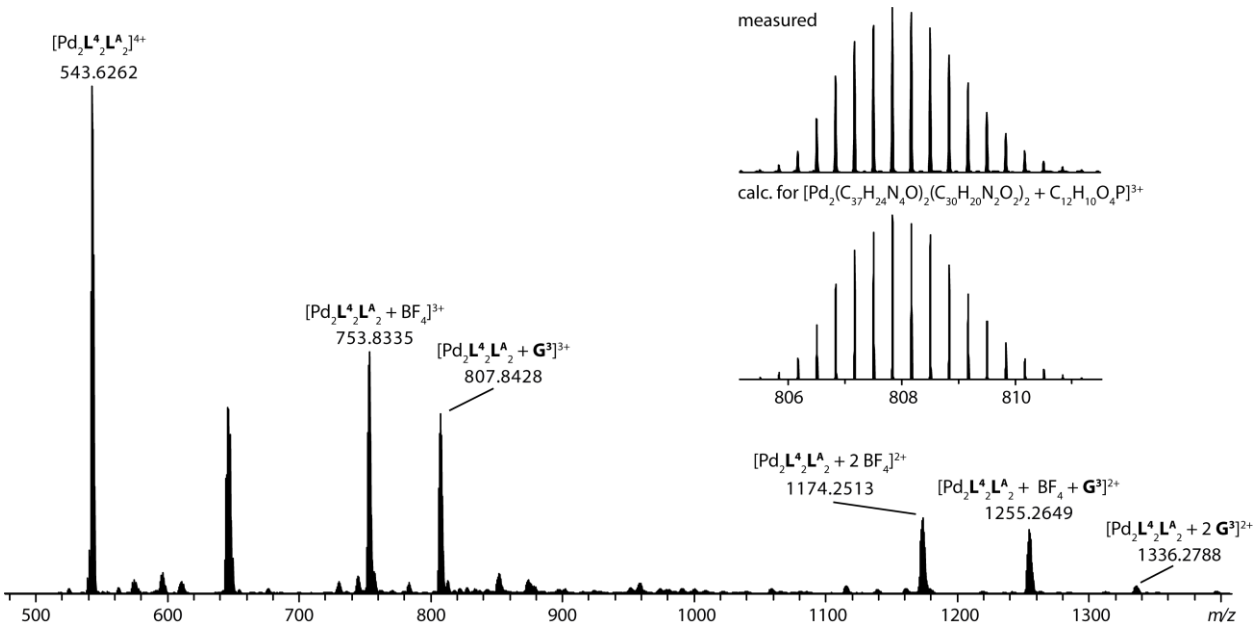

Figure 4.184: ESI-MS spectrum of $[Pd_2\mathbf{L^4}{}_2\mathbf{L^A}{}_2$ + m $\mathbf{G^3}$ + n $BF_4]^{(4-[m+n])+}$ and inset of comparison of measured and calculated mass.

4.6.17 Titration of G^3 to $Pd_2L^1{}_2L^A{}_2$ in DMF-d_7

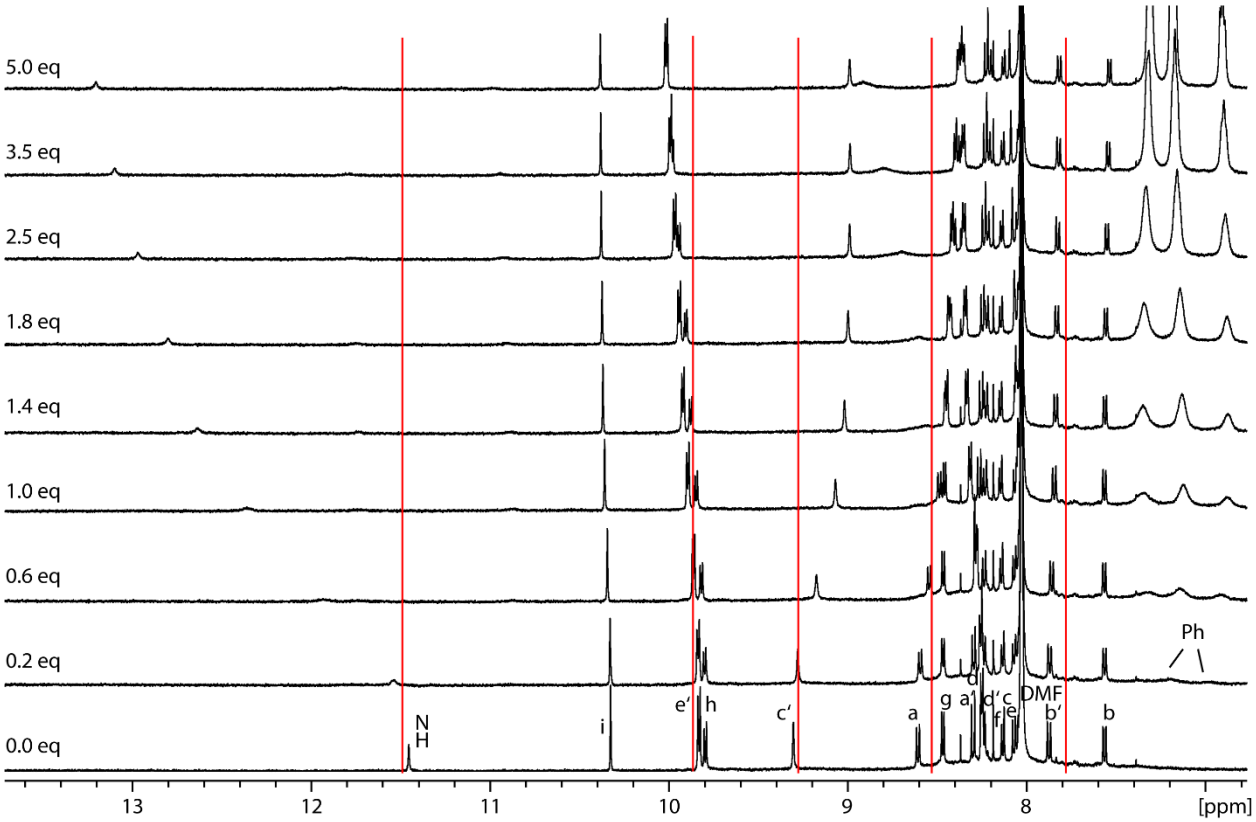

Figure 4.185: Stacked partial ^{1}H NMR spectra (500 MHz, 298 K, DMF-d_7) of $\mathbf{G^3}$@$Pd_2\mathbf{L^1}{}_2\mathbf{L^A}{}_2$.

4.6.18 Titration of G^3 to $Pd_2L^2_2L^A_2$ in DMF-d_7

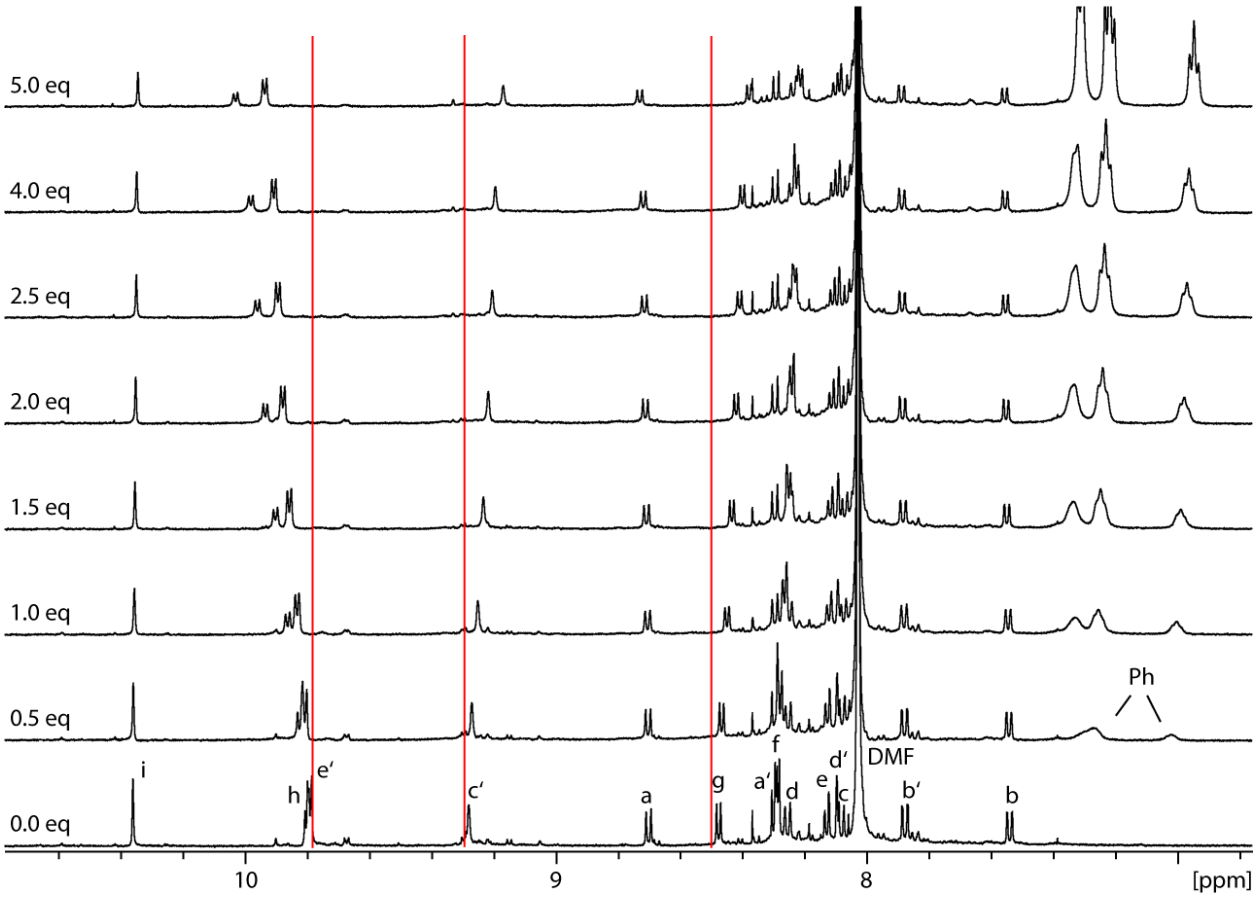

Figure 4.186: Stacked partial ^{1}H NMR spectra (500 MHz, 298 K, DMF-d_7) of $\mathbf{G^3}$@$Pd_2\mathbf{L^2}_2\mathbf{L^A}_2$.

Table 4.1: Overview of obtained binding constants K [M^{-1}].

DMSO-d_6	$\mathbf{G^3}$	$\mathbf{G^5}$	$\mathbf{G^6}$
$Pd_2\mathbf{L^1}_2\mathbf{L^A}_2$	2062 ± 31	1432 ± 117	513 ± 17
$Pd_2\mathbf{L^1}_2\mathbf{L^B}_2$	98 ± 1		
$Pd_2\mathbf{L^2}_2\mathbf{L^A}_2$	77 ± 3		
$Pd_2\mathbf{L^2}_2\mathbf{L^B}_2$	no binding		
$Pd_2\mathbf{L^3}_2\mathbf{L^A}_2$	128 ± 3		
$Pd_2\mathbf{L^4}_2\mathbf{L^A}_2$	46 ± 2		
$Pd_2\mathbf{L^1}_2\mathbf{L^C}_2$	33 ± 1		
$Pd_2\mathbf{L^1}_2\mathbf{L^D}_2$	149 ± 1		
DMF-d_7	$\mathbf{G^3}$		
$Pd_2\mathbf{L^1}_2\mathbf{L^A}_2$	1734 ± 97		
$Pd_2\mathbf{L^2}_2\mathbf{L^A}_2$	199 ± 6		

4.7 Guest Competition Experiments

Since it was not possible to determine binding constants for the aliphatic guest molecules, we performed guest competition experiments to test for the relative binding affinity of aliphatic **G⁴** compared to aromatic **G³**, qualitatively. Therefore, first 1 eq of **G⁴** was added to a solution of $Pd_2\mathbf{L^1}_2\mathbf{L^A}_2$, followed by 1 eq of **G³**. NMR spectra were recorded immediately and 24 and 48 h after addition of **G³**. As a result, compared to the spectrum of pure $\mathbf{G^3}@Pd_2\mathbf{L^1}_2\mathbf{L^A}_2$, the aliphatic guest was found to be fully replaced by the aromatic one, indicating that **G³** has a higher affinity to the host than **G⁴**.

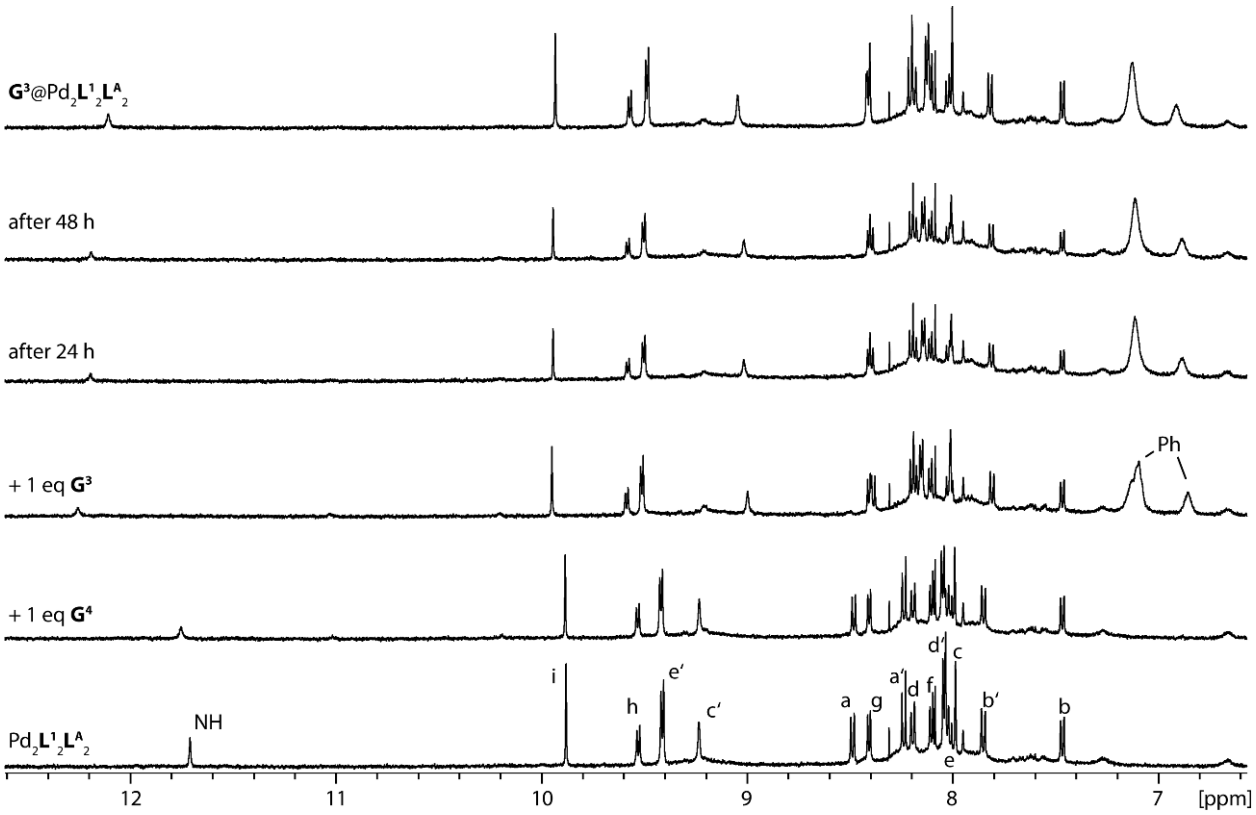

Figure 4.187: Stacked partial ^{1}H NMR spectra (500 MHz, 298 K, DMSO-d_6) of guest competition titration.

Next, the order of guest addition was exchanged. First, 1 eq of **G³** was added, yielding the host-guest complex $\mathbf{G^3}@Pd_2\mathbf{L^1}_2\mathbf{L^A}_2$, followed by addition of 1 eq of **G⁴**, leading to only a slight further downfield shift of the inward pointing NH proton, expected for a situation where **G³** is the stronger binding guest (the additional downfield shift is explainable by the doubling of the phosphate guest concentration in this experiment, regardless of substituent). Again, this experiment confirms that **G³** is the stronger binding guest.

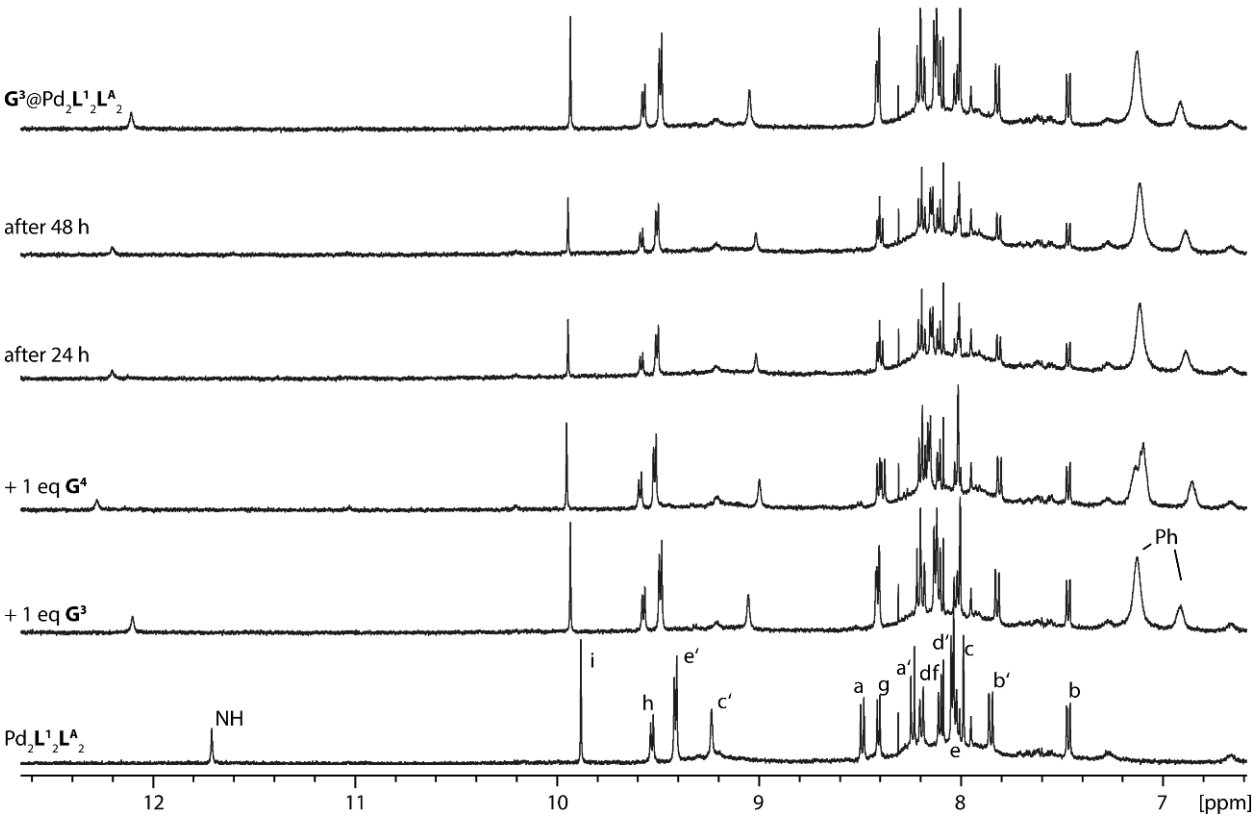

Figure 4.188: Stacked partial ^{1}H NMR spectra (500 MHz, 298 K, DMSO-d_6) of guest competition titration.

4.8 Single-Crystal X-ray Structure Analysis

Crystal preparation, measurement and refinement was performed by Dr. S. Hasegawa and Dr. J. J. Holstein. The structures of complexes [$Pd_2\mathbf{L^1}_2\mathbf{L^A}_2$], [$\mathbf{G^3}$@$Pd_2\mathbf{L^1}_2\mathbf{L^A}_2$] and [$\mathbf{G^5}$@$Pd_2\mathbf{L^1}_2\mathbf{L^A}_2$] were studied using single-crystal X-ray crystallography. Due to very thin plate-shaped crystals, the analysis was hampered by the limited scattering power of the samples not allowing to reach the desired (sub-)atomic resolution using our modern microfocussed X-ray in-house CuKα source. Gaining detailed structural insight required cryogenic crystal handling and highly brilliant synchrotron radiation. Hence, diffraction data of all three supramolecular assemblies was collected during two beamtime shifts at macromolecular synchrotron beamline P11, PETRA III, DESY.[187] Counterion and solvent flexibility required carefully adapted macromolecular refinement protocols employing geometrical restraint dictionaries, similarity restraints and restraints for anisotropic displacement parameters (ADPs).

Table 4.2: Crystal data and structure refinement for cage assemblies $[Pd_2L^1{}_2L^A{}_2]$, $[G^3@Pd_2L^1{}_2L^A{}_2]$ and $[G^5@Pd_2L^1{}_2L^A{}_2]$

Compound	$[Pd_2\mathbf{L^1}_2\mathbf{L^A}_2]$	$[\mathbf{G^3}@Pd_2\mathbf{L^1}_2\mathbf{L^A}_2]$	$[\mathbf{G^5}@Pd_2\mathbf{L^1}_2\mathbf{L^A}_2]$
CIF ID	**ap136d**	**ap214**	**ap217_sq**
CCDC number	**2180522**	**2180523**	**2180524**
Empirical formula	$C_{176}H_{140}B_4F_{16}N_{12}O_6Pd_2$	$C_{170}H_{142}B_2F_8N_{12}O_{17}P_2Pd_2$	$C_{324}H_{240}B_4F_{16}N_{24}O_{28}P_4Pd_4$
Formula weight	3079.03	3073.31	5814.11
Temperature [K]	100(2)	100(2)	100(2)
Crystal system	triclinic	monoclinic	monoclinic
Space group (number)	$P\bar{1}$ (2)	$C2/c$ (15)	$C2/c$ (15)
a [Å]	17.287(4)	44.284(9)	44.281(9)
b [Å]	20.596(4)	17.110(3)	16.740(3)
c [Å]	22.355(5)	21.142(4)	21.175(4)
α [Å]	78.53(3)	90	90
β [Å]	76.99(3)	96.51(3)	96.36(3)
γ [Å]	85.78(3)	90	90
Volume [Å^3]	7597(3)	15916(6)	15600(5)
Z	2	4	2
ρ_{calc} [g/cm^3]	1.346	1.283	1.238
μ [mm^{-1}]	0.291	0.293	0.399
F(000)	3168	6344	5968
Crystal size [mm^3]	0.060×0.020×0.010	0.300×0.300×0.001	0.100×0.100×0.005
Crystal colour	colourless	colourless	colourless
Crystal shape	plate	plate	plate
Radiation	synchrotron (λ=0.6888 Å)	synchrotron (λ=0.6888 Å)	synchrotron (λ=0.77491 Å)
2Θ range [°]	1.84 to 55.38 (0.74 Å)	1.79 to 55.66 (0.74 Å)	2.02 to 55.88 (0.83 Å)
Index ranges	-20 ≤ h ≤ 20 -26 ≤ k ≤ 26 -29 ≤ l ≤ 29	-53 ≤ h ≤ 53 -20 ≤ k ≤ 19 -26 ≤ l ≤ 26	-45 ≤ h ≤ 45 -19 ≤ k ≤ 20 -25 ≤ l ≤ 24
Reflections collected	93015	95335	66738
Independent reflections	25824 R_{int} = 0.0260 R_{sigma} = 0.0236	16159 R_{int} = 0.0285 R_{sigma} = 0.0189	10988 R_{int} = 0.0211 R_{sigma} = 0.0138
Completeness	84.5 %	96.2 %	77.8 %
Data/Restraints/Parameters	25824/4462/2336	16159/270/1023	10988/1384/912
Goodness-of-fit on F^2	1.008	1.051	1.140
Final *R* indexes [$I \geq 2\sigma(I)$]	R_1=0.0794, wR_2=0.2675	R_1=0.06, wR_2=0.2012	R_1=0.0720, wR_2=0.2351
Final *R* indexes [all data]	R_1=0.0844, wR_2=0.2733	R_1=0.071, wR_2=0.2096	R_1=0.078, wR_2=0.2475
Largest peak/hole [eÅ^{-3}]	4.13/-0.98	1.56/-1.09	0.76/-1.06

4.8.1 Data Collection and Refinement Details of $[Pd_2L^1{}_2L^A{}_2]$, ap136d

Single crystals were grown by slow diffusion of toluene into a solution of $[Pd_2\mathbf{L^1}_2\mathbf{L^A}_2]$ in DMF. A single crystal of $[Pd_2\mathbf{L^1}_2\mathbf{L^A}_2]$ in mother liquor was pipetted onto a glass slide containing NVH oil. To avoid cracking of the crystal, the crystal was quickly mounted onto a 0.06 mm nylon loop and immediately flash cooled in liquid nitrogen. Crystals were stored at cryogenic temperature in dry shippers, in which they were safely transported to macromolecular beamline P11 at Petra III, DESY, Germany. A wavelength of λ = 0.6888 Å was chosen using a liquid N_2 cooled double crystal monochromator. Single crystal X-ray diffraction data was collected at 100(2) K on a single axis goniometer, equipped with an Oxford Cryostream 800 open flow cooling device and an Eiger 2 12M detector.

3600 diffraction images were collected in a 360° φ sweep at a detector distance of 154 mm, 100% filter transmission, 0.1° step width and 50 ms exposure time per image. Data integration and reduction were undertaken using XDS.[188] The structure was solved by intrinsic phasing/direct methods using SHELXT[189] and refined with SHELX[190] using 22 cpu cores for full-matrix least-squares routines on F^2 and ShelXle[191] as a graphical user interface and the DSR program plugin was employed for modeling.[192,193]

The asymmetric unit contains a full cage. Two of the four co-crystallised tetrafluoroborate was modelled with two discrete positions refining their occupancy factor to 78:22 using a free variable. Four of the five co-crystallised toluene molecules as well as one of the two co-crystallised DMF molecules were modelled disordered refining their occupancy factor with a free variable for to 66%:34% for Toluene in residue 21-22 and 78%:22% for Dimethylformamide in residue 11-12. An additional free variable was refined to occupancy of 67%:53% for Toluene in residues 19-20, 24-25, 28-29 as well as Tetrafluoroborate in residues 9-10, al of which are in closed proximity to each other.

Despite reaching 0.74 Å resolution, disorder and poor crystal quality required stereochemical restraints to be employed for ensuring a sensible geometry of the organic part of the structure.

Stereochemical restraints for the ligands $\mathbf{L^1}$ (residue class ICZ) and $\mathbf{L^A}$ (residue class MPR) and co-crystallised Toluene (residue class TOL) and Dimethylformamide (residue class DMF) solvent molecules were generated by the GRADE program using the GRADE Web Server (http://grade.globalphasing.org) and applied in the refinement. A GRADE dictionary for SHELXL contains target values and standard deviations for 1,2-distances (DFIX) and 1,3-distances (DANG), as well as restraints for planar groups (FLAT). All

displacements for non-hydrogen atoms were refined anisotropically. The refinement of ADP's for carbon, nitrogen, oxygen, boron and fluorine atoms was enabled by a combination of similarity restraints (SIMU) with lowered standard deviation of [0.02 0.04] and rigid bond restraints (RIGU).[194] For disordered toluene molecules in residues 24-25 additional ISOR restraints were applied.

4.8.2 Data Collection and Refinement Details of [G^3@$Pd_2L^1{}_2L^A{}_2$], ap214

Single crystals were grown by slow diffusion of diethylether into a solution of [$\mathbf{G^3}$@$Pd_2\mathbf{L^1}_2\mathbf{L^A}_2$] in DMF. A single crystal of [$\mathbf{G^3}$@$Pd_2\mathbf{L^1}_2\mathbf{L^A}_2$] in mother liquor was pipetted onto a glass slide containing NVH oil. To avoid cracking of the crystal, the crystal was quickly mounted onto a 0.3 mm nylon loop and immediately flash cooled in liquid nitrogen. Crystals were stored at cryogenic temperature in dry shippers, in which they were safely transported to macromolecular beamline P11 at Petra III, DESY, Germany. A wavelength of λ = 0.6888 Å was chosen using a liquid N_2 cooled double crystal monochromator. Single-crystal X-ray diffraction data was collected at 100(2) K on a single axis goniometer, equipped with an Oxford Cryostream 800 open flow cooling device and an Eiger 2 12M detector.

3600 diffraction images were collected in a 360° φ sweep at a detector distance of 154 mm, 100% filter transmission, 0.1° step width and 10 ms exposure time per image. Data integration and reduction were undertaken using XDS.[188] The structure was solved by intrinsic phasing/direct methods using SHELXT[189] and refined with SHELXL[190] using 22 cpu cores for full-matrix least-squares routines on F^2 and ShelXle[191] as a graphical user interface and the DSR program plugin was employed for modeling.[192,193]

The asymmetric unit contains half a cage, one diphenylphosphate (residue class POB), one tetrafluoroborate counter ion (residue class BF4), three diethylether as well as one dimethylformamide solvent molecules. One of the three co-crystallised diethylether solvent molecules is close to a special position (2-fold axis) and was therefore modelled with negative PART and a fixed occupancy factor of 50%.

Despite reaching 0.74 Å resolution, disorder and poor crystal quality required stereochemical restraints to be employed for ensuring a sensible geometry of the solvent part of the structure.

Stereochemical restraints for the co-crystallised diethyether (residue class ETO) and dimethylformamide (residue class DMF) solvent molecules were generated by the

GRADE program using the GRADE Web Server (http://grade.globalphasing.org) and applied in the refinement. A GRADE dictionary for SHELXL contains target values and standard deviations for 1,2-distances (DFIX) and 1,3-distances (DANG), as well as restraints for planar groups (FLAT). All displacements for non-hydrogen atoms were refined anisotropically. The refinement of ADP's for carbon, nitrogen, oxygen, boron and fluorine atoms of dimethylformamide and diethylether in residues classes DMF and ETO was enabled by a combination of similarity restraints (SIMU) and rigid bond restraints (RIGU).[194] Rigid bond restraints (RIGU) were also employed for the phosphonate guest (G3) in residue class POB.

4.8.3 Data Collection and Refinement Details of [$\mathbf{G^5}$@$Pd_2\mathbf{L^1}_2\mathbf{L^A}_2$], ap217_sq

Single crystals were grown by slow diffusion of diethylether into a solution of [$\mathbf{G^5}$@$Pd_2\mathbf{L^1}_2\mathbf{L^A}_2$] in DMF. A single crystal of [$\mathbf{G^5}$@$Pd_2\mathbf{L^1}_2\mathbf{L^A}_2$] in mother liquor was pipetted onto a glass slide containing NVH oil. To avoid cracking of the crystal, the crystal was quickly mounted onto a 0.1 mm nylon loop and immediately flash cooled in liquid nitrogen. Crystals were stored at cryogenic temperature in dry shippers, in which they were safely transported to macromolecular beamline P11 at Petra III, DESY, Germany. A wavelength of λ = 0.77491 Å was chosen using a liquid N_2 cooled double crystal monochromator. Single crystal X-ray diffraction data was collected at 100(2) K on a single axis goniometer, equipped with an Oxford Cryostream 800 open flow cooling device and an Eiger 2 12M detector.

3600 diffraction images were collected in a 360° φ sweep at a detector distance of 154 mm, 100% filter transmission, 0.1° step width and 10 ms exposure time per image. Data integration and reduction were undertaken using XDS.[188] The structure was solved by intrinsic phasing/direct methods using SHELXT[189] and refined with SHELXL[190] using 22 cpu cores for full-matrix least-squares routines on F^2 and ShelXle[191] as a graphical user interface and the DSR program plugin was employed for modeling.[192,193]

The asymmetric unit contains half a cage, one ditoloylphosphate (residue class POT), one tetrafluoroborate counter ion (residue class BF4) and a co-crystallised dimethylformamide solvent molecule. Despite reaching 0.83 Å resolution, poor crystal quality required stereochemical restraints to be employed for ensuring a sensible

geometry of the solvent part of the structure.

Stereochemical restraints for the co-crystallised dimethylformamide (residue class DMF) solvent molecule were generated by the GRADE program using the GRADE Web Server (http://grade.globalphasing.org) and applied in the refinement. A GRADE dictionary for SHELXL contains target values and standard deviations for 1,2-distances (DFIX) and 1,3-distances (DANG), as well as restraints for planar groups (FLAT). All displacements for non-hydrogen atoms were refined anisotropically. The refinement of ADP's for carbon, nitrogen, oxygen, boron and fluorine atoms was enabled by a combination of similarity restraints (SIMU) and rigid bond restraints (RIGU).[194] The contribution of the electron density from disordered solvent molecules, which could not be modeled with discrete atomic positions were handled using the SQUEEZE[195] routine in PLATON.[196] The solvent mask file (.fab) computed by PLATON were included in the SHELXL refinement via the ABIN instruction leaving the measured intensities untouched.

4.9 Ion Mobility Measurements

Ion mobility measurements were performed on a Bruker timsTOF instrument combining a trapped ion mobility (TIMS) with a time-of-flight (TOF) mass spectrometer in one instrument.

In contrast to the conventional drift tube method to determine mobility data, where ions are carried by an electric field through a stationary drift gas, the TIMS method is based on an electric field ramp to hold ions in place against a carrier gas pushing them in the direction of the analyzer. Consequently, larger sized ions that experience more carrier gas impacts leave the TIMS units first and smaller ions elute later. This method offers a much higher mobility resolution despite a smaller device size.

Measurement: After the generation of ions by electrospray ionisation (ESI, analyte concentration: 0.07 mM, solvent: acetonitrile, capillary voltage: 3600 V, end plate offset voltage: 500 V, nebulizer gas pressure: 0.3 bar, dry gas flow rate: 3.0 $L \cdot min^{-1}$, dry temperature: 75 °C) the desired ions were orthogonally deflected into the TIMS cell consisting of an entrance funnel, the TIMS analyser (carrier gas: N_2, temperature: 305 K, entrance pressure: 2.55 mbar, exit pressure: 0.89 mbar, IMS imeX ramp end: 1.92 K_0^{-1}, IMS imeX ramp start: 0.54 K_0^{-1}) and an exit funnel. As a result, the ions are stationary trapped. After accumulation (accumulation time: 10 ms), a stepwise reduction of the

electric field strength leads to a release of ion packages separated by their mobility. After a subsequent focussing, the separated ions are transferred to the TOF-analyser.

The ion mobility *K* was directly calculated from the trapping electric field strength *E* and the velocity of the carrier gas stream v_g *via*

$$K = \frac{v_g}{E} = \frac{A}{U_{release} - U_{out}} \qquad (1)$$

where *A* is a calibration constant (based on calibration standards), $U_{release}$ is the voltage at which the ions are released from the analyser and U_{out} is the voltage applied to the exit of the tube. The ion mobility is corrected to standard gas density *via*

$$K_0 = K \frac{P}{1013\ \text{hPa}} \frac{273\ \text{K}}{T} \qquad (2)$$

to obtain the reduced mobility K_0, where *P* is the pressure and *T* is the temperature. By using the MASON-SCHAMP equation, the collisional cross-section Ω can be calculated:

$$\Omega = \frac{(18\pi)^{\frac{1}{2}}}{16} \frac{ze}{(k_B T)^{\frac{1}{2}}} \left[\frac{1}{\mu}\right]^{\frac{1}{2}} \frac{1}{K_0} \frac{1}{N_0} \qquad (3)$$

where *ze* is the ion charge, k_B is the BOLTZMANN constant, μ is the reduced mass of analyte and carrier gas and N_0 is the number density of the neutral gas.[197–199]

For calibration of both the TIMS and TOF analysers, commercially available Agilent ESI tuning mix was used. The instrument was calibrated before each measurement, including each change in the ion mobility resolution mode ("imeX" settings: survey, detect or ultra).

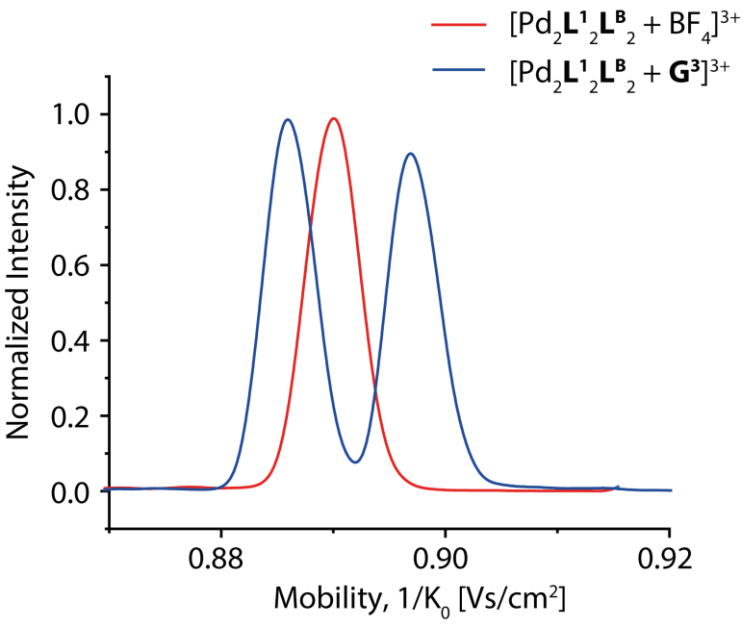

Figure 4.189: Ion-mobility mass spectra of $[Pd_2\mathbf{L}^{\mathbf{1}}{}_2\mathbf{L}^{\mathbf{B}}{}_2 + BF_4]^{3+}$ and $[Pd_2\mathbf{L}^{\mathbf{1}}{}_2\mathbf{L}^{\mathbf{B}}{}_2 + \mathbf{G}^{\mathbf{3}}]^{3+}$.

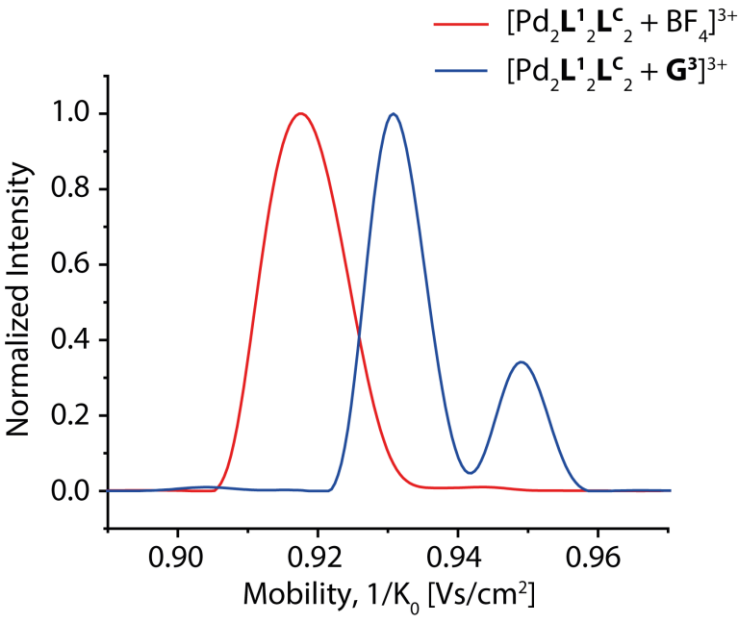

Figure 4.190: Ion-mobility mass spectra of $[Pd_2\mathbf{L}^{\mathbf{1}}{}_2\mathbf{L}^{\mathbf{C}}{}_2 + BF_4]^{3+}$ and $[Pd_2\mathbf{L}^{\mathbf{1}}{}_2\mathbf{L}^{\mathbf{C}}{}_2 + \mathbf{G}^{\mathbf{3}}]^{3+}$.

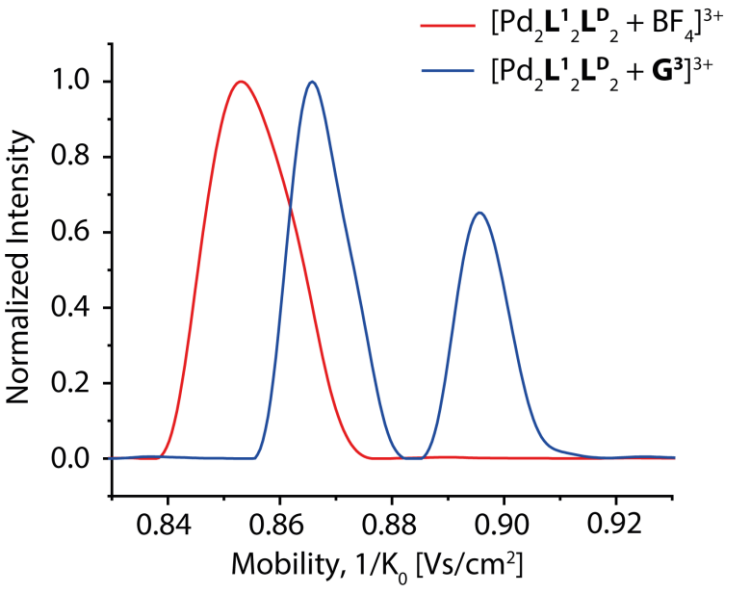

Figure 4.191: Ion-mobility mass spectra of $[Pd_2\mathbf{L}^{\mathbf{1}}{}_2\mathbf{L}^{\mathbf{D}}{}_2 + BF_4]^{3+}$ and $[Pd_2\mathbf{L}^{\mathbf{1}}{}_2\mathbf{L}^{\mathbf{D}}{}_2 + \mathbf{G}^{\mathbf{3}}]^{3+}$.

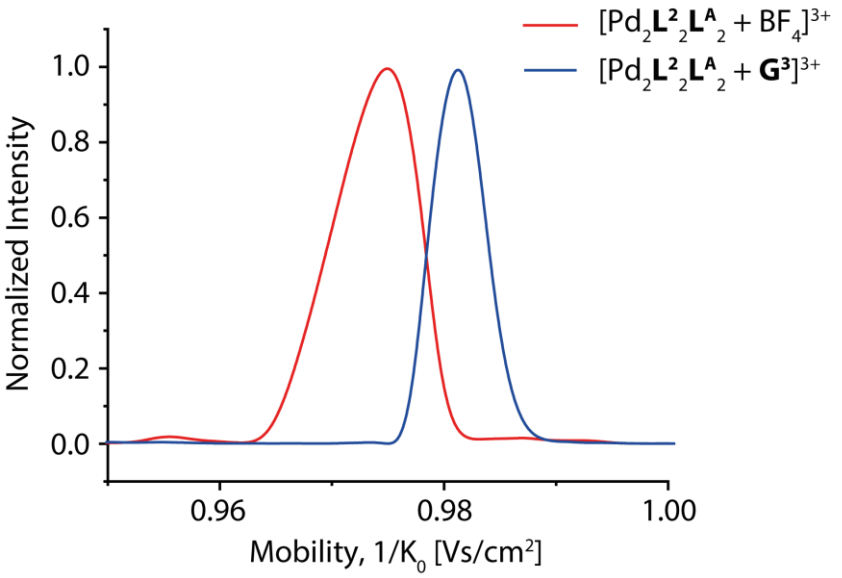

Figure 4.192: Ion-mobility mass spectra of $[Pd_2\mathbf{L}^{\mathbf{2}}{}_2\mathbf{L}^{\mathbf{A}}{}_2 + BF_4]^{3+}$ and $[Pd_2\mathbf{L}^{\mathbf{2}}{}_2\mathbf{L}^{\mathbf{A}}{}_2 + \mathbf{G}^{\mathbf{3}}]^{3+}$.

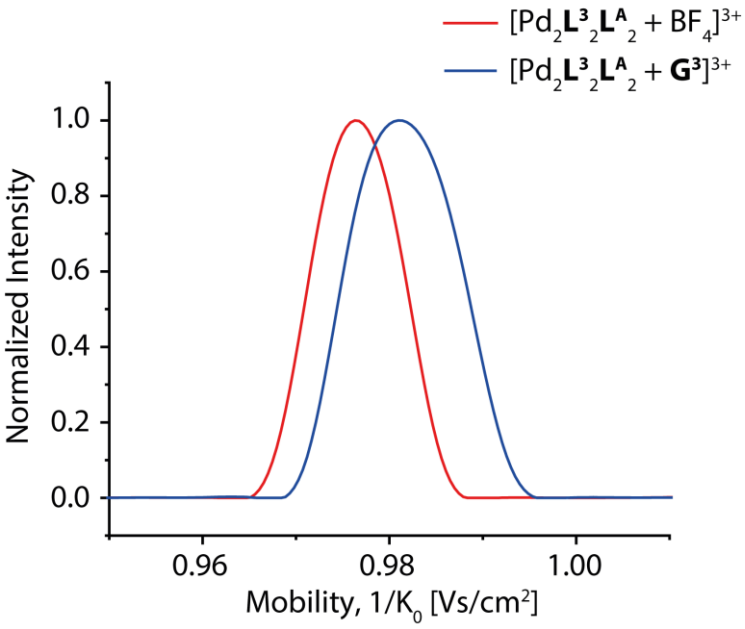

Figure 4.193: Ion-mobility mass spectra of $[Pd_2\mathbf{L}^{\mathbf{3}}{}_2\mathbf{L}^{\mathbf{A}}{}_2 + BF_4]^{3+}$ and $[Pd_2\mathbf{L}^{\mathbf{3}}{}_2\mathbf{L}^{\mathbf{A}}{}_2 + \mathbf{G}^{\mathbf{3}}]^{3+}$.

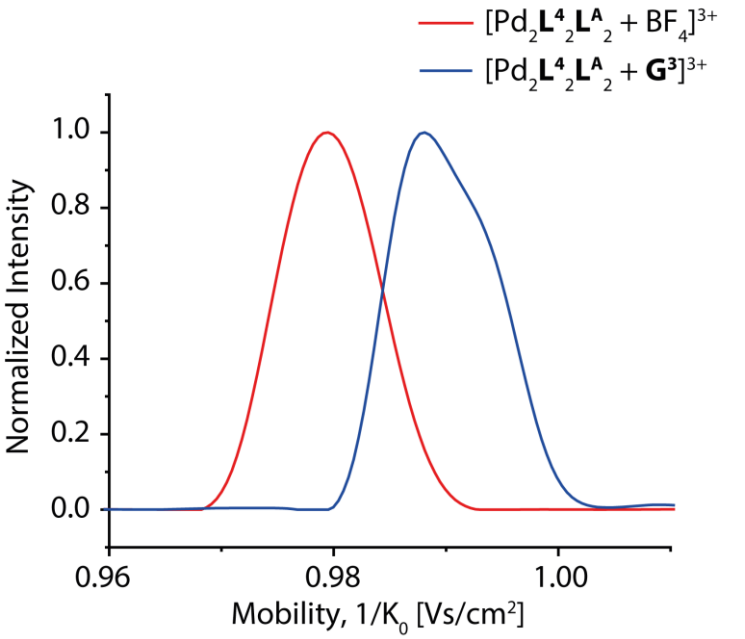

Figure 4.194: Ion-mobility mass spectra of $[Pd_2\mathbf{L}^{\mathbf{4}}{}_2\mathbf{L}^{\mathbf{A}}{}_2 + BF_4]^{3+}$ and $[Pd_2\mathbf{L}^{\mathbf{4}}{}_2\mathbf{L}^{\mathbf{A}}{}_2 + \mathbf{G}^{\mathbf{3}}]^{3+}$.

Taking a close look at the measured ion mobility spectra we observe that the signals are mostly gaussian-shaped or have slight shoulders. For some of the species with bound guest we observe two prominent mobility signals, indicating different co-conformers of the host-guest complexes in the gas phase, probably due to different positions of the guest inside the cage. However, we were not able to differentiate between different conformers by means of theoretical CCS calculations (compare below). In all cases, the measured mobilities of the host-guest complexes are close to the mobilities of the hosts containing

only a BF_4^- anion, indicating encapsulation inside the cavity (with – depending on the guest – slight protrusion of guest features, i.e. the phosphate's alkyl or aryl substituents outside the cage's apertures).

4.10 Modeling and Theoretical Collisional Cross Sections calculations (CCS)

The host-guest systems were optimized using the quantum chemistry software package ORCA (version 5.0.2),[200] by DFT methods on a PBE/def2-SVP level of theory. The theoretical collisional cross sections ($^{Theo}CCS_{N2}$) of the optimized models were then calculated with Collidoscope (version 1.4).[201] The number of energy states was set to 16 and the temperature to 303 K. The used CM5 point charges[202] were calculated using the `xtb` software (version 6.4.1) and the semiempirical model GFN1-xTB.[203]

Table 4.3: Measured and calculated collisional cross sections (CCS) of Host-Guest-Complexes.

Complex	Measured CCS [Å²]	Calculated CCS [Å²]	Δ%
$[Pd_2\mathbf{L^1}_2\mathbf{L^A}_2 + BF_4]^{3+}$	595.1	637.273	+7.1%
$[Pd_2\mathbf{L^1}_2\mathbf{L^A}_2]^{3+} + BF_4$ **outside**	-	640.175	+7.6%
$[Pd_2\mathbf{L^1}_2\mathbf{L^A}_2 + \mathbf{G^1}]^{3+}$	604.2	649.624	+7.5%
$[Pd_2\mathbf{L^1}_2\mathbf{L^A}_2 + \mathbf{G^2}]^{3+}$	605.4	652.593	+7.8%
$[Pd_2\mathbf{L^1}_2\mathbf{L^A}_2 + \mathbf{G^3}]^{3+}$	603.7	652.774	+8.1%
$[Pd_2\mathbf{L^1}_2\mathbf{L^A}_2]^{3+} + \mathbf{G^3}$ **outside**	-	688.833	+14.1%
$[Pd_2\mathbf{L^1}_2\mathbf{L^A}_2 + \mathbf{G^4}]^{3+}$	601.1	647.946	+7.8%
$[Pd_2\mathbf{L^1}_2\mathbf{L^A}_2 + \mathbf{G^5}]^{3+}$	601.7	655.126	+8.9%
$[Pd_2\mathbf{L^1}_2\mathbf{L^A}_2 + \mathbf{G^6}]^{3+}$	599.0	652.191	+8.9%
$[Pd_2\mathbf{L^1}_2\mathbf{L^B}_2 + BF_4]^{3+}$	545.6	585.424	+7.3%
$[Pd_2\mathbf{L^1}_2\mathbf{L^B}_2 + \mathbf{G^3}]^{3+}$	549.2	594.947	+8.3%
$[Pd_2\mathbf{L^1}_2\mathbf{L^C}_2 + BF_4]^{3+}$	555.1	620.360	+11.8%
$[Pd_2\mathbf{L^1}_2\mathbf{L^C}_2 + \mathbf{G^3}]^{3+}$	562.7	626.520	+11.3%
$[Pd_2\mathbf{L^1}_2\mathbf{L^D}_2 + BF_4]^{3+}$	516.6	573.185	+11.0%
$[Pd_2\mathbf{L^1}_2\mathbf{L^D}_2 + \mathbf{G^3}]^{3+}$	523.9	575.587	+9.9%
$[Pd_2\mathbf{L^2}_2\mathbf{L^A}_2 + BF_4]^{3+}$	597.0	-	
$[Pd_2\mathbf{L^2}_2\mathbf{L^A}_2 + \mathbf{G^3}]^{3+}$	600.3	-	
$[Pd_2\mathbf{L^3}_2\mathbf{L^A}_2 + BF_4]^{3+}$	590.5	639.362	+8.3%
$[Pd_2\mathbf{L^3}_2\mathbf{L^A}_2 + \mathbf{G^3}]^{3+}$	592.7	643.551	+8.6%
$[Pd_2\mathbf{L^4}_2\mathbf{L^A}_2 + BF_4]^{3+}$	592.3	644.968	+8.9%
$[Pd_2\mathbf{L^4}_2\mathbf{L^A}_2 + \mathbf{G^3}]^{3+}$	597.0	642.655	+7.6%

For this system we observe a relatively large average deviation, around +7.5%, of the theoretical value compared to the experimental data. This could be due to neglecting dynamic cage motions in the CCS calculation technique and due to the funnel-like shape

of the cage that may be problematic in the used trajectory method. The error is especially large for the $[Pd_2\mathbf{L}^{\mathbf{1}}{}_2\mathbf{L}^{\mathbf{C}}{}_2 + X]^{3+}$ species, which can be attributed to the two hexyl side chains, which are considered straight in the DFT models but may adopt more folded conformations in the gas phase. The slight increase of the CCS value by replacing a BF_4^- anion with a guest, as observed experimentally, could be reproduced in the computations. As discussed in the main text, considering a guest binding mode outside of the cage would lead to very high deviations between measured and calculated CCS values, which is why we assume the guest to be always inside the cage during the TIMS measurement.

4.11 UV/Vis and CD Spectroscopy

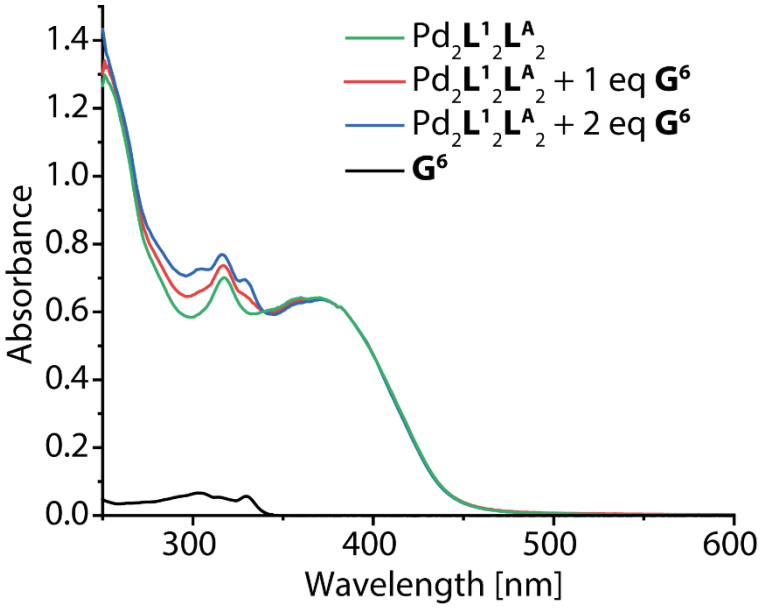

Figure 4.195: UV/vis spectra of $Pd_2\mathbf{L}^{\mathbf{1}}{}_2\mathbf{L}^{\mathbf{A}}{}_2$ (green, c = 0.07 mM), $\mathbf{G}^{\mathbf{6}}@Pd_2\mathbf{L}^{\mathbf{1}}{}_2\mathbf{L}^{\mathbf{A}}{}_2$ (1 eq red, 2 eq blue, c = 0.07 mM) and $\mathbf{G}^{\mathbf{6}}$ (black, c = 0.07 mM).

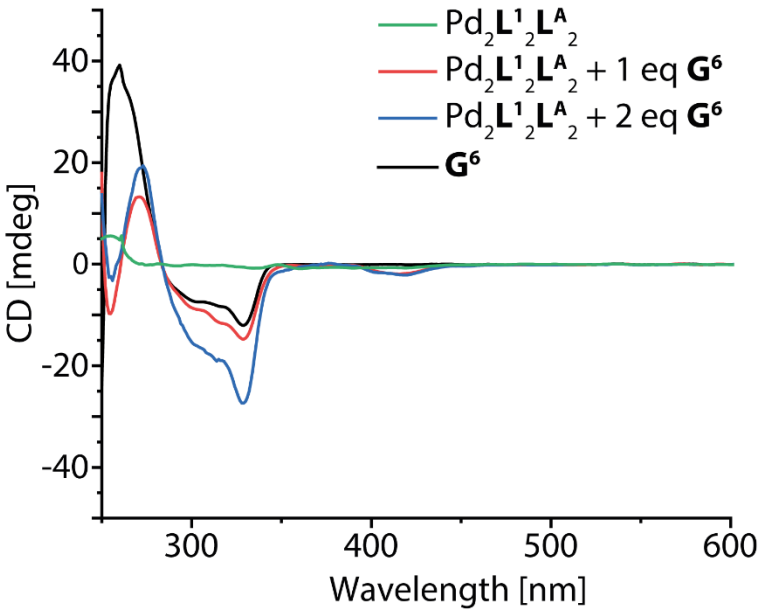

Figure 4.196: CD spectra of $Pd_2\mathbf{L}^{\mathbf{1}}{}_2\mathbf{L}^{\mathbf{A}}{}_2$ (green, c = 0.07 mM), $\mathbf{G}^{\mathbf{6}}$@$Pd_2\mathbf{L}^{\mathbf{1}}{}_2\mathbf{L}^{\mathbf{A}}{}_2$ (1 eq red, 2 eq blue, c = 0.07 mM) and $\mathbf{G}^{\mathbf{6}}$ (black, c = 0.07 mM).

A CD signal in the absorption range of the host-guest complex was observed, indicating a chirality transfer from the guest to the host.

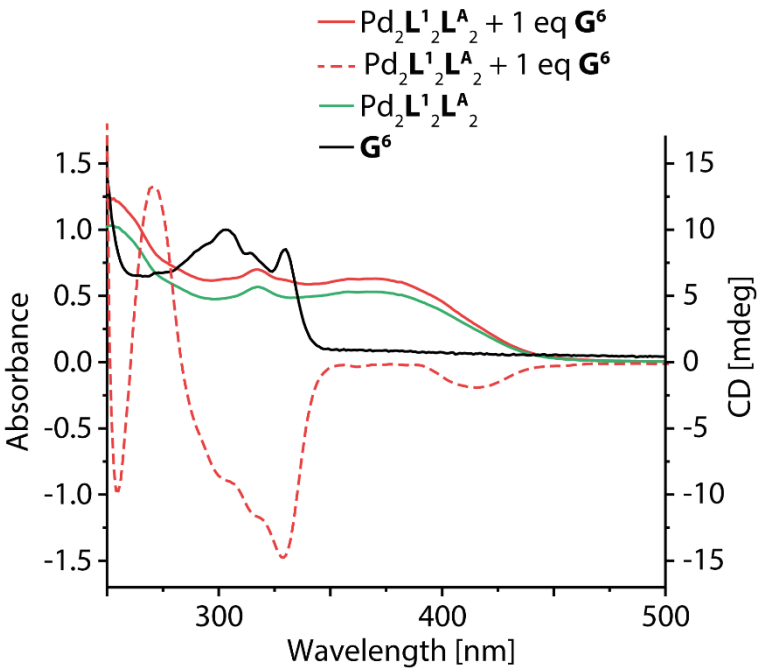

Figure 4.197: Overlay of UV/Vis (solid lines) and CD (dashed line) spectra of $Pd_2\mathbf{L}^{\mathbf{1}}{}_2\mathbf{L}^{\mathbf{A}}{}_2$ (green, c = 0.07 mM), $\mathbf{G}^{\mathbf{6}}$@$Pd_2\mathbf{L}^{\mathbf{1}}{}_2\mathbf{L}^{\mathbf{A}}{}_2$ (1 eq red, c = 0.07 mM) and $\mathbf{G}^{\mathbf{6}}$ (black, c = 0.7 mM).

5 Experimental Section II

5.1 General Information

NMR spectroscopic data was measured on the spectrometers Bruker AV 400 Avance III HD NanoBay (**A**), Bruker AV 500 Avance NEO (**B**), AV 500 Avance III HD (**C**), AV 600 Avance III HD (**D**), AV 700 Avance III HD (**E**) and Agilent Technologies DD2 500 MHz (**F**). For ^{1}H NMR spectra, chemical shifts were calibrated to the solvent lock signal.[184]. Chemical shifts δ are given in ppm, coupling constants J in Hz. All spectra were recorded in standard 5 mm NMR tubes at 25 °C, if not mentioned otherwise. ^{1}H DOSY NMR spectra were recorded with a *dstebpgp3s* (D_{cc}) pulse sequence or *ledbpgp2s* (*D*) pulse sequence, respectively, with diffusion delays D20 of 0.08 to 0.09 s and gradient durations P30 of 900 to 2300 µs.[97–99] T1 analyses of the corresponding signals in the 1D spectra were performed to obtain the diffusion coefficients *D* using the STEJSKAL-TANNER-Equation.[185,186] Hydrodynamic radii r_H were calculated using the STOKES-EINSTEIN-Equation.[84] Syntheses of the ligands $\mathbf{L^{ACR1\text{-}6}}$ were performed according to the protocols described in the literature.[66,174] *p*-toluene sulfonic acid (*p*-TSA) and 2-phenoxyethanol (2-POE) were purchased from SigmaAldrich and used without further purification. Deuterated solvents (99%+ D atom) were purchased from Deutero or Eurisotop and used without further purification.

5.2 ^{1}H DOSY NMR Measurements of *p*-TSA and 2-POE

To follow the decrease of the signal intensity during the 1D DOSY measurements of the analytes in a precise way, the residual solvent signals were subtracted digitally before the processing procedure.

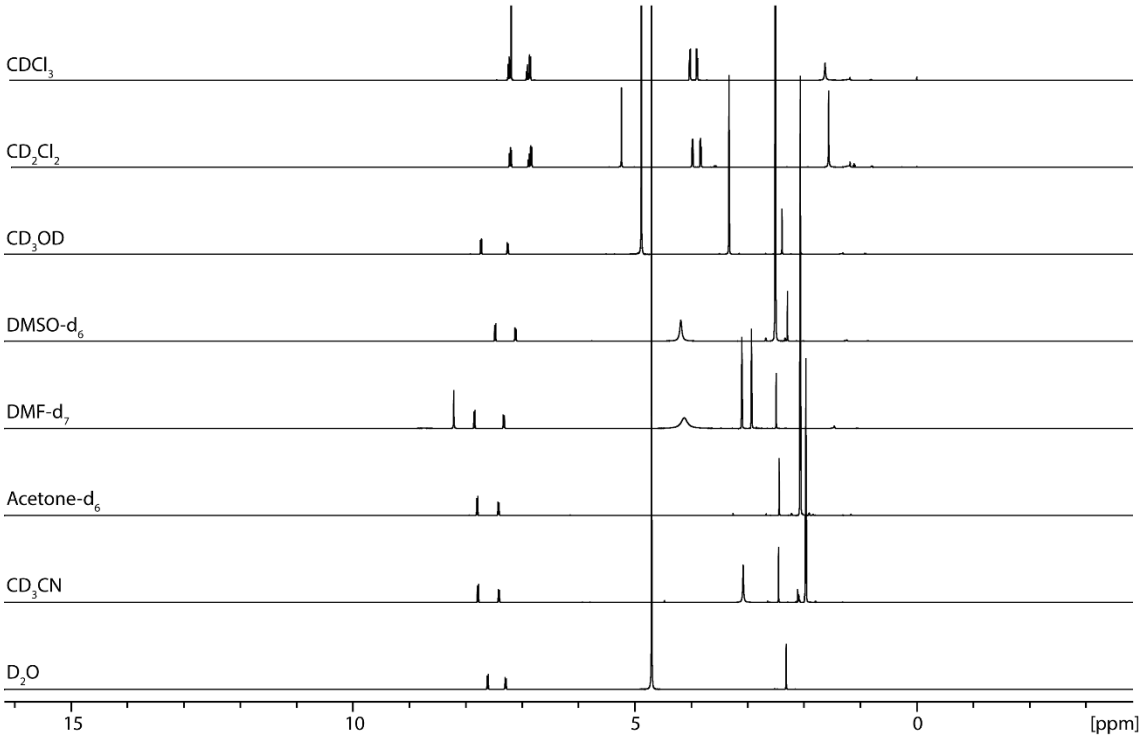

Figure 5.1: Stacked ^{1}H NMR spectra (400 MHz, 298 K, spectrometer **A**) of *p*-TSA and 2-POE in the mentioned solvents.

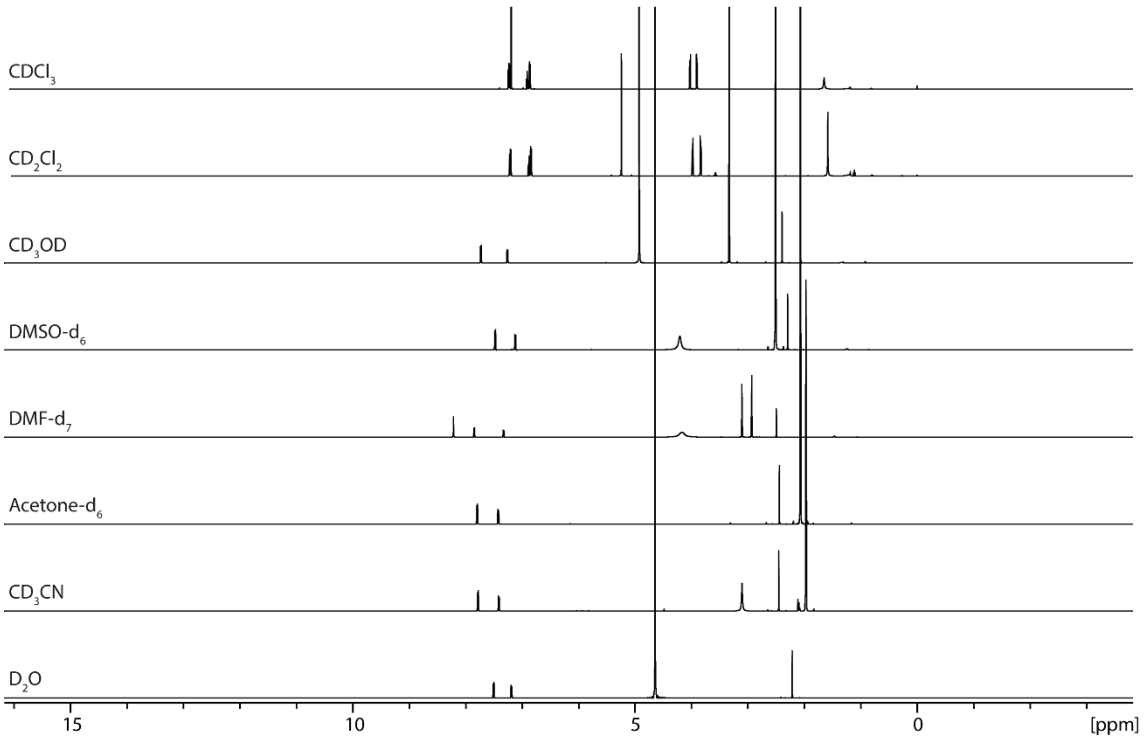

Figure 5.2: Stacked ^{1}H NMR spectra (500 MHz, 298 K, spectrometer **C**) of *p*-TSA and 2-POE in the mentioned solvents.

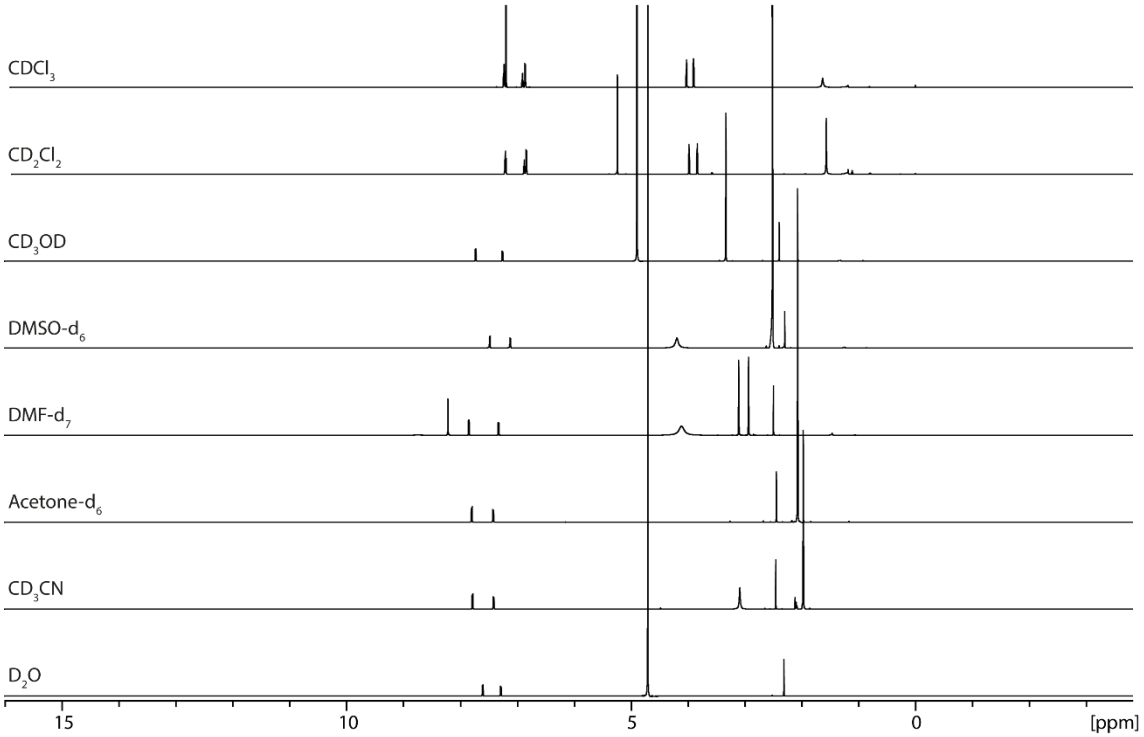

Figure 5.3: Stacked ^{1}H NMR spectra (600 MHz, 298 K, spectrometer **D**) of *p*-TSA and 2-POE in the mentioned solvents.

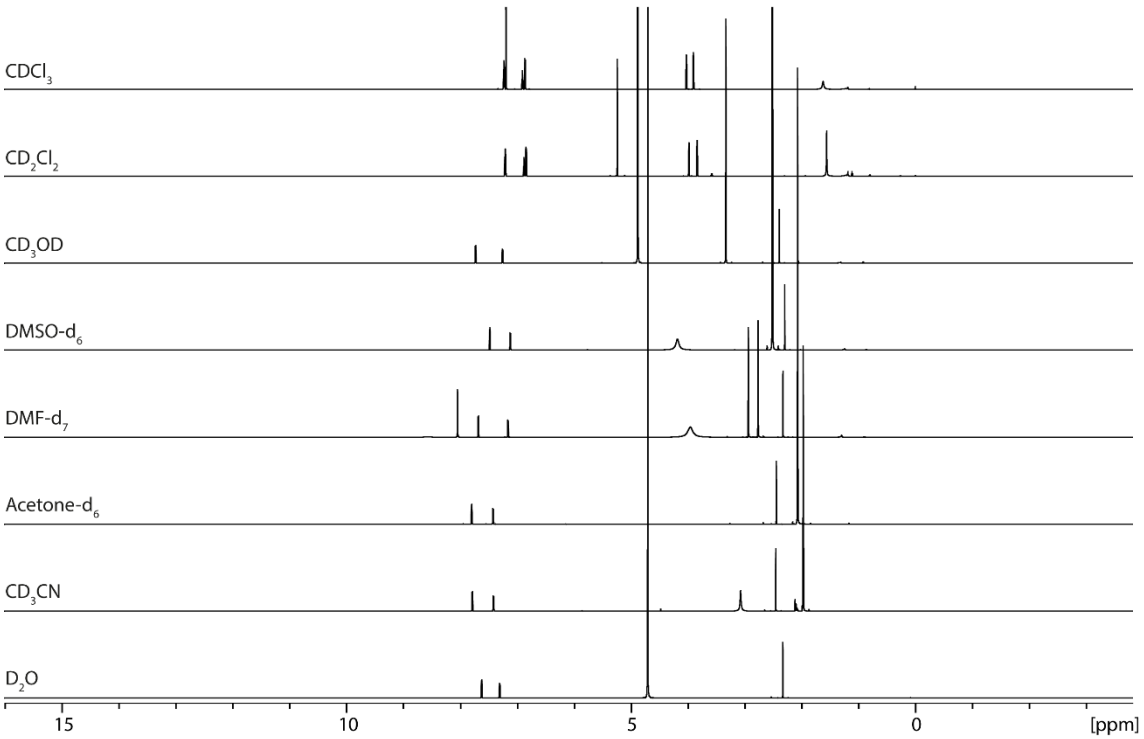

Figure 5.4: Stacked ^{1}H NMR spectra (700 MHz, 298 K, spectrometer **E**) of *p*-TSA and 2-POE in the mentioned solvents.

5.2.1 ^{1}H DOSY Measurements at Spectrometer A

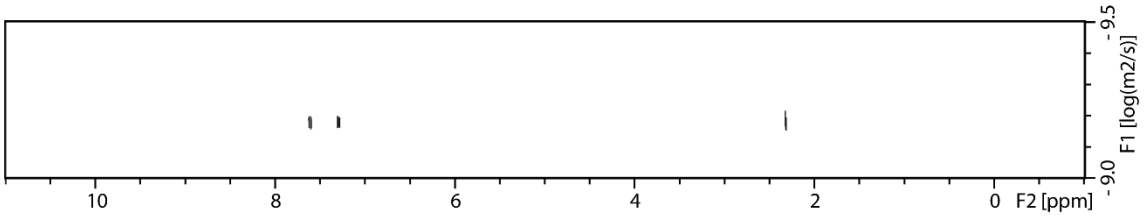

Figure 5.5: ^{1}H DOSY NMR (400 MHz, D_2O, 298 K) of *p*-TSA with *ledbpgp2s* pulse sequence.

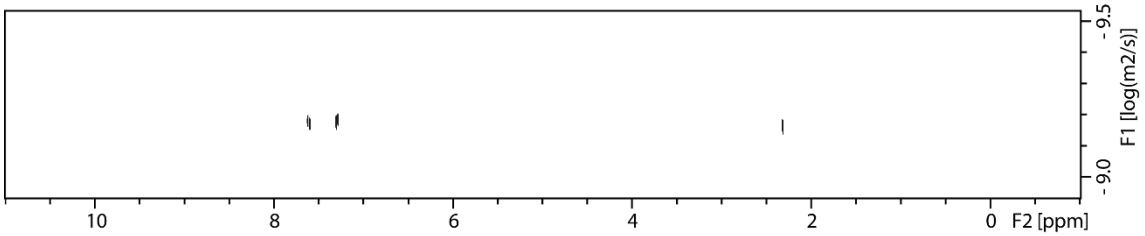

Figure 5.6: ^{1}H DOSY NMR (400 MHz, D_2O, 298 K) of *p*-TSA with *dstebpgp3s* pulse sequence.

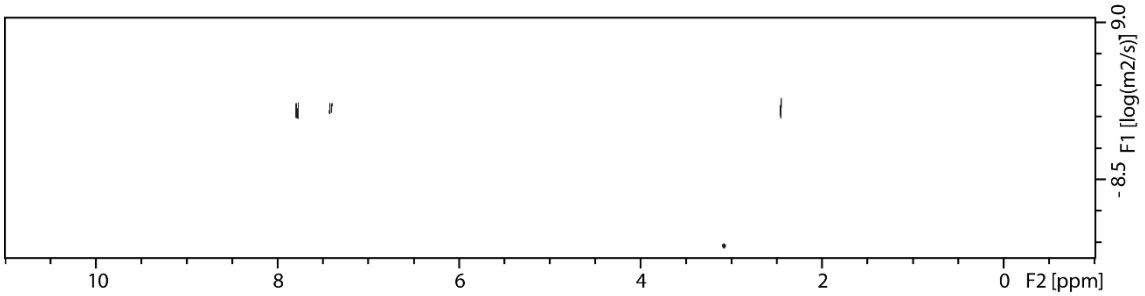

Figure 5.7: ^{1}H DOSY NMR (400 MHz, CD_3CN, 298 K) of *p*-TSA with *ledbpgp2s* pulse sequence.

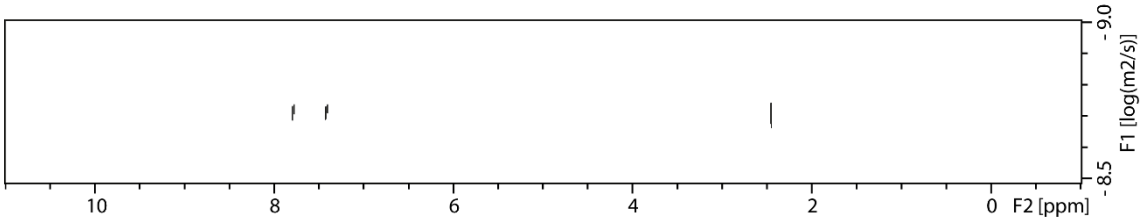

Figure 5.8: ^{1}H DOSY NMR (400 MHz, CD_3CN, 298 K) of *p*-TSA with *dstebpgp3s* pulse sequence.

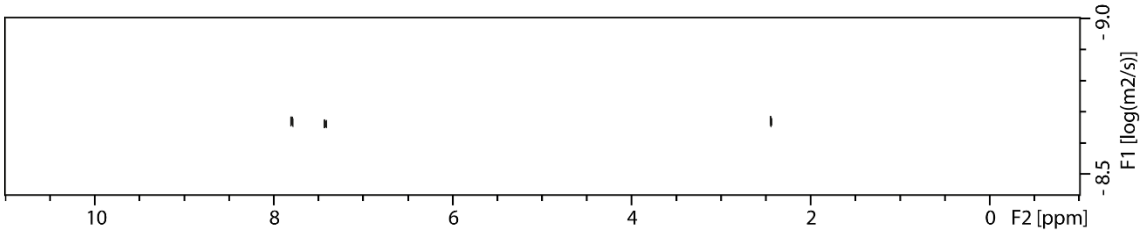

Figure 5.9: ^{1}H DOSY NMR (400 MHz, acetone-d_6, 298 K) of *p*-TSA with *ledbpgp2s* pulse sequence.

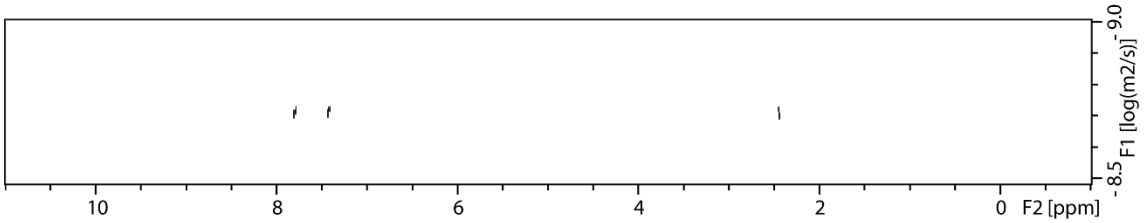

Figure 5.10: ^{1}H DOSY NMR (400 MHz, acetone-d_6, 298 K) of *p*-TSA with *dstebpgp3s* pulse sequence.

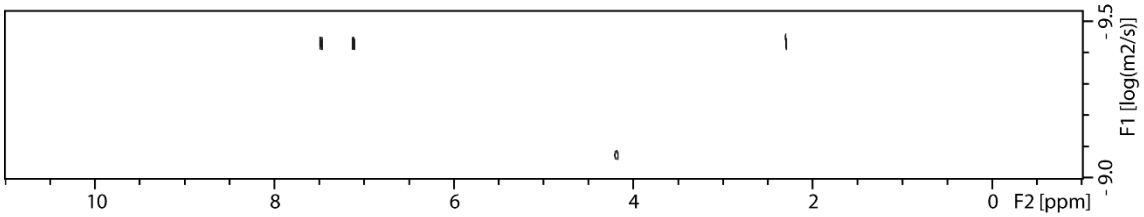

Figure 5.11: ^{1}H DOSY NMR (400 MHz, DMSO-d_6, 298 K) of *p*-TSA with *ledbpgp2s* pulse sequence.

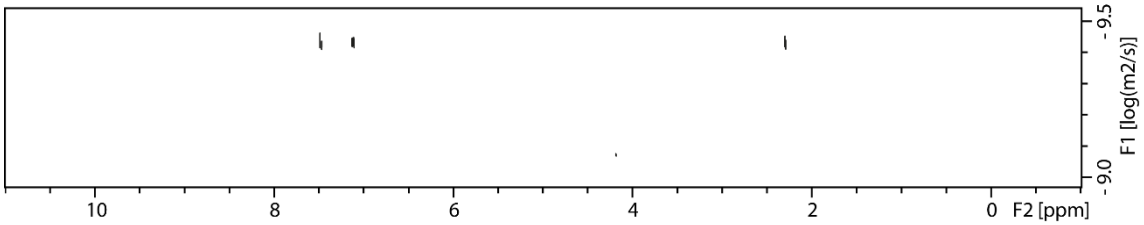

Figure 5.12: ^{1}H DOSY NMR (400 MHz, DMSO-d_6, 298 K) of *p*-TSA with *dstebpgp3s* pulse sequence.

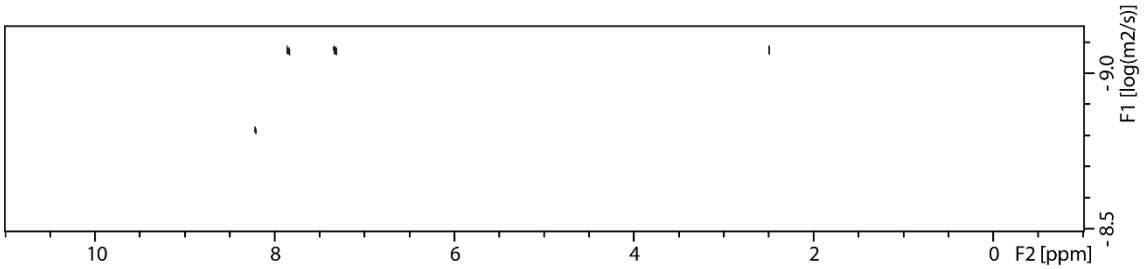

Figure 5.13: ^{1}H DOSY NMR (400 MHz, DMF-d_7, 298 K) of *p*-TSA with *ledbpgp2s* pulse sequence.

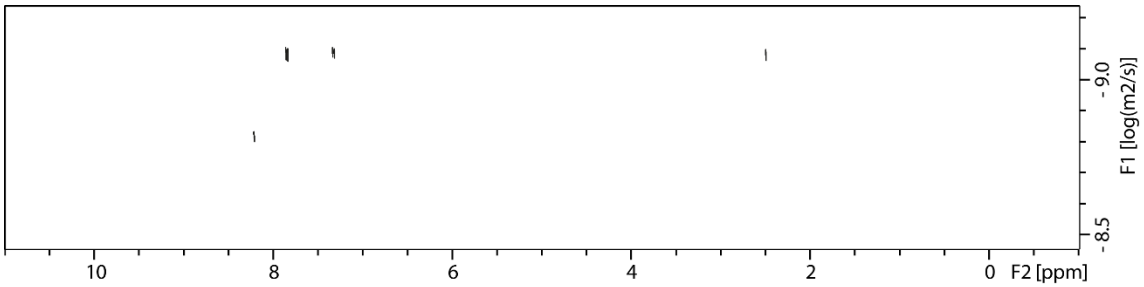

Figure 5.14: ^{1}H DOSY NMR (400 MHz, DMF-d_7, 298 K) of *p*-TSA with *dstebpgp3s* pulse sequence.

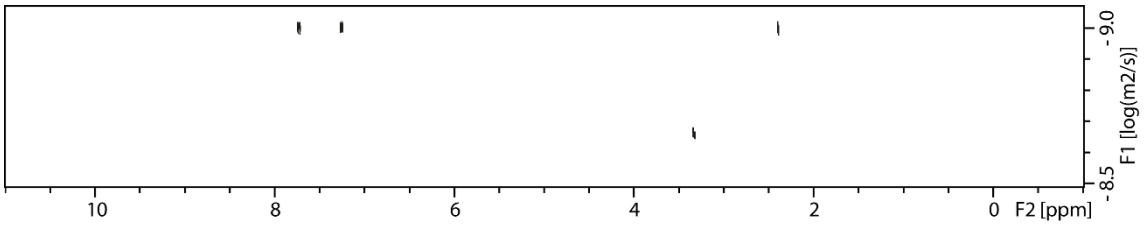

Figure 5.15: ^{1}H DOSY NMR (400 MHz, CD_3OD, 298 K) of *p*-TSA with *ledbpgp2s* pulse sequence.

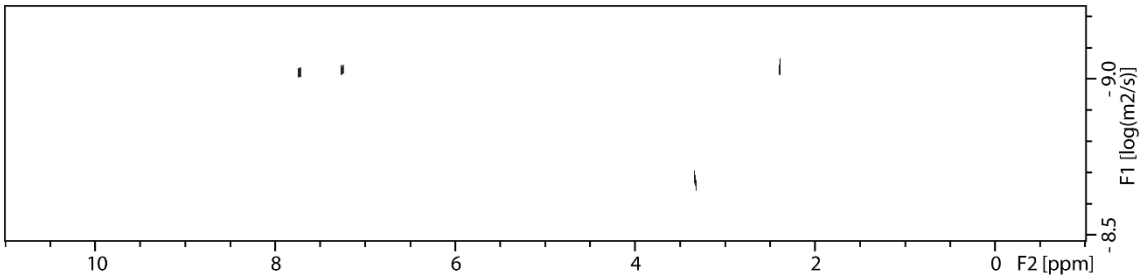

Figure 5.16: ^{1}H DOSY NMR (400 MHz, CD_3OD, 298 K) of *p*-TSA with *dstebpgp3s* pulse sequence.

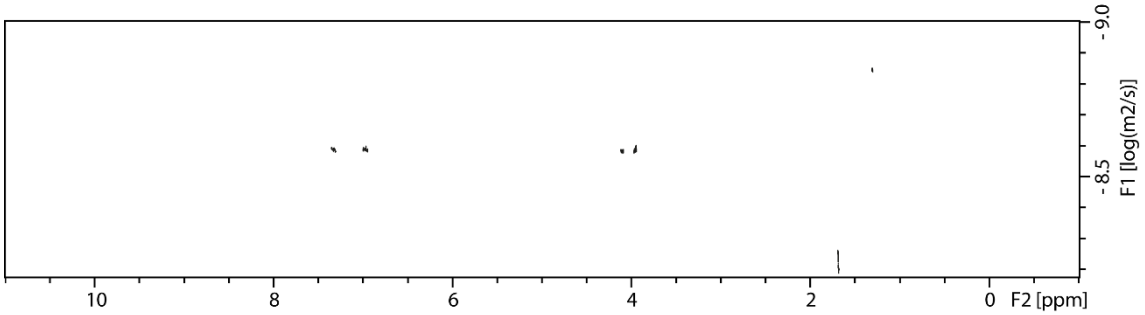

Figure 5.17: ^{1}H DOSY NMR (400 MHz, CD_2Cl_2, 298 K) of 2-POE with *ledbpgp2s* pulse sequence.

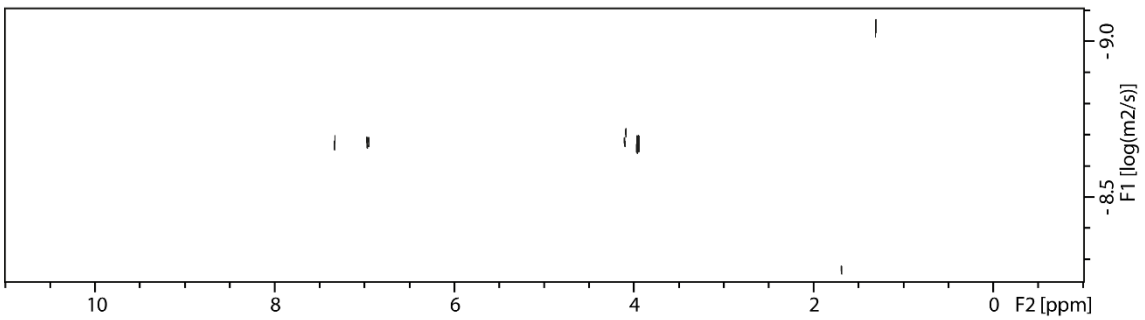

Figure 5.18: ^{1}H DOSY NMR (400 MHz, CD_2Cl_2, 298 K) of 2-POE with *dstebpgp3s* pulse sequence.

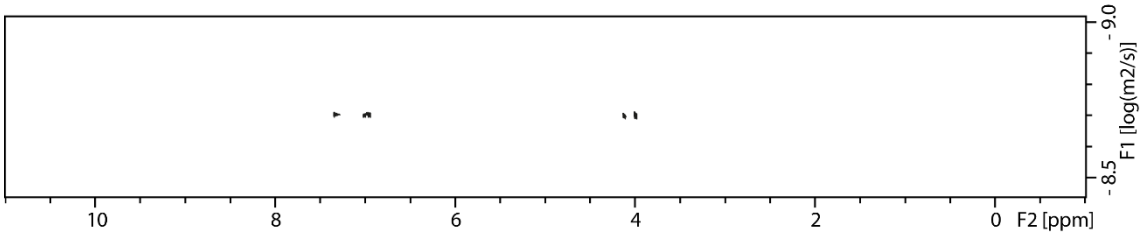

Figure 5.19: ^{1}H DOSY NMR (400 MHz, $CDCl_3$, 298 K) of 2-POE with *ledbpgp2s* pulse sequence.

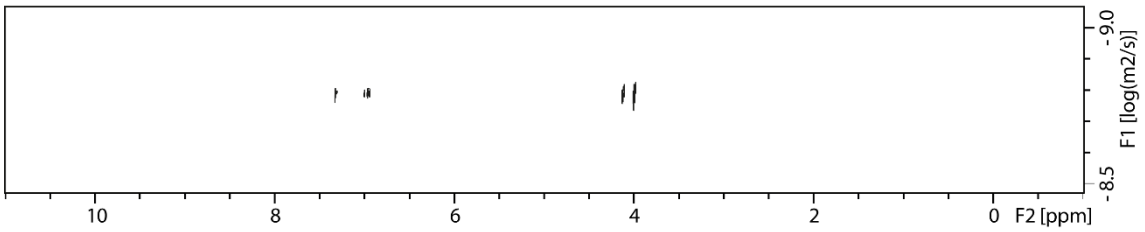

Figure 5.20: ^{1}H DOSY NMR (400 MHz, $CDCl_3$, 298 K) of 2-POE with *dstebpgp3s* pulse sequence.

5.2.2 ^{1}H DOSY Measurements at Spectrometer B

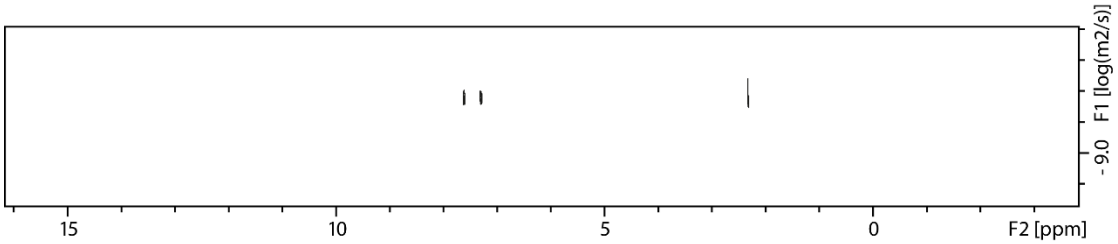

Figure 5.21: ^{1}H DOSY NMR (500 MHz, D_2O, 298 K) of *p*-TSA with *ledbpgp2s* pulse sequence.

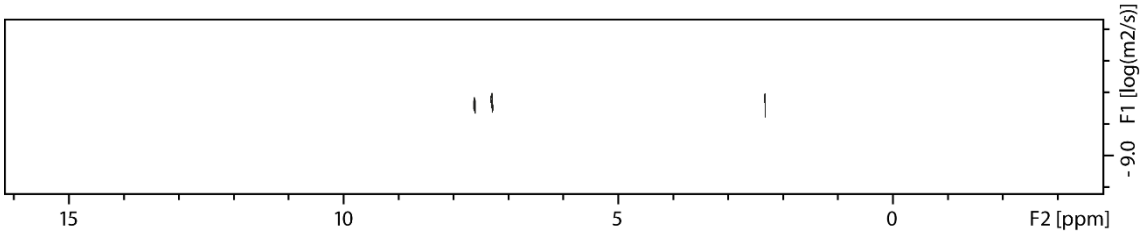

Figure 5.22: ^{1}H DOSY NMR (500 MHz, D_2O, 298 K) of *p*-TSA with *dstebpgp3s* pulse sequence.

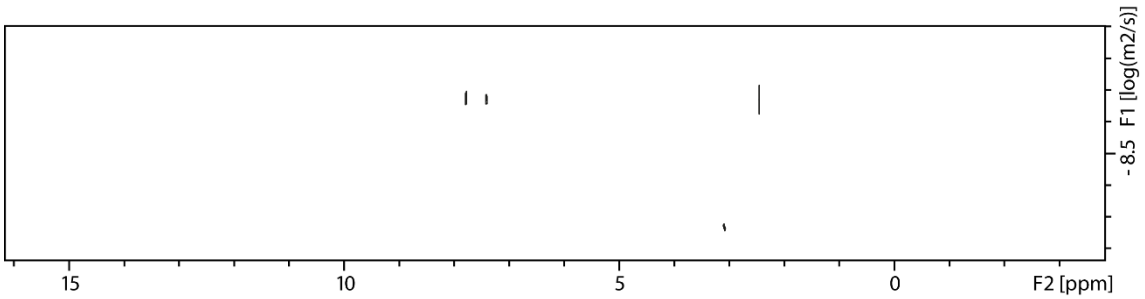

Figure 5.23: ^{1}H DOSY NMR (500 MHz, CD_3CN, 298 K) of *p*-TSA with *ledbpgp2s* pulse sequence.

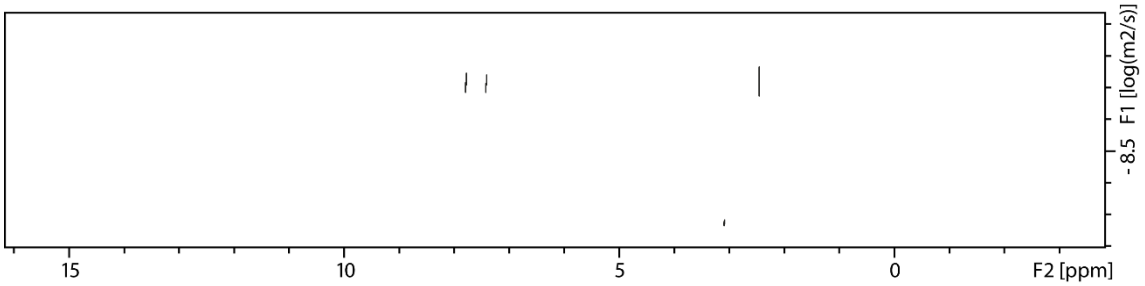

Figure 5.24: ^{1}H DOSY NMR (500 MHz, CD_3CN, 298 K) of *p*-TSA with *dstebpgp3s* pulse sequence.

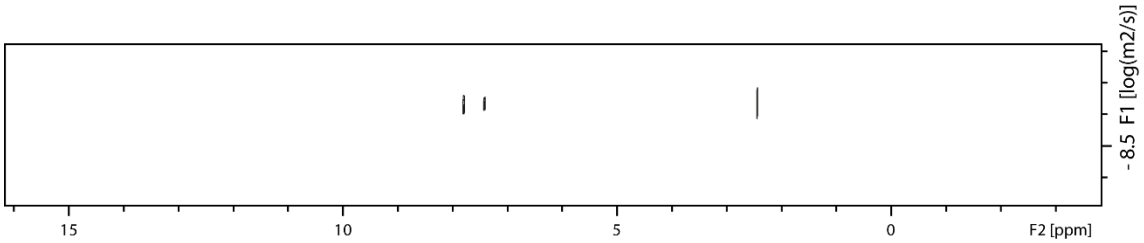

Figure 5.25: ^{1}H DOSY NMR (500 MHz, acetone-d_6, 298 K) of *p*-TSA with *ledbpgp2s* pulse sequence.

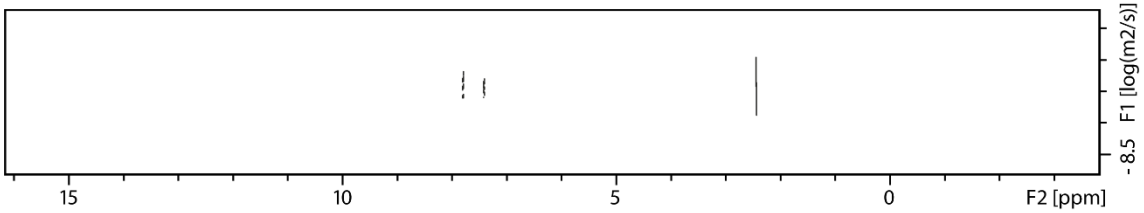

Figure 5.26: ^{1}H DOSY NMR (500 MHz, acetone-d_6, 298 K) of *p*-TSA with *dstebpgp3s* pulse sequence.

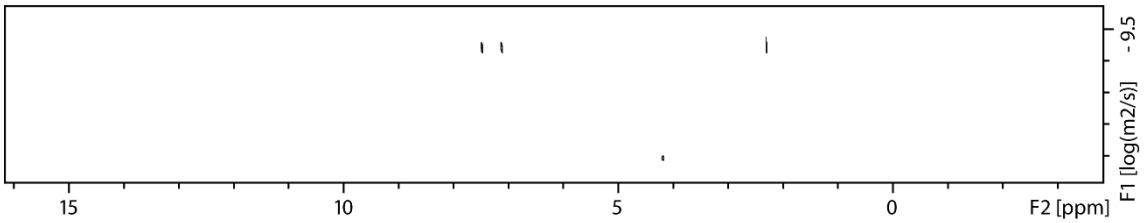

Figure 5.27: ^{1}H DOSY NMR (500 MHz, DMSO-d_6, 298 K) of *p*-TSA with *ledbpgp2s* pulse sequence.

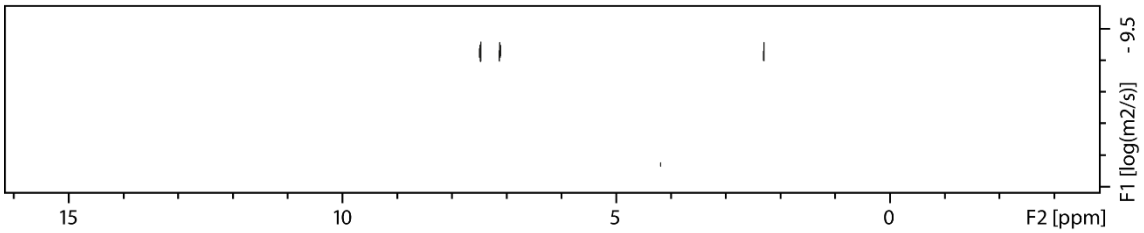

Figure 5.28: ^{1}H DOSY NMR (500 MHz, DMSO-d_6, 298 K) of *p*-TSA with *dstebpgp3s* pulse sequence.

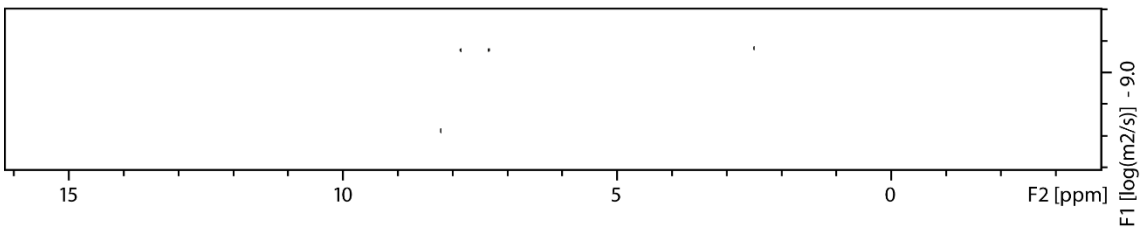

Figure 5.29: ^{1}H DOSY NMR (500 MHz, DMF-d_7, 298 K) of *p*-TSA with *ledbpgp2s* pulse sequence.

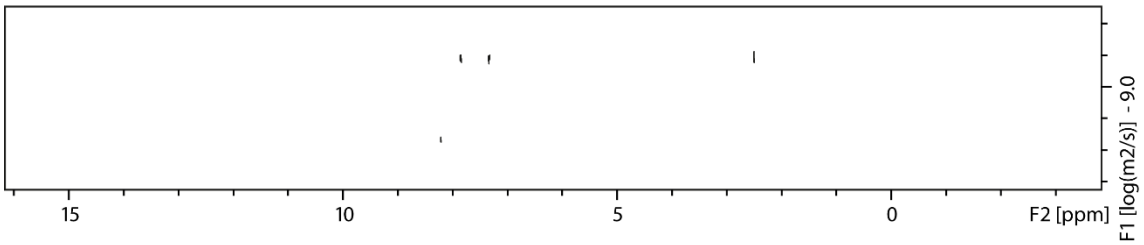

Figure 5.30: ^{1}H DOSY NMR (500 MHz, DMF-d_7, 298 K) of *p*-TSA with *dstebpgp3s* pulse sequence.

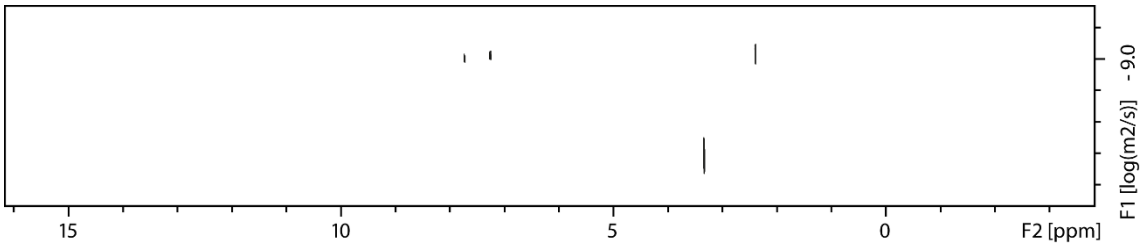

Figure 5.31: ^{1}H DOSY NMR (500 MHz, CD_3OD, 298 K) of *p*-TSA with *ledbpgp2s* pulse sequence.

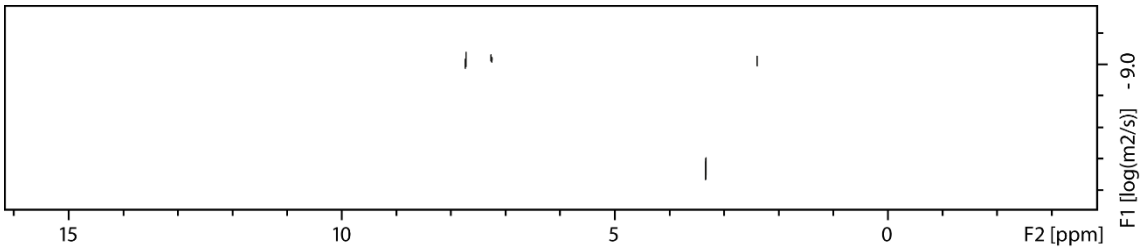

Figure 5.32: ^{1}H DOSY NMR (500 MHz, CD_3OD, 298 K) of *p*-TSA with *dstebpgp3s* pulse sequence.

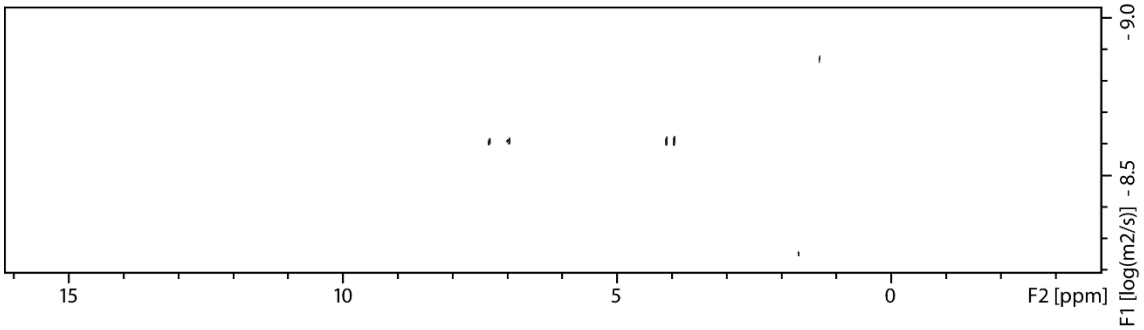

Figure 5.33: ^{1}H DOSY NMR (500 MHz, CD_2Cl_2, 298 K) of 2-POE with *ledbpgp2s* pulse sequence.

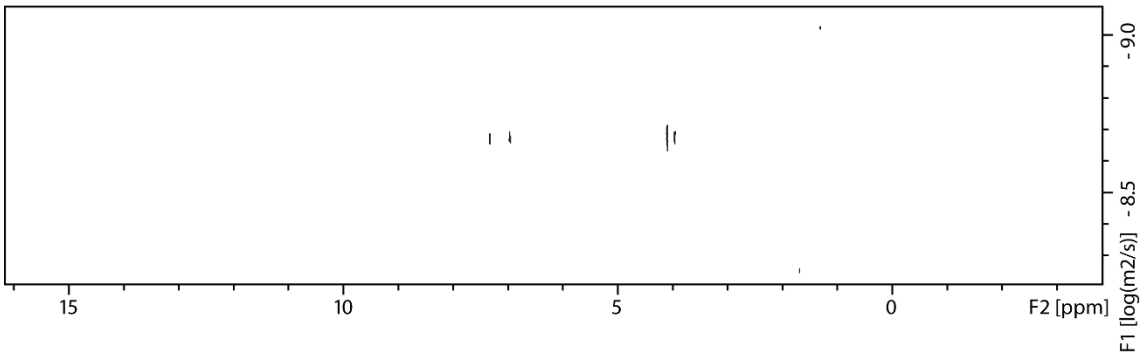

Figure 5.34: ^{1}H DOSY NMR (500 MHz, CD_2Cl_2, 298 K) of 2-POE with *dstebpgp3s* pulse sequence.

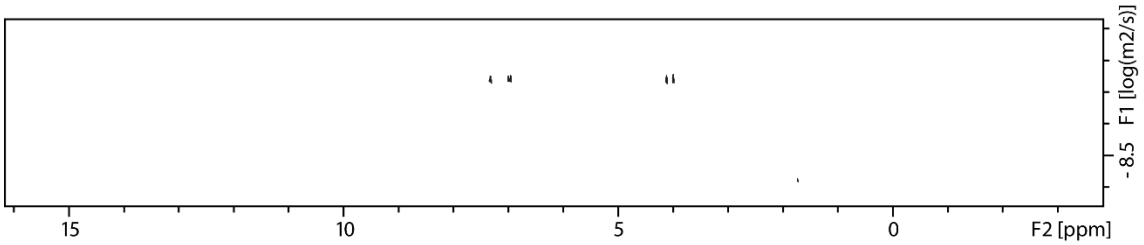

Figure 5.35: ^{1}H DOSY NMR (500 MHz, $CDCl_3$, 298 K) of 2-POE with *ledbpgp2s* pulse sequence.

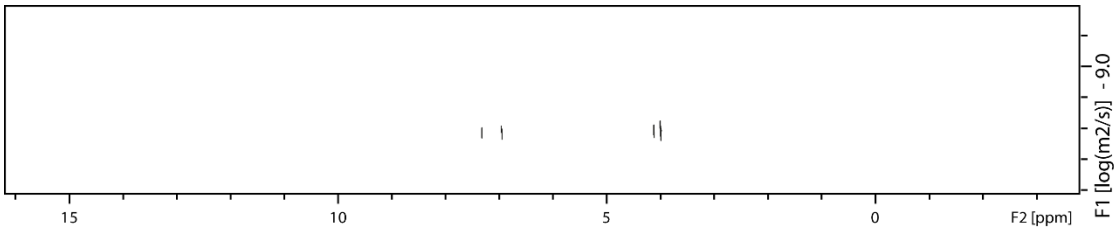

Figure 5.36: ^{1}H DOSY NMR (500 MHz, $CDCl_3$, 298 K) of 2-POE with *dstebpgp3s* pulse sequence.

5.2.3 ^{1}H DOSY Measurements at Spectrometer C

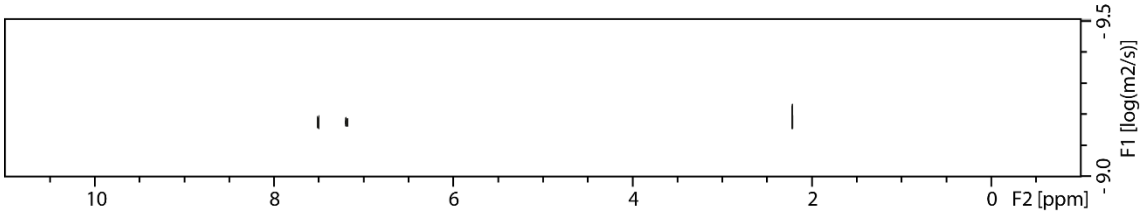

Figure 5.37: ^{1}H DOSY NMR (500 MHz, D_2O, 298 K) of *p*-TSA with *ledbpgp2s* pulse sequence.

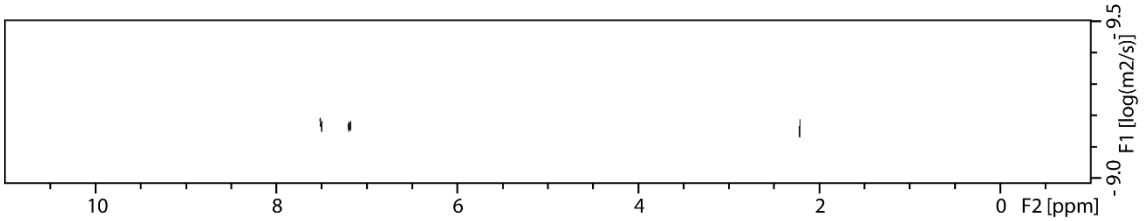

Figure 5.38: ^{1}H DOSY NMR (500 MHz, D_2O, 298 K) of *p*-TSA with *dstebpgp3s* pulse sequence.

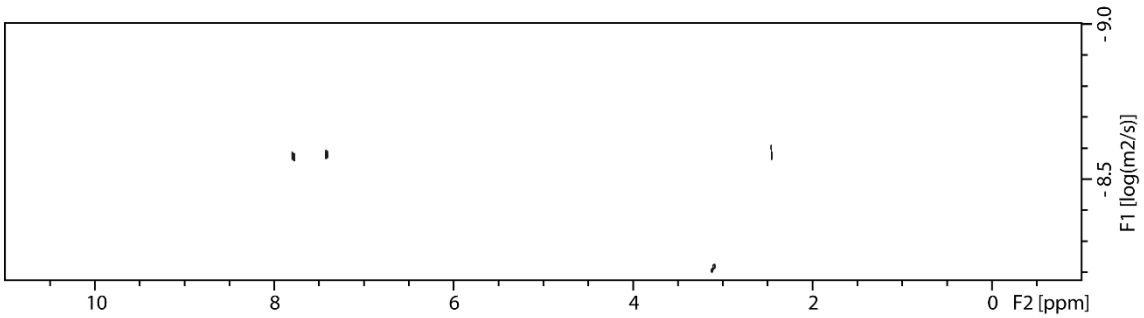

Figure 5.39: ^{1}H DOSY NMR (500 MHz, CD_3CN, 298 K) of *p*-TSA with *ledbpgp2s* pulse sequence.

Figure 5.40: ^{1}H DOSY NMR (500 MHz, CD_3CN, 298 K) of *p*-TSA with *dstebpgp3s* pulse sequence.

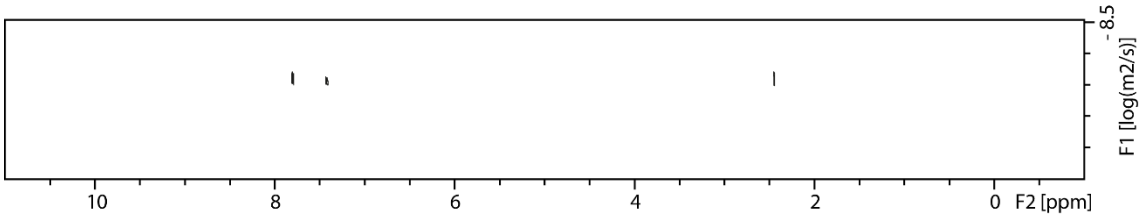

Figure 5.41: ^{1}H DOSY NMR (500 MHz, acetone-d_6, 298 K) of *p*-TSA with *ledbpgp2s* pulse sequence.

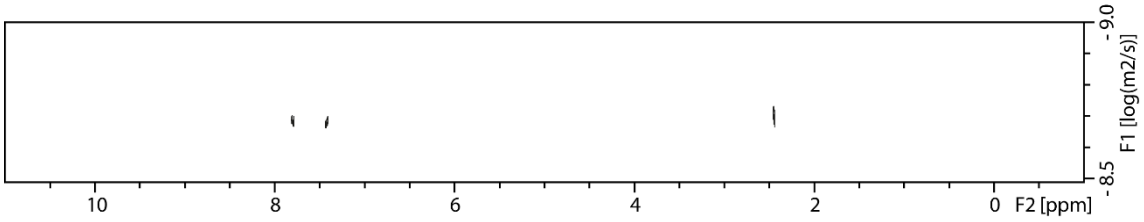

Figure 5.42: ^{1}H DOSY NMR (500 MHz, acetone-d_6, 298 K) of *p*-TSA with *dstebpgp3s* pulse sequence.

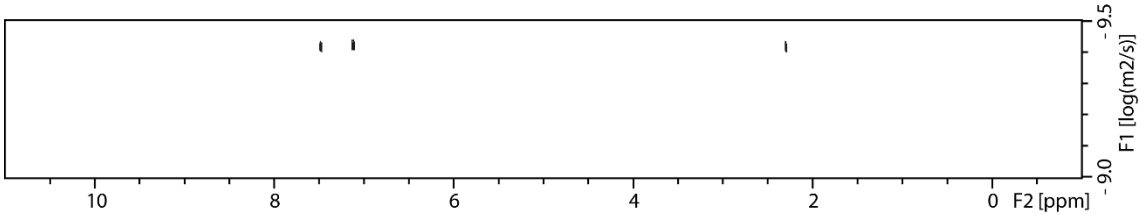

Figure 5.43: ^{1}H DOSY NMR (500 MHz, DMSO-d_6, 298 K) of *p*-TSA with *ledbpgp2s* pulse sequence.

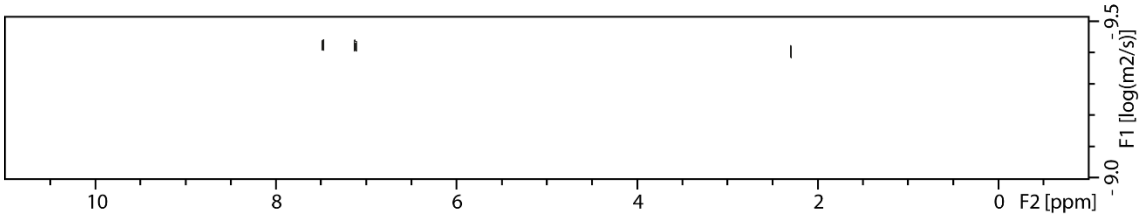

Figure 5.44: ^{1}H DOSY NMR (500 MHz, DMSO-d_6, 298 K) of *p*-TSA with *dstebpgp3s* pulse sequence.

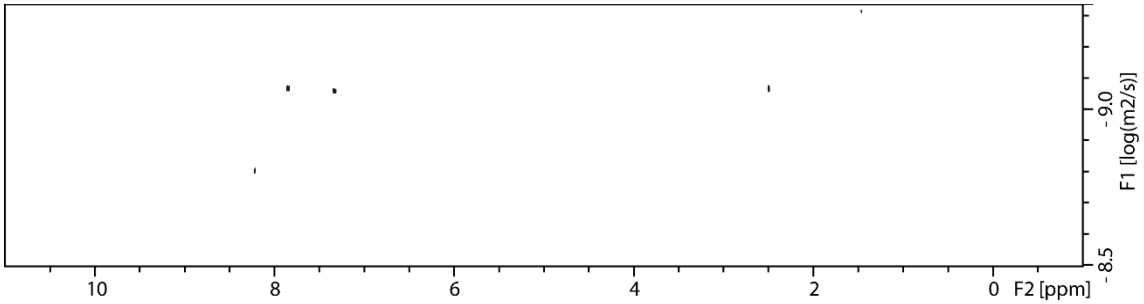

Figure 5.45: ^{1}H DOSY NMR (500 MHz, DMF-d_7, 298 K) of *p*-TSA with *ledbpgp2s* pulse sequence.

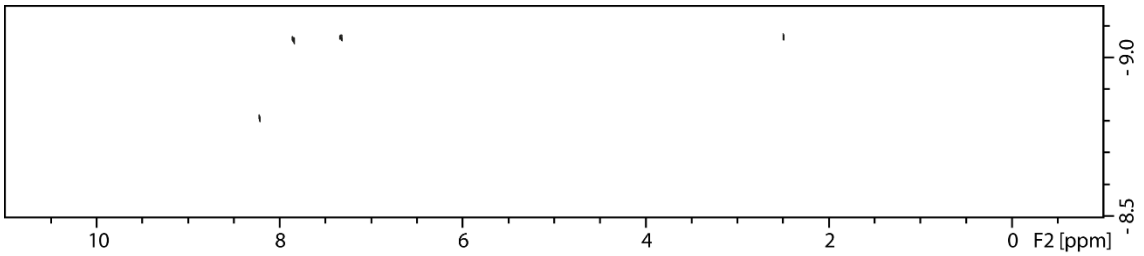

Figure 5.46: ^{1}H DOSY NMR (500 MHz, DMF-d_7, 298 K) of *p*-TSA with *dstebpgp3s* pulse sequence.

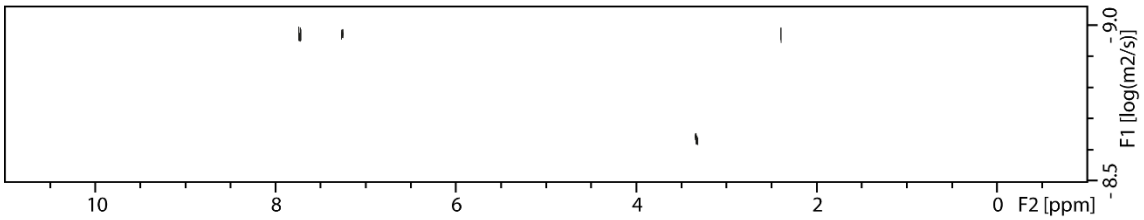

Figure 5.47: ^{1}H DOSY NMR (500 MHz, CD_3OD, 298 K) of *p*-TSA with *ledbpgp2s* pulse sequence.

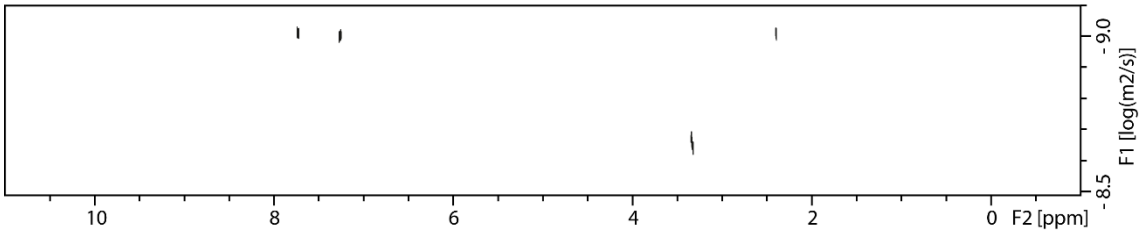

Figure 5.48: ^{1}H DOSY NMR (500 MHz, CD_3OD, 298 K) of *p*-TSA with *dstebpgp3s* pulse sequence.

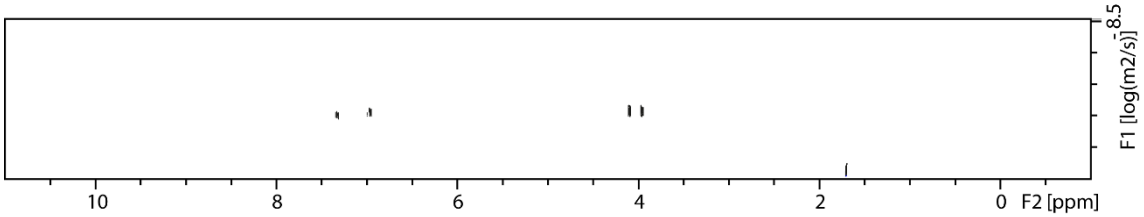

Figure 5.49: ^{1}H DOSY NMR (500 MHz, CD_2Cl_2, 298 K) of 2-POE with *ledbpgp2s* pulse sequence.

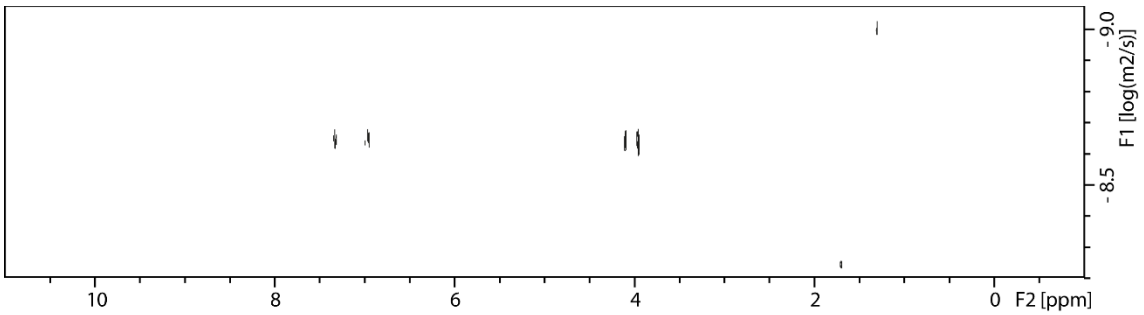

Figure 5.50: ^{1}H DOSY NMR (500 MHz, CD_2Cl_2, 298 K) of 2-POE with *dstebpgp3s* pulse sequence.

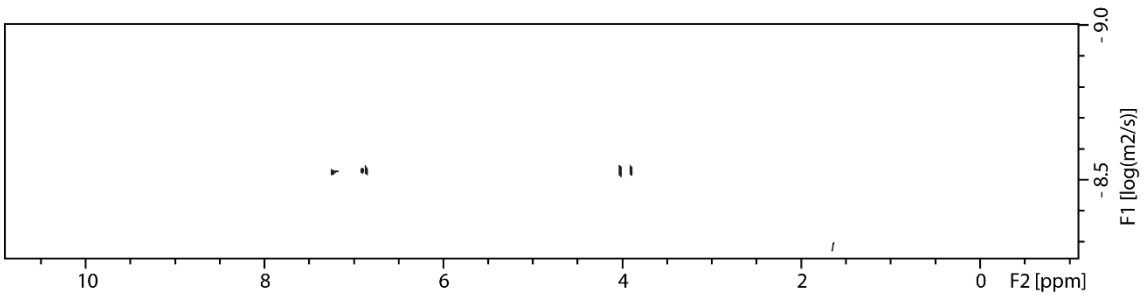

Figure 5.51: ^{1}H DOSY NMR (500 MHz, $CDCl_3$, 298 K) of 2-POE with *ledbpgp2s* pulse sequence.

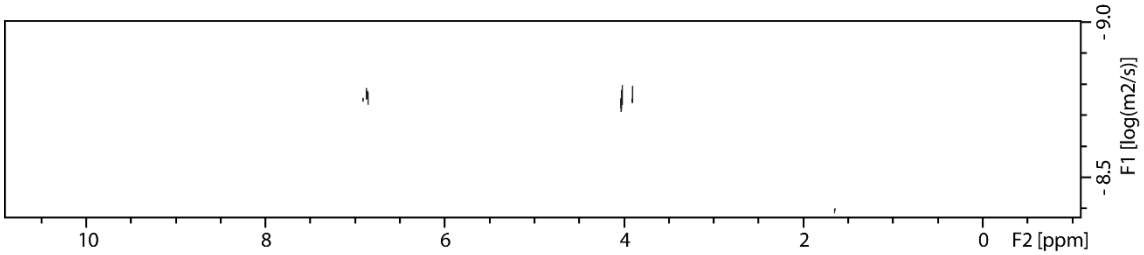

Figure 5.52: ^{1}H DOSY NMR (500 MHz, $CDCl_3$, 298 K) of 2-POE with *dstebpgp3s* pulse sequence.

5.2.4 ^{1}H DOSY Measurements at Spectrometer D

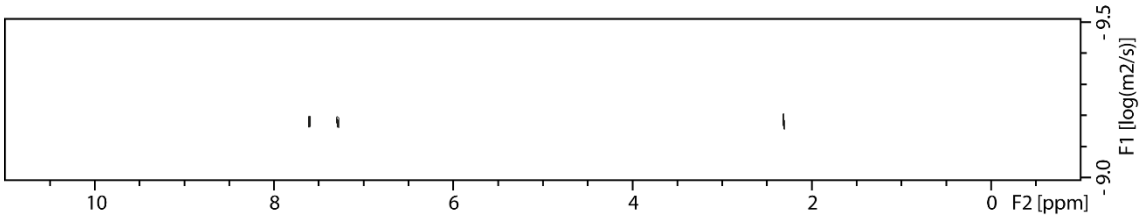

Figure 5.53: ^{1}H DOSY NMR (600 MHz, D_2O, 298 K) of *p*-TSA with *ledbpgp2s* pulse sequence.

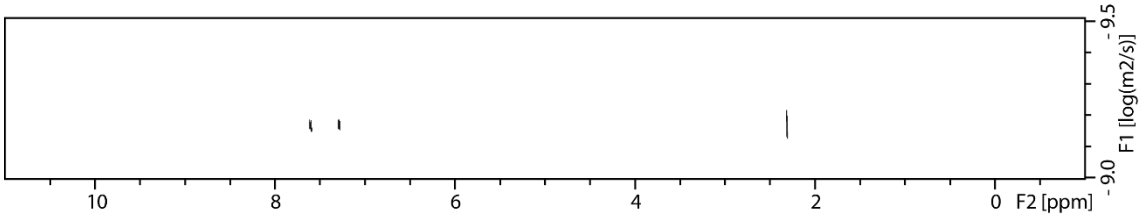

Figure 5.54: ^{1}H DOSY NMR (600 MHz, D_2O, 298 K) of *p*-TSA with *dstebpgp3s* pulse sequence.

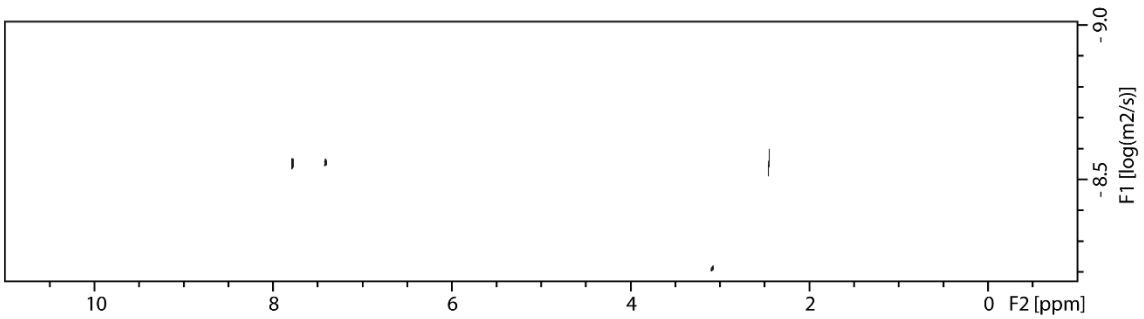

Figure 5.55: ^{1}H DOSY NMR (600 MHz, CD_3CN, 298 K) of *p*-TSA with *ledbpgp2s* pulse sequence.

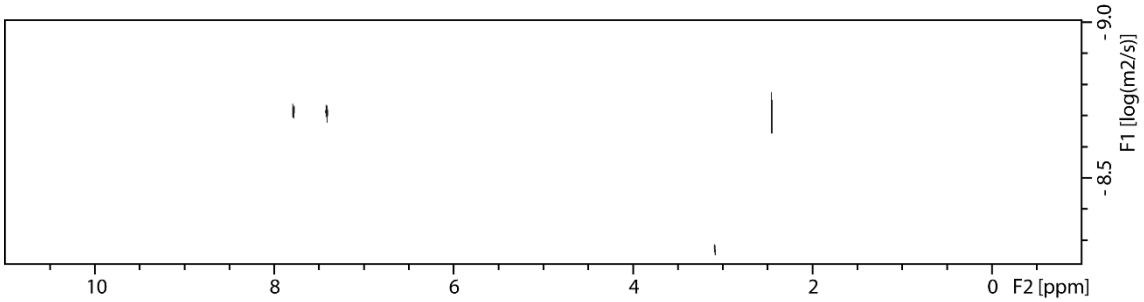

Figure 5.56: ^{1}H DOSY NMR (600 MHz, CD_3CN, 298 K) of *p*-TSA with *dstebpgp3s* pulse sequence

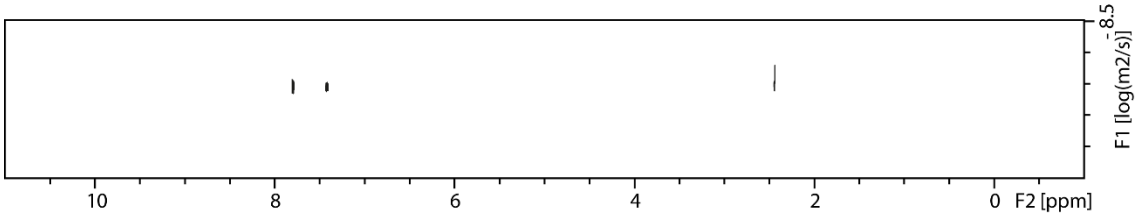

Figure 5.57: ^{1}H DOSY NMR (600 MHz, acetone-d_6, 298 K) of *p*-TSA with *ledbpgp2s* pulse sequence.

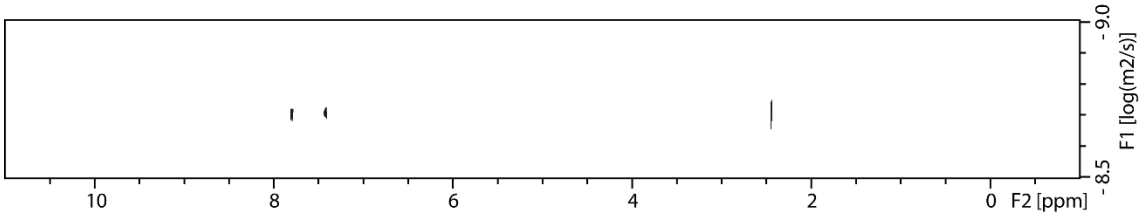

Figure 5.58: ^{1}H DOSY NMR (600 MHz, acetone-d_6, 298 K) of *p*-TSA with *dstebpgp3s* pulse sequence.

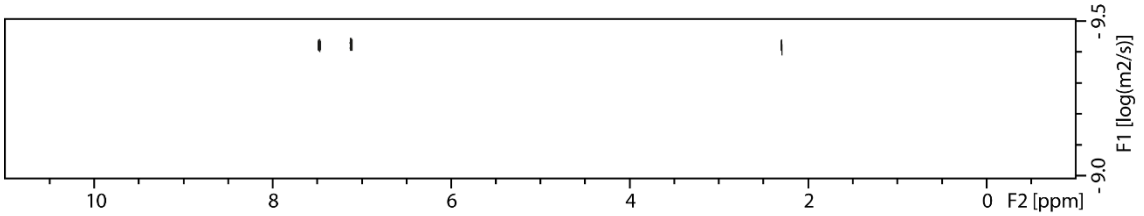

Figure 5.59: ^{1}H DOSY NMR (600 MHz, DMSO-d_6, 298 K) of *p*-TSA with *ledbpgp2s* pulse sequence.

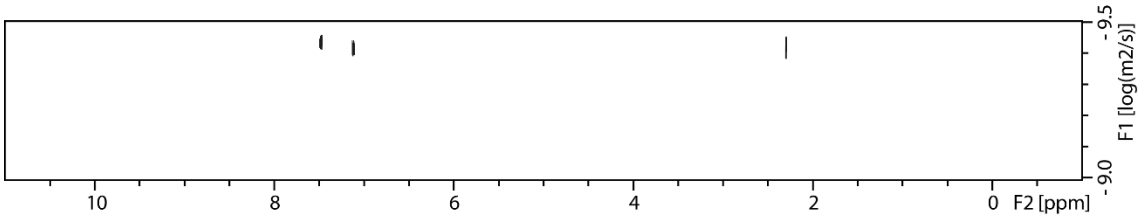

Figure 5.60: ^{1}H DOSY NMR (600 MHz, DMSO-d_6, 298 K) of *p*-TSA with *dstebpgp3s* pulse sequence.

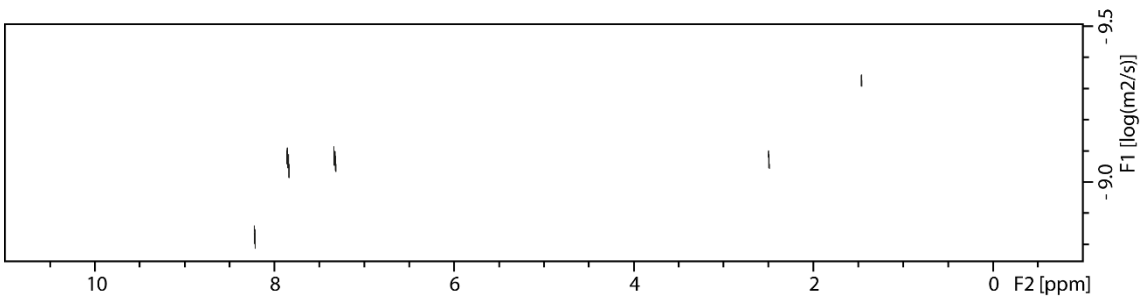

Figure 5.61: ^{1}H DOSY NMR (600 MHz, DMF-d_7, 298 K) of *p*-TSA with *ledbpgp2s* pulse sequence.

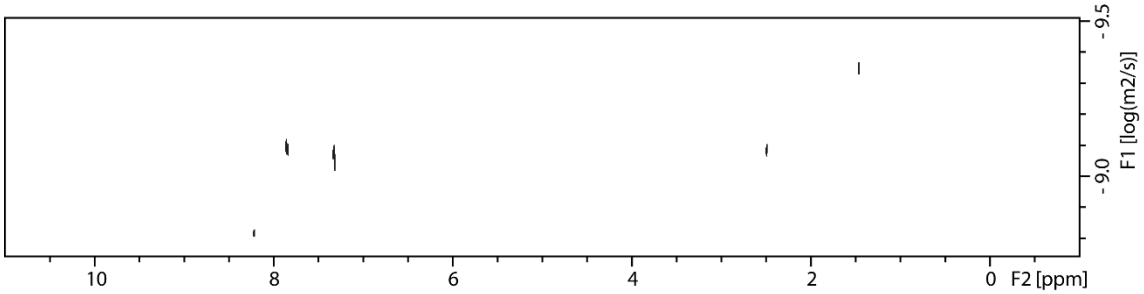

Figure 5.62: ^{1}H DOSY NMR (600 MHz, DMF-d_7, 298 K) of *p*-TSA with *dstebpgp3s* pulse sequence.

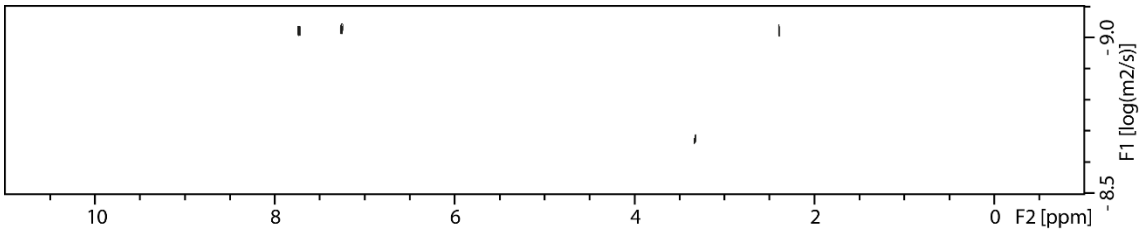

Figure 5.63: ^{1}H DOSY NMR (600 MHz, CD_3OD, 298 K) of *p*-TSA with *ledbpgp2s* pulse sequence.

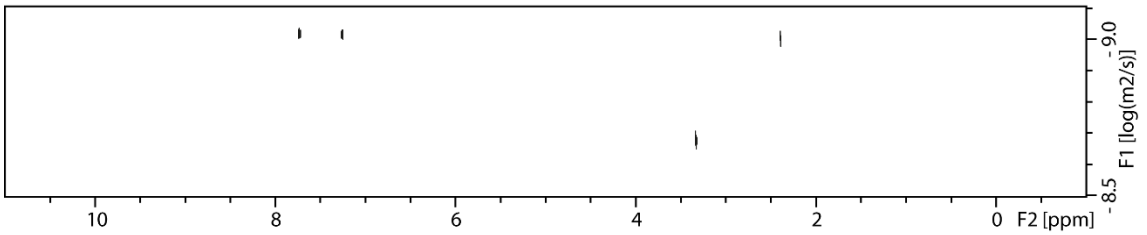

Figure 5.64: ^{1}H DOSY NMR (600 MHz, CD_3OD, 298 K) of *p*-TSA with *dstebpgp3s* pulse sequence.

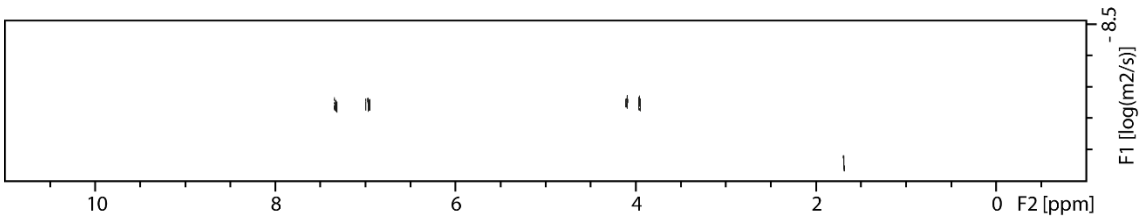

Figure 5.65: ^{1}H DOSY NMR (600 MHz, CD_2Cl_2, 298 K) of 2-POE with *ledbpgp2s* pulse sequence.

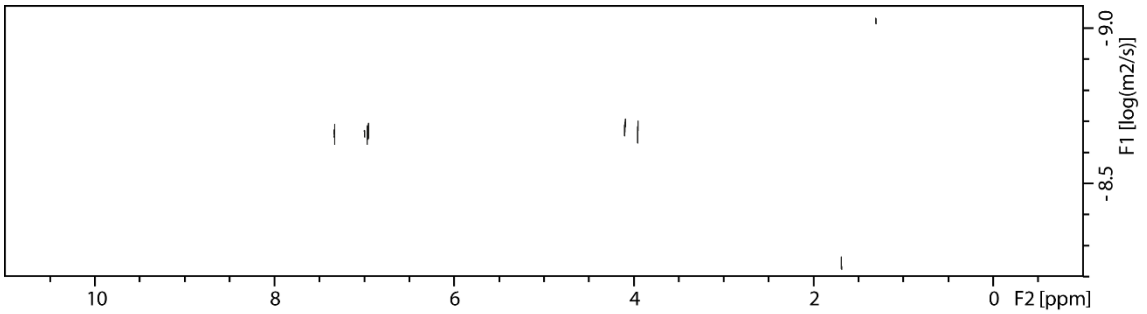

Figure 5.66: ^{1}H DOSY NMR (600 MHz, CD_2Cl_2, 298 K) of 2-POE with *dstebpgp3s* pulse sequence.

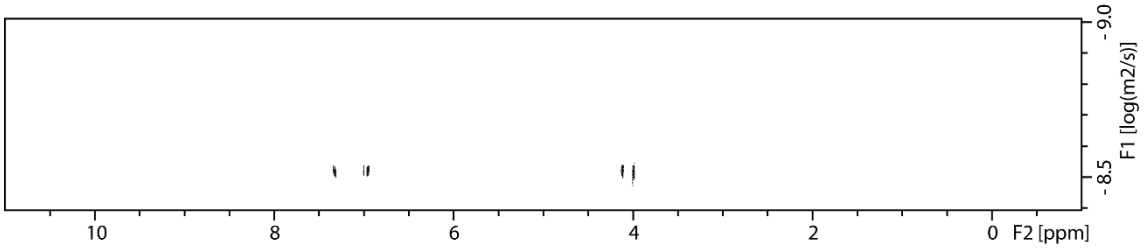

Figure 5.67: ^{1}H DOSY NMR (600 MHz, $CDCl_3$, 298 K) of 2-POE with *ledbpgp2s* pulse sequence.

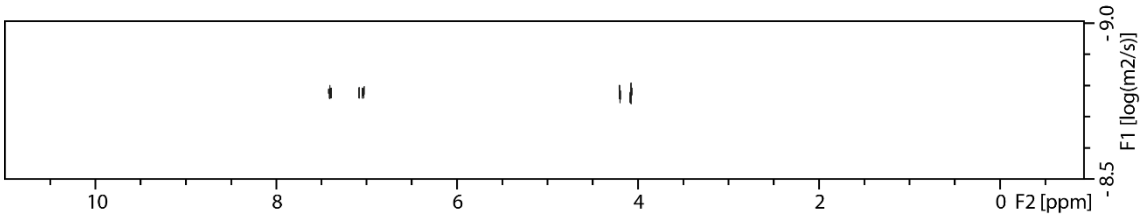

Figure 5.68: ^{1}H DOSY NMR (600 MHz, $CDCl_3$, 298 K) of 2-POE with *dstebpgp3s* pulse sequence.

5.2.5 ^{1}H DOSY Measurements at Spectrometer E

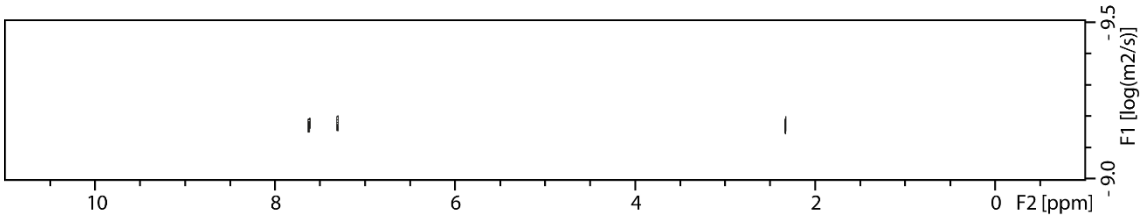

Figure 5.69: ^{1}H DOSY NMR (700 MHz, D_2O, 298 K) of *p*-TSA with *ledbpgp2s* pulse sequence.

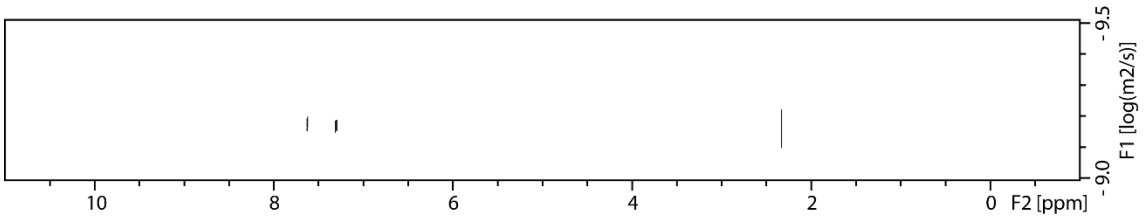

Figure 5.70: ^{1}H DOSY NMR (700 MHz, D_2O, 298 K) of *p*-TSA with *dstebpgp3s* pulse sequence.

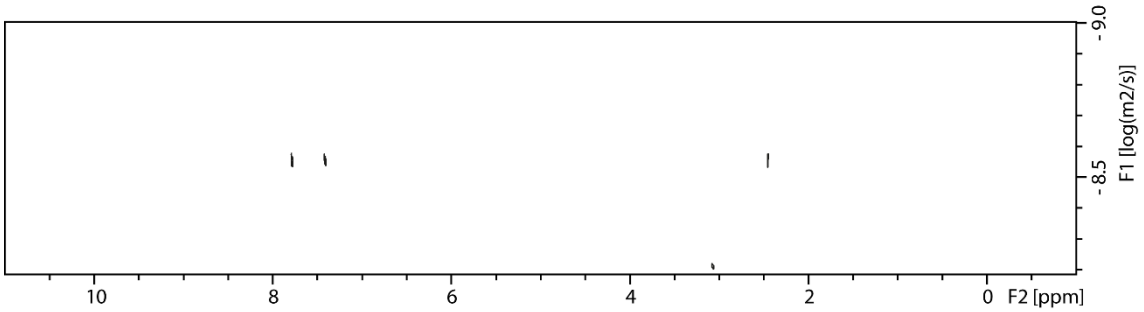

Figure 5.71: ^{1}H DOSY NMR (700 MHz, CD_3CN, 298 K) of *p*-TSA with *ledbpgp2s* pulse sequence.

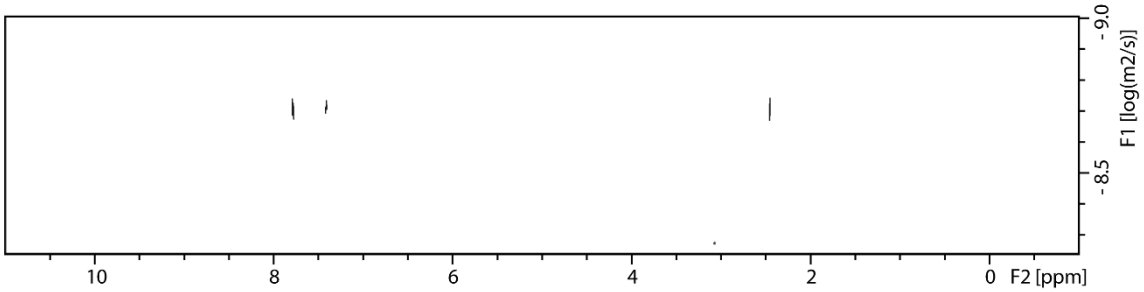

Figure 5.72: ^{1}H DOSY NMR (700 MHz, CD_3CN, 298 K) of *p*-TSA with *dstebpgp3s* pulse sequence.

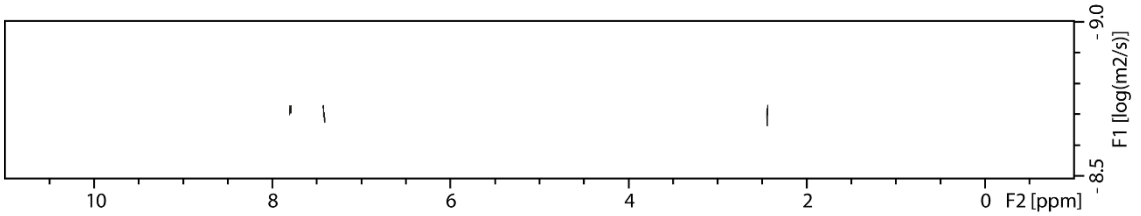

Figure 5.73: ^{1}H DOSY NMR (700 MHz, acetone-d_6, 298 K) of *p*-TSA with *ledbpgp2s* pulse sequence.

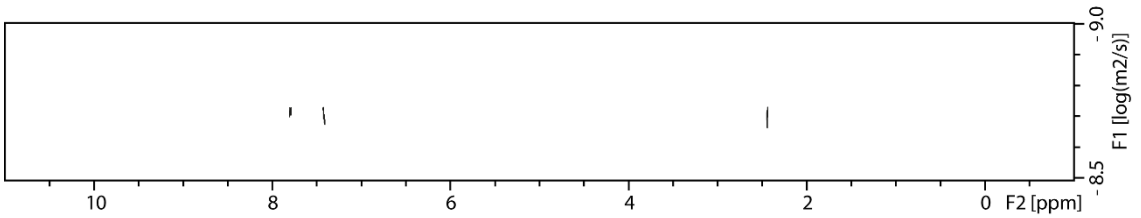

Figure 5.74: ^{1}H DOSY NMR (700 MHz, acetone-d_6, 298 K) of *p*-TSA with *dstebpgp3s* pulse sequence.

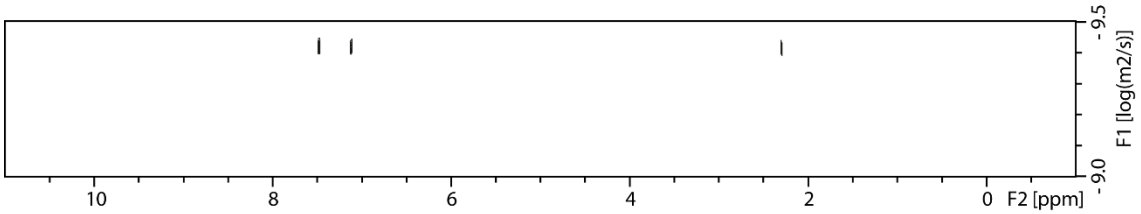

Figure 5.75: ^{1}H DOSY NMR (700 MHz, DMSO-d_6, 298 K) of *p*-TSA with *ledbpgp2s* pulse sequence.

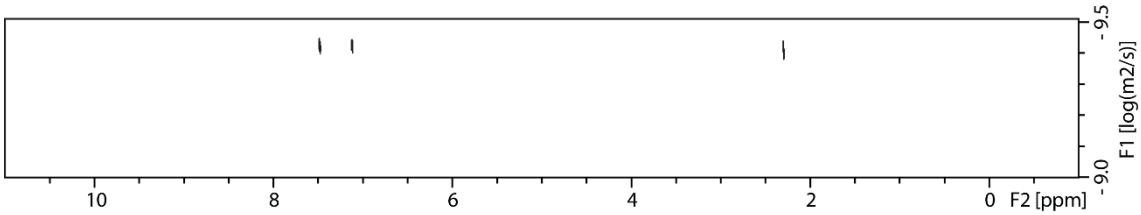

Figure 5.76: ^{1}H DOSY NMR (700 MHz, DMSO-d_6, 298 K) of *p*-TSA with *dstebpgp3s* pulse sequence.

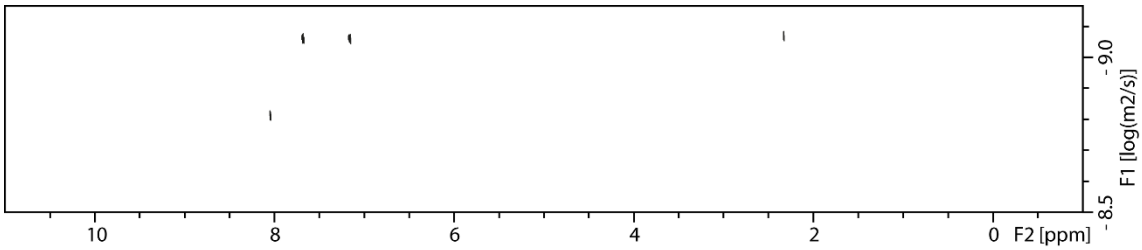

Figure 5.77: ^{1}H DOSY NMR (700 MHz, DMF-d_7, 298 K) of *p*-TSA with *ledbpgp2s* pulse sequence.

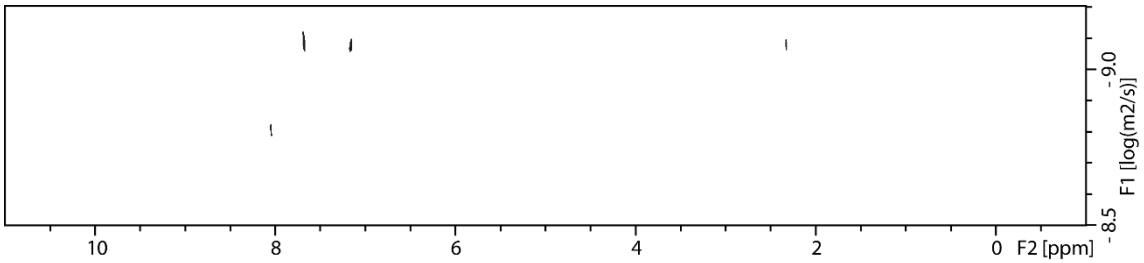

Figure 5.78: ^{1}H DOSY NMR (700 MHz, DMF-d_7, 298 K) of *p*-TSA with *dstebpgp3s* pulse sequence.

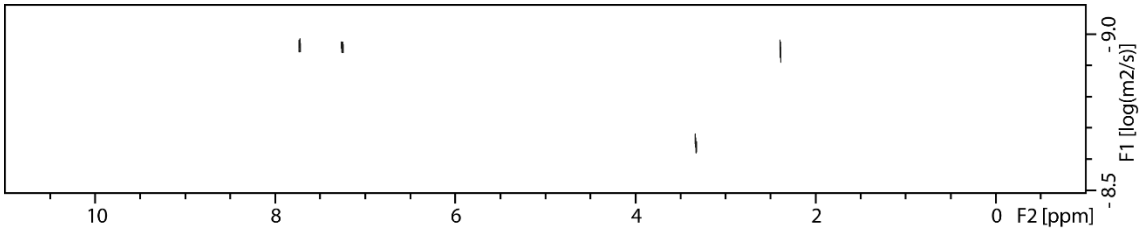

Figure 5.79: ^{1}H DOSY NMR (700 MHz, CD_3OD, 298 K) of *p*-TSA with *ledbpgp2s* pulse sequence.

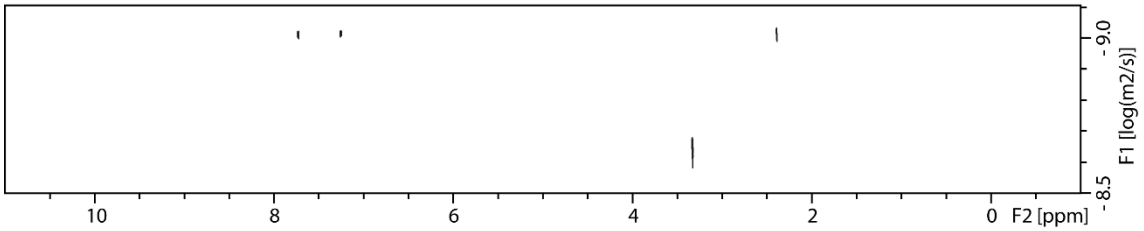

Figure 5.80: ^{1}H DOSY NMR (700 MHz, CD_3OD, 298 K) of *p*-TSA with *dstebpgp3s* pulse sequence.

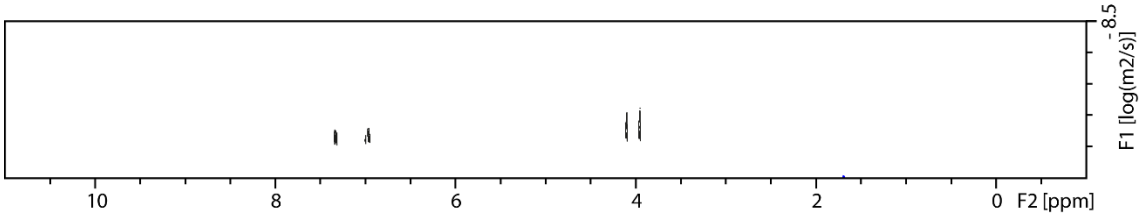

Figure 5.81: ^{1}H DOSY NMR (700 MHz, CD_2Cl_2, 298 K) of 2-POE with *ledbpgp2s* pulse sequence.

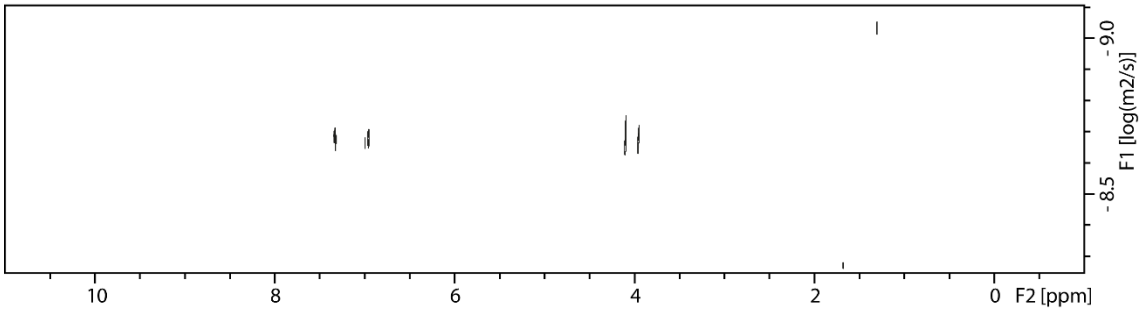

Figure 5.82: ^{1}H DOSY NMR (700 MHz, CD_2Cl_2, 298 K) of 2-POE with *dstebpgp3s* pulse sequence.

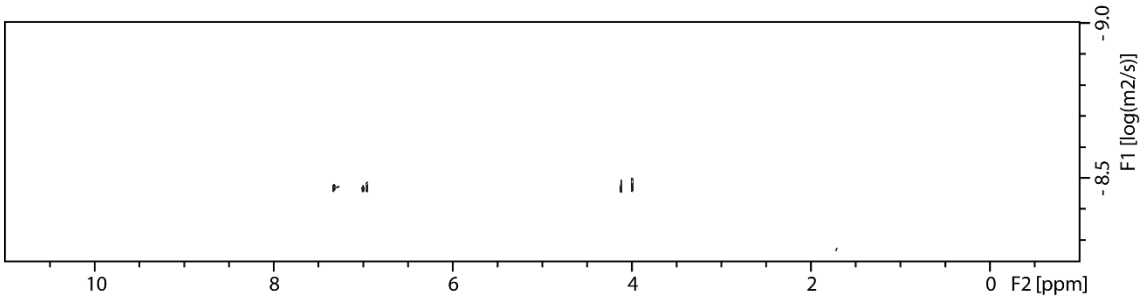

Figure 5.83: ^{1}H DOSY NMR (700 MHz, $CDCl_3$, 298 K) of 2-POE with *ledbpgp2s* pulse sequence.

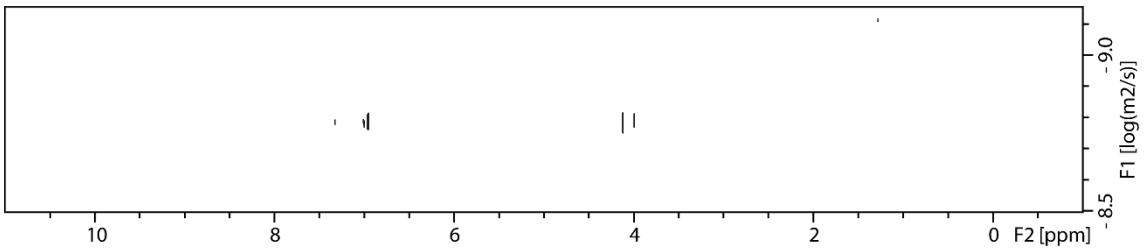

Figure 5.84: ^{1}H DOSY NMR (700 MHz, $CDCl_3$, 298 K) of 2-POE with *dstebpgp3s* pulse sequence.

5.2.6 Overview on the Obtained Diffusion Coefficients from the ^{1}H DOSY Measurements

Table 5.1: Obtained diffusion coefficients $\boldsymbol{D_{cc}}$ and $\boldsymbol{D}$ in $10^{-10} \cdot m^2 \cdot s^{-1}$ for the ^{1}H DOSY NMR measurements on spectrometers **A-F**.

D_2O	**A**	**B**	**C**	**D**	**E**	**F**
$\boldsymbol{D_{cc}}$	6.688 ± 0.005	6.738 ± 0.004	6.857 ± 0.003	6.486 ± 0.004	6.646 ± 0.007	7.490 ± 0.002
$\boldsymbol{D}$	6.693 ± 0.005	6.799 ± 0.001	6.778 ± 0.002	6.303 ± 0.003	6.792 ± 0.001	7.370 ± 0.001
CD_2Cl_2	**A**	**B**	**C**	**D**	**E**	**F**
$\boldsymbol{D_{cc}}$	21.19 ± 0.04	21.07 ± 0.09	22.73 ± 0.11	21.46 ± 0.07	20.75 ± 0.10	22.10 ± 0.10
$\boldsymbol{D}$	25.87 ± 0.04	24.42 ± 0.01	61.47 ± 0.05	56.81 ± 0.06	73.75 ± 0.07	22.50 ± 0.02
CD_3CN	**A**	**B**	**C**	**D**	**E**	**F**
$\boldsymbol{D_{cc}}$	19.63 ± 0.05	19.76 ± 0.10	20.14 ± 0.07	19.03 ± 0.06	19.69 ± 0.06	20.07 ± 0.06
$\boldsymbol{D}$	19.04 ± 0.01	21.12 ± 0.11	26.83 ± 0.02	27.33 ± 0.03	28.43 ± 0.01	20.10 ± 0.02
acetone-d_6	**A**	**B**	**C**	**D**	**E**	**F**
$\boldsymbol{D_{cc}}$	19.48± 0.05	19.03 ± 0.06	20.82 ± 0.04	19.51 ± 0.06	19.74 ± 0.03	21.10 ± 0.05
$\boldsymbol{D}$	21.70 ± 0.01	23.67 ± 0.06	48.62 ± 0.03	49.39 ± 0.04	44.59 ± 0.03	20.80 ± 0.02

DMSO-d_6	A	B	C	D	E	F
D_{cc}	3.734 ± 0.005	3.748 ± 0.003	3.843 ± 0.007	3.741 ± 0.002	3.766 ± 0.006	4.06 ± 0.008
D	3.741 ± 0.008	3.627 ± 0.004	3.825 ± 0.002	3.654 ± 0.002	3.822 ± 0.001	3.920 ± 0.002
DMF-d_7	A	B	C	D	E	F
D_{cc}	8.171 ± 0.004	8.082 ± 0.005	8.679 ± 0.003	8.197 ± 0.006	8.224 ± 0.004	8.930 ± 0.003
D	8.508 ± 0.001	8.380 ± 0.005	8.678 ± 0.001	8.457 ± 0.002	8.660 ± 0.002	8.780 ± 0.007
CD_3OD	A	B	C	D	E	F
D_{cc}	9.421 ± 0.002	9.588 ± 0.004	9.956 ± 0.002	6.688 ± 0.002	9.612 ± 0.003	10.50 ± 0.03
D	10.06 ± 0.01	9.895 ± 0.003	10.77 ± 0.02	9.101 ± 0.002	11.02 ± 0.08	10.20 ± 0.09
$CDCl_3$	A	B	C	D	E	F
D_{cc}	16.31 ± 0.07	15.95 ± 0.09	17.40 ± 0.10	16.58 ± 0.05	16.45 ± 0.10	17.30 ± 0.06
D	19.98 ± 0.02	18.19 ± 0.07	29.58 ± 0.02	29.70 ± 0.03	34.20 ± 0.03	16.90 ± 0.01

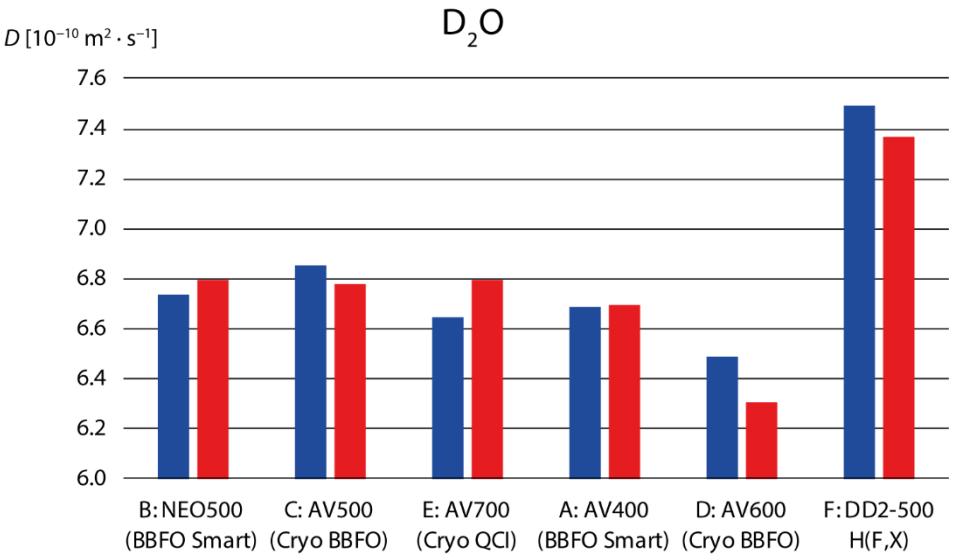

Figure 5.85: Plotted values for D_{cc} (blue) and D (red) for measurements in D_2O.

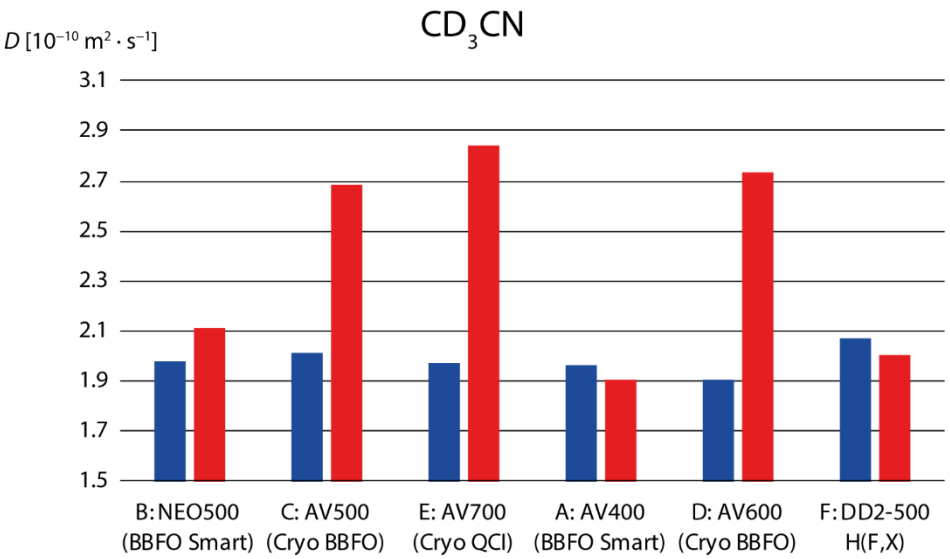

Figure 5.86: Plotted values for D_{cc} (blue) and D (red) for measurements in CD_3CN.

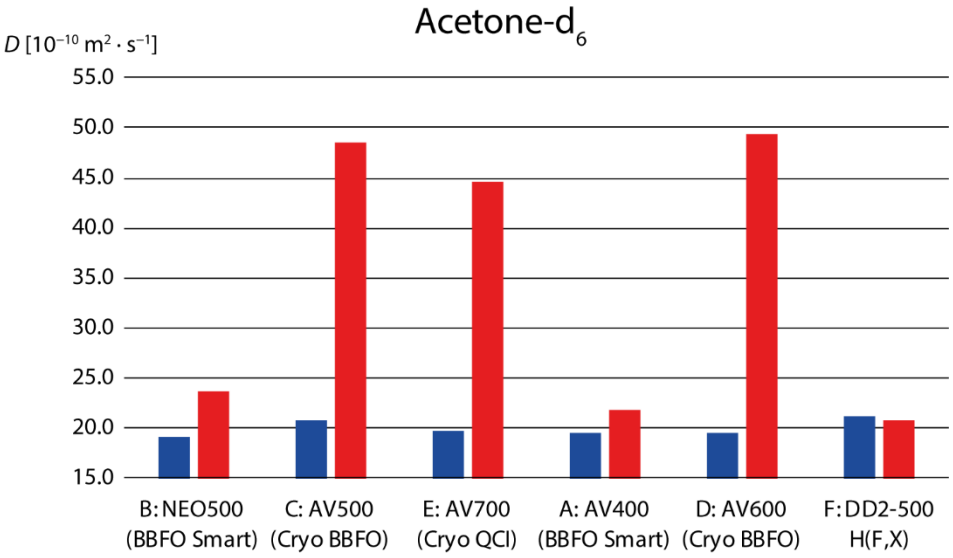

Figure 5.87: Plotted values for D_{cc} (blue) and D (red) for measurements in acetone-d_6.

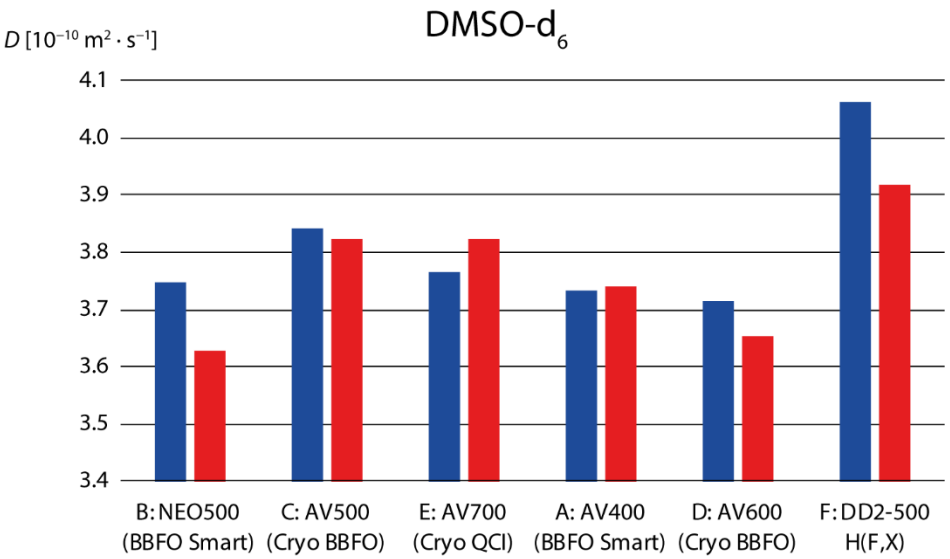

Figure 5.88: Plotted values for D_{cc} (blue) and D (red) for measurements in DMSO-d_6.

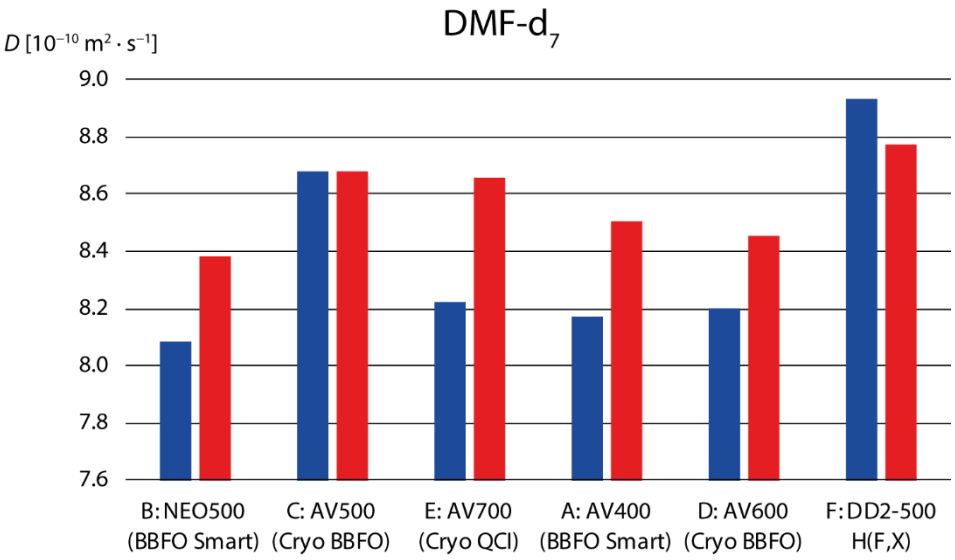

Figure 5.89: Plotted values for D_{cc} (blue) and D (red) for measurements in DMF-d_7.

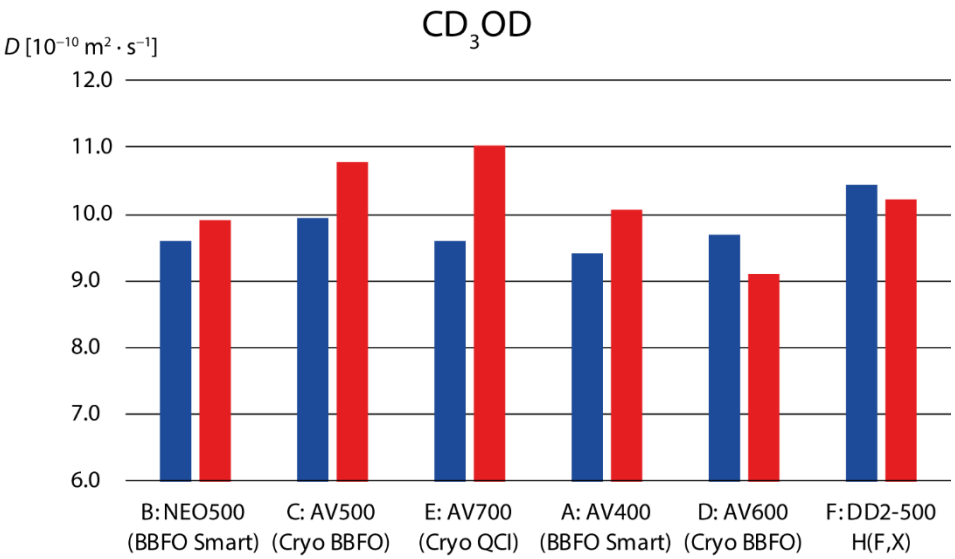

Figure 5.90: Plotted values for D_{cc} (blue) and D (red) for measurements in CD_3OD.

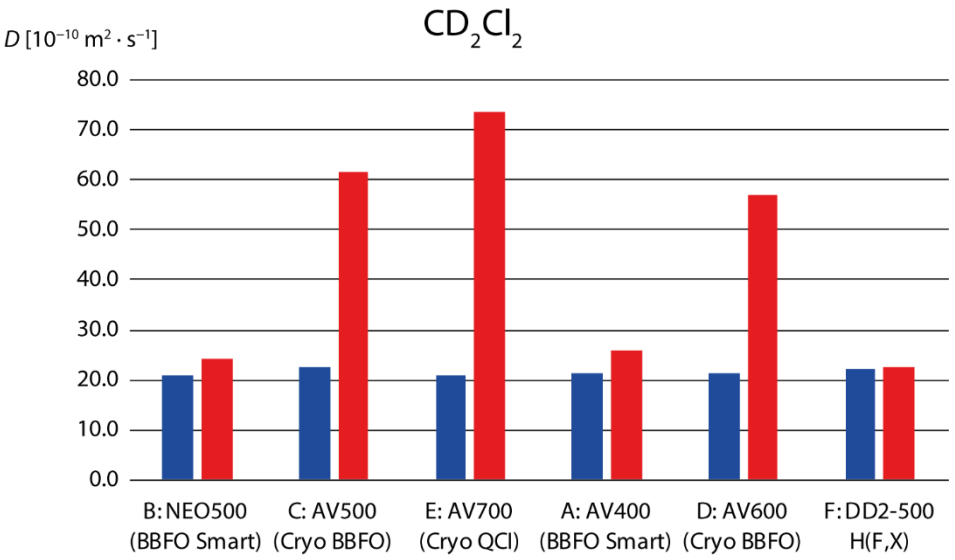

Figure 5.91: Plotted values for D_{cc} (blue) and D (red) for measurements in CD_2Cl_2.

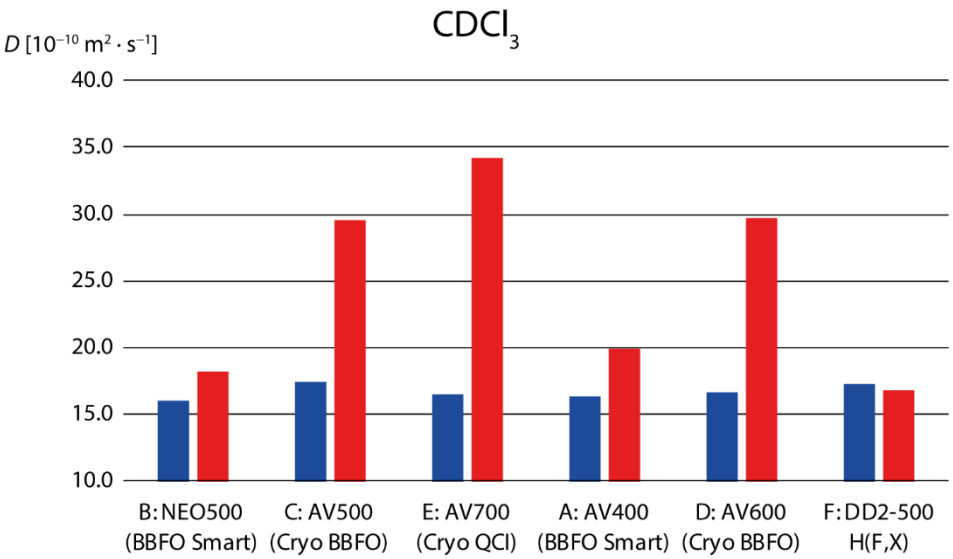

Figure 5.92: Plotted values for D_{cc} (blue) and D (red) for measurements in $CDCl_3$.

5.2.7 Convection Tests on Spectrometer E

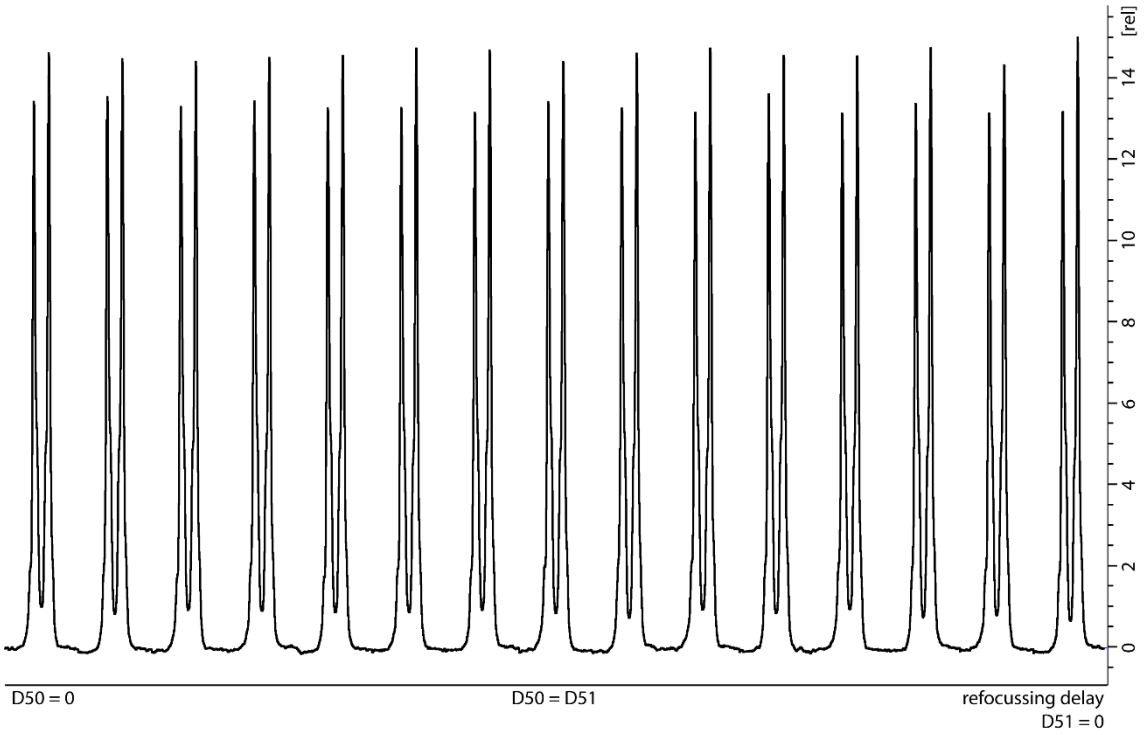

Figure 5.93: Plot of the signal intensity (700 MHz, T = 298 K, D_2O) of proton **1** against the refocusing delays D50 and D51.

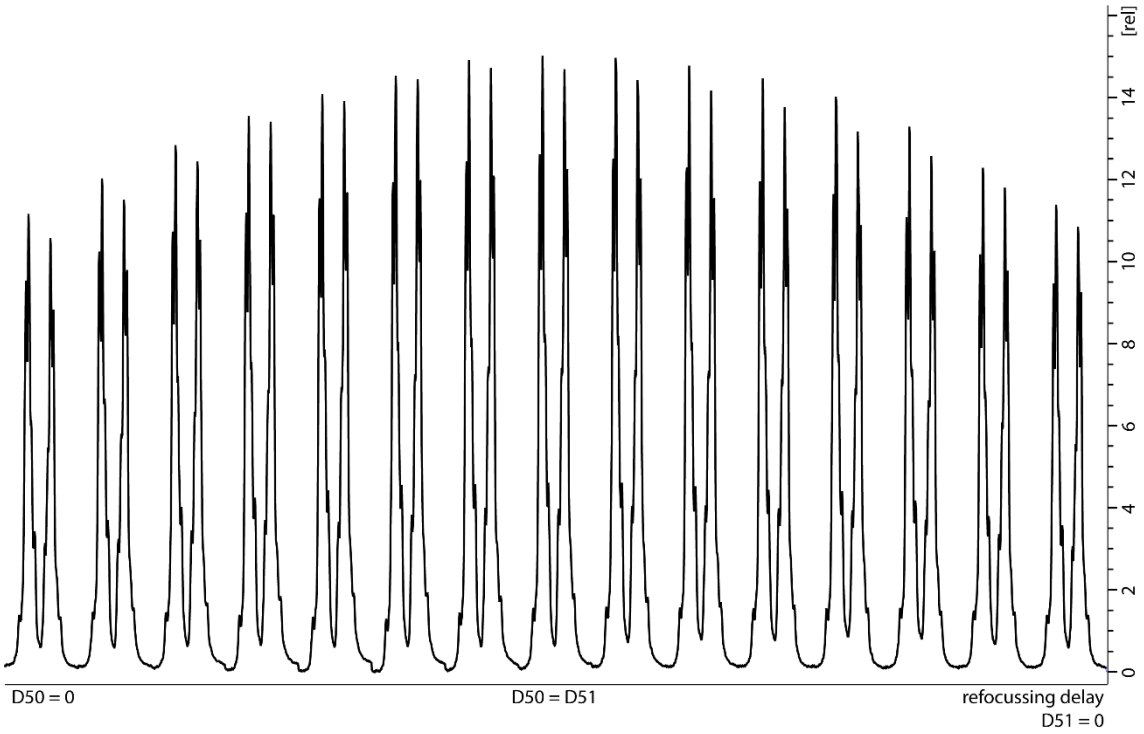

Figure 5.94: Plot of the signal intensity (700 MHz, T = 298 K, CD_2Cl_2) of proton **1** against the refocusing delays D50 and D51.

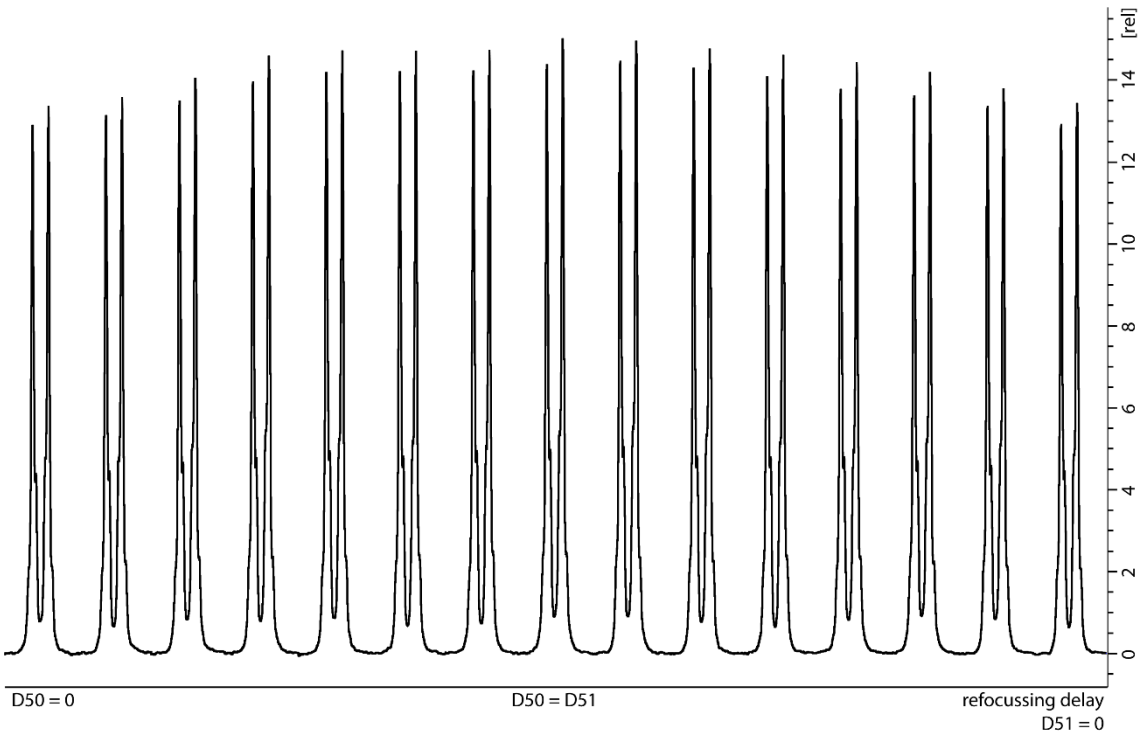

Figure 5.95: Plot of the signal intensity (700 MHz, T = 298 K, CD_3CN) of proton **1** against the refocusing delays D50 and D51.

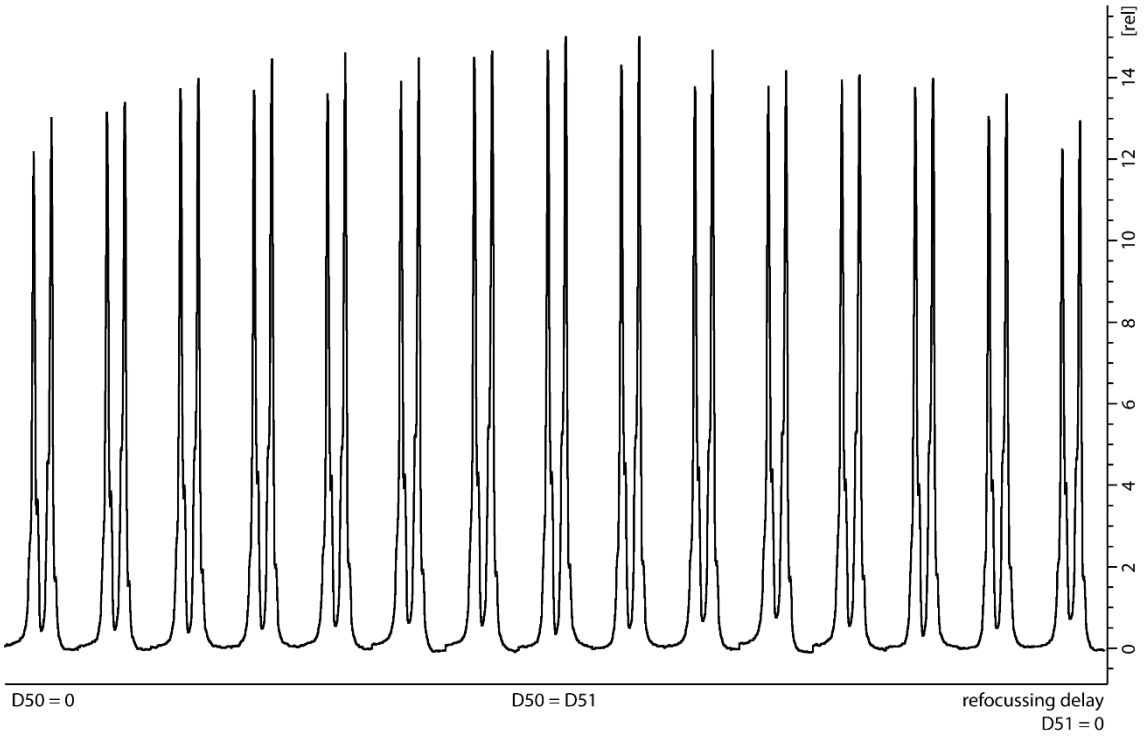

Figure 5.96: Plot of the signal intensity (700 MHz, T = 298 K, acetone-d_6) of proton **1** against the refocusing delays D50 and D51.

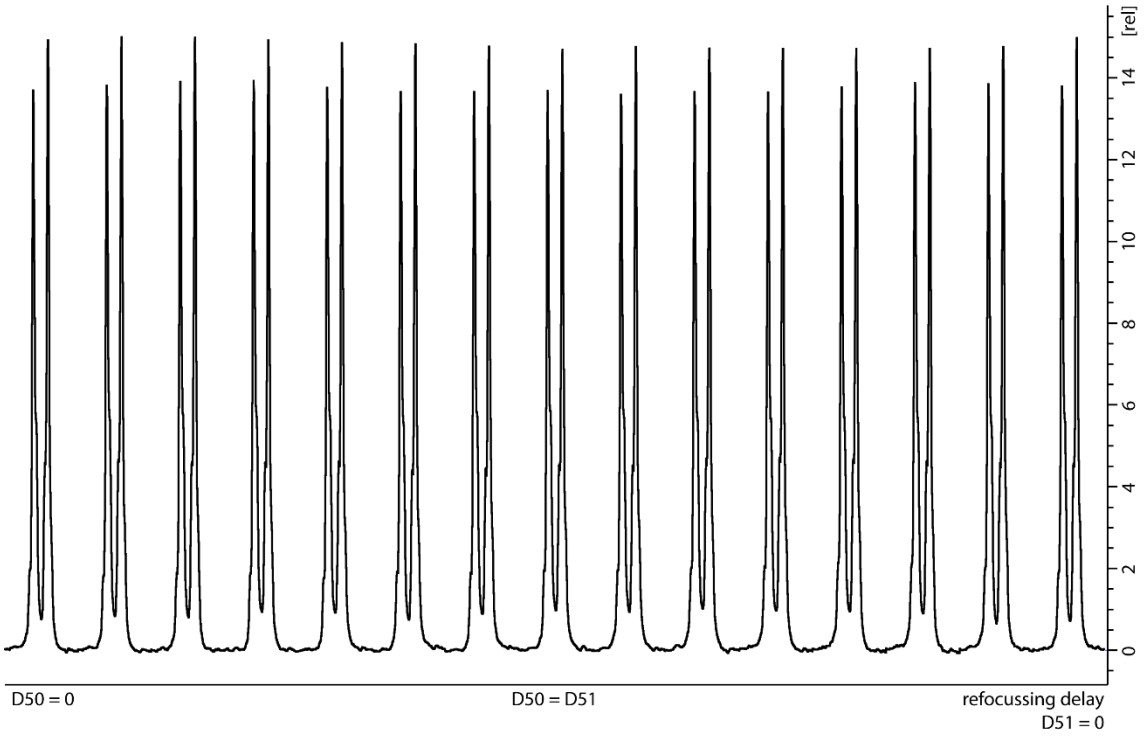

Figure 5.97: Plot of the signal intensity (700 MHz, T = 298 K, DMF-d_7) of proton **1** against the refocusing delays D50 and D51.

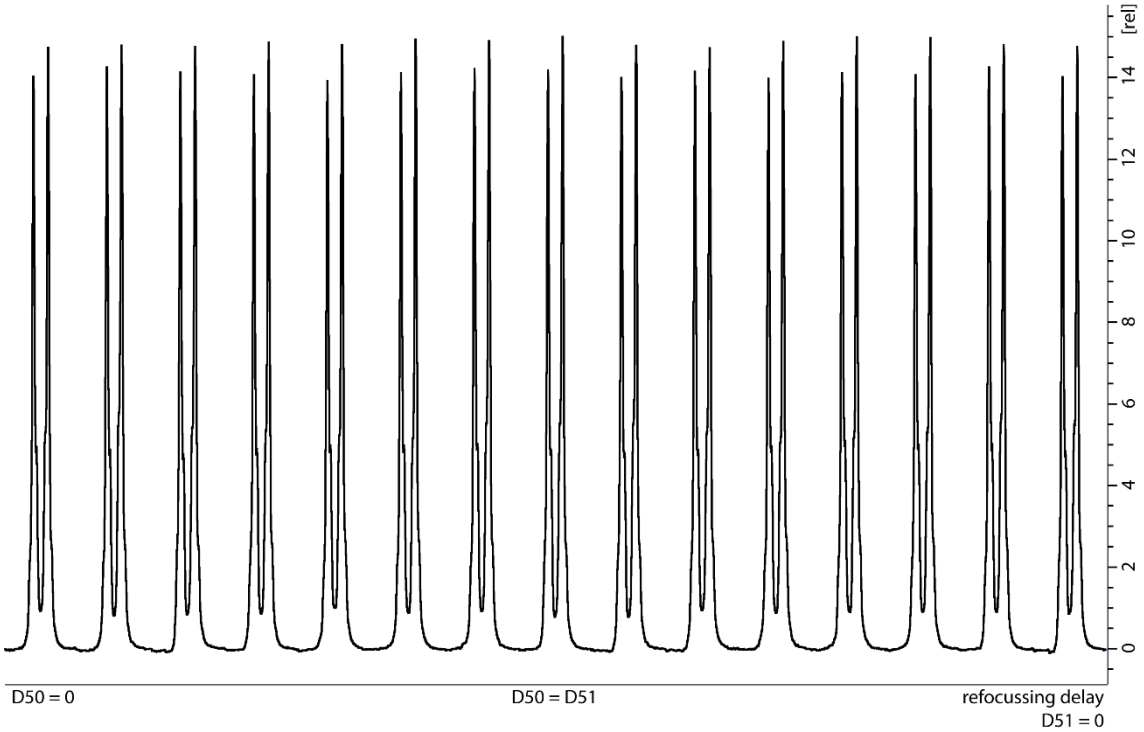

Figure 5.98: Plot of the signal intensity (700 MHz, T = 298 K, DMSO-d_6) of proton **1** against the refocusing delays D50 and D51.

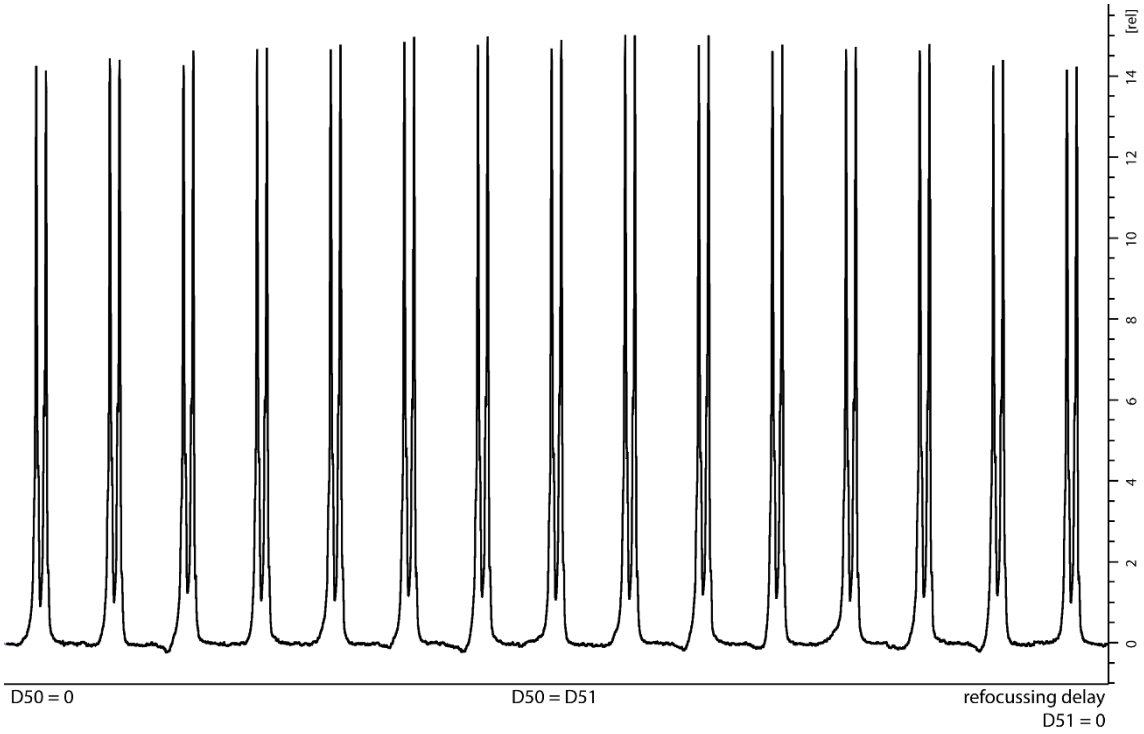

Figure 5.99: Plot of the signal intensity (700 MHz, T = 298 K, CD_3OD) of proton **1** against the refocusing delays D50 and D51.

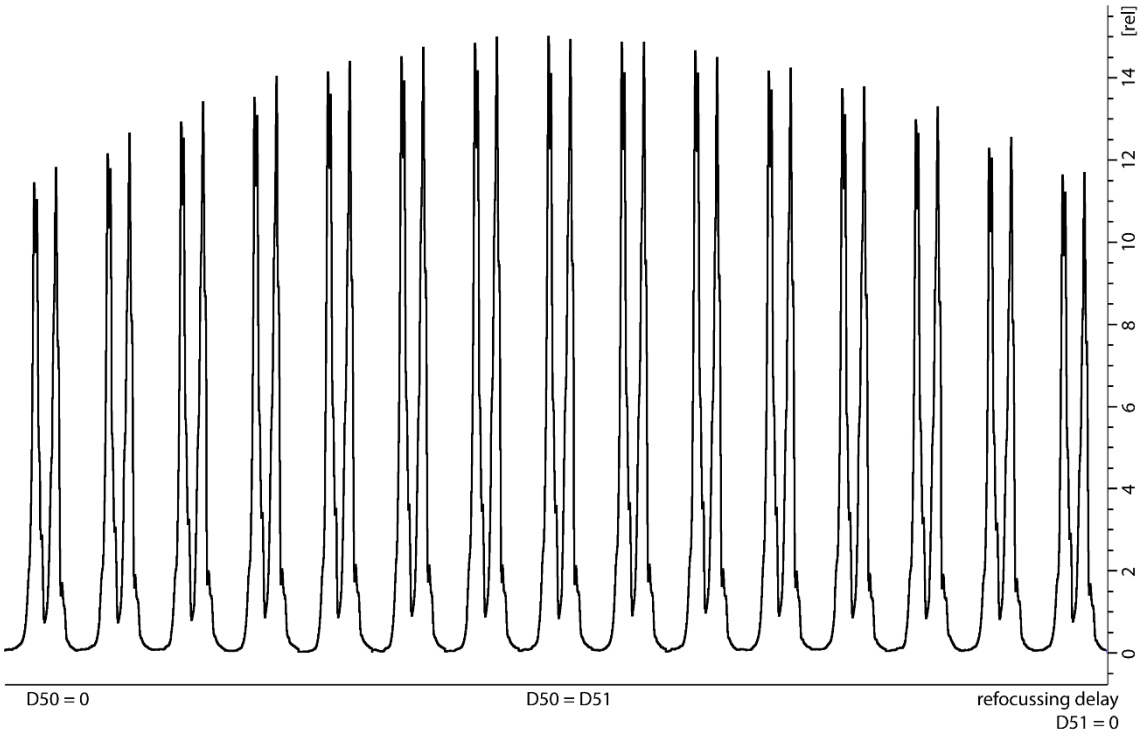

Figure 5.100: Plot of the signal intensity (700 MHz, T = 298 K, $CDCl_3$) of proton **1** against the refocusing delays D50 and D51.

5.3 VT ^{1}H DOSY NMR Measurements of $3BF_4@Pd_4L^{ACR1\text{-}6}{}_8$

Note: VT experiments were carried out for $3BF_4@Pd_4L^{ACR2}{}_8$, $3BF_4@Pd_4L^{ACR3}{}_8$, $3BF_4@Pd_4L^{ACR4}{}_8$ and $3BF_4@Pd_4L^{ACR6}{}_8$. DOSY data for $3BF_4@Pd_4L^{ACR1}{}_8$ was obtained only at 25 °C and $3BF_4@Pd_4L^{ACR5}{}_8$ has not been successfully synthesized by the end of this doctoral work due to time reasons. All spectra were recorder in CD_3CN. The sample was equilibrated to the exact temperature for at least 10 min, prior measurement.

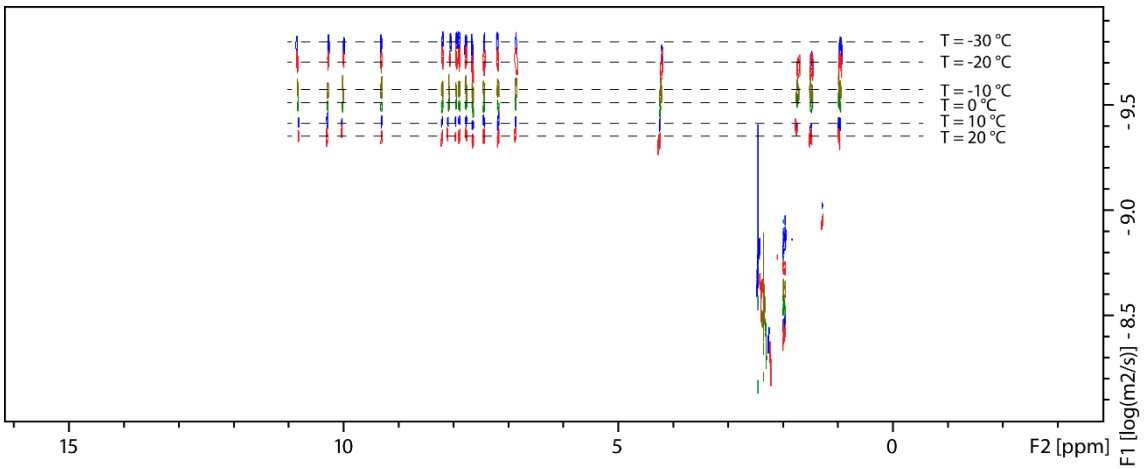

Figure 5.101: Stack of VT ^{1}H DOSY NMR (500 MHz, CD_3CN, *dstebpgp3s*) spectra of $3BF_4@Pd_4L^{ACR2}{}_8$ measured at the mentioned temperatures.

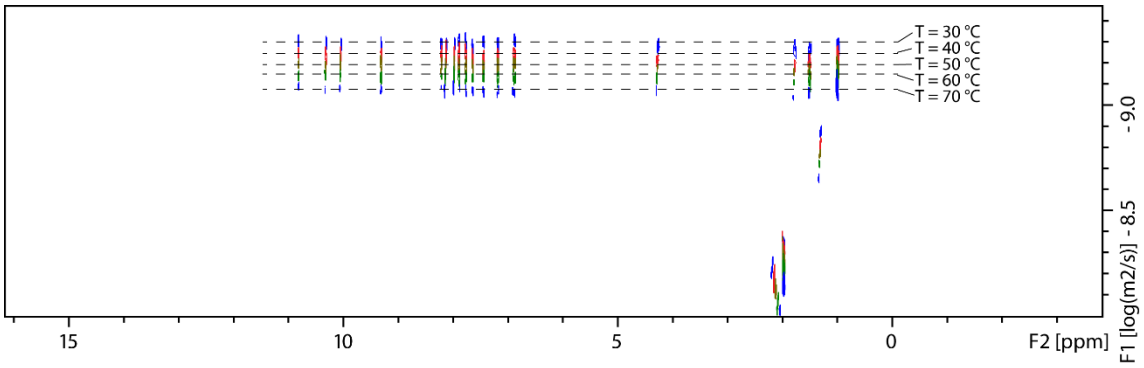

Figure 5.102: Stack of VT ^{1}H DOSY NMR (500 MHz, CD_3CN, *dstebpgp3s*) spectra of $3BF_4@Pd_4\mathbf{L}^{\mathbf{ACR2}}{}_8$ measured at the mentioned temperatures.

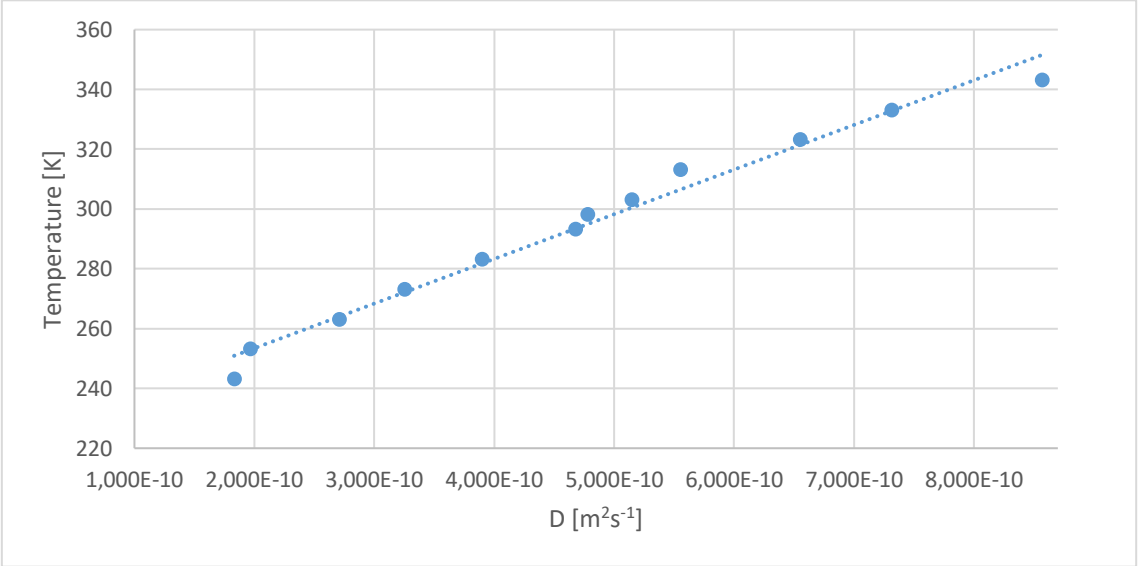

Figure 5.103: Plot of obtained values for D against temperature for $3BF_4@Pd_4\mathbf{L}^{\mathbf{ACR2}}{}_8$.

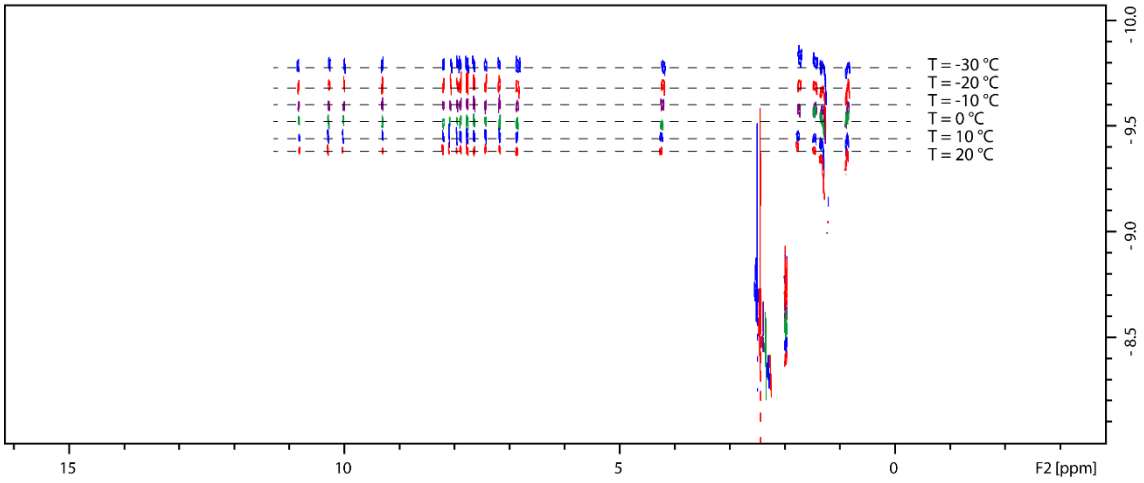

Figure 5.104: Stack of VT ^{1}H DOSY NMR (500 MHz, CD_3CN, *dstebpgp3s*) spectra of $3BF_4@Pd_4\mathbf{L}^{\mathbf{ACR3}}{}_8$ measured at the mentioned temperatures.

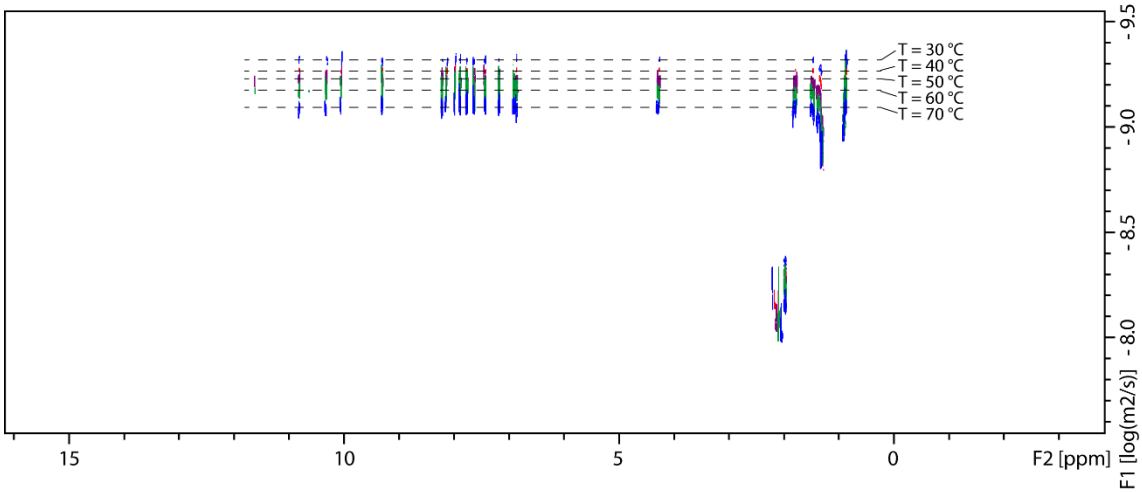

Figure 5.105: Stack of VT ^{1}H DOSY NMR (500 MHz, CD_3CN, *dstebpgp3s*) spectra of $3BF_4@Pd_4\mathbf{L}^{\mathbf{ACR3}}_{\mathbf{8}}$ measured at the mentioned temperatures.

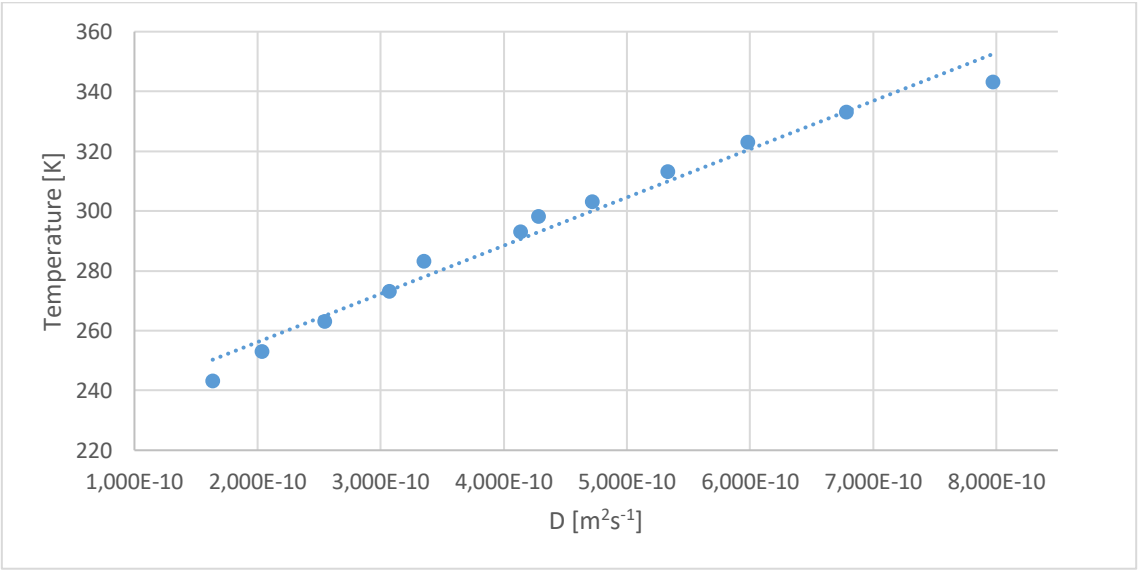

Figure 5.106: Plot of obtained values for D against temperature for $3BF_4@Pd_4\mathbf{L}^{\mathbf{ACR3}}_{8.}$

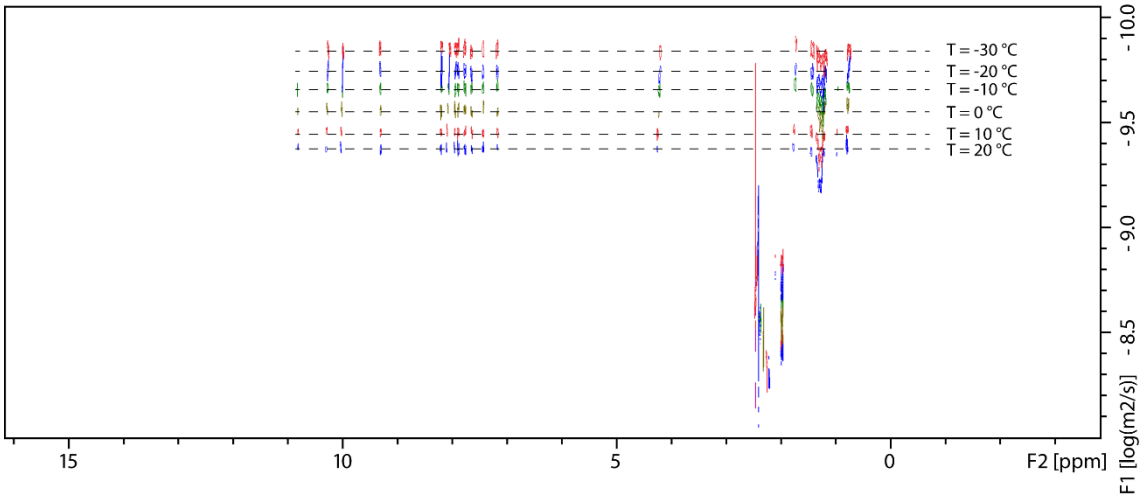

Figure 5.107: Stack of VT ^{1}H DOSY NMR (500 MHz, CD_3CN, *dstebpgp3s*) spectra of $3BF_4@Pd_4\mathbf{L}^{\mathbf{ACR4}}_{\mathbf{8}}$ measured at the mentioned temperatures.

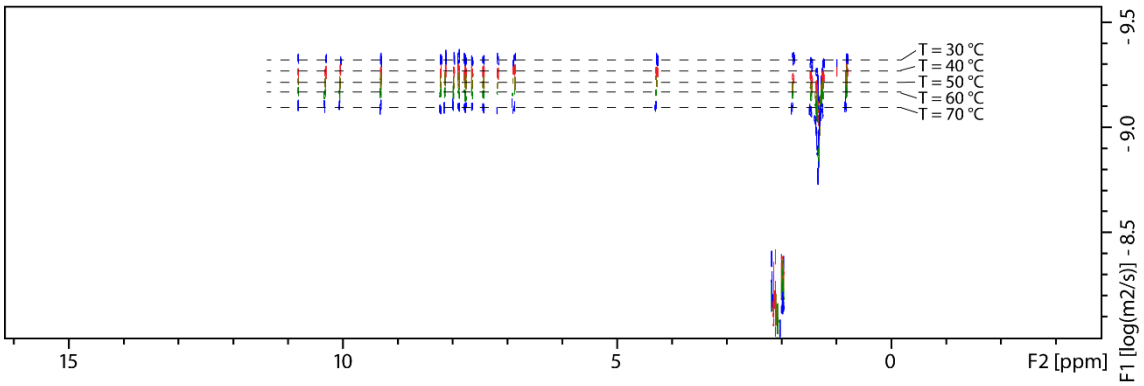

Figure 5.108: Stack of VT ^{1}H DOSY NMR (500 MHz, CD_3CN, *dstebpgp3s*) spectra of $3BF_4@Pd_4\mathbf{L}^{\mathbf{ACR4}}_{\mathbf{8}}$ measured at the mentioned temperatures.

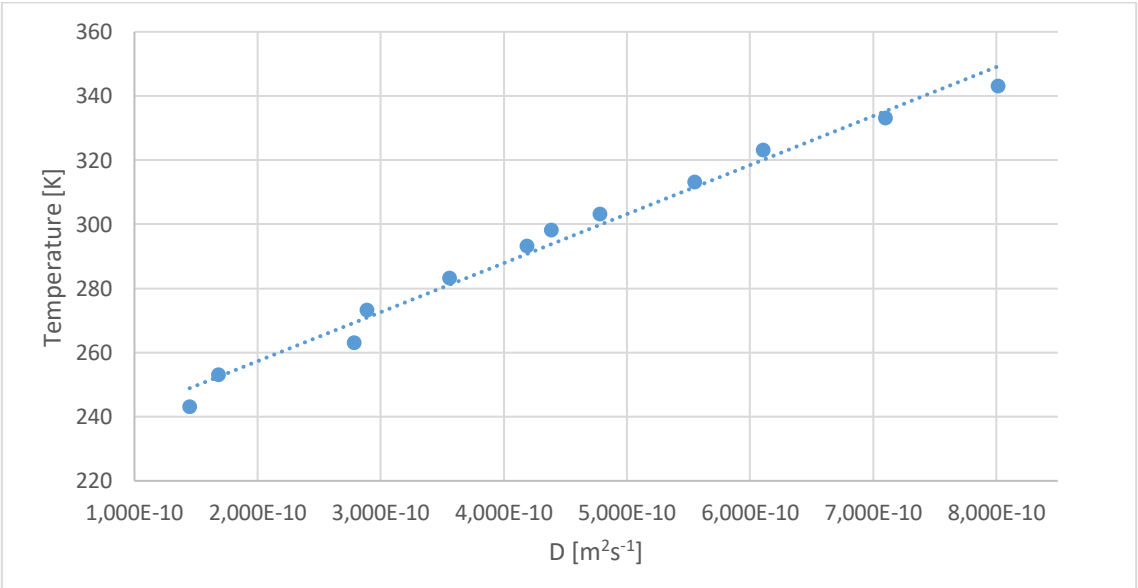

Figure 5.109: Plot of obtained values for D against temperature for $3BF_4@Pd_4\mathbf{L}^{\mathbf{ACR4}}_{8.}$

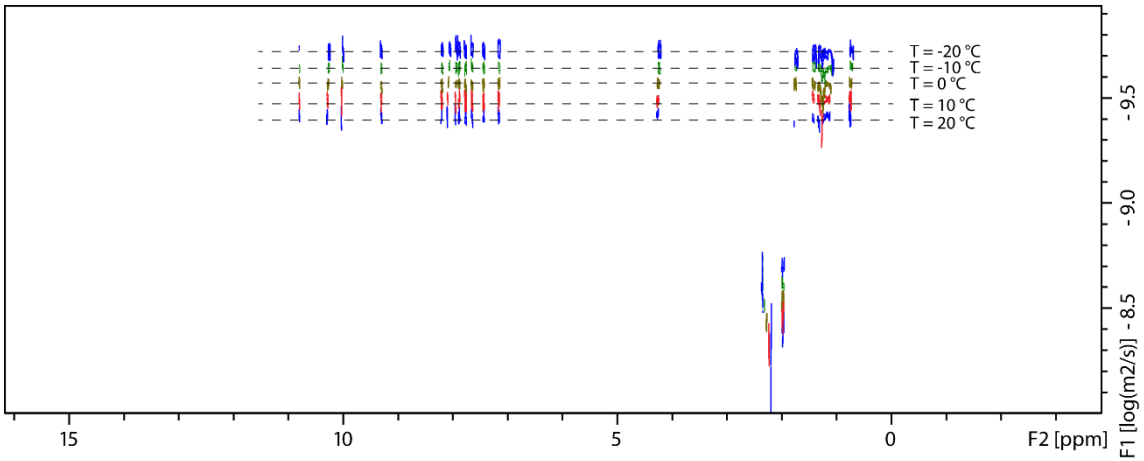

Figure 5.110: Stack of VT ^{1}H DOSY NMR (500 MHz, CD_3CN, *dstebpgp3s*) spectra of $3BF_4@Pd_4\mathbf{L}^{\mathbf{ACR6}}{}_{\mathbf{8}}$ measured at the mentioned temperatures.

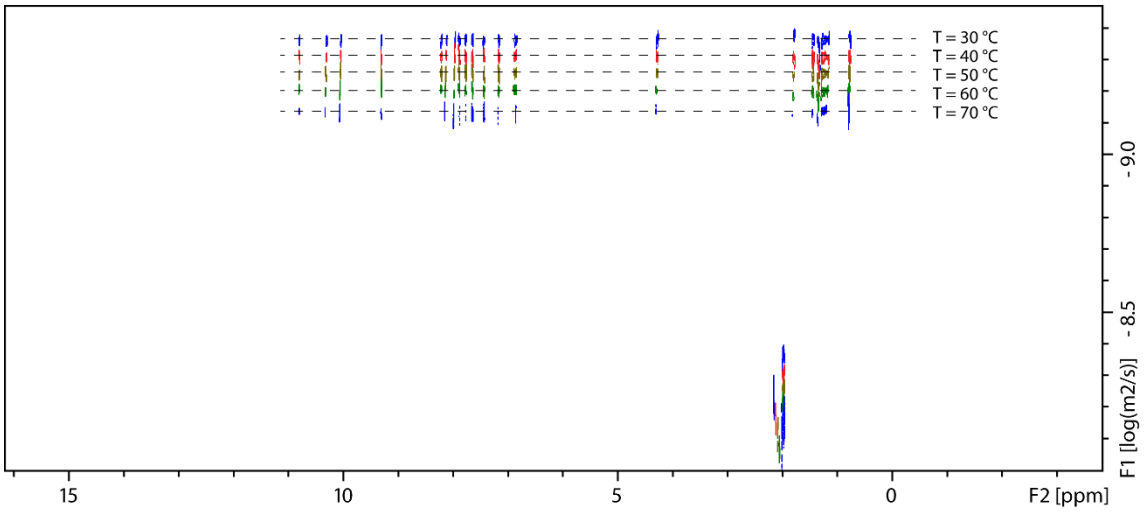

Figure 5.111: Stack of VT ^{1}H DOSY NMR (500 MHz, CD_3CN, *dstebpgp3s*) spectra of $3BF_4@Pd_4\mathbf{L}^{\mathbf{ACR6}}{}_{\mathbf{8}}$ measured at the mentioned temperatures.

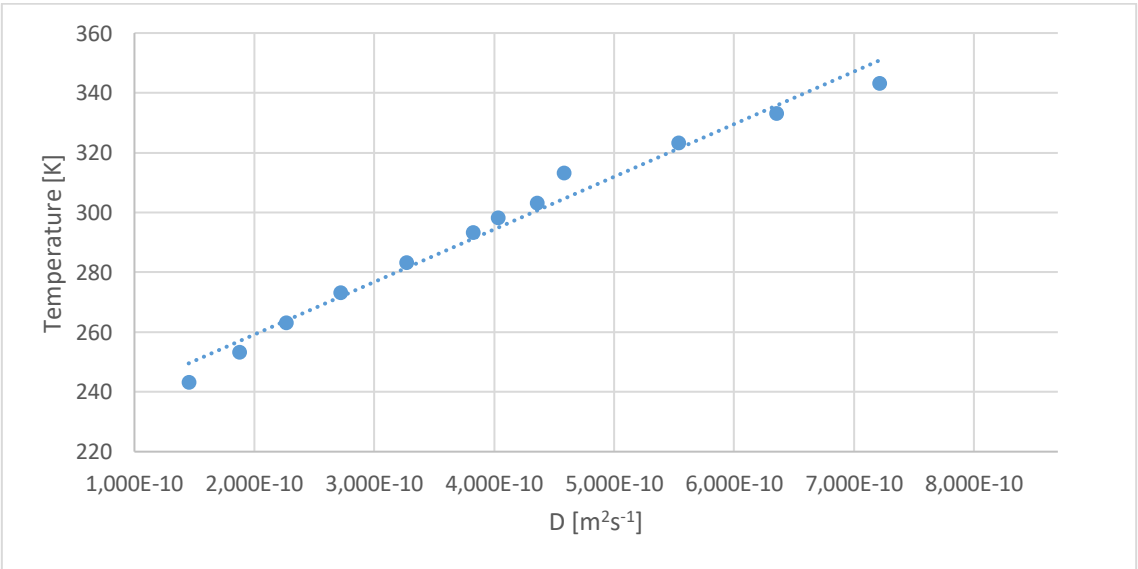

Figure 5.112: Plot of obtained values for D against temperature for $3BF_4@Pd_4\mathbf{L}^{\mathbf{ACR6}}{}_{\mathbf{8}}$.

5.3.1 VT ^{1}H DOSY NMR Measurement Parameters

Table 5.2: Values for gradient duration P30 and diffusion time D20 during the VT DOSY experiments.

	$3BF_4@Pd_4L^{ACR1}_8$		**$3BF_4@Pd_4L^{ACR2}_8$**		**$3BF_4@Pd_4L^{ACR3}_8$**	
T [°C]	D20 [s]	P30 [µs]	D20 [s]	P30 [µs]	D20 [s]	P30 [µs]
-30			0.08	2200	0.09	2100
-20			0.08	1800	0.09	1700
-10			0.08	1700	0.09	1700
0			0.08	1400	0.09	1500
10			0.08	1300	0.09	1400
20			0.08	1200	0.08	1200
25	0.09	1200	0.08	1200	0.08	1200
30			0.08	1100	0.08	1200
40			0.08	1100	0.08	1200
50			0.08	1100	0.08	1100
60			0.08	1000	0.08	1000
70			0.08	1000	0.08	900

	$3BF_4@Pd_4L^{ACR4}_8$		**$3BF_4@Pd_4L^{ACR6}_8$**	
T [°C]	D20 [s]	P30 [µs]	D20 [s]	P30 [µs]
-30	0.08	2300	0.08	2300
-20	0.08	200	0.08	2100
-10	0.08	1800	0.08	1900
0	0.08	1600	0.08	1700
10	0.08	1400	0.08	1600
20	0.08	1200	0.08	1500
25	0.08	1200	0.08	1400
30	0.08	1200	0.08	1400
40	0.08	1100	0.08	1300
50	0.08	1100	0.08	1200
60	0.08	1000	0.08	1100
70	0.08	900	0.08	1100

5.3.2 ^{1}H DOSY NMR Measurements at Room Temperature

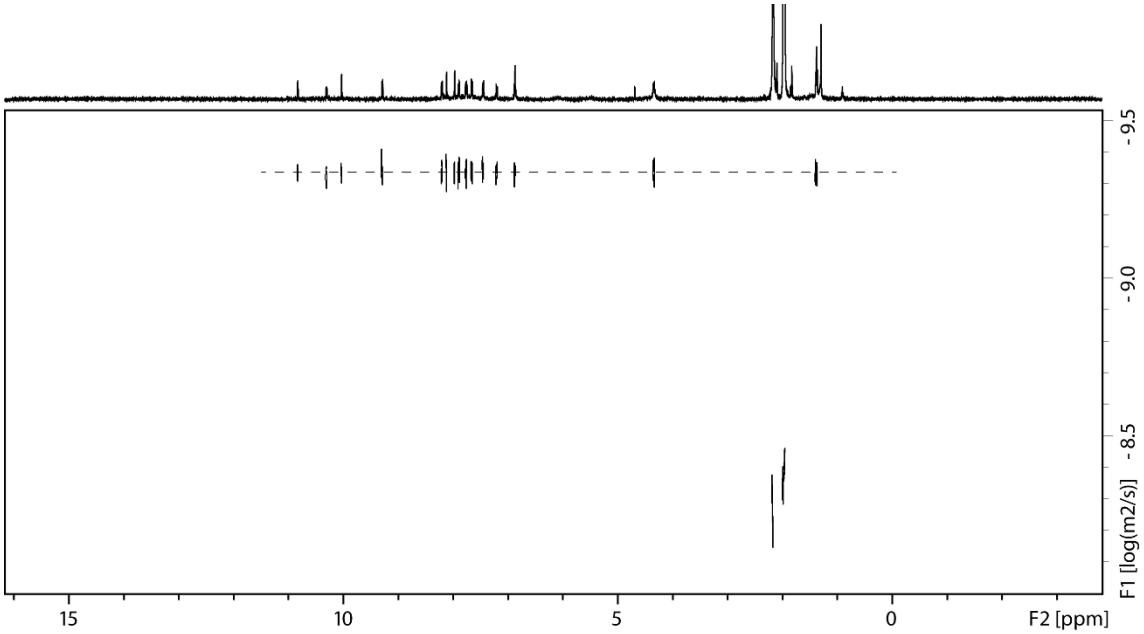

Figure 5.113: ^{1}H DOSY NMR (500 MHz, 298 K CD_3CN, *dstebpgp3s*) spectrum of $3BF_4@Pd_4\mathbf{L}^{\mathbf{ACR1}}_{\mathbf{8}}$.

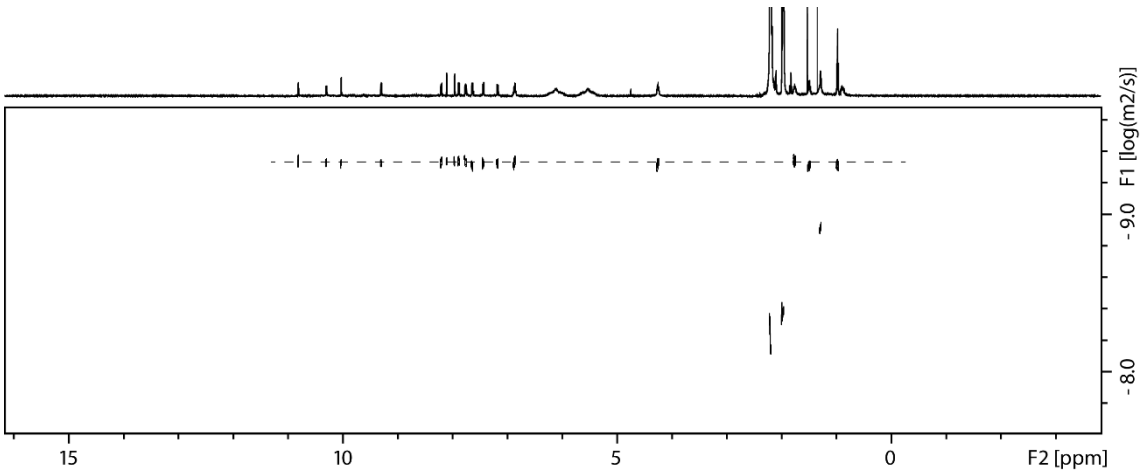

Figure 5.114: ^{1}H DOSY NMR (500 MHz, 298 K CD_3CN, *dstebpgp3s*) spectrum of $3BF_4@Pd_4\mathbf{L}^{\mathbf{ACR2}}_{\mathbf{8}}$.

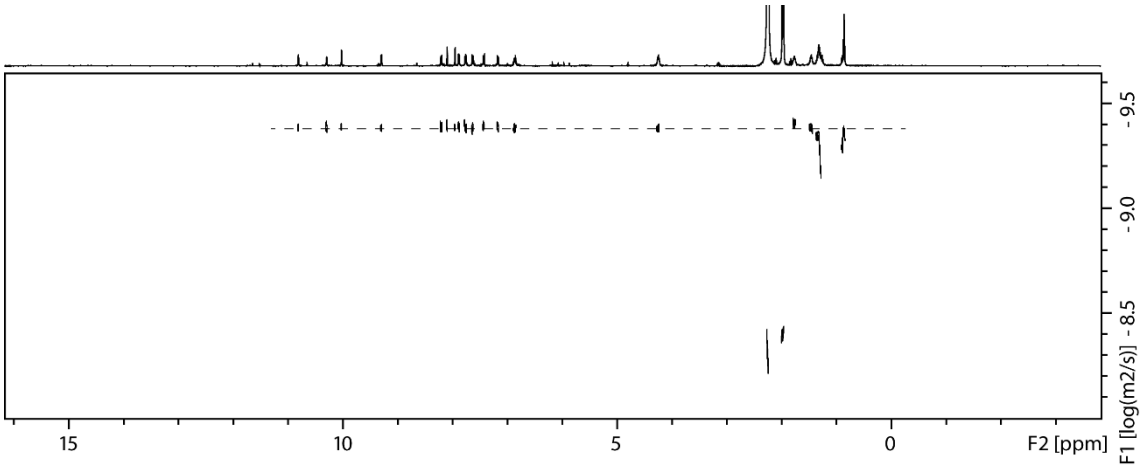

Figure 5.115: ^{1}H DOSY NMR (500 MHz, 298 K CD_3CN, *dstebpgp3s*) spectrum of $3BF_4@Pd_4\mathbf{L}^{\mathbf{ACR3}}{}_{\mathbf{8}}$.

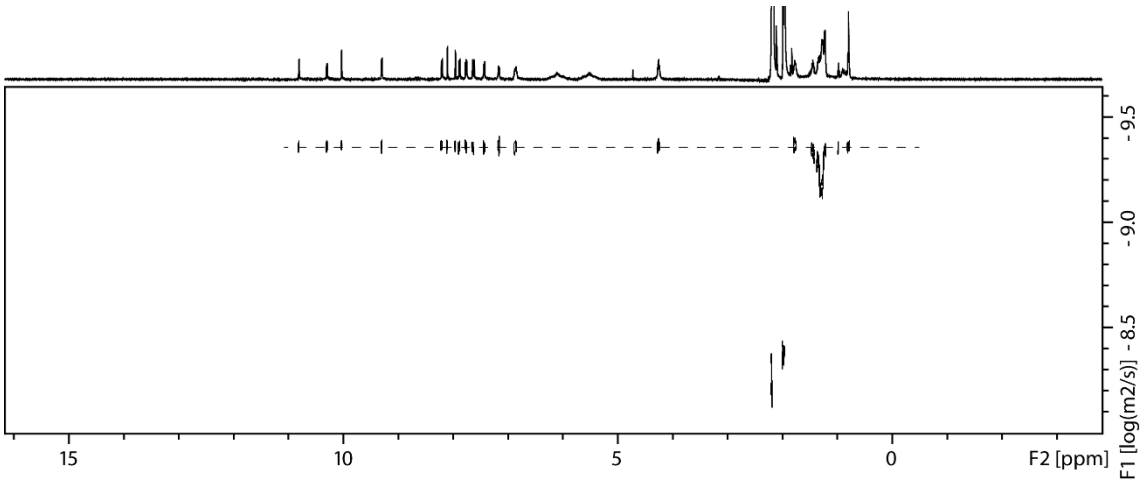

Figure 5.116: ^{1}H DOSY NMR (500 MHz, 298 K CD_3CN, *dstebpgp3s*) spectrum of $3BF_4@Pd_4\mathbf{L}^{\mathbf{ACR4}}{}_{\mathbf{8}}$.

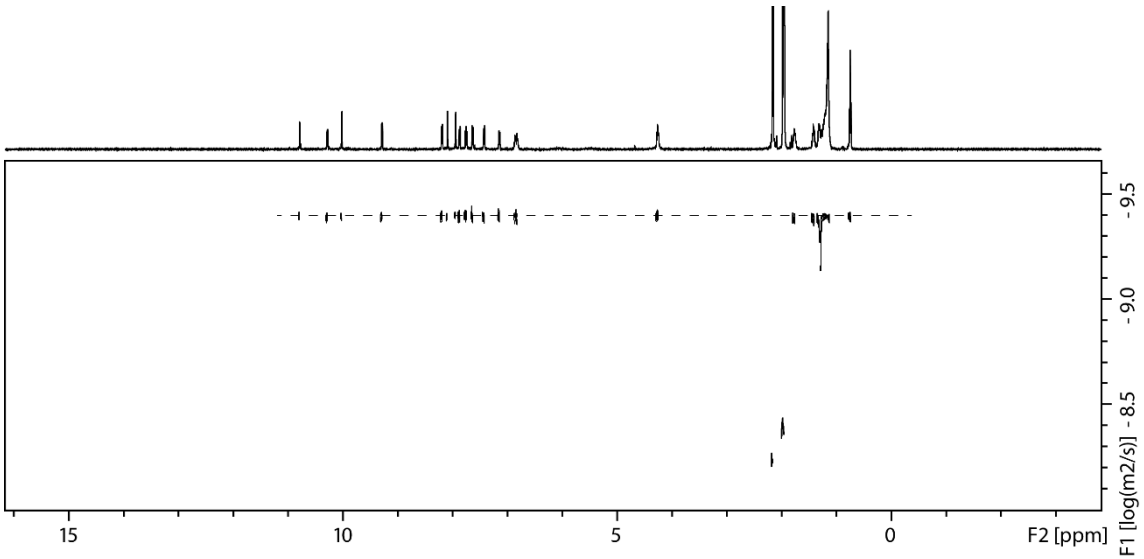

Figure 5.117:^{1}H DOSY NMR (500 MHz, 298 K CD_3CN, *dstebpgp3s*) spectrum of $3BF_4@Pd_4\mathbf{L}^{\mathbf{ACR6}}{}_{\mathbf{8}}$.

Danksagung

Diesen doch recht emotionalen Teil meiner Dissertation werde ich auf Deutsch verfassen.

Als allererstes möchte ich Herrn Prof. Dr. Guido Clever danken, für die Möglichkeit diese Arbeit in seinem Arbeitskreis anzufertigen, für die Motivation und Unterstützung in der Zeit. Als nächstes möchte ich meinem Zweitgutachter Herrn Prof. Dr. Wolf Hiller danken, für viele Diskussionen und sehr viel Hilfe am NMR.

Herrn Dr. Julian Holstein und Herrn Dr. Shota Hasegawa danke ich für die Messung und Prozessierung der Kristallstrukturdaten. Frau Laura Schneider danke ich für die Messung der Massen- und Ionenmobilitätsspektren sowie Herrn Christoph Drechsler für die Berechnung der theoretischen Ionenmobilitäten. Frau Dr. Qian-Qian Yan danke ich für die Aufnahme von UV- und CD-Spektren. Für die sehr erfolgreiche Kooperation danke ich Herrn Prof. Dr. Lars Schäfer und Frau Selina Juber, welche meine Forschung mit MD-Simulationen stark unterstützen konnten. Dem NMR-Service Team danke ich für die Messung von zahlreichen ^{13}C und 2D Messungen. Herrn Dr. Jacopo Tessarolo möchte ich für intensive Diskussionen im Rahmen der Subgroup-Meetings danken. Darüber hinaus danke ich meinen Studenten Cem Yurtseven für eine sehr erfolgreiche Bachelorarbeit und Florian Thys, der meine Forschung durch ein Masterpraktikum unterstützt hat sowie meiner Auszubildenen Franziska Klutzny, die sehr viel mit Ihrer Hilfe zu dieser Arbeit beigetragen hat.

So viel zum wissenschaftlichen Support, nun kommt das Wichtigste: In der Zeit im CleverLab und auch in den 10 Jahren zuvor an der Fakultät CCB habe ich bemerkenswerte Menschen kennengelernt, diese möchte ich an dieser Stelle erwähnen.

Alex Klauke, dich kenne ich am längsten in dem Laden und ich möchte dir für die großartige Zeit danken, die wir zusammen im Praktikum und in der Ausgabe gearbeitet haben und dafür von dir gelernt zu haben, wie dieser ganze Haufen eigentlich so funktioniert…

Gabi Trötscher-Kaus, auch dich kenne ich schon gefühlt ewig, viele Dank für allen Support, den ich von dir bekommen habe, schon während des Studiums und dann vor allem während der Promotion.

Birgit Thormann. Beste Sekretärin von die Welt. Danke für die ganze Hilfe und Unterstützung in den letzten Jahren, sei es für ein offenes Ohr, Diskussionen über Fussball und alles was so in Dortmund passiert, die ganzen Reiseanträge, Verwaltungskram oder die Erinnerungen Urlaubsanträge zu stellen: „na, hast du nicht was vergessen?“ Wir sehen uns im Sommer bei unserem Spaziergang!

Maike, Laura, Franzi und Kristian haben den Laden mit ihrem Einsatz am Laufen gehalten und bei allem geholfen, was man so brauchte, vielen Dank dafür.

Oben schon erwähnt, nochmal danke ans NMR-Team. Ben und Jan, vielen Dank für die ganzen Sonderwünsche, die ich in den Jahren hatte und für die Hilfe, die ich bei technischen Problemen bei euch bekommen habe. Basti, dir auch herzlichen Dank für die Diskussionen bei Problemen und die Hilfen am Spektrometer. Allen drein aber am meisten Dank für die geniale Arbeitsatmosphäre unten im Keller.

Herrn Prof. Dr. Klaus Jurkschat, bei Ihnen in der Gruppe fing meine wissenschaftliche Karriere an und ich danke Ihnen für alles, was ich von Ihnen gelernt habe und für die Diskussionen und Hilfe auch noch während der Promotion. Nun genießen Sie Ihren Ruhestand!

Das CleverLab. Vielen Dank für die tolle Arbeitsatmosphäre. Ich möchte besonders meine Laborkollegen hervorheben, die immer geholfen haben und zu einer tollen Zeit beigetragen haben. Danke an Marcel, Subhadeep, Sudhakar, Cem, Franzi und Erti!

Mein Büro, das Boys-Office, herzlichen Dank für die tausenden von Lachern in der Zeit, Diskussionen und Lästereien über die Arbeit, danke an Christoph, Bo und Rujin, und natürlich an Rob. Du hast mir viel geholfen im Labor, bei allem unterstützt und mich dazu gebracht endlich den Angelschein zu machen. Bei unseren Angeltrips kam dann aber heraus: Angeln ist Scheiße. (Du weißt, wie ich das meine…). Dann kam Covid, und das Büro wurde aufgelöst, ich wurde in die vierte Etage verbannt aber hatte dort einen verdammt coolen Bürokollegen, danke für die geniale Zeit ¡muchas gracias por tu ajuda Pedro!

Viele von den Menschen, die im CleverLab gearbeitet haben oder arbeiten sind von Arbeitskollegen zu Freunden geworden. Dies sind vor allem Shota (ich weiß ich hab dir immer gesagt hör auf danke zu sagen und nun mach ich es selbst…), Jacopo (mille grazie), Q2, Pedro, Sudhakar und Flipse, danke euch für die mega Zeit in Dortmund und

für alles was ich durch euch über eure Heimatländer lernen konnte. Ich hoffe wir treffen uns bald in Japan, Korea (oder von mir aus auch Italien), China, Mexiko, Indien und in der Schweiz. Ach ja, falls Jacopo meckert, dass das auf Deutsch geschrieben ist, dann lern endlich die Sprache!

Die Pfeffi Friday Crew! Danke dass ihr mit unseren Abenden dazu beigetragen habt, dass das alles eine mega Zeit war. Danke auch, dass ihr bis nach Hannover gekommen seid und kommt! Danke an Björn, Maike, Franzi, Jenny, Olli, Simon, Hannah, Laura, Kathi, Shaian für diese legendären Abende.

Auch außerhalb der Arbeitsgruppe habe ich an der Uni Menschen kennengelernt, die nun zu meinen engsten Freunden zählen und denen auch diese Arbeit gewidmet ist. Die Rede ist von Jonathan, Lars, Marvin und Stefan. Es fing an mit Fussball gucken, einfach sitzen und saufen, gemeinsame Mittagessen und ging bis hin zu gemeinsamen Urlauben. Danke für diese tolle Zeit. Auch wenn wir nicht mehr zusammen in Dortmund leben glaube ich, dass unsere Freundschaft weiter gehen wird. Ich hab euch lieb.

Einen ganz besonderen Menschen habe ich noch nicht erwähnt. Kennengelernt an der Uni in Dortmund und mittlerweile leben wir zusammen seit über sieben Jahren zusammen. Danke für alles in dieser Zeit. Danke für die vielen Momente, die ich mit dir erleben durfte. Für unsere Reisen zu den entferntesten Plätzen in dieser Welt, die, wie ich immer sagte, niemals sehen werde. Danke für den nie endenden Support während der Promotion. Danke, dass du ohne nachzudenken mit mir den Weg nach Hannover angetreten hast. Danke Kristina. Ich liebe dich.

Ohne euch hätte das alles hier niemals funktioniert. Danke an meine Familie für all die Unterstützung in den letzten Jahren.

Falls jemand meint, ich hätte hier wen vergessen, dann tuts mir leid, kommt vorbei, auch in Hannover gibt es Bier.

Es gibt Nie Nie Nie einen anderen Verein!

6 Appendix

6.1 Abbreviations

2,7-DBC	2,7-dibromo carbazole
2-POE	2-Phenoxy ethanol
ADP	Adenosine diphosphate
AMP	Adenosine monophosphate
ATP	Adenosine triphosphate
BINOL	1,1-Binaphthol
Boc	*tert*-butyl oxycarbonyl
CD	Circular dichroism
COSY	Correlation spectroscopy
CSE	Coordination sphere engineering
CSS	Collisional cross section
CW	continuous wave
DCM	Dichloromethane
DIPEA	Diisopropylethylamine
DMAP	4-Dimethylaminopyridine
DMF	Dimethylformamide
DMSO	Dimethylsulfoxide
DNA	Desoxyribonucleic acid
DOPC	1,2-Dipalmitoylphosphatidylcholine
DOSY	Diffusion ordered spectroscopy
Dpa	Dipicoylamine
eCCS	experimental collisional cross section
eq	Equivalents
ESI	Electron spray ionization
Et	Ethyl
Et_2O	Diethylether
EtOAc	Ethyl acetate
EtOH	Ethanol
EXSY	Exchange spectroscopy
FID	Free induction decay
G	Guest
GC/EI	Gaschromatography electron ionization
GPC	Gel permeation chromatography
H	Host
HG	Host-Guest Complex
HR	High-Resolution
L	Ligand

M	Metal
MD	Molecular dynamics
Me	Methyl
MeOH	Methanol
MS	Mass spectrometry
NMR	Nuclear magnetic resonance
NOESY	Nuclear Overhauser enhancement spectroscopy
NS	Number of scans
p	para
PFG	Pulsed field gradient
PFT	Pulse FOURIER transform
Ph	Phenyl
PM6	Parameterization method 6
PSYCHE	Pure shift yielded by chirp excitation
presat	Presaturation
p-TSA	*para*-toluene sulfonic acid
R	Receptor
rt	room temperature
SCA	Shape complementary assembly
S/N	Signal-to-noise
t	tertiary
T1	Longitudinal relaxation time
T2	Transversal relaxation time
tCCS	theoretical collisional cross section
THF	Tetrahydrofuran
TIMS	Trapped ion mobility mass spectrometry
TLC	Thin layer chromatography
TMS	Tetramethylsilane
TOF	Time of flight
UFOs	Unique fluorescent open structure
UV/Vis	Ultraviolet/visible
VT	Variable temperature

6.2 List of Figures

6.3 List of Schemes

6.4 List of Tables

7 Literature

[1] J. W. Steed, J. L. Atwood, *Supramolecular Chemistry*, John Wiley & Sons Ltd, Chichester, **2022**.

[2] B. Dietrich, J. M. Lehn, J. P. Sauvage, *Tetrahedron Lett.* **1969**, *10*, 2885.

[3] B. Dietrich, J. M. Lehn, J. P. Sauvage, *Tetrahedron Lett.* **1969**, *10*, 2889.

[4] J.-M. Lehn, *Acc. Chem. Res.* **1978**, *11*, 49.

[5] J. M. Lehn, *Pure Appl. Chem.* **1978**, *50*, 871.

[6] D. J. Cram, G. M. Lein, *J. Am. Chem. Soc.* **1985**, *107*, 3657.

[7] C. J. Pedersen, *J. Am. Chem. Soc.* **1967**, *89*, 7017.

[8] D. J. Cram, T. Kaneda, G. M. Lein, R. C. Helgeson, *Chem. Commun.* **1979**, 948b.

[9] M. Tominaga, K. Suzuki, T. Murase, M. Fujita, *J. Am. Chem. Soc.* **2005**, *127*, 11950.

[10] Q. Sun, S. Sato, M. Fujita, *Angew. Chem. Int. Ed.* **2014**, *53*, 13510.

[11] Q.-F. Sun, S. Sato, M. Fujita, *Nat. Chem.* **2012**, *4*, 330.

[12] M. Fujita, M. Tominaga, A. Hori, B. Therrien, *Acc. Chem. Res.* **2005**, *38*, 369.

[13] M. Yoneya, S. Tsuzuki, T. Yamaguchi, S. Sato, M. Fujita, *ACS Nano* **2014**, *8*, 1290.

[14] D. K. Chand, K. Biradha, M. Kawano, S. Sakamoto, K. Yamaguchi, M. Fujita, *Chem. Asian J.* **2006**, *1*, 82.

[15] H. Yokoyama, Y. Ueda, D. Fujita, S. Sato, M. Fujita, *Chem. Asian J.* **2015**, *10*, 2292.

[16] K. Harris, D. Fujita, M. Fujita, *Chem. Commun.* **2013**, *49*, 6703.

[17] K. Harris, Q.-F. Sun, S. Sato, M. Fujita, *J. Am. Chem. Soc.* **2013**, *135*, 12497.

[18] R. Chakrabarty, P. S. Mukherjee, P. J. Stang, *Chem. Rev.* **2011**, *111*, 6810.

[19] S. Saha, I. Regeni, G. H. Clever, *Coord. Chem. Rev.* **2018**, *374*, 1.

[20] Q.-F. Sun, J. Iwasa, D. Ogawa, Y. Ishido, S. Sato, T. Ozeki, Y. Sei, K. Yamaguchi, M. Fujita, *Science* **2010**, *328*, 1144.

[21] D. Fujita, Y. Ueda, S. Sato, H. Yokoyama, N. Mizuno, T. Kumasaka, M. Fujita, *Chem.* **2016**, *1*, 91.

[22] D. Fujita, Y. Ueda, S. Sato, N. Mizuno, T. Kumasaka, M. Fujita, *Nature* **2016**, *540*, 563.

[23] K. Suzuki, M. Tominaga, M. Kawano, M. Fujita, *Chem. Commun.* **2009**, 1638.

[24] S. Ghorai, S. Maji, B. Paul, K. Samanta, S. K. Sen, R. Natarajan, *Chem. Asian J.* **2023**, e202201312.

[25] E. O. Bobylev, D. A. Poole, B. de Bruin, J. N. H. Reek, *J. Am. Chem. Soc.* **2022**, *144*, 15633.

[26] K. Suzuki, M. Kawano, M. Fujita, *Angew. Chem. Int. Ed.* **2007**, *46*, 2819.

[27] D. R. Martir, L. Delforce, D. B. Cordes, A. M. Z. Slawin, S. L. Warriner, D. Jacquemin, E. Zysman-Colman, *Inorg. Chem. Front.* **2020**, *7*, 232.

[28] T. Zhang, L.-P. Zhou, X.-Q. Guo, L.-X. Cai, Q.-F. Sun, *Nat. Commun.* **2017**, *8*, 15898.

[29] M. Han, Y. Luo, B. Damaschke, L. Gómez, X. Ribas, A. Jose, P. Peretzki, M. Seibt, G. H. Clever, *Angew. Chem. Int. Ed.* **2016**, *55*, 445.

[30] J. Tessarolo, H. Lee, E. Sakuda, K. Umakoshi, G. H. Clever, *J. Am.Chem. Soc.* **2021**, *143*, 6339.

[31] C. Klein, C. Gütz, M. Bogner, F. Topić, K. Rissanen, A. Lützen, *Angew. Chem. Int. Ed.* **2014**, *53*, 3739.

[32] T. Tateishi, T. Kojima, S. Hiraoka, *Inorg. Chem.* **2018**, *57*, 2686.

[33] A. Schmidt, A. Casini, F. E. Kühn, *Coord. Chem. Rev.* **2014**, *275*, 19.

[34] C. Desmarets, T. Ducarre, M. N. Rager, G. Gontard, H. Amouri, *Materials* **2014**, *7*, 287.

[35] W. M. Bloch, S. Horiuchi, J. J. Holstein, C. Drechsler, A. Wuttke, W. Hiller, R. A. Mata, G. H. Clever, *Chem. Sci.* **2023**, *14*, 1524.

[36] W. M. Bloch, Y. Abe, J. J. Holstein, C. M. Wandtke, B. Dittrich, G. H. Clever, *J. Am. Chem. Soc.* **2016**, *138*, 13750.

[37] T. Nakamura, H. Ube, M. Shiro, M. Shionoya, *Angew. Chem. Int. Ed.* **2013**, *52*, 720.

[38] C. R. P. Fulong, S. Kim, A. E. Friedman, T. R. Cook, *Front. Chem.* **2019**, *7*, 567.

[39] S. J. Dalgarno, N. P. Power, J. L. Atwood, *Coord. Chem. Rev.* **2008**, *252*, 825.

[40] D. Bardhan, D. K. Chand, *Chem. Eur. J.* **2019**, *25*, 12241.

[41] M. M. J. Smulders, I. A. Riddell, C. Browne, J. R. Nitschke, *Chem. Soc. Rev.* **2012**, *42*, 1728.

[42] B. H. Northrop, Y.-R. Zheng, K.-W. Chi, P. J. Stang, *Acc. Chem. Res.* **2009**, *42*, 1554.

[43] N. B. Debata, D. Tripathy, D. K. Chand, *Coord. Chem. Rev.* **2012**, *256*, 1831.

[44] M. Han, D. M. Engelhard, G. H. Clever, *Chem Soc Rev* **2014**, *43*, 1848.

[45] S. Hasegawa, G. H. Clever, *Chem.* **2020**, *6*, 5.

[46] S. Hasegawa, S. L. Meichsner, J. J. Holstein, A. Baksi, M. Kasanmascheff, G. H. Clever, *J. Am. Chem. Soc.* **2021**, *143*, 9718.

[47] B. Chen, J. J. Holstein, A. Platzek, L. Schneider, K. Wu, G. H. Clever, *Chem. Sci.* **2022**, *13*, 1829.

[48] B. Chen, J. J. Holstein, S. Horiuchi, W. G. Hiller, G. H. Clever, *J. Am. Chem. Soc.* **2019**, *141*, 8907.

[49] B. Chen, S. Horiuchi, J. J. Holstein, J. Tessarolo, G. H. Clever, *Chem. Eur. J.* **2019**, *25*, 14921.

[50] A. Kumar, S.-S. Sun, A. J. Lees, *Coord. Chem. Rev.* **2008**, *252*, 922.

[51] J. E. M. Lewis, A. Tarzia, A. J. P. White, K. E. Jelfs, *Chem. Sci.* **2020**, *11*, 677.

[52] J. Lewis, J. Crowley, *ChemPlusChem* **2020**, *85*, 815.

[53] W. M. Bloch, G. H. Clever, *Chem. Commun.* **2017**, *53*, 8506.

[54] S. Pullen, J. Tessarolo, G. H. Clever, *Chem. Sci.* **2021**, *12*, 7269.

[55] M. Yamashina, T. Yuki, Y. Sei, M. Akita, M. Yoshizawa, *Chem. Eur. J.* **2015**, *21*, 4200.

[56] A. M. Johnson, R. J. Hooley, *Inorg. Chem.* **2011**, *50*, 4671.

[57] R. Zhu, W. M. Bloch, J. J. Holstein, S. Mandal, L. V. Schäfer, G. H. Clever, *Chem. Eur. J.* **2018**, *24*, 12976.

[58] S. Hiraoka, Y. Kubota, M. Fujita, *Chem. Commun.* **2000**, 1509.

[59] D. Preston, J. E. Barnsley, K. C. Gordon, J. D. Crowley, *J. Am. Chem. Soc.* **2016**, *138*, 10578.

[60] S. Sudan, R.-J. Li, S. M. Jansze, A. Platzek, R. Rudolf, G. H. Clever, F. Fadaei-Tirani, R. Scopelliti, K. Severin, *J. Am. Chem. Soc.* **2021**, *143*, 1773.

[61] W. M. Bloch, J. J. Holstein, W. Hiller, G. H. Clever, *Angew. Chem. Int. Ed.* **2017**, *56*, 8285.

[62] K. E. Ebbert, L. Schneider, A. Platzek, C. Drechsler, B. Chen, R. Rudolf, G. H. Clever, *Dalton Trans.* **2019**, *48*, 11070.

[63] M. Han, R. Michel, B. He, Y. Chen, D. Stalke, M. John, G. H. Clever, *Angew. Chem. Int. Ed.* **2013**, *52*, 1319.

[64] R.-J. Li, J. J. Holstein, W. G. Hiller, J. Andréasson, G. H. Clever, *J. Am. Chem. Soc.* **2019**, *141*, 2097.

[65] S. Freye, J. Hey, A. Torras-Galán, D. Stalke, R. Herbst-Irmer, M. John, G. H. Clever, *Angew. Chem. Int. Ed.* **2012**, *51*, 2191.

[66] S. Löffler, J. Lübben, L. Krause, D. Stalke, B. Dittrich, G. H. Clever, *J. Am. Chem. Soc.* **2015**, *137*, 1060.

[67] S. Löffler, A. Wuttke, B. Zhang, J. J. Holstein, R. A. Mata, G. H. Clever, *Chem. Commun.* **2017**, *53*, 11933.

[68] S. Pullen, S. Löffler, A. Platzek, J. J. Holstein, G. H. Clever, *Dalton Trans.* **2020**, *49*, 9404.

[69] I. Regeni, B. Chen, M. Frank, A. Baksi, J. J. Holstein, G. H. Clever, *Angew. Chem. Int. Ed.* **2020**, *60*, 5673.

[70] M. Frank, J. Ahrens, I. Bejenke, M. Krick, D. Schwarzer, G. H. Clever, *J. Am. Chem. Soc.* **2016**, *138*, 8279.

[71] S. Saha, B. Holzapfel, Y.-T. Chen, K. Terlinden, P. Lill, C. Gatsogiannis, H. Rehage, G. H. Clever, *J. Am. Chem. Soc.* **2018**, *140*, 17384.

[72] M. Yoshizawa, M. Tamura, M. Fujita, *Science* **2006**, *312*, 251.

[73] K. N. Raymond, *Acc. Chem. Res.* **1991**, 975.

[74] C. J. Hastings, M. D. Pluth, R. G. Bergman, K. N. Raymond, *J. Am. Chem. Soc.* **2010**, *132*, 6938.

[75] J. Jiao, C. Tan, Z. Li, Y. Liu, X. Han, Y. Cui, *J. Am. Chem. Soc.* **2018**, *140*, 2251.

[76] P. Howlader, P. Das, E. Zangrando, P. S. Mukherjee, *J. Am. Chem. Soc.* **2016**, *138*, 1668.

[77] M. Yoshizawa, J. K. Klosterman, M. Fujita, *Angew. Chem. Int. Ed.* **2009**, *48*, 3418.

[78] C. M. A. Gangemi, A. Pappalardo, G. T. Sfrazzetto, *RSC Adv.* **2015**, *5*, 51919.

[79] C. Schalley, *Analytical Methods in Supramolecular Chemistry*, Wiley-VCH, Weinheim, **2007**.

[80] H. Friebolin, *Basic One- and Two-Dimensional NMR Spectroscopy*, Wiley VCH, Weinheim, **2011**.

[81] T. D. W. Claridge, *High-Resolution NMR Techniques in Organic Chemistry*, Elsevier, Cambridge, **2016**.

[82] Y. Cohen, S. Slovak, L. Avram, *Chem. Commun.* **2021**, *57*, 8856.

[83] O. Mayzel, Y. Cohen, *Chem. Commun.* **1994**, 1901.

[84] A. Einstein, *Ann. Phys.* **1905**, *322*, 549.

[85] J. Gmehling, U. Onken, "Dortmund Data Bank" can be found under http://www.ddbst.com/ddb.html.

[86] M. M. Tirado, C. L. Martínez, J. G. de la Torre, *J. Chem. Phys.* **1984**, *81*, 2047.

[87] P. H. Elworthy, *J. Chem. Soc.* **1962**, 3718.

[88] H. C. Chen, S. H. Chen, *J. Phys. Chem.* **1984**, *88*, 5118.

[89] A. Macchioni, G. Ciancaleoni, C. Zuccaccia, D. Zuccaccia, *Chem. Soc. Rev.* **2007**, *37*, 479.

[90] P. W. Atkins, J. de Paula, *Physical Chemistry*, **2006**.

[91] P. Stilbs, *Prog. Nucl. Magn. Reson. Spectrosc.* **1987**, *19*, 1.

[92] E. L. Hahn, *Phys. Rev.* **1950**, *80*, 580.

[93] C. S. Johnson. Jr., *Prog. Nucl. Mag. Reson. Spectrosc.* **1999**, *34*, 203.

[94] S. V. Kharlamov, S. K. Latypov, *Russ. Chem. Rev.* **2010**, *79*, 635.

[95] R. Evans, G. D. Poggetto, M. Nilsson, G. A. Morris, *Anal. Chem* **2018**, *90*, 3987.

[96] Y. Cohen, S. Slovak, *Org. Chem. Front.* **2019**, *6*, 1705.

[97] D. H. Wu, A. D. Chen, C. S. Johnson, *J. Magn. Reson.* **1995**, *115*, 260.

[98] A. Jerschow, N. Müller, *J. Magn. Reson.* **1997**, *125*, 372.

[99] A. Jerschow, N. Müller, *J. Magn. Reson.* **1996**, *123*, 222.

[100] A. Platzek, S. Juber, C. Yurtseven, S. Hasegawa, L. Schneider, C. Drechsler, K. E. Ebbert, R. Rudolf, Q. Yan, J. J. Holstein, L. V. Schäfer, G. H. Clever, *Angew. Chem. Int. Ed.* **2022**, *61*, e202209305.

[101] C. Graebe, C. Glaser, *Ann. Chem. Pharm.* **1872**, 343.

[102] W. R. Abdel-Monem, T. E. Ali, *Int. J. Chem.* **2007**, *17*, 303.

[103] I. A. Tonks, A. C. Durrell, H. B. Gray, J. E. Bercaw, *J. Am. Chem. Soc.* **2012**, *134*, 7301.

[104] T. Karmakar, M. Mukherjee, D. P. Chakraborty, *Curr. Sci.* **1986**, *55*, 828.

[105] G. H. Kulkarni, R. H. Naik, S. K. Tandel, S. Rajappa, *Tetrahedron* **1991**, *47*, 1249.

[106] A. H. Winter, H. H. Gibson, D. E. Falvey, *J. Org. Chem.* **2007**, *72*, 8186.

[107] A. Kamal, N. A. V. Reddy, P. B. Sattur, *Heterocycles* **1986**, *24*, 3397.

[108] V. H. K. Fell, A. Mikosch, A.-K. Steppert, W. Ogieglo, E. Senol, D. Canneson, M. Bayer, F. Schoenebeck, A. Greilich, A. J. C. Kuehne, *Macromolecules* **2017**, *50*, 2338.

[109] K. Moon, H. Kim, E. Lee, M. Lee, *Angew. Chem. Int. Ed.* **2007**, *46*, 6807.

[110] V. Malavade, M. Patil, M. Patil, *Eur. J. Org. Chem.* **2020**, *2020*, 561.

[111] D.-H. Chen, L. Lin, T.-L. Sheng, Y.-H. Wen, S.-M. Hu, R.-B. Fu, C. Zhuo, H.-R. Li, X.-T. Wu, *CrystEngComm* **2017**, *19*, 2632.

[112] R. Zhu, J. Lübben, B. Dittrich, G. H. Clever, *Angew. Chem. Int. Ed.* **2015**, *54*, 2796.

[113] A. Hüttermann, *The Hydrogen Bond, A Bond for Life*, Walter De Gruyter GmbH, Berlin/Boston, **2019**.

[114] J. Teyssandier, S. D. Feyter, K. S. Mali, *Chem. Commun.* **2016**, *52*, 11465.

[115] P. Ballester, *Chem. Soc. Rev.* **2010**, *39*, 3810.

[116] F. J. Rizzuto, L. K. S. von Krbek, J. R. Nitschke, *Nat. Rev. Chem.* **2019**, *3*, 204.

[117] A. Galan, P. Ballester, *Chem. Soc. Rev.* **2016**, *45*, 1720.

[118] M. Frank, J. M. Dieterich, S. Freye, R. A. Mata, G. H. Clever, *Dalton Trans.* **2013**, *42*, 15906.

[119] G. H. Clever, P. Punt, *Acc. Chem. Res.* **2017**, *50*, 2233.

[120] T. R. Schulte, J. J. Holstein, G. H. Clever, *Angew. Chem. Int. Ed.* **2019**, *58*, 5562.

[121] A. Pastor, E. Martínez-Viviente, *Coord. Chem.Rev.* **2008**, *252*, 2314.

[122] P. Thordarson, *Chem. Soc. Rev.* **2010**, *40*, 1305.

[123] R. G. Bryant, *J. Chem. Educ.* **1983**, *60*, 933.

[124] D. B. Hibbert, P. Thordarson, *Chem Commun.* **2016**, *52*, 12792.

[125] "BindFit v0.5," can be found under http://app.supramolecular.org/bindfit/.

[126] N. Sewald, H. Jakubke, *Peptides: Chemistry and Biology*, Wiley-VCH, Weinheim, **2002**.

[127] J. M. Berg, J. L. Tymoczko, L. Stryer, *Biochemistry*, **2002**.

[128] M. F. Fiore, S. T. de Lima, W. W. Carmichael, S. M. K. McKinnie, J. R. Chekan, B. S. Moore, *Harmful Algae* **2020**, *92*, 101737.

[129] S. V. Levchik, E. D. Weil, *J. Fire Sci.* **2006**, *24*, 345.

[130] P. J. A. Kleinman, A. N. Sharpley, R. W. McDowell, D. N. Flaten, A. R. Buda, L. Tao, L. Bergstrom, Q. Zhu, *Plant Soil* **2011**, *349*, 169.

[131] H. P. Jarvie, A. N. Sharpley, D. Flaten, P. J. A. Kleinman, A. Jenkins, T. Simmons, *J. Environ. Qual.* **2015**, *44*, 1049.

[132] D. Cordell, J.-O. Drangert, S. White, *Glob. Environb Change* **2009**, *19*, 292.

[133] A. K. Greaves, R. J. Letcher, D. Chen, D. J. McGoldrick, L. T. Gauthier, S. M. Backus, *Environ. Res.* **2016**, *150*, 255.

[134] I. van der Veen, J. de Boer, *Chemosphere* **2012**, *88*, 1119.

[135] J. L. Sessler, P. A. Gale, W.-S. Cho, Anion Receptor Chemistry, **2007**, 27.

[136] P. A. Gale, E. N. W. Howe, X. Wu, M. J. Spooner, *Coord. Chem. Rev.* **2018**, *375*, 333.

[137] V. Amendola, L. Fabbrizzi, L. Mosca, *Chem. Soc. Rev.* **2010**, *39*, 3889.

[138] N. Busschaert, C. Caltagirone, W. V. Rossom, P. A. Gale, *Chem. Rev.* **2015**, *115*, 8038.

[139] S. Pal, T. K. Ghosh, R. Ghosh, S. Mondal, P. Ghosh, *Coord. Chem. Rev.* **2020**, *405*, 213128.

[140] A. K. H. Hirsch, F. R. Fischer, F. Diederich, *Angew. Chem. Int. Ed.* **2007**, *46*, 338.

[141] N. H. Evans, P. D. Beer, *Angew. Chem. Int. Ed.* **2014**, *53*, 11716.

[142] A. E. Hargrove, S. Nieto, T. Zhang, J. L. Sessler, E. V. Anslyn, *Chem. Rev.* **2011**, *111*, 6603.

[143] E. A. Katayev, Y. A. Ustynyuk, J. L. Sessler, *Coord. Chem. Rev.* **2006**, *250*, 3004.

[144] B. D. Kubena, H. Luecke, H. Rosenberg, F. A. Quiocho, *J. Biol. Chem.* **1986**, *261*, 7995.

[145] H. Luecke, F. A. Quiocho, *Nature* **1990**, *347*, 402.

[146] C. Nakai, W. Glinsmann, *Biochemistry* **1977**, *16*, 5636.

[147] B. Dietrich, M. W. Hosseini, J. M. Lehn, R. B. Sessions, *J. Am. Chem. Soc.* **1981**, *103*, 1282.

[148] E. Kimura, M. Kodama, T. Yatsunami, *J. Am. Chem. Soc.* **1982**, *104*, 3182.

[149] E. García-España, P. Díaz, J. M. Llinares, A. Bianchi, *Coord. Chem. Rev.* **2006**, *250*, 2952.

[150] M. J. Chmielewski, M. Charon, J. Jurczak, *Org. Lett.* **2004**, *6*, 3501.

[151] J. R. Hiscock, C. Caltagirone, M. E. Light, M. B. Hursthouse, P. A. Gale, *Org. Biomol. Chem.* **2009**, *7*, 1781.

[152] D. Curiel, A. Cowley, P. D. Beer, *Chem. Commun.* **2004**, 236.

[153] M. N. Piña, M. C. Rotger, A. Costa, P. Ballester, P. M. Deyà, *Tetrahedron Lett.* **2004**, *45*, 3749.

[154] C. Raposo, N. Pérez, M. Almaraz, M. L. Mussons, M. C. Caballero, J. R. Morán, *Tetrahedron Lett.* **1995**, *36*, 3255.

[155] P. Piątek, V. M. Lynch, J. L. Sessler, *J. Am. Chem. Soc.* **2004**, *126*, 16073.

[156] S. C. Hirst, P. Tecilla, S. J. Geib, E. Fan, A. D. Hamilton, *Isr. J. Chem.* **1992**, *32*, 105.

[157] J. A. Tovilla, R. Vilar, A. J. P. White, *Chem. Commun.* **2005**, 4839.

[158] J. A. Tovilla, P. Carlqvist, J. Benet-Buchholz, F. Maseras, R. Vilar, *Supramol. Chem.* **2007**, *19*, 599.

[159] C. Mendoza, J. Benet-Buchholz, M. A. Pericás, R. Vilar, *Dalton Trans.* **2009**, 2974.

[160] A. Ojida, I. Hamachi, *Bull. Chem. Soc. Jpn.* **2006**, *79*, 35.

[161] A. Ojida, M. Inoue, Y. Mito-oka, H. Tsutsumi, K. Sada, I. Hamachi, *J. Am. Chem. Soc.* **2006**, *128*, 2052.

[162] A. Ojida, S. Park, Y. Mito-oka, I. Hamachi, *Tetrahedron Lett.* **2002**, *43*, 6193.

[163] A. Ojida, Y. Mito-oka, M. Inoue, I. Hamachi, *J. Am. Chem. Soc.* **2002**, *124*, 6256.

[164] J. Wongkongkatep, Y. Miyahara, A. Ojida, I. Hamachi, *Angew. Chem. Int. Ed.* **2006**, *45*, 665.

[165] A. Ojida, Y. Mito-oka, K. Sada, I. Hamachi, *J. Am. Chem. Soc.* **2004**, *126*, 2454.

[166] A. Ojida, T. Kohira, I. Hamachi, *Chem. Lett.* **2004**, *33*, 1024.

[167] A. Ojida, Y. Miyahara, T. Kohira, I. Hamachi, *Pept. Sci.* **2004**, *76*, 177.

[168] C. G. P. Taylor, J. R. Piper, M. D. Ward, *Chem. Commun.* **2016**, *52*, 6225.

[169] C. G. P. Taylor, A. J. Metherell, S. P. Argent, F. M. Ashour, N. H. Williams, M. D. Ward, *Chem. Eur. J.* **2020**, *26*, 3065.

[170] J. L. Bolliger, A. M. Belenguer, J. R. Nitschke, *Angew. Chem. Int. Ed.* **2013**, *52*, 7958.

[171] V. Martí-Centelles, R. L. Spicer, P. J. Lusby, *Chem. Sci.* **2020**, *11*, 3236.

[172] C. G. Avila-Ortiz, L. Díaz-Corona, E. Jiménez-González, E. Juaristi, *Molecules* **2017**, *22*, 1328.

[173] M. Frank, M. D. Johnstone, G. H. Clever, *Chem. Eur. J.* **2016**, *22*, 14104.

[174] A. Platzek, Systematic NMR Studies on Acridone- Based Interpenetrated Coordination Cages, Master Thesis, TU Dortmund University, **2018**.

[175] C. Drechsler, A. Baksi, A. Platzek, M. Acar, J. J. Holstein, C. J. Stein, G. H. Clever, *Manuscript in Preparation* **2024**.

[176] A. J. McConnell, *Chem. Soc. Rev.* **2022**, *51*, 2957.

[177] F. Octa-Smolin, M. Thiele, R. Yadav, A. Platzek, G. H. Clever, J. Niemeyer, *Org. Lett.* **2018**, *20*, 6153.

[178] S. Pullen, A. Hegmans, W. G. Hiller, A. Platzek, E. Freisinger, B. Lippert, *ChemistryOpen* **2021**, *10*, 28.

[179] J. Tessarolo, G. H. Clever, *Manuscript in preparation*

[180] K. Zangger, H. Sterk, *J. Magn. Reson.* **1997**, *124*, 486.

[181] M. Foroozandeh, R. W. Adams, N. J. Meharry, D. Jeannerat, M. Nilsson, G. A. Morris, *Angew. Chem. Int. Ed.* **2014**, *53*, 6990.

[182] K. Zangger, *Prog. Nucl. Magn. Reson. Spectrosc.* **2015**, *86*, 1.

[183] K. E. Ebbert, G. H. Clever, *Manuscript in preparation*

[184] G. R. Fulmer, A. J. M. Miller, N. H. Sherden, H. E. Gottlieb, A. Nudelman, B. M. Stoltz, J. E. Bercaw, K. I. Goldberg, *Organometallics*, **2010**, *29*, 2176.

[185] E. O. Stejskal, J. E. Tanner, *J. Chem. Phys.* **1965**, *42*, 288.

[186] J. E. Tanner, E. O. Stejskal, *J. Chem. Phys.* **1968**, *49*, 1768.

[187] A. Burkhardt, T. Pakendorf, B. Reime, J. Meyer, P. Fischer, N. Stübe, S. Panneerselvam, O. Lorbeer, K. Stachnik, M. Warmer, P. Rödig, D. Göries, A. Meents, *Eur. Phys. J. Plus* **2016**, *131*, 56.

[188] W. Kabsch, *Acta Crystallogr. D* **2010**, *66*, 125.

[189] G. M. Sheldrick, *Acta Crystallogr. A* **2015**, *71*, 3.

[190] G. M. Sheldrick, *Acta Crystallogr. C* **2015**, *71*, 3.

[191] C. B. Hübschle, G. M. Sheldrick, B. Dittrich, *J. Appl. Crystallogr.* **2011**, *44*, 1281.

[192] D. Kratzert, J. J. Holstein, I. Krossing, *J. Appl. Crystallogr.* **2015**, *48*, 933.

[193] D. Kratzert, I. Krossing, *J. Appl. Crystallogr.* **2018**, *48*, 928.

[194] A. Thorn, B. Dittrich, G. M. Sheldrick, *Acta Crystallogr. A* **2012**, *68*, 448.

[195] A. L. Spek, *Acta Crystallogr. C* **2015**, *71*, 9.

[196] A. L. Spek, *Acta Crystallogr. D* **2009**, *65*, 148.

[197] F. A. Fernandez-Lima, D. A. Kaplan, M. A. Park, *Rev. Sci. Instrum.* **2011**, *82*, 126106.

[198] D. R. Hernandez, J. D. DeBord, M. E. Ridgeway, D. A. Kaplan, M. A. Park, F. Fernandez-Lima, *Analyst* **2014**, *139*, 1913.

[199] J.-F. Greisch, J. Chmela, M. E. Harding, D. Wunderlich, B. Schäfer, M. Ruben, W. Klopper, D. Schooss, M. M. Kappes, *Phys. Chem. Chem. Phys.* **2017**, *19*, 6105.

[200] F. Neese, *Wiley Interdiscip Rev Comput Mol Sci* **2018**, *8*, DOI 10.1002/wcms.1327.

[201] S. A. Ewing, M. T. Donor, J. W. Wilson, J. S. Prell, *J. Am. Soc. Mass Spectr.* **2017**, *28*, 587.

[202] A. V. Marenich, S. V. Jerome, C. J. Cramer, D. G. Truhlar, *J. Chem. Theory Comput.* **2012**, *8*, 527.

[203] S. Grimme, C. Bannwarth, P. Shushkov, *J. Chem. Theory Comput.* **2017**, *13*, 1989.